NGGM/MAGIC – Science Support Study During Phase A

"MAGIC"

ESA Contract No. RFP/3-17035/20/NL/FF/tfd

Final Report

Issue 1.0

ESA STUDY CONTRACT REPORT		
ESA Contract No: RFP/3-17035/20/NL/FF/tfd	Subject: Final Report NGGM/MAGIC – Science Support Study During Phase A	Contractor: Technische Universität München
*ESA CR( ) No.	No. of Volumes: 1 This is Volume No.: 1	Contractors Reference: Roland Pail
Abstract: Final Report of ESA study *NGGM/MAGIC – Science Support Study During Phase A*		
The work described in this report was done under ESA Contract. Responsibility for the contents resides in the author or organisation that prepared it.		
Names of Authors: Roland Pail, TBD		
** NAME OF ESA STUDY MANAGER: Ilias Daras DIV: Mission Science Division DIRECTORATE: Earth Observation Programmes	** ESA BUDGET HEADING	

NGGM/MAGIC – Science Support Study During Phase A	*Final Report*	
	Doc. Nr:	MAGIC_FR
	Issue:	1.0
	Date:	15.11.2022
	Page:	3 of 466

Authors

Roland Pail (Editor)	TUM
Petro Abrykosov	TUM
Betty Heller-Kaikov	TUM
Pieter Visser	TUD
Markus Hauk	AEI
Frank Flechtner	GFZ
Josefine Wilms	GFZ
Pieter Visser	TUD
Sean Bruinsma	CNES
Jean-Charles Marty	CNES
Andreas Güntner	GFZ
Annette Eicker	HCU
Bert Wouters	TUD
Carla Braitenberg	UTR
Chris Hughes	ULP
Laurent Longuevergne	URE

Document Change Record

ISSUE /REV.	DATE	REASON FOR CHANGE	CHANGED PAGES / PARAGRAPHS
1.0	10 Oct. 2022	Initial Issue	

Table of Contents

PREFACE

This Final Report reports on the results of the project "NGGM/MAGIC – Science Support Study During Phase A. It addresses all tasks defined in the SoW and the corresponding work packages defined in the WBS:

Part no.	Title	Task	WP	TN
1	Closed-loop simulations with baseline and improved software	1	100	D2
2	Generation of a 2nd baseline implementation for closed-loop simulations	2	200	D4
3	DORIS aided orbit and gravity field determination	3	300	D7
4	Closed-loop simulator improvement and analysis	4	400	D8
5	Elaborated alternative orbit scenarios	4	420	D9
6	Analysis of results and match against requirements	5	510, 520	D13
7	Science impact analysis	6	520, 600	D15
8	Calibration of accelerometers	7	700	D17
9	Sensitivity Analysis on Inter-Satellite Distance	Ad-hoc	--	AH1

A summary of the main findings of this project phase, the main conclusions, and an outlook to research topics that have been popped up during this project are given in the Executive Summary.

EXECUTIVE SUMMARY

In November 2020 it was decided at ESA's Ministerial Conference to investigate a European next-generation gravity mission (NGGM) in Phase A as first Mission of Opportunity in the FutureEO Programme. The Mass-change And Geoscience International Constellation (acronym: MAGIC) is a joint investigation with NASA's MCDO study resulting in a jointly accorded Mission Requirements Document (MRD) responding to global user community needs. On NASA side, a pre-Phase A study to address these needs started in summer 2021. On ESA side, the MAGIC concept is currently being investigated in two parallel industry Phase A studies, and was complemented by this "NGGM/MAGIC – Science Support Study during Phase A". Further information on this project can be found at the website: https://www.asg.ed.tum.de/iapg/magic/.

1) Evaluation of various constellations and detail studies on specific subjects

In the frame of this science study, several potential mission constellations were investigated and numerically simulated in great depth, in order to narrow down the trade space of a potential MAGIC constellation, to provide feedback to parallel system Phase A industry studies, and to identify an optimum constellation set-up regarding science return, technical feasibility, and costs.

In order to study the impact of different values for the period of a repeat orbit or (sub)cycle and the impact of a change of height, several scenarios were defined for Bender-type constellations consisting of one pair flying in a (near-)polar orbit and one pair in an inclined orbit (Table 2-1). In addition, a few sun-synchronous orbital (SSO) and pendulum missions were defined. The nominal baseline length is equal to 220 km for all satellite pairs and scenarios. For the scenarios 3d_H and 5d_LL also pendulum pairs with angles of 15^0, 30^0, and 45^0 were defined.

Table E.1: Orbits sets for inclined and polar pairs. The ID shows the number of sub-cycle days for which the set is optimized and an additional information about the altitudes: (M)id, (H)igh. Note that the semi-major axis is reduced by 6378 km for highlighting differences in altitude. The other columns provide information about the homogeneity of the ground track patterns).

ID	Sats 1 (IP)		Sats 2 (PP)		h_{l1} [-]	h_{l2} [-]	$\Delta(\text{Lon})_1$ [deg]	$\Delta(\text{Lon})_2$ [deg]	Sub-cycles [days]
	Alt. [km]	Incl. [deg]	Alt. [km]	Incl. [deg]					
3d_M	409	70	440	89	1.368	1.383	2.308	2.384	2, 3, 8, 11, 30
3d_H	432	70	463	89	1.451	1.449	-3.076	-3.067	3, 7, 31
5d_Ma	396	65	434	89	1.397	1.383	-1.499	-1.458	2, 3, 5, 13, 18, 31
5d_Mb	397	70	425	87	1.168	1.167	0.736	0.733	2, 5, 27, 32
5d_H	465	75	488	89	1.185	1.190	0.762	0.781	4, 5, 29
7d_M	389	70	417	87	1.238	1.253	0.743	0.786	2, 7, 30
7d_H	432	70	463	89	1.218	1.226	0.672	0.692	3, 7, 31
SSO for 3d_H	477	97	463	89	1.454	1.449	-3.097	-3.067	3, 7, 31
SSO for 7d_H	477	97	463	89	1.201	1.226	0.622	0.692	3, 7, 31
5d_LL	344	70	376	89	1.423	1.410	-1.671	-1.628	1, 2, 5, 12, 29
5d_LH	344	71.5	492	89	1.169	1.172	-0.732	-0.790	5, (32-31)

Figure E-1 shows an overview of the performance of various constellation designs.
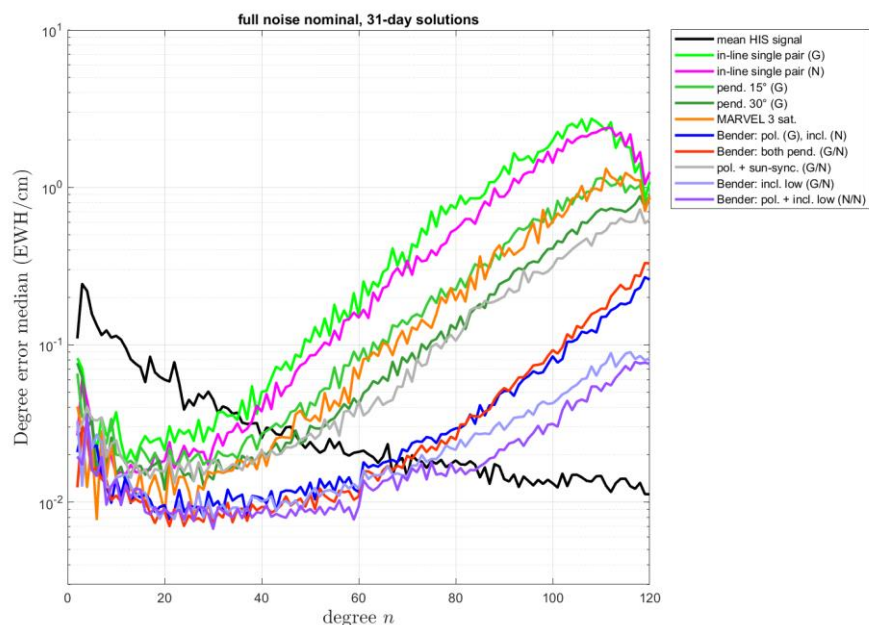
Figure E.1: Degree error medians of various mission constellations. G means "SuperStar", N "MicroStar" accelerometer performance.

These results, which are mainly based on the 3d_H scenario including realistic error models for the key instruments and tidal and non-tidal background errors, clearly demonstrate the superior performance of Bender double-pair mission concepts over all other potential constellations,

such as single-pair inline or pendulum missions. There is no added value by flying a pendulum pair as part of a Bender-type constellation. Also the concept of a chronometric 3-satellite pendulum mission was ruled out by these results. In general, temporal aliasing errors are the dominant error source. However, an improved accelerometer ($\sim 10^{-11}$ m/s^2/$\sqrt{\text{Hz}}$) has relatively higher impact in double pair constellations (due to improved de-aliasing capabilities).

Among others, detailed numerical studies were also performed regarding the following aspects:

a) Dependence of performance on the altitude of the satellites/satellite pairs

It could be confirmed that the altitude is the main performance driver. Since in a Bender double-pair scenario the relative contribution of the inclined pair to the total performance is more than 90% in the areas covered with measurements, a low altitude together with a high-performance instrumentation of the inclined pair is essential.

b) Optimum inter-satellite distance

The choice of the inter-satellite distance is a compromise between sensitivity (which improves with distance) and spatial resolution (which degrades with distance). As optimum an inter-satellite distance of 200-250 km is recommended.

c) Double-pair: sensitivity w.r.t. inclination of inclined pair

A rather low inclination of second pair (≤70°) is paramount for the de-aliasing capability of the constellation. Raw (unfiltered) 70° solutions are more stripy (about 50%) than 65° solutions in the covered areas, due to worse estimates of (near-)sectorials, but are better (by about 50%) in the polar areas, due to smaller polar gaps and better estimates of the polar wedge. Post-processed (filtered) 65° solutions are on global average up to 10% better than 70° solutions. This holds for both covered and polar regions. However, this percentage numbers vary with the choice of the filter. An obvious severe disadvantage of 65° inclined orbit is that it results into a larger unobserved region near the poles as stand-alone mission. Therefore, a more conservative 70° inclination of the inclined pair is recommended.

d) Impact of ground track sampling on gravity performance and heterogeneity

Figure E.2 shows the simulation set-up for a 3-day solution using polar and inclined orbits with 3-day and/or 5-day sub-cycles polar and inclined orbit (mixture of orbits of the scenarios given in Table 2-1), leading to homogeneous coverage (3d_H), spatial gaps of the polar tracks (U3d5d_H) or gaps in both pairs (U5d_H). Evidently, a non-homogeneous ground track pattern of the polar pair (blue curve in Figure E.3) is acceptable, but leads to slightly larger errors in higher spherical harmonic (SH) degrees compared to the homogeneous ground track sampling of both pairs (red curve). However, combining a polar pair having a non-homogeneous ground track pattern with an inclined pair also having a non-homogeneous ground track pattern with coinciding gaps in the 3-day ground tracks of both pairs results in a severe degradation over the whole spectral range, and thus hampers significantly the homogenous quality especially of short-term (NRT) solutions required for operational service applications.
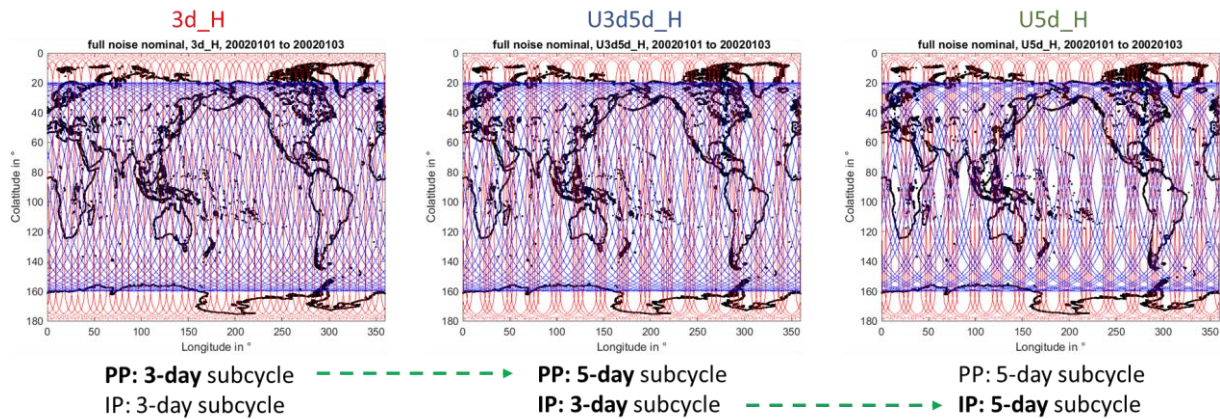
Figure E.2: Ground track patterns of simulation set-ups with varying ground track homogeneity.
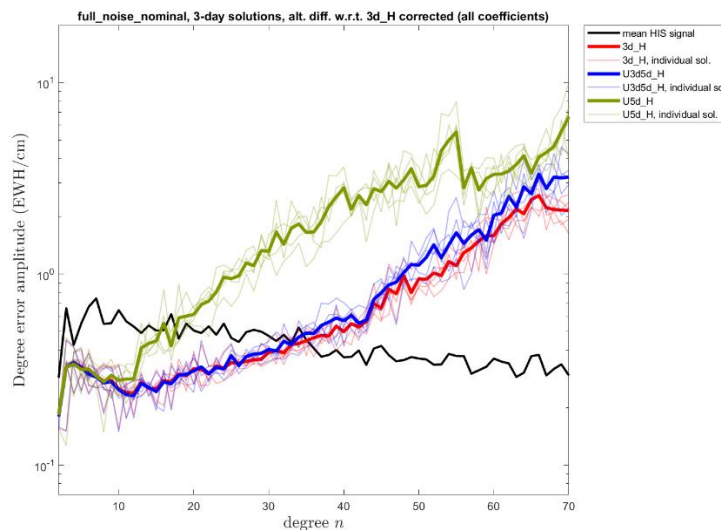
Figure E.3: Degree error RMS of gravity field retrievals related to the scenarios shown in Figure 2.

e) Impact on drag-free conditions and accelerometer performance

Various scenarios representing a combination of the MicroSTAR instrument performance combined with different levels of imperfect drag compensation for the inclined satellite pair in regard to different atmospheric conditions ranging from a "best-case" full 3D (blue curve in Figure E.4) to a "worst-case" 1D drag compensation in along-track direction and with maximum atmospheric conditions (red curve), have been analyzed. In all cases, the same assumption on the polar pair of a SuperSTAR ACC is applied. Figure E.5 a shows, that in the product-noise only case, a degradation of varying extent of all scenarios compared to the reference scenario (black curve) is visible, with the maximum impact up to degree/order 30. It should be emphasized, that a stochastic stochastic modelling of the tone error peaks at multiples of the orbital frequency (cf. Figure E.4) as part of the gravity adjustment process is

indispensable to avoid significant degradation of the retrieval performance.. In case of the full-noise simulation scenario (Figure E.5 b) where de-aliasing is applied for the AO and OT components with the HIS component as target signal, the differences between the investigated scenarios are much smaller, because most of the impact of the drag compensation is covered by the temporal aliasing.
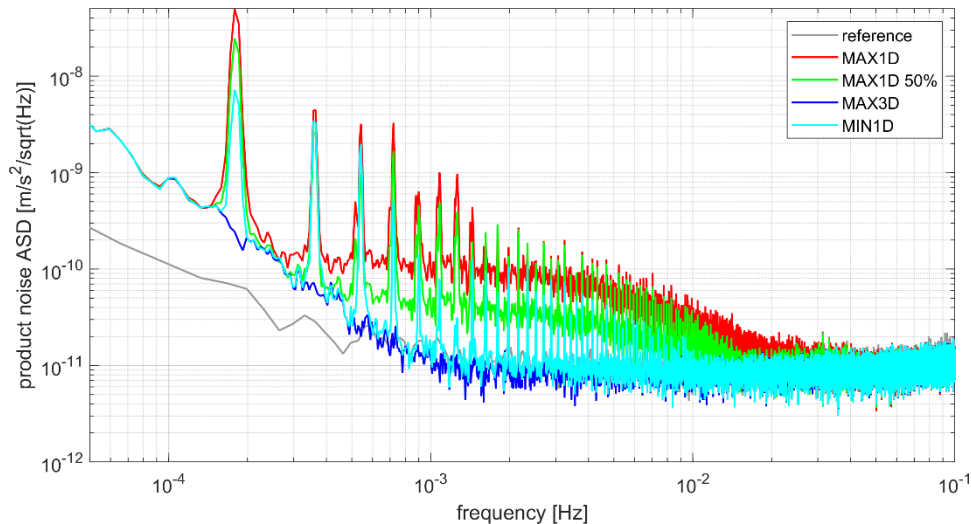
Figure E.4: Product noise amplitude spectral densities (ASD) for various set-ups of ACC performance and drag-free conditions. The terms "MAX" and "MIN" denote a maximal or minimal atmospheric activity, respectively, while the terms "1D" and "3D" denote whether drag compensation is applied exclusively in along-track or in all three spatial directions. The "reference" scenario denotes in essence the performance of a MicroSTAR-type accelerometer and differs from the "MAX3D" scenario only by its lower low-frequency noise increase (1/f instead of 1/f²).
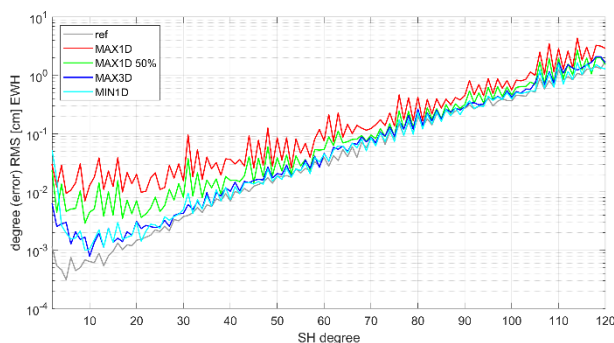
a)   b)
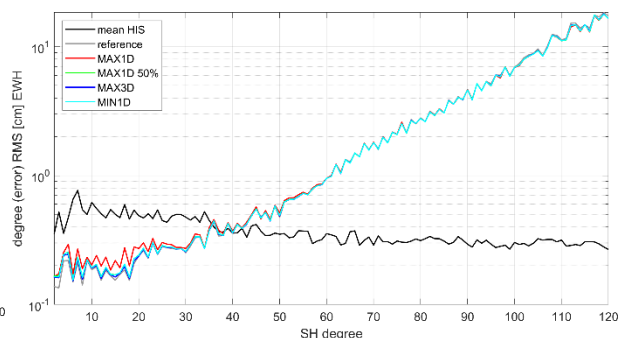
Figure E.5: Degree error RMS of gravity field retrievals related to the scenarios shown in Figure E.4, a) product-noise only case, b) full noise case.

f) Scaling of performance with retrieval period

As to be expected, in the product-noise only case the performance can be scaled linearly with the number of observations (= retrieval period). We found out that this linear scaling can also be roughly applied to the full-noise solutions (including background model errors) down to about 3 days. In contrast, co-estimated as well as stand-alone daily solutions perform even better than predicted by linear scaling.

g) Capabilities of short-term (near-real time) retrieval

Short-term daily co-estimates (proposed by Wiese et al. 2011) are possible up to SH degree 15 to 20 for double-pair scenarios. In specific cases this parameterization causes "bumps" in the degree variance plots at higher degrees. This happens whenever the inclined pair has a very high weighting compared to the polar pair, for example if it has a significantly lower altitude or a much better instrument (accelerometer) performance. In this case, alternatives to the classical "Wiese parameterization" will have to be applied, such as the DMD method (cf. section 4 c).

h) Raw vs. post-processed (filtered) solutions, effect of filtering

Depending on the post-processing strategy, a wide range of results can be achieved in comparison to the MRD/IUGG requirements. It is recommended to use the raw (unfiltered) solution as the baseline strategy for the evaluation of mission performances, keeping in mind that this composes the "worst case" compared to the IUGG requirements, which assumed a certain degree of post-processing.

i) Effect of tone errors

The effect of tone errors is clearly visible in product-only cases, where mainly the low-degree zonal SH coefficients are affected. An adequate stochastic modelling of tone errors is paramount to avoid significant degradation of higher-degree coefficients. Increasing the amplitude of tone errors by a factor of 10 w.r.t. the original SRD specifications, their impact reaches the error level of the full-noise solution, where the effect of tone errors is partly mixing with other error sources. Based on these results, it was recommended to relax the SRD requirements regarding tone error amplitudes by a factor of 10.

2) Second software implementation

In order to validate the TUM numerical simulation results and to prove that these results are reliable, a second implementation of the simulator was done at GFZ based on the EPOS software package. The inter-comparison was performed not only on the final result, but also selected intermediate products, such as orbits, background models and corrections. After some software adaption on both sides, a very good agreement both for product-only and full-noise scenarios could be achieved, even though these two packages are based on different evaluation methods (short-arc approach at TUM vs. numerical integration approach at GFZ). As an example, Figure E.6 shows the TUM and GFZ results for a 3d_H double pair scenario. In general, the RMS deviation between the two solutions is less than 5% of the resulting error

level of the simulation. Also co-estimated daily ("Wiese") parameters show a very similar performance.

With this, two very comparable software systems are available for further simulation studies.
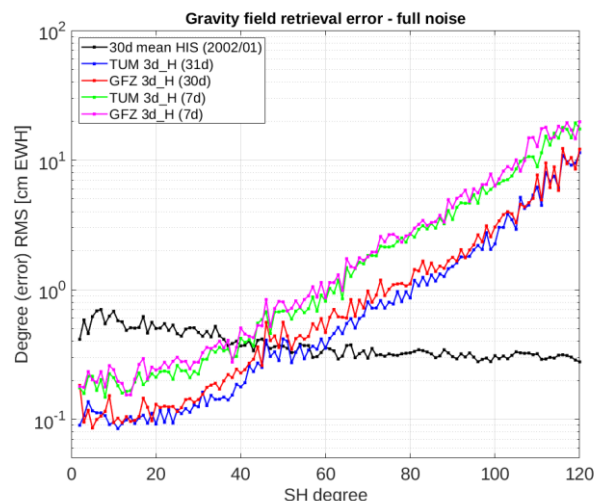
Figure E.6: Full noise solutions of the 3d_H Bender scenario simulated by GFZ (red and magenta) and TUM (blue and green) in terms of SH degree error amplitudes. The monthly averaged HIS signal is displayed in black.

3) Match against MRD requirements

All simulation scenarios performed in this study were evaluated in terms of cumulative EHW errors, and the results were compared against the MRD requirements, which are largely based on the IUGG user requirements (Pail et al., 2015).

Figure E.7 a shows the cumulative EWH errors of various scenarios in the product-only noise case for a monthly (31 day) retrieval period. Evidently, in the absence of background model errors and related temporal aliasing the results come very close to fulfil even the very ambitious target requirements

Figure E.7 b shows the same quantities for the full-noise scenarios. Here, the threshold requirements can largely be reached, with the exception of the low degrees. This significant reduction of performance for the full-noise case compared to the product-only noise case again demonstrates the dominant role of background model errors in the total error budget. However, it should be emphasized that the simulations are based on very conservative assumptions of the background model errors. Additionally, the cumulative error curves are based on the raw solutions, i.e. without any a-posteriori filtering, while the IUGG requirements assumed some degree of post-processing. It is expected that in the near future, the overall performance of the mission, which is currently not limited by the key payload and system design, will be improved by improvements of geophysical background models, going hand in hand with further improvements in processing methodology to reduce the impact of temporal aliasing.

a)   b)
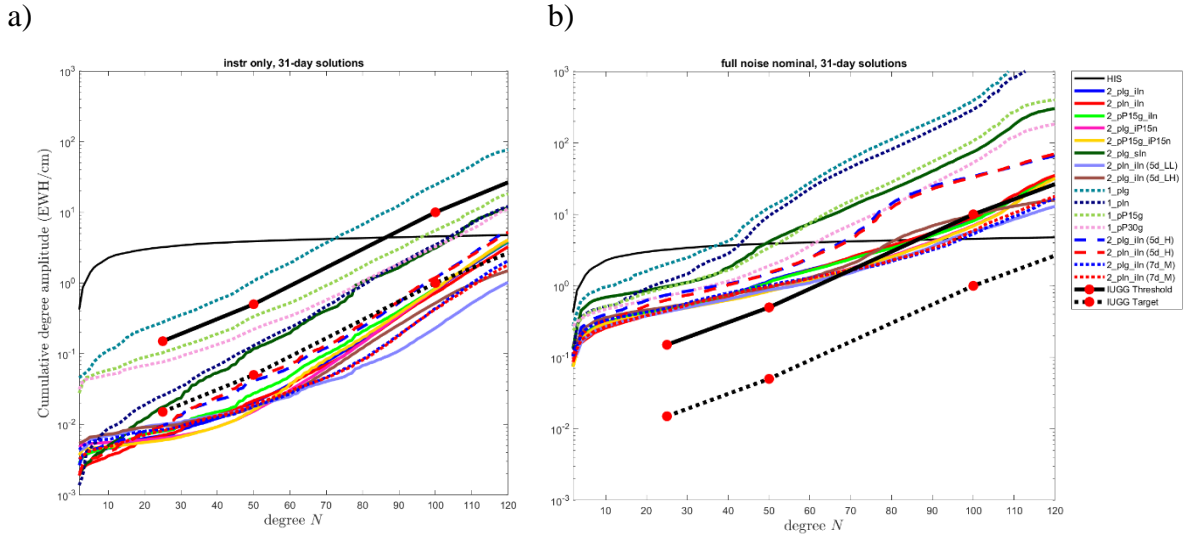
Figure E.7: Cumulative RMS curves for a 31-day d/o 120 a) product-only noise, and b) full-noise simulation results, compared to the IUGG threshold and target requirements. For each individual scenario, the mean curve of the cumulative RMS curves of two subsequent 31-day solutions is shown.

Also the match for sub-monthly periods was analyzed. As an example, Figure E.8 visualizes cumulative errors of simulations using a 3 day retrieval period (up to SH degree 100). The monthly MRD threshold and target requirements were scaled to a 3-day period (cf. 1f) by multiplying with a factor of sqrt(31/3). Similar conclusions as for the monthly retrieval period also hold for the sub-monthly period.

a)   b)
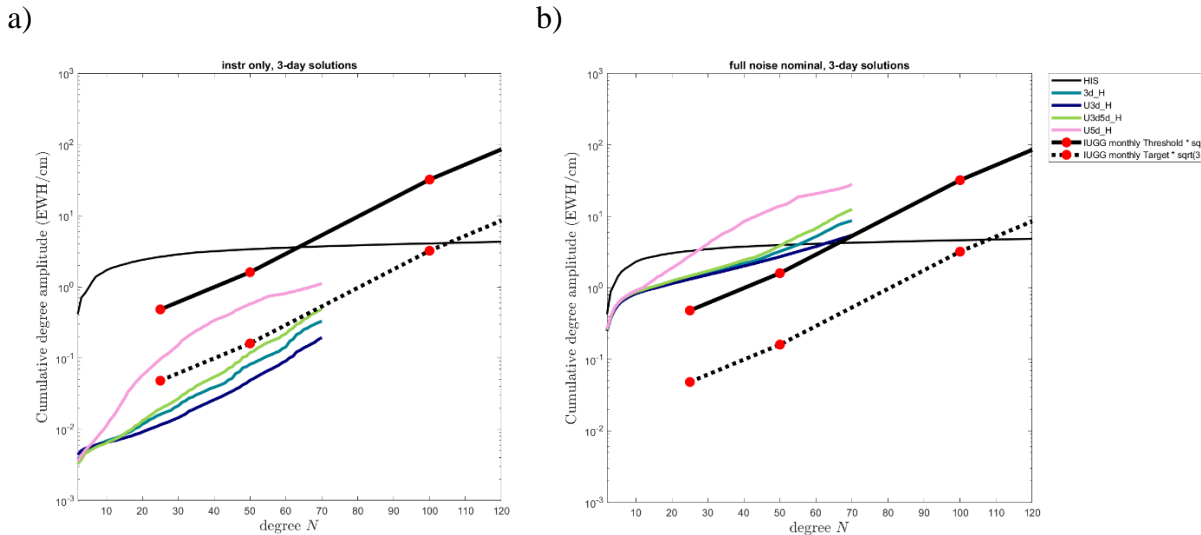
Figure E.8: Cumulative RMS curves for a 3-day d/o 100 a) product-only noise, and b) full-noise simulation results, compared to the MRD threshold and target requirements (monthly req. scaled by sqrt(31/3)). For each individual scenario, the mean curve of the cumulative RMS curves of 20 subsequent 3-day solutions is shown.

4) Development of improved processing methods

In the frame of this project, improved processing strategies have been developed, implemented, numerically analyzed and compared to the performance of the baseline strategy.

a) Optimal application of de-aliasing models

In order to investigate the impact of temporal aliasing errors in more detail, tidal and non-tidal aliasing errors were assessed individually, by excluding either the one or the other error signal from the simulation, but keeping the same product-error assumptions for all simulations. Results demonstrate that the orbit altitude is the main performance driver, either omitting ocean tide errors or omitting errors due to non-tidal aliasing. If non-tidal AO signals are included in the simulation, lower orbit altitudes lead to significantly reduced temporal aliasing errors, even in the longer wavelength spectrum, as temporal aliasing errors due to AO error is the dominating error contributor. In this context, it is to mention that the altitude of the inclined pair is crucial since an altitude, which is much lower (e.g. below 400 km) than the one of the polar pair, results into smaller retrieval errors, also in the high frequency spectrum. If no AO signals are included in the simulation and tidal aliasing errors are dominating, the performances of gravity field solutions of double pair formations having different altitudes show similar behavior at the low-to-mid degree spectrum. In that case, the role of orbit altitude becomes more important for the performance at the mid-to-high frequency spectrum. For sub-monthly retrievals, the length of the respective retrieval period plays an important role as well, next to the altitude. This is especially true if non-tidal AO signals are included.

b) Treatment of ocean tides in NRT analysis and post-processing

It could be shown by Hauk and Pail (2018) that the co-estimation of ocean tide parameters is possible and reduces temporal aliasing errors. However, this method requires long observation time series and is therefore not applicable in near-real time (NRT) analysis. Therefore, an alternative method was developed and applied to Bender double-pair constellations. It is based on the idea to introduce ocean tide background model errors as additional stochastic model into the parameter adjustment, and to propagate it through the whole process to the parameter estimates. Details of the method and a detailed analysis for single- and double pair scenarios can be found in Abrykosov et al. (2021).

a)   b)
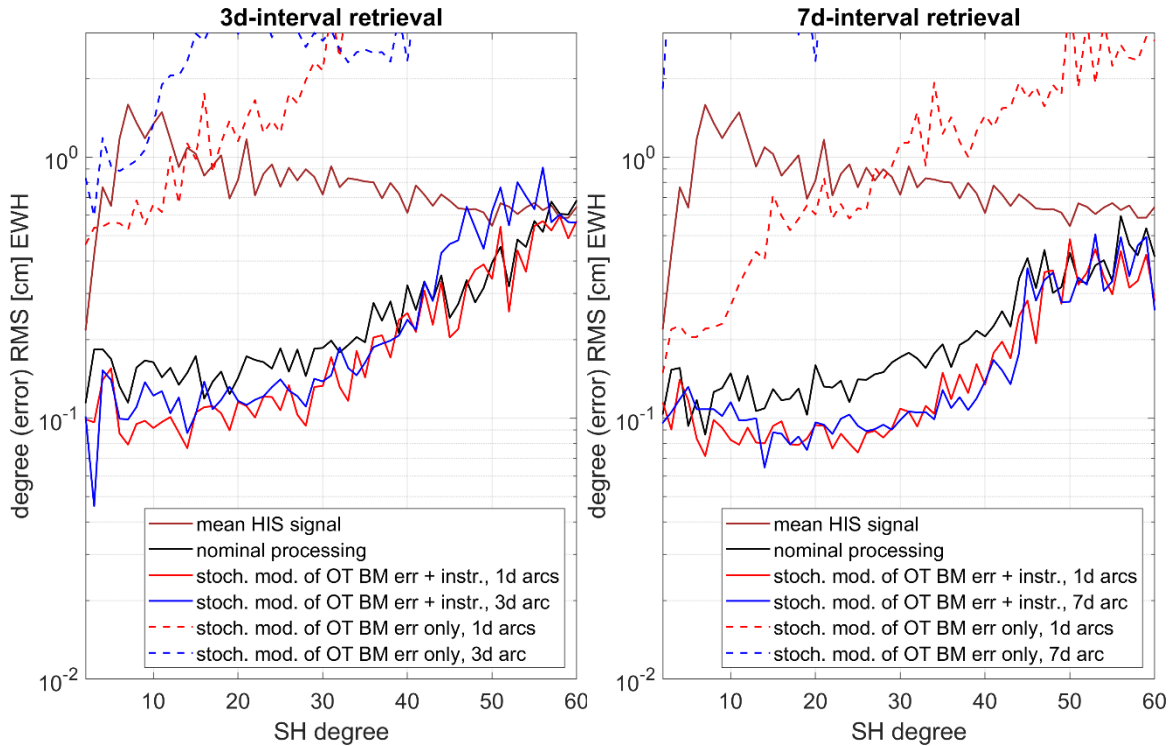
Figure E.9: Retrieval performance of scenarios including tidal and non-tidal gravity signal as well as instrument noise when stochastic modelling is applied for OT BM errors only, OT BM errors and instrument noise or no stochastic modelling of OT is applied at all. Retrieval period is a) 3 days (left), and b) 7 days.

The results of Figure E.9, which are based on a 3d_H Bender-type double-pair scenario, demonstrate that stochastic modelling of OT background errors has the potential to significantly improve the retrieval performance. This method can be applied not only to the retrieval of long-term, e.g. monthly, solutions, but also short-interval fields. It thus poses a valid processing strategy for estimating NRT-type gravity field solutions. The main limiting factor are non-tidal (AOD) background model errors. In future research, it is planned to develop a similar strategy for stochastic modelling of non-tidal background model errors, and apply it together with the OT method discussed here.

c) Optimal signal parametrization with respect to space and time

An alternative method for the co-estimation of daily long-wavelength gravity fields together with coefficients of higher SH degrees ("Wiese approach"), the data-driven multi-step self-de-aliasing (DMD) method, has been developed (Abrykosov et al. 2022a), originally for the "self-dealiasing" of the single-pair missions GRACE and GRACE-FO. In the course of this, a detailed analysis of the space-time pattern of temporal gravity signals was performed, showing that also long-term signals create high-frequency spatial structures. Therefore, the standard concept proposed by Wiese et al. (2011) is not able to fully capture these signals. It was demonstrated that especially in this case of a single-pair scenario long-wavelength, high-amplitude signal components are mapped into other spectral bands, thus degrading the retrieval performance. Therefore, the decoupling of daily low-degree and multi-daily higher-degree

estimates, as done in DMD, is of great benefit especially for single-pair scenarios, because the effect of aliasing reduction by means of daily estimates is larger than the spectral leakage due to decoupling of low and higher degrees.

In the frame of this project, the DMD concept was transferred to double-pair constellations. Here, compared to single-pair constellations the behavior of DMD is somewhat different, because of the intrinsic aliasing reduction of the double-pair constellation due to the additional inclined pair, leading to a lower gain of additional de-aliasing relative to the spectral leakage effect. The DMD performance depends on the amplitude of the signal (being a potential source of aliasing) and the resolution of the gravity field product (defining the relative contribution of spectral leakage errors). Figures E.10 a and E.10 b show the results when using only AO or the full AOHIS signal as an input, respectively. Evidently, the classical Wiese parameterization performs slightly better for the present simulation set-up including the full AOHIS signal up to degree/order 50. However, both classical Wiese and DMD perform generally better than the nominal processing without additional parametrization.

a)   b)
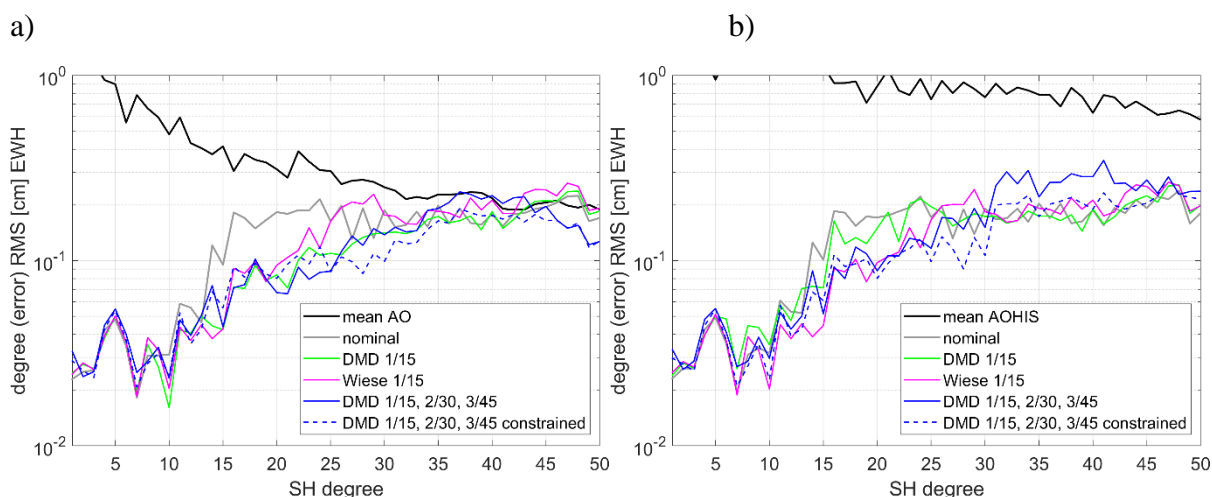
Figure 10: Degree error RMS of gravity field retrievals related to various parameterization schemes.

In addition, expanding the classic "Wiese approach" with additional intermediate steps in terms of successively longer periods increases the processing complexity, but has not shown any improvements in achievable gravity performance. In contrast, as shown in Figure E.10, a DMD multi-step approach has some potential to further improve the results.

d) Analysis of need for long-term trend estimation

Linear trend parameters have been co-estimated together with monthly temporal gravity fields for a 10-year period in the frame of a joint adjustment. Comparing the monthly solutions with and without co-estimation, there is no indication of a benefit when the long-term trend is co-estimated.

e) Analysis of need for post-processing

An optimal filter technique for post-processing of Bender-type gravity field solutions was developed. Methods based on non-isotropic smoothing by approximate decorrelation and regularization (DDK), and time variable decorrelation (VADER/VDK filters) were investigated. The VDK filter usually outperforms the DDK filter. Exemplarily, Figure E.11 shows the results of a raw and a VDK-filtered solution of the Bender-pair scenario 3d_H. Comparing single and double-pair solutions, a much lower filter strength has to be applied to reduce the residual striping of double-pair missions.
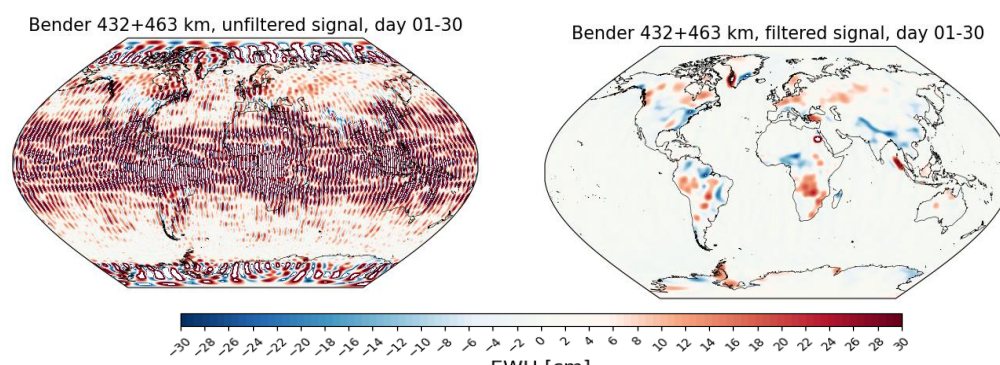
Figure E.11: Spatial comparison of filtered and unfiltered monthly retrieval periods for Bender double-pair scenario 3dH.

The filtered gravity fields are then further evaluated against the true reference signal as well as unfiltered fields at the example of river basins and ice sheets. Results demonstrate, that VDK filtering of Bender-type gravity fields can be useful in order to extract the signal of interest by reducing temporal aliasing effects significantly. Depending on the region to be investigated, it is advisable to look at the error distribution of the 'raw' retrieval on a spatial scale first and then decide which type of gravity field (filtered or unfiltered) to be used.

5) Science impact analysis

The science impact analyses for the fields of hydrology, cryosphere, oceanography and solid Earth revealed significant added value of MAGIC constellations for unravelling and understanding mass transport and mass change processes in the Earth system. For hydrological applications, the number of hydrological units, e.g. river basins, that can be analyzed for water storage variations within the limits of MRD requirements will markedly increase compared to a GRACE-like mission. At a comparatively high spatial resolution, the threshold accuracy (10.1 cm at N=77) can be fulfilled by MAGIC for more than 90% of the river basins worldwide (compared to 2.5% with GRACE-type missions), and even higher accuracies that may be required for several hydrological applications can be met in a large number of basins (Figure E.12). In contrast, the current MRD requirement at the lower spatial resolution of 400 km cannot be met by MAGIC for any river basin. However, relaxing this threshold accuracy to 2.5 cm or 3.5 cm, which can be expected to be still acceptable for many hydrological applications, will allow for resolving TWS variations in 67% and 90% (0.5% and 2.5% for

GRACE-type missions) of the river basins, respectively. For the optimally filtered solutions, the improvement of MAGIC relative to GRACE in terms of RMSD errors of basin-average water storage variations worldwide amounts to a factor of 1.5 to 5, where the largest improvements occur for basin in low-latitude regions, which are hampered most by temporal aliasing errors.
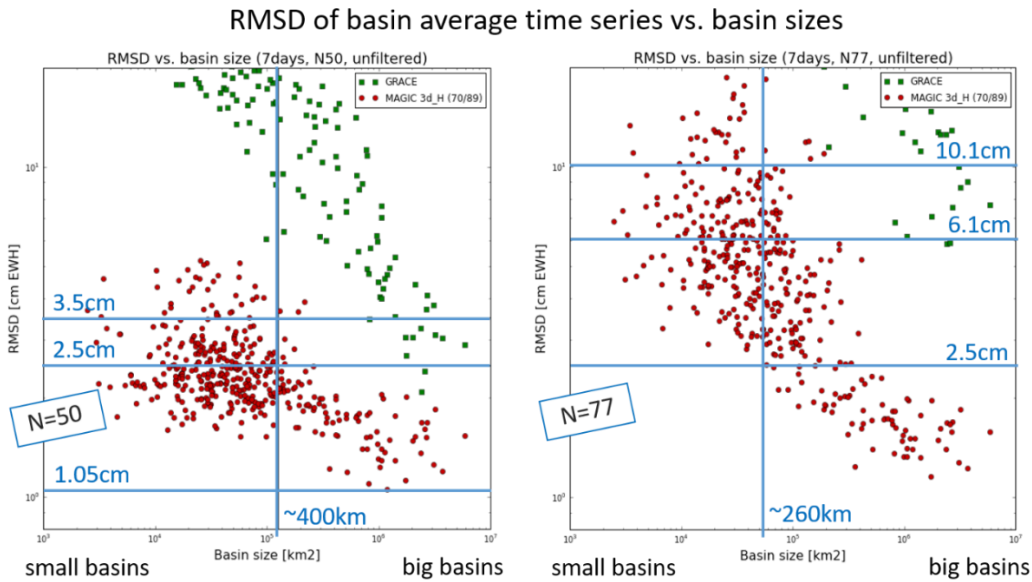
Figure E.12: Root-mean square deviations of weekly basin-average water storage variations for GRDC river basins worldwide, truncated at N= 50 (left) and N=77 (right), for the MAGIC 3d_H and a GRACE-like configuration. Different accuracy requirements are given by blue horizontal lines. The vertical blue lines represent the spatial extent of spherical caps with 400km and 260km diameter, respectively.

Climate change impacts on the global water cycle such as its intensification will be markedly better be observed by a MAGIC double pair mission than by a GRACE-like mission. While, according to our simulations, a GRACE-like mission can only detect the projected changes of the annual amplitude of continental water storage in 36% of the land area after 30 years of observation, MAGIC-like missions would be able to identify such changes in 64% of the land area (Figure E.13). Similarly, the projected 30-years phase change of water storage can be detected by the single-pair scenario in 30% of the land area while a significant increase of this portion (56% of land area) can be achieved with the MAGIC constellation.
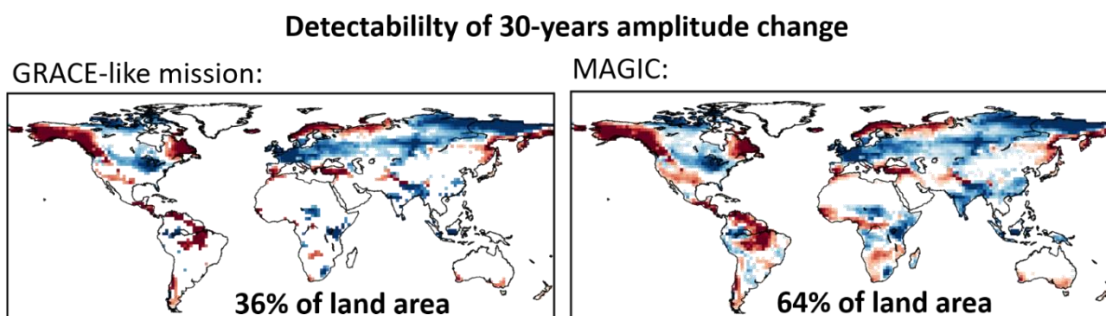
Figure E.13: Detectability of the projected climate-change induced annual amplitude change of terrestrial water storage after 30 years of satellite gravimetry observations: coloured pixels denote where projected amplitude change exceeds the magnitude of the GRACE or MAGIC accuracy.

For cryosphere applications, our analysis shows that the double-pair MAGIC configurations will drastically improve our ability to monitor mass displacements on the ice sheets compared to what is currently possible. It is shown that it should be feasible to separate mass signals in the interior of Greenland or Antarctica from those in the coastal zones (Figure E.14), which is of high scientific interest. While for the hydrology, ocean and solid Earth analyses the MAGIC 3d_H, 5d_Ma and 5d_Mb constellations performed very similar, the 5d_Mb configuration shows the best performance for the cryosphere applications, which is related to the lower altitude of the polar pair compared to scenario 3d_H, and the higher inclination of the inclined pair compared to scenario 5d_Ma. Correspondingly, scenario 5d_Mb shows the largest number of basins passing the threshold and target criteria and the lowest RMSE. At a 250 km resolution, the threshold accuracy for monthly time scales (5.5 cm RMSE) is met for 40 out of the 45 basins, and at daily-to-weekly time scales (6.3 cm RMSE) still for 37 basins. For the Antarctic Peninsula as a region of rapid ice loss, the added scientific value of a double-pair mission is far-reaching as the RMSE drops to an order of magnitude lower than what is currently achievable with a single-pair mission.
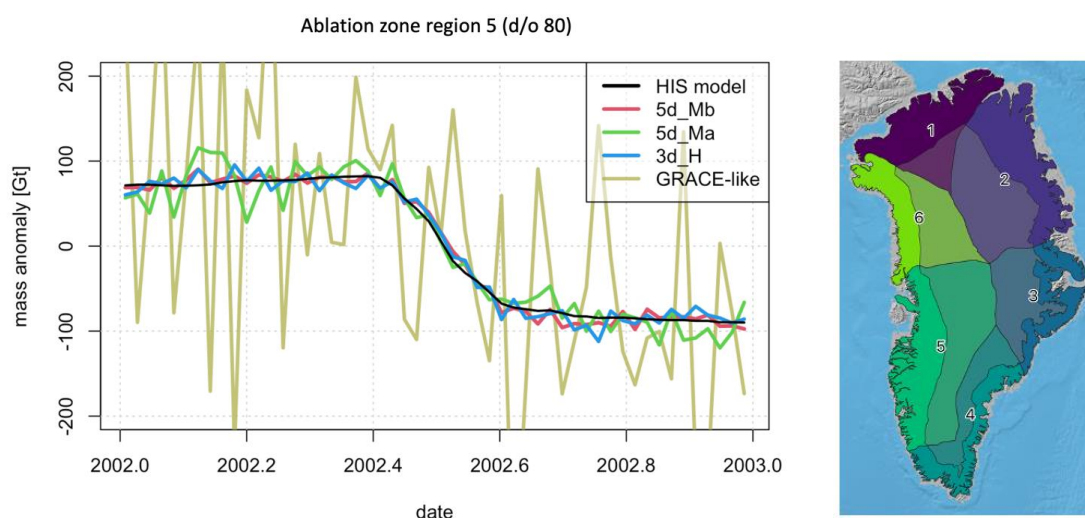
Figure E.14: Mass variations in the ablation zone of Greenland basin 5 simulated by the HIS model and retrieved from the 4 mission configurations simulations.

In the field of oceanography, the MAGIC double-pair configurations produce a dramatic improvement in ocean bottom pressure determination over the single pair GRACE-style configuration. While the present state GRACE measurements cover only the large-scale fluctuations over the range of degrees from about 5 to 15-30 which are of little climatic interest, the new configurations extend the valuable information out to degrees up to between degree 50 and 80, depending on the signal. This is a game-changing extension, permitting clear physical interpretation of aspects of the ocean circulation which are of most relevance to the Earth System, including the potential to monitor meridional overturning circulation changes on time scales of years and decades. The Caribbean Sea example shows a change from barely detectable signals (at about 1 cm RMS) to clearly detectable ones, increasing the explained variance from about 50% of the single-pair to 80%-90% with the double-pair configuration (Figure E.15).
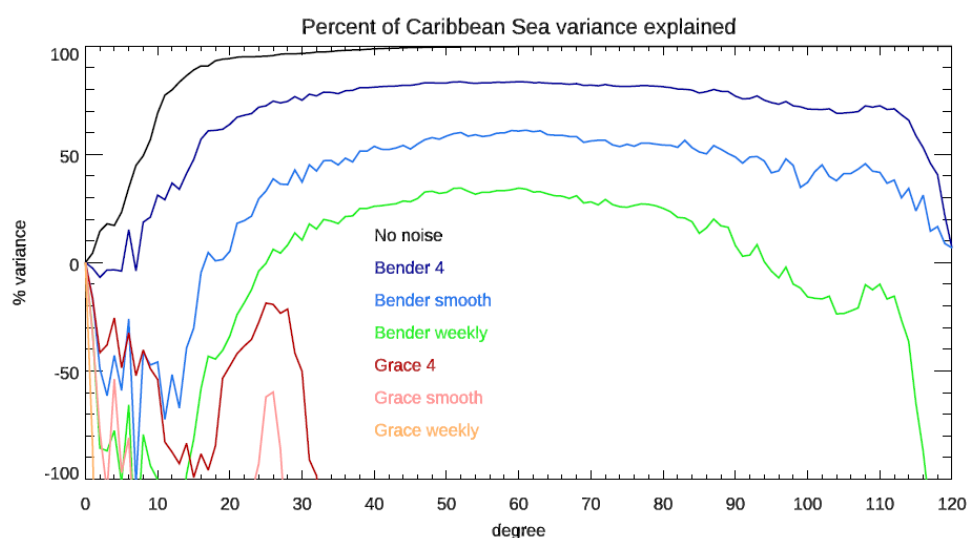
Figure E.15: Percentage variance explained, of the Caribbean Sea basin-averaged bottom pressure, by the pressures truncated at different spherical harmonic degrees and with noise of different amplitudes added. "4" means noise has been reduced by a factor of square root of 4 (in order to propagate the weekly values for the noise to 4-weekly (monthly) means). "smooth" means 4-week averages were used instead of weekly data.

Our analysis of the MAGIC performance in detecting a gravity signal generated by an earthquake of a magnitude *M* shows that it will bring a definitive improvement compared to the present observation technologies of a GRACE-like configuration. When comparing single and double pair configurations with weekly solutions, the double pair significantly lowers the detectable moment magnitude from *M*=8.8 to *M*=8.2, and increases the highest observable degree up to about 60 (333 km resolution). Lowering the time resolution to 1 year, the Bender configuration would detect earthquakes with magnitude *M*=7.4 upwards (Figure E.16).
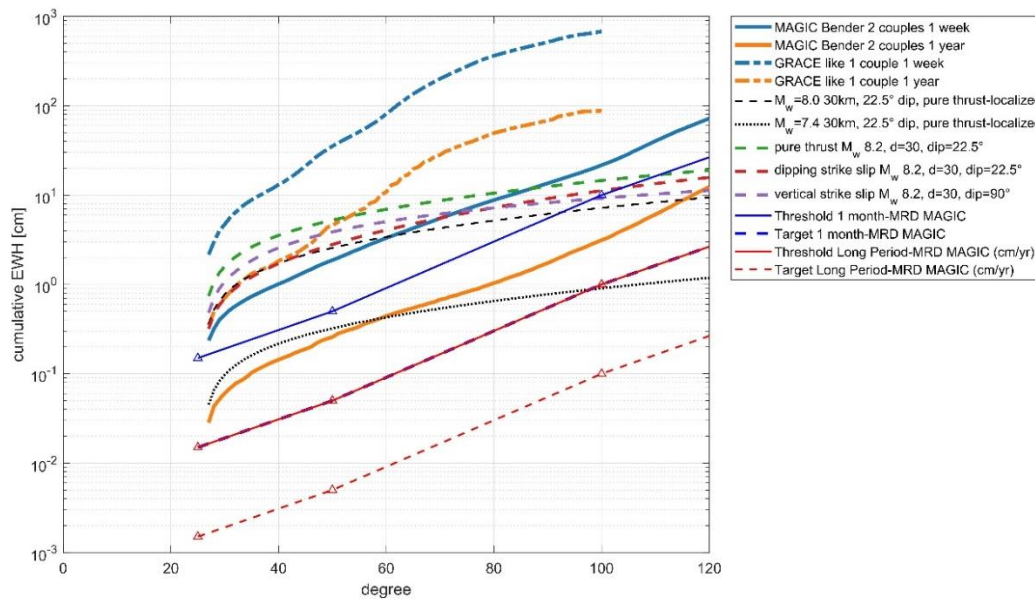
Figure E.16: Cumulative noise curves and cumulative spectral signal curves for some selected earthquake mechanisms. EWH amplitude spectra. The blue and red triangles correspond to the MRD threshold and target requirements (Table 12 of MRD-ESA document; threshold requirement monthly:of 0.15 cm EWH@degree 25, 0.5 cm EWH@degree 50, 10 cm EWH@degree 100, and 50 cm EWH@degree 133, 500 cm EWH@degree 200 (month). The monthly target curves are scaled by a factor 10. The long period error curves in cm/yr values correspond to a division by factor 10 of the monthly values.

6) DORIS-aided orbit and gravity field determination

The impact of embarking DORIS receivers on board of the gravity field satellites was investigated. It will be assessed if DORIS, in addition to precise cm-level kinematic orbit solutions derived from GNSS observations, has the capability to enhance the quality of retrieved temporal gravity field models. The use of satellite tandems allows to form differential DORIS observations, which mitigates some common errors such as tropospheric delay correction errors. Therefore, the gravity field retrieval simulations included solutions based on both absolute and differential DORIS observations. The gravity field retrieval simulations have been conducted for the scenario 3d_H. It was verified that TU Delft and CNES software lead to comparable gravity field retrieval simulation results. The DORIS differential measurement type, even the ideal case tested in the gravity field retrieval simulations, does not provide additional information, i.e. accuracy, to the solution. In reality, the errors in the DORIS differential measurements will be much larger as they will for an important part not cancel out, as was shown with real Sentinel 3A/3B data. The DORIS receiver can therefore only be considered as a back-up instrument for the GNSS receiver in the unlikely event of its failure.

7) Accelerometer calibration

Connected to the studies on the DORIS-aided orbit and gravity field determination (section 6), it was also investigated if such a scenario has the potential to enhance the calibration of accelerometers. Also in this case, the calibration simulations were based on scenario 3d_H and

included solutions based on both absolute and differential DORIS observations. The accelerometer calibration assessment was based on having one accelerometer in the center-of-mass with a GRACE-type noise. The biggest contribution for precise accelerometer calibration comes from the kinematic orbit coordinates (GNSS). The addition of DORIS or ll-SST observation hardly improves the accelerometer calibration by POD.

Drag-free flight leaves a very small non-gravitational signal to be observed by the accelerometers, which makes the estimation of accelerometer scale factors less crucial and also very unstable. A proper maneuver scheme allows a very accurate kinematic orbit based calibration of the scale factor of the accelerometers: very accurate values can be obtained for the X and Z axes (accuracy generally better than 0.001), and more reliable estimates for the Y axis scale factors are obtained (better than 0.05). Periods of a few hours with thrust of the order of 50 nm/s^2 might be sufficient. Accurate estimates of scale factors can be obtained as well when not flying drag-free (e.g. during the commissioning phase), especially for the X axis (much better than 0.001 during solar maximum, better than 0.01 during solar minimum). For the Y and Z axes, the performance is an order of magnitude worth, even more so for the Z axis during solar minimum.

A proposed implementation is to have 3 accelerometers on board of each satellite, with 1 accelerometer in the center-of-mass of the satellite and the other two symmetrically located with respect to this center-of-mass. This possibly leads to a $\sqrt{3}$ noise reduction when for example using a 3-accelerometer common-mode in case of accelerometer calibration by POD. The exact impact of such a possible reduction is yet to be assessed. Heritage from GOCE shows that similar results are obtained for 2-accelerometer and 1-accelerometer calibration by POD, but also that other calibration schemes, e.g. by comparison with star tracker observations, are feasible for at least the accelerometer scale factors.

8) Conclusions

In the frame of this MAGIC/Science project, which was performed in parallel to two industry system studies, the trade space of a wide range of satellite constellations could be narrowed down, leading to a clear recommendation for a Bender-type double pair mission concept. The performance of the constellation is mainly driven by the inclined pair. Therefore, at least the inclined pair has to fly a coordinated orbit with a ground-track pattern forming short sub-cycles, in order to guarantee homogeneous performance of short-term solutions which is an indispensable requirement for operational service applications. All simulation results were compared against the MRD requirements In the full-noise case, which includes very conservative assumptions especially regarding background model errors as the dominant error contributors, the double-pair results can largely meet the threshold requirements for monthly solutions, with the exception of the low degrees. This is also true for short-term solutions of a few days.

The scientific potential was assessed in the main fields of applications continental hydrology, cryosphere, ocean, solid Earth, and climate research. Based on the analysis of single- and double pair simulation scenarios spanning over 1year, the latter could demonstrate significant added value in all analyzed thematic fields. This is reflected, e.g., by a much larger number of

hydrological units that can be analyzed for water storage variations within the limits of MRD requirements, an increase in capability to detect the projected climatic changes of the annual amplitude of continental water storage from 36% to 64% of the land area after 30 years of observation, a drastic improvement to monitor mass displacements on the ice sheets including the feasibility to separate mass signals in the interior of Greenland or Antarctica from those in the coastal zones, and the ability to detect earthquakes with magnitude M=7.4 upwards for a time resolution of 1 year. In the field of oceanography, the MAGIC double-pair configuration would be a game changer, permitting clear physical interpretation of aspects of the ocean circulation, including the potential to monitor meridional overturning circulation changes on time scales of years and decades.

During this science study, several interactions with the parallel system Phase A studies existed, leading, e.g. to the identification of the optimum inter-satellite distance, the impact of various accelerometer and drag free scenarios, and a loosening of the requirements for tone errors. The reliability of the simulation results were guaranteed by an independent second implementation of a numerical simulator based on GFZ's EPOS software, which produces very comparable results to TUM's numerical simulator for all tested scenarios. In the frame of this projects, also several methodological improvements were developed, implemented and assessed, such as the treatment of ocean tides (OT) in near-real time (NRT) processing based on the stochastic modelling of OT background model errors, Science impact analysis, a data-driven multi-step self-de-aliasing (DMD) method for better treatment of short-term atmosphere and ocean signals and corresponding reduction of temporal aliasing, or the optimal application of de-aliasing models. Additionally, impact of embarking DORIS receivers on board of the gravity field satellites was investigated. In full-scale simulation, it was found out that the DORIS differential measurement type does not provide additional information to GNSS.

In summary, important lessons regarding the optimum set-up of a MAGIC double-pair mission, the tuning of its key parameters, and its optimized processing could be learnt during this project, providing also valuable feedback for the parallel system studies and paving the way for a significantly improved monitoring of mass transport processes from space.

References

Abrykosov P, Murböck M, Hauk M, Pail R, Flechtner F (2022a): Data-driven multi-step self-de-aliasing approach for GRACE and GRACE-FO data processing, Geophysical Journal International, ggac340, doi: https://doi.org/10.1093/gji/ggac340.

Abrykosov P, Sulzbach R, Pail R, Dobslaw H, Thomas M (2022b): Treatment of ocean tide background model errors in the context of GRACE/GRACE-FO data processing. Geophysical Journal International 228 (2022). 1850-1865, doi: https://doi.org/10.1093/gji/ggab421.

Hauk M, Pail R (2018): Treatment of ocean tide aliasing in the context of a next generation gravity field mission. Geophysical Journal International 214, 345-365, doi: https://doi.org/10.1093/gji/ggy145.

Mission Requirements Document, Next Generation Gravity Mission as a Mass-change And Geosciences International Constellation (MAGIC) - A joint ESA/NASA double-pair mission based on NASA's MCDO and ESA's NGGM studies (2020). ESA-EOPSM-FMCC-MRD-3785

Pail R, Bingham R, Braitenberg C, Dobslaw H, Eicker A, Güntner A, Horwath M, Ivins E, Longuevergne L, Panet I, Wouters B (2015): Science and User Needs for Observing Global Mass Transport to Understand Global Change and to Benefit Society. Surveys in Geophysics, 36(6):743-772, doi: https://doi.org/10.1007/s10712-015-9348-9.

Wiese DN, Visser P, Nerem RS (2011): Estimating low resolution gravity fields at short time itnervals to reduce temporal aliasing errors. Advances in Space Research 48 (2011), 1094-1107, doi: https://doi.org/10.1016/j.asr.2011.05.027.

ABBREVIATIONS AND ACRONYMS

ACC   Accelerometer
AO   Non-tidal atmosphere and Ocean
AOD   Atmosphere and ocean de-aliasing
AOerr   Atmosphere and ocean error
AOHIS   Atmosphere Ocean Hydrology Ice Solid-earth
AP   Advanced Pendulum
ASD   Amplitude Spectral Density
ATT   Attitude
BM   Background model
d/o   degree and order
DFC   Drag-Free Control
DORIS   Doppler Orbitography and Radiopositioning Integrated by Satellite
EPOS   Earth Parameter and Orbit System software
ESA   European Space Agency
ESM   Earth System Model
EWH   Equivalent Water Height
GFZ   GeoForschungZentrum Potsdam – Helmholtz Center for Geosciences
GNSS   Global Navigation Satellite Systems
GOCE   Gravity field and steady-state Ocean Circulation Explorer
GRACE   Gravity Recovery and Climate Experiment
HCU   HafenCityUniversität Hamburg
HIS   Hydrology, Ice and Solid-earth (temporal gravity)
ICGEM   International Centre for Global Earth Models
IERS   International Earth Rotation Service
ISD   Inter-satellite distance
ITRF   International Terrestrial Reference Frame
IUGG   International Union of Geodesy and Geophysics
ll-SST   low-low Satellite-to-Satellite Tracking
LRI   Laser ranging interferometer
MAGIC   Mass change And Geosciences International Constellation
NGGM   Next Generation Gravity Mission
OT   Ocean tides
PWL   Piecewise Linear
RB   Requirements Baseline
RMS   Root-Mean-Square
SDS   Science Data System
SF   Scale factor
SH   Spherical Harmonic
SST   satellite-to-satellite tracking
TUD   Delft University of Technology
TUM   Technical University of Munich
ULP   The University of Liverpool
URE   Université de Rennes
UTR   University of Trieste

WBS   Work Breakdown Structure

PART 1:

CLOSED-LOOP SIMULATIONS WITH BASELINE AND IMPROVED SOFTWARE

1 INTRODUCTION

This Part 1 refers to Task 1 of the SoW and covers the work performed under WP 100 of the WBS. It refers to the deliverable document TN D2 "Closed-loop simulations with baseline and improved software".

The main purpose is to investigate various MAGIC mission scenarios based on numerical closed-loop simulations and to interpret and assess the resulting performance.

2 CONSTELLATION SCENARIOS

2.1 INTRODUCTION

In order to study the impact of different values for the period of a repeat orbit or (sub)cycle and the impact of a change of height, several scenarios were defined for Bender-type constellations consisting of one pair flying in a (near-)polar orbit and one pair in an inclined orbit (Table 2-1). In addition, a few sun-synchronous orbital (SSO) and pendulum missions were defined. The nominal baseline length is equal to 220 km for all satellite pairs and scenarios. For the scenarios 3d_H and 5d_LL additional tandems were defined, including inline tandems with a baseline length of 100 km, 150 km, and 180 km, and pendulum pairs with angles of 15^0, 30^0, and 45^0 (Table 2-2).

Table 2-1 Orbits sets for inclined and polar pairs. The ID shows the number of sub-cycle days for which the set is optimized and an additional information about the altitudes: (M)id, (H)igh. Note that the semi-major axis is reduced by 6378 km for highlighting differences in altitude. The other columns provide information about the homogeneity of the ground track patterns (for more details is referred to [RD-1]).

ID	Sats 1 (IP)		Sats 2 (PP)		h_{l1} [-]	h_{l2} [-]	$\Delta(Lon)_1$ [deg]	$\Delta(Lon)_2$ [deg]	Sub-cycles [days]
	Alt. [km]	Incl. [deg]	Alt. [km]	Incl. [deg]					
3d_M	409	70	440	89	1.368	1.383	2.308	2.384	2, 3, 8, 11, 30
3d_H	432	70	463	89	1.451	1.449	-3.076	-3.067	3, 7, 31
5d_Ma	396	65	434	89	1.397	1.383	-1.499	-1.458	2, 3, 5, 13, 18, 31
5d_Mb	397	70	425	87	1.168	1.167	0.736	0.733	2, 5, 27, 32
5d_H	465	75	488	89	1.185	1.190	0.762	0.781	4, 5, 29
7d_M	389	70	417	87	1.238	1.253	0.743	0.786	2, 7, 30
7d_H	432	70	463	89	1.218	1.226	0.672	0.692	3, 7, 31
SSO for 3d_H	477	97	463	89	1.454	1.449	-3.097	-3.067	3, 7, 31
SSO for 7d_H	477	97	463	89	1.201	1.226	0.622	0.692	3, 7, 31

5d_LL	344	70	376	89	1.423	1.410	-1.671	-1.628	1, 2, 5, 12, 29
5d_LH	344	71.5	492	89	1.169	1.172	-0.732	-0.790	5, (32-31)

Table 2-2 Scenarios for which Kepler elements were computed for additional tandems.

3d_H	Inline baselines: 100, 150, 180 & 220 km
	Pendulum 15^0 & 30^0: baselines 100 & 220 km
	Pendulum 45^0: baseline 220 km
5d_LL	Inline baselines: 100, 150, 180 & 220 km

2.2 GENERATION OF OSCULATING KEPLER ELEMENTS

A procedure was established to obtain proper orbital initial conditions for the orbit scenarios outlined in Table 2-1. The procedure is largely identical to the one used in previous studies to a Next Generation Gravity Mission (NGGM) [RD-2][RD-3][RD-4]. The procedure incorporates the possibility of taking into account a common drift of the ground track pattern for the (near-)polar and inclined satellite pairs. The reason for this incorporation is the choice of a number of relatively short repeat periods or (sub)cycles, e.g., as low as 3 days for scenario **3d_H** in Table 2-1. In case such a repeat period would be exact, the associated ground track spacing would not allow for high-degree gravity field recoveries for longer periods. For example, typically 47 orbital revolutions are completed in a 3-day period, which allows for a homogeneous gravity field retrieval only to spherical harmonic degree 23 according to the Nyquist-Colombo sampling rule for space-borne gravimetry [RD-5]. Therefore, a common drift to both the polar and inclined orbits can be applied, such that over longer time spans the distance between adjacent tracks becomes smaller. For example, for the 3-day near-repeat **3d_H** scenario the common ground track pattern shifts by about 3 degrees after 3 days. This way, it is guaranteed that for example after a month a gravity field retrieval up to, e.g., at least spherical degree and order 150 is possible.

The procedure consists of the following steps:

1. Simulation of time series of Cartesian X, Y and Z coordinates in a true-of-date pseudo-inertial Earth-centered reference frame according to a perfectly circular drifting repeat orbit. The force model consists of the central and J_2 terms of the Earth's gravity field. The time step is 1 hr. The time series is nominally 30 days long.

2. Estimation of osculating Kepler elements at epoch by a dynamic orbit fit through the Cartesian coordinates of step 1. The satellites are assumed to fly drag free, which means that only gravitational force models are taken into account (GOCO05s complete to degree and order 120 [RD-7], EGM-96 based model for the solid-earth and ocean tides [RD-8], 3rd body perturbations). The GEODYN software, version 0712, is used that was kindly provided by the NASA Goddard Space Flight Center, Greenbelt, Maryland [RD-7].

Typically, the fit of the Cartesian coordinates is of the order of a 1.5-5 km. The epoch of the Kepler elements is 1 January 2002, 00:00:00, GPS time. It has to be noted that largely the same dynamical models were used as those to be used in the analysis of the possible DORIS contribution (WPs 300 and 700 of this project). The differences between the used force model

consist of (1) different tide model, and (2) inclusion of remaining non-gravitational accelerations equivalent to as described in [RD-4]. These force model differences cause orbit differences that are typically less than 1 km after 30 days and do thus not significantly change the ground track pattern and baseline stability. The Kepler elements are provided in the *J2000* reference frame.

3 VERIFICATION OF ORBIT GEOMETRIES

For all the satellite tandems and Bender constellation scenarios listed in Table 2-1, the baseline stability has been checked by computing the mean and RMS-about-mean of the orbit differences in flight, radial and cross-track directions, and the distances, for the two satellites that form the associated tandem. This has been done for a 30-day period for all satellite pairs and the time series of orbit differences and distances has been plotted as well (GIF images). In addition, the maximum gap between adjacent tracks at the equator has been computed for several combinations of ground tracks (see, e.g., Table 3-1 for scenario **3d_H**). For each scenario, the associated Figures and ground track information is provided in an electronic archive (3.1). It was found that for all scenarios and satellite pairs, the baseline never deviates more than typically a few hundreds of meters from the nominal length of 220 km for the inline pairs (also for other baseline lengths, the deviations were of this order of magnitude), and that the baselines for the pendulum pairs are in agreement with the desired 15^0 or 30^0 pendulum-motion.

In addition, for all scenarios in Table 2-1 it was checked if the ground track patterns are consistent with the specifications in [RD-1].

Table 3-1 Check of ground track for scenario 3d_H. The maximum distance between adjacent tracks at the equator is indicated for only the ascending or descending tracks, or for all tracks, for sub-cycles of 3 and 7 days.

Satellite(s)	3-day subcycle			7-day sub-cycle		
	Ascending			Ascending		
	Min (deg)	Max (deg)	Ratio	Min (deg)	Max (deg)	Ratio
Sat1/polar	6.82	9.91	1.45	0.67	3.76	5.58
Sat1/inclined	6.77	9.87	1.46	0.85	3.95	4.63
Sat2/polar	6.82	9.91	1.45	3.07	3.76	1.22
Sat2/inclined	6.77	9.87	1.46	0.85	3.95	4.63
	Descending			Descending		
Sat1/polar	6.82	9.91	1.45	3.07	3.75	1.22

Sat1/inclined	6.77	9.87	1.46	0.85	3.95	4.65
Sat2/polar	6.82	9.91	1.45	3.07	3.75	1.22
Sat2/inclined	6.77	9.87	1.46	0.94	3.95	4.21
	Asc & Des			Asc & Des		
Sat1/polar	3.39	6.51	1.92	0.31	3.09	9.81
Sat1/inclined	3.38	6.48	1.92	0.37	3.01	8.06
Sat2/polar	3.39	6.51	1.92	0.32	3.09	9.81
Sat2/inclined	3.38	6.49	1.92	0.37	3.01	8.04
	Bender			Bender		
Sat1/pol+inc	0.54	3.38	6.43	0.21	2.43	11.57
Sat2/pol+inc	0.53	3.48	6.56	0.20	2.42	11.97

3.1 ELECTRONIC DELIVERABLES

The products to be provided by WP 120 and 410 are the Keplerian elements. An example is provided in Figure 3-1.
In addition, checks have been conducted to assess if the baselines for the different satellite pairs and scenarios are stable, i.e., do not drift away too much (e.g., more than a few km) from the nominal 220 km (or other length if so specified). For each satellite pair and for each scenario, Figures have been provided that demonstrate sufficient baseline stability (GIF format). An example is included below (Figure 3-2).

Moreover, it has been verified that the ground track patterns of both polar and inclined pairs have an identical drift for each scenario and also satisfy the sub-cycle/repeat period specification. To this aim, Figures (animated GIF format) were produced and provided as well such as the one below in Figure 3-3. Finally, as stated in Section 2, for all scenario's the maximum gap between adjacent tracks has been computed for relevant sub-cycles. Associated numbers are included in ASCII text files.

Thus, the electronic supplement incudes (all uploaded to TU Munich LRZ server [RD-9]):
- Osculating Kepler elements at epoch in the *J2000* reference frame (ASCII text files);
- Information about the ground tracks for sub-cycles (ASCII text files);
- Images displaying evolution of baselines (GIF);
- Animated images of drifting ground track patterns for selected sub-cycles (GIF).

```
PLEASE NOTE THAT TIME SYSTEM IS UTC, NOT GPS (USED FOR SP3 FILES)

 DATE   GREENWICH TIME        A             E              I          RA ASC NODE      ARC PERIGEE      MEAN ANOMALY
YYMMDD  HHMM  SECONDS      (METERS)                    (DEGREES)      (DEGREES)        (DEGREES)        (DEGREES)
020101  0000  0.000000   6846058.138  0.00165585454   88.997236132   359.981873073    28.199409842     331.085529881
020101  0000  0.000000   6846061.861  0.00166631056   88.997236202   359.981889635    28.818288775     331.305620485
020101  0000  0.000000   6815259.195  0.00086208786   70.016625375     3.971420249     4.992907115     354.288098763
020101  0000  0.000000   6815262.582  0.00086477282   70.016622926     3.971830396     6.359334258     353.764506377
020101  0000  0.000000   6858709.382  0.00150382295   96.991325534   359.986138963    24.054779405     335.237208935
020101  0000  0.000000   6858712.595  0.00151283437   96.991324206   359.985993073    24.757990347     335.371524929
020101  0000  0.000000   6846061.920  0.00166587189   88.997290256     0.198627364    28.814290182     331.305925309
020101  0000  0.000000   6815263.056  0.00086458106   70.016649117     4.203534810     6.187443472     353.857257502
020101  0000  0.000000   6846061.972  0.00166548588   88.997341066     0.400594844    28.810508392     331.306275890
020101  0000  0.000000   6815263.430  0.00086437889   70.016674082     4.419449141     6.027948707     353.943028009
020101  0000  0.000000   6846055.435  0.00167700488   88.997232771   359.981912706    29.576264262     331.554948941
020101  0000  0.000000   6815256.945  0.00086682759   70.016604620     3.972322383     8.003702712     353.131544035
020101  0000  0.000000   6858705.688  0.00152217161   96.991327473   359.985817952    25.622458300     335.512089669
020101  0000  0.000000   6846055.728  0.00167611412   88.997352528     0.458735969    29.567453860     331.555656181
020101  0000  0.000000   6815259.771  0.00086654572   70.016666414     4.482072712     7.626508408     353.334673827
020101  0000  0.000000   6846055.982  0.00167540886   88.997466144     0.903064692    29.558822790     331.556773136
020101  0000  0.000000   6815262.034  0.00086617013   70.016729002     4.957085727     7.279584607     353.519387415
020101  0000  0.000000   6846056.190  0.00167490286   88.997565065     1.284618379    29.550869449     331.558293077
020101  0000  0.000000   6815263.655  0.00086577345   70.016789062     5.364988955     6.986294502     353.673285873
```

Figure 3-1 Osculating Kepler elements for scenario 3d_H from [RD-1] at epoch 1 January 2002, 00:00:00 UTC time.
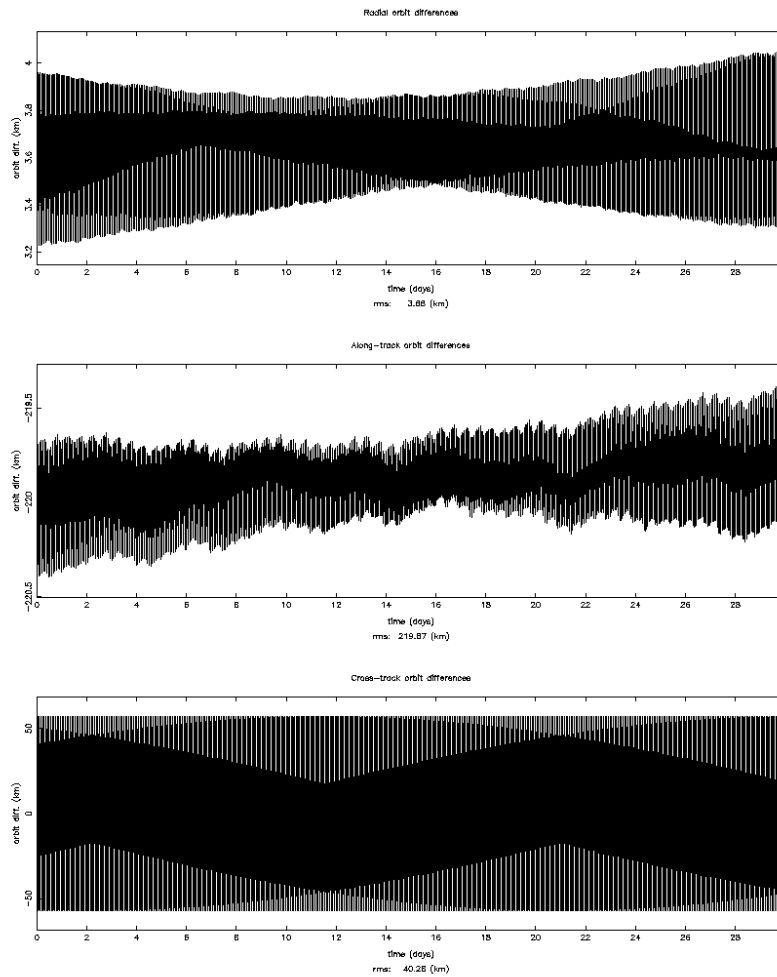
Figure 3-2 Differences between the orbits of the two satellites of the 15⁰ pendulum pair for scenario 3d_H (Table 2-1). The radial, along-track and cross-track differences are displayed for a 30-day period (1-30 January 2002). The along-track difference does not deviate by more than a few hundreds of meters from the nominal baseline length of 220 km in the flight direction. The pendulum motion can be nice observed on the cross-track direction.
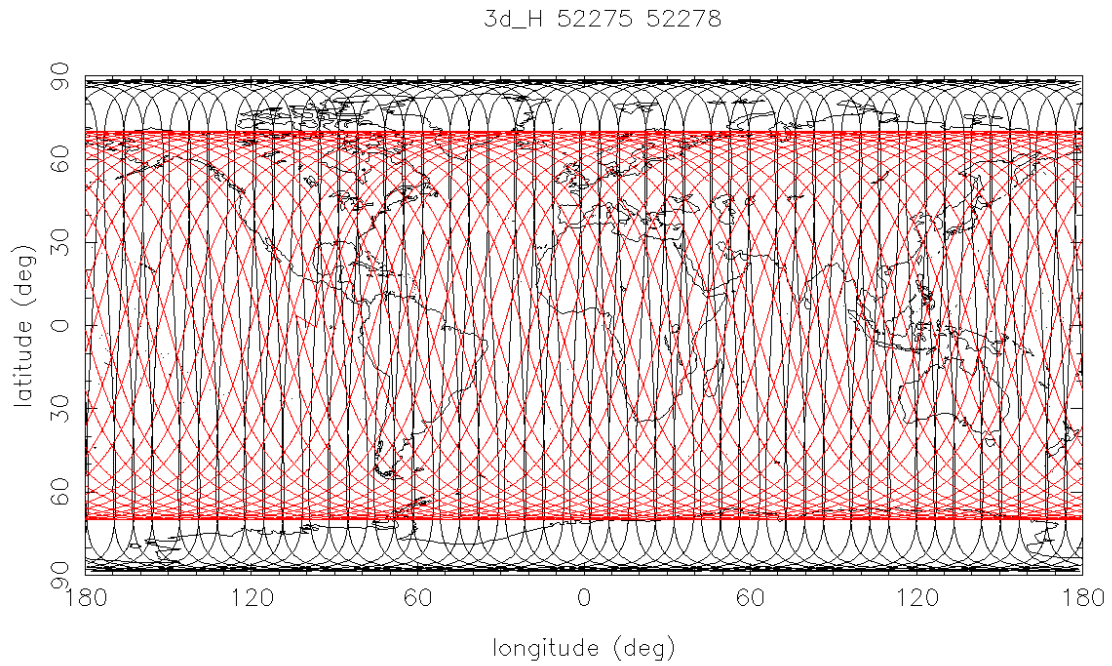
Figure 3-3 Ground track patterns (animated GIF in original Word document) for 10 consecutive 3-day sub-cycles (scenario 3d_H in Table 2-1).

4   VALIDATION OF THE INTEGRATED ORBITS

For each of the orbit configurations introduced in sections 1 and 2, orbit time series over the 2-month time period starting from January 1st, 2002 were computed by TUM. The initial state parameters of the satellites are defined by the osculating Kepler elements provided by TUD. We numerically integrate force models for the static gravity field, the ocean tide signal and the AOHIS signal. In the following, we present a detailed analysis of the orbits obtained by numerical integration from the TUM full-scale simulation software, and thereby validate the properties of the orbits described in sections 1 and 2.

The properties analysed are the inclination of the orbits and the presence of a "pendulum" angle between the satellite orbits, the stability of the inter-satellite distance over a 2-month period, the longitude shift of the groundtracks, the duration of the repeat subcycles as well as the homogeneity of the groundtrack coverage in subsequent subcycles over time.

The corresponding plots are given by Figure 4-1 to Figure 4-14. The respective panels a and b show the groundtracks of the leading satellite (in blue) and the trailing satellite (in green) over a time period of 1 day (January 1st, 2002). The global groundtrack plots (panels a) visualize the inclination of the orbits, as well as the data coverage within a one-day time span. The smaller section (panel b) visualizes the angle of the orbital planes of the two satellites, which is 0° for the in-line orbits and 15° or 30° for the pendulum orbits.

The inter-satellite distance over the 2-month simulation time span starting from January 1st, 2002 is shown by the respective panels c. The nominal inter-satellite distance of 220 km (or 150 km, or 180 km, respectively) is marked as a red horizontal line. It can be seen that the distance between the two satellites stays within +/- 1km at the nominal distance for the in-line pairs. For the pendulum pairs, the maximum deviation from the nominal inter-satellite distance is 8 km (15° opening angle) and about 25 km (30° opening angle) within the considered 2-month period. Figure 4-15 additionally visualizes the stability of the inter-satellite distance in the case of the 3d_H and 5d_LL orbits with 150 km and 180 km inter-satellite distance.

With respect to the analysis of the subcycle stability and longitude shifts, we give an overview of the nominal values in Table 4-1, which also includes which subcycles are explicitly validated in Figures Figure 4-1 to Figure 4-14.

Panel d of Figure 4-1 to Figure 4-14 shows the longitude shift of the groundtrack after the completion of an integer number of subcycles, where the longitude shift is measured as distance between the groundtrack equator crossings at the beginning and the end of the subcycle interval. The lengths of the subcycles as well as the nominal longitude shift of the individual orbit configurations are given by Table 2-1 and are repeated for convenience in Table 4-1. The longitude shift for the individual subcycles determined from the computed orbit data can be read in the legend of the panel d plots. The comparison of the nominal shift value and the shift determined from the orbit data is given in the figure captions. For all orbit configurations, the deviations between the nominal and determined values are very small.

The stability of the subcycle lengths is shown by panels e and f of Figure 4-1 to Figure 4-14. We confirm the presence of the nominal subcycle lengths as well as their stability within 2 months.

Panels g to n of Figure 4-1 to Figure 4-14 visualize the homogeneity of the groundtrack coverage of individual subcycles, as well as the direction of the longitude shift. A green marker is plotted at the beginning of the respective groundtrack segment, and a red marker at the end of it. As an example, panel g of Figure 4-1 shows the groundtrack of the leading satellite from January 1st to January 3rd, 2002, which represents the first 3-day subcycle of the polar 3d_H orbit. The red marker is located to the west of the green marker, visualizing the negative (westward) longitude drift of the 3-day subcycle. Panel h of Figure 4-1 shows the groundtrack for day 4 to 6 and panel i shows the groundtrack for day 58-63, visualizing that the groundtrack coverage is stable over time.

Equivalent observations can be made in panels j to l of Figure 4-1 for the 7-day subcycle, as well as in panels m and n of Figure 4-1 for the 31-day subcycle.

Table 4-1 Longitude shift and subcycle lengths for selected orbit configurations. Data is extracted from Table 2-1. The last column gives the subcycles which are validated using integrated orbits in

	Longitude shift (polar pair)	Longitude shift (inclined pair)	Subcycles in days	Validated subcycles
3d_H	-3.076°/3 days	-3.076°/3 days	3, 7, 31	3, 7, 31
5d_LL	-1.628°/5 days	-1.671°/5 days	1, 2, 5, 12, 29	5, 29
5d_LH	-0.790°/5 days	-0.732°/5 days	5, PP: 31, IP: 32	5, 31, 32
5d_H	0.781°/5 days	0.762°/5 days	4, 5, 29	5, 29
7d_M	0.786°/7 days	0.743°/7 days	2, 7, 30	7, 30
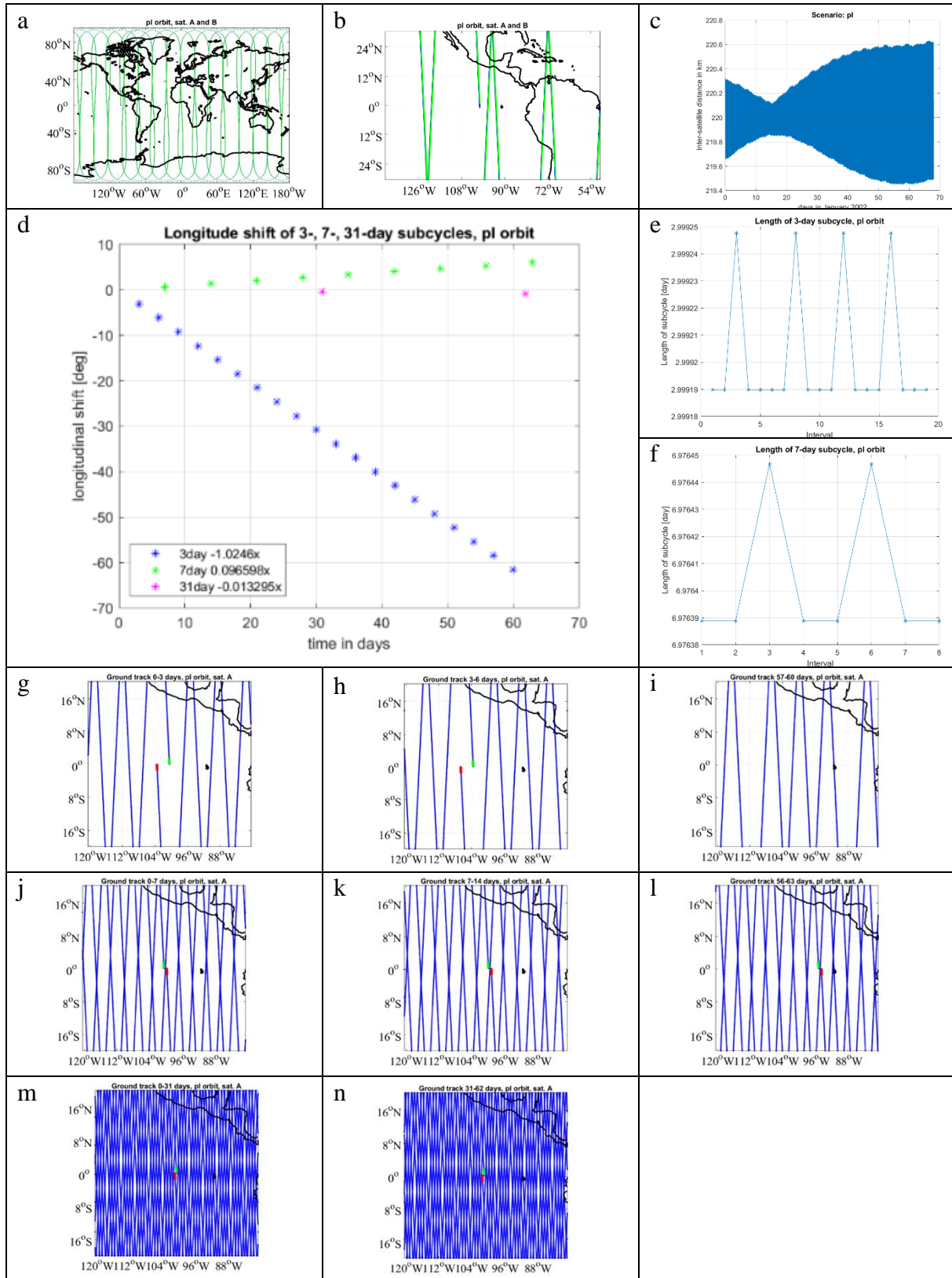
Figure 4-1 Orbit validation plots for the polar in-line pair (pI, 3d_H). Determined longitude shift: -3.0738°/3 days. Nominal longitude shift (3d_H): -3.076°/3 days. The stability of the 3- and 7-day subcycles is visualized in panels e and f. The groundtrack coverage within 3-day, 7-day and 31-day segments is shown by the panels g to i, j to l and m to n, respectively.
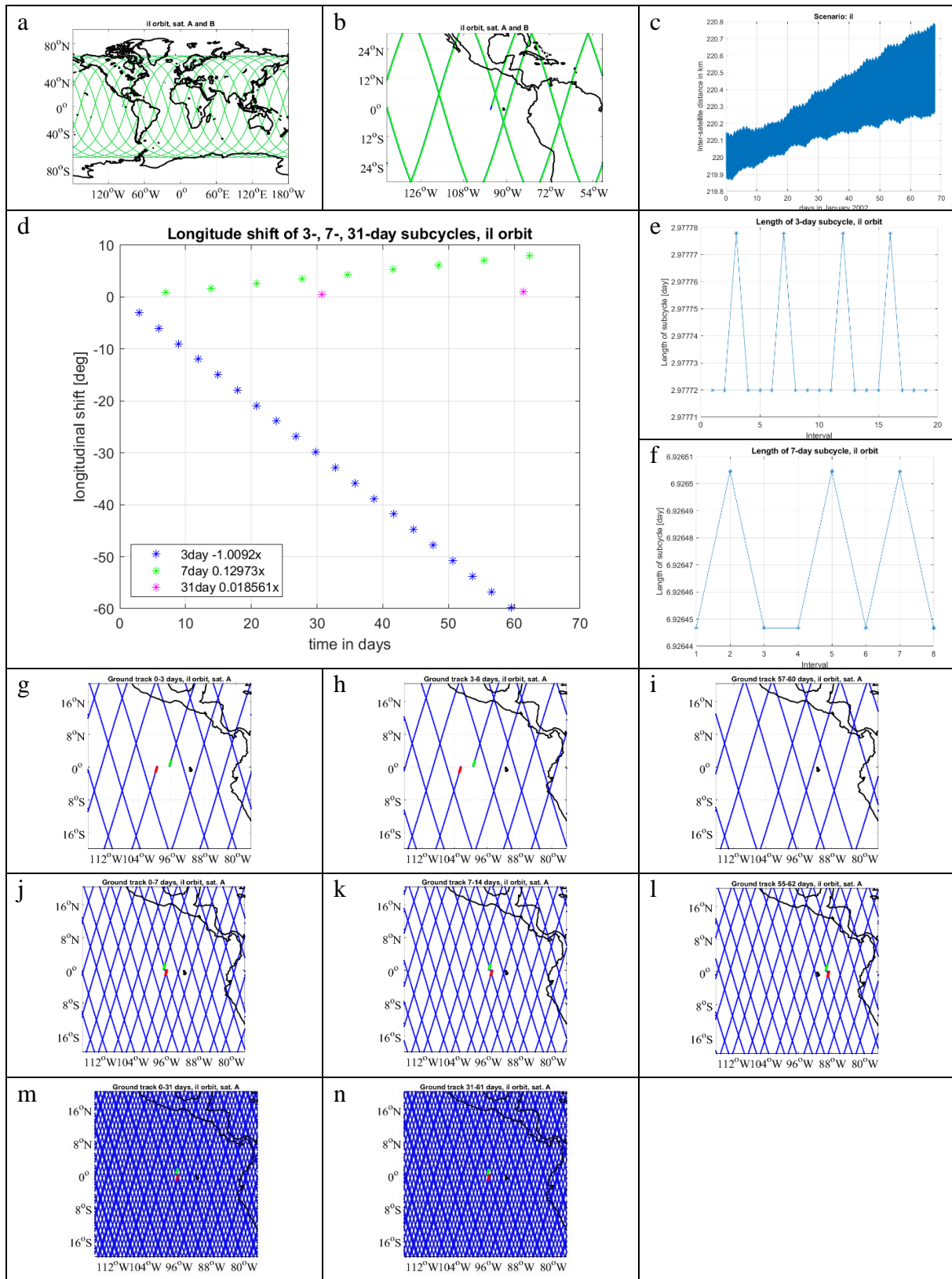
Figure 4-2 Orbit validation plots for the inclined in-line pair (iI, 3d_H). Determined longitude shift (leading satellite): -3.0276°/3 days. Nominal longitude shift (3d_H): -3.076°/3 days. The stability of the 3- and 7-day subcycles is visualized in panels e and f. The groundtrack coverage within 3-day, 7-day and 31-day segments is shown by the panels g to i, j to l and m to n, respectively.
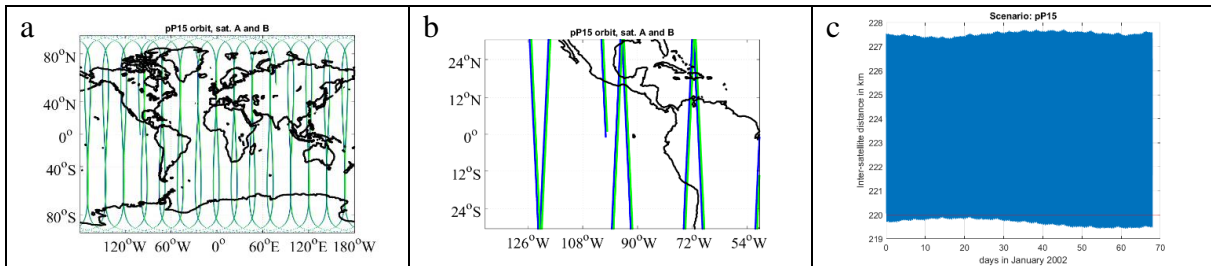
Figure 4-3 Polar pendulum pair with 15° opening angle (pP15, 3d_H)
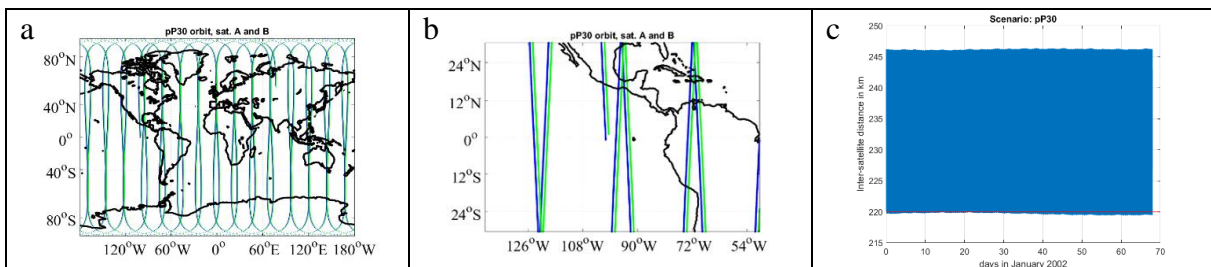
Figure 4-4 Polar pendulum pair with 30° opening angle (pP30, 3d_H)
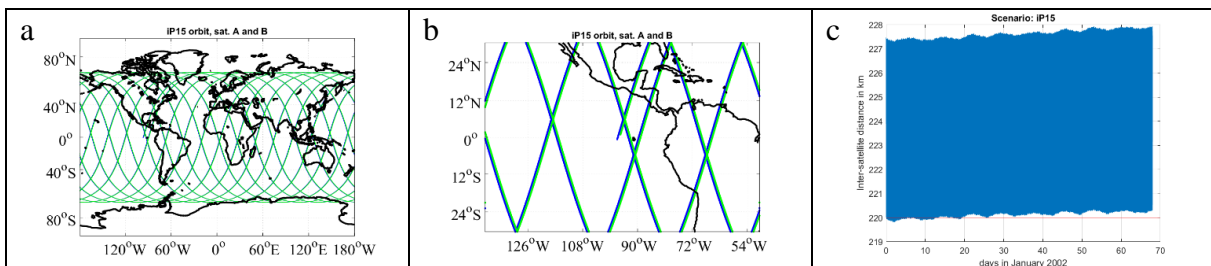
Figure 4-5 Inclined pendulum pair with 15° opening angle (iP15, 3d_H)

NGGM/MAGIC – Science Support Study During Phase A	*Final Report*	
	Doc. Nr:	MAGIC_FR
	Issue:	1.0
	Date:	15.11.2022
	Page:	43 of 466
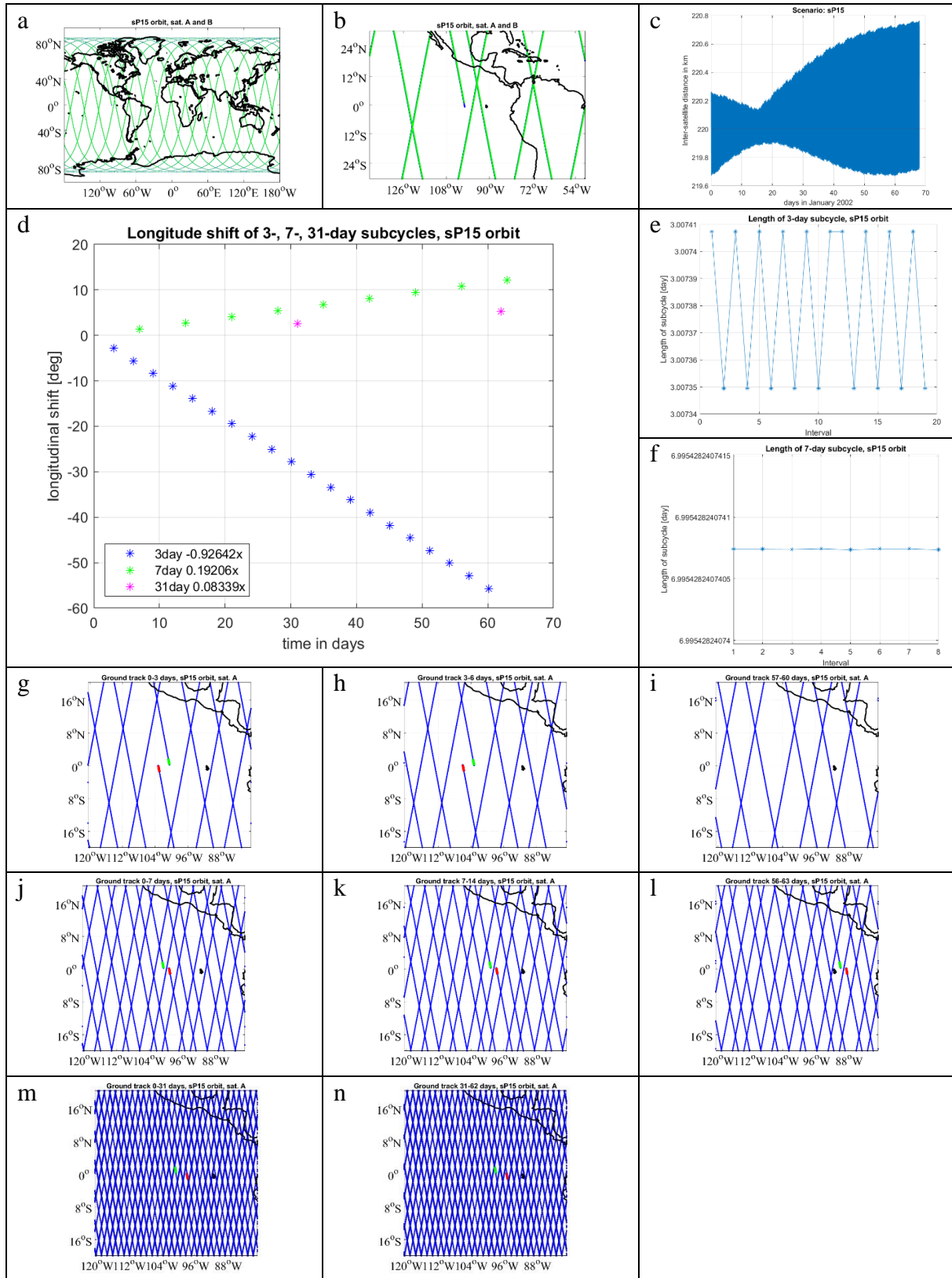
Figure 4-6 Orbit validation plots for the sun-synchronous in-line pair (sI, 3d_H). Determined longitude shift (leading satellite): -2.77926°/3 days. Nominal longitude shift (3d_H): -3.076°/3 days. The stability of the 3- and 7-day subcycles is visualized in panels e and f. The groundtrack coverage within 3-day, 7-day and 31-day segments is shown by the panels g to i, j to l and m to n, respectively.
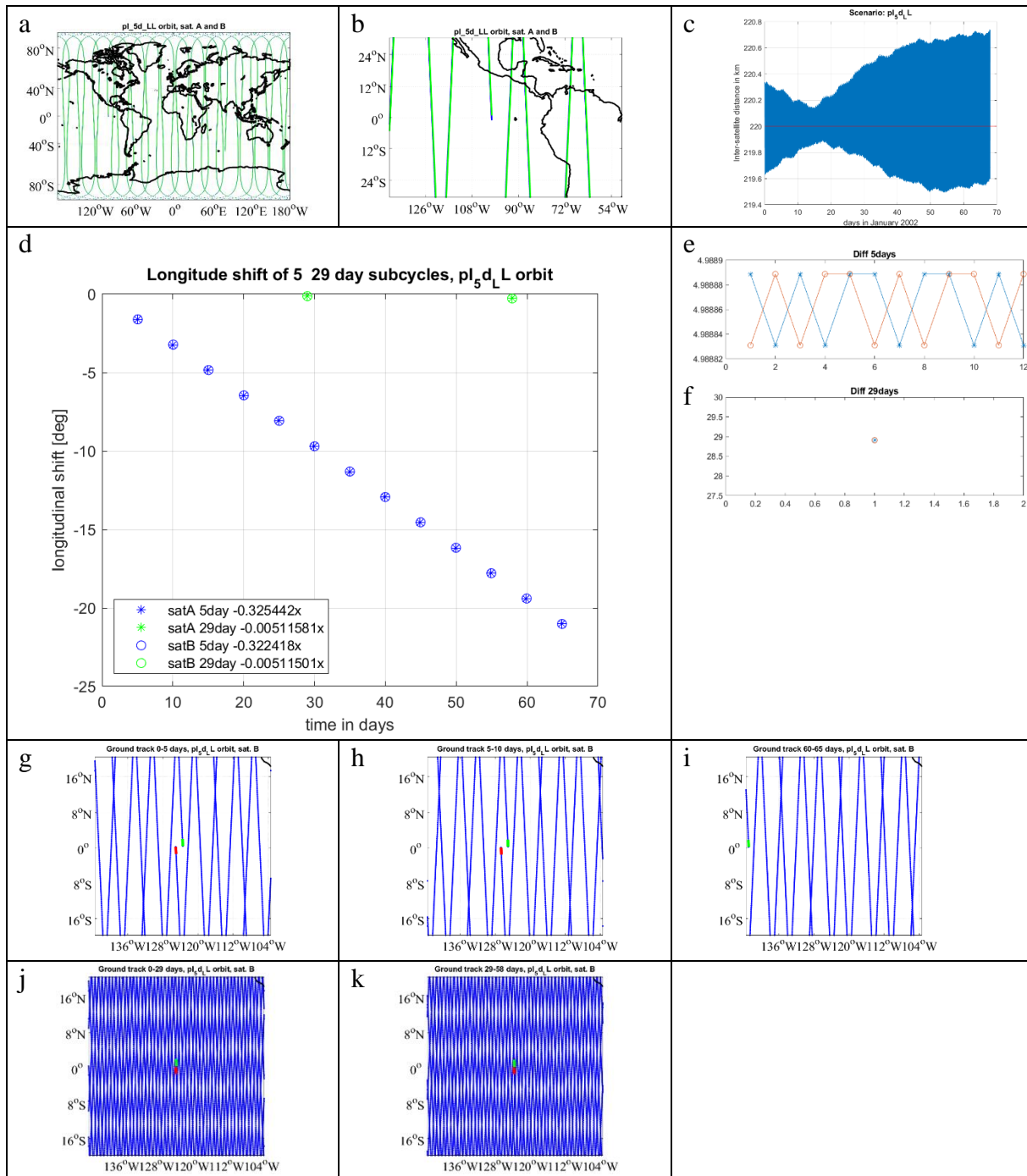
Figure 4-7 Orbit validation plots for the polar in-line pair (pI, 5d_LL). Determined longitude shift (leading satellite): -1.62721°/5 days. Nominal longitude shift (5d_LL): -1.628°/5 days. The stability of the 5- and 29-day subcycles is visualized in panels e and f. The groundtrack coverage within 5-day and 29-day segments is shown by the panels g to i and j to k, respectively.
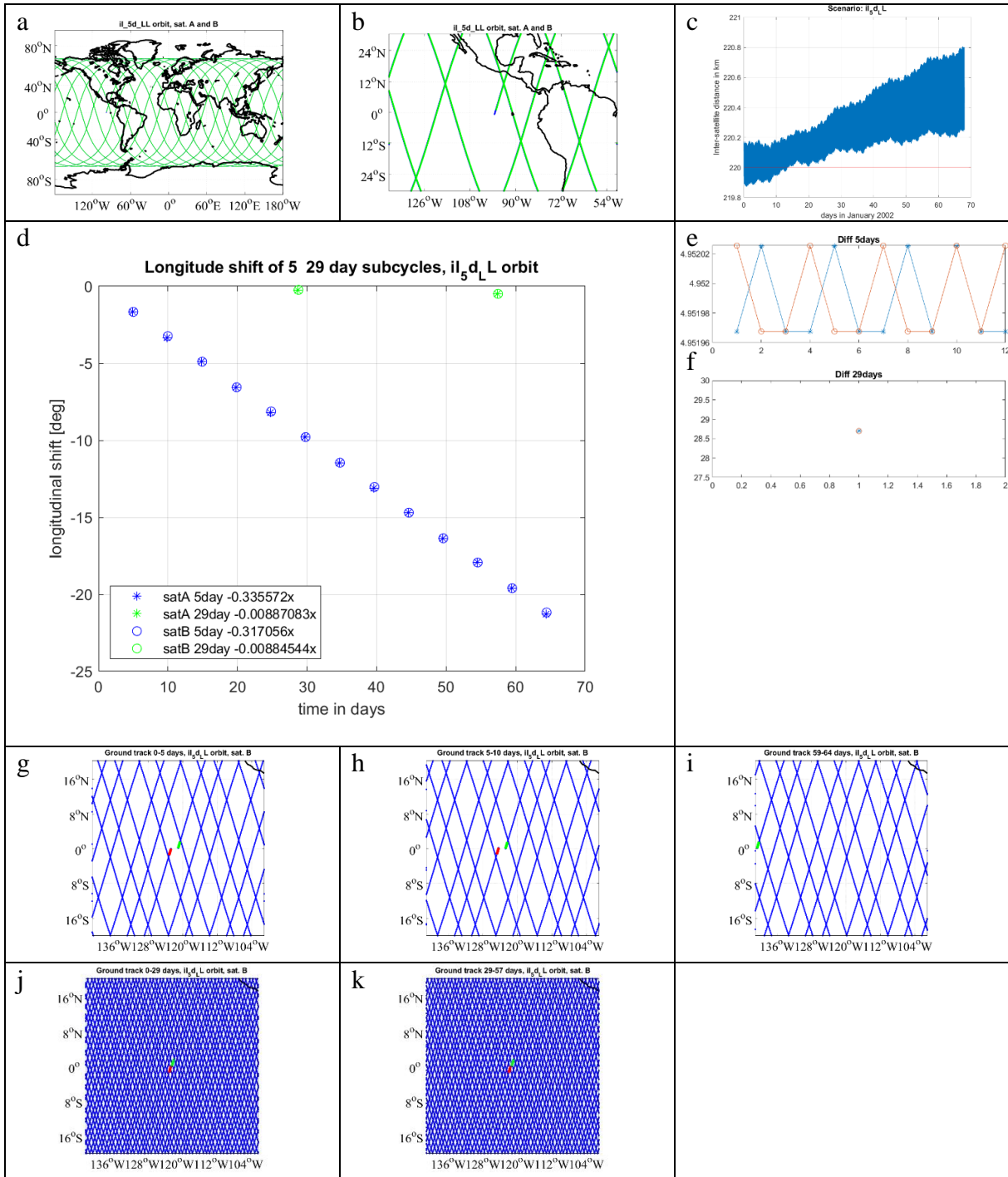
Figure 4-8 Orbit validation plots for the inclined in-line pair (iI, 5d_LL). Determined longitude shift (leading satellite): -1.67786°/5 days. Nominal longitude shift (5d_LL): -1.671°/5 days. The stability of the 5- and 29-day subcycles is visualized in panels e and f. The groundtrack coverage within 5-day and 29-day segments is shown by the panels g to i and j to k, respectively.
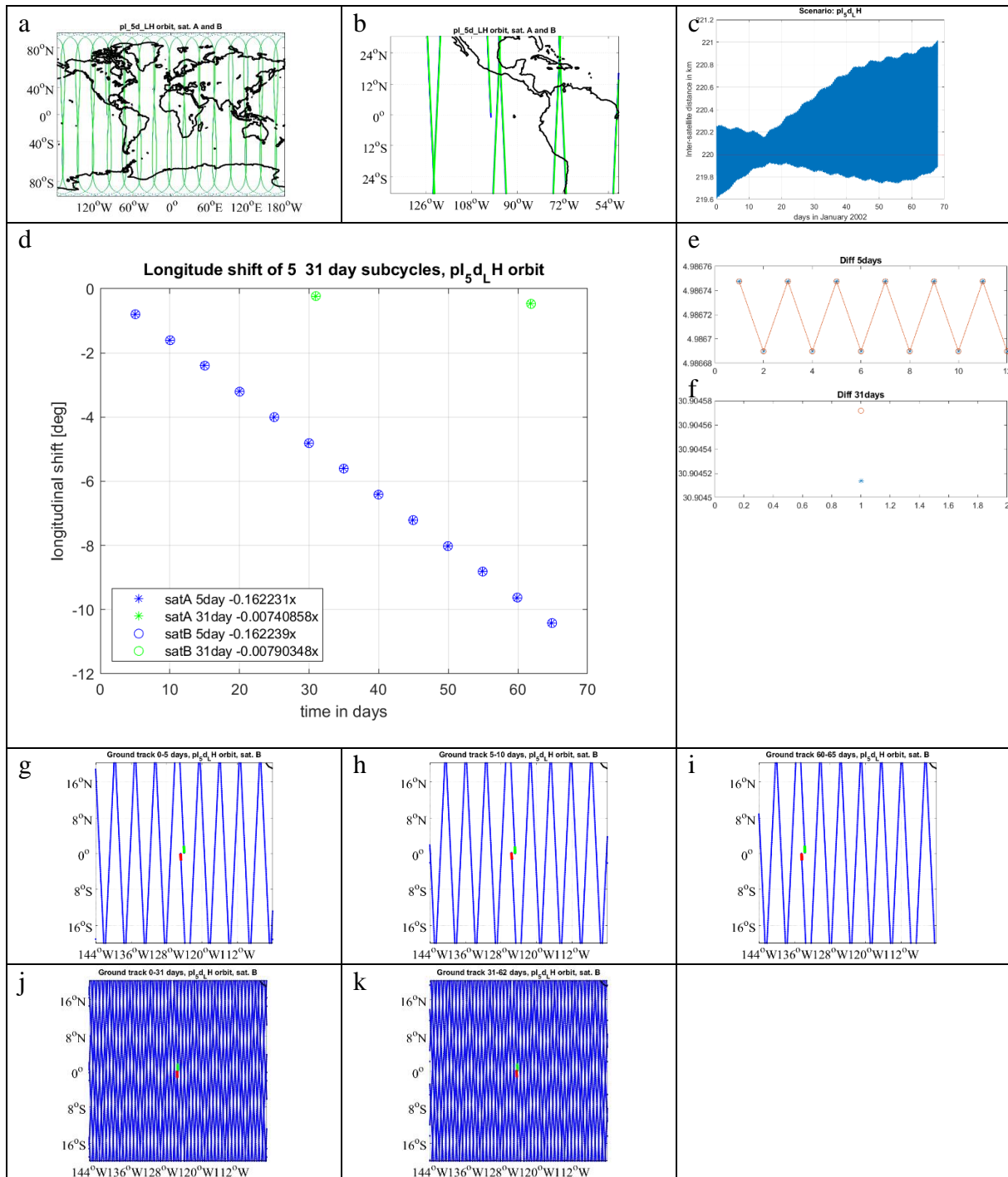
Figure 4-9 Orbit validation plots for the polar in-line pair (pI, 5d_LH). Determined longitude shift (leading satellite): -0.811155°/5 days. Nominal longitude shift (5d_LH): -0.790°/5 days. The stability of the 5- and 31-day subcycles is visualized in panels e and f. The groundtrack coverage within 5-day and 31-day segments is shown by the panels g to i and j to k, respectively.
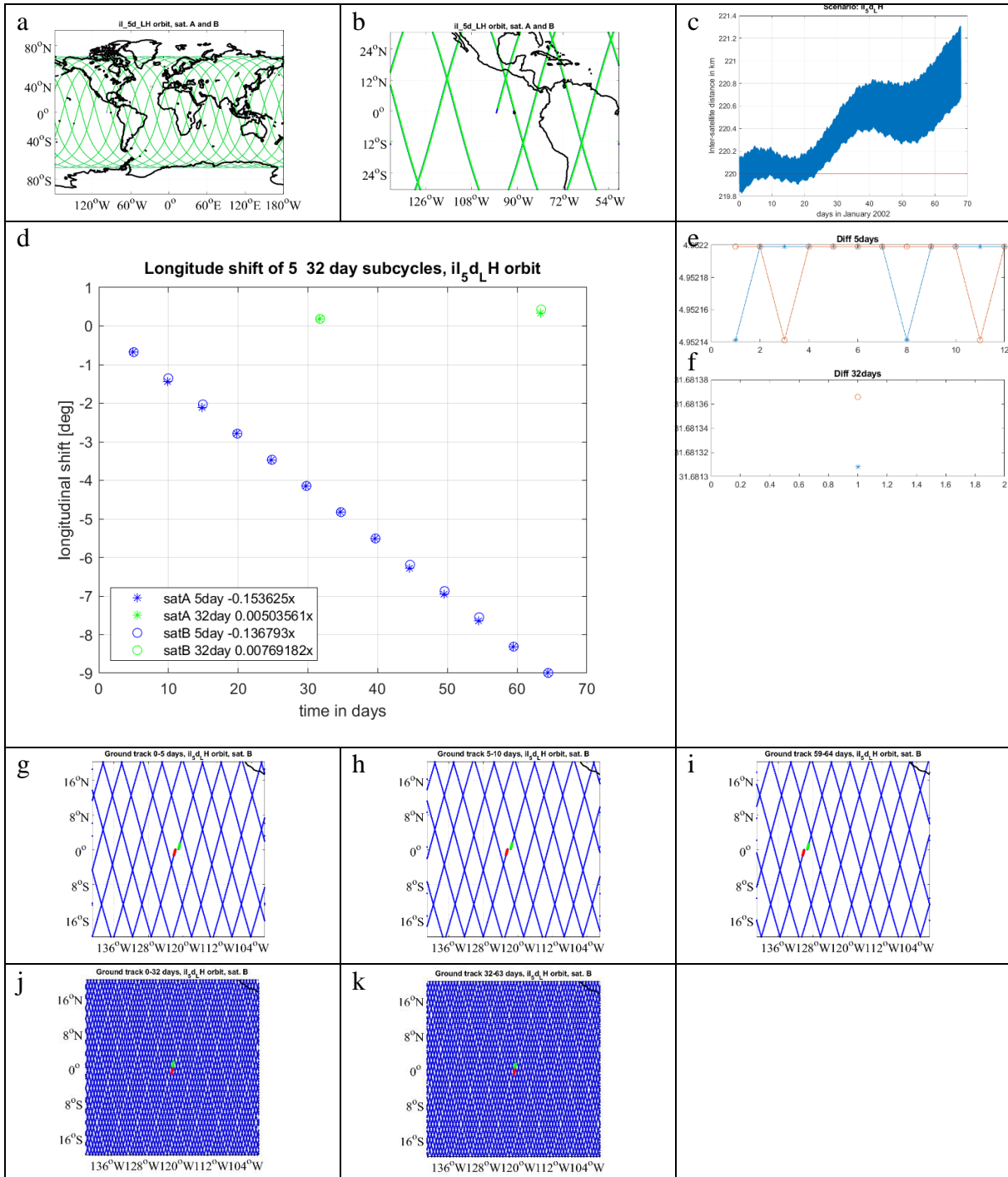
Figure 4-10 Orbit validation plots for the inclined in-line pair (iI, 5d_LH). Determined longitude shift (leading satellite): -0.768125°/5 days. Nominal longitude shift (5d_LH): -0.732°/5 days. The stability of the 5- and 32-day subcycles is visualized in panels e and f. The groundtrack coverage within 5-day and 32-day segments is shown by the panels g to i and j to k, respectively.

NGGM/MAGIC – Science Support Study During Phase A	*Final Report*	
	Doc. Nr:	MAGIC_FR
	Issue:	1.0
	Date:	15.11.2022
	Page:	48 of 466
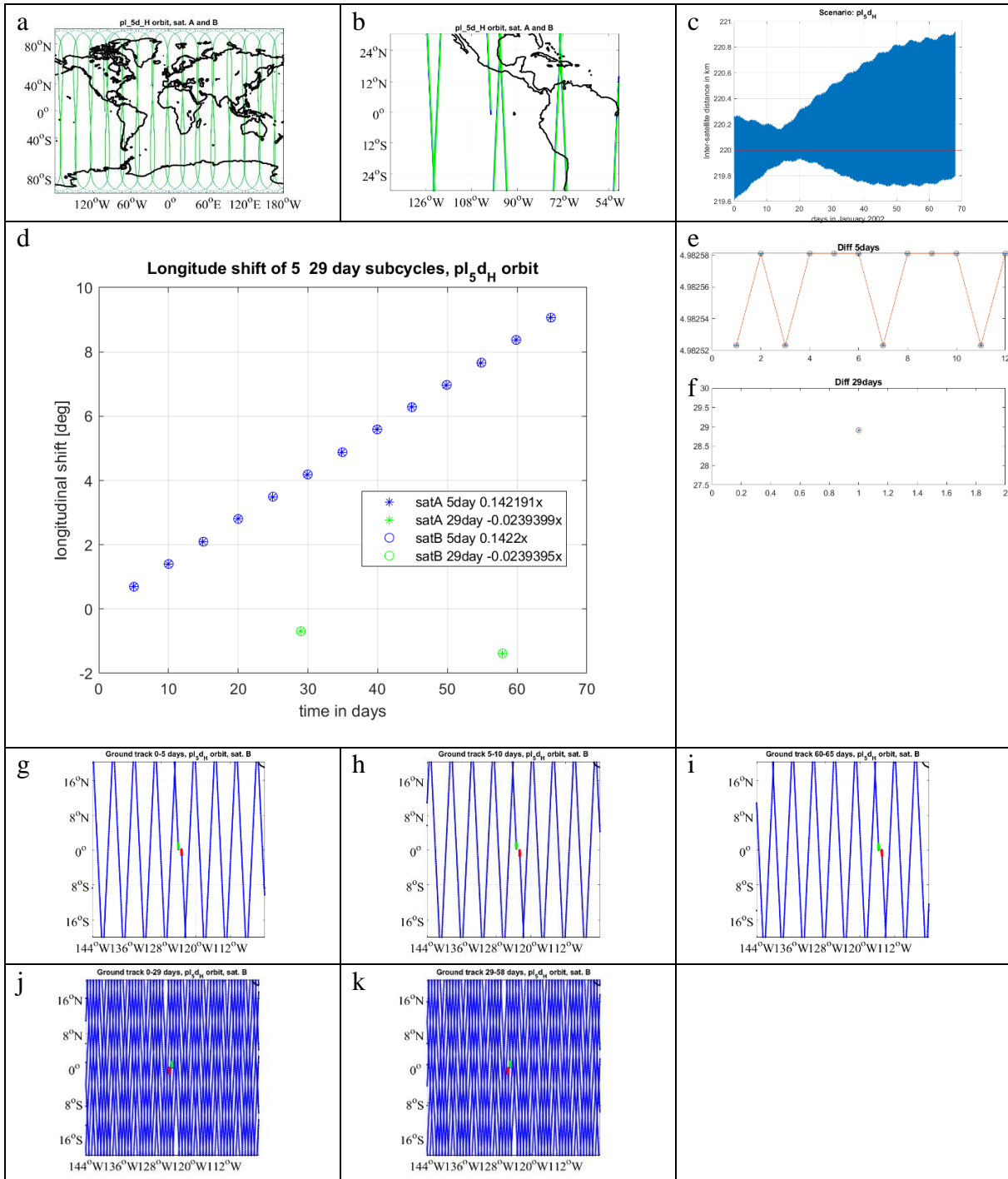
Figure 4-11 Orbit validation plots for the polar in-line pair (pI, 5d_H). Determined longitude shift (leading satellite): 0.710955°/5 days. Nominal longitude shift (5d_H): 0.781°/5 days. The stability of the 5- and 29-day subcycles is visualized in panels e and f. The groundtrack coverage within 5-day and 29-day segments is shown by the panels g to i and j to k, respectively.
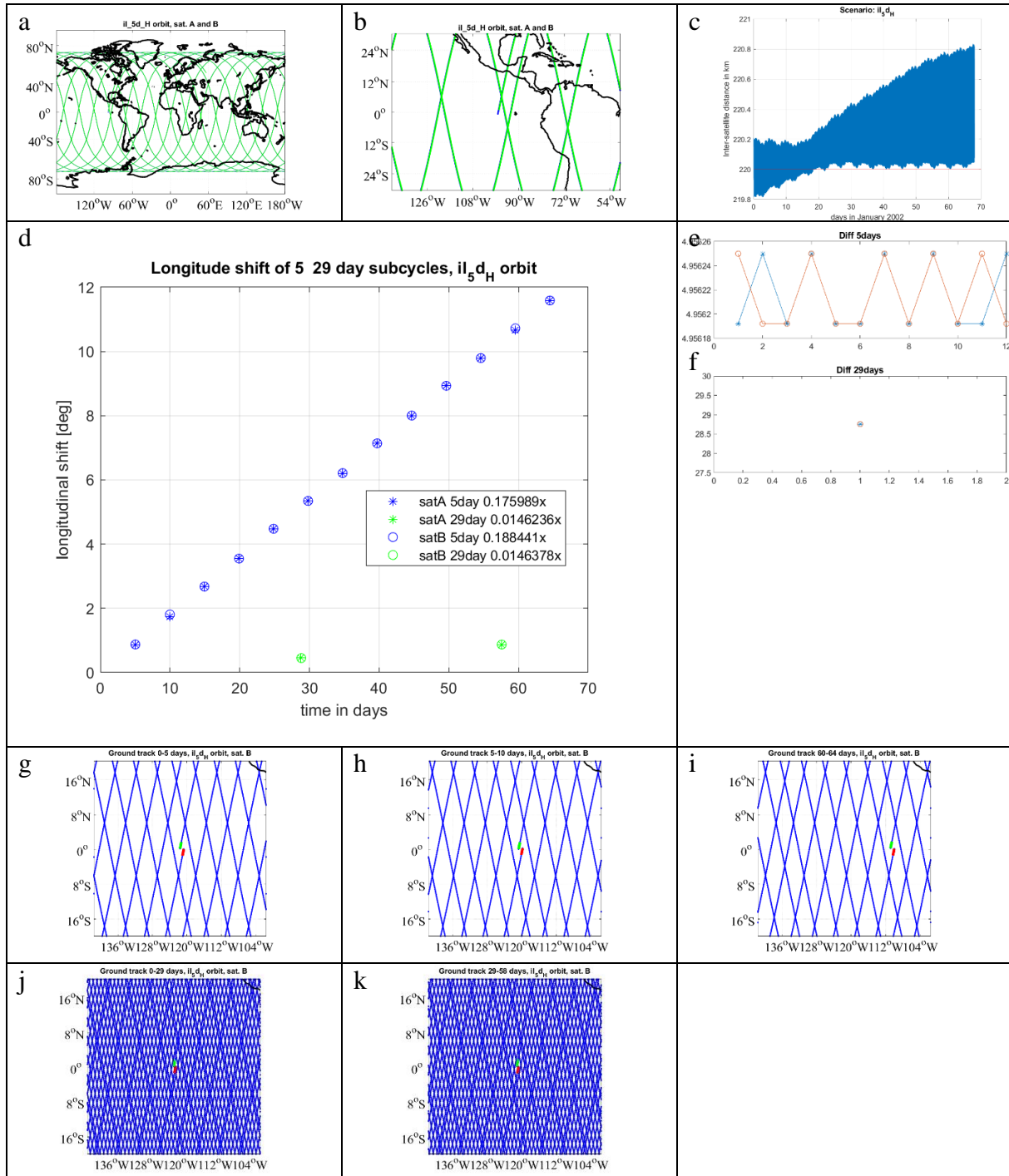
Figure 4-12 Orbit validation plots for the inclined in-line pair (iI, 5d_H). Determined longitude shift (leading satellite): 0.879945°/5 days. Nominal longitude shift (5d_H): 0.762°/5 days. The stability of the 5- and 29-day subcycles is visualized in panels e and f. The groundtrack coverage within 5-day and 29-day segments is shown by the panels g to i and j to k, respectively.
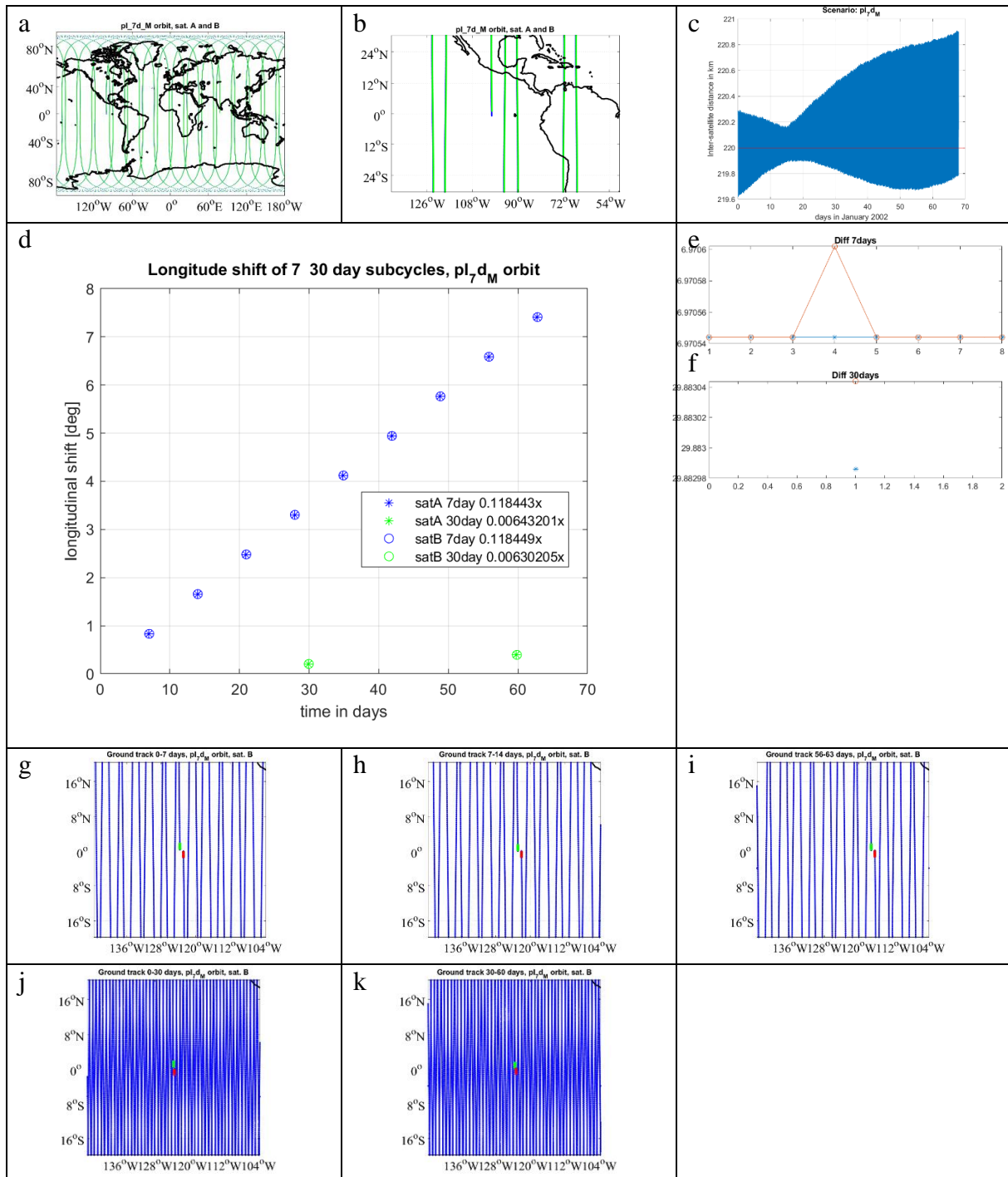
Figure 4-13 Orbit validation plots for the polar in-line pair (pI, 7d_M). Determined longitude shift (leading satellite): 0.829101°/7 days. Nominal longitude shift (7d_M): 0.786°/7 days. The stability of the 7- and 30-day subcycles is visualized in panels e and f. The groundtrack coverage within 7-day and 30-day segments is shown by the panels g to i and j to k, respectively.
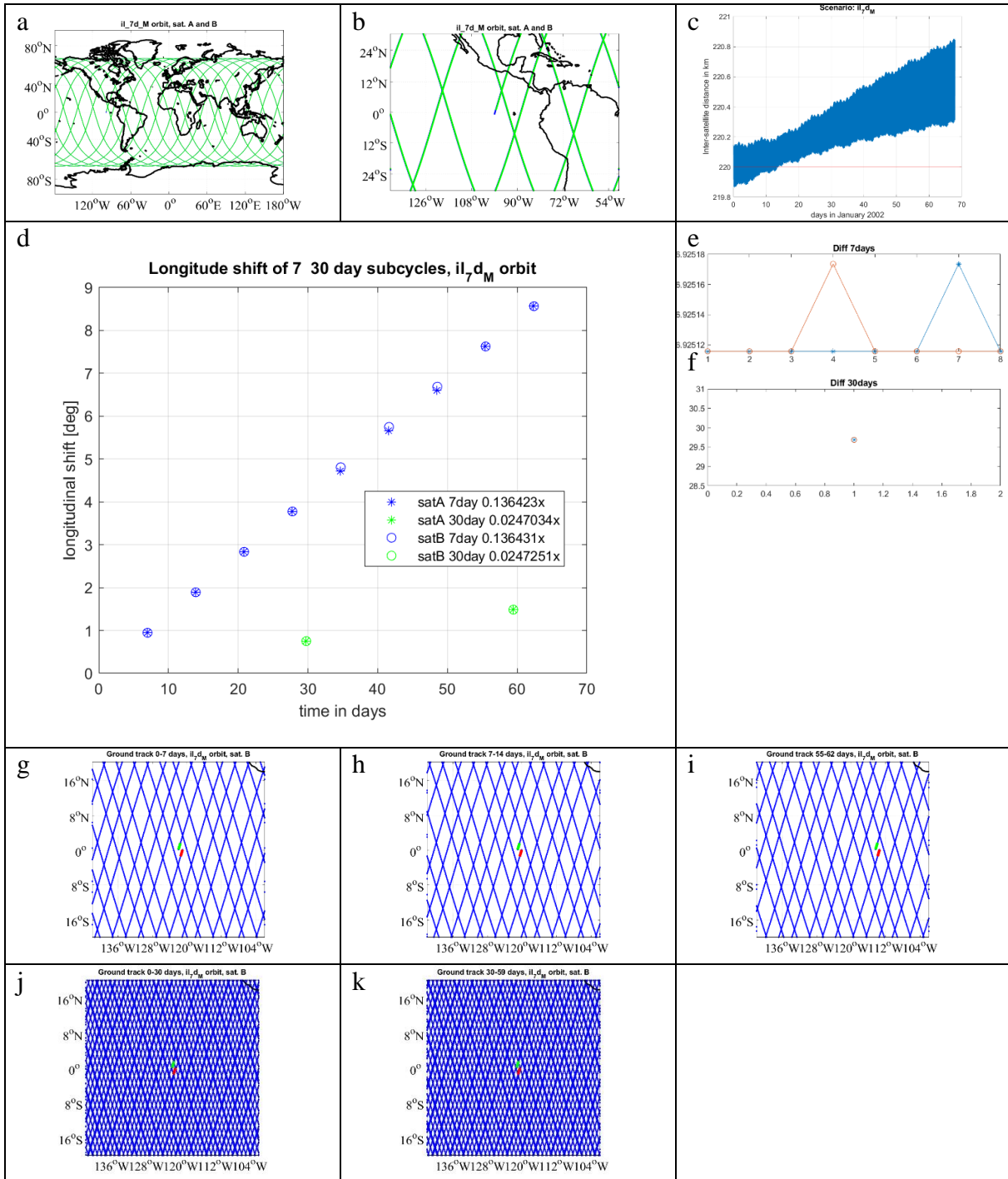
Figure 4-14 Orbit validation plots for the inclined in-line pair (iI, 7d_M). Determined longitude shift (leading satellite): 0.954961°/7 days. Nominal longitude shift (7d_M): 0.743°/7 days. The stability of the 7- and 30-day subcycles is visualized in panels e and f. The groundtrack coverage within 7-day and 30-day segments is shown by the panels g to i and j to k, respectively.

Polar in-line pair (**pI, 3d_H, ISD = 150 km**)	Polar in-line pair (**pI, 3d_H, ISD = 180 km**)
Incl. in-line pair (**iI, 3d_H, ISD = 150 km**)	Incl. in-line pair (**iI, 3d_H, ISD = 180 km**)
Polar in-line pair (**pI, 5d_LL, ISD = 150 km**)	Polar in-line pair (**pI, 5d_LL, ISD = 180 km**)
Incl. in-line pair (**iI, 5d_LL, ISD = 150 km**)	Incl. in-line pair (**iI, 5d_LL, ISD = 180 km**)
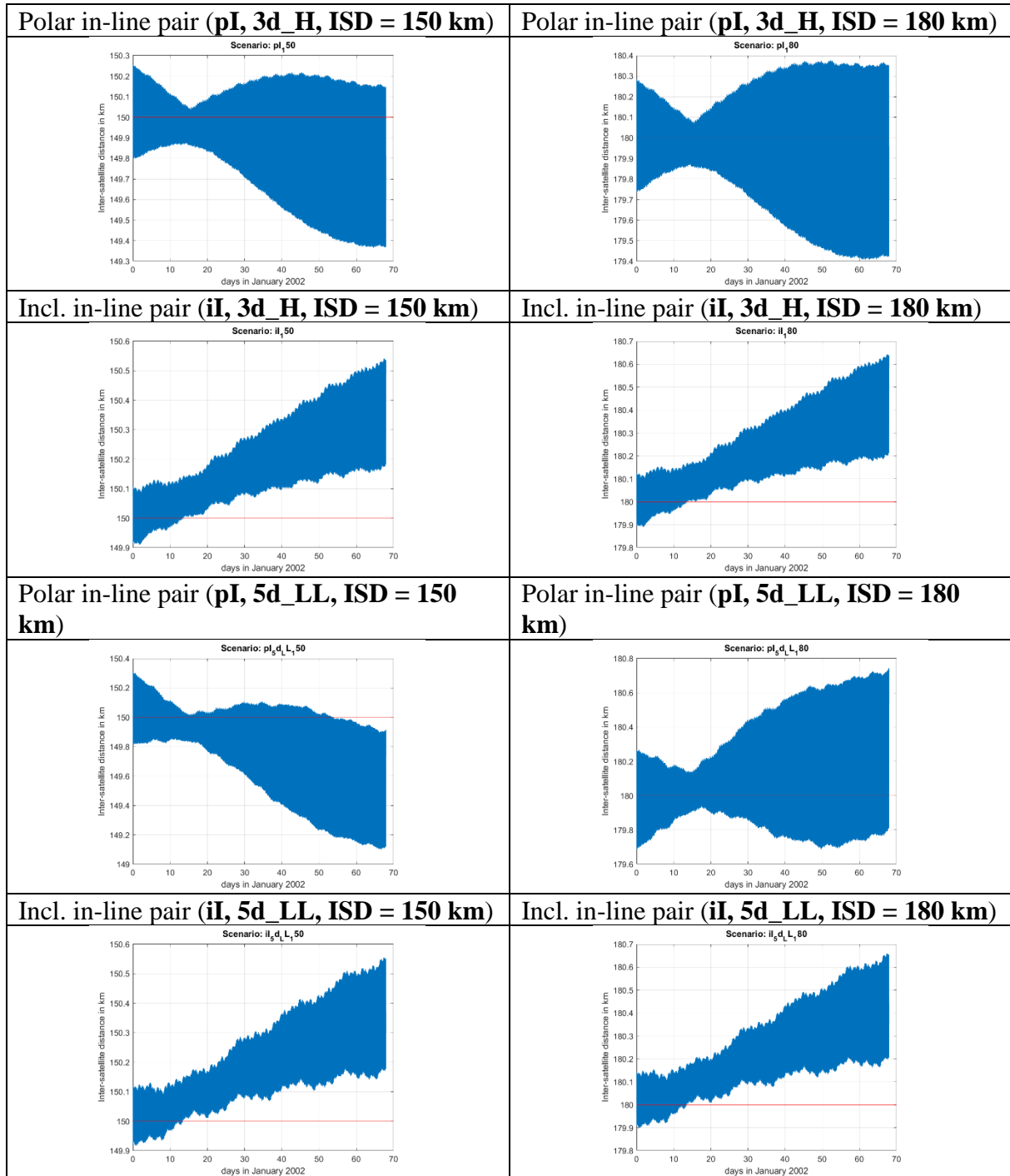
Figure 4-15 Visualization of the stability of the inter-satellite distance for the polar and inclined in-line pairs for 3d_H and 5d_LL in the cases of 150 km and 180 km inter-satellite distance.

5 PERFORMANCE AND ANALYSIS OF SCENARIOS 1-13

5.1 INTRODUCTION AND INITIAL ANALYSIS OF SCENARIOS 1-13

In this section, we present the full-scale gravity retrieval simulation results for various single- and double pair ll-sst configurations. Table 5-1 summarizes the orbit configurations for the scenarios 1 to 13. For scenarios 1 to 9, 3d_H orbits according to Table 2-1 are used. For scenario 12 and 13, 5d_LL and 5d_LH orbits are used, respectively.

The naming convention for the scenarios is as follows: "1" stands for a single-pair scenario, "2" for a double-pair scenario, respectively. "p" stands for the polar satellite pair, while "i" stands for the inclined satellite pair and "s" for the sun-synchronous satellite pair, respectively. "I" means that the satellites of a pair are flying in-line, while "P" is denoting a pendulum formation with the opening angle of the orbital planes of the leading and trailing satellite being specified in degrees after the "P". The letter "g" of "n" specifies which instrument noise is assumed for the respective satellite pair. "g" stands for GRACE-I noise and "n" for NGGM noise.

In the GRACE-I noise case, we assume three equally good accelerometer axes with a noise ASD of

$$acc_{x,y,z} = 1 \cdot 10^{-10} \sqrt{1 + \frac{0.005\ Hz}{f}} \quad \frac{m}{s^2/\sqrt{Hz}}. \tag{1}$$

In the NGGM noise case, we assume an ACC noise model of

$$acc_{los} = 1 \cdot 10^{-11} \sqrt{\left(\frac{10^{-3}Hz}{f}\right)^2 \bigg/ \left(\left(\frac{10^{-5}Hz}{f}\right)^2 + 1\right) + 1 + \left(\frac{f}{10^{-1}Hz}\right)^4} \quad \frac{m}{s^2/\sqrt{Hz}} \tag{2}$$

along the line of sight between the two satellites of a pair.

For both the GRACE-I and the NGGM noise case, we assume a LRI performance of

$$lri = 1.5 \cdot 10^{-9} \sqrt{\left(\left(\frac{0.028\ Hz}{f}\right)^3 + 1\right) \cdot \frac{\left(\frac{0.02\ Hz}{f}\right)}{\left(\left(\frac{0.00115\ Hz}{f}\right)^4 + 1\right)}} \quad \frac{m}{\sqrt{Hz}}. \tag{3}$$

and an orbit noise of

$$gps = 1 \cdot 10^{-2} \frac{m}{\sqrt{Hz}}. \tag{4}$$

The analytical amplitude spectral densities (ASDs) given by Equations (1) to (3) are visualized in Figure 5-1. The reason why we assume three good accelerometer axes in the GRACE-I noise case instead of assuming a degraded y axis is that the simulation list includes scenarios involving pendulum formations. In the TUM full-scale simulation software, the x axis of the accelerometer coordinate system is aligned along the orbit of the respective satellite. In the case

of a pendulum formation, this means that the accelerometer component which is directed towards the respective other satellite of a pair is changing periodically.

Table 5-1 Overview of the orbit configurations underlying the single- and double-pair full-scale simulations for the scenarios 1 to 13.

No.	Scenario	Pair 1			Pair 2		
		Incl.	In-line/ pend.	ACC noise	Incl.	In-line/ pend.	ACC noise
1	2_pIg_iIn	89	In-line	GRACE-I	70	In-line	NGGM
1a	1_pIg	89	In-line	GRACE-I	---	---	---
1b	1_iIn	70	In-line	NGGM			
2	2_pIn_iIn	89	In-line	NGGM	70	In-line	NGGM
2a	1_pIn	89	In-line	NGGM	---	---	---
3	1_pP15g	89	Pendulum 15°	GRACE-I	---	---	---
4	1_pP30g	89	Pendulum 30°	GRACE-I	---	---	---
5	2_pP15g_iIn	89	Pendulum 15°	GRACE-I	70	In-line	NGGM
6	2_pP30g_iIn	89	Pendulum 30°	GRACE-I	70	In-line	NGGM
7	2_pIg_iP15n	89	In-line	GRACE-I	70	Pendulum 15°	NGGM
8	2_pP15g_iP15n	89	Pendulum 15°	GRACE-I	70	Pendulum 15°	NGGM
9	2_pIg_sIn	89	In-line	GRACE-I	97	In-line	NGGM
10*	tbd	89	In-line	GRACE-I	89	Pendulum 15 or 30°	NGGM
11*	tbd	89	In-line	GRACE-I	89	Pendulum 15 or 30°	NGGM
12	2_pIn_iln (5d_LL)	89	In-line	NGGM	70	In-line	NGGM
13	2_pIg_iln (5d_LH)	89	In-line	GRACE-I	71.5	In-line	NGGM
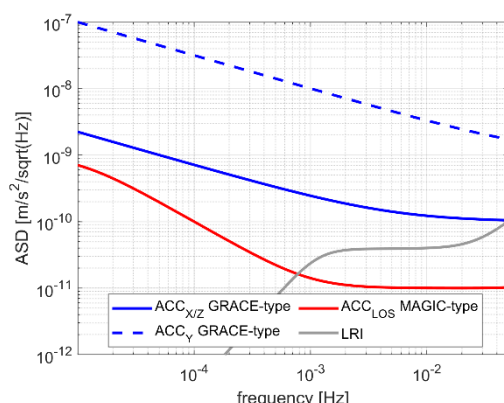
Figure 5-1 Amplitude spectral densities of the GRACE-I and the NGGM accelerometer and laser ranging interferometer noise assumed for the full-scale simulations for the scenarios 1 to 13. The dashed blue curve is not used: Instead, we assume ACC_y = ACC_x/z in the GRACE-I noise case. [Path: Various_Data_and_Models/ACC_LRI_Noise/]

between the x- and the y- axis, giving a significant reduction in the gravity retrieval performance of pendulum formations. As we assume that in a potential real pendulum satellite mission, either accelerometers with three well-performing axes or accelerometers which are able to rotate such that the accelerometer x-axis would be constantly aligned along the satellites' line of sight would be used, we assume three equally good axes in our simulations.

For all scenarios, we compare the simulation results in the instrument-only case (which just includes the static gravity field as signal and mainly shows the impact of the instrument noise specifications on the retrieved gravity field), the full noise nominal case (which additionally includes the temporal aliasing errors due to the ocean tide as well as the AOHIS signal as well as an estimate for the atmosphere and ocean background model error) as well as the full noise wiese case (in which daily gravity fields up to d/o 15 are co-estimated). The resulting retrieved gravity field coefficients represent a zero signal-field in the case of the instrument-only simulations, the estimated HIS field in the case of the full noise nominal simulations, and the estimated AOHIS field in the case of the full noise wiese simulations.

For all cases, we compute two subsequent 31-day solutions and nine subsequent 7-day solutions, starting from January 1st, 2002. These retrieval periods correspond to the repeat orbit subcycles of the 3d_H orbits. As shown in Section 3, the groundtrack coverage is equally good for subsequent subcycles, which is the prerequisite for subsequent short-term gravity solutions of the same quality.

In the following, we analyse the coefficients and the formal errors of the instrument-only case, the coefficient differences w.r.t. the mean HIS field of the full noise nominal case and the coefficient differences w.r.t. the mean AOHIS field in the full noise wiese case, thereby analysing the retrieval errors in all cases. All simulations are computed up to a maximum SH d/o of 120, except from the 7-day single pair simulations, where a reduced d/o of 100 is used because the groundtrack coverage of the single pair scenarios after 7 days does not suffice to resolve the coefficients of larger SH degrees.

Figure 5-2 shows the retrieval errors of the instrument-only case in terms of degree amplitudes. Panels a and b show the formal errors, while panels c and d show the retrieved coefficients. The

single-pair scenarios are displayed by the dotted curves, the double-pair scenarios by the solid curves, respectively.

First of all, we analyse the performance of the single-pair scenarios:

Among the single polar pairs, the in-line pair with the improved NGGM noise assumption, 1_pIn, shows the best performance and even outperforms the pendulum scenarios 1_pP15g and 1_pP30g. This shows that in the instrument-only case, i.e. in the case of zero temporal aliasing and background model errors, the benefit of replacing the GRACE-I noise by the NGGM noise is larger than the benefit of multi-directional observations that the pendulum configuration provides.

Considering the single polar pairs in the full noise case (Figure 5-3, panels a and b), we see that in the full noise case, the benefit of replacing an in-line by a pendulum configuration is larger than the benefit of reducing the accelerometer noise. This shows that the multi-directional observations of the pendulum configuration are especially beneficial for reducing the large temporal aliasing errors which are included in the full noise case.

In both the instrument-only and the full noise cases, increasing the opening angle of the pendulum orbits from 15 to 30 degrees improves the results, as the observation direction changes over a larger angle during the pendulum motion.

The solving of the normal equations for the single inclined pair scenario 1_iIn requires a regularization, because of the data gaps over the polar caps. We apply a spherical cap regularization, in which normal equations for a grid filling the polar gaps are assembled, the observations on which are set to zero such that the resulting gravity field solutions are pushed towards zero over the poles. This can be done with various weighting factors for the regularization matrix. We present three solutions for 1_iIn, which differ only in the weighting factor chosen for the regularization matrix. As shown by Figure 5-6, changing the regularization weight only affects the resulting solution over the polar caps. In the data-covered region, the resulting solution does not change, demonstrating that the regularization only applies where it should: in the regions of missing data. In the 2-dimensinal SH domain, the polar gaps map to the near-zonal coefficients, which can be seen by comparing the three 1_iIn solutions.

Now, we analyse the double-pair scenarios:

Comparing the double-pair scenarios in Figure 5-2 shows that the worst performing double pair is 2_pIn_sIn, which includes a satellite pair flying in sun-synchronous orbit as the second satellite pair. The reason for the bad performance of 2_pIn_sIn compared to the remaining double-pair scenarios is the too small angle between the orbital planes of the polar and the sun-synchronous pair, the inclination of which is 97° compared to the 70° inclination of the inclined pairs included in the other double-pair scenarios. This effect is even more prominent in the full noise case (Figure 5-3 a and b), where the 2_pIn_sIn scenario is outperformed by the pendulum single pair scenario 1_pP30g.

Figure 5-2 and Figure 5-3 show that the performance of most of the double-pair scenarios is very similar to each other. We especially note that including one or two pendulum pairs as part of a double-pair configuration does not show a large impact compared to the standard Bender configuration. The improvement by using the NGGM noise assumption for both satellite pairs

(which is done for scenario 2_pIn_iIn) which is visible in the formal errors (see Figure 5-2 a and b) becomes masked by the larger-amplitude temporal aliasing errors in the full noise case (see Figure 5-3 a and b).

Comparing the 3d_H double pair scenarios to the 5d_LL and 5d_LH scenarios in Figure 5-2 and Figure 5-3, we see an improvement by lowering the orbit altitude, especially in the large SH degrees.

As can be seen in panels c and d of Figure 5-3, the relative behaviour of the double-pair configurations in the full noise wiese case is similar to the full noise nominal case.

Figure 5-4 and Figure 5-5 show the degree median plots corresponding to the degree amplitude plots shown by Figure 5-2 and Figure 5-3. The reason why we show them additionally here is that the degree median curves are less dominated by individual worse-resolved SH coefficients compared to the degree amplitude curves. Thereby, e.g. the performance of the single inclined pair within the data-covered region can be assessed more realistically: The degree medians of scenario 1_iIn are smaller than the degree medians of the single polar pairs. Especially for SH degrees above about 50, the performance of 1_iIn as estimated from the degree medians comes close to the performance of the analysed double pair scenarios.
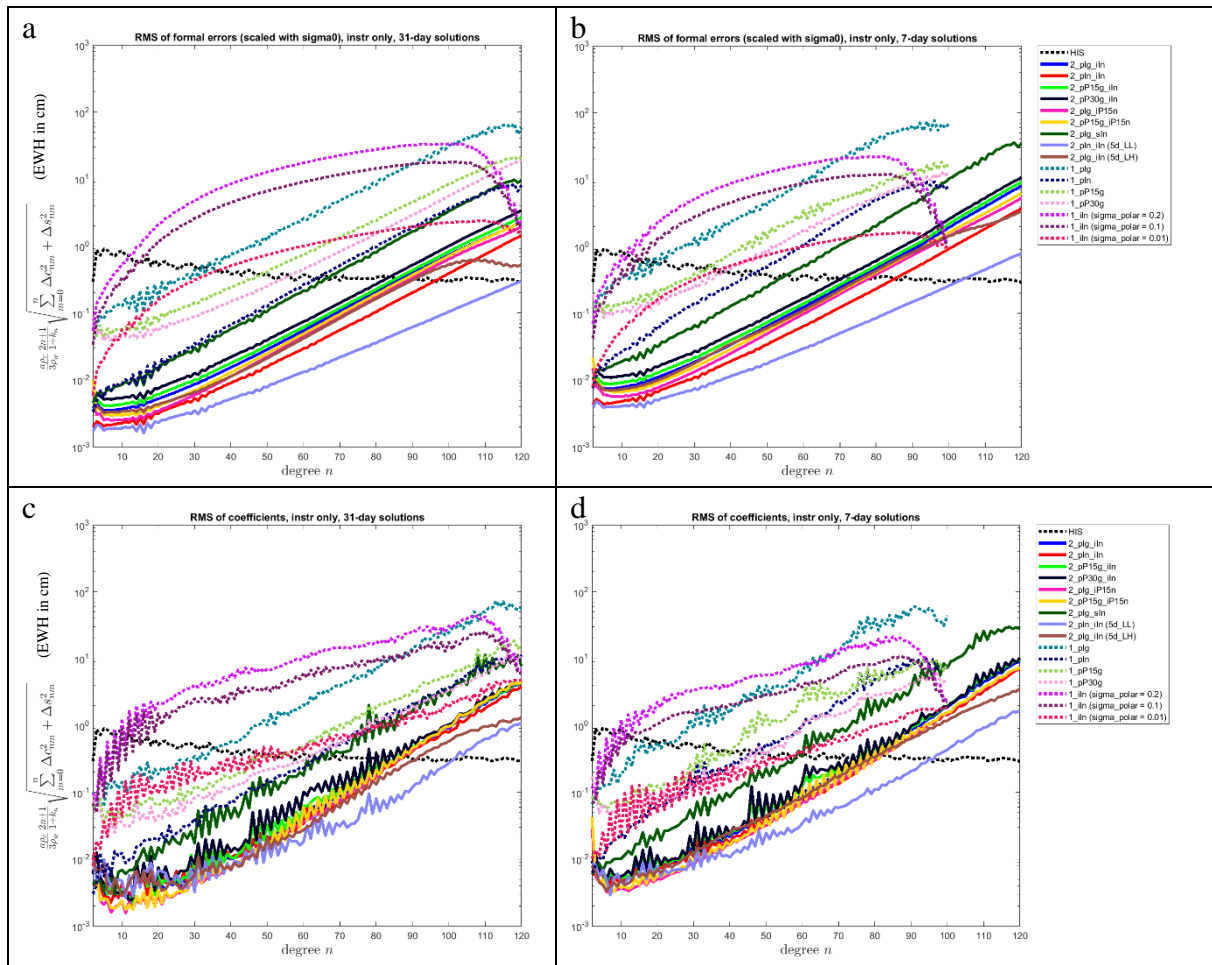
Figure 5-2 Degree amplitude plots of the instrument-only full-scale simulations of the scenarios 1 to 9 and 12 to 13 of Table 5-1. Panels a and b show the formal errors scaled by the a posteriori variance factor. Panels c and d show the retrieved coefficients. The plots in the left column show the curves averaged over two 31-day solutions, while the plots in the right column show the curves averaged over nine 7-day solutions. Single-pair scenarios are shown by dotted lines while double-pair scenarios are shown by solid lines. [Path: Deliverables/D1/simulation_results/full_scale_simulator_v009/old_noise_scaling/instrument_only/]
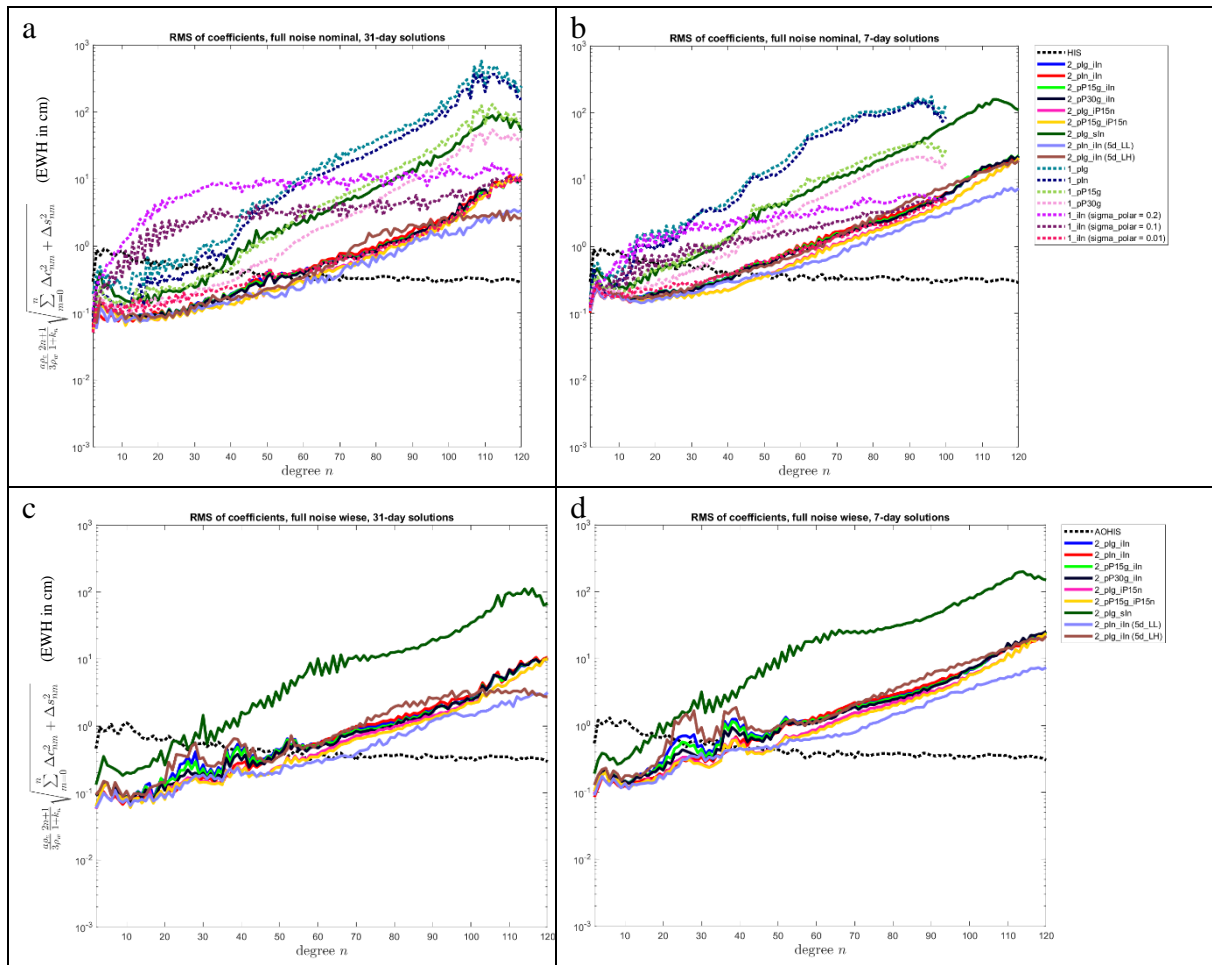
Figure 5-3 Degree amplitude plots of the full-noise full-scale simulations of the scenarios 1 to 9 and 12 to 13 of Table 5-1. Panels a and b show the coefficient differences of the full noise nominal simulations w.r.t. the mean HIS signal. Panels c and d show the coefficient differences of the full noise wiese simulations w.r.t. the mean AOHIS signal. The plots in the left column show the curves averaged over two 31-day solutions, while the plots in the right column show the curves averaged over nine 7-day solutions. Single-pair scenarios are shown by dotted lines while double-pair scenarios are shown by solid lines. [Path: Deliverables/D1/simulation_results/full_scale_simulator_v009/old_noise_scaling/]

Figure 5-4 Degree median plots of the instrument-only full-scale simulations of the scenarios 1 to 9 and 12 to 13 of Table 5-1. Panels a and b show the formal errors scaled by the a posteriori variance factor. Panels c and d show the retrieved coefficients. The plots in the left column show the curves averaged over two 31-day solutions, while the plots in the right column show the curves averaged over nine 7-day solutions. Single-pair scenarios are shown by dotted lines while double-pair scenarios are shown by solid lines. [Path: Deliverables/D1/simulation_results/full_scale_simulator_v009/old_noise_scaling/instrument_only/]
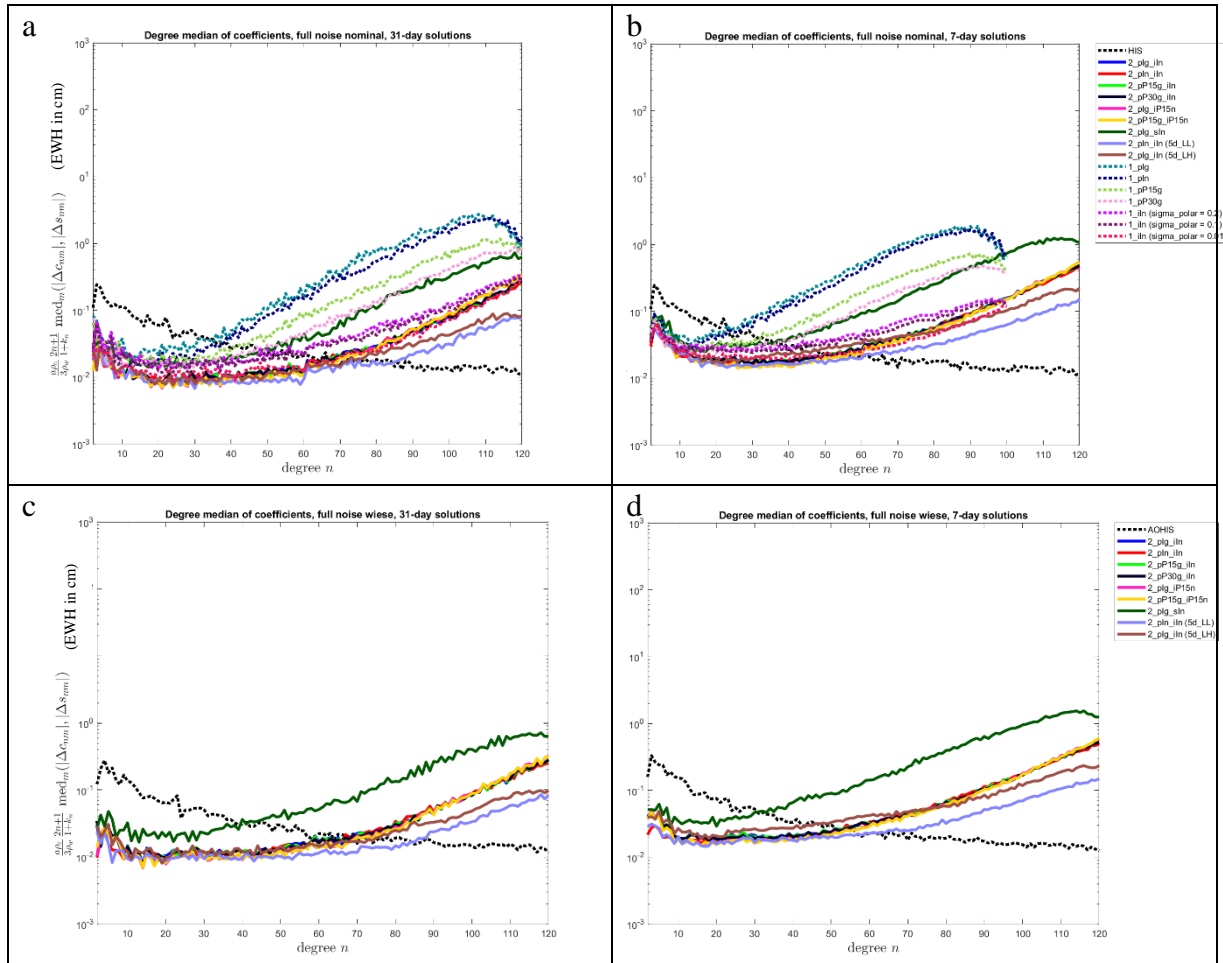
Figure 5-5 Degree median plots of the full-noise full-scale simulations of the scenarios 1 to 9 and 12 to 13 of Table 5-1. Panels a and b show the coefficient differences of the full noise nominal simulations w.r.t. the mean HIS signal. Panels c and d show the coefficient differences of the full noise wiese simulations w.r.t. the mean AOHIS signal. The plots in the left column show the curves averaged over two 31-day solutions, while the plots in the right column show the curves averaged over nine 7-day solutions. Single-pair scenarios are shown by dotted lines while double-pair scenarios are shown by solid lines. [Path: Deliverables/D1/simulation_results/full_scale_simulator_v009/old_noise_scaling/]

Figure 5-6 Triangle plots and spatial EWH grids of the 31-day simulation results for the single inclined pair (1_iIn, 3d_H), with three different weighting factors of the regularization matrix applied. For the plots in the left column, the applied regularization is weakest; for the plots in the right column, it is strongest. Panels a to f show the instrument only solutions and panels g to l the full noise solutions, respectively. All plots are displayed with one consistent colour scale. [Path: Deliverables/D1/simulation_results/full_scale_simulator_v009/old_noise_scaling/]

The more detailed comparison of the performance of the individual scenarios can be done using the triangle plots and spatial EWH grids of the retrieval errors shown by Figure 5-7 to Figure 5-14. Figure 5-7 and Figure 5-8 show the instrument only and full noise nominal simulation results for the four polar single pair scenarios. A comparison of the instrument only and full noise results reveals that the temporal aliasing errors included in the full noise results are especially visible in the sectorial coefficients in the triangle plots and show up as longitudinal striping pattern in the EWH grids. These errors become reduced in the pendulum scenarios. Since these errors are not included in the instrument only computations, the benefit of the pendulum is not as pronounced in Figure 5-7. In the instrument only results, as noted above, especially the benefit of an improved accelerometer is visualized, which is especially pronounced for the low SH degrees.

The instrument-only, full noise nominal and full noise wiese results of the double-pair scenarios are shown by Figure 5-9, Figure 5-10 and Figure 5-11 for the double in-line pairs, and Figure 5-12, Figure 5-13 and Figure 5-14 for the double pairs including at least one pendulum pair. Compared to the single-pair results, the double-pair formations show considerably smaller retrieval errors, which is expected due to the number of observations, the groundtrack coverage and the contained multi-directional observations. As already observed in the degree amplitude and median plots, the best-performing satellite configuration among the analysed scenarios is 2_pIn_iIn (5d_LL), which can mainly be explained by the lower orbit of the satellites. Also, the observation that there is no added value by flying a pendulum pair as part of a Bender-type constellation can be repeated.

In order to assess the contributions of the polar and the inclined pair in a standard Bender double-pair configuration, we plot the coefficient error triangles of the scenarios 1_pIn, 1_iIn and 2_pIn_iIn side by side in Figure 5-15.

As the normal equation system of the double pair scenarios are computed by adding the normal equation systems of the polar and the inclined pair, we assume that the weight of the individual NEQ systems in the combined solution can be visualized by looking at the coefficient errors of the respective single-pair solutions. As the single inclined pair solution 1_iIn needs a regularization to be solved, we keep in mind that the coefficients in the 1_iIn solution that are affected by the regularization (these are the near-zonal coefficients) are actually given much smaller weights in the combination with the 1_pIn NEQ system than suggested by the errors in the regularized 1_iIn single-pair solution.

As shown by Figure 5-15, the retrieval errors of the coefficients outside the "polar gap wedge" of the 1_iIn solution are comparable to the respective coefficients in the 2_pIn_iIn solution. This is the case both for the instrument only and the full noise simulation results. That means that for the coefficients that can be resolved by the inclined pair, the 2_pIn_iIn solution is dominated by the 1_iIn NEQs. The 1_pIn NEQs are however required in order to achieve a global solution: For the near-zonal coefficients, the observations of the polar pair are needed.
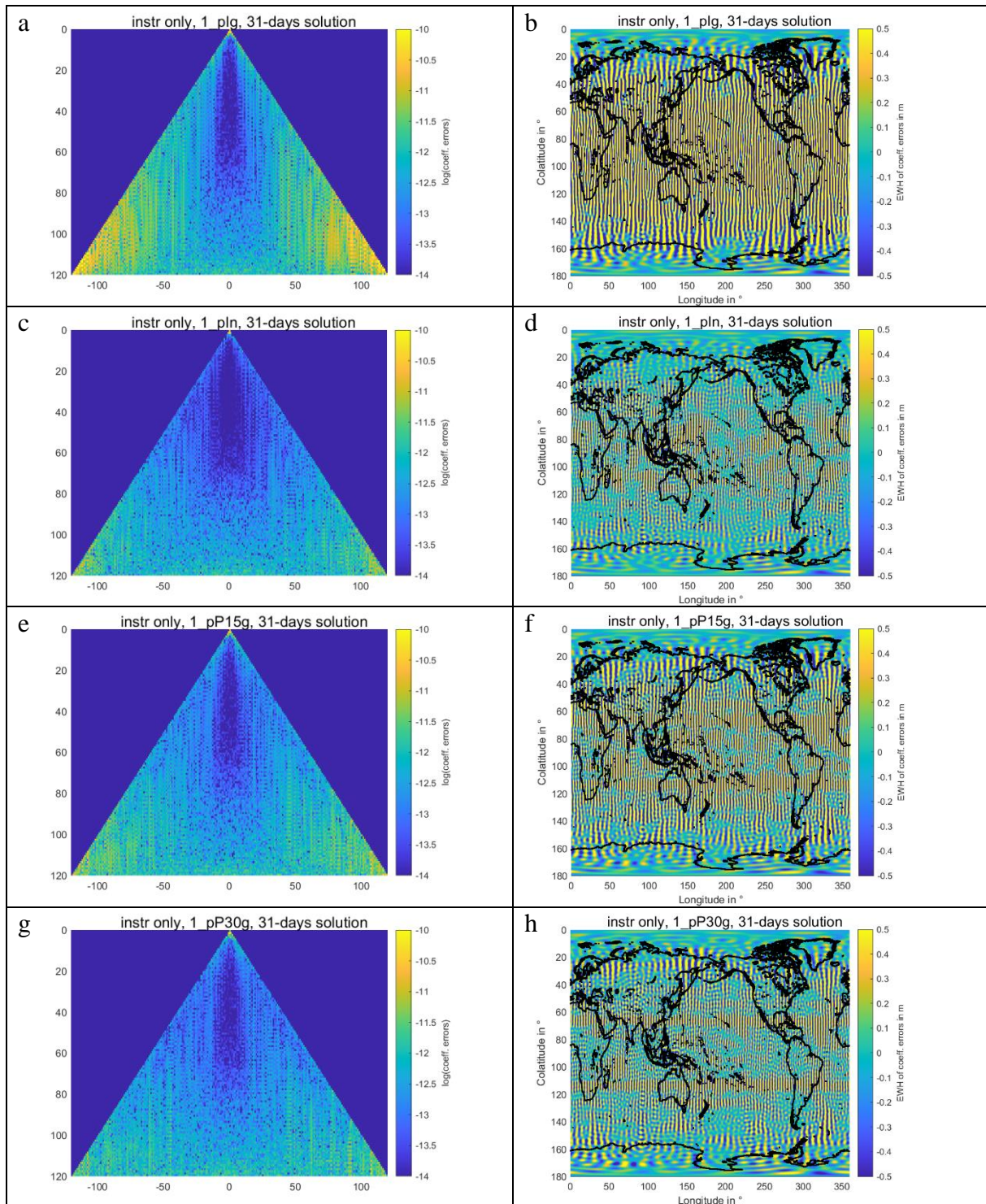
Figure 5-7 Triangle plots and spatial EWH grids of the 31-day instrument-only simulation results for the single-pair scenarios 1_pIg (panels a and b), 1_pIn (panels c and d), 1_pP15g (panels e and f) and 1_pP30g (panels g and h). The scenarios are defined in Table 5-1. All plots are displayed with one consistent colour scale. [Path: Deliverables/D1/simulation_results/full_scale_simulator_v009/old_noise_scaling/instrument_only/]

|		Final Report	
NGGM/MAGIC – Science Support Study During Phase A		Doc. Nr:	MAGIC_FR
		Issue:	1.0
		Date:	15.11.2022
		Page:	65 of 466

Figure 5-8 Triangle plots and spatial EWH grids of the 31-day full noise nominal simulation results for the single-pair scenarios 1_pIg (panels a and b), 1_pIn (panels c and d), 1_pP15g (panels e and f) and 1_pP30g (panels g and h). The scenarios are defined in Table 5-1. All plots are displayed with one consistent colour scale. [Path: Deliverables/D1/simulation_results/full_scale_simulator_v009/old_noise_scaling/full_noise_nominal/]
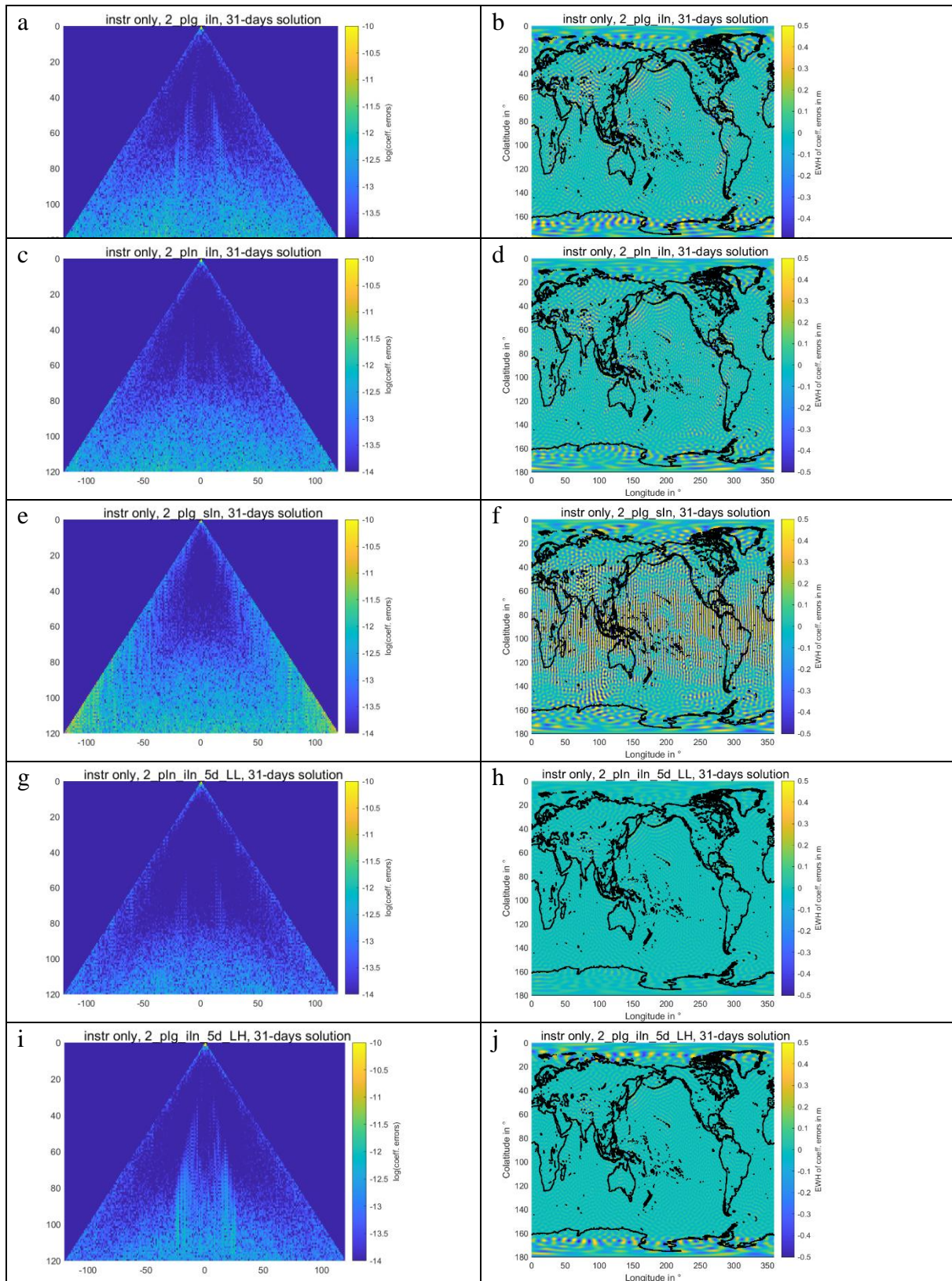
Figure 5-9 Triangle plots and spatial EWH grids of the 31-day instrument only simulation results for the double in-line pair scenarios 2_pIg_iIn (panels a and b), 2_pIn_iIn (panels c and d), 2_pIg_sIn (panels e and f), 2_pIn_iIn (5d_LL) (panels g and h) and 2_pIg_iIn (5d_LH) (panels i and j). The scenarios are defined in Table 5-1. All plots are displayed with one consistent colour scale. [Path: Deliverables/D1/simulation_results/full_scale_simulator_v009/old_noise_scaling/instrument_only/]
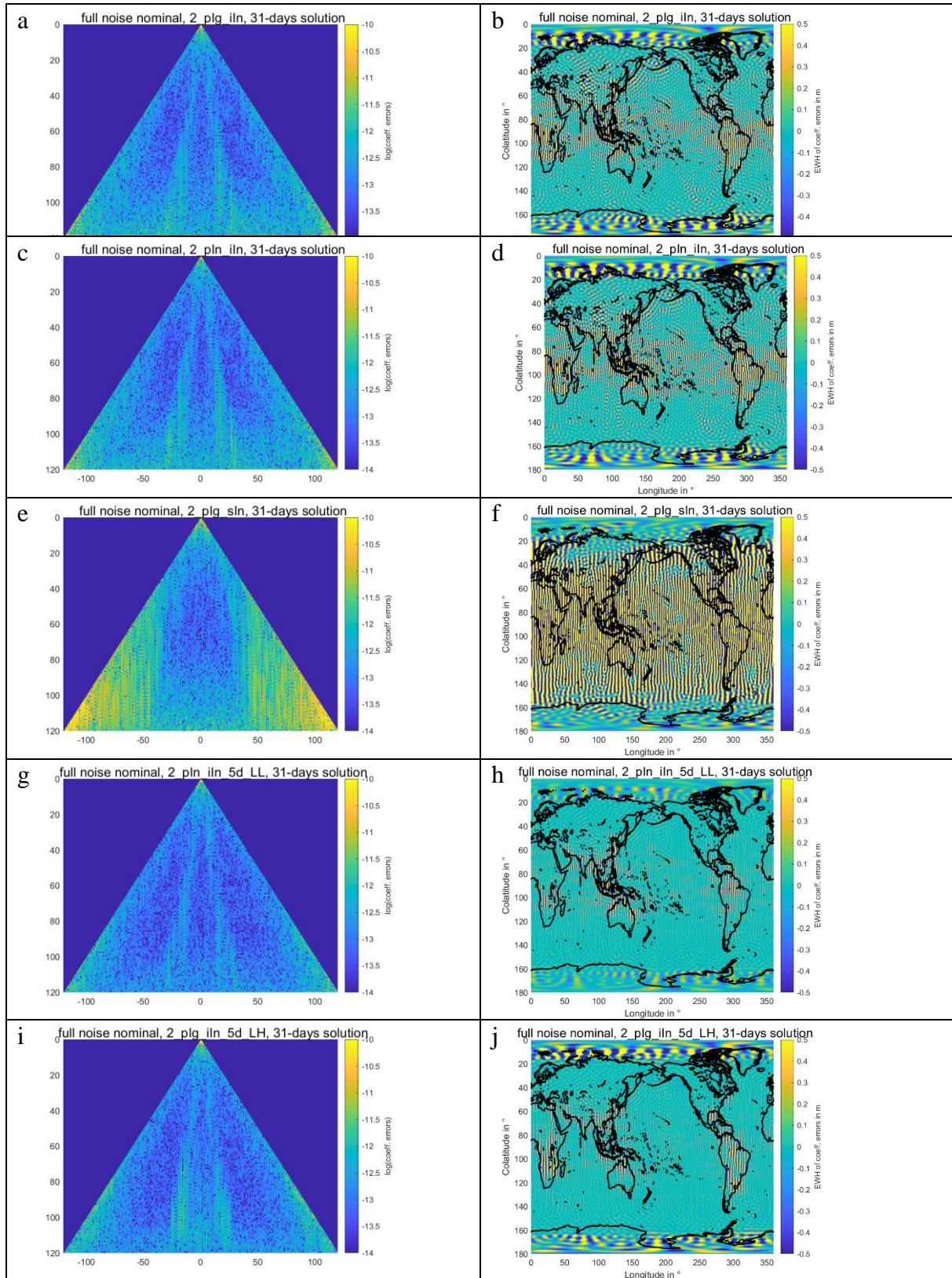
Figure 5-10 Triangle plots and spatial EWH grids of the 31-day full noise nominal simulation results for the double in-line pair scenarios 2_pIg_iIn (panels a and b), 2_pIn_iIn (panels c and d), 2_pIg_sIn (panels e and f), 2_pIn_iIn (5d_LL) (panels g and h) and 2_pIg_iIn (5d_LH) (panels i and j). The scenarios are defined in Table 5-1. All plots are displayed with one consistent colour scale. [Path: Deliverables/D1/simulation_results/full_scale_simulator_v009/old_noise_scaling/full_noise_nominal/]
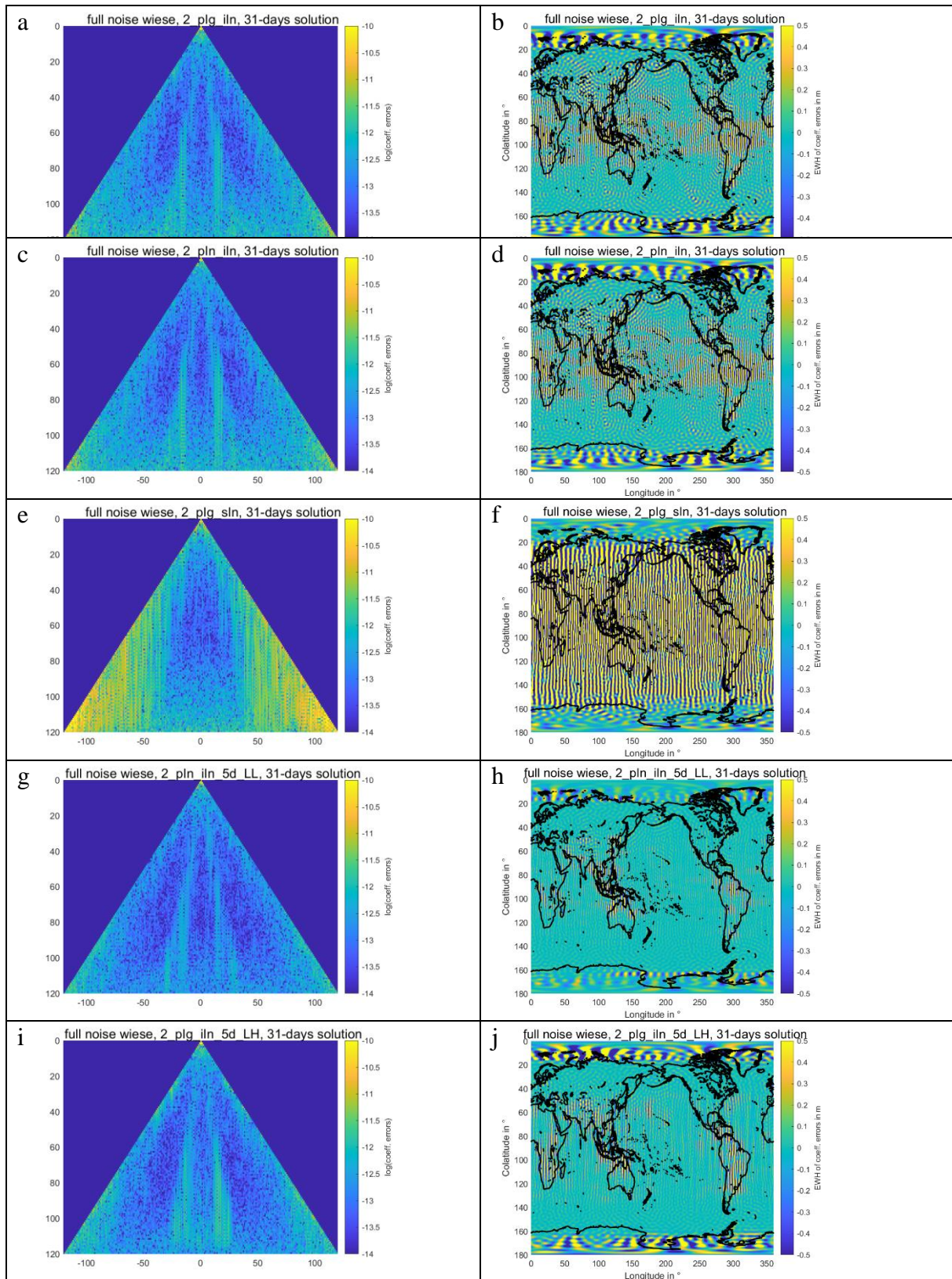
Figure 5-11 Triangle plots and spatial EWH grids of the 31-day full noise wiese simulation results for the double in-line pair scenarios 2_pIg_iIn (panels a and b), 2_pIn_iIn (panels c and d), 2_pIg_sIn (panels e and f), 2_pIn_iIn (5d_LL) (panels g and h) and 2_pIg_iIn (5d_LH) (panels i and j). The scenarios are defined in Table 5-1. All plots are displayed with one consistent colour scale. [Path: Deliverables/D1/simulation_results/full_scale_simulator_v009/old_noise_scaling/full_noise_wiese/]
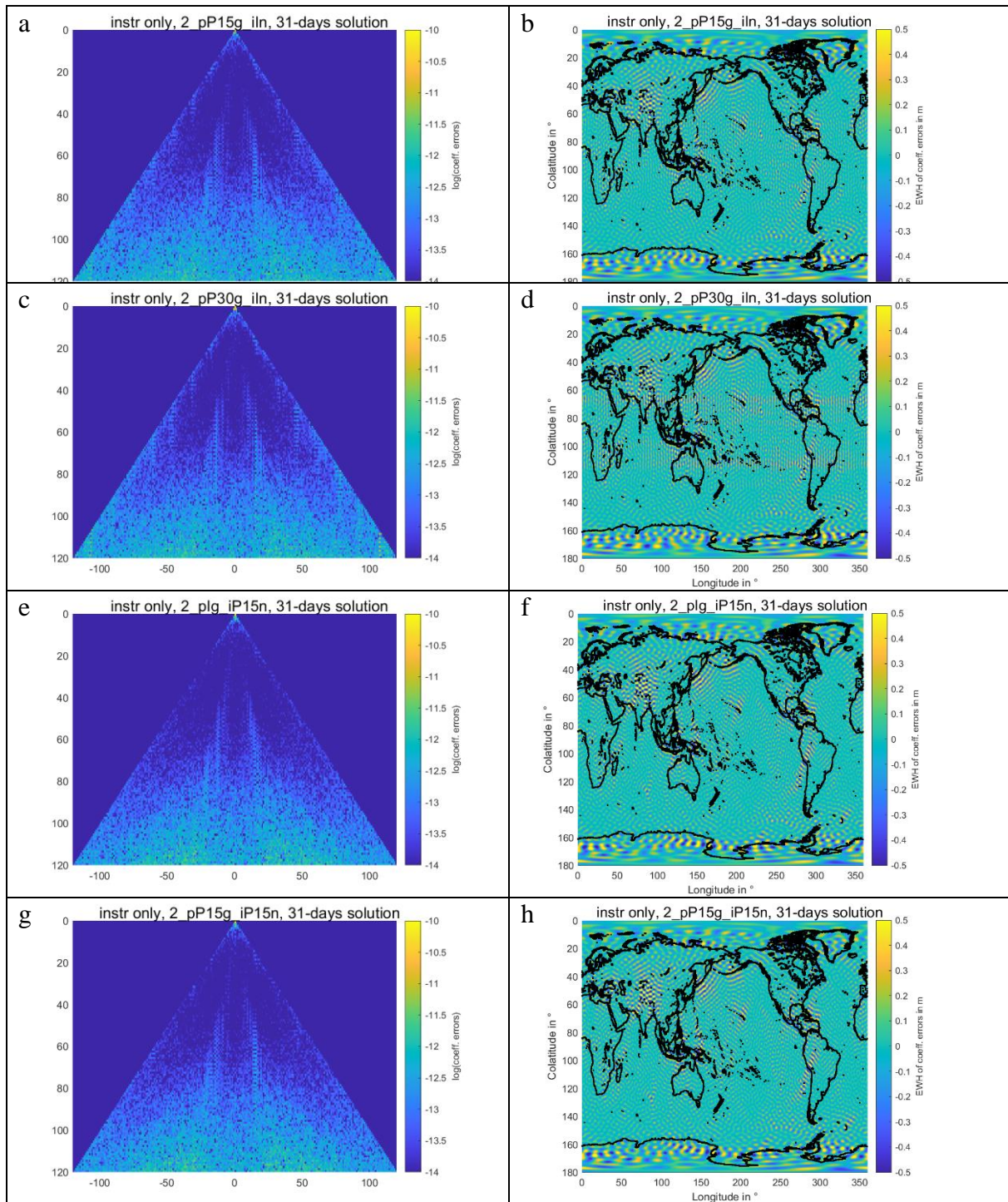
Figure 5-12 Triangle plots and spatial EWH grids of the 31-day instrument only simulation results for the double pair scenarios including at least one pendulum pair: 2_pP15g_iIn (panels a and b), 2_pP30g_iIn (panels c and d), 2_pIg_iP15n (panels e and f) and 2_pP15g_iP15n (panels g and h). The scenarios are defined in Table 5-1. All plots are displayed with one consistent colour scale. [Path: Deliverables/D1/simulation_results/full_scale_simulator_v009/old_noise_scaling/instrument_only/]
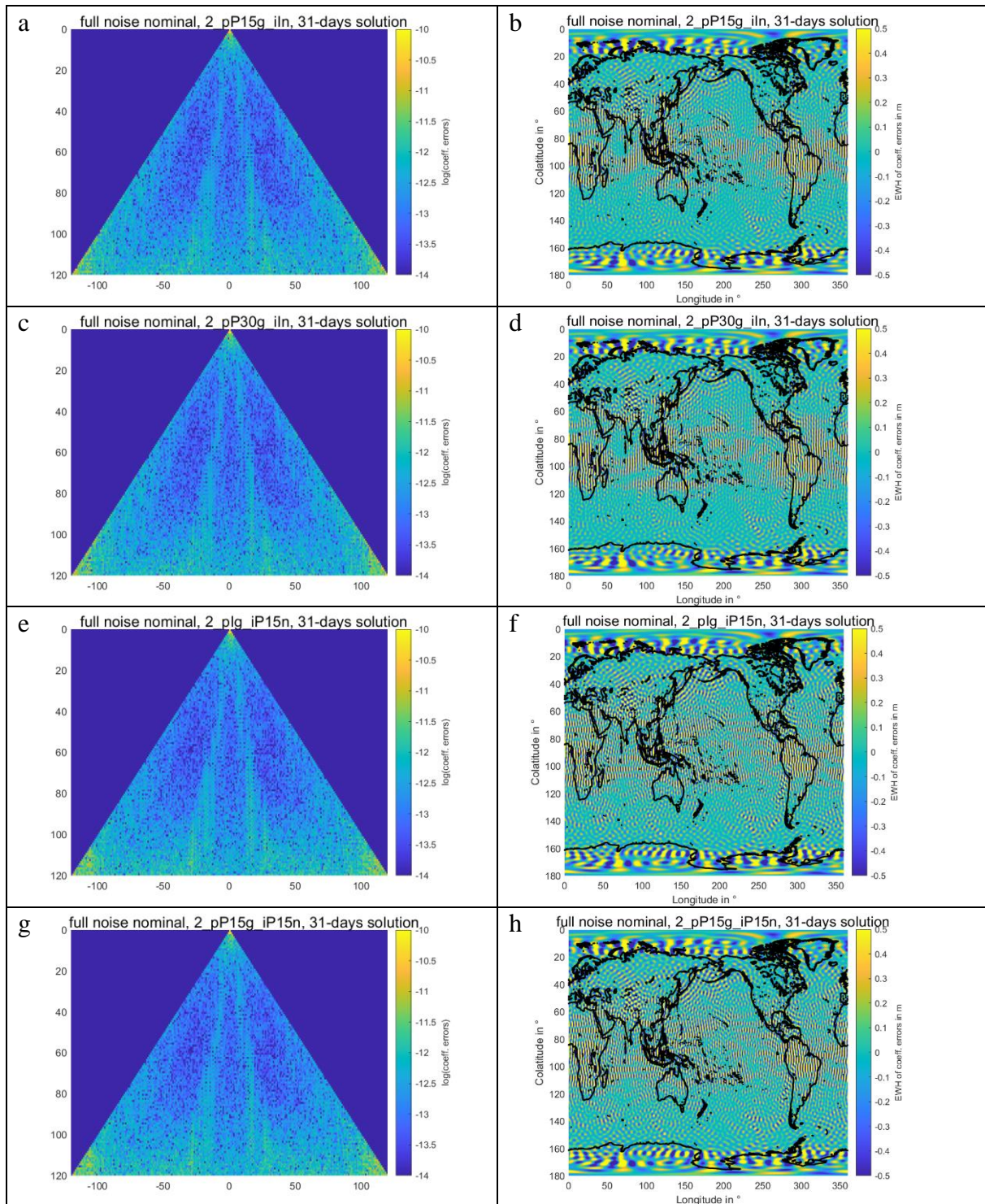
Figure 5-13 Triangle plots and spatial EWH grids of the 31-day full noise nominal simulation results for the double pair scenarios including at least one pendulum pair: 2_pP15g_iIn (panels a and b), 2_pP30g_iIn (panels c and d), 2_pIg_iP15n (panels e and f) and 2_pP15g_iP15n (panels g and h). The scenarios are defined in Table 5-1. All plots are displayed with one consistent colour scale. [Path: Deliverables/D1/simulation_results/full_scale_simulator_v009/old_noise_scaling/full_noise_nominal/]
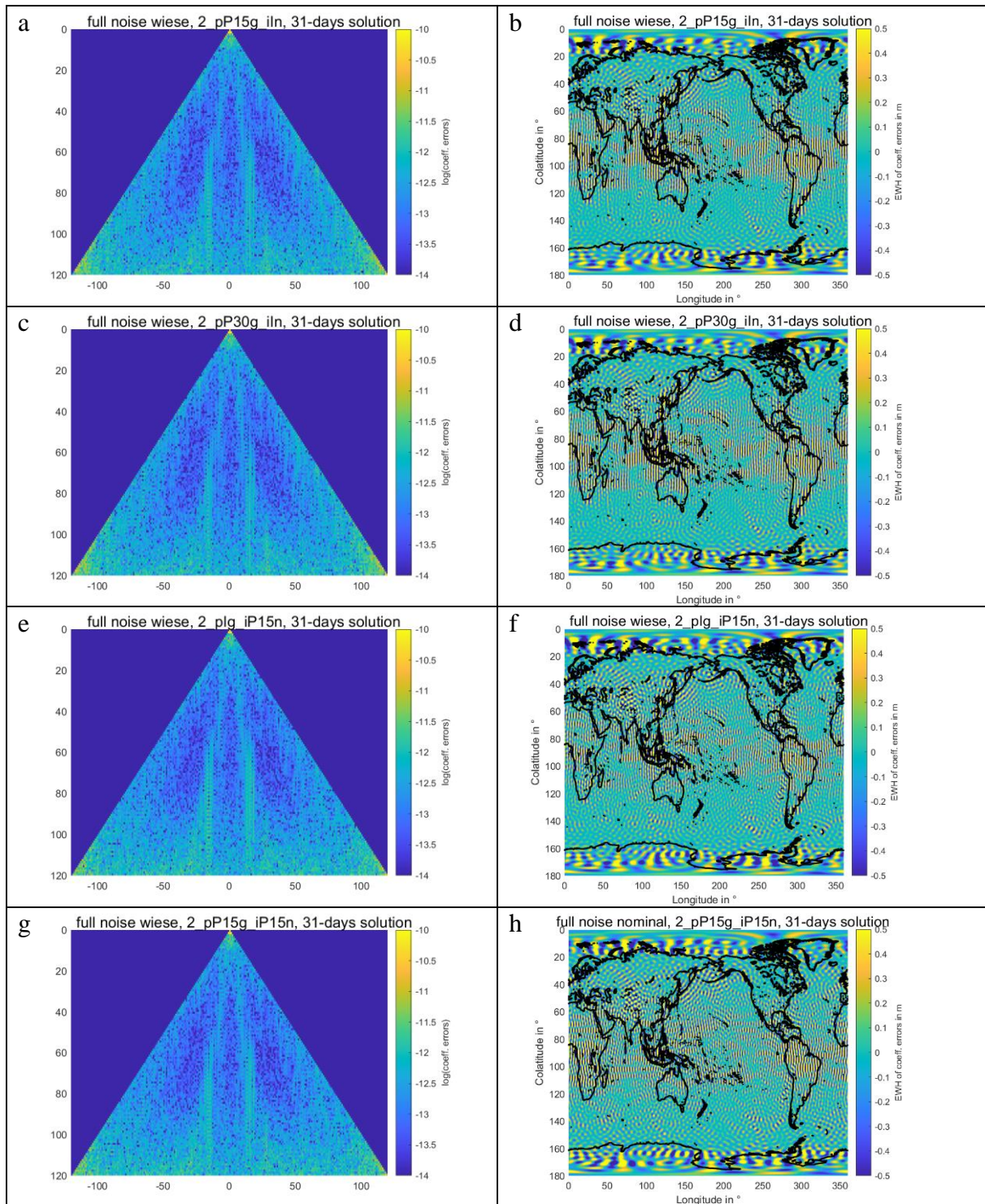
Figure 5-14 Triangle plots and spatial EWH grids of the 31-day full noise wiese simulation results for the double pair scenarios including at least one pendulum pair: 2_pP15g_iIn (panels a and b), 2_pP30g_iIn (panels c and d), 2_pIg_iP15n (panels e and f) and 2_pP15g_iP15n (panels g and h). The scenarios are defined in Table 5-1. All plots are displayed with one consistent colour scale. [Path: Deliverables/D1/simulation_results/full_scale_simulator_v009/old_noise_scaling/full_noise_wiese/]
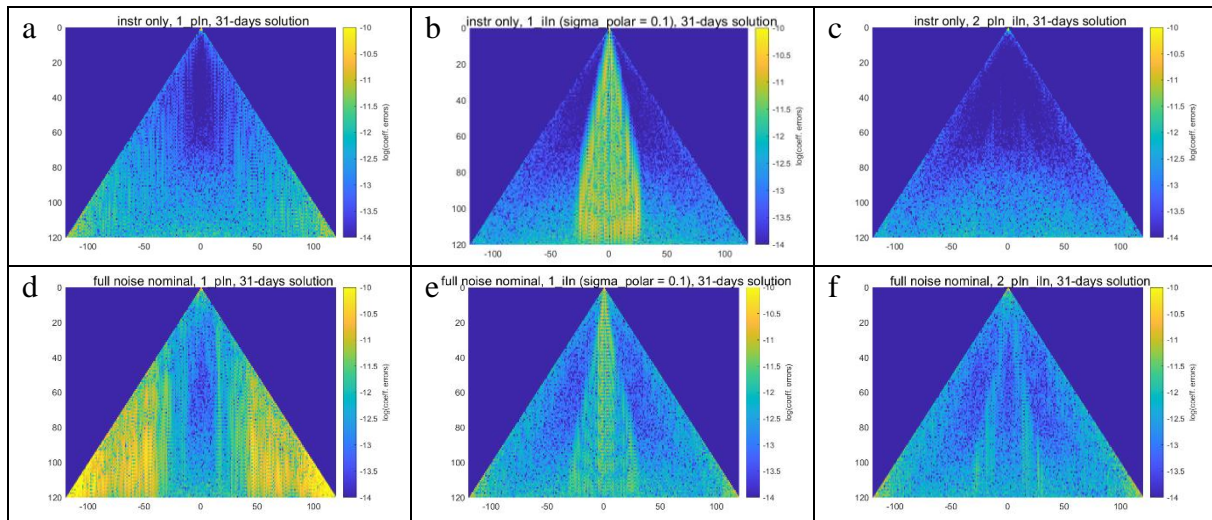
Figure 5-15 Comparison of the retrieval errors in the instrument only (top row) and full noise nominal (bottom row) cases for the single-pair scenarios 1_pIn and 1_iIn and the double-pair scenario 2_pIn_iIn, in order to estimate the contributions of the NEQ systems of the polar and inclined pairs in the 2_pIn_iIn solution. [Path: Deliverables/D1/simulation_results/full_scale_simulator_v009/old_noise_scaling/]

5.2 COMPARISON OF SCENARIOS 1 AND 13 IN THE LOW SH DEGREES

In this section, we analyze the retrieval error behavior of the scenarios 1 (2_pIg_iIn, 3d_H) and 13 (2_pIg_iIn, 5d_LH) in the low SH degrees. In the orbit scenario 3d_H, the altitudes of the satellites are 463 km (polar pair) and 432 km (inclined pair), respectively, while in the orbit scenario 5d_LH, the altitudes of the satellites are 492 km (polar pair) and 344 km (inclined pair). Thus, the main difference of the scenarios 1 and 13 is the altitude of the inclined pair, which is much lower for the 5d_LH orbits. In the following, we analyze the impact of the lower altitude of the inclined pair of scenario 13 on the retrieved low-degree SH coefficients.
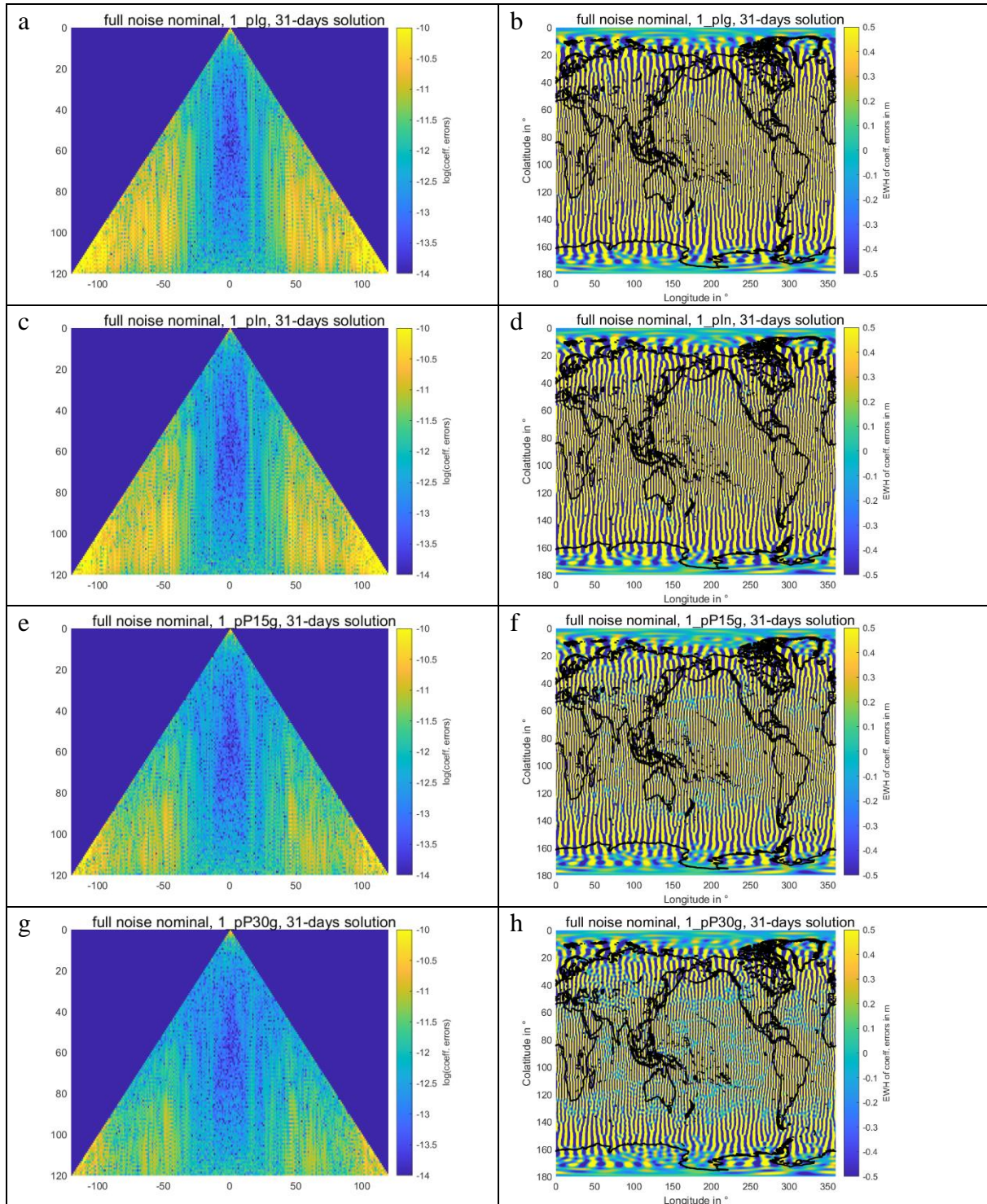
Figure 5-16 shows the degree amplitudes of scenarios 1 to 13 up to SH d/o 50. By comparing the dark blue curve (corresponding to scenario 1) to the brown curve (corresponding to scenario 13), we see the reduced formal errors for scenario 13 especially in the 31-day solutions. In the corresponding triangle plots shown by Figure 5-17, it can be seen that this improvement of the formal errors exists for all SH degrees and orders.

Since the coefficient errors of the instrument-only simulations are much more noisy compared to the corresponding formal errors, the above-described improvement is more difficult to identify in the corresponding plots (panels c, d of Figure 5-16 and Figure 5-17).

Comparing the performance of the scenarios 1 and 13 in the full noise nominal case, we do not see a very pronounced difference in the retrieval errors (see the panels e, f of Figure 5-16 and Figure 5-17).

In the corresponding full noise Wiese simulations, there is a visible difference in the behavior of scenario 1 and 13: As can be seen in panels g and h of Figure 5-16, the "bumps" in the degree amplitude curves of the full noise Wiese simulations are more strongly pronounced for scenario 13, decreasing the performance of scenario 13 compared to scenario 1 in the full noise Wiese case. These bumps are caused by larger errors of (near-)sectorial SH coefficients of specific SH orders, as can be seen by investigating panels g and h of Figure 5-17. Additional analysis on this phenomenon is presented in Section 5.3.

To summarize the findings of this section: We found an improved performance of scenario 13 compared to scenario 1 in the formal errors of the instrument-only simulations, which is mainly caused by the lower orbit altitude of the inclined pair of the 5d_LH orbits compared to the 3d_H orbits and can be observed across the SH spectrum. This improvement is however smaller than the impact of temporal aliasing errors, which cause the retrieval errors of the full noise nominal simulations of most of the double-pair scenarios among the scenarios 1 to 13 to be very similar to each other. In the full noise Wiese case, differences in the strength of the "bump" artefacts in the degree amplitudes of scenario 1 and 13 were observed.
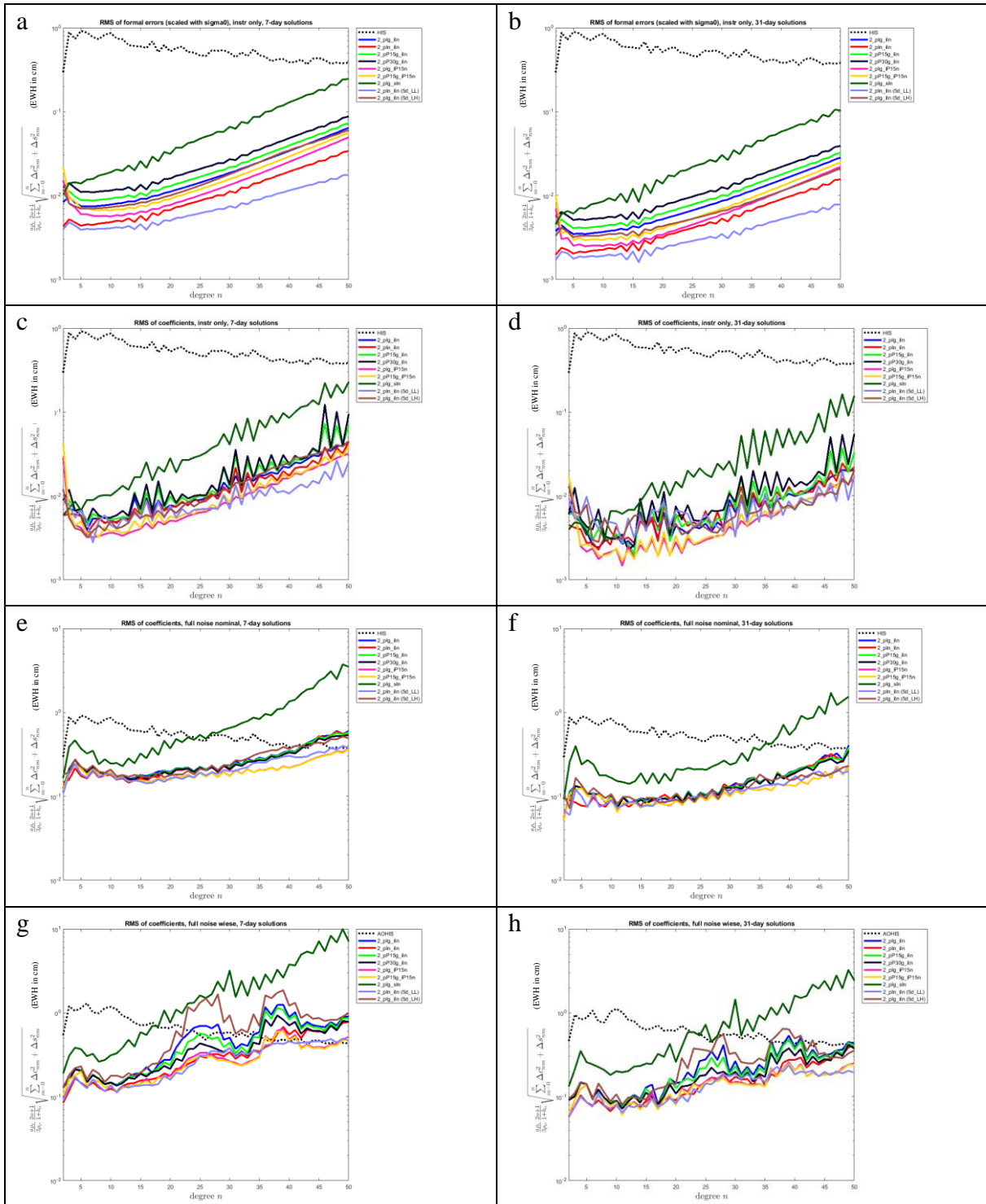
Figure 5-16 Degree amplitude plots showing the retrieval errors (a, b: formal errors, c, d: coefficient errors of instrument-only simulations, e, f: coefficient errors of full noise nominal simulations, g, h: coefficient errors of full noise Wiese simulations) for the double-pair cases among the scenarios 1 to 13 up to SH d/o 50. The dark blue curves correspond to scenario 1, the brown curves to scenario 13, respectively. The retrieval period is 7 days (left column) and 31 days (right column), respectively. [Path: Deliverables/D1/simulation_results/full_scale_simulator_v009/old_noise_scaling/]
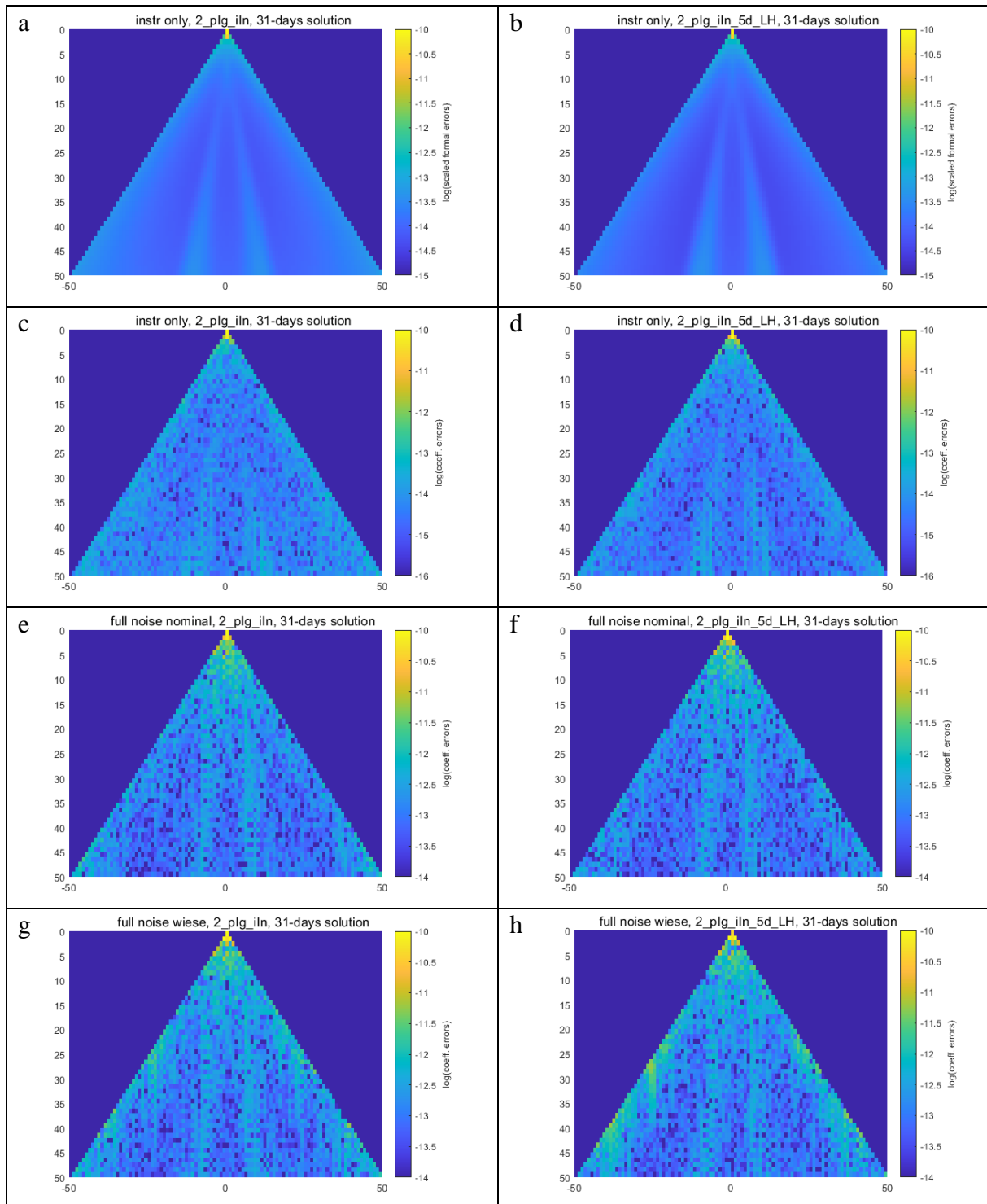
Figure 5-17 Triangle plots showing the retrieval errors (a, b: formal errors, c, d: coefficient errors of instrument-only simulations, e, f: coefficient errors of full noise nominal simulations, g, h: coefficient errors of full noise Wiese simulations) for scenarios 1 (left column) and 13 (right column) up to SH d/o 50. [Path: Deliverables/D1/simulation_results/full_scale_simulator_v009/old_noise_scaling/]

5.3 ARTEFACTS IN THE FULL NOISE WIESE SOLUTIONS

As could be seen in the analysis of the scenarios 1 to 13 presented in the preceding sections, the full noise Wiese retrieval errors of (near-)sectorial SH coefficients of specific SH orders are anomalously large, leading to bump-shaped anomalies in the corresponding degree amplitude curves. In this section, we investigate this behavior and try to explain it.

As a first step, we investigate the formal errors of the full noise nominal and full noise Wiese simulations in terms of degree amplitudes. As can be observed in Figure 5-18, the bump-shaped artifacts that we observed in the coefficient errors of the full noise Wiese results (e.g. see panels g and h of Figure 5-16) indeed also occur in the corresponding formal errors of the full noise Wiese results. This indicates that the phenomenon could be related to an unstable inversion of the NEQ matrix $A^T PA$, the inverse of which is formed both in order to compute the formal errors as well as to retrieve the SH coefficients. The fact that the formal errors of the full noise nominal results do not show this behavior indicates that the reason for the unstable inversion could be the additional daily gravity field coefficients that are co-parametrized in the case of the full noise Wiese solutions.

We further investigate this presumption by computing several test cases for scenario 2_pIg_iIn (5d_LH), which showed the strongest anomalies in the corresponding Wiese solutions compared to the remaining scenarios. If it is true that the bump-shaped artifacts in the degree amplitude curves of the Wiese simulations are caused by an unstable inversion of the corresponding NEQ matrix, the amplitudes of the bumps should increase if the maximum SH degree of the co-parametrized Wiese daily solutions is increased (as more unknown parameters are solved for). By varying this so-called "Wiese degree" between 0 and 20 (see Figure 5-19) we are indeed able to observe the presumed behavior. Also, we see that not only the amplitude of the bump feature is increasing with increasing Wiese degree, but also the range in SH degrees which are affected is increasing. In this specific scenario, the Wiese degree can maximally amount to 5 if the artifact should be avoided.

Alternatively to decreasing the Wiese degree, the bump artifact can also be avoided if the instrument noise that is included in the simulation is increased (in which we also imply an adaptation of the used weighting matrix *P*), which is visualized in Figure 5-20: If we replace the instrument noise as well as the P matrix in the scenario 2_pIg_iIn (5d_LH), the artifact is not visible any more, as the overall retrieval performance of the scenario is considerably decreased.

In summary, regarding the "bump artifacts" that we observed in the degree amplitudes of full noise Wiese simulations, we came to the interpretation that these effects are caused by an unstable inversion of the related NEQ matrix. The features can be avoided by either significantly decreasing the maximum SH degree of the daily Wiese solutions, or by decreasing the overall performance of the scenario (which e.g. is reached by worsening the assumed instrument noise performance). In order to further refine our interpretation of this behavior, we would need to investigate the numerical stability of the individual parts (i.e. the part related to the overall retrieved solution as well as the daily blocks related to the daily Wiese solutions) of the NEQ matrix in detail.
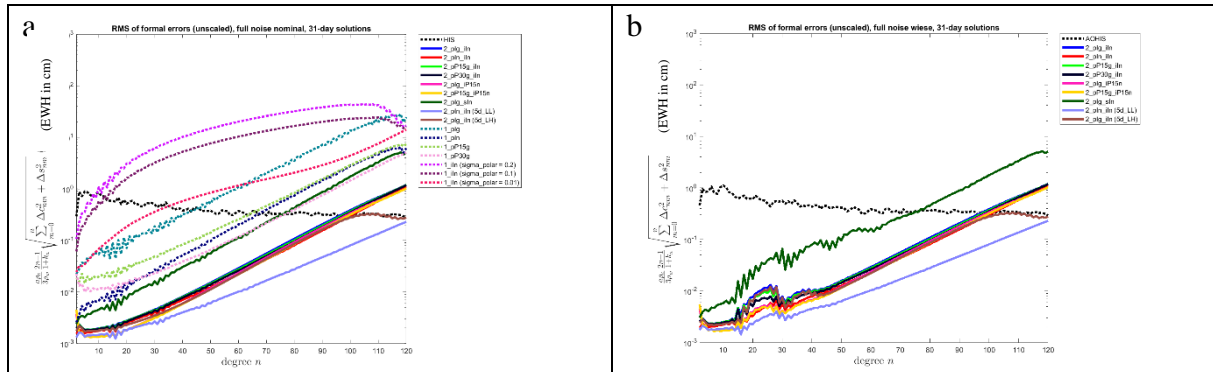
Figure 5-18 Degree amplitudes of the formal errors of the full noise nominal (panel a) and full noise Wiese (panel b) simulations for scenarios 1 to 13. [Path: Deliverables/D1/simulation_results/full_scale_simulator_v009/old_noise_scaling/]
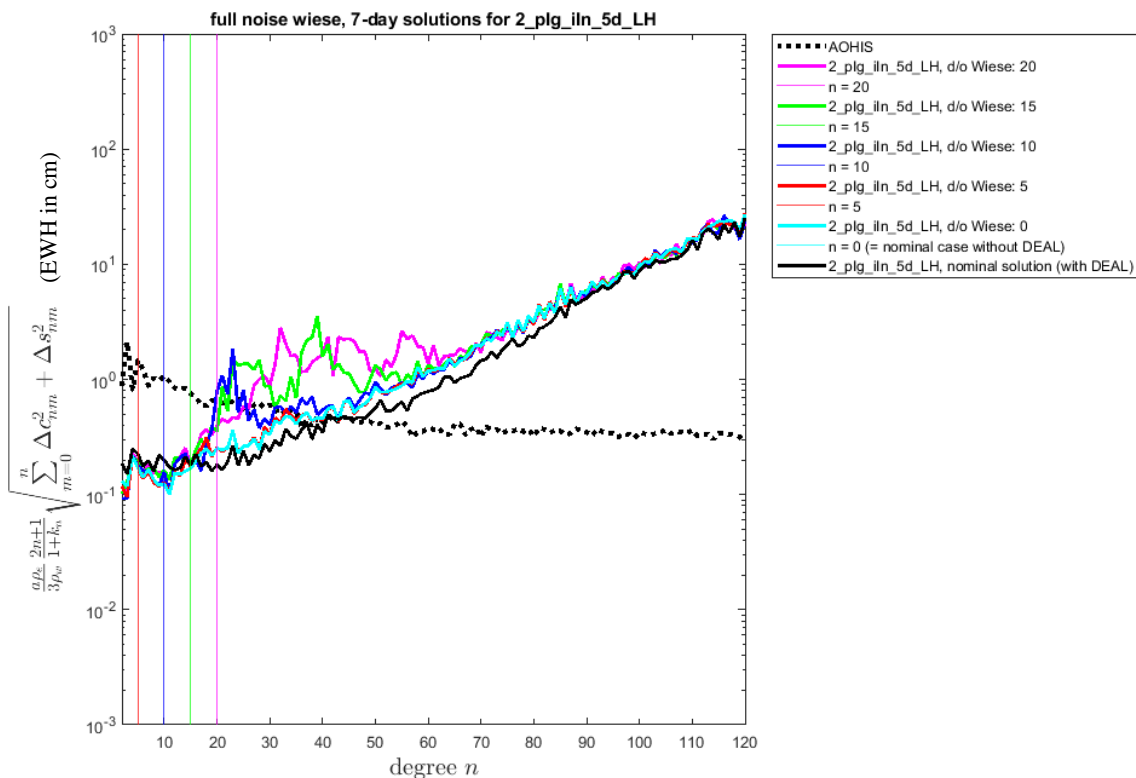
Figure 5-19 Degree amplitude plot based on the coefficient errors of 7-day d/o 120 full noise Wiese simulations for scenario 2_pIg_iIn (5d_LH). The maximum SH d/o of the daily Wiese solutions is varied in steps of 5 between 0 and 20. Additionally, the black curve shows the corresponding full noise nominal simulation result (including the usage of a background model for dealiasing) for comparison.
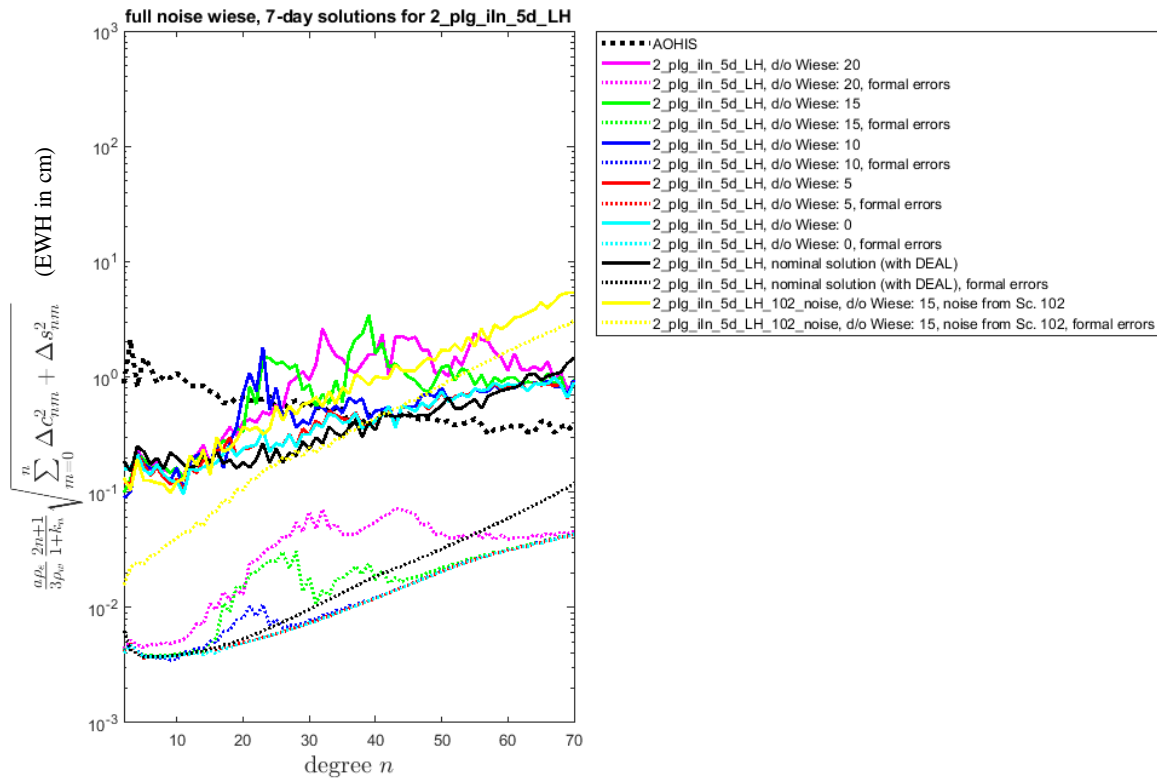
Figure 5-20 Degree amplitude plot based on the retrieval errors (solid lines: coefficient errors, dotted lines: formal errors) of 7-day d/o 70 full noise Wiese simulations for scenario 2_pIg_iIn (5d_LH). The maximum SH d/o of the daily Wiese solutions is varied in steps of 5 between 0 and 20. Additionally, the black curves show the corresponding full noise nominal simulation results (including the usage of a background model for dealiasing). The yellow curve shows the full noise Wiese simulation for a scenario similar to scenario 2_pIg_iIn (5d_LH), but using a higher instrument noise level.

5.4 SCALING OF 3-DAY, 7-DAY AND 31-DAY SOLUTIONS

In this section, we investigate if the scaling factor sqrt(x/y) between the retrieval errors of x-day and y-day solutions is valid for instrument-only as well as for full noise nominal simulations.

For this purpose, we show the results of 3-day, 5-day, 7-day and 31-day instrument only and full noise nominal simulations for the scenario 2_pIn_iIn in Figure 5-21. In order to check if sqrt(x/y) is indeed the factor between the solutions of retrieval periods x and y, we plot the up-scaled error degree amplitudes of the 31-day solutions as dotted lines. By comparing the solid and dotted curves of the same color in Figure 5-21, we find that indeed the theoretical factor that reflects the decrease in the retrieval error by increasing the number of observations is valid both for instrument-only as well as for the full noise nominal simulations. Especially, we observe that this factor is also valid for the 5-day retrieval period which does not correspond to a subcycle of the 3d_H orbits underlying the 2_pIn_iIn scenario. This shows that for the global performance of a specific constellation, the chosen retrieval period for data processing does not have to correspond to a subcycle of the underlying orbits in order to provide error levels that scale according to the amount of data samples.

It should be noted that for this study, the maximum d/o of the solutions for the individual retrieval periods has been adjusted in order to account for the decreasing spatial coverage for shorter retrieval periods. For the considered double-pair scenario 2_pIn_iIn, a maximum SH d/o of 120 for 31-day and 7-day solutions, d/o 100 for 5-day solutions and d/o 70 für 3-day solutions has been determined to give good results.

In order to complete our investigation, we also show the error degree amplitudes of d/o 15 daily Wiese solutions in Figure 5-21, panel b. It can be seen that for these solutions, the error levels do not scale corresponding to the sqrt(x/y) rule but are smaller. This could be because in the full noise Wiese processing, the degree n > 15 signals are absorbed by the co-estimated higher-resolved multiple-day solution and therefore do not disturb the daily solutions.

To summarize, we found in this section that the global error levels of both the instrument-only as well as the full noise nominal solutions scale with the number of observations included, i.e. the retrieval period. This is only the case if the maximum SH degree for the specific solution is adjusted for the spatial coverage reached after the considered period of time. We especially note that the scaling of the errors with the number of observations is independent of a match of the retrieval period with one of the subcycles of the underlying satellite orbits.
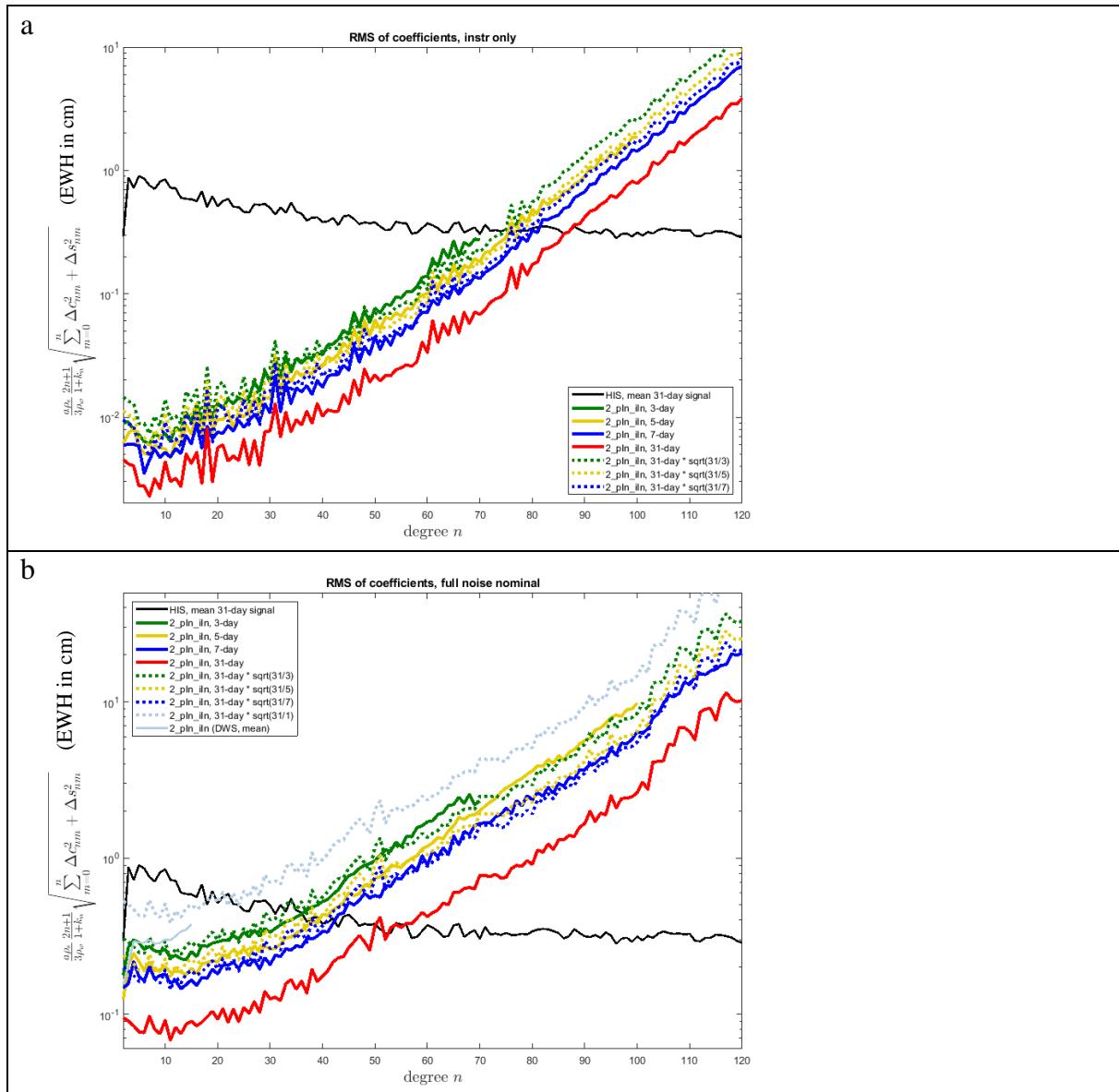
Figure 5-21 Degree amplitudes of instrument-only (panel a) and full noise nominal (panel b) simulations for the scenario 2_pIn_iIn. The solid lines are computed based on the respective coefficient errors of 3-day d/o 70, 7-day d/o 100 and 31-day d/o 120 solutions, while the dotted lines show the 31-day curve upscaled by a factor of sqrt(31/x) to approximate the x-day curve. Panel b additionally shows the degree amplitude curve of a d/o 15 daily Wiese solution, to also visualize the error level for a retrieval period of 1 day. [Path: Deliverables/D1/simulation_results/full_scale_simulator_v009/old_noise_scaling/instrument_only/2_pIn_iIn/ and Deliverables/D1/simulation_results/full_scale_simulator_v009/old_noise_scaling/full_noise_nominal/2_pIn_iIn/]

5.5 IMPACT OF MATCH BETWEEN RETRIEVAL PERIOD AND SUBCYCLE LENGTH

As presented in Section 5.4, the retrieval errors of simulated scenarios differing by their retrieval period only scale with the number of observations included in a solution. Especially, it was found that this holds both if the retrieval period matches one of the subcycles of the underlying orbits or not. This was investigated based on degree amplitudes averaged among multiple subsequent solutions of the same retrieval period.

Here, we additionally investigate the amount of scatter between individual solutions of a chosen retrieval period, using the scenario 2_pIn_iIn (5d_LL). The relevant subcycles of the underlying 5d_LL orbits are 5 and 29 days. We compute multiple subsequent 5-day, 7-day, 29-day and 31-day gravity field solutions and analyze if there is a dependency of the scattering of the performance of the individual subsequent solutions on their match between retrieval period and subcycle length.

Figure 5-22 and Figure 5-23 show the global retrieval errors of 5-, 7-, 29- and 31-day instrument-only and full noise nominal solutions, respectively. By comparing the amount of scatter among the individual solutions for a retrieval period of 5 or 7 days and 29 or 31 days, we see that the global quality of the individual solutions does not differ depending on if the chosen retrieval period does or does not match the subcycles of the underlying orbits.
In order to compare the quality of individual subsequent solutions in more detail, Figure 5-24 and Figure 5-25 show the retrieval errors of selected individual instrument-only solutions in the SH and the space domain. By comparing the performance of the two depicted individual solutions of the same retrieval period, we cannot find an indication of a dependency of the scatter among individual solutions on their match between retrieval period and orbit subcycle length.

To sum up, we compared the retrieval errors of subsequent individual solutions and did not find a dependency on the match between the chosen retrieval period and one of the subcycles of the underlying satellite orbits. In connection with the findings of Section 5.4, this shows that the fit between retrieval period and subcycle length does not have a major impact on the quality of the retrieved gravity field solutions.
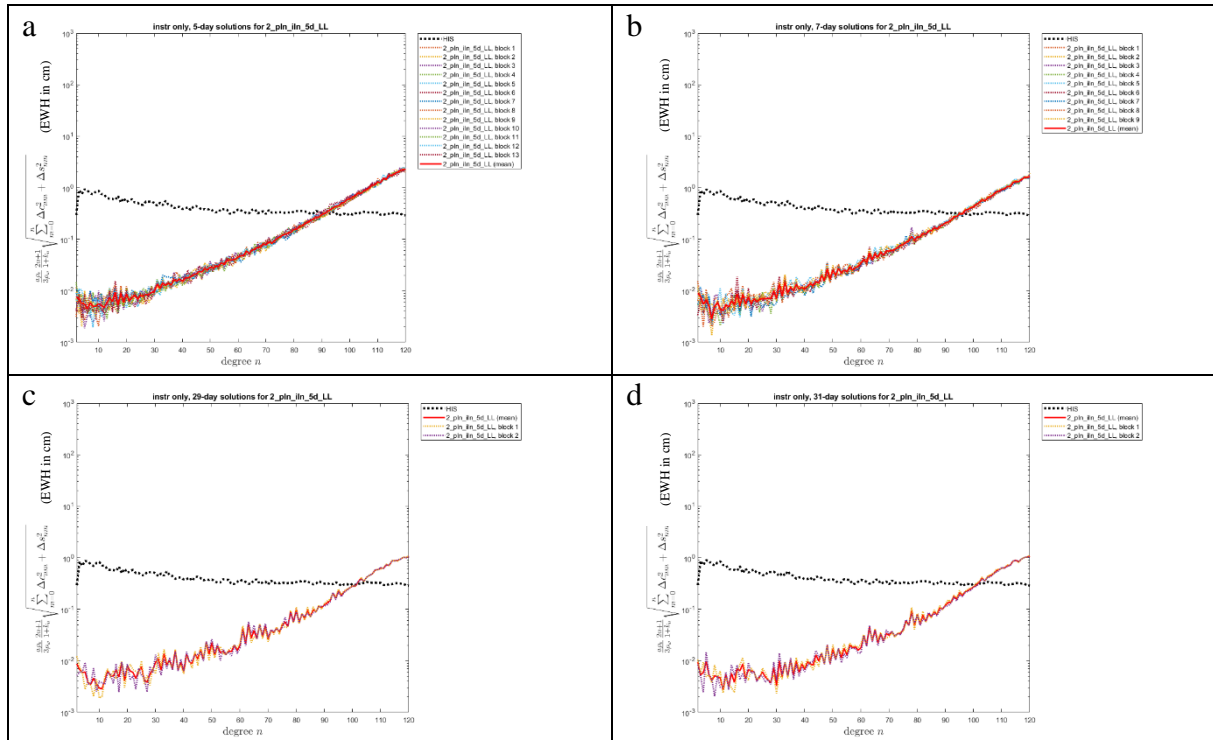
Figure 5-22 Degree amplitudes of 5-day (panel a), 7-day (panel b), 29-day (panel c) and 31-day (panel d) instrument only simulations for the scenario 2_pIn_iIn (5d_LL). The curves for the individual solutions are depicted with light dotted curves while the mean of the individual curves is represented by the red curve. The relevant subcycles of the 5d_LL orbits are 5 and 29 days. [Path: Deliverables/D1/simulation_results/full_scale_simulator_v009/old_noise_scaling/instrument_only/2_pIn_iIn_5d_LL/]
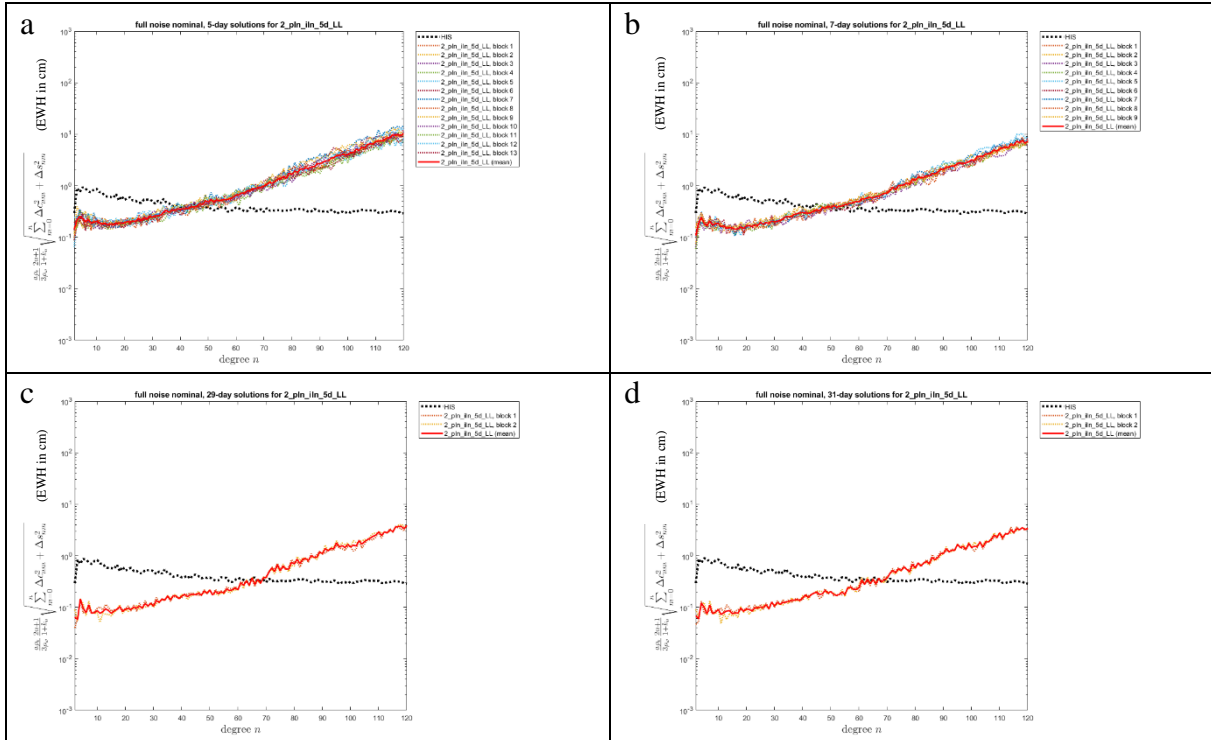
Figure 5-23 Degree amplitudes of 5-day (panel a), 7-day (panel b), 29-day (panel c) and 31-day (panel d) full noise nominal simulations for the scenario 2_pIn_iIn (5d_LL). The curves for the individual solutions are depicted with light dotted curves while the mean of the individual curves is represented by the red curve. The relevant subcycles of the 5d_LL orbits are 5 and 29 days. [Path: Deliverables/D1/simulation_results/full_scale_simulator_v009/old_noise_scaling/full_noise_nominal/2_pIn _iIn_5d_LL/]
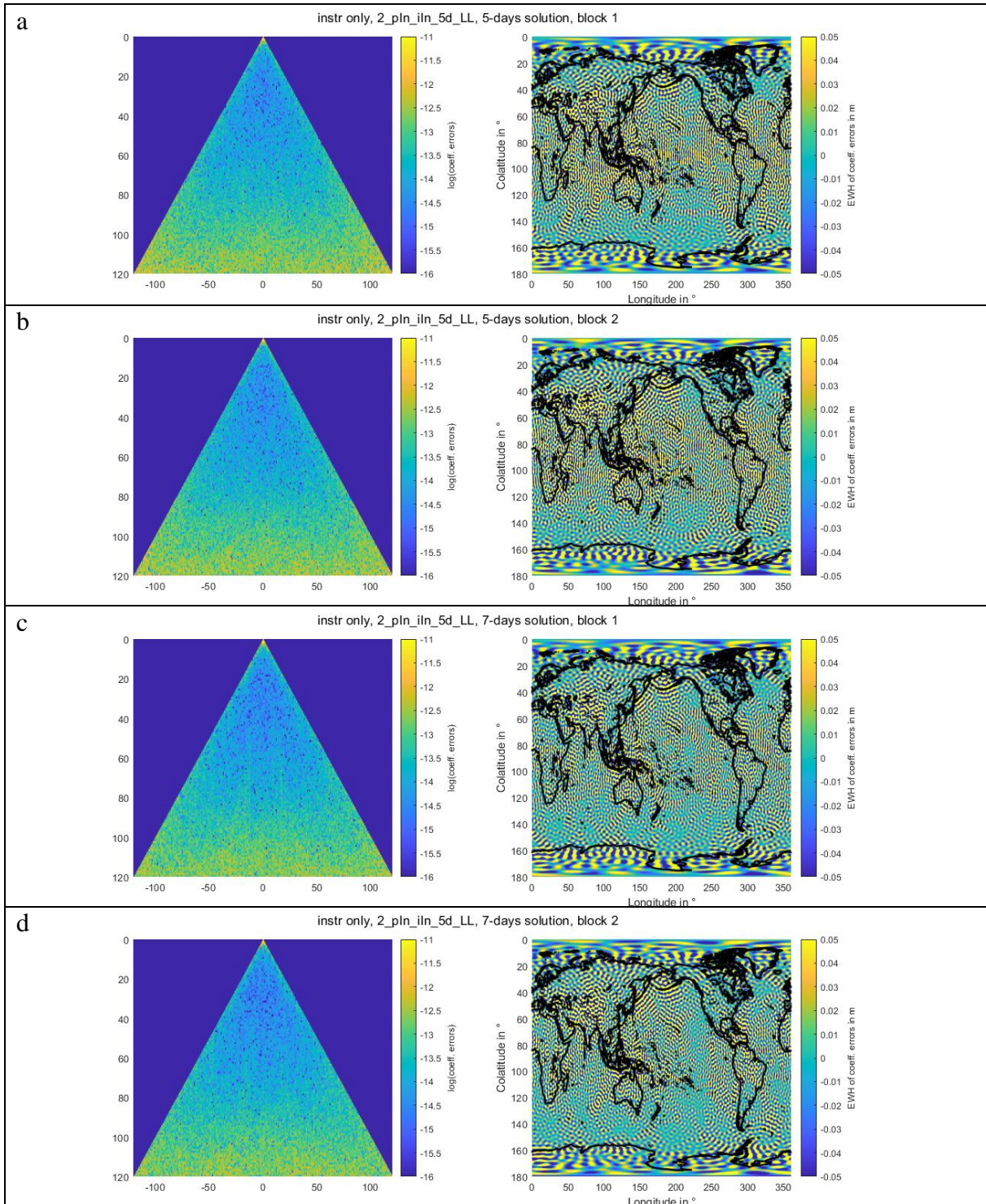
Figure 5-24 Triangle plots and spatial EWH grid plots visualizing the retrieval errors of individual instrument-only simulations for the scenario 2_pIn_iIn (5d_LL). Panel a: 5-day solution for 01.-05.01.2002, panel b: 5-day solution for 06.-10.01.2002, panel c: 7-day solution for 01.-07.01.2002, panel d: 7-day solution for 8.-14.01.2002. The relevant subcycle of the 5d_LL orbits is 5 days. [Path: Deliverables/D1/simulation_results/full_scale_simulator_v009/old_noise_scaling/instrument_only/2_pIn_iIn_5d_LL/]
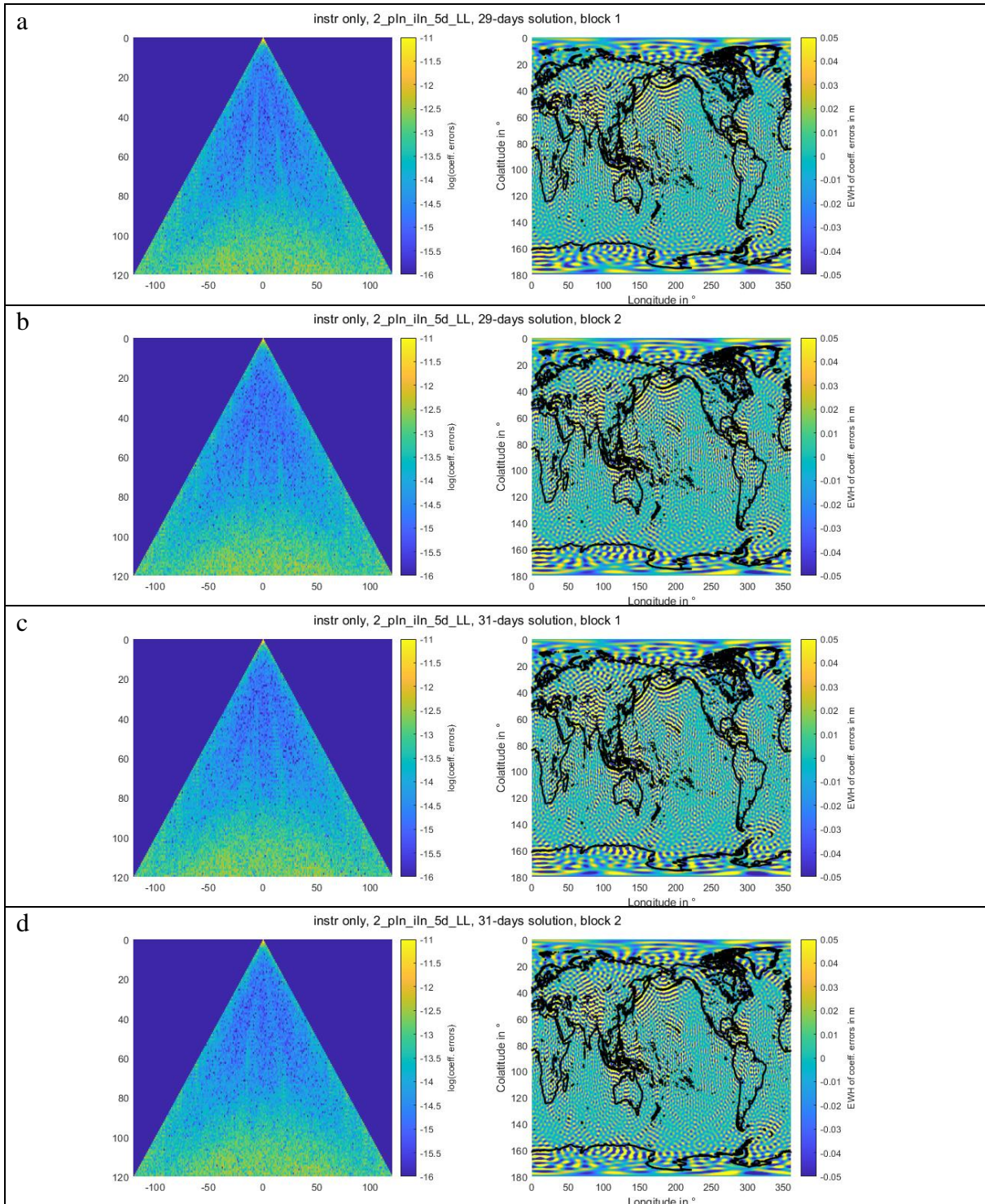
Figure 5-25 Triangle plots and spatial EWH grid plots visualizing the retrieval errors of individual instrument-only simulations for the scenario 2_pIn_iIn (5d_LL). Panel a: 29-day solution for 01.-29.01.2002, panel b: 29-day solution for 30.01.-27.02.2002, panel c: 31-day solution for 01.-31.01.2002, panel d: 31-day solution for 01.01.-03.03.2002. The relevant subcycle of the 5d_LL orbits is 29 days. [Path: Deliverables/D1/simulation_results/full_scale_simulator_v009/old_noise_scaling/instrument_only/2_pIn_iIn_5d_LL/]

6 COMPARISON OF 3D_H, 5D_H AND 7D_M SCENARIOS

In this section, the impact of the orbit altitude on the retrieval errors is analysed by comparing the results for the single and double pair scenarios 1 to 2a (cf. Table 5-1) using 3d_H, 5d_H and 7d_M orbits as defined by Table 2-1. For convenience, we summarize the orbit altitude and subcycles of the analysed orbit scenarios in Table 6-1.

As we already computed one scenario (2_pIn_iIn) using 5d_LL orbits and one scenario (2_pIg_iIn) using 5d_LH orbits, we additionally add these results to our comparison.

Figure 6-1 shows the degree amplitude plots of the formal errors as well as the coefficient errors of the instrument only and the full noise nominal simulations. By comparing the retrieval errors of the same satellite configuration between the 3d_H, 5d_H and 7d_M orbit cases, we observe that mostly, the 7d_M orbits provide the best performance, followed by the 3d_H orbits and again followed by the 5d_H orbits. This order can be understood by comparing the orbit altitudes of the individual orbits in Table 6-1: The scenarios using the lowest orbit alitudes give the smallest retrieval errors.

As can be seen in Figure 6-1, this effect becomes increasingly pronounced with increasing SH degree: The degree amplitude curves of the same colour (i.e., of the same satellite configuration) but different line styles (i.e., different orbit altitudes used) split up towards higher SH degrees.

The only scenario for which this effect cannot be observed in Figure 6-1 is 1_iIn, as these curves are dominated by the near-zonal worse-resolved SH coefficients of the single inclined pair simulation.

Comparing the individual single and double pair scenarios among each other (e.g. 2_pIg_iIn versus 2_pIn_iIn), we observe that the improving effect of the NGGM noise versus the GRACE-I noise which is visible for low SH degrees becomes secondary for increasing degrees, where a lower orbit altitude can compensate a worse instrument noise performance. This shows that the orbit altitude has to be considered as the main performance driver of satellite gravity missions.

Comparing the instrument only and the full noise results, we observe again that as soon as temporal aliasing errors are included, the benefit of an improved instrument noise performance which can be especially seen in the instrument only single-pair results, becomes secondary as the temporal aliasing errors are larger compared to the errors introduced by the instrument noise: The difference between 1_pIg and 1_pIn becomes much smaller in the full noise case compared to the instrument only case. The effect of the orbit altitude, however, still remains significant in the full noise case.

For completeness, we also show the corresponding degree median plots in Figure 6-2. They allow for the same observations as Figure 6-1 and additionally provide a more realistic evaluation of the scenario 1_iIn w.r.t. the other scenarios.

Figure 6-3 and Figure 6-4 give the triangle plots and spatial EWH grids of the double in-line scenario 2_pIn_iIn for the orbit scenarios 5d_H, 3d_H, 7d_M and 5d_LL. We ordered them

with decreasing orbit altitude, to directly visualise the effect of increasing retrieval performance. The triangle plots show that this improvement is found throughout the SH spectrum.

Table 6-1 Orbit altitude and subcycles of selected orbit types. Data is extracted from Table 2-1 and repeated here for convenience.

	Altitude in km (polar pair)	Altitude in km (inclined pair)	Subcycles in days
3d_H	463	432	3, 7, 31
5d_LL	376	344	1, 2, 5, 12, 29
5d_LH	492	344	5, PP: 31, IP: 32
5d_H	488	465	4, 5, 29
7d_M	417	389	2, 7, 30
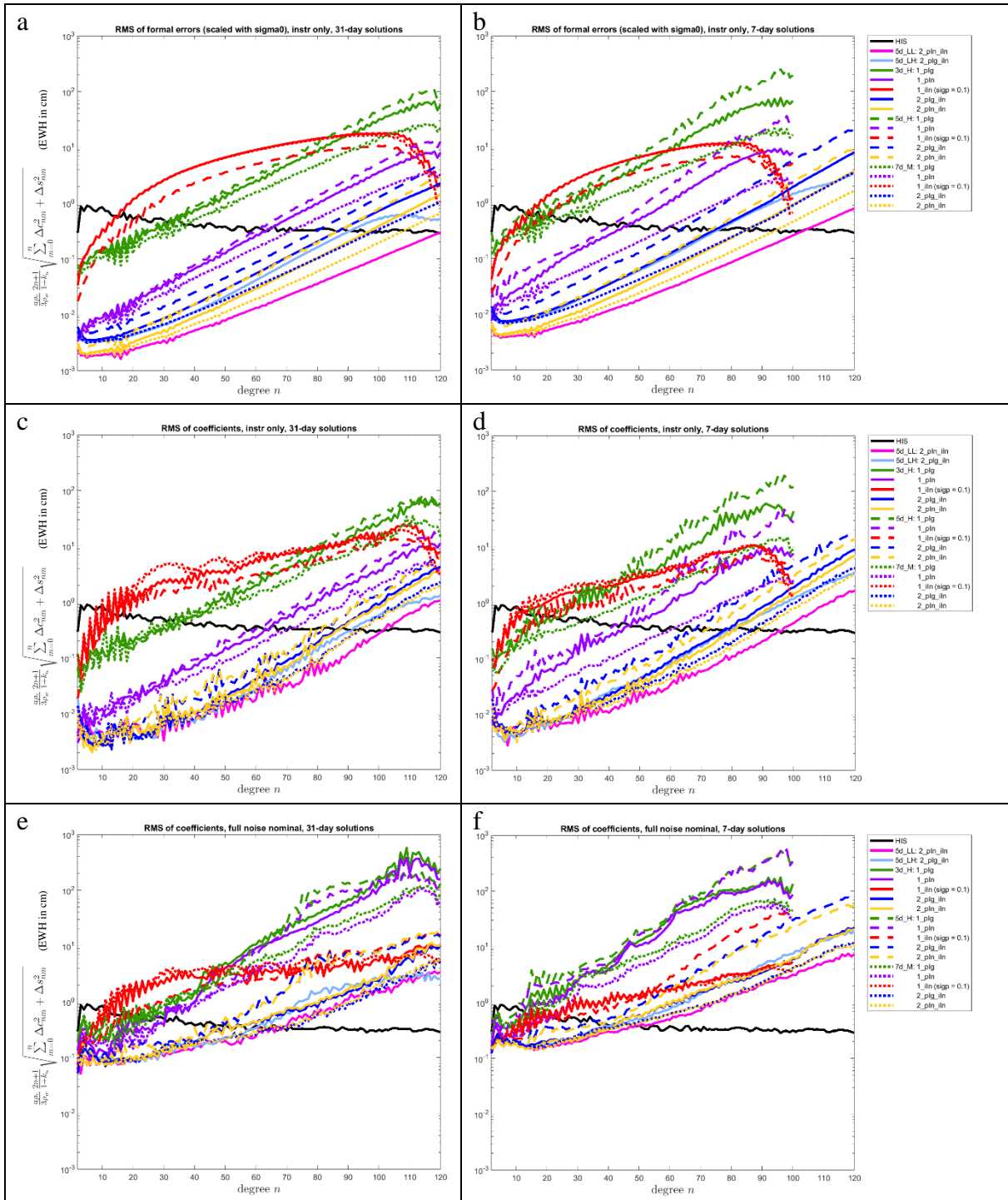
Figure 6-1 Degree amplitude plots of the full-scale simulations of the scenarios 1_pIg, 1_pIn, 1_iIn, 2_pIg_iIn and 2_pIn_iIn defined in Table 5-1. Compared are the results obtained when using 3d_H (solid curves), 5d_H (dashed curves) and 7d_M (dotted curves) orbits, as defined by Table 2-1. Additionally, the results for the scenarios 2_pIn_iIn (5d_LL orbits) and 2_pIg_iIn (5d_LH orbits) are shown. Panels a and b show the formal errors scaled by the a posteriori variance factor. Panels c and d show the retrieved coefficients of the instrument only case. Panels e and f show the coefficient errors of the full noise nominal case. The plots in the left column show the curves averaged over two 31-day solutions, while the plots in the right column show the curves averaged over nine 7-day solutions. [Path: Deliverables/D1/simulation_results/full_scale_simulator_v009/old_noise_scaling/]

Figure 6-2 Degree median plots of the full-scale simulations of the scenarios 1_pIg, 1_pIn, 1_iIn, 2_pIg_iIn and 2_pIn_iIn defined in Table 5-1. Compared are the results obtained when using 3d_H (solid curves), 5d_H (dashed curves) and 7d_M (dotted curves) orbits, as defined by Table 2-1. Additionally, the results for the scenarios 2_pIn_iIn (5d_LL orbits) and 2_pIg_iIn (5d_LH orbits) are shown. Panels a and b show the formal errors scaled by the a posteriori variance factor. Panels c and d show the retrieved coefficients of the instrument only case. Panels e and f show the coefficient errors of the full noise nominal case. The plots in the left column show the curves averaged over two 31-day solutions, while the plots in the right column show the curves averaged over nine 7-day solutions. [Path: Deliverables/D1/simulation_results/full_scale_simulator_v009/old_noise_scaling/]

Figure 6-3 Triangle plots and spatial EWH grids of the 31-day instrument only simulations for the double in-line pair scenario 2_pIn_iIn, to analyse the effect of the orbit altitude on the retrieval errors. Shown are the results obtained by using 5d_H (panels a, b), 3d_H (panels c, d), 7d_M (panels e, f) and 5d_LL (panels g, h) orbits, as defined by Table 2-1. The solutions are ordered such that the orbit altitude is decreasing from top to the bottom row (cf. Table 6-1). [Path: Deliverables/D1/simulation_results/full_scale_simulator_v009/old_noise_scaling/instrument_only/]
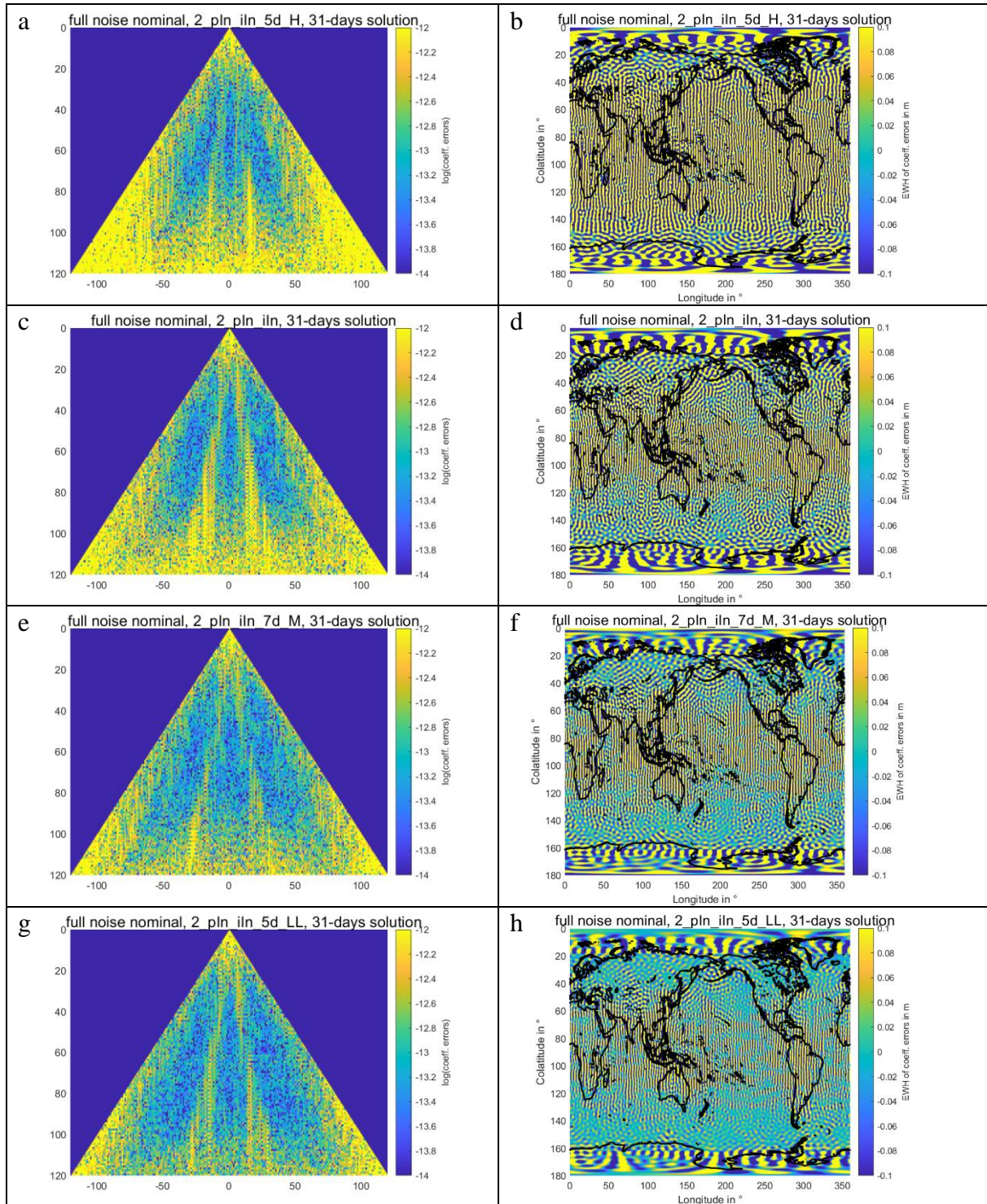
Figure 6-4 Triangle plots and spatial EWH grids of the 31-day full noise nominal simulations for the double in-line pair scenario 2_pIn_iIn, to analyse the effect of the orbit altitude on the retrieval errors. Shown are the results obtained by using 5d_H (panels a, b), 3d_H (panels c, d), 7d_M (panels e, f) and 5d_LL (panels g, h) orbits, as defined by Table 2-1. The solutions are ordered such that the orbit altitude is decreasing from top to the bottom row (cf. Table 6-1). [Path: Deliverables/D1/simulation_results/full_scale_simulator_v009/old_noise_scaling/full_noise_nominal/]

7 ANALYSIS OF THE INTER-SATELLITE DISTANCE

7.1 INITIAL ANALYSIS

In this section, we analyse the impact of the inter-satellite distance (ISD) dependency of the LRI noise on the retrieved gravity field solution. For this analysis, we use four different simulation scenarios: Firstly, we show the results obtained if the ISD is 220 km, but the LRI noise remains without scaling (which corresponds to the LRI noise in the case of an ISD of 100 km). This is the situation as used for the simulation scenarios 1 to 14, where the ISD dependency of the LRI noise is not taken into account. The remaining three cases show the results obtained for an ISD of 150, 180 and 220 km, respectively, and an appropriately scaled LRI noise for these ISD values. We scale the LRI noise by a factor of ISD/100 km, which represents an increase of the LRI noise with increasing ISD.

The above described four cases w.r.t. ISD and LRI noise scaling are considered for the Bender double-pair configuration corresponding to scenario 2_pIn_iIn (two in-line pairs with MAGIC-type accelerometers). We present the results both for the 3d_H orbits and the 5d_LL orbits, in order to compare the magnitudes of the ISD effect to the effect the orbit altitude has on the retrieved gravity field model.

Figure 7-1 shows the amplitude spectral densities (ASDs) of the pre-fit range rate residuals in the instrument-only case. They include the instrument noise (as can be seen by comparing the pre-fit residuals ASDs to the analytical ASDs of the noise models) as well as numerical errors (which produce the deviations of the shape between the pre-fit residuals ASDs and the ASDs of the noise models). The curves show that the noise in the ll-sst residuals is dominated by the ACC noise for frequencies below $7*10^{-4}$ Hz and therefore does not change between the considered scenarios. For larger frequencies, the scaling factor in the LRI noise is visible: For larger ISDs, the noise level is larger.

Panels a and b of Figure 7-2 show the degree amplitudes of the retrieved coefficients in the instrument-only case, and panels c and d of Figure 7-2 the corresponding plot with the formal errors. For the three scenarios where the LRI noise is scaled according to the ISD, the retrieval errors are smaller if the ISD is larger. This shows that the increase of the signal-to-noise ratio (SNR) by increasing the ISD is dominating over the effect of the increased LRI noise by increasing the ISD. However, it has to be noted that the impact of the ISD on the retrieval errors is much smaller compared to the effect that the satellite orbit altitude has: Especially in the degrees larger than about 50, the decreased orbit altitude improves the retrieval errors significantly. For a fixed orbit altitude, the best performance is reached if ISD=220 km and the unscaled LRI noise is used, which is expected, as the positive effects of the increased ISD and the lower LRI noise levels are interfering. The fact that the curves for ISD=220 km, LRI noise scaled for 100 km distance and ISD=220 km, LRI noise scaled for 220 km distance are so close to each other demonstrates that the ISD-dependency of the LRI noise plays a secondary role in our simulations.

If the errors due to temporal aliasing and background model errors are included (see panels e and f of Figure 7-2), both the effects of the ISD and the LRI noise scaling disappear, showing

that these effects play a secondary role after the errors introduced if temporal gravity signals are considered.
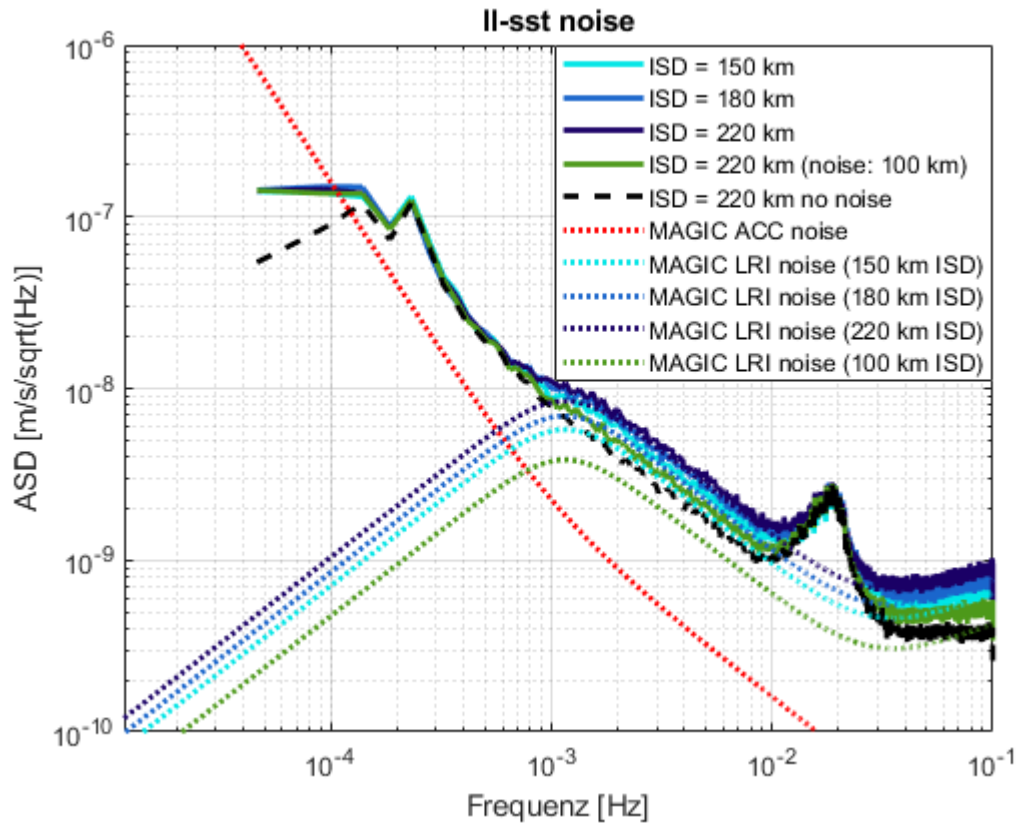
Figure 7-1 Amplitude spectral densities (ASDs) of the instrument-only pre-fit range rate residuals for the polar in-line pair using MAGIC-type ACC and LRI noise (pIn), in the case of various inter-satellite distances (ISDs) and accordingly scaled LRI noise (blue solid lines) and in the case of ISD = 220 km and unscaled LRI noise (green solid line). The dashed black curve shows the corresponding pre-fit spectrum if no orbit, ACC and LRI noise is used. The dotted lines give the analytical noise ASDs of the used ACC and LRI noise models.
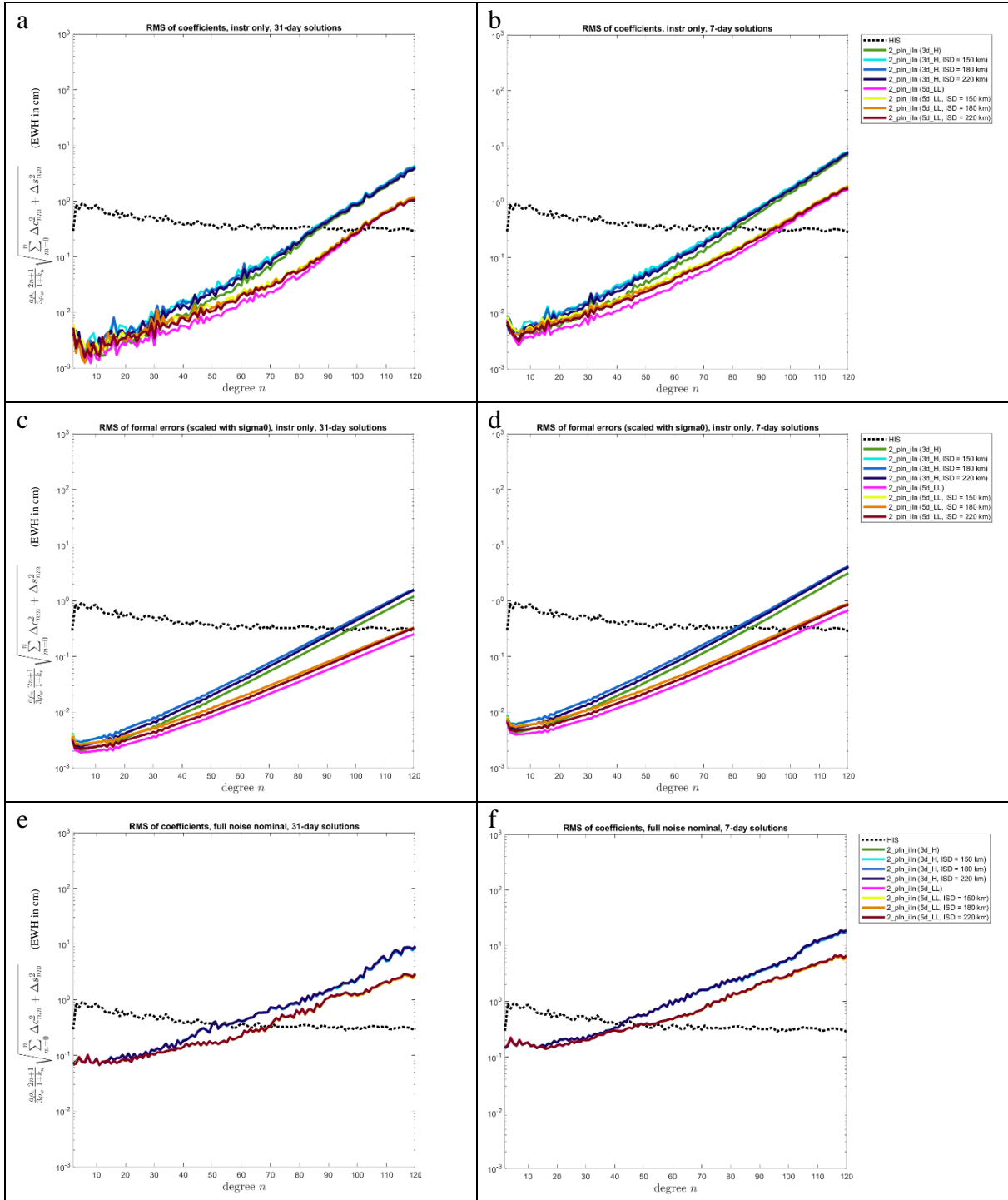
Figure 7-2 Degree amplitude plots of the coefficients (top row) and formal errors (middle row) of the instrument-only simulations, as well as the coefficient errors of the full noise simulations (bottom row). Panels a, c and e show the results for the 31-day retrieval period; panels b, d and f show the results for the 7-day retrieval period.

7.2 REPEATED ANALYSIS USING CORRECTED SCALING FACTOR

As has been pointed out in Milestone Meeting 1, the scaling factor for the LRI noise of ISD/100 km, which has been used for the initial analysis presented in Section 7.1, is wrong and the correct scaling factor is supposed to be ISD/220 km. For this reason, the analysis presented in Section 7.1 is now repeated using the correct scaling factor for the LRI noise.

First of all, we give an update for Figure 7-1 in Figure 7-3. By comparing the two figures, we see the expected effect that the noise amplitudes are now smaller with the new scaling factor of ISD/220 km. As smaller noise amplitudes are used, the relative importance of the instrument noise compared to the numerical errors in the software is decreasing, as can be seen in Figure 7-3: Now, for all considered cases the numerical errors (visualized by the ASD of the no noise prefit residuals) are dominating for most of the spectral range except for the low frequencies < 1e-4 Hz where the ACC noise is still stronger than the numerical errors.

An update of Figure 7-2 is given in Figure 7-4. Qualitatively, the results are similar to the findings presented in Section 7.1: For larger ISDs, the improving effect of the gain in signal is predominating the degrading effect of the increased LRI noise, resulting in smaller coefficient errors for larger ISDs. The fact that the sigma 0-scaled formal errors are smaller compared to the instrument only coefficient errors (especially towards the larger SH degrees) could be due to the numerical errors which are contained in the coefficient errors but not in the formal errors.

We note that in Figure 7-4, in contrast to Figure 7-2, we are using retrieval periods of 29 and 5 days for the 5d_LL scenario, in order to show solutions with retrieval periods matching the subcycle lengths of the underlying orbits for all cases. The different amount of observations contained in the 5- and 7-day solutions of the 3d_H and 5d_LL scenarios is presumably the reason for the intersection of the corresponding degree amplitude curves which could be avoided by scaling the curves corresponding to their retrieval period.

All in all, the repeated analysis of the ISD-dependence of the LRI noise and its impact on the retrieval errors could confirm our previous findings using the wrong scaling factor for the LRI noise.
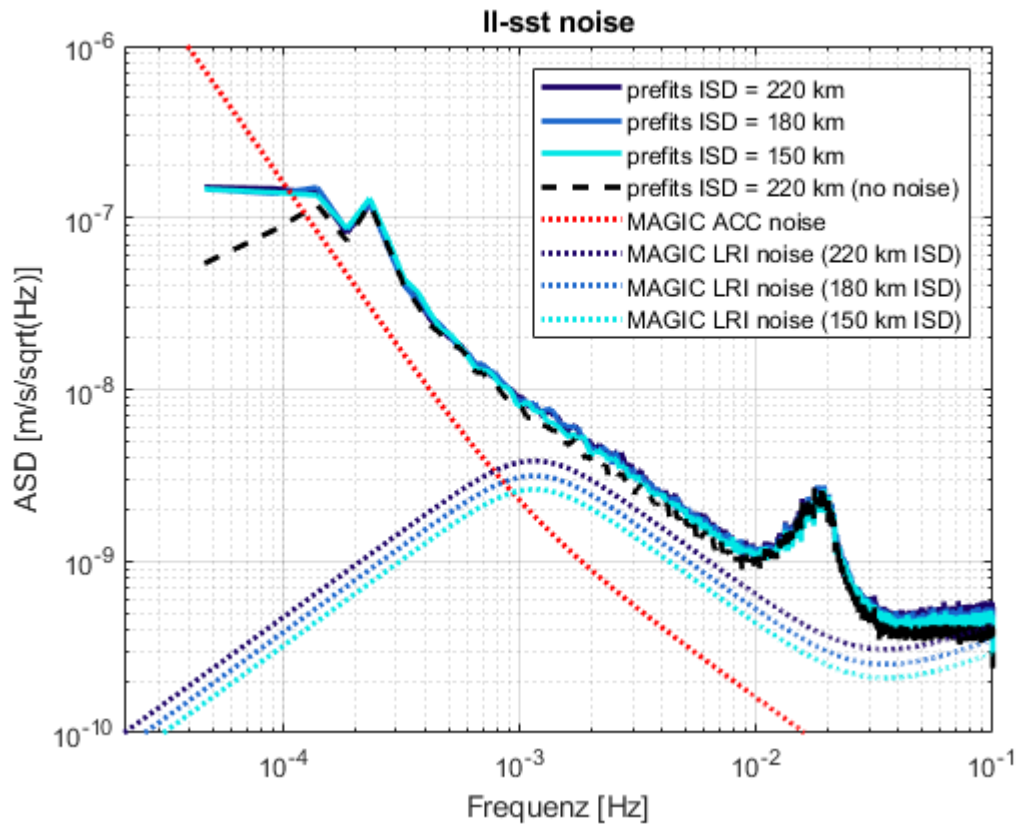
Figure 7-3 Update of Figure 7-1, now using the correct scaling factor of ISD/220 km for the LRI noise.
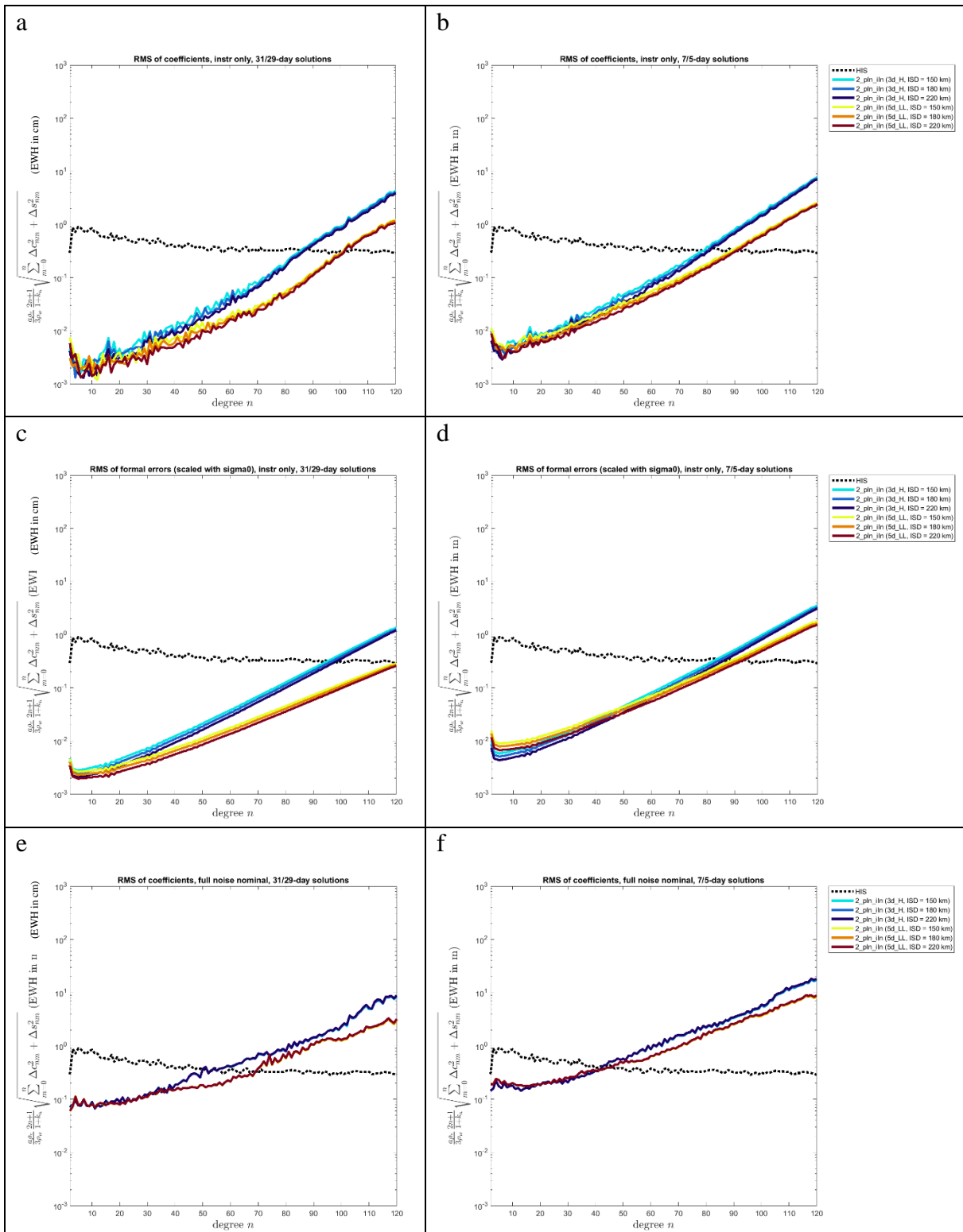
Figure 7-4 Update of Figure 7-2, now using the correct scaling factor of ISD/220 km for the LRI noise. [Path: Deliverables/D1/simulation_results/full_scale_simulator_v009/old_noise_scaling/instrument_only/2_pIn_iI n_5d_LL/]

8 ANALYSIS OF ADDITIONAL DOUBLE-PAIR SCENARIOS

8.1 IMPACT OF THE ACC PERFORMANCE OF THE INCLINED PAIR

In this section, we compare the previously investigated scenario 2_pIg_iIn (3d_H) to the new scenario 2_pIg_iIg (3d_H). The only difference between the two scenarios is the accelerometer noise assumed for the inclined satellite pair: In the newly computed scenario 2_pIg_iIg (3d_H), the NGGM-like ACC on the inclined pair is replaced by a GRACE-like ACC. The aim is to find out what the impact of the ACC performance of the inclined pair is on the retrieval errors of a double pair constellation.

Figure 8-1 to Figure 8-3 give an overview of the instrument only and full noise nominal simulation results for retrieval periods of 7 and 31 days. As shown by Figure 8-1, the impact of the ACC performance of the inclined pair is clearly visible in the instrument only results: Especially towards the low SH degrees, 2_pIg_iIn outperforms 2_pIg_iIg by a factor of up to 10 for the lowest degrees. This effect is both visible in the coefficient errors (solid lines) and the formal errors (dotted lines) in panels a and b of Figure 8-1. In the full noise nominal simulations, in contrast, this effect becomes overwhelmed by the amplitude of temporal aliasing errors (see panels c and d of Figure 8-1).

In order to visualize in more detail which SH coefficients are mostly affected by the change in the ACC performance of the inclined pair, we plot the ratio of the coefficient errors as triangle plots in Figure 8-2. As shown by the respective panels a and b, mostly the (near-)sectorial coefficients of the instrument only results are affected. This is expected, since the sectorial coefficients are mainly determined by the inclined pair, which provides observations including a component in east-west direction. In the ratio of the retrieval errors of the full noise nominal simulations shown by panels c and d of Figure 8-2, we do not find any major difference between the two considered scenarios.

For completeness, we also show the performance of the computed simulation results in space domain in Figure 8-3. The improvement of the (near-)sectorial coefficient in the instrument only case can be observed in panels a to d of Figure 8-3 in the form of reduced striping noise patterns for scenario 2_pIg_iIn compared to 2_pIg_iIg. As observed before, the full noise results do not show such an impact.

Summing up, we found that the impact of an improved ACC for the satellites of the inclined pair in a double-pair constellation is mainly the improvement of the (near-)sectorial SH coefficients in instrument-only simulations. If temporal gravity signals are included in the simulation, this effect however disappears behind the temporal aliasing errors which are dominating the retrieval errors in the full noise case. For the reduction of temporal aliasing errors, mainly the inclination of the second pair plays a role.
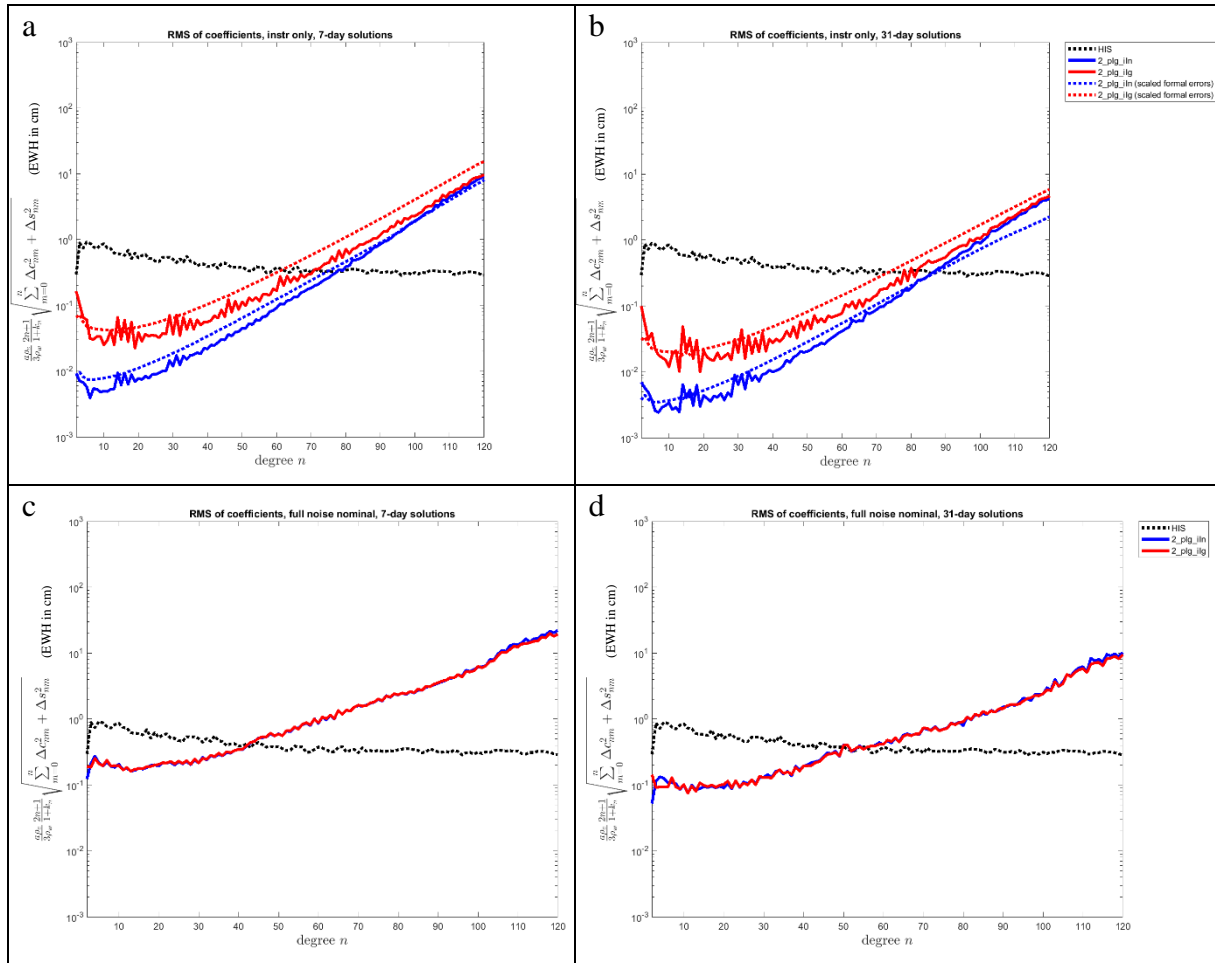
Figure 8-1 Degree amplitudes of instrument-only (panels a, b) and full noise nominal (panels c, d) simulations for the double-pair scenarios 2_pIg_iIn and 2_pIg_iIg. The retrieval period amounts to 7 days (panels a, c) and 31 days (panels b, d), respectively. [Path: Deliverables/D1/simulation_results/full_scale_simulator_v009/old_noise_scaling/]
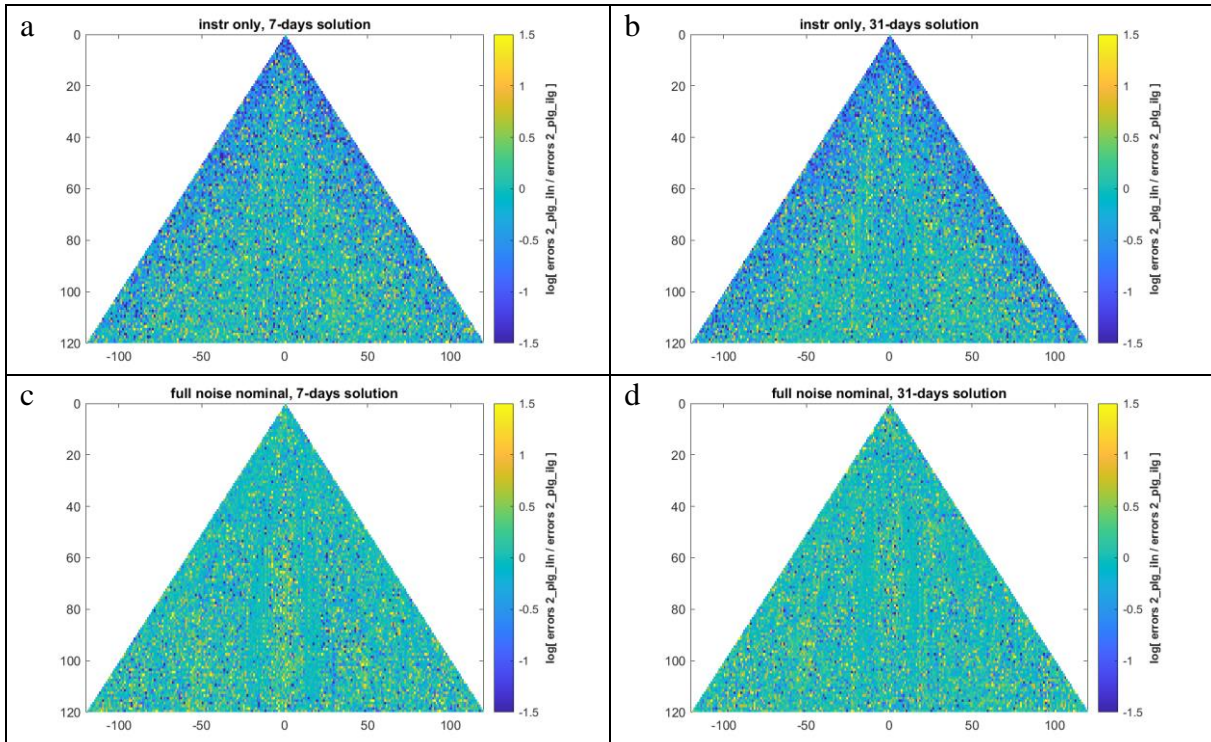
Figure 8-2 Triangle plots showing the ratio of the coefficient errors of instrument-only (panels a, b) and full noise nominal (panels c, d) simulations of the scenarios 2_pIg_iIn and 2_pIg_iIg on a logarithmic scale. Blue colors indicate that 2_pIg_iIn performs better than 2_pIg_iIg. [Path: Deliverables/D1/simulation_results/full_scale_simulator_v009/old_noise_scaling/]
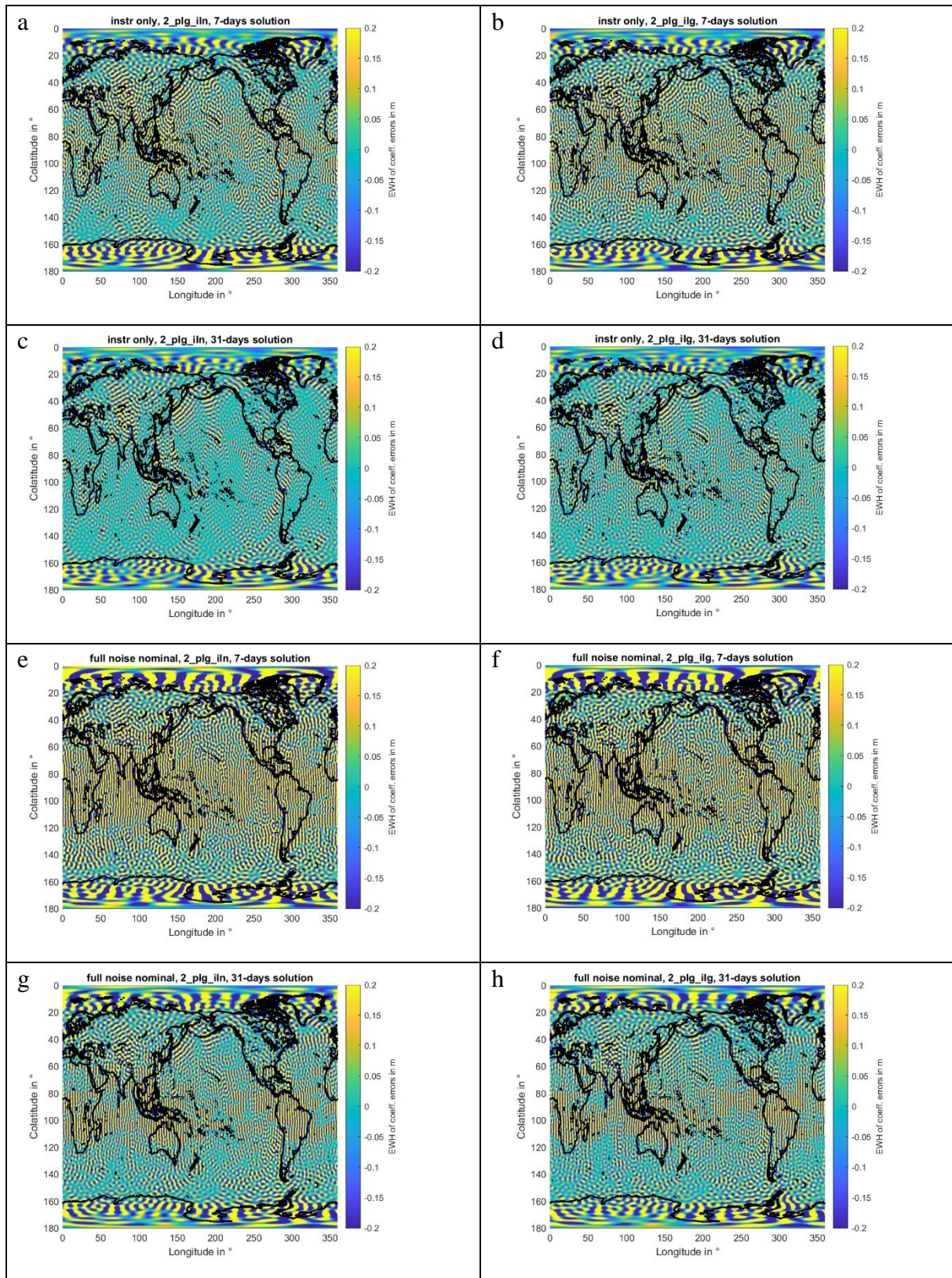
Figure 8-3 Spatial plots visualizing the retrieval performance of the scenarios 2_pIg_iIn (left column) and 2_pIg_iIg (right column) in terms of EWHs. Panels a to d show the results of the instrument only simulations, while panels e to f show the results of the full noise nominal simulations. The retrieval period amounts to 7 days (panels a, b, e, f) and 31 days (panels c, d, g, h), respectively. [Path: Deliverables/D1/simulation_results/full_scale_simulator_v009/old_noise_scaling/]

8.2 REPLACING THE POLAR BY A SUN-SYNCHRONOUS PAIR

In this section, we compare the previously investigated scenario 2_pIn_iIn (3d_H) to the new scenario 2_sIn_iIn (3d_H) in which the polar pair (89° inclination) is replaced by a sun-synchronous pair (97° inclination). The sun-synchronous orbit has polar gaps of 7° radius, which are not covered by any data in the scenario 2_sIn_iIn since the polar pair is missing. However, in the data-covered region of 2_sIn_iIn, the combination of the given inclinations could be beneficial in terms of the multi-directionality of the observations.

Both for the 2_pIn_iIn and the 2_sIn_iIn scenario, we do not apply any regularization. In order to compare the global performance of 2_sIn_iIn to the previously computed 3d_H scenarios, we compute the degree medians of the respective retrieval errors, since the degree amplitudes of 2_sIn_iIn are strongly degraded by the near-zonal SH coefficients of the polar gaps of the 2_sIn_iIn constellation. As can be seen from the plots in the left column of Figure 8-4, the global performance of scenario 2_sIn_iIn in terms of degree medians is very similar to the other depicted 3d_H double-pair scenarios in the full noise case. The formal errors of 2_sIn_iIn are, however, larger than the formal errors of 2_pIn_iIn up to degree 50 (which could be related to the missing data over the polar caps which are needed to constrain the long-wavelength features of the gravity field), and comparable to the formal errors of 2_pIn_iIn for degrees > 50.

To obtain a more detailed picture of the relative performance of 2_pIn_iIn and 2_sIn_iIn, we plot the logarithmic ratio of the respective instrument only and full noise nominal retrieval errors in panels b and e of Figure 8-4. Blue colors indicate that 2_pIn_iIn outperforms 2_sIn_iIn, while yellow colors indicate that 2_sIn_iIn outperforms 2_pIn_iIn. In the instrument-only case, the main effect visible is the degradation of 2_sIn_iIn in the near-zonal SH coefficients, caused by the missing data in the polar gaps of the sun-synchronous orbit. In the full-noise case, besides the polar gap effect, we additionally see that 2_sIn_iIn outperforms 2_pIn_iIn in the SH coefficients which are outside the polar gaps of the sun-synchronous orbit, but inside the polar gaps of the inclined orbit. That means that in the areas which are not covered by the inclined pair, and therefore the double-pair performance is solely determined by the first (i.e., the polar or the sun-synchronous pair), the larger inclination of the sun-synchronous pair is beneficial for reducing temporal aliasing errors (which are included in the full noise case). If no temporal aliasing errors are present (which is the case in the instrument only computation), no significant benefit of replacing the polar by a sun-synchronous pair could be found.

To compare the performance of 2_pIn_iIn and 2_sIn_iIn in the spatial domain, we show the respective EWH grids as stereographic projections in Figure 8-5 and Figure 8-6. In the instrument-only case, 2_pIn_iIn shows a homogeneous performance, also above the poles, while 2_sIn_iIn shows large retrieval errors above the 7° polar gaps of the sun-synchronous pair. In the full noise nominal case, the additional effect that 2_sIn_iIn outperforms 2_pIn_iIn in the near-polar region between 70° and a bit less than 80° latitude can be seen (the zonal noise in the retrieval errors for 2_sIn_iIn slightly exceeds the 7° polar gaps of the sun-synchronous pair as probably the north-south-directed observations of the polar pair are missing).

To sum up, by comparing 2_pIn_iIn and 2_sIn_iIn, we found that replacing the polar pair of a double-pair constellation by a sun-synchronous pair is beneficial to reduce temporal aliasing errors in part of the polar gap regions of the inclined pair, but introduces large zonal noise in the vicinity of the polar gap regions of the sun-synchronous pair.
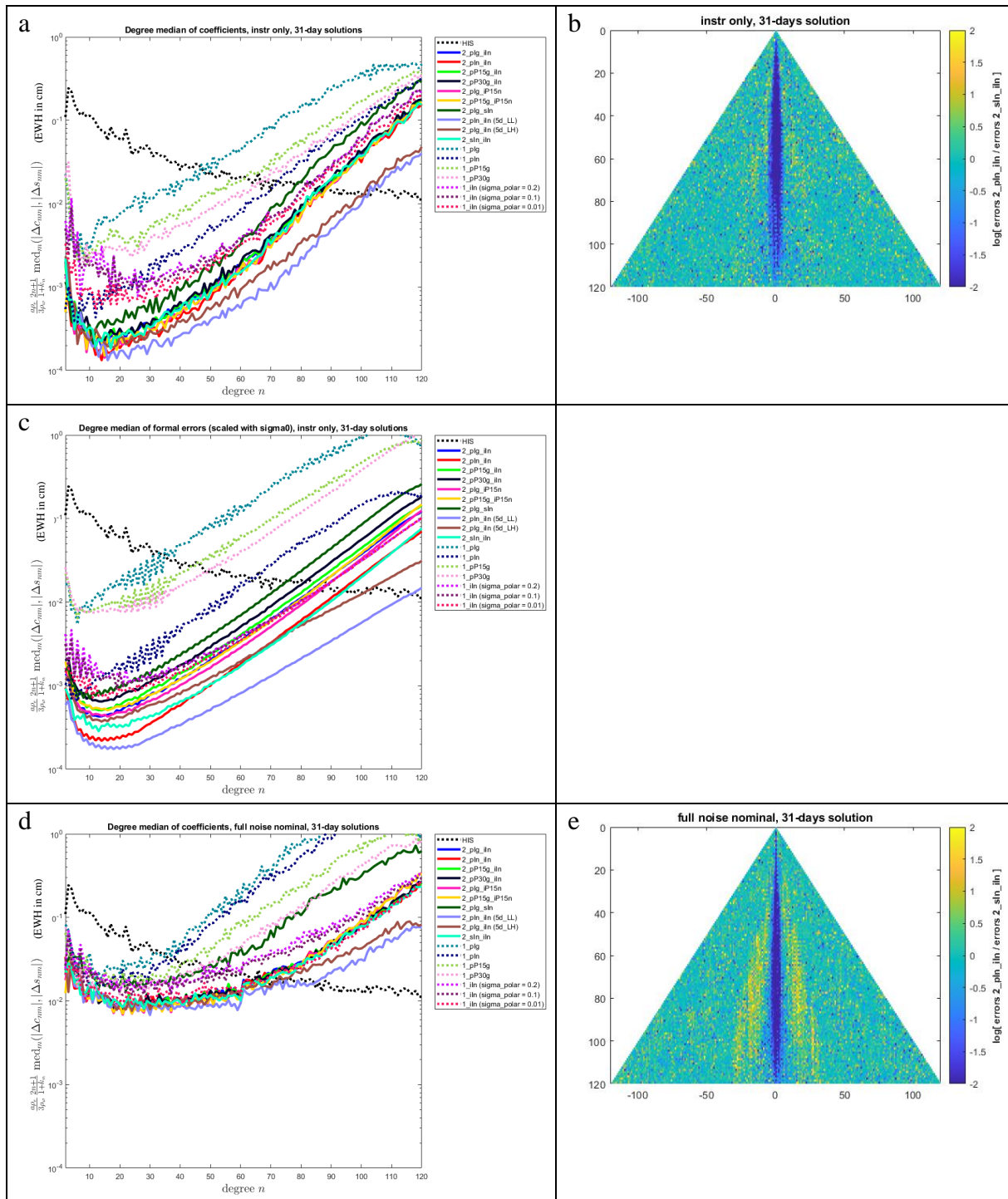
Figure 8-4 Left: Degree medians of previously computed scenarios 1 to 13 (a: coefficient errors of instrument-only simulations, c: formal errors of instrument-only simulations, d: coefficient errors of full noise nominal simulations), with the newly computed results of scenario 2_sIn_iIn depicted by the cyan solid curves. Right: Logarithmic ratio of coefficient errors of scenarios 2_pIn_iIn and 2_sIn_iIn in the instrument only (panel b) and the full noise nominal (panel e) case. [Path: Deliverables/D1/simulation_results/full_scale_simulator_v009/old_noise_scaling/]
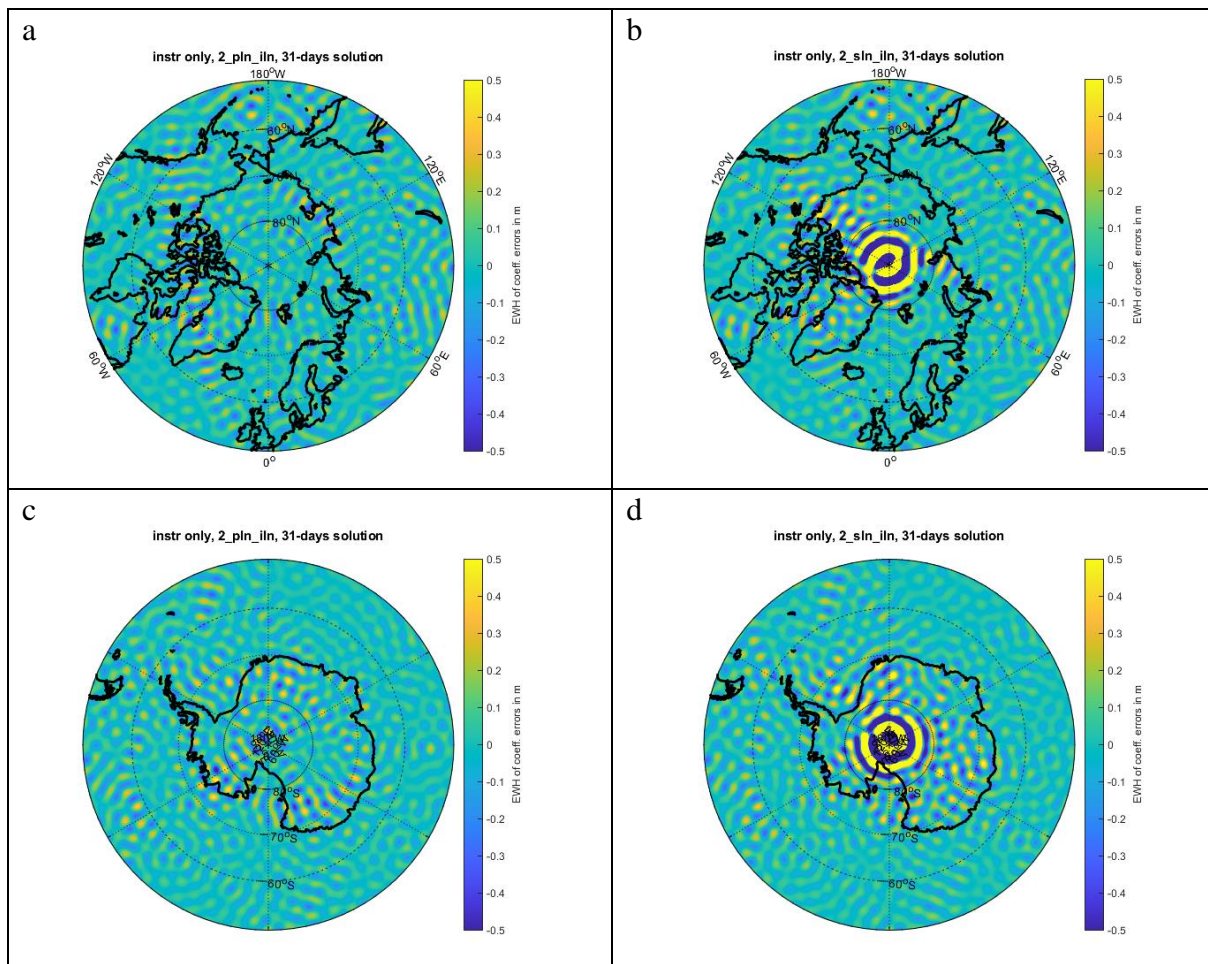
Figure 8-5 Stereographic projection of the instrument only retrieval errors in terms of EWHs, for the scenarios 2_pIn_iIn (left column) and 2_sIn_iIn (right column), in the northern (top row) and southern (bottom row) hemisphere. [Path: Deliverables/D1/simulation_results/full_scale_simulator_v009/old_noise_scaling/instrument_only/]
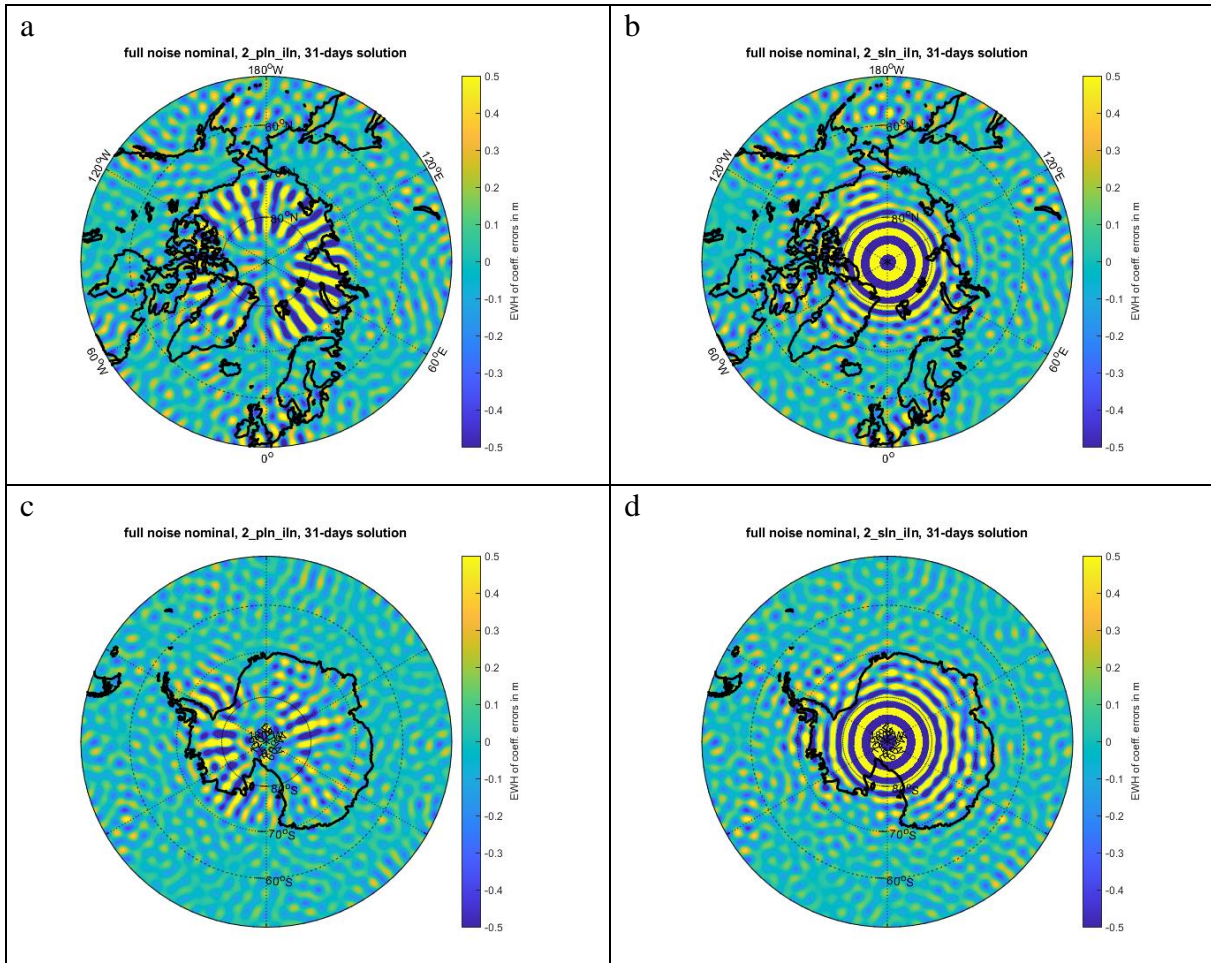
Figure 8-6 Stereographic projection of the full noise nominal retrieval errors in terms of EWHs, for the scenarios 2_pIn_iIn (left column) and 2_sIn_iIn (right column), in the northern (top row) and southern (bottom row) hemisphere. [Path: Deliverables/D1/simulation_results/full_scale_simulator_v009/old_noise_scaling/full_noise_nominal/]

8.3 IMPACT OF THE INCLINATION OF THE SECOND PAIR

The aim of this section is to analyze how the inclination of the second pair in a double-pair constellation affects the gravity retrieval errors. To this end, we compute 3-, 5- and 31-day instrument only and full noise nominal solutions for the scenarios 2_pIg_iIn (5d_Ma) and 2_pIg_iIn (5d_Mb). The altitudes of the 5d_Ma and 5d_Mb orbits are comparable, such that the main difference between these two orbit scenarios is the inclination of the second pair: For scenario 5d_Ma, the inclined pair is flying at 65° inclination while for scenario 5d_Mb, the inclined pair is flying at an inclination of 70°.

In general, a lower inclination of the inclined pair brings the benefit of a larger angle between the observation directions of the polar and the inclined pair, thereby reducing temporal aliasing errors in the latitudinal band where both satellites observe. This is, however, at the cost of a lower data coverage in the polar regions, where the double-pair performance is mainly given by the performance of the single polar pair. Therefore, the question is how small the inclination of the inclined pair could be made without decreasing the retrieval performance in the (near-)polar areas too strongly.

We start by investigating the error degree amplitudes of the computed solutions, although they only provide an insight into the global performance of the scenarios. As shown by Figure 8-7, the 5d_Ma scenario shows a better global retrieval performance than 5d_Mb for most cases. However, especially for the 5- and 31-day solutions, there are also intersections of the curves which indicate that the relative performance of the two investigated scenarios is not the same across the complete SH spectrum.

In order to better see which SH coefficients are better resolved by the 5d_Ma or the 5d_Mb scenario, we show the corresponding triangle plots in Figure 8-8. It is visible that for the (near-)sectorial coefficients, 5d_Ma performs better, which is due to the larger east-west component of the observation direction of the inclined pair of 5d_Ma that helps to constrain the variations of the gravity field in east-west direction.

For the near-zonal coefficients, in general, there is a certain pattern that shows up especially in the full noise case: The very low order-SH coefficients are well constrained, due to the higher number of polar-pair observations close to the poles where the groundtracks of the polar pair converge. Going to slightly larger SH orders, bands of increased retrieval errors are visible in the 2-d SH domain. These bands of decreased performance reflect the large temporal aliasing errors in the polar gaps of the inclined pair, where only the north-south directed observations of the polar pair are available. This phenomenon occurs more strongly for the 5d_Ma scenario which has a larger polar gap of the inclined pair compared to the 5d_Mb scenario. These two counteracting effects that a lower inclination of the second pair improves the retrieval performance for the sectorial coefficients but degrades the performance in the above-described near-zonal band explains the observation that the degree amplitudes of the retrieval errors of 5d_Ma and 5d_Mb show intersections, especially in the full noise case.

Complementing this analysis in the SH domain, we show the reduction of temporal aliasing errors outside the polar gap regions and the error increase in the polar regions for 5d_Ma compared to 5d_Mb in the spatial domain, see Figure 8-9.

As described, the relative performance of the 5d_Ma and the 5d_Mb scenario is mainly dependent on latitude. Therefore, we build RMS values of the EWH grid values plotted in Figure 8-9 along parallels and plot them in Figure 8-10 as a function of latitude. This visualization could be used to decide, based on requirements given by the cryosphere community, which minimal inclination of the inclined pair in a double-pair constellation would be acceptable such that the performance in the polar regions is not too much degraded.
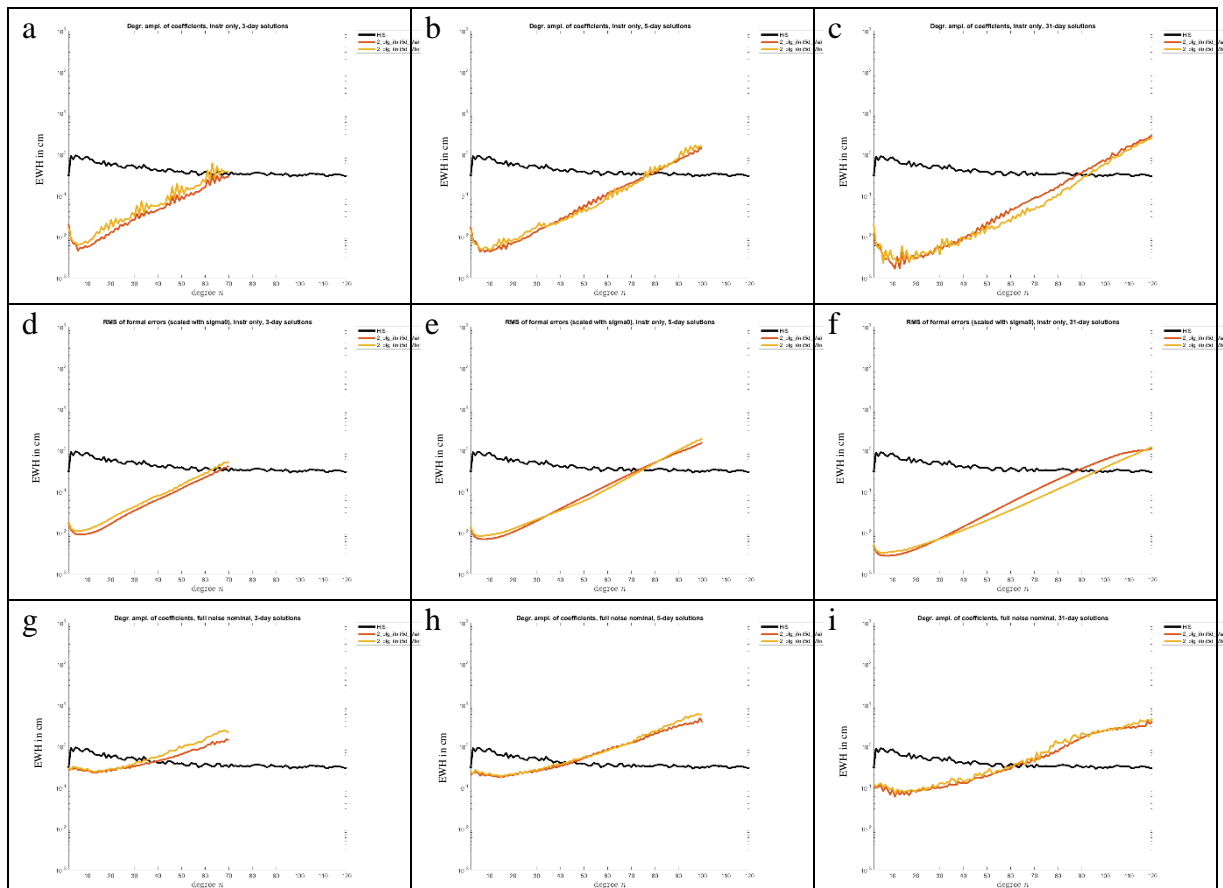
Figure 8-7 Degree amplitudes of the coefficient errors of instrument-only solutions (top row), the formal errors of instrument-only solutions (middle row) and the coefficient errors of full noise nominal solutions (bottom row), respectively. The retrieval period is 3 days (left column), 5 days (middle column) and 31 days (right column), respectively. The red curves show the retrieval errors of scenario 2_pIg_iIn (5d_Ma) while the yellow curves show the retrieval errors of scenario 2_pIg_iIn (5d_Mb). [Path: Deliverables/D1/simulation_results/full_scale_simulator_v009/old_noise_scaling/]
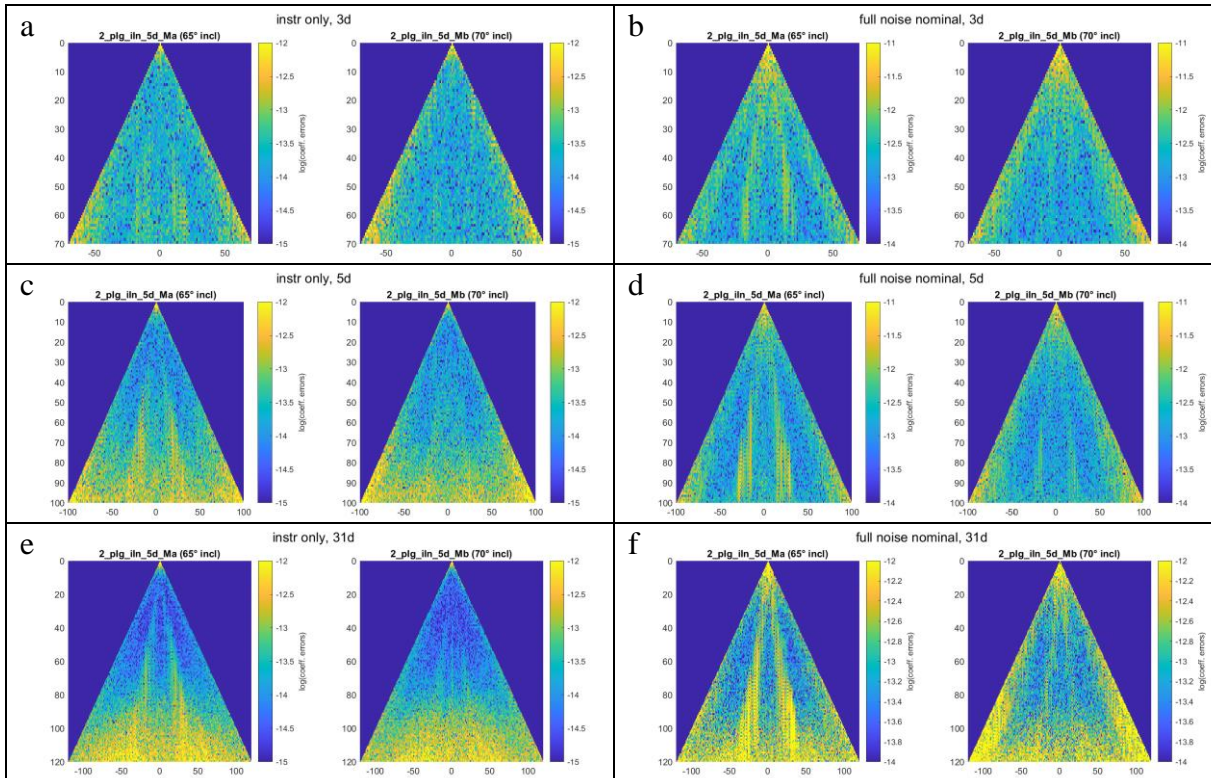
Figure 8-8 Retrieval errors of instrument-only (left column) and full noise nominal (right column) simulations for the scenarios 2_pIg_iIn (5d_Ma) and 2_pIg_iIn (5d_Mb). The retrieval period is 3 days (top row), 5 days (middle row) and 31 days (bottom row). Note the different maximum SH d/o until which the respective solutions are computed. [Path: Deliverables/D1/simulation_results/full_scale_simulator_v009/old_noise_scaling/]
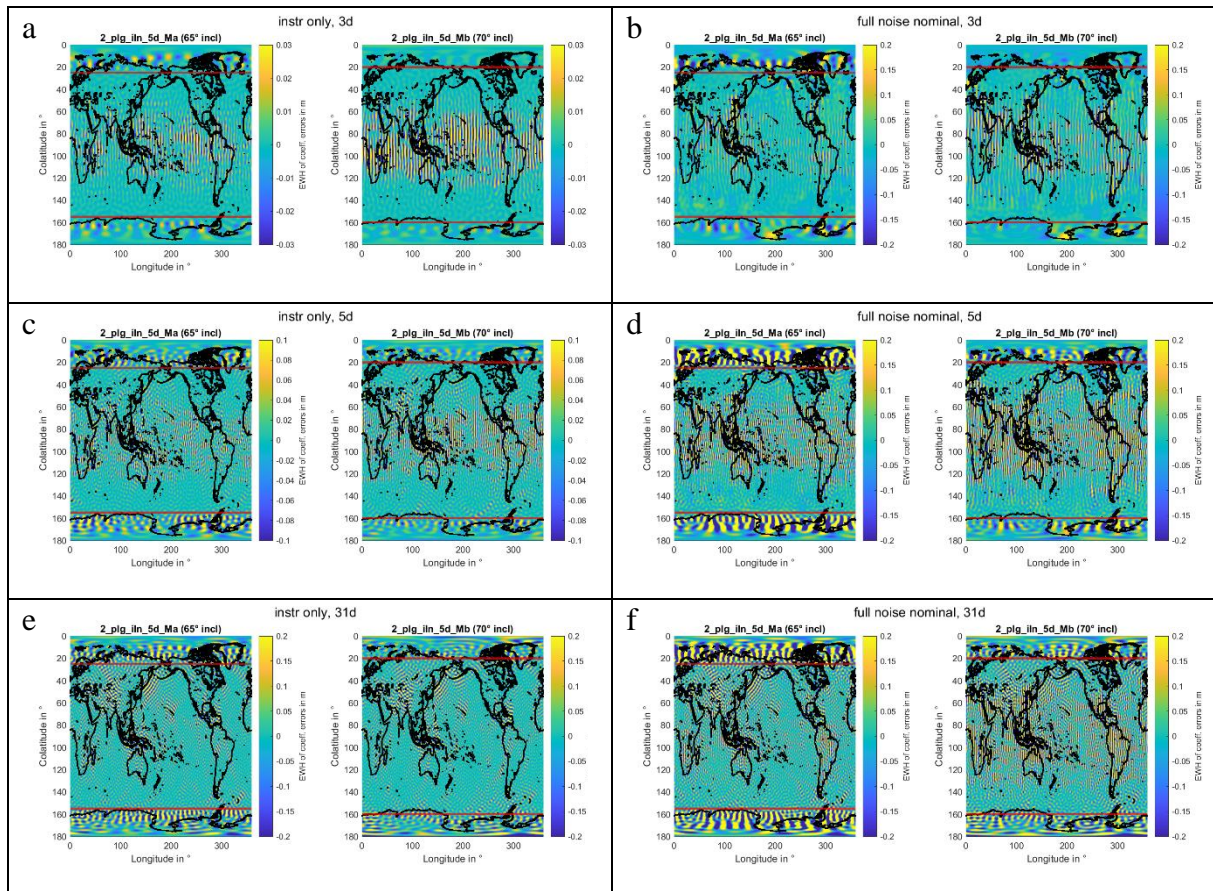
Figure 8-9 Retrieval errors of instrument-only (left column) and full noise nominal (right column) solutions in terms of spatial EWH grids. Shown are the solutions for the scenarios 2_pIg_iIn (5d_Ma) and 2_pIg_iIn (5d_Mb) for retrieval periods of 3 days (top row), 5 days (middle row) and 31 days (bottom row). The red horizontal lines in the figures marks the inclination of the inclined pair of the respective constellation (65° for 5d_Ma and 70° for 5d_Mb). [Path: Deliverables/D1/simulation_results/full_scale_simulator_v009/old_noise_scaling/]
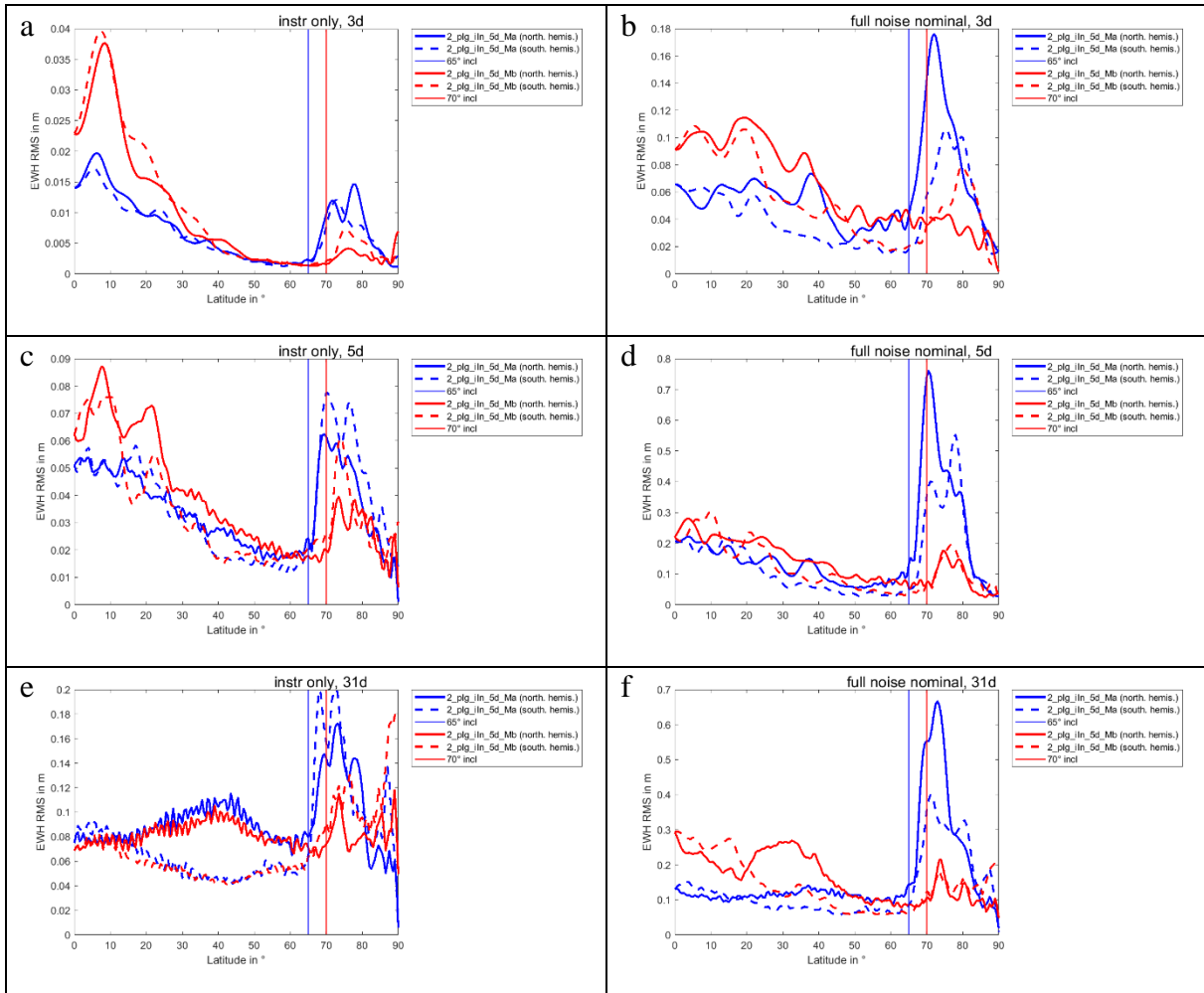
Figure 8-10 Root-mean-square values of the EWH grid values computed along parallels based on the EWH grid points shown by Figure 8-9. On the x axes, 0 denotes the equator and 90 the north pole (for the solid curves) and the south pole (for the dashed curves). The blue curves correspond to the scenario 2_pIg_iIn (5d_Ma) and the red curves to the scenario 2_pIg_iIn (5d_Mb), respectively. The vertical lines mark the inclination of the respective second pair (65° for 5d_Ma and 70° for 5d_Mb). [Path: Deliverables/D1/simulation_results/full_scale_simulator_v009/old_noise_scaling/]

NGGM/MAGIC – Science Support Study During Phase A	Final Report	
	Doc. Nr:	MAGIC_FR
	Issue:	1.0
	Date:	15.11.2022
	Page:	111 of 466

9 IMPACT OF ACC PERFORMANCE AND BM ERRORS

9.1 FULL-SCALE RESULTS FOR SCENARIOS SR-1, SR-5 AND S-5

In this section, we present results for some of the newly defined scenarios listed in Table 9-1. The main difference to the previously analyzed scenarios is the assumed ACC instrument: For the new scenarios, we consider the coarse- or fine-pointing superSTAR accelerometer as well as the fine-pointing microSTAR accelerometer. For each combination of an ACC instrument and an assumption for the drag compensation of the satellite (no drag-free, drag compensation along the x axis only, drag compensation along all three axes), the frequency-dependent ACC product noise (given along the satellites' line of sight) has to be pre-specified in terms of an Amplitude Spectral Density (ASD). The dependence of the ACC ASD on the satellite altitude is rather weak.

Figure 9-1 shows these given ACC ASDs for four cases, as the yellow curves in the four panels. Panels a and b show the coarse- and fine-pointing superSTAR ACC in no drag-free mode for a satellite altitude of 488 km. Panels c and d show the microSTAR ACC assuming drag compensation along the x-axis, for satellite altitudes of 465 and 488 km, respectively.

Based on these ACC ASDs and the ASDs for the LRI instrument, combined ACC+LRI noise time series with a sampling rate of dt = 5 s have been computed. For that, our procedure to generate noise time series based on given ASDs has been adapted such that the factor of 1/sqrt(2*dt) is now applied to the noise time series and not in the computation of the ASD. This was done in order to adjust the computation of noise time series to the industry partner TASI. In order to avoid an unrealistic increase in the derived retrieval errors due to ACC noise in the very low frequencies < 1e-4 Hz, we highpass-filter our noise time series such that their ASDs (orange curves in Figure 9-1) become flat for f < 1e-4 Hz and do not increase in amplitude towards lower frequencies, as it is shown by the given ACC ASDs (yellow curves in Figure 9-1). This procedure can be justified as also real ACC data can be highpass-filtered to improve the gravity field retrieval in the real data processing case.

The blue curves shown by Figure 9-1 are the ASDs of the instrument only pre-fit range rate residuals computed by our simulation software, which represent the observation vector of the associated NEQ system. The difference in amplitude between the pre-fit spectra shown by the blue curves and the input noise time series shown by the orange curves is caused by the numerical errors of the simulation. We note that due to the meanwhile very low instrument-noise levels, which are additionally reduced by dividing the noise time series by sqrt(2*dt), the instrument noise levels are lower than the numerical noise levels across almost the full spectral range, except for the coarse-pointing superSTAR case where the instrument noise levels are still large enough. The limitation of the simulations due to the large numerical noise levels is a problem specific to the full-scale simulation software (version v009) used at TUM and is not present in the software used at GFZ. Meanwhile (towards the end of the project), the numerical noise in the TUM software could be significantly reduced, such that this limitation is not present any more when using the updated simulator version (v010).

We show the d/o 120 31-day simulation results for the scenarios SR-1, SR-5 and S-5 in Figure 9-2. By comparing the coefficient errors (panel a) and the formal errors (panel b) of the

instrument-only case, we see that especially for scenario S-5 where the microSTAR accelerometer is used, the coefficient errors are larger than the formal errors. This could be due to numerical errors which are contained in the coefficient errors (as they include the right-hand-side of the NEQ system) but not in the formal errors. In the full noise nominal results shown by panel c, the error budget is dominated by temporal aliasing errors, therefore the difference between SR-5 and S-5 becomes minor.

In order to find out if the impact of replacing a fine-pointing superSTAR ACC (no drag compensation) by a fine-pointing microSTAR ACC (drag compensation along the x-axis) becomes visible in the full noise nominal case if the amount of background model (BM) errors is reduced, we additionally consider the full noise case with only 75% of the BM errors included. With this, we attempt to obtain an idea of the performance of the individual scenarios if in several years, the BMs will have been improved.

The full noise 75% BM error case is implemented as follows: To simulate an improvement of the ocean tide model errors by 25%, we still use the eot model for the forward computation. For the inversion, we use a newly created OT model which is created as eot + 0.75 * (got-eot), such that the new difference of the two used models amounts to 0.75 * (got-eot) which corresponds to 75% of the OT model error that we include in the usual full noise nominal computations. To simulate a 25% improvement of the atmosphere and ocean dealiasing model, we exchange the dealiasing model used for the usual full noise nominal computations (DEAL + 1 * AOerr) by DEAL + 0.75 * AOerr.

Panel d of Figure 9-2 shows the results for the full noise (75% BM error) simulations. Comparing these to the retrieval errors of the 100% BM error case shown by panel c, we see a slight improvement if the BM errors are reduced. This impact, however, is rather small, as also in the 75% BM error case, the temporal aliasing errors lie well above the instrument-only error level. I.e., also in the case of 25% reduced BM errors, the impact of replacing the superSTAR by a microSTAR accelerometer is negligible, given the still much larger temporal aliasing errors.

To summarize, we found that in the case of much reduced instrument error levels (especially the fine-pointing superSTAR and microSTAR ACC instruments), the numerical errors in our simulation software influence the instrument-only results significantly. In the full noise nominal case, independently of applying 100% or 75% BM errors, the impact of different accelerometers is hidden behind the much larger temporal aliasing errors.

Table 9-1 Overview on the additional scenarios SR-1 to S-8 using the superSTAR coarse (ssc), superSTAR fine (ssf) and microSTAR fine (msf) accelerometers in no drag-free, 1 axis drag-free and 3-axes drag-free mode.

ID	Polar pair					Inclined pair				
	orbit	alt./km	incl./°	ACC	d.-free	orbit	alt./km	incl./°	ACC	d.-free
SR-1	5d_H	488	89	ssc	no					
SR-2	5d_H	488	89	ssf	no					
SR-3	5d_H	488	89	ssf	1 axis					
SR-4	5d_H	488	89	ssf	no	5d_E	488	75	ssf	no
SR-5	5d_H	488	89	ssf	no	5d_H	465	75	ssf	1 axis
S-1	5d_H	488	89	msf	no					
S-2	5d_H	488	89	msf	1 axis					
S-3	5d_H	488	89	ssf	no	5d_H	465	75	msf	1 axis
S-4	5d_H	488	89	msf	no	5d_H	465	75	msf	1 axis
S-5	5d_H	488	89	msf	1 axis	5d_H	465	75	msf	1 axis
S-6	3d_H	463	89	msf	no	3d_H	432	70	msf	1 axis
S-7	3d_H	463	89	msf	1 axis	3d_H	432	70	msf	1 axis
S-8	5d_LH	492	89	msf	no	5d_LH	344	71.5	msf	3 axes
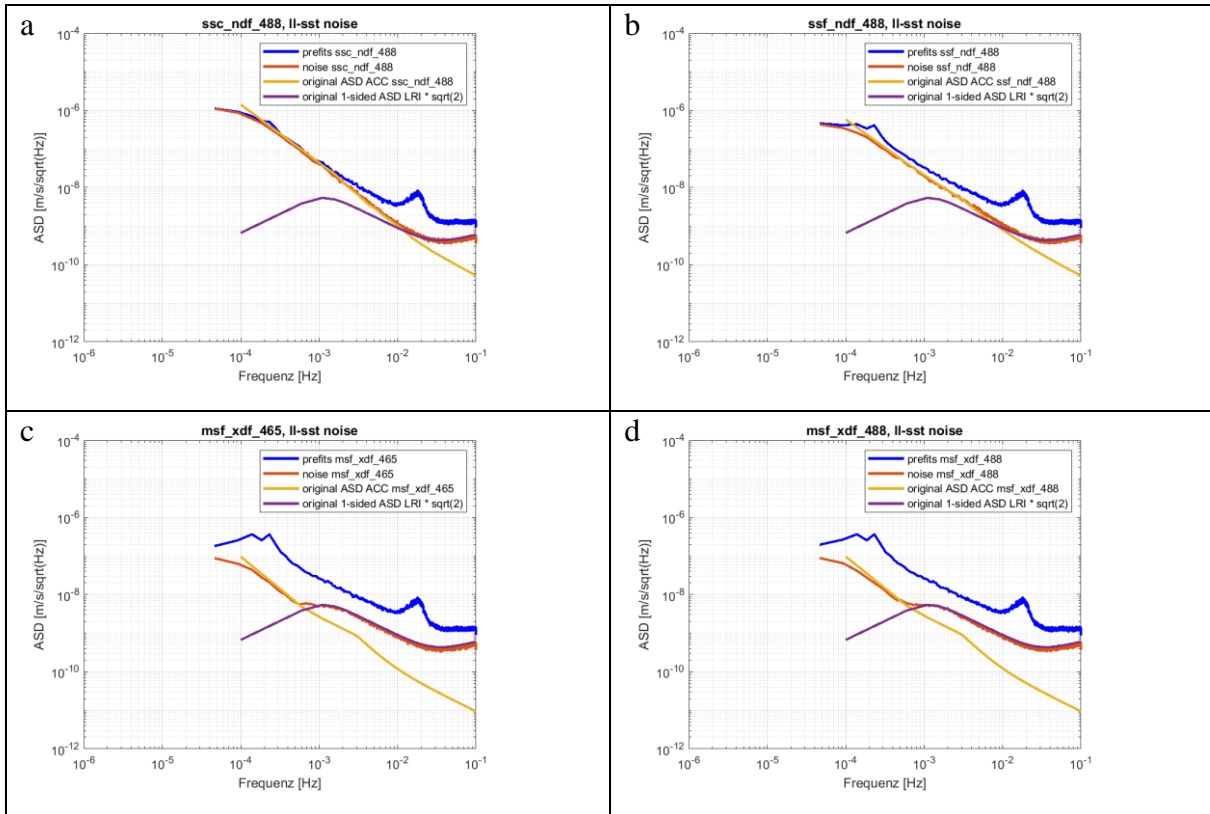
Figure 9-1 Amplitude spectral densities (ASDs) of the combined ACC + LRI instrument noise along the line of sight of the two satellites. The panels differ by the ACC instrument noise included. Panel a: superSTAR coarse-pointing ACC in no drag-free mode (for an altitude of 488 km), panel b: superSTAR fine-pointing ACC in no drag-free mode (for an altitude of 488 km), panels c and d: microSTAR fine-pointing ACC with drag compensation in x direction (for an altitude of 465 km for panel c and 488 km for panel d)).
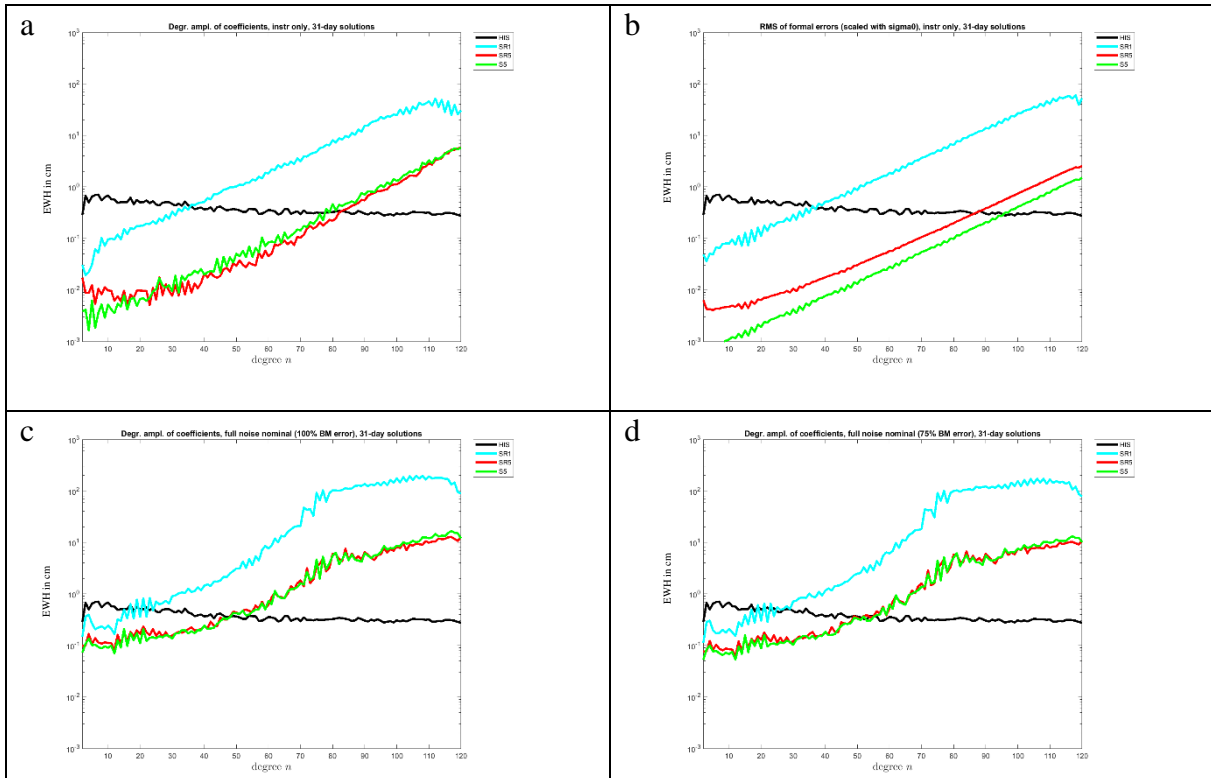
Figure 9-2 Degree amplitudes of the retrieval errors for 31-day simulations for the scenarios SR-1, SR-5 and S-5. Panels a and b show the retrieval errors of instrument-only simulations (a: coefficient errors, b: formal errors). Panels c and d show the retrieval errors of full noise nominal simulations (c: usual full noise nominal results, d: full noise nominal results if the AO and OT background model errors are reduced by 25%). [Path: Deliverables/D1/simulation_results/full_scale_simulator_v009/1_by_sqrt(10)_noise_scaling/ and Deliverables/AdHoc/20220209_SR1_SR5_S5]

9.2 REDUCED-SCALE RESULTS FOR SCENARIOS SR-5 AND S-5

As has been shown in Section 9.1, the results for the scenarios SR-1, SR-5 and S-5 computed by the full-scale simulation software are partly strongly affected by numerical errors in the software. For this reason, we additionally show here some results computed using the reduced-scale simulation software available at TUM.

Figure 9-3 visualizes the relative magnitude of the error contributors for the SR-5 and S-5 scenarios. The green and cyan curves show the retrieval errors introduced by the instrument noise in the two scenarios. We note that the error level of the instrument-only results as shown here would be larger if the instrument noise time series was not scaled by the factor 1/sqrt(10) (see Section 9.1 for more background information on this factor). By comparing the instrument-only results for SR-5 and S-5, we see that contrary to the corresponding full-scale simulation results shown in panel a of Figure 9-2, the results computed by the reduced-scale simulator do not suffer from numerical errors that strongly, which is why we repeat part of our analysis presented in Section 9.1 in the present section.

The impact of the temporal aliasing errors introduced in the full noise case due to non-tidal AO and ocean tide background model errors is separately shown by the blue and red curves in Figure 9-3. First of all, in comparison to the instrument-only curves, it is visible that the part of the retrieval errors that is caused by background model errors is up to 1-2 orders of magnitude larger compared to the part introduced by the instrument noise. Secondly, it can be seen that even if the background model errors were reduced by 25%, the impact of improving the accelerometer noise level is still negligible if background model errors of this magnitude are included.

To summarize this section, using the reduced-scale simulation software which does not suffer from numerical errors as strongly as the full-scale simulation software, we could confirm our results on the relative importance of the instrument noise and the background model errors shown in Section 9.1: Even if the background model errors were reduced by 25%, the impact of replacing the superSTAR accelerometer used for SR-5 by the microSTAR accelerometer used for S-5 is negligible in view of the retrieval error levels introduced by background model errors.
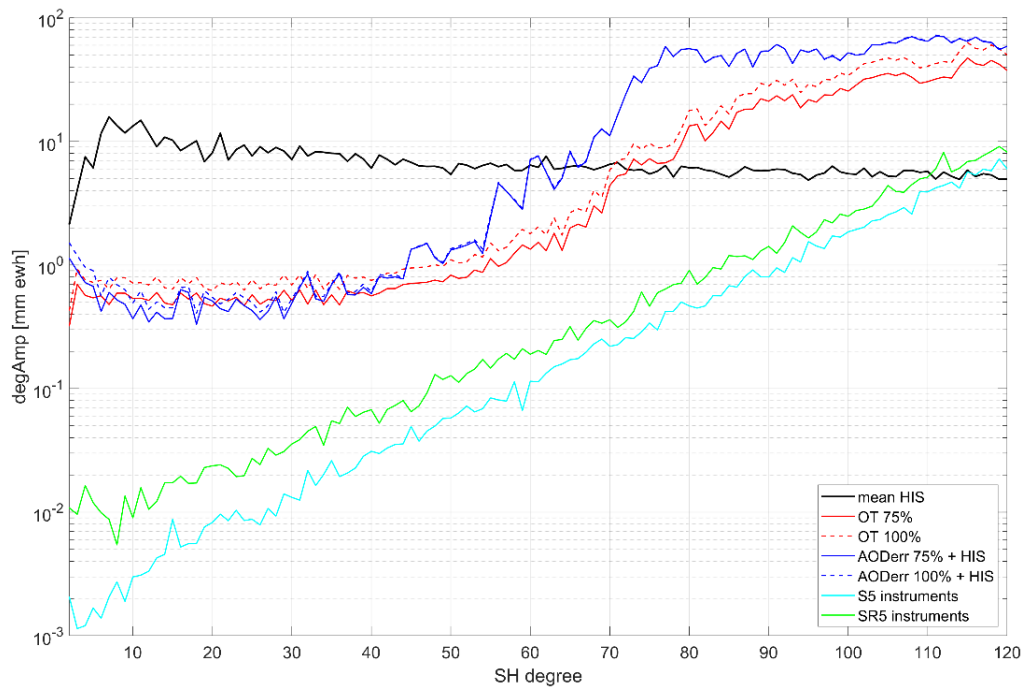
Figure 9-3 Degree amplitudes of the simulation results for the double-pair scenarios SR-5 and S-5 using the reduced-scale simulation software. The green and cyan curves show the retrieval errors of the instrument-only simulations for the SR-5 and S-5 scenario, respectively. The blue curves show the retrieval errors if temporal aliasing errors due to non-tidal background model errors are included, while the red curves show the retrieval errors if temporal aliasing errors due to ocean tide background model errors are included. In the case of the dashed lines, the respective background model error is fully included, while in the case of the solid lines, the respective background model error is reduced by 25%. [Path: Deliverables/AdHoc/20220209_SR1_SR5_S5/reduced_scale/]

9.3 FULL-SCALE RESULTS FOR MICROSTAR INCLUDING DRAG COMPENSATION

In this subchapter, we investigate the impact of various product noise scenarios on the double-pair-based gravity retrieval performance. These scenarios represent a combination of the MicroSTAR instrument performance combined with different levels of imperfect drag compensation for the inclined satellite pair in regard to different atmospheric conditions ranging from a "best-case" full, i.e. 3D, drag compensation (here, the performance does not depend on whether the atmospheric activity is minimal or maximal) to a "worst-case" 1D drag compensation, i.e. in along-track direction, considering maximum atmospheric conditions. The noise scenarios are denoted as MAX1D, MAX1D 50%, MAX3D (equivalent to MIN1D) and MIN1D (equivalent to MIN1D prima), and their specifications are depicted in Figure 9-4 in terms of ASDs. Note that the product noise performance for the polar pair remains unchanged to all other conducted simulations, i.e. here we consider the SuperSTAR ACC in combination with the LRI based on eq. (3). The retrieval is carried out for a time span of 7 days for a product-noise-only as well as for a full-noise (i.e. including time-variable gravity field) case.
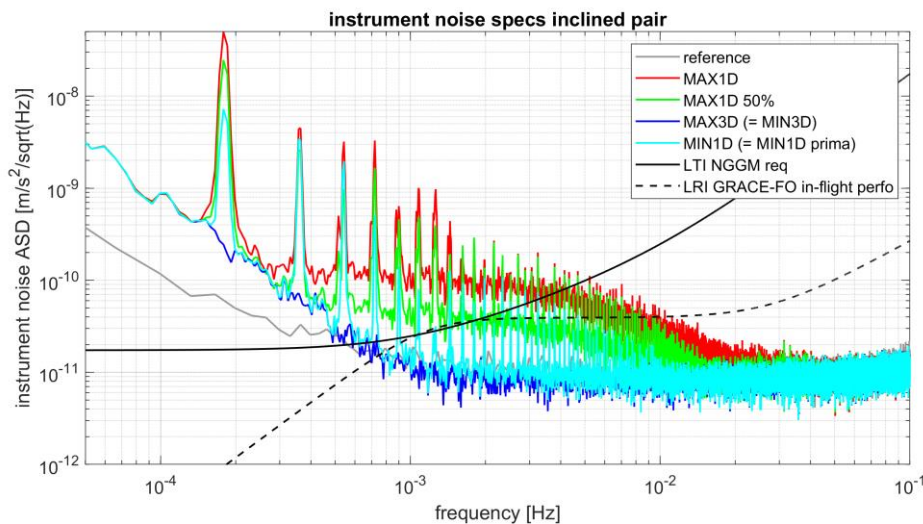
Figure 9-4 Investigated product noise specifications

The retrieval errors in case of a product-noise-only retrieval scenario are depicted in Figure 9-5. It is evident that the reference scenario shows – as expected – the best performance due to its overall lowest level of the product noise on the inclined pair. The scenarios MIN1D, MIN1D prima, MAX3D and MAX1D show a very similar noise performance among each other, but perform worse than the reference case up to d/o 30. It can thus be concluded that here an optimally applied stochastic modelling can for the most part compensate for the drag-related "spikes" at multiples of the orbital frequency. A further degradation occurs if the MAX1D 50% scenario is considered, where a decreased gravity retrieval performance can be asserted primarily in the spectral bands up to d/o 50 in comparison to e.g. MAX3D. This behaviour could be expected due to the on one hand with the overall higher noise level in the low frequencies and on the other hand with the significantly increased drag-related spikes. This behaviour is even further amplified in the MAX1D scenario. It is also notable that both in case of MAX1D and MAX1D 50% the error curves shown in Figure 9-5 feature a high level of oscillation between subsequent spectral bands, which is evidently related to the extremely high

spikes which in this case cannot be optimally handled even through specifically tailored stochastic modelling.
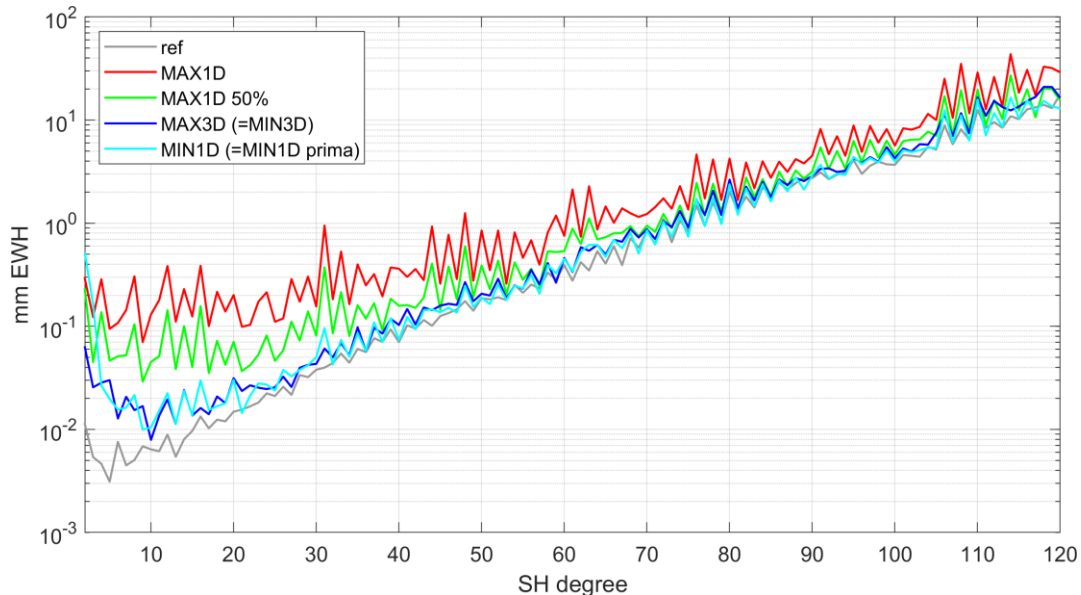
Figure 9-5 Retrieval error for the product-noise-only simulation scenarios
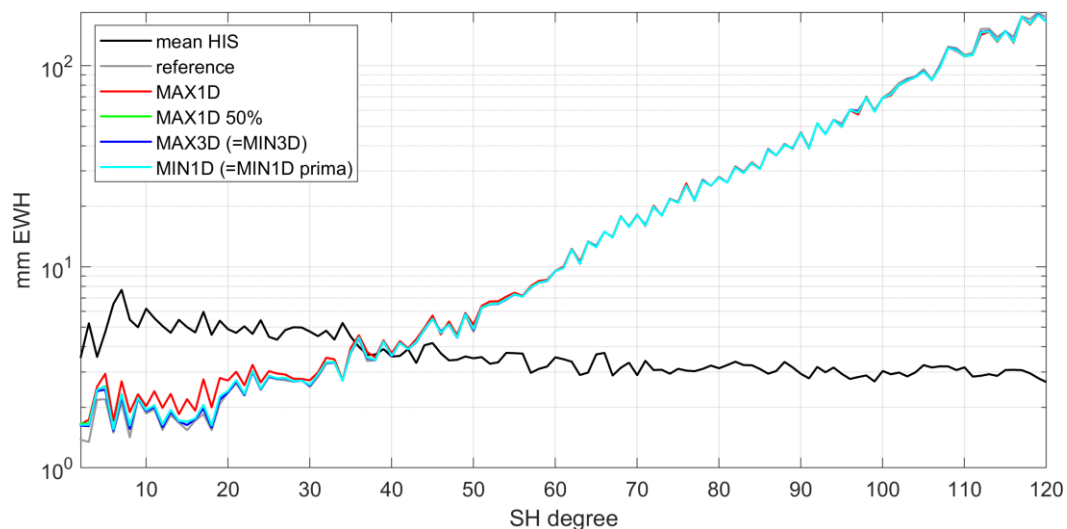
Figure 9-6 Retrieval error for the full-noise simulation scenarios

In case of the full-noise simulation scenario where de-aliasing is applied for the AO and OT components with the HIS component as target signal, the variations between the investigated scenarios are much smaller (cf. Figure 9-6). Clearly much of the impact of the drag compensation is covered by the temporal aliasing induced by the gravity field's temporal variability. Here, only minor deviations to the reference scenario can be established for MAX3D, MIN1D and MAX1D 50% in the lowest spatial frequencies. Larger deviations can be seen up around to d/o 25 in case of MAX1D, which is, as already noted in the product-noise-only simulations, related to the spikes' impact. However, although this behaviour is of course undesirable, the signal-to-noise ration remains well below 1 even in this case, and thus can be expected to not significantly hamper the gravity retrieval.

10 REPROCESSING WITH METHODOLOGY UPDATES AND ANALYSIS OF RESULTS (GFZ)

In this chapter results related to the application of the 2-step or data-driven multi-step self-de-aliasing (DMD) approach are assessed. Originally, the DMD approach was developed in order to improve single-pair-based gravity fields instead of using the Wiese approach. Tests based on real GRACE data have shown significant improvements in terms of reduced aliasing errors for a typical monthly solution compared to a nominally derived gravity field solution. In order to evaluate whether this approach is also able to improve Bender-type derived gravity field solutions, it has been applied in the simulation world using GFZ's EPOS software. The approach has been applied at the example of the Bender 3dH scenario for monthly and sub-monthly retrievals.

10.1 DMD APPROACH FOR SINGLE-PAIR FORMATION

The strategy of the DMD approach is to capture the short-periodic long-wavelength signals, which are predominantly related to the time-variable AO component, within the interval fields and thus prevented from manifesting as temporal aliasing effects, i.e. striping, within the long-term solution

The gravity field observations are split into intervals of e.g. one day of length for which individual low-resolution gravity fields up to a certain harmonic degree (based on previous made tests for real GRACE and GFO data this value has been set to d/o 12) are estimated, disregarding the fact that the observations contain also high-degree signals and thus allowing for a certain amount of spectral leakage. Treating the latter prior to the estimation of the interval fields is crucial, as otherwise the entirety of the corresponding signal would be parametrized into the low-degree spectrum, thus inducing a large-scale error. Therefore, its short-wavelength components are reduced and retain the low-degree part, i.e. the estimation of the interval fields is done while fixing the high-degree spectrum to the static signal's values.

These fields then represent valid stand-alone gravity solutions for the respective interval and are further used to compute reference observations which in a subsequent step are reduced from the original ones. Based on the reduced observations a long-term, e.g. monthly, solution is estimated up to the usually chosen maximum d/o of 96 for real data solved fields and, in a final step, restore the mean of the interval estimates to the low degrees of the long-term solution. In fact, the latter is done in an alternative approach, where the interval fields' mean value can be computed already after the estimation of the short-term interval fields and already restored to them instead of restoring the low degrees of the long-term solution, so that the reference observations used for the de-aliasing step are only comprised of variations with respect to the total signal's long-term mean.

The approach has already been tested on real GRACE/GFO data showing significant reduction of retrieval errors for dedicated monthly periods. As an example, the monthly averaged gravity field recovery of the year 2007 together with the result when applying the DMD approach are displayed in Figure 10-1. It is to mention that the GFZ related results were computed based on the RL06 processing scheme.
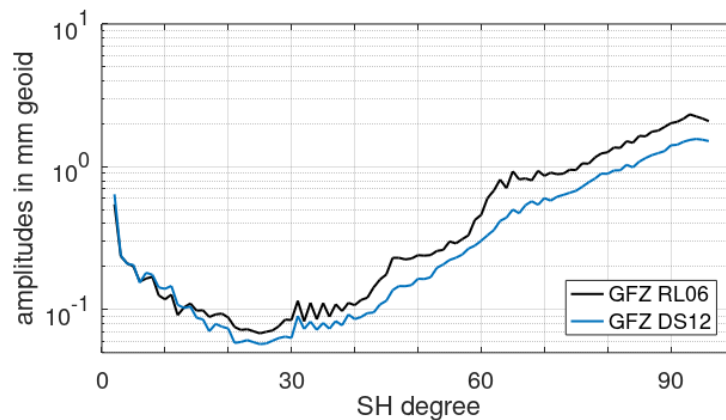
Figure 10-1: Monthly averaged degree amplitudes in mm geoid of the year 2007 for GFZ RL06 nominally processed fields (black) and for fields including the 2-step approach (blue).

In order to check whether the approach is working in the simulation world as well, it was applied to a single pair GFO-like formation flying at 490 km altitude, at first. Identical instrument noise assumptions were used as for all the polar pairs of the Bender-type formations simulated in this study. The fixing of the high-degree spectrum when estimating the daily fields (up to d/o 12) was done by means of a static field (GOCO05s). Figure 10-2 shows the performance of the single pair when applying the nominal processing scheme and when applying the DMD method. Results demonstrate that the DMD-processed solution benefits from reduced aliasing errors for the majority of the spectrum, except for the very low degrees. This result is consistent to the results obtained with real GRACE data.
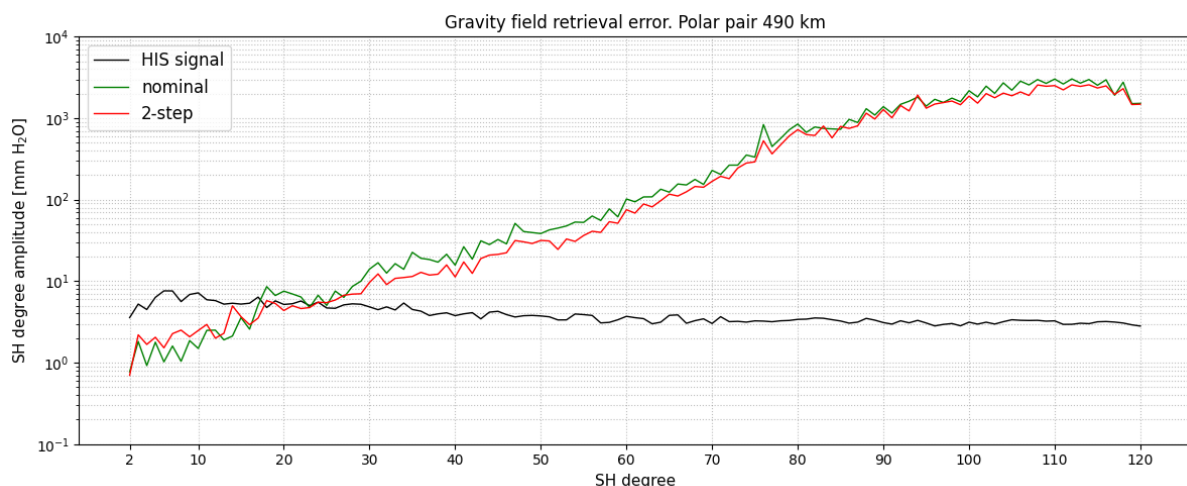
Figure 10-2: Degree error amplitudes in mm EWH for a single-pair formation based on a monthly retrieval when using the nominal processing scheme (green) and when applying the DMD approach (red). The reference signal is displayed in black.

10.2 DMD APPROACH FOR DOUBLE-PAIR FORMATION

The test with the single pair formation has shown that the application of the DMD approach works in the simulation world as well. In a next step the approach was applied to the Bender 3dH scenario. The gravity field recovery has been done in terms of estimating the full AOHIS signal (without using an AOD model) as well as estimating the HIS signal (when an AOD model is applied). Daily gravity fields were estimated up to d/o 12, 16 and 20 as the doubled amount of observations as well as the observation geometry allow for a higher maximum resolved daily retrieval. Figure 10-3 displays the performances of the daily fields used as additional de-aliasing model in the second step when performing the long-term (monthly or sub-monthly) gravity field recovery. The plotted retrieval errors show that the truth signal can be resolved up to d/o 20 without dominating error signals indicating a high quality of the daily estimated to be used in the second step.
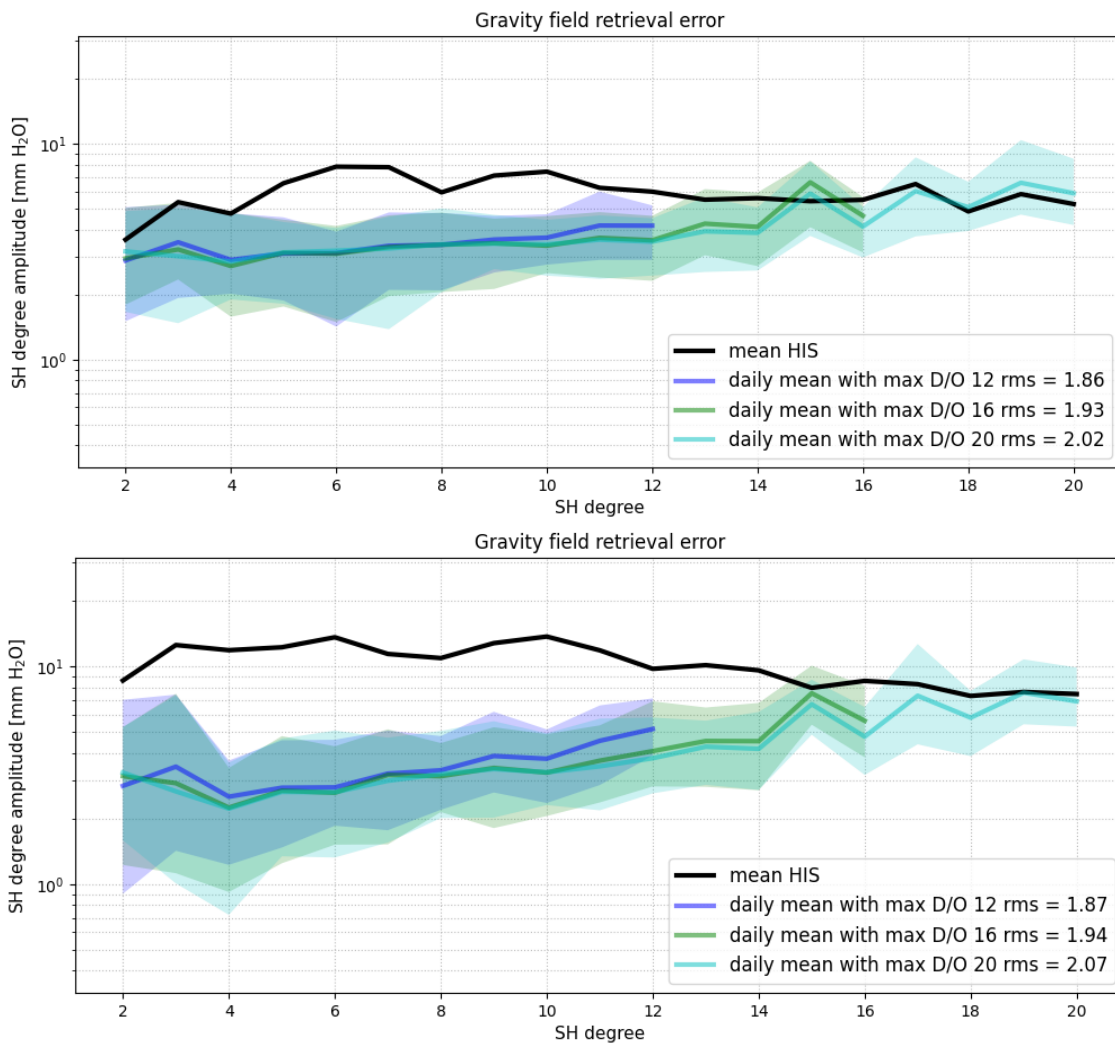
Figure 10-3; Degree error amplitudes in mm EWH for the 3dH scenario of all daily fields from January 2002 resolved up to max. d/o 12 (blue) 16 (green) and 20 (cyan). Solid lines represent the average of the daily amplitudes, respectively. The reference signal HIS (top) and AOHIS (bottom) is displayed in black.

The differently resolved daily fields were applied as additional de-aliasing product for the gravity field recovery of the 3dH case. The resulting gravity fields were compared against the nominal solution and the Wiese solution, respectively.

Figure 10-4 shows the monthly retrieval errors for the different solutions in case of not using an AOD model and resolving the full AOHIS signal. The DMD related solutions show a similar performance as the Wiese solution for the low degree spectrum indicating a successful de-aliasing of AO signals in this wavelength spectrum. Further, it is seen that the DMD solutions degrade between degree 20 and 35 (the degradation is getting less prominent when solving the daily fields up to a smaller max. d/o) but show less error signals for degrees between 35 and 50 compared to the nominal and the Wiese solutions. DMD results indicate that higher resolved daily fields lead to additional error signals in the monthly recovery for a dedicated bandwidth where the satellite constellation itself de-aliases the system due to the long time span of one month, already. The corresponding spatial representations are displayed in Figure 10-5.

Figure 10-4: Degree error amplitudes in mm EWH of a monthly retrieval for the 3dH formation without using an AOD model. The reference signal (AOHIS) is plotted in black.

Figure 10-5: Global grids of monthly retrieval errors of the 3dH formation solved up to d/o 60 without including an AOD model.

Figure 10-6 displays the monthly retrieval errors where an AOD model was included during the processing. All results perform relatively similar, however, the DMD solutions based on higher resolved daily fields (up to d/o 16 and 20) show again increased error signals in the spectrum between 20 and 35 due to the same reasons as stated before. The corresponding global grids are shown in Figure 10-7. Due to the fact of increased errors for the bandwidth between degrees 20 and 35, DMD related monthly solutions do not show an improved performance compared to the nominal and Wiese solutions, for both cases, with and without including an AOD model.

Figure 10-6: Degree error amplitudes in mm EWH of a monthly retrieval for the 3dH formation when using an AOD model. The reference signal (HIS) is plotted in black.

Figure 10-7: Global grids of monthly retrieval errors of the 3dH formation solved up to d/o 60 including an AOD model.

The DMD approach has been tested for sub-monthly retrievals as well. Figure 10-8 and Figure 10-9 show the retrieval errors for a solution based on the first 7 days of January 2002 when the AOD model was not included. Again, the DMD solutions perform similar compared to the Wiese solution for the low degree spectrum indicating a successful de-aliasing of A and O signals. Further, it is seen that the DMD solutions do not show increased error signals between degrees 20 and 35 anymore as it was seen for the monthly retrievals. This might be caused by the shorter retrieval period which hampers the system to further de-alias A and O signals so that the DMD additionally helps to de-correlate the system. The amount of retrieval error of the monthly nominal solution is significantly smaller than the retrieval error of the 7-day nominal solution, especially in the spectrum between degrees 2 and 40. Therefore, the potential of the DMD approach is exploited better for shorter retrievals (e.g. 7 days) compared to a monthly retrieval. The additional de-aliasing effect of the DMD approach can be even further increased when solving the underlying daily fields up to a higher spatial resolution (e.g. d/o 20).

Figure 10-8: Degree error amplitudes in mm EWH of a 7-day retrieval for the 3dH formation without using an AOD model. The reference signal (AOHIS) is plotted in black.
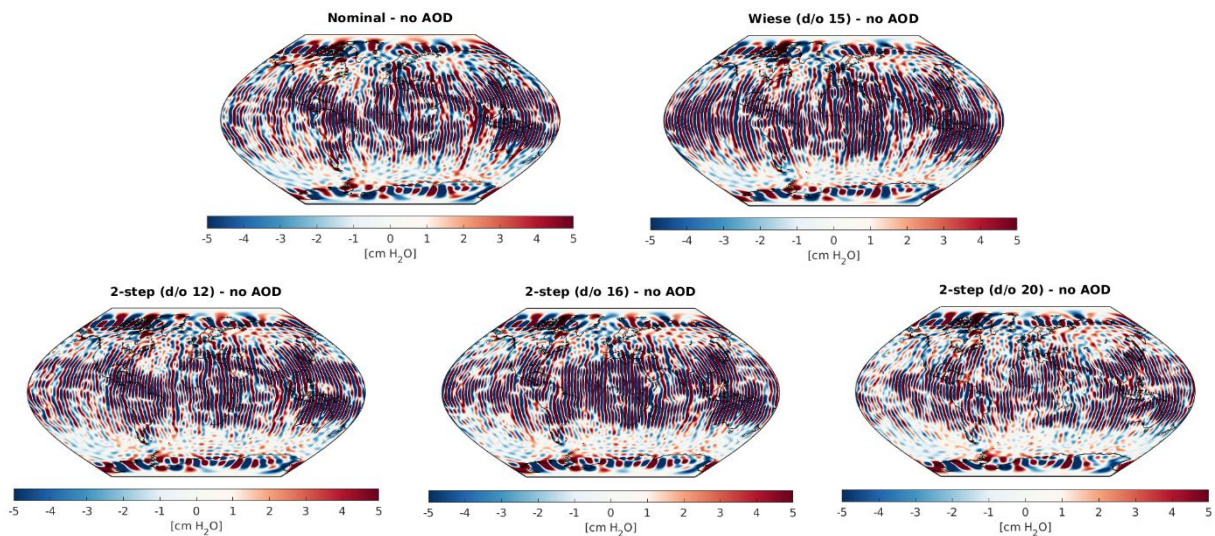
Figure 10-9: Global grids of 7-day retrieval errors of the 3dH formation solved up to d/o 60 without including an AOD model.

Figure 10-10 and Figure 10-11 show the retrieval errors when an AOD model was included during processing. The performance of the DMD solutions among each other is similar and also the performance compared to the nominal and Wise solutions does not differ much. The possible benefit of the DMD approach is smaller or even not existent when using an AOD model for de-aliasing A and O signals as the signals, to which the DMD approach aims at (as well as the Wiese approach), are already de-aliased by the AOD model. However, a small benefit is visible for the DMD solution, which is based on d/o 20 resolved daily fields, wrt. the nominal solution
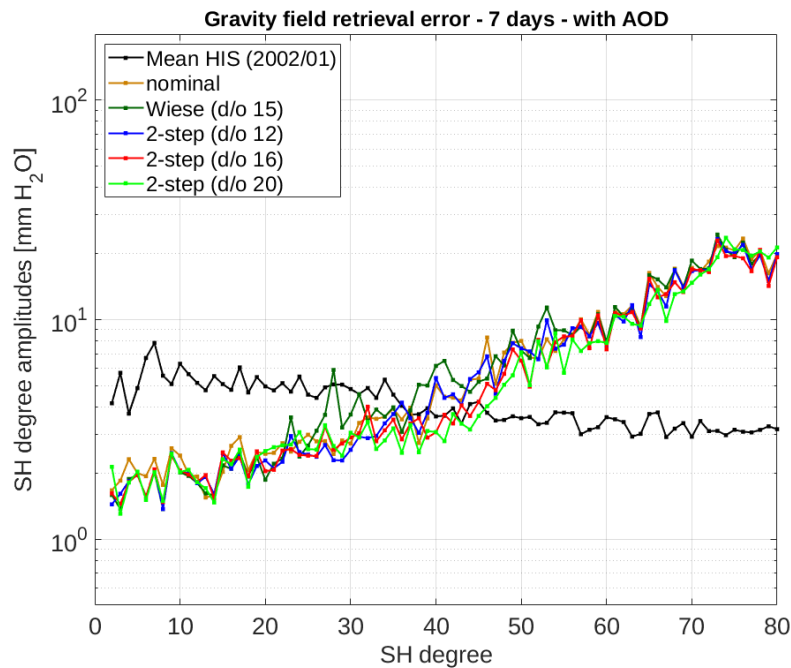
Figure 10-10: Degree error amplitudes in mm EWH of a 7-day retrieval for the 3dH formation when using an AOD model. The reference signal (HIS) is plotted in black.
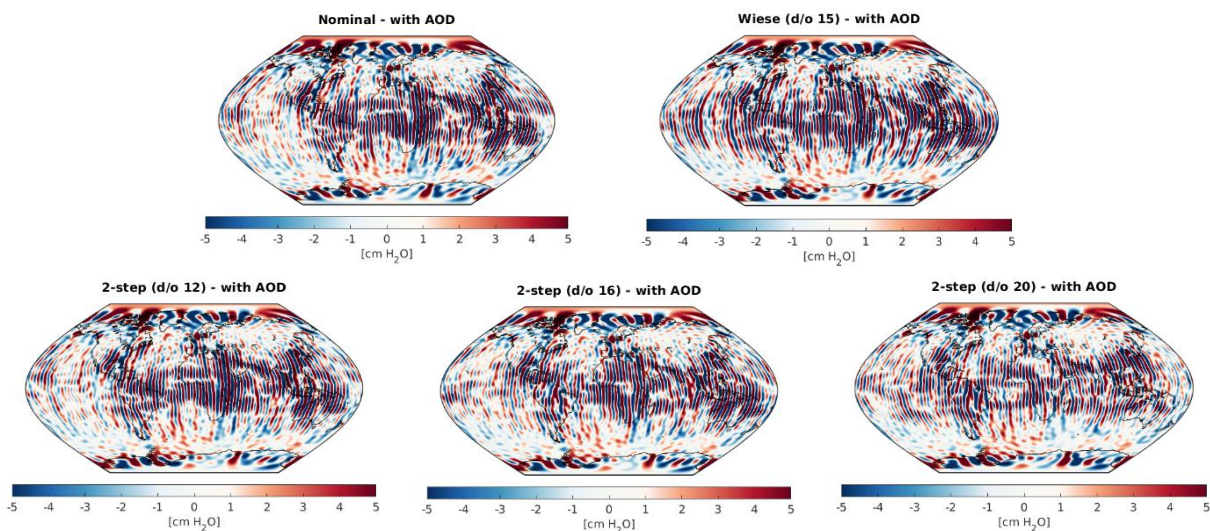
Figure 10-11: Global grids of 7-day retrieval errors of the 3dH formation solved up to d/o 60 including an AOD model.

The results for the retrieval of the first 3 days of January 2002 without using an AOD model can be seen in Figure 10-12 and Figure 10-13. Similar to the 7-day retrievals, the 3-day DMD results (especially the solutions based on higher resolved daily fields) show reduced aliasing signals between degrees 10 and 40 compared to the nominal and Wiese solutions. However, the DMD solution based on d/o 20 daily fields shows larger error signals at the very high frequency spectrum.

Figure 10-12: Degree error amplitudes in mm EWH of a 3-day retrieval for the 3dH formation without using an AOD model. The reference signal (AOHIS) is plotted in black.
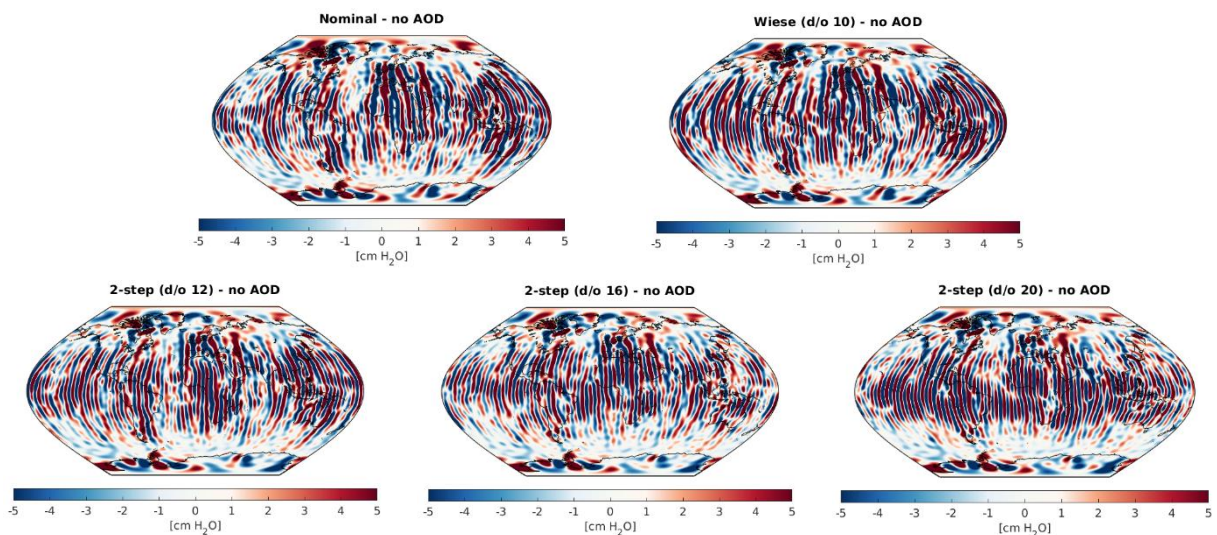
Figure 10-13: Global grids of 3-day retrieval errors of the 3dH formation solved up to d/o 50 without including an AOD model,

The 3-day solutions including an AOD model are displayed in Figure 10-14 and Figure 10-15. Similar to the 7-day solutions, the 3-day DMD solutions show only marginal improvements compared to the nominal and Wiese solutions as de-aliasing is mostly done by the AOD model.
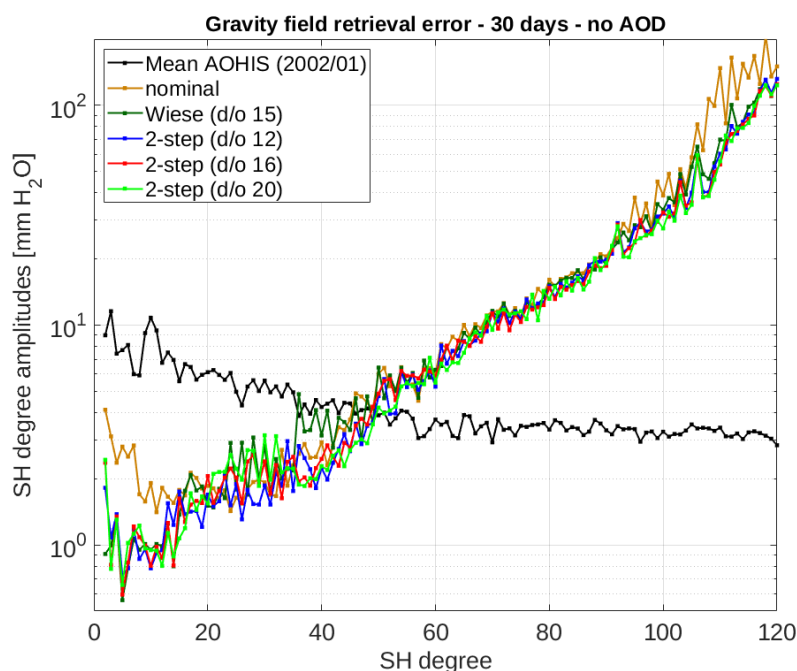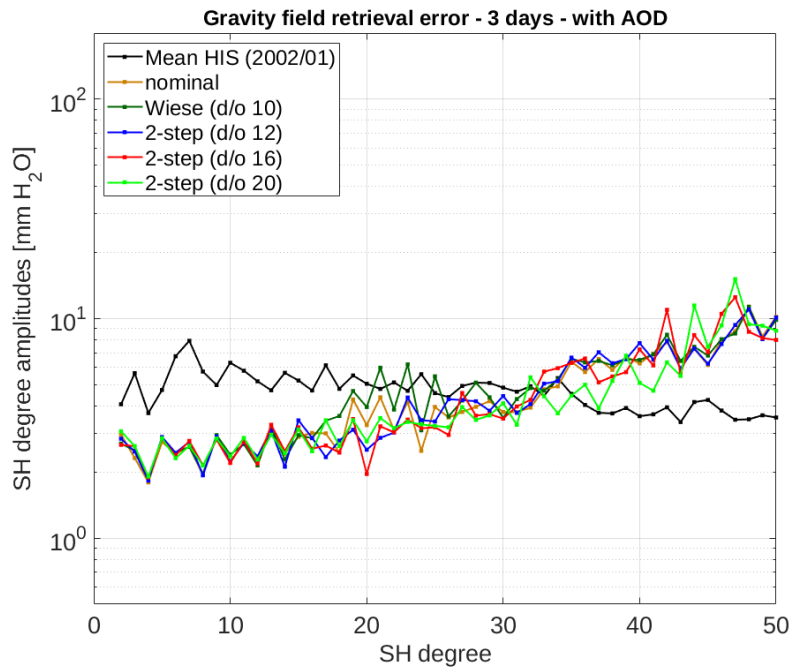
Figure 10-14: Degree error amplitudes in mm EWH of a 3-day retrieval for the 3dH formation when using an AOD model. The reference signal (HIS) is plotted in black.
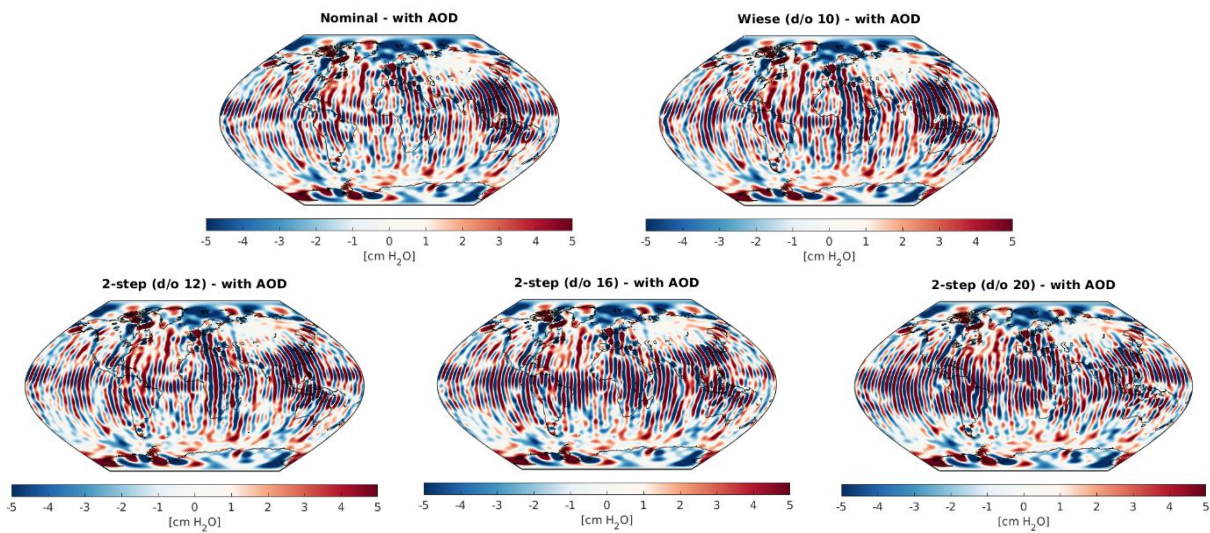
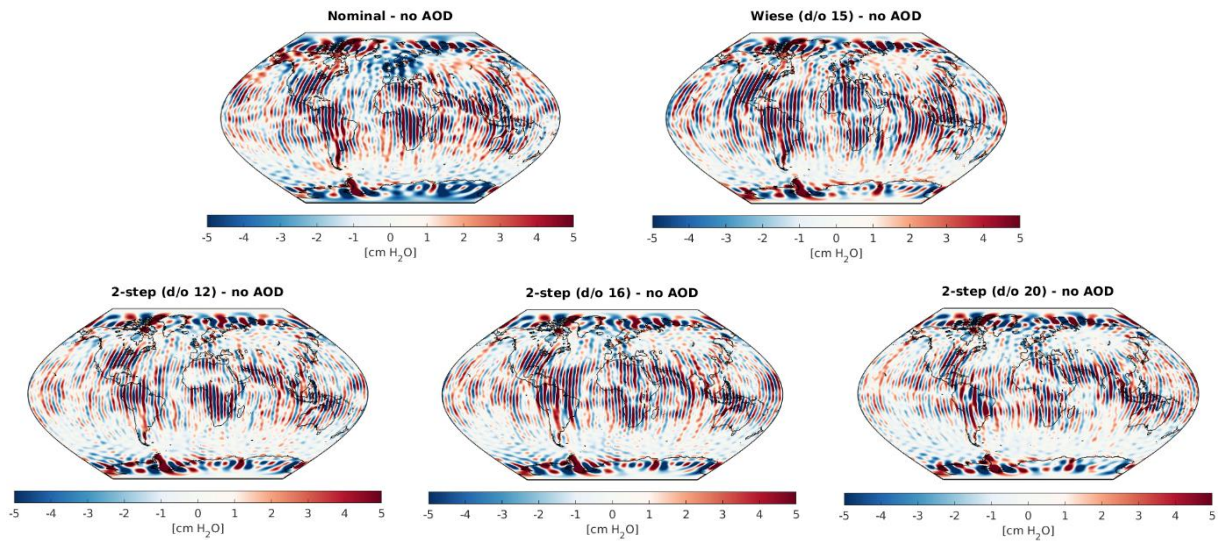**Figure 10-15: Global grids of 3-day retrieval errors of the 3dH formation solved up to d/o 50 including an AOD model.**

A quantitative overview about the results can be found in Table 10-1.

Table 10-1: Cumulative error in mm EWH for different retrieval periods and different processing strategies for the 3d_H scenario.

Scenario	Cumul. error d/o 50 – no AOD [mm EWH]	Cumul. error d/o 50 – with AOD [mm EWH]
3 days nominal	42.7	-35.7
3 days Wiese d/o 10	47.7	37.4
3 days 2-step d/o 12	43.1	36.0
3 days 2-step d/o 16	38.5	36.8
3 days 2-step d/o 20	46.9	36.5
7 days nominal	32.6	26.1
7 days Wiese d/o 15	37.2	27.7
7 days 2-step d/o 12	29.5	24.7
7 days 2-step d/o 16	30.6	22.2
7 days 2-step d/o 20	24.0	20.9
30 days nominal	18.3	15.2
30 days Wiese d/o 15	18.6	13.7
30 days 2-step d/o 12	14.4	13.4
30 days 2-step d/o 16	15.2	13.1
30 days 2-step d/o 20	14.7	13.2

10.3 APPLICATION OF THE DMD APPROACH BASED ON DAILY FIELDS WITH THE HIGH DEGREE SPECTRUM FIXED TO A VDK FILTERED MONTHLY/SUB-MONTHLY RECOVERY

Results presented in the previous section are based on daily gravity fields whose high degree spectrum has been fixed to a static field (GOCO05s) when estimating them. A second set of simulations has been performed while fixing the high degree spectrum to a VDK filtered monthly/sub-monthly gravity field retrieval. This strategy was chosen in order to assess a possible benefit in the long-term recovery when using a gravity field, which represents the reality in a more appropriate way instead of a static field, when fixing the high degree spectrum for daily estimates.

Figure 10-17 depicts the monthly retrieval errors without an AOD model included. Compared to the monthly retrievals presented in the previous section, now the DMD related solutions show a much smoother behaviour in the spectrum between degree 20 and 35. Spatial grids for the three DMD results can be seen in Figure 10-16.
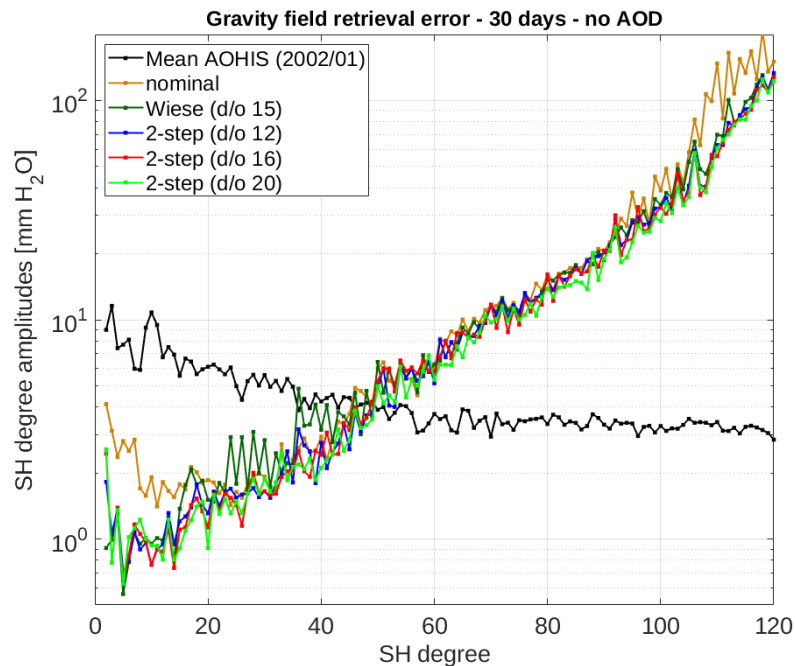
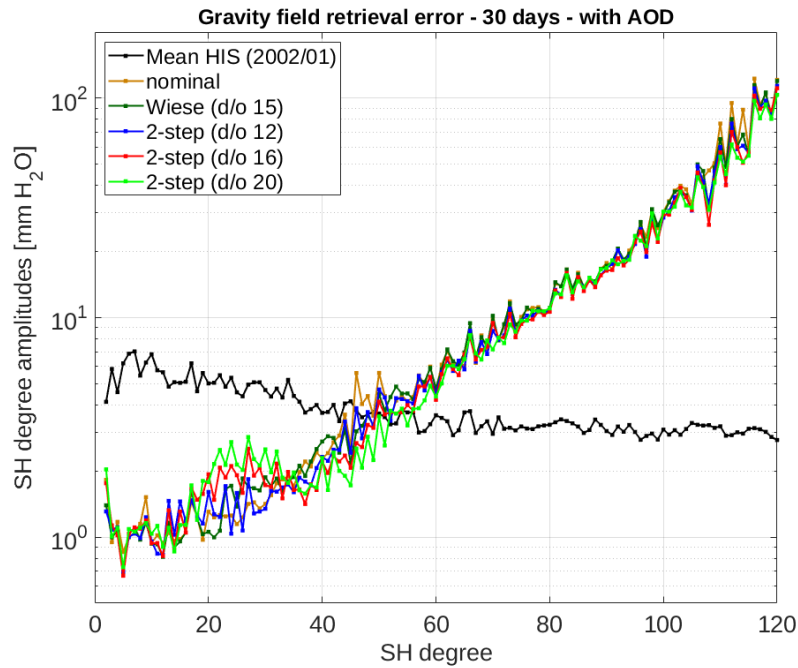**Figure 10-17: Degree error amplitudes in mm EWH of a monthly retrieval for the 3dH formation without using an AOD model. Daily estimates are based on fixing the high degree spectrum to a VDK filtered monthly gravity field. The reference signal (AOHIS) is plotted in black.**
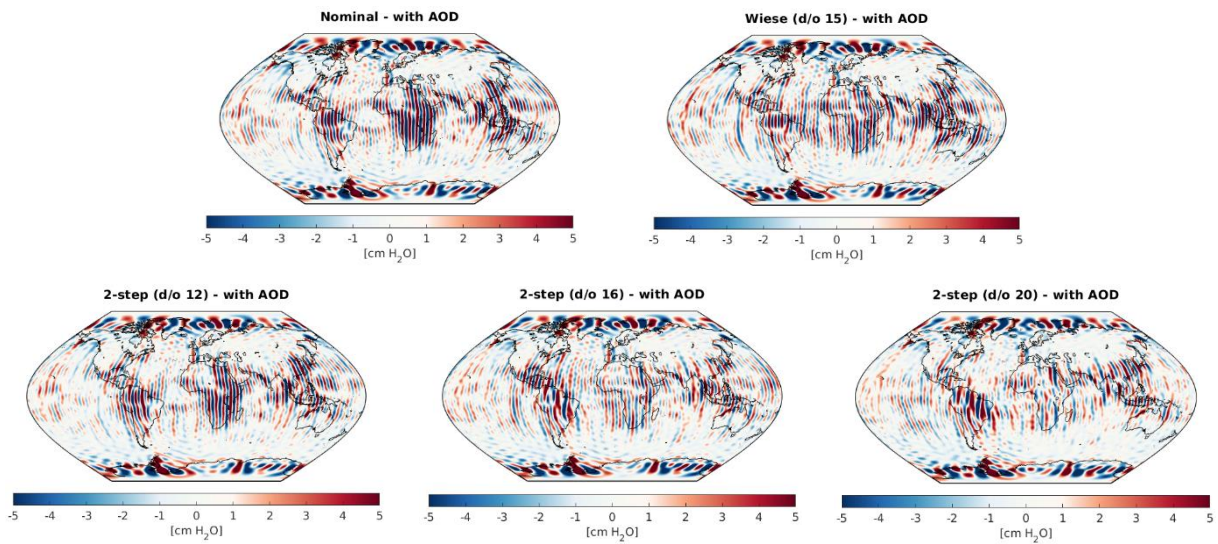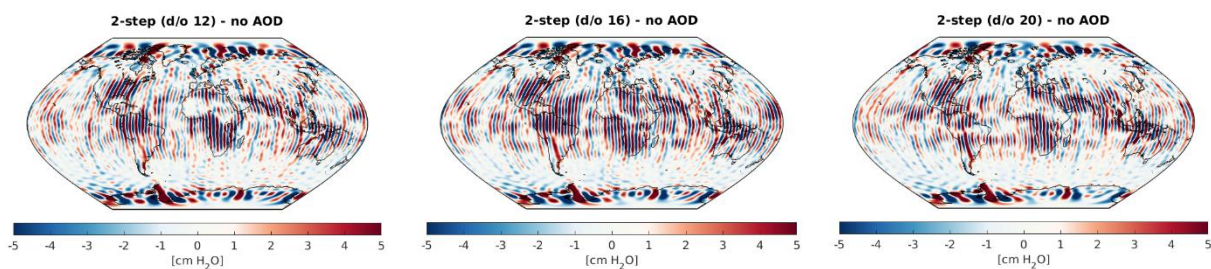

Figure 10-16: Global grids of monthly retrieval errors of the 3dH formation solved up to d/o 60 without including an AOD model. Daily estimates are based on fixing the high degree spectrum to a VDK filtered monthly gravity field.

Figure 10-18 shows the monthly results for the case with an AOD model included during gravity field recovery. Similar observations can be made as for the simulation case without using an AOD model. Additional de-aliasing can be achieved for the spectrum between degree 40 and 60, especially when using daily estimates resolved up to d/o 20, compared to the nominal result. The corresponding spatial grids for the three DMD results can be found in Figure 10-19.
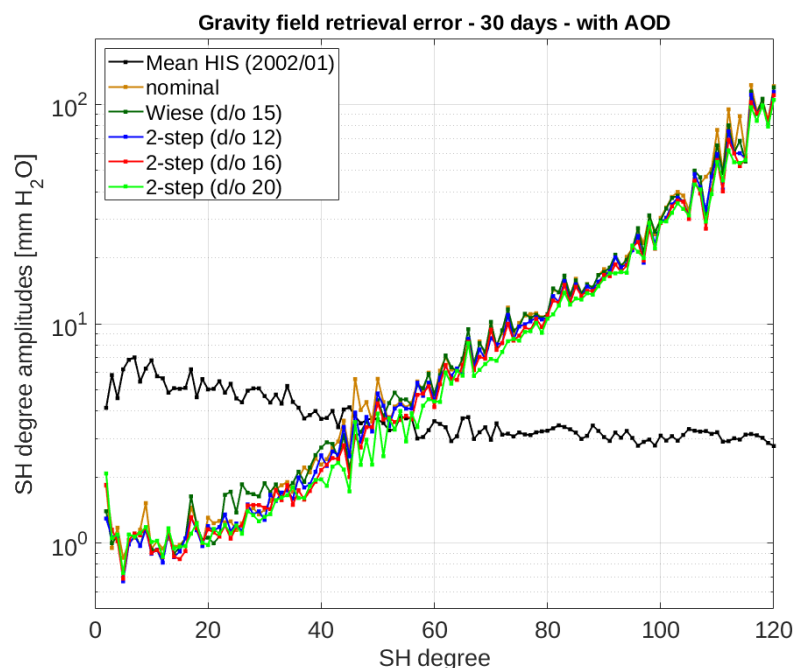
Figure 10-18: Degree error amplitudes in mm EWH of a monthly retrieval for the 3dH formation when using an AOD model. Daily estimates are based on fixing the high degree spectrum to a VDK filtered monthly gravity field. The reference signal (AOHIS) is plotted in black.
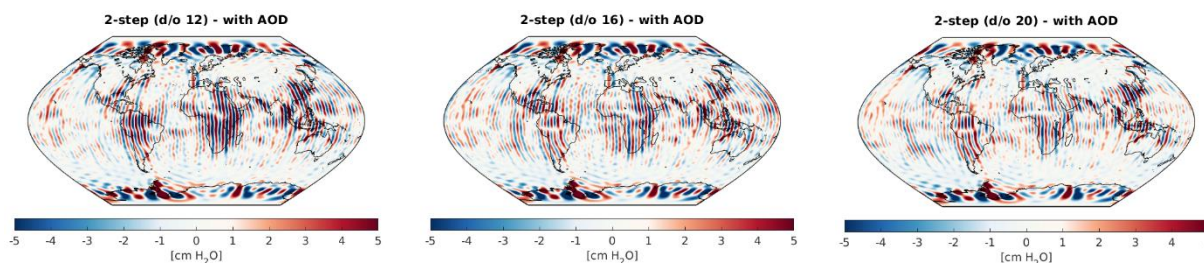
Figure 10-19: Global grids of monthly retrieval errors of the 3dH formation solved up to d/o 60 including an AOD model. Daily estimates are based on fixing the high degree spectrum to a VDK filtered monthly gravity field.

The monthly DMD related retrievals indicate that the Bender formation benefits from daily estimates which are less affected by leakage error signals introduced from the fixing of the high degree spectrum.

Figure 10-20 shows the results for the 7-day retrieval. The DMD related solutions perform similar compared to the solutions based on the fixing of the high degree spectrum to the static field. Additional benefit for the DMD based 7-day retrieval cannot be seen as it is seen for the monthly solutions when fixing the high degree spectrum to a VDK filtered solution.
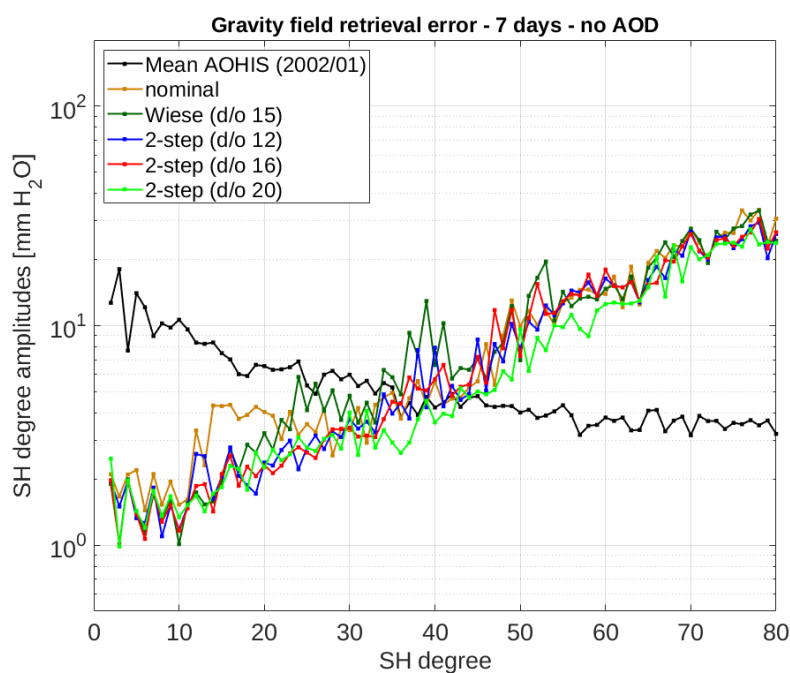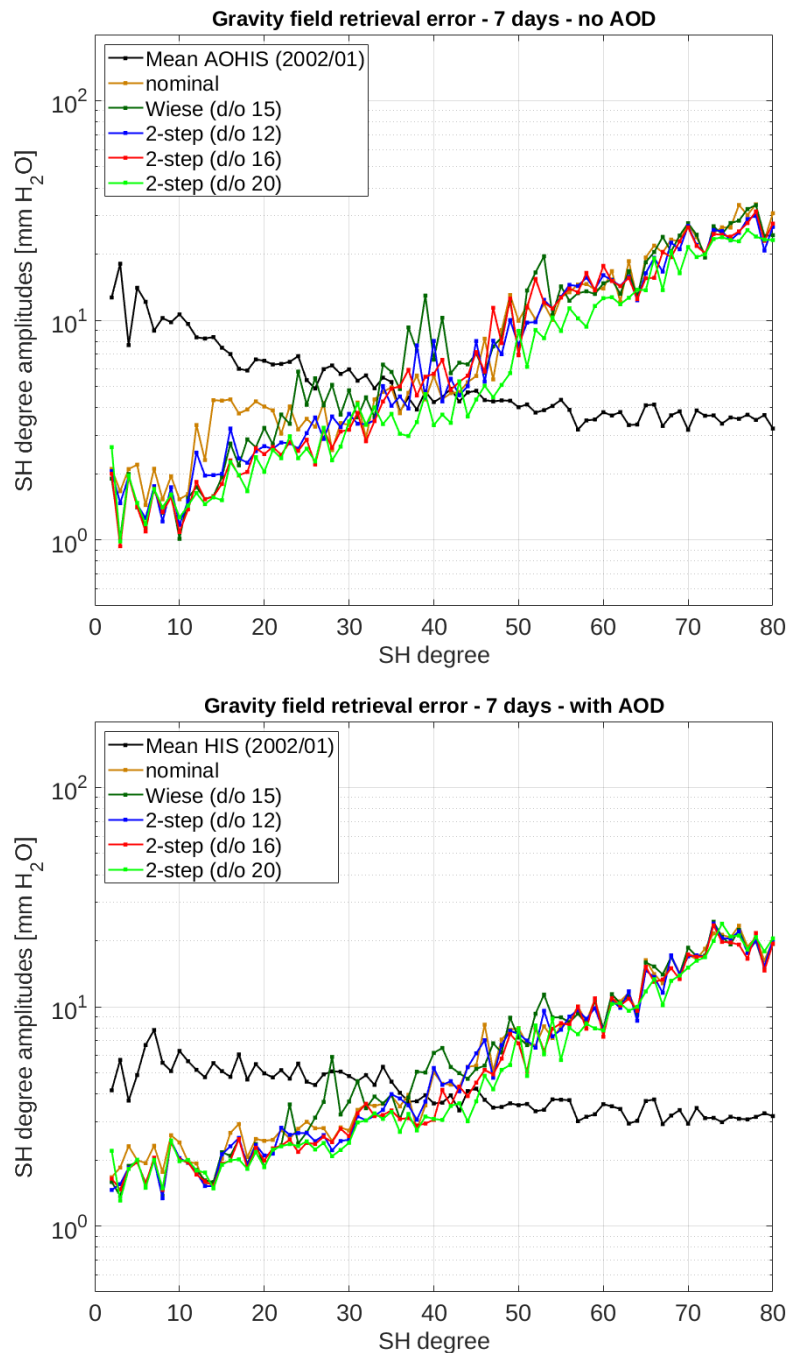
Figure 10-20: Degree error amplitudes in mm EWH of a 7-day retrieval for the 3dH formation without using an AOD model (top) and when using an AOD model (bottom). Daily estimates are based on fixing the high degree spectrum to a VDK filtered monthly gravity field. The reference signal is plotted in black.

The results representing a 3-day retrieval are shown in Figure 10-21. Again, DMD related retrieval errors perform similar to the solutions based on the fixing of the high degree spectrum to the static field. A quantitative assessment of the DMD results, which are based on daily estimated fixed to VDK filtered gravity fields, can be found in Table 10-2.

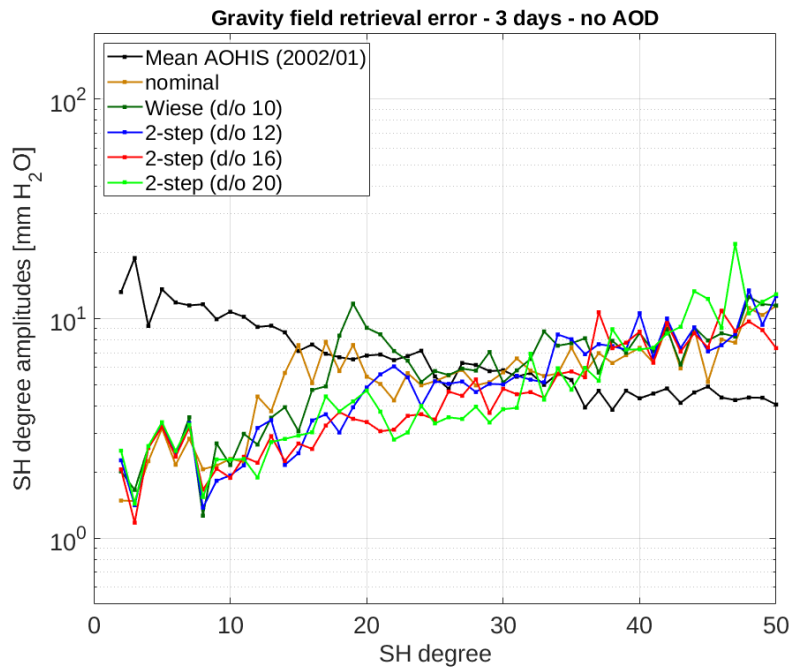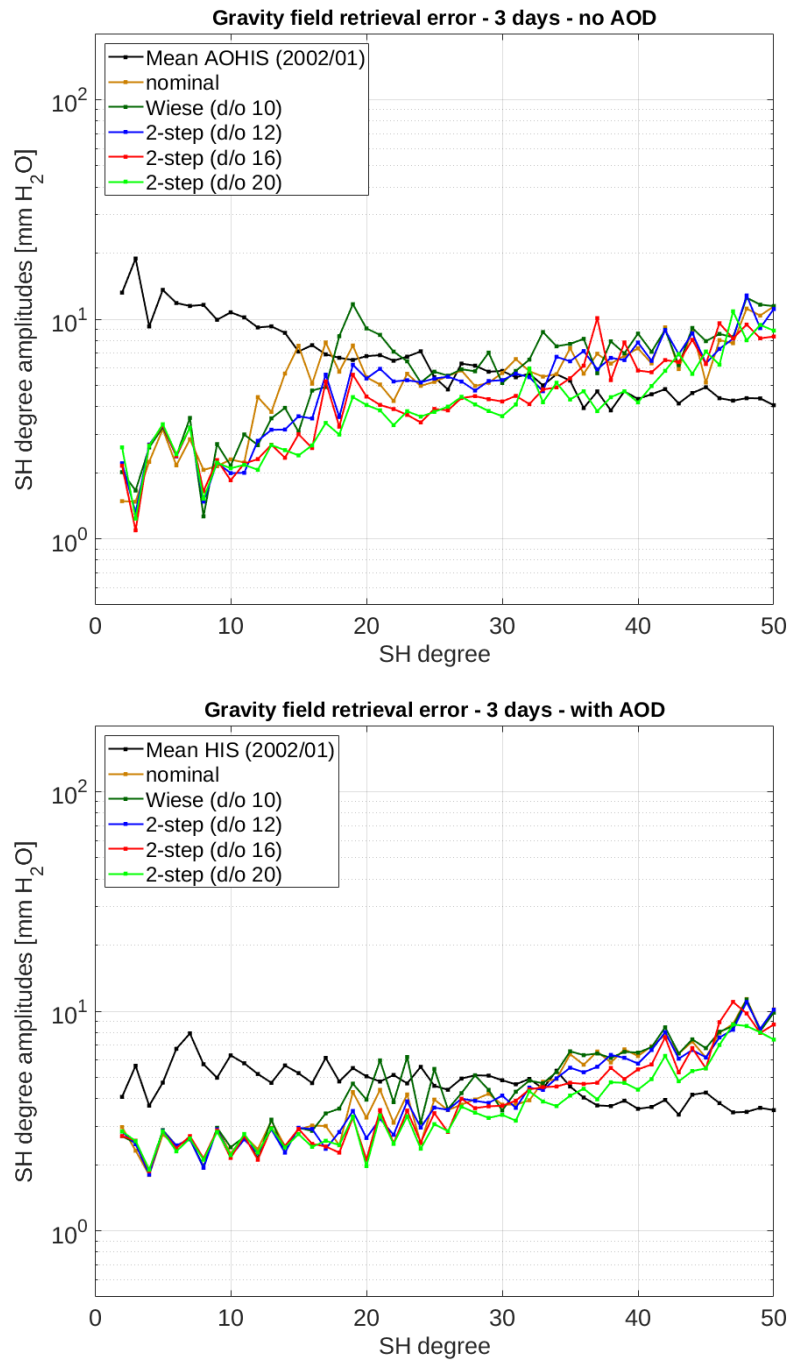**Figure 10-21: Degree error amplitudes in mm EWH of a 3-day retrieval for the 3dH formation without using an AOD model (top) and when using an AOD model (bottom). Daily estimates are based on fixing the high degree spectrum to a VDK filtered monthly gravity field. The reference signal is plotted in black.**

Table 10-2: Cumulative error in mm EWH for different retrieval periods for the 3d_H scenario based on the DMD processing strategy when fixing the high degree spectrum to VDK filtered monthly/sub-monthly gravity fields.

Scenario	Cumul. error d/o 50 – no AOD [mm EWH]	Cumul. error d/o 50 – with AOD [mm EWH]
3 days 2-step d/o 12	40.9	34.3
3 days 2-step d/o 16	36.3	32.9
3 days 2-step d/o 20	32.8	29.2
7 days 2-step d/o 12	29.8	25.0
7 days 2-step d/o 16	31.0	22.3
7 days 2-step d/o 20	22.9	20.7
30 days 2-step d/o 12	14.6	13.3
30 days 2-step d/o 16	14.7	12.4
30 days 2-step d/o 20	14.0	11.5

The application of the DMD approach at the 3dH Bender-type formation has shown some improvements wrt. the nominal and Wiese solutions if an AOD model is not included during processing. The benefit of this approach can be exploited for shorter or sub-monthly retrievals as the overall de-correlation of the system is damped by the shorter retrieval period. Additional benefit can be reached when solving the daily fields up to a higher maximum resolution (e.g. d/o 16 or 20). Results also showed that additional error signals arise for the monthly retrieval between degrees 20 and 35 if the high degree spectrum is fixed to a static field when solving for the daily fields. These coefficients already experienced de-aliasing, mainly from the optimized observation geometry of the Bender formation, due to the longer retrieval period. However, the monthly solutions based on DMD processing strategy can be improved when fixing the high degree spectrum to a time-variable VDK filtered gravity field retrieval including less leakage error signals. In case of sub-monthly retrievals, the benefit of using VDK filtered fields instead of using a static field is rather small. The DMD results including an AOD model show smaller improvements compared to the nominal and Wiese solutions for all different retrieval periods due to already de-aliased A and O signals

11 IMPACT OF VADER FILTERING ON SIMULATION RESULTS

In order to evaluate the effect of post processing on the gravity retrieval errors derived in our simulations, we use time-variable decorrelation (VADER) filters as defined by Horvath et al. (2018):

$$x_\alpha = (N + \alpha M)^{-1} \, N \, x = W_\alpha \, x$$

where x and x_α are the vectors of unfiltered and filtered SH coefficients, respectively, N is the NEQ matrix ($A^T P A$), which is equal to the inverse of the error variance-covariance matrix, M is the inverse of the signal variance matrix, α is the scaling factor and W_α is the filter matrix. The matrix M is a diagonal matrix containing the reciprocal squares of the SH coefficients of the monthly HIS signal. The value of α is determined as to minimize the RMS of the global error grid of the filtered model.

The error Δx_α of the VADER-filtered gravity field solution x_α

$$
\begin{aligned}
\Delta x_\alpha &= x_\alpha - HIS \\
&= W_\alpha \, x \, - HIS \\
&= W_\alpha \, (HIS + \Delta x) - HIS \\
&= W_\alpha \Delta x + (W_\alpha - 1) \, HIS
\end{aligned}
$$

consists of two parts: The filtered retrieval error $W_\alpha \Delta x$ and the HIS signal dampening $(W_\alpha - 1) \, HIS$. Applying a stronger filter (e.g. using a larger value for α) leads to a decrease of $W_\alpha \Delta x$, as the error part contained in the retrieved field is increasingly dampened, but also to an increase of $(W_\alpha - 1) \, HIS$, as also the (HIS) signal part contained in the retrieved field is increasingly dampened which also increases the value of Δx_α.

In the following sections 11.1 and 11.2, we analyze the effect of VADER-filtering on the retrieval errors of simulations being based on 5d_Ma and 5d_Mb orbits (section 11.1) and 3d_H orbits (section 11.2).

11.1 IMPACT OF THE SECOND PAIR'S INCLINATION IN POST-PROCESSED SOLUTIONS

As described in section 8.3, the consequences of choosing a lower value of the inclination of the second pair in a double-pair configuration are reduced temporal aliasing errors in the low-latitude region covered by both pairs, as well as larger polar gaps of the inclined pair's orbit leading to a larger region where only the single-polar pair performance is reached. In this section, the impact of applying VADER filters to the 31-day full noise simulation results for the scenarios 2_pIg_iIn (5d_Ma) and 2_pIg_iIn (5d_Mb) is analyzed.

As shown by the defining formula of the VADER filter matrix (see the introduction of section 11), the VADER filter of a solution is adapted to its specific error structure, as introduced by the matrix N. That means for the present case that in the 5d_Ma scenario, especially the near-zonal coefficients are filtered more strongly, while for the 5d_Mb scenario, this is the case for the sectorial coefficients.

Figure 11-1 and Figure 11-2 show the impact of the filtering on the two considered solutions. For both solutions, the VADER filter considerably reduces the striping errors, leading to an increased SNR of the filtered solution. The striping errors in the low-latitude region contained by both unfiltered solutions are stronger for the 5d_Mb scenario. This difference in quality for the two solutions, however, becomes significantly reduced when comparing the filtered results. It has to be noted that, as described above, although after the filtering, the 5d_Mb solution is more similar to the 5d_Ma solution in the low-latitude region, this is achieved by a stronger filtering in the 5d_Mb case compared to the 5d_Ma case, as can be derived by comparing the error amplitudes of the unfiltered solutions.

Figure 11-3 shows how the errors of the unfiltered and filtered solutions behave as a function of latitude. Also here, it is visible that the error levels of the two scenarios are more similar after filtering. The distinct peaks visible in the curves associated with the northern hemisphere are induced by the HIS signal dampening, as will be described below. With respect to the comparison of the filtered solutions of the scenarios 5d_Ma and 5d_Mb, we would like to note that their relative behavior (as a function of latitude) strongly depends on the chosen method for computing the signal variance matrix M, which is why we do not further analyze the differences of the filtered solutions for 5d_Ma and 5d_Mb in more detail here.

Figure 11-4 shows in more detail how the filtering affects the errors of the individual SH coefficients of the solutions. This visualizes how the VADER filter is adapted to the error structure of the respective solution: Less well determined coefficients are filtered more strongly, while better determined coefficients are much less affected by the filter. In the present case, in the 5d_Ma solution, especially the near-zonal polar gap coefficients are improved by the filtering, while in the 5d_Mb solution, especially the sectorial coefficients are improved.

By considering the errors of the filtered solutions in Figure 11-1 and Figure 11-2, it is noticeable that their structure is determined by high-frequency signal-correlated errors. To analyze their origin, we investigate the error components of the VADER-filtered solutions in Figure 11-5 and Figure 11-6. This shows us that the observed high-frequency errors are introduced by the HIS signal dampening. As the VADER filter is constructed based on the error variance-covariance information of the retrieved solution, it especially eliminates high-SH degree model contents,

which, besides the high-degree noise, also include high-SH degree signal components. In our simulations where the signal corresponds to the HIS model, this effect can most prominently be seen in Greenland, where large-SH degree time-variable signal structures are present, as well as in the vicinity of the Nile, where the HIS models contain the signal of a newly built dam and the region of Sumatra, where the HIS models contain the signal of a strong earthquake. Both the dam as well as the earthquake events changed the gravity signature of the respective region permanently, which means that for real data applications, the error contributions in these two regions can be ignored.

Finally, we analyze how the error of the filtered solutions and its components change if cutting the SH spectrum at some maximum degree N_{max}. Figure 11-7 shows the errors as a function of latitude, for N_{max} values between 20 and 120. It can be observed that for increasing values of N_{max}, the contribution of the HIS signal dampening to the error of the filtered solution is increasing. Up to about $N_{max} = 80$, the error budget of the filtered solutions is determined by the filtered retrieval errors. This effect can also be observed in the panels c of Figure 11-5 and Figure 11-6.

To summarize, the performance of the 5d_Ma and 5d_Mb scenarios is comparable if considering VADER-filtered results. However, in the case of the scenario with the lower inclination of the second pair (i.e., 5d_Ma), a weaker filter is required to reach this performance.

Figure 11-1 31-day full noise nominal simulation for scenario 2_pIg_iIn (5d_Ma). Top row: unfiltered solution (left) and its difference to the HIS reference field (right). Middle row: VADER-filtered solution (left) and its difference to the HIS reference field (right). Bottom row: HIS reference field. [Path: Deliverables/D1/simulation_results/full_scale_simulator_v009/old_noise_scaling/full_noise_nominal/2_pIg_iIn_5d_Ma/]
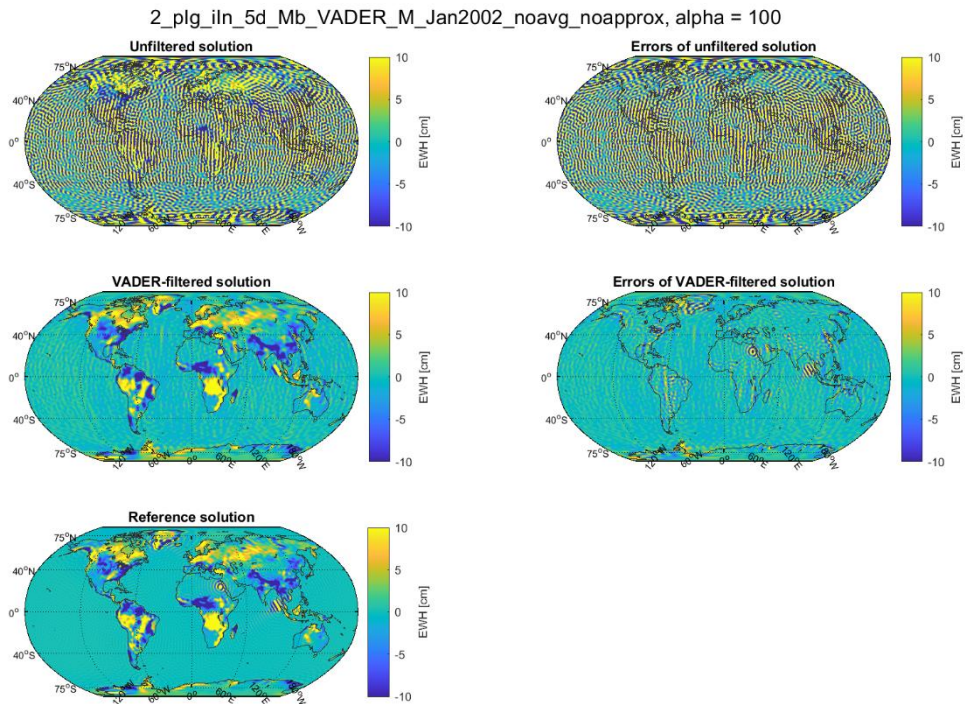
Figure 11-2 31-day full noise nominal simulation for scenario 2_pIg_iIn (5d_Mb). Top row: unfiltered solution (left) and its difference to the HIS reference field (right). Middle row: VADER-filtered solution (left) and its difference to the HIS reference field (right). Bottom row: HIS reference field. [Path: Deliverables/D1/simulation_results/full_scale_simulator_v009/old_noise_scaling/full_noise_nominal/2_pIg _iIn_5d_Mb/]

NGGM/MAGIC – Science Support Study During Phase A	*Final Report*	
	Doc. Nr:	MAGIC_FR
	Issue:	1.0
	Date:	15.11.2022
	Page:	141 of 466

Figure 11-3 Root-mean-square values of the EWH grid values computed along parallels based on the EWH grid points shown by Figure 11-1 and Figure 11-2 (right column). On the x axes, 0 denotes the equator and 90 the north pole (for the solid curves) and the south pole (for the dashed curves). The blue curves correspond to the scenario 2_pIg_iIn (5d_Ma) and the red curves to the scenario 2_pIg_iIn (5d_Mb), respectively. The vertical lines mark the inclination of the respective second pair (65° for 5d_Ma and 70° for 5d_Mb). [Path: Deliverables/D1/simulation_results/full_scale_simulator_v009/old_noise_scaling/full_noise_nominal/]
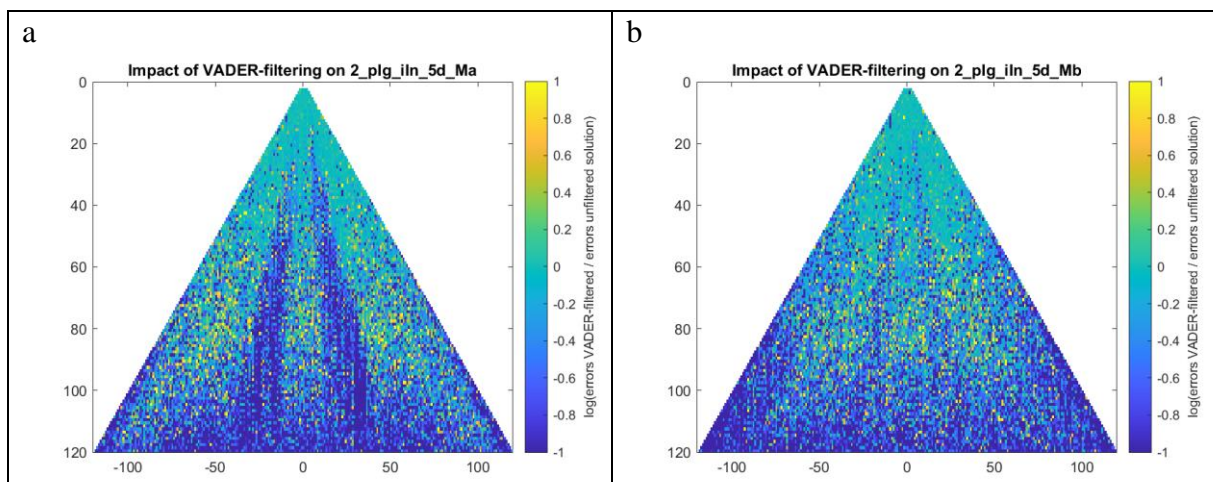
Figure 11-4 Impact of applying a VADER filter to the 31-day full noise solutions of 2_pIg_iIn (5d_Ma, left) and 2_pIg_iIn (5d_Mb, right). Shown is the logarithm of the quotient of the errors of the VADER-filtered solution and the errors of the unfiltered solution. The stronger the shade of blue, the stronger the error reduction from the unfiltered to the post-processed solution. [Path: Deliverables/D1/simulation_results/full_scale_simulator_v009/old_noise_scaling/full_noise_nominal/]
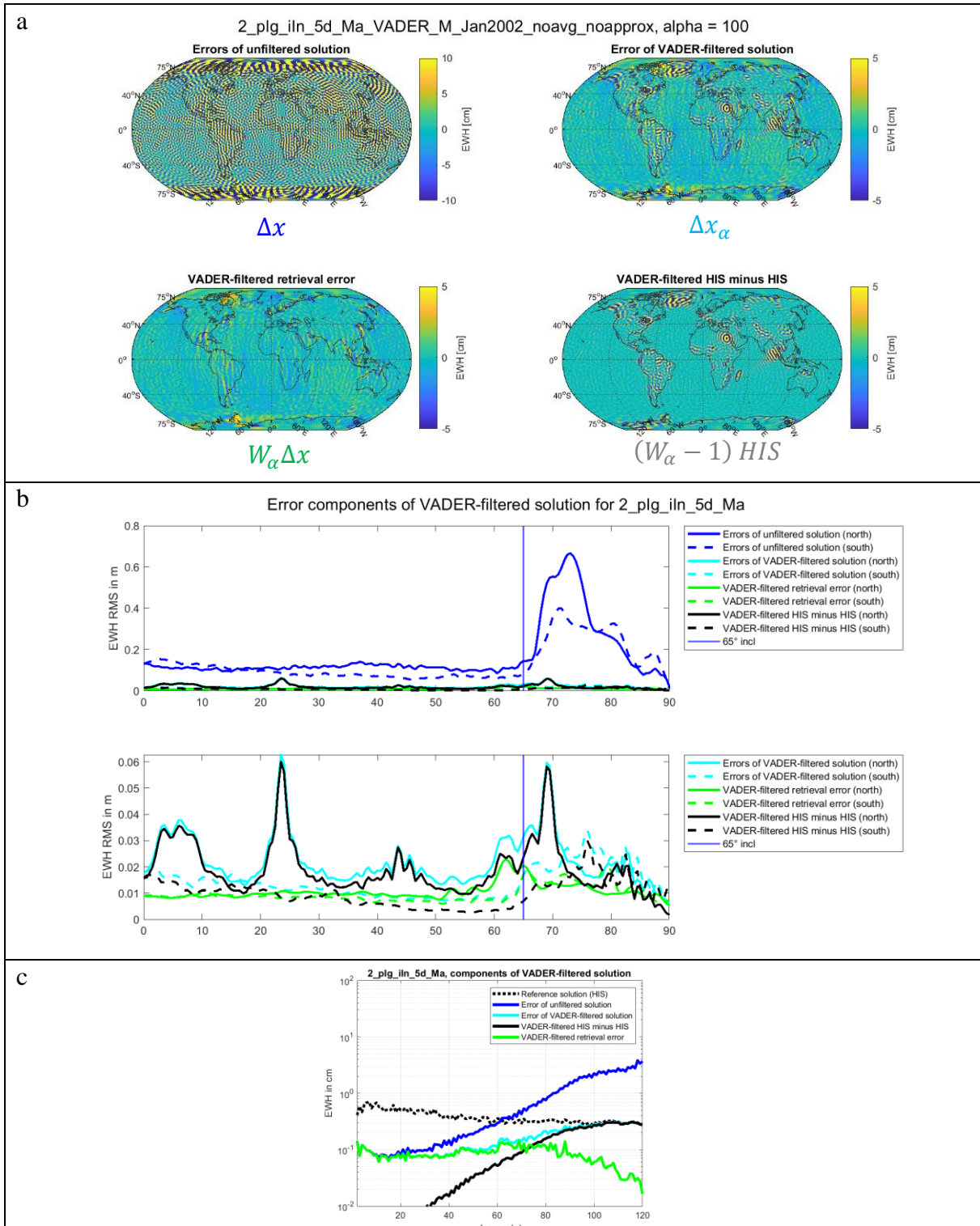
Figure 11-5 Analysis of the error components of the VADER-filtered 31-day full noise solution for the scenario 2_pIg_iIn (5d_Ma). Δx is the error of the unfiltered solution. Δx_α is the error of the filtered solution, consisting of the filtered retrieval error $W_\alpha \Delta x$ and the HIS signal dampening effect $(W_\alpha - 1) HIS$. Panel a shows the error components as spatial EWH grids, panel b shows the RMS values of the EWH grid values along the parallels, and panel c shows the degree amplitude curves associated to the individual fields. [Path: Deliverables/D1/simulation_results/full_scale_simulator_v009/old_noise_scaling/full_noise_nominal/2_pIg_iIn_5d_Ma/]

Figure 11-6 Analysis of the error components of the VADER-filtered 31-day full noise solution for the scenario 2_pIg_iIn (5d_Mb). Δx is the error of the unfiltered solution. Δx_α is the error of the filtered solution, consisting of the filtered retrieval error $W_\alpha \Delta x$ and the HIS signal dampening effect $(W_\alpha - 1)HIS$. Panel a shows the error components as spatial EWH grids, panel b shows the RMS values of the EWH grid values along the parallels, and panel c shows the degree amplitude curves associated to the individual fields. [Path: Deliverables/D1/simulation_results/full_scale_simulator_v009/old_noise_scaling/full_noise_nominal/2_pIg_iIn_5d_Mb/]

Figure 11-7 RMS values of EWH error grids computed along the parallels, as a function of latitude, for the southern hemisphere. The underlying EWH grids are computed based on coefficient errors of SH d/o 2 to N_{max}, where we vary N_{max} from 20 to 120 (top to bottom panel). The color coding of the left panel (scenario 2_pIg_iIn (5d_Ma)) corresponds to the color coding applied in Figure 11-5. The color coding of the right panel (scenario 2_pIg_iIn (5d_Mb)) corresponds to the one in Figure 11-6. [Path: Deliverables/D1/simulation_results/full_scale_simulator_v009/old_noise_scaling/full_noise_nominal/]

11.2 POST-PROCESSED 3D_H SCENARIOS

In this section, we present the effect of applying a VADER filter to 52 subsequent 7-day full noise nominal solutions for the scenarios 1_pIg (3d_H) (maximum degree: 100) and 2_pIn_iIn (3d_H) (maximum degree: 120). Figure 11-8 to Figure 11-11 show the effect of the filtering: The errors become smaller and less order-dependent. This can especially be seen in the triangle plots that show a much more homogeneous error structure for the filtered solutions compared to the unfiltered solutions. It should be noted that the formal errors of the filtered solutions only represent the propagated instrument noise and do not contain the errors produced by temporal aliasing and the filter bias.

The filter bias (also: regularization bias) is a measure for the strength of the regularization introduced by the VADER filter. It is the part of the error of the filtered gravity field solution that is introduced by the filter (in contrast to the part of the error that is remaining from the unfiltered gravity field solution, which consists of a stochastic component (introduced by the instrument noise) and a deterministic component (introduced by temporal aliasing errors)). Further information on the VADER filter bias can be found in Horvath (2017).

Comparing the effect of the filtering for the scenarios 1_pIg and 2_pIn_iIn reveals that the difference between the errors of the unfiltered and filtered solutions is smaller for the double-pair than for the single-pair solution. This is explained by the fact the VADER filter is designed based on the variance-covariance information of the specific solution it is applied to, and the retrieval errors of the single-pair solution are larger than for the double-pair solution, such that the single-pair solution becomes filtered more strongly.

Figure 11-12 shows the effect of the filtering as a function of latitude. Before the filtering, the 1_pIg solution shows an error increase towards the equator, which is produced by the large striping errors contained in the single-pair solutions. The 2_pIn_iIn solution, in contrast, shows an error increase towards the poles, where only the data of the polar satellite pair is available. After the filtering, the latitude dependency of the errors becomes significantly reduced, and the performance of the two scenarios becomes more similar.

Figure 11-13 shows how the error of the 52 subsequent solutions varies over time. Before the filtering, the quality variation among subsequent solutions is much larger for 1_pIg than for 2_pIn_iIn. This variation of the errors over time is due to the „random" sampling of time-variable signals that lead to aliasing. For the filtered solutions, the errors become more constant over time.

The degree amplitude plots in Figure 11-14 show how the error of the solutions is globally reduced by the filtering. The error of the filtered solution can be split in the formal error, the filter bias and a contribution from temporal aliasing errors. The fact that the filter bias is smaller in the case of 1_pIg compared to 2_pIn_iIn shows one of the advantages of the double-pair configuration: a weaker filter is required than for the single-pair solution.
Figure 11-15 shows the VADER filter bias spatially for the two scenarios. Also here, it can be seen that the bias is larger for the filter applied to the single-pair scenario 1_pIg compared to the double-pair scenario 2_pIn_iIn.

Figure 11-16 and Figure 11-17 show the error components of the filtered solutions. As the filter applied to 1_pIg is stronger than the filter applied to 2_pIn_iIn, the signal dampening component is larger for the 1_pIg filtered solution compared to the 2_pIn_iIn filtered solution.
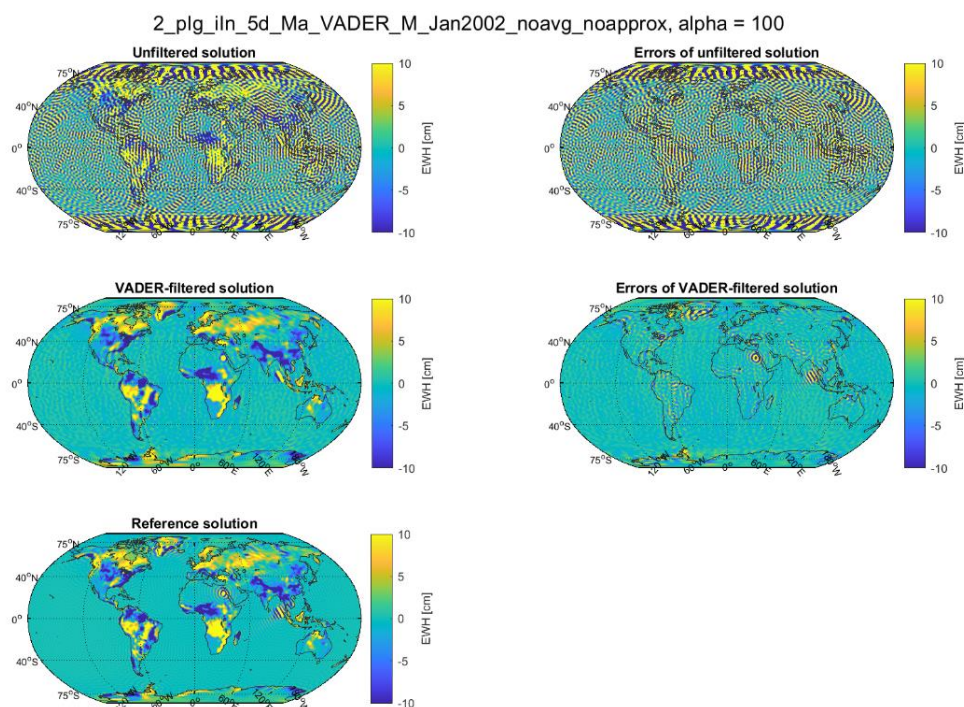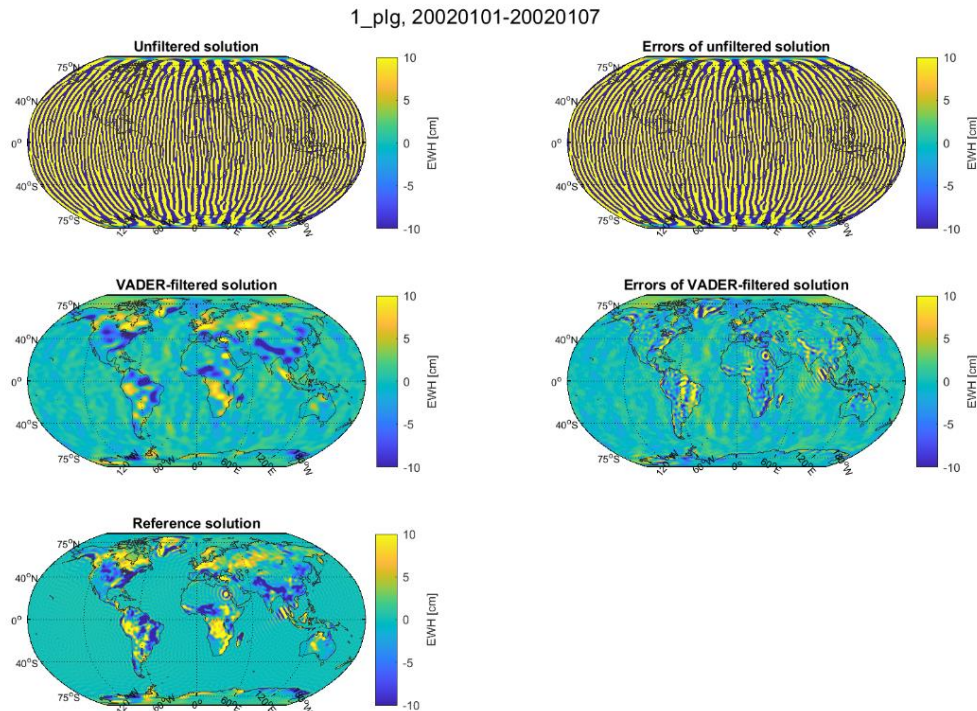

Figure 11-8 7-day d/o 100 full noise nominal simulation for scenario 1_pIg (3d_H). Top row: unfiltered solution (left) and its difference to the HIS reference field (right). Middle row: VADER-filtered solution (left) and its difference to the HIS reference field (right). Bottom row: HIS reference field. [Path: Deliverables/D1/simulation_results/full_scale_simulator_v009/old_noise_scaling/full_noise_nominal_1year _solutions/1_pIg_3d_H/]
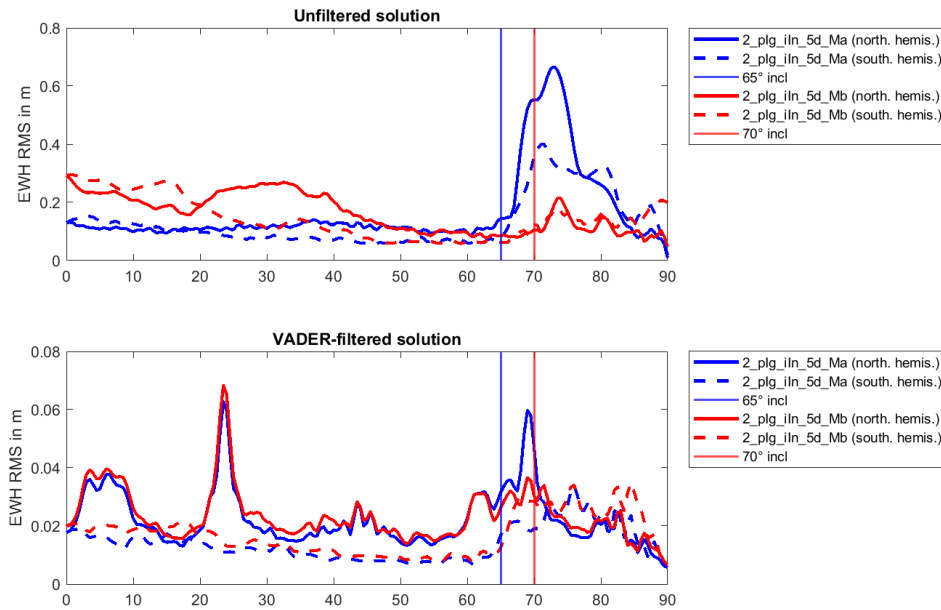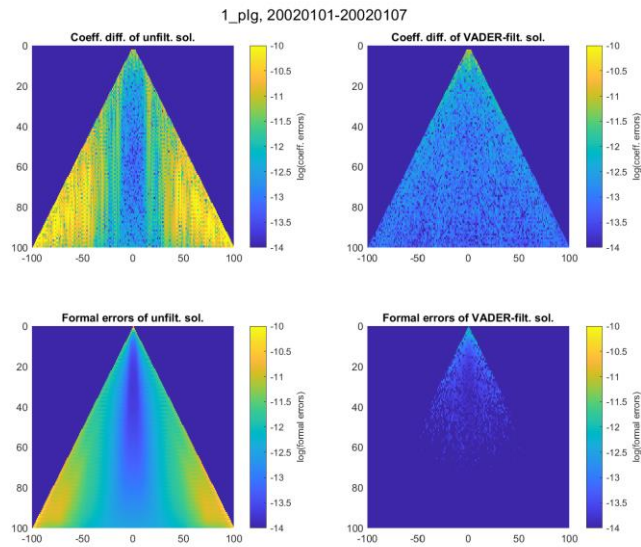
Figure 11-9 Coefficient (top row) and formal (bottom row) errors of a 7-day d/o 100 full noise nominal simulation for scenario 1_pIg (3d_H). Left: Errors of unfiltered solution, right: errors of VADER-filtered solution. [Path: Deliverables/D1/simulation_results/full_scale_simulator_v009/old_noise_scaling/full_noise_nominal_1year _solutions/1_pIg_3d_H/]
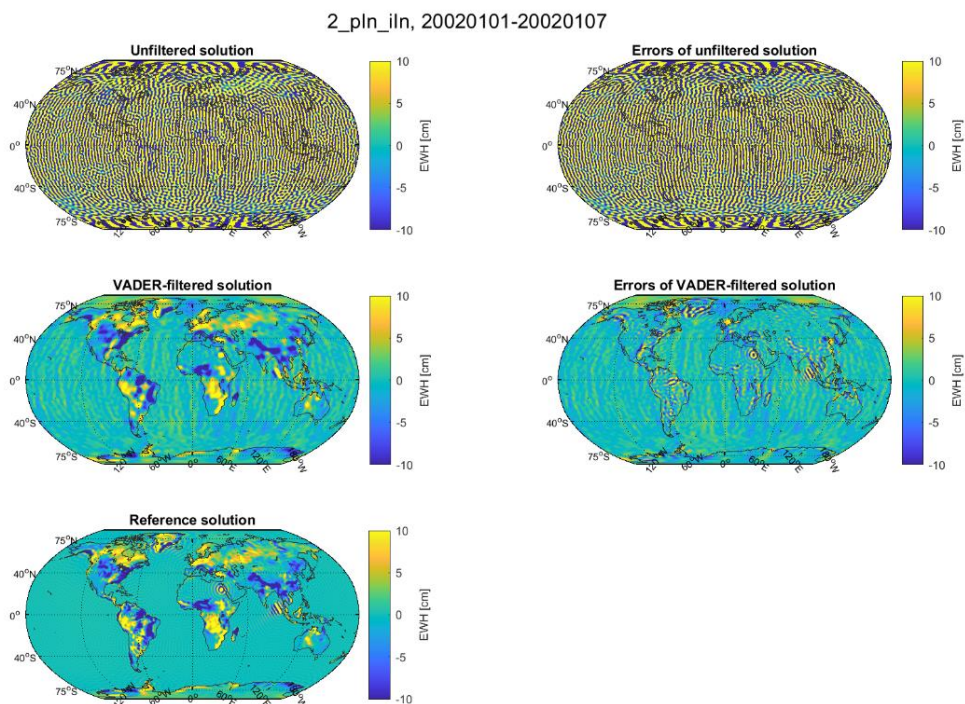
Figure 11-10 7-day d/o 120 full noise nominal simulation for scenario 2_pIn_iIn (3d_H). Top row: unfiltered solution (left) and its difference to the HIS reference field (right). Middle row: VADER-filtered solution (left) and its difference to the HIS reference field (right). Bottom row: HIS reference field. [Path: Deliverables/D1/simulation_results/full_scale_simulator_v009/old_noise_scaling/full_noise_nominal_1year _solutions/2_pIn_iIn_3d_H/]
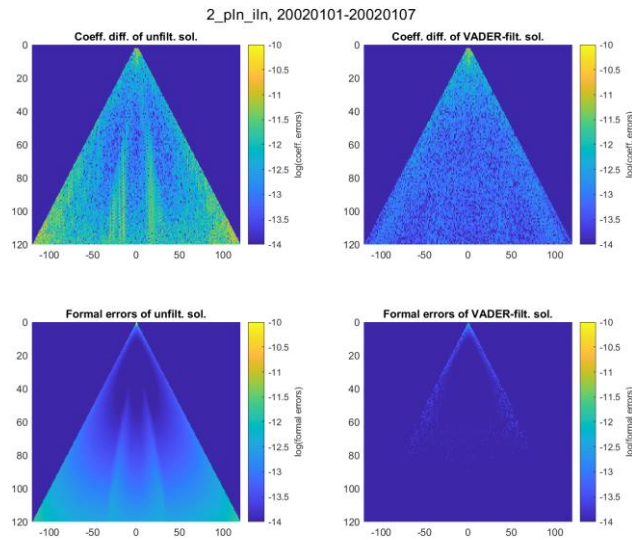
Figure 11-11 Coefficient (top row) and formal (bottom row) errors of a 7-day d/o 120 full noise nominal simulation for scenario 2_pIn_iIn (3d_H). Left: Errors of unfiltered solution, right: errors of VADER-filtered solution. [Path: Deliverables/D1/simulation_results/full_scale_simulator_v009/old_noise_scaling/full_noise_nominal_1year _solutions/2_pIn_iIn_3d_H/]
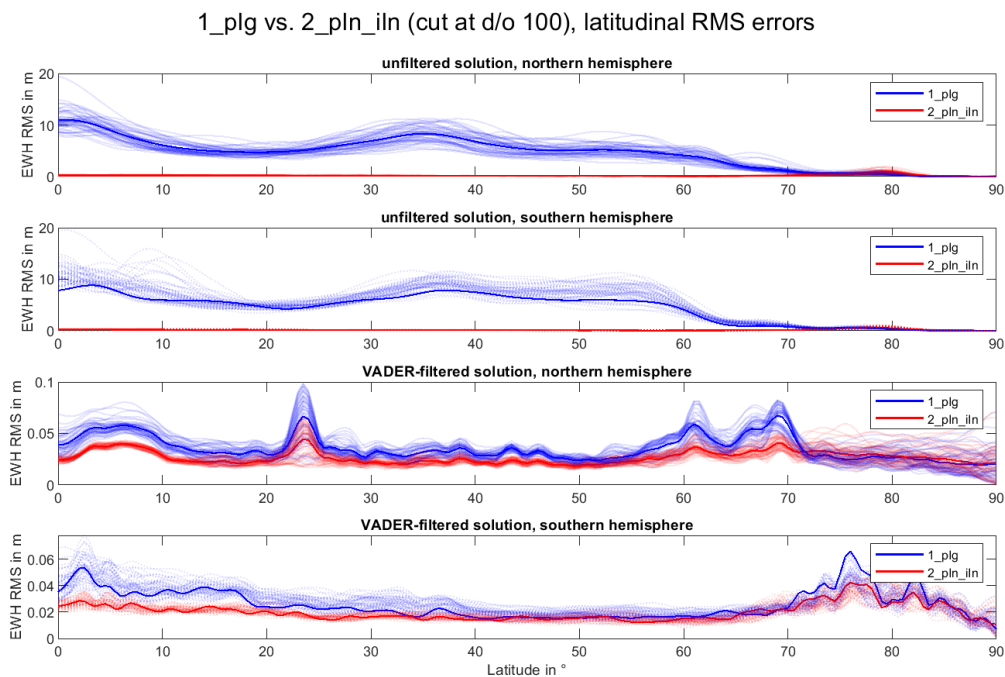

Figure 11-12 RMS values of EWH error grids computed along the parallels, as a function of latitude. The underlying EWH error grids are computed based on 7-day full noise nominal solutions for the scenarios 1_pIg (3d_H) and 2_pIn_iIn (3d_H), where SH coefficients from d/o 2 to 100 have been used. [Path: Deliverables/D1/simulation_results/full_scale_simulator_v009/old_noise_scaling/full_noise_nominal_1year _solutions/]
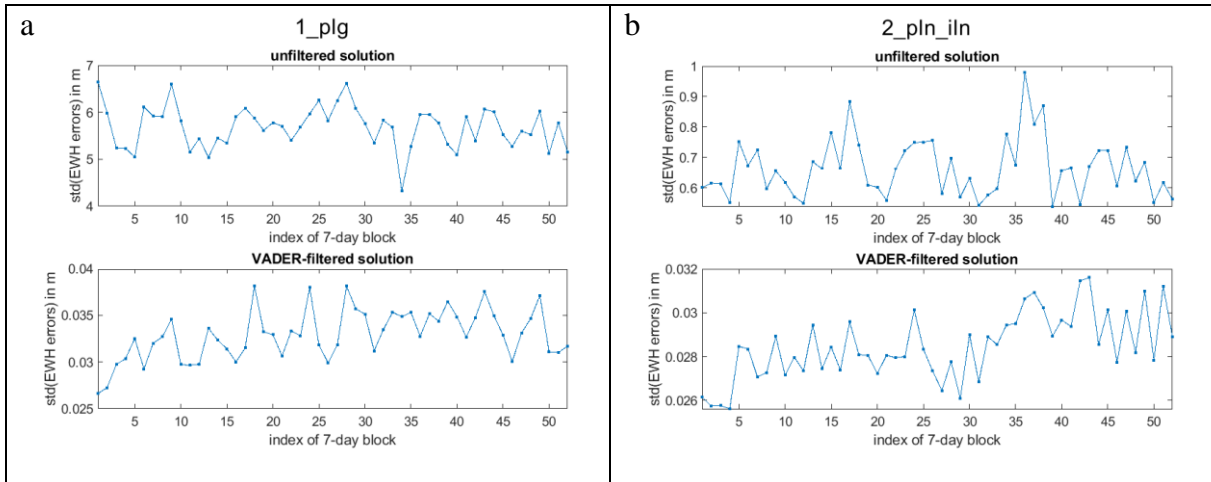
Figure 11-13 Standard deviation of EWH error grids for the 52 subsequent 7-day d/o 100 full noise nominal solutions for the scenario 1_pIg (3d_H) (panel a) and 2_pIn_iIn (3d_H) (panel b), as a function of time. Top: EWH errors of the unfiltered solutions, bottom: EWH errors of the VADER-filtered solutions. [Path: Deliverables/D1/simulation_results/full_scale_simulator_v009/old_noise_scaling/full_noise_nominal_1year _solutions/]

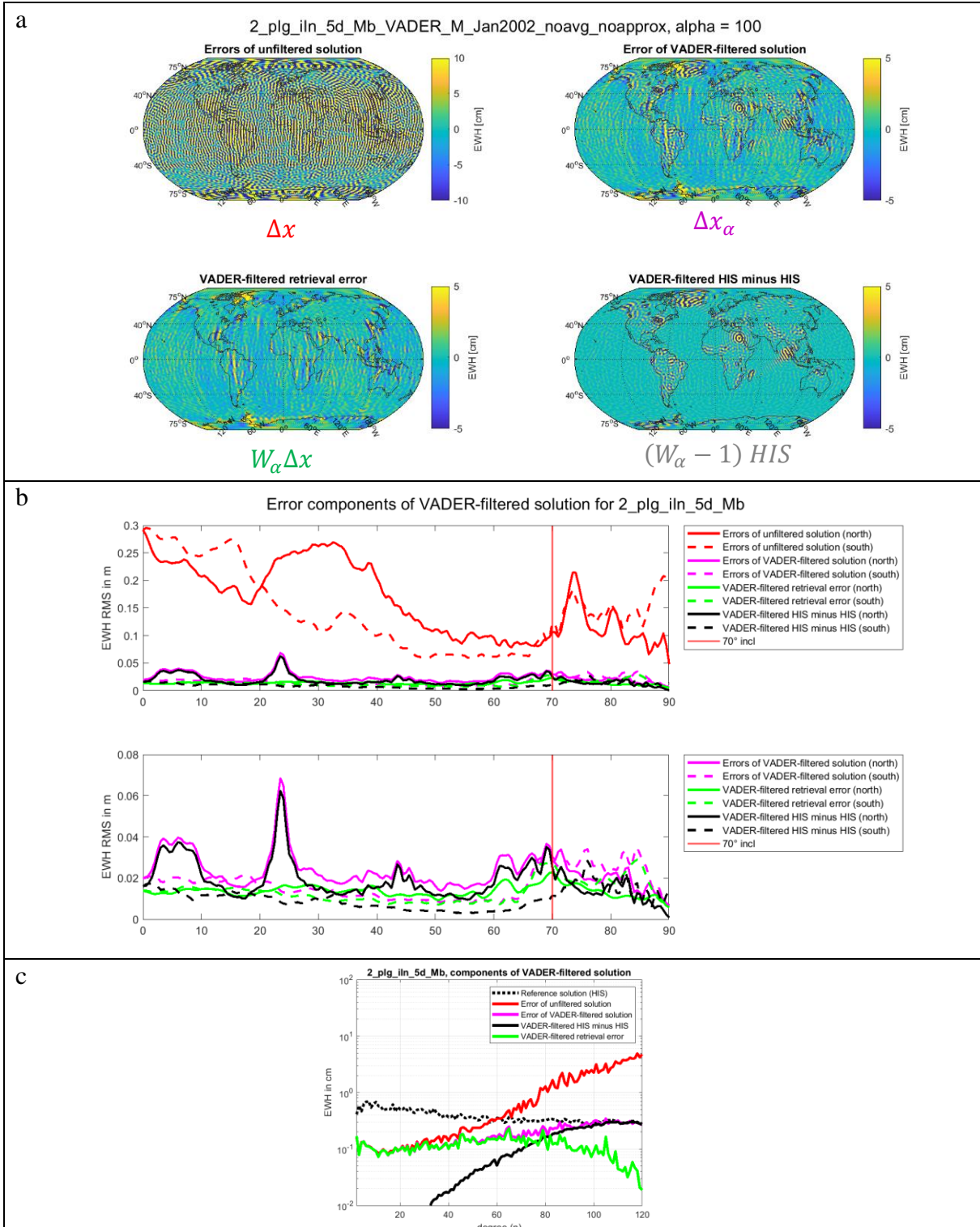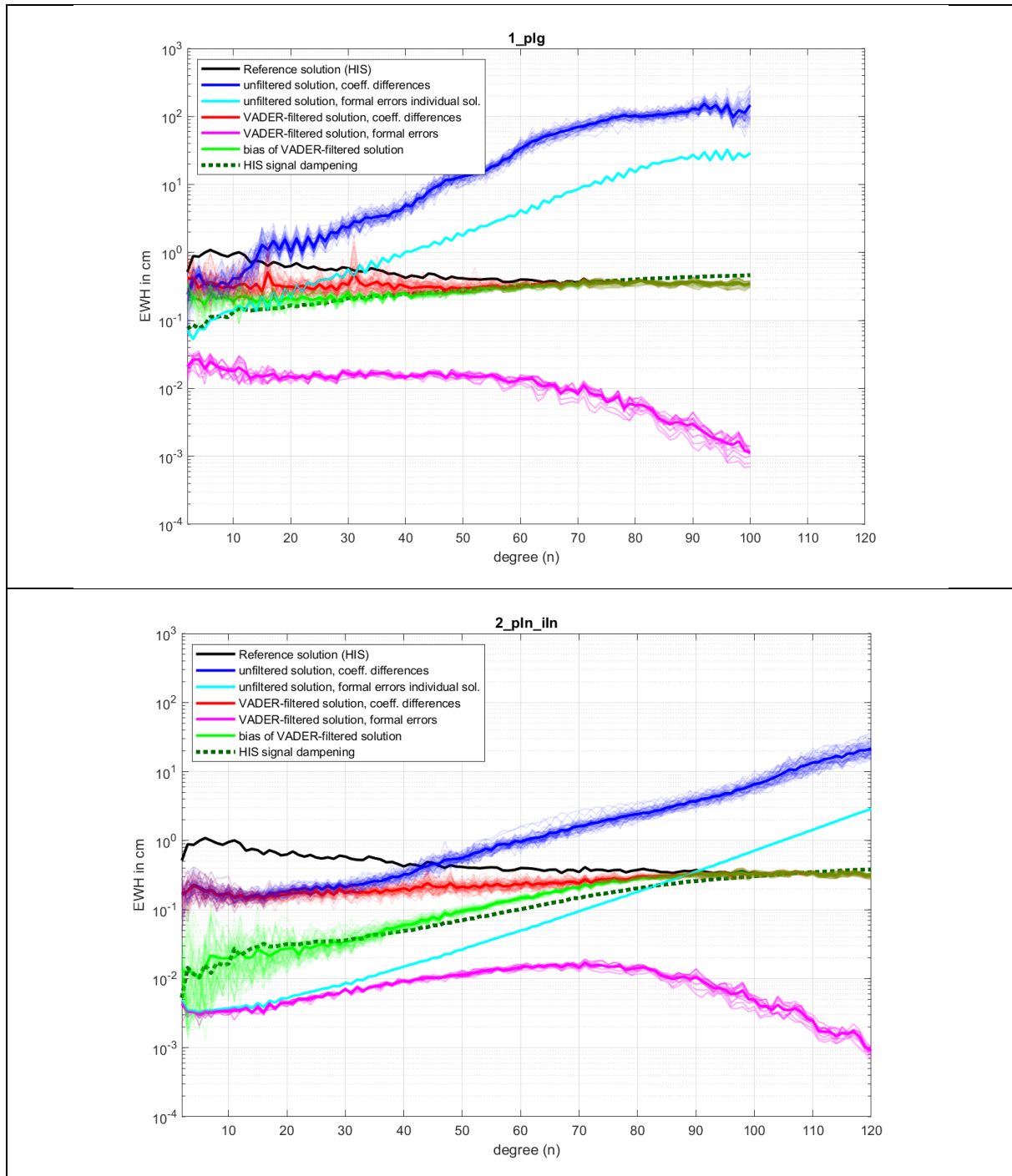**Figure 11-14 Degree amplitude curves for the 52 subsequent 7-day full noise nominal solutions for the scenarios 1_pIg (3d_H) (top) and 2_pIn_iIn (3d_H) (bottom). Shown are the curves for the unfiltered solutions (dark blue: coefficient errors, cyan: formal errors), the curves for the VADER-filtered solutions (red: coefficient errors, magenta: formal errors) and the bias of the VADER filters applied to the solutions (green). The dark green dotted lines additionally show the HIS signal dampening for the filter applied to the first 7-day solution. [Path: Deliverables/D1/simulation_results/full_scale_simulator_v009/old_noise_scaling/full_noise_nominal_1year _solutions/]**
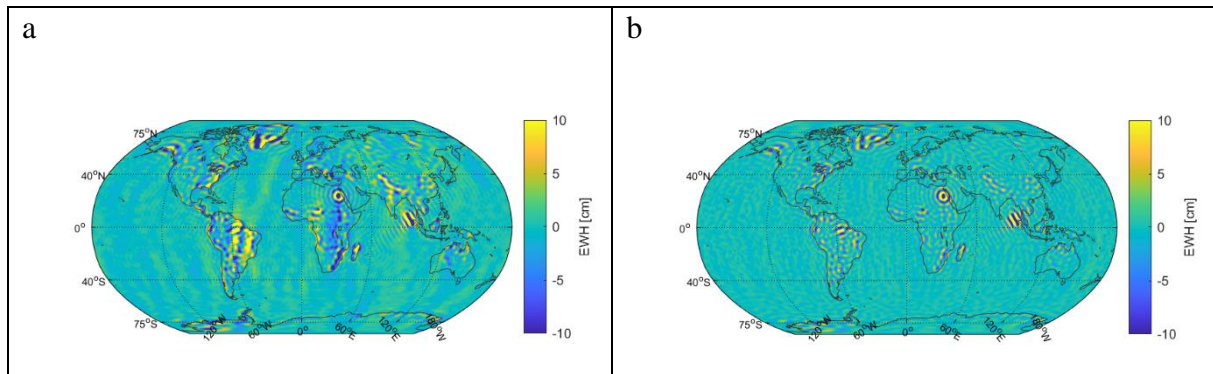
Figure 11-15 Spatial plots of the bias of the VADER filters applied to the 7-day full noise nominal solutions for the scenarios 1_pIg (3d_H) (panel a) and 2_pIn_iIn (3d_H) (panel b). [Path: Deliverables/D1/simulation_results/full_scale_simulator_v009/old_noise_scaling/full_noise_nominal_1year _solutions/]
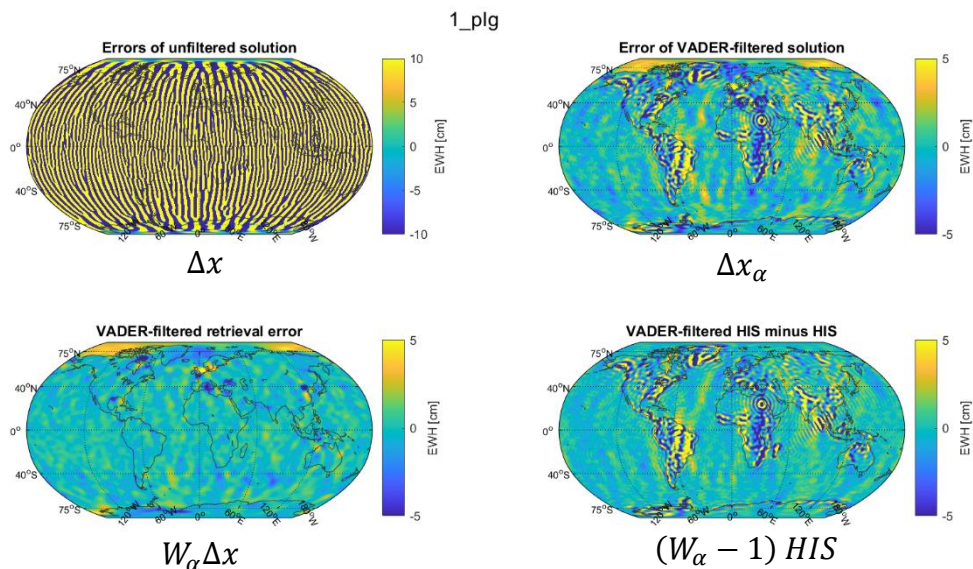
Figure 11-16 Error components of the VADER-filtered 7-day full noise solution for the scenario 1_pIg (3d_H). Δx is the error of the unfiltered solution. Δx_α is the error of the filtered solution, consisting of the filtered retrieval error $W_\alpha \Delta x$ and the HIS signal dampening effect $(W_\alpha - 1)HIS$. [Path: Deliverables/D1/simulation_results/full_scale_simulator_v009/old_noise_scaling/full_noise_nominal_1year _solutions/]
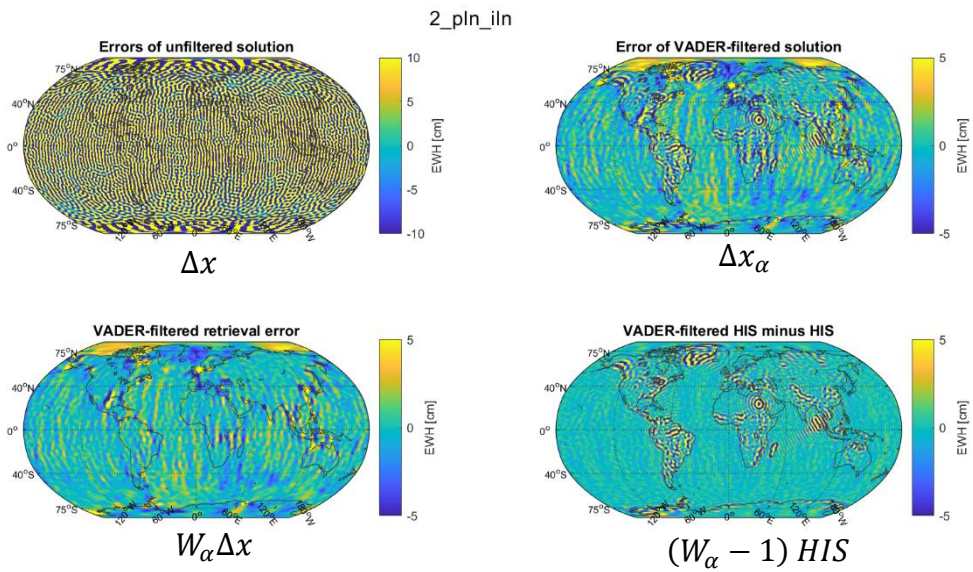
Figure 11-17 Error components of the VADER-filtered 7-day full noise solution for the scenario 2_pIn_iIn (3d_H). Δx is the error of the unfiltered solution. Δx_α is the error of the filtered solution, consisting of the filtered retrieval error $W_\alpha \Delta x$ and the HIS signal dampening effect $(W_\alpha - 1)HIS$. [Path: Deliverables/D1/simulation_results/full_scale_simulator_v009/old_noise_scaling/full_noise_nominal_1year _solutions/]

12 IMPROVEMENT OF DOUBLE-PAIR SOLUTIONS OVER THE POLES

The motivation of this section is the observation that Bender-type double-pair (DP) solutions show larger errors in the polar areas compared to the corresponding single polar pair (SP) solutions. The reason for this is that, although only the observations of the polar pair are supposed to control the DP solutions for latitudes $|\varphi| > i_2$ (i_2 being the inclination of the inclined pair), correlations of the SH coefficients among each other are responsible for a degradation of the derived solution over the poles when the NEQs of the inclined pair are incorporated to the system. The latitude from which the SP solution is outperforming the DP solution is larger than i_2, since the knowledge derived from the inclined pair's gravity data extends beyond $|\varphi| = i_2$.

Our solution strategy for improving DP solutions in the polar areas is to separately compute corresponding SP solutions up to the same SH degree and order N_{max} as the DP solution and use some of the SP solution coefficients as pseudo observations to regularize the DP NEQs. To this end, we exclusively use those coefficients of the SP solution that are related to the polar areas of latitudes $|\varphi| > \varphi_1$, where the parameter $\varphi_1 > i_2$ is optimized, as will be described below. These polar-gap coefficients are defined by the degree n-dependent maximum order

$$m_{max}(n) = \left| \frac{\pi}{2} - \varphi_1 \right| \cdot n$$

The regularization NEQ system is defined as

$$(A^T A)_{reg} \, x = (A^T l)_{reg}$$

where $(A^T A)_{reg}$ is a $N_{max}{}^2$-by-$N_{max}{}^2$ diagonal matrix with diagonal entries $= 1$ on the position of SH coefficients with orders $\leq m_{max}(n)$ and zero entries else, and $(A^T l)_{reg}$ is a $N_{max}{}^2$-by-1 vector that on the position of SH coefficients with orders $\leq m_{max}(n)$ contains the SP solution coefficients and is zero on all other positions.

The regularized DP solution is computed using the equation

$$x_{DP, \, reg} = \left[(A^T PA)_{DP} + \alpha (A^T A)_{reg} \right]^{-1} \left[(A^T Pl)_{DP} + \alpha (A^T l)_{reg} \right]$$

where $(A^T PA)_{DP}, (A^T Pl)_{DP}$ define the NEQ system of the DP and α is the weighting parameter determining the strength of the regularization.

The two parameters φ_1 and α are optimized using the criteria that the RMS value of the global EWH errors becomes minimal.

To test our method, firstly we apply it to a 7-day d/o 100 full noise solution of the scenario 2_pIn_iIn (3d_H). Figure 12-1 and Figure 12-2 show how the performances of the SP solution 1_pIn and the DP solution 2_pIn_iIn compare. At about $\varphi \approx 83°$, the SP solution starts to outperform the DP solution. As shown by Figure 12-2 c, the near-zonal SH coefficients are responsible for the relative performance of the two solutions over the poles.

Figure 12-3 shows the results of the regularization. As can be seen in panels a and b, the regularized DP solution performs at least as well as the original DP solution for all latitudes, and almost reaches the SP solution performance over the poles. Comparing the coefficient errors of the regularized and original DP solution by considering panel d reveals that our regularization method exclusively improves the polar gap-related coefficients of the DP solution, while the remaining coefficients stay unaffected. Thus, we conclude that for d/o 100 7-day solutions, our method is able to improve DP solutions over the poles by using the corresponding SP solutions.

As a second test, we apply our method to a 31-day d/o 120 full noise nominal solution of the same scenario as above. The longer retrieval period is chosen as the groundtrack coverage of the single polar pair within 7 days does not allow to retrieve the gravity field up to d/o 120.

Figure 12-4 shows the results of our regularization method. It can be seen that by applying the found optimum values for the parameters α and φ_1, the regularized DP solution shows almost no difference to the original DP solution and the SP performance over the poles is not reached.

In order to visualize why our method does not work as well for the d/o 120 solution as for the d/o 100 solution, we compare the spatial patterns produced by the polar gap-related SH coefficients of the d/o 120 SP and DP solution in Figure 12-5. Panel a shows that although over the poles, the SP solution contains smaller errors than the DP solution, the polar gap-related SH coefficients of the SP solution produce large errors in the lower-latitude region, showing that these coefficients are more correlated in the SP solution than in the DP solution. For this reason, a regularization of the d/o 120 DP solution using the polar gap-related coefficients of the SP solution would be able to decrease the errors of the DP solution over the poles, but at the same time would increase them for lower latitudes. As we optimize the regularization parameters α and φ_1 by minimizing the EWH errors globally, the determined parameter values lead to a rather weak regularization effect, which is why in the case of the d/o 120 solution, the regularized DP solution is very similar to the original DP solution.

To conclude, we found that it is possible to improve DP solutions over the poles by regularizing them using those SH coefficients of the corresponding SP solution that are related to the polar areas. We showed that applying this method to a d/o 100 7-day solution significantly improves the DP solution over the poles, and also provides a slightly improved performance in a global sense (which, however, would only slightly impact the cumulative error curves of this solution). For a d/o 120 31-day solution, we found that the method cannot provide a global improvement of the DP solution when improving it over the poles, as the polar gap-related SH coefficients of the corresponding SP solution are strongly correlated.
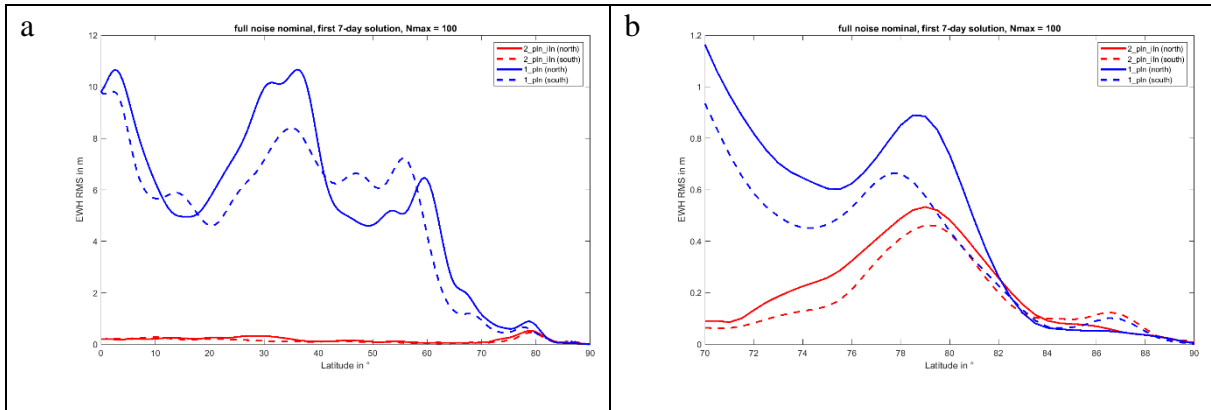
Figure 12-1 RMS values of EWH error grids computed along the parallels, as a function of latitude. On the x axes, 0 denotes the equator and 90 the north pole (for the solid curves) and the south pole (for the dashed curves). The underlying EWH error grids for the scenarios 1_pIn (3d_H) (blue curves) and 2_pIn_iIn (3d_H) (red curves) are shown by Figure 12-2. Panel b shows the same curves as panel a, for the latitude interval from 70° to 90°. [Path: Deliverables/D1/simulation_results/full_scale_simulator_v009/old_noise_scaling/full_noise_nominal/]
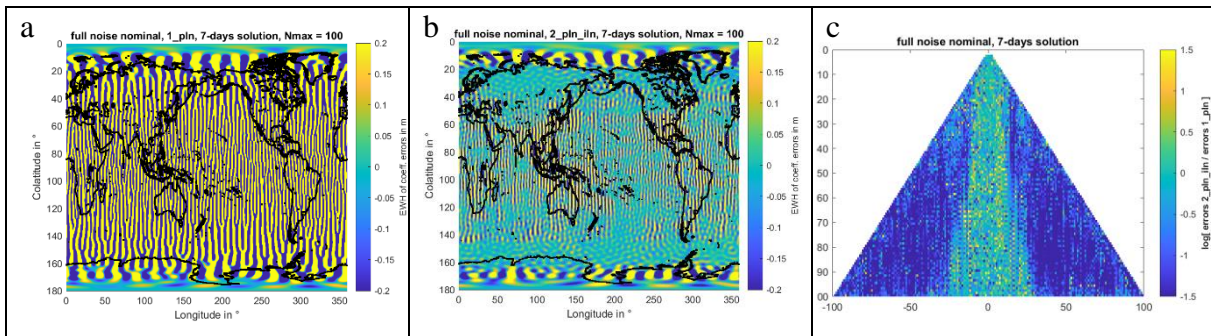
Figure 12-2 EWH error grids for d/o 100 7-day full noise nominal simulations for the scenarios 1_pIn (3d_H) (panel a) and 2_pIn_iIn (3d_H) (panel b). Panel c shows the ratio of the coefficient errors of the scenario 2_pIn_iIn divided by the scenario 1_pIn, on a logarithmic scale. [Path: Deliverables/D1/simulation_results/full_scale_simulator_v009/old_noise_scaling/full_noise_nominal/]
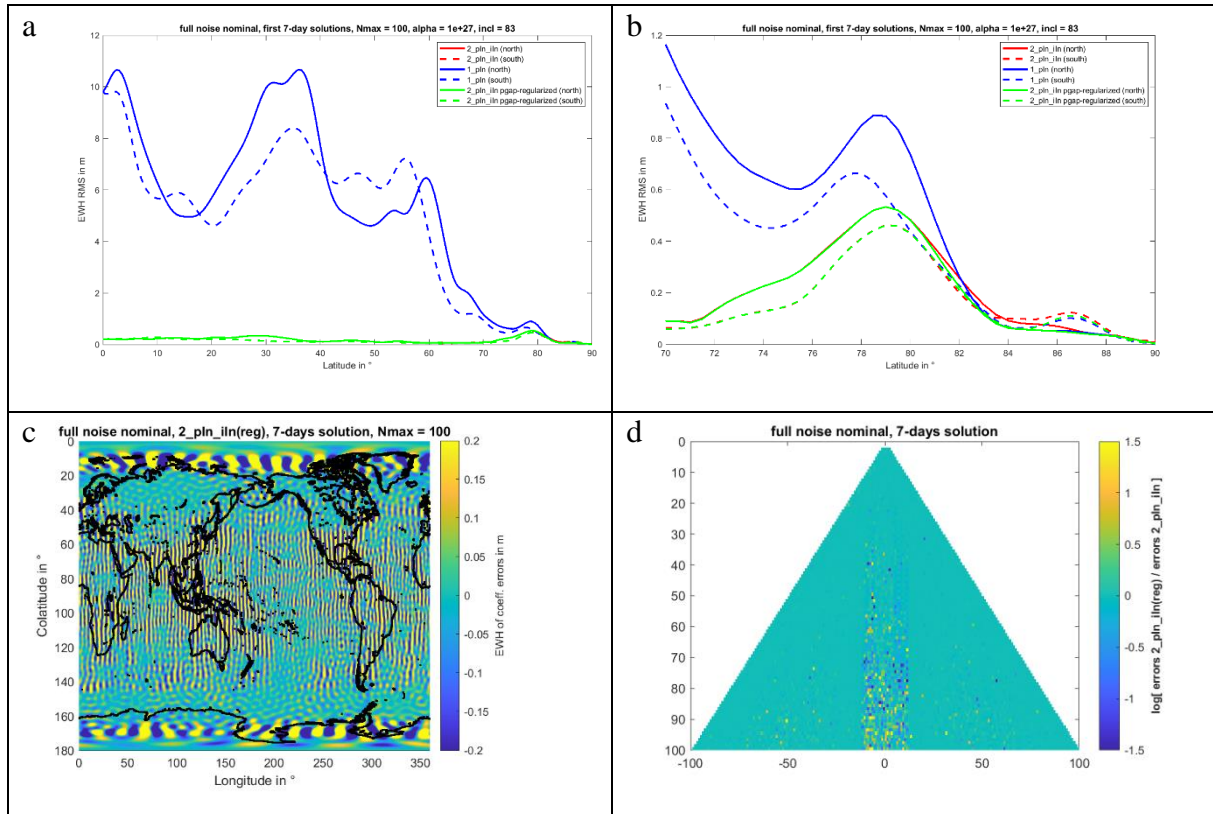
Figure 12-3 Result of the regularization of the 7-day d/o 100 full noise nominal DP solution 2_pIn_iIn (3d_H) using the corresponding SP solution 1_pIn (3d_H) as described in the text. As optimal regularization parameters, we found $\alpha = 10^{27}$ and $\varphi = 83°$. In panels a and b, the regularized DP solution is shown by the green line. Panel c shows the global EWH error grid of the regularized DP solution, and panel d shows the ratio of the coefficient errors of the regularized DP solution divided by the original DP solution, on a logarithmic scale.
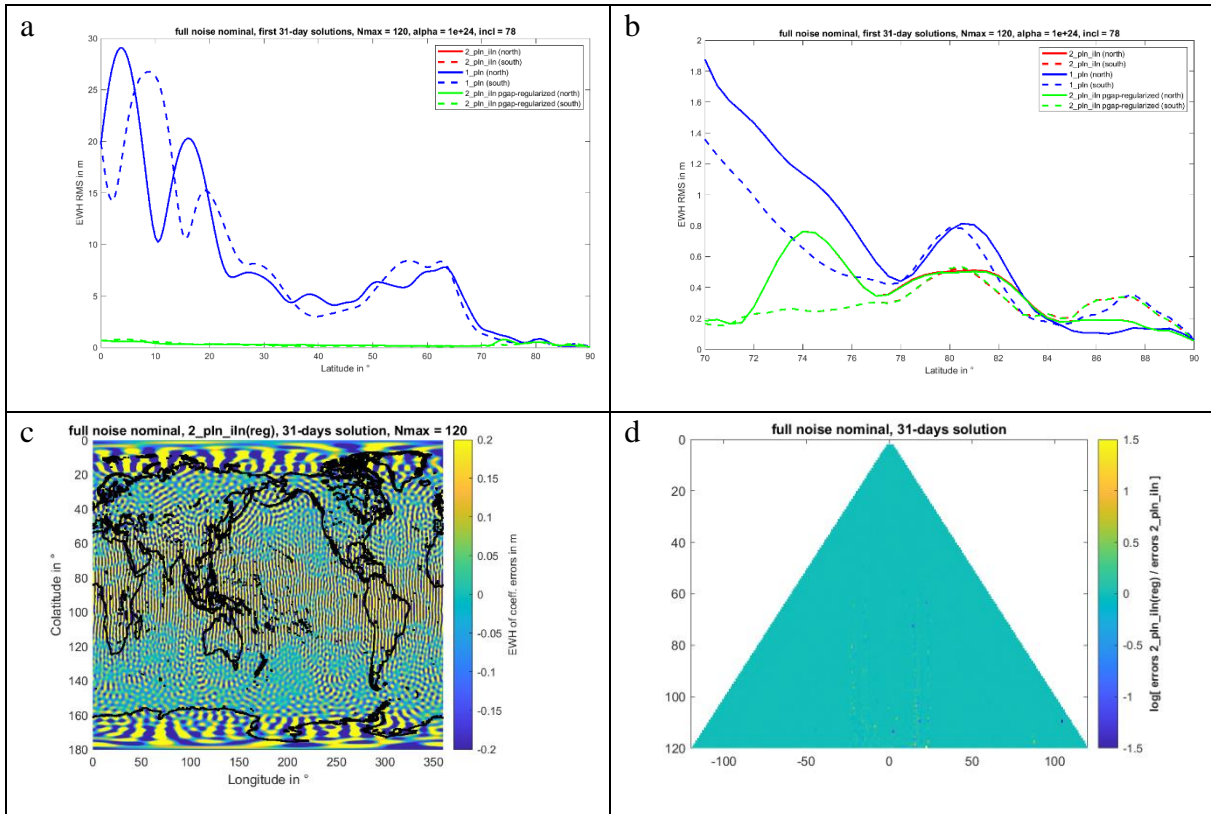
Figure 12-4 Result of the regularization of the 31-day d/o 120 full noise nominal DP solution 2_pIn_iIn (3d_H) using the corresponding SP solution 1_pIn (3d_H) as described in the text. As optimal regularization parameters, we found $\alpha = 10^{24}$ and $\varphi = 78°$. Panels are as in Figure 12-4.
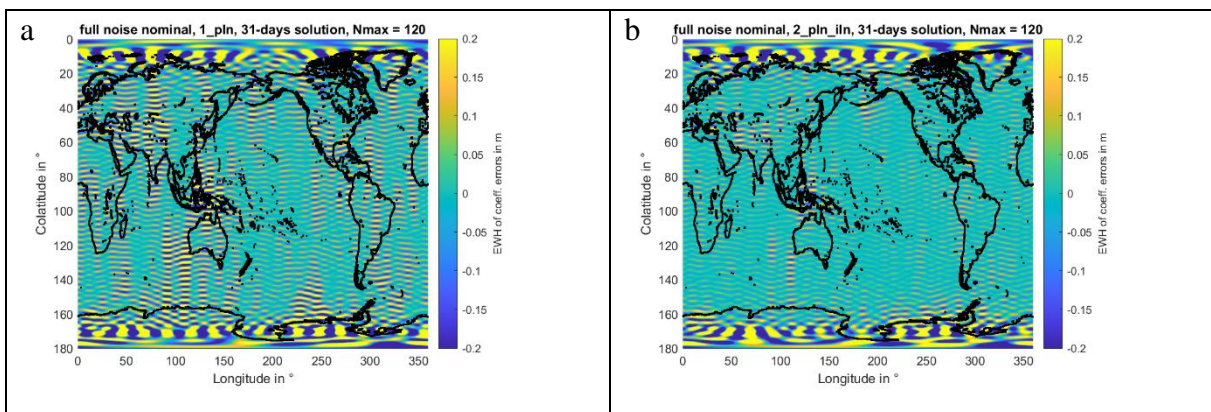
Figure 12-5 EWH error grids computed based on the polar gap (defined by $\varphi = 78°$)-related SH coefficients of the 31-day d/o 120 full noise nominal solutions for the scenario 1_pIn (panel a) and 2_pIn_iIn (panel b). [Path: Deliverables/D1/simulation_results/full_scale_simulator_v009/old_noise_scaling/full_noise_nominal/]

13 ORBIT DESIGN ASPECTS FOR 3-DAY GRAVITY RETRIEVAL

In this section, we evaluate how the orbits of the polar and the inclined pair need to be designed for retrieving short-term (3-day) gravity solutions from the data of a Bender-type double-pair configuration. On the one hand, the necessity of the fit of the orbit subcycle lengths to the 3-day retrieval period is tested. On the other hand, the impact of a common drift rate of the polar and inclined pair on the relative performance of subsequent solutions is investigated.

To this end, we compute five subsequent d/o 70 3-day full noise nominal solutions for the scenario 2_pIg_iIn, for the four different orbit scenarios listed in Table 13-1. Our reference orbit scenario is 3d_H, in which both the polar and the inclined pair have 3-day subcycles and a common westward longitudinal drift of about 1 degree per day. To evaluate the impact of the 3-day subcycle of the polar pair, we compare 3d_H to the scenario U3d5d_H. For investigating the impact of the 3-day subcycle of the inclined pair in the case of a missing 3-day subcycle of the polar pair, we compare U3d5d_H to the scenario U5d_H. To analyze how the common drift rate of the polar and the inclined pair impacts the relative performance of subsequent solutions, we compare 3d_H to the scenario U3d_H, in which both pairs have 3-day subcycles but their orbits drift at different rates such that the double-pair ground track pattern is different each of the subsequent 3-day periods.

Figure 13-1 visualizes the double-pair ground track for the first 3-day period for the scenarios 3d_H, U3d5d_H and U5d_H. It can be seen how missing 3-day subcycles of the polar and the inclined pair lead to gaps in the ground tracks and thereby to a spatially uneven data coverage within 3 days. For the scenario U3d5d_H, the ground track gaps of the polar pair are filled by the ground tracks of the inclined pair up to $|\varphi| = 70°$. As for U5d_H, both the polar and the inclined pair have no 3-day, but 5-day subcycles, the gaps in the 3-day ground tracks of the two satellite pairs coincide which leads to especially large gaps at low latitudes.

The degree amplitude curves of the resulting full noise nominal solutions are shown by panel a of Figure 13-2. Panel b shows the corresponding curves after eliminating the impact of the varying orbit altitudes (cf. Table 13-1) between the scenarios from the curves. In the following, we describe our altitude correction method:

The impact of the satellite altitude on the retrieval errors originates from the fact that the gravity signal decays with distance from the Earth, but at the same time the (instrument) noise obscuring the signal in the satellite data is altitude-independent. Assuming that in the case of low-low satellite-to-satellite tracking missions, the main quantity measured by the satellites is the range rate, which is related to gravity accelerations, i.e. the first spatial derivative of the gravity potential, the radius dependency of the signal in the data is given by the degree n-dependent factor $\left(\frac{1}{r}\right)^{n+2}$. For r, we use the mean radius of the polar and inclined pair of the considered scenario (we found that the effect of using e.g. the inclined satellites' height instead is very small). Assuming that the measured data is the sum of the $\left(\frac{1}{r}\right)^{n+2}$ - dependent signal and the noise, the retrieval error (being the difference between the SH coefficients derived from the noisy data and the true SH coefficients of the signal) contains the radius-dependent factor r^{n+2}. Thus, the ratio of the retrieval errors of two scenarios due to the changed orbital height will be

$\left(\frac{r_1}{r_2}\right)^{n+2}$. Using 3d_H (with mean radius of polar and inclined pair of r_{ref}) as reference scenario, we correct the retrieval errors of a specific scenario (with mean radius of polar and inclined pair of r) by multiplying them by $\left(\frac{r_{ref}}{r}\right)^{n+2}$.

The impact of this height correction on the retrieval errors can be seen by comparing panels a and b of Figure 13-2. It can be seen that for n<40, the three better-performing scenarios move together in their performance after the height correction. In the following, we assume that after applying this height correction, the impact of the varying orbital heights between the scenarios is eliminated.

Firstly, we investigate the necessity of a match between the subcycle lengths of the polar and inclined pair to the 3-day retrieval period by considering Figure 13-2, Figure 13-3 and Figure 13-4.

The comparison of the retrieval errors of 3d_H and U3d5d_H shows that the gaps in the polar pair's ground track present for U3d5d_H slightly degrade the solution for larger n, while for small n, no impact can be seen. In the spatial plots, it can be seen that especially the resolution of small-scale features at low latitudes is affected, while the convergence of the polar pair's ground tracks towards the poles prevents a significant degradation of the U3d5d_H solution over the poles.

Comparing the retrieval errors of U3d5d_H and U5d_H shows that the common gaps in the ground track patterns of the polar and inclined pair of U5d_H significantly degrade the solution globally. The fact that the error amplitudes are spatially strongly correlated with the ground track gaps reveals that these gaps are responsible for the degradation of the 3-day solutions of U5d_H. As in the polar areas, the ground tracks of U3d5d_H and U5d_H are similar, also the error patterns in these areas are very similar between the scenarios.

From these observations, we conclude that short-term (3-day) solutions are indeed affected by a match between the subcycle length and the retrieval period. A missing 3-day subcycle of the polar pair is acceptable, but affects the resolution of small-scale features at low latitudes. However, if the polar pair orbit is uncontrolled, an orbit control for the inclined pair to maintain the 3-day ground track subcycles is crucial for the homogeneous quality of the 3-day solutions.

Finally, we investigate the necessity of a common longitudinal drift rate between the polar and the inclined pair's orbits for a homogenous quality of subsequent 3-day solutions. For this, we compare the error spread of the five subsequent 3-day solutions for the scenarios 3d_H and U3d_H. As the inclination of the second satellite pair is different between these scenarios, the main impact on the relative retrieval errors between these scenarios is the inclination of the second pair. Therefore, for our purpose of analyzing the impact of the coordination of the longitudinal drift between the two pairs, we do not compare the retrieval errors themselves but only how the retrieval errors of the individual solutions scatter about their mean performance. As shown by Figure 13-5, no difference in the error spread of individual solutions about their mean performance can be observed between the scenarios 3d_H and U3d_H. Therefore, we conclude that if stable subcycles matching the retrieval period are provided for both pairs, a common longitudinal drift between the ground tracks of the two pairs is not necessary to provide a homogeneous quality of subsequent 3-day solutions. That means, the double-pair

ground track pattern does not need to be exactly equal between the subsequent 3-day solutions, as long as there is no strong spatial variation in the ground track density, as has been shown in the above-described analysis of the necessity of the orbit subcycles.

Table 13-1 Orbit scenarios for evaluating the impact of orbit subcycles and drift rates on 3-day gravity retrieval.

ID	Sats 1 (IP)		Sats 2 (PP)		h_{l1} [-]	h_{l2} [-]	$\Delta(Lon)_1$ [deg]	$\Delta(Lon)_2$ [deg]	Sub-cycles [days]	Retrieval period [days]	MRD
	Alt. [km]	Incl. [deg]	Alt. [km]	Incl. [deg]							Requirements
Coordinated											
3d_H	432	70	463	89	1.451	1.449	-3.076	-3.067	3, 7, 31	3	MRD-040 – **Fulfilled** MRD-050 – **Fulfilled** MRD-060 – **Fulfilled**
Uncoordinated											
U3d5d_H	432	70	492	89	1.451 (3d)	1.172 (5d)	-3.076 (3d)	-0.790 (5d)	IP: 3, 31 PP: 5, 31	3	MRD-040 – **Violated** MRD-050 – **Violated** MRD-060 – **Violated**
U5d_H	460	70	492	89	1.061 (5d)	1.172 (5d)	-0.284 (5d)	-0.790 (5d)	IP: 5 PP: 5, 31	3	MRD-040 – **Violated** MRD-050 – **Violated** MRD-060 – **Violated**
U3d_H	402	65	463	89	1.382	1.449	2.380	-3.067	IP: 3, 29-30 PP: 3, 7, 31	3	MRD-040 – **Fulfilled** MRD-050 – **Violated** MRD-060 – **Violated**
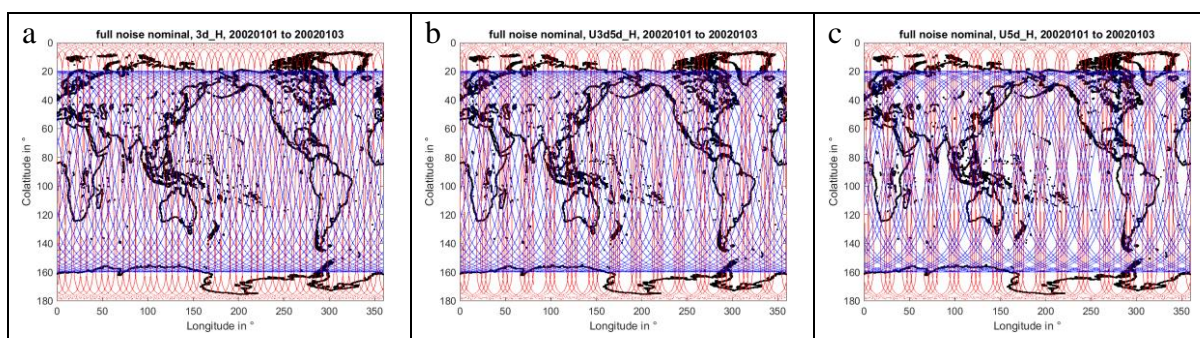
Figure 13-1 3-day double-pair groundtrack pattern for the orbit scenarios 3d_H (panel a), U3d5d_H (panel b) and U5d_H (panel c), as described in Table 13-1. [Path: Deliverables/D1/simulation_results/full_scale_simulator_v009/1_by_sqrt(10)_noise_scaling/full_noise_nominal/]

Figure 13-2 Degree amplitude curves of five subsequent d/o 70 3-day full noise nominal solutions for the scenario 2_pIg_iIn (3d_H, U3d5d_H, U5d_H and U3d_H). The characteristics of the underlying orbits are given in Table 13-1. Panel a shows the uncorrected cures, panel b the curves after the altitude correction as described in the text. Panel c gives the legend for both figures. [Path: Deliverables/D1/simulation_results/full_scale_simulator_v009/1_by_sqrt(10)_noise_scaling/full_noise_nominal/]
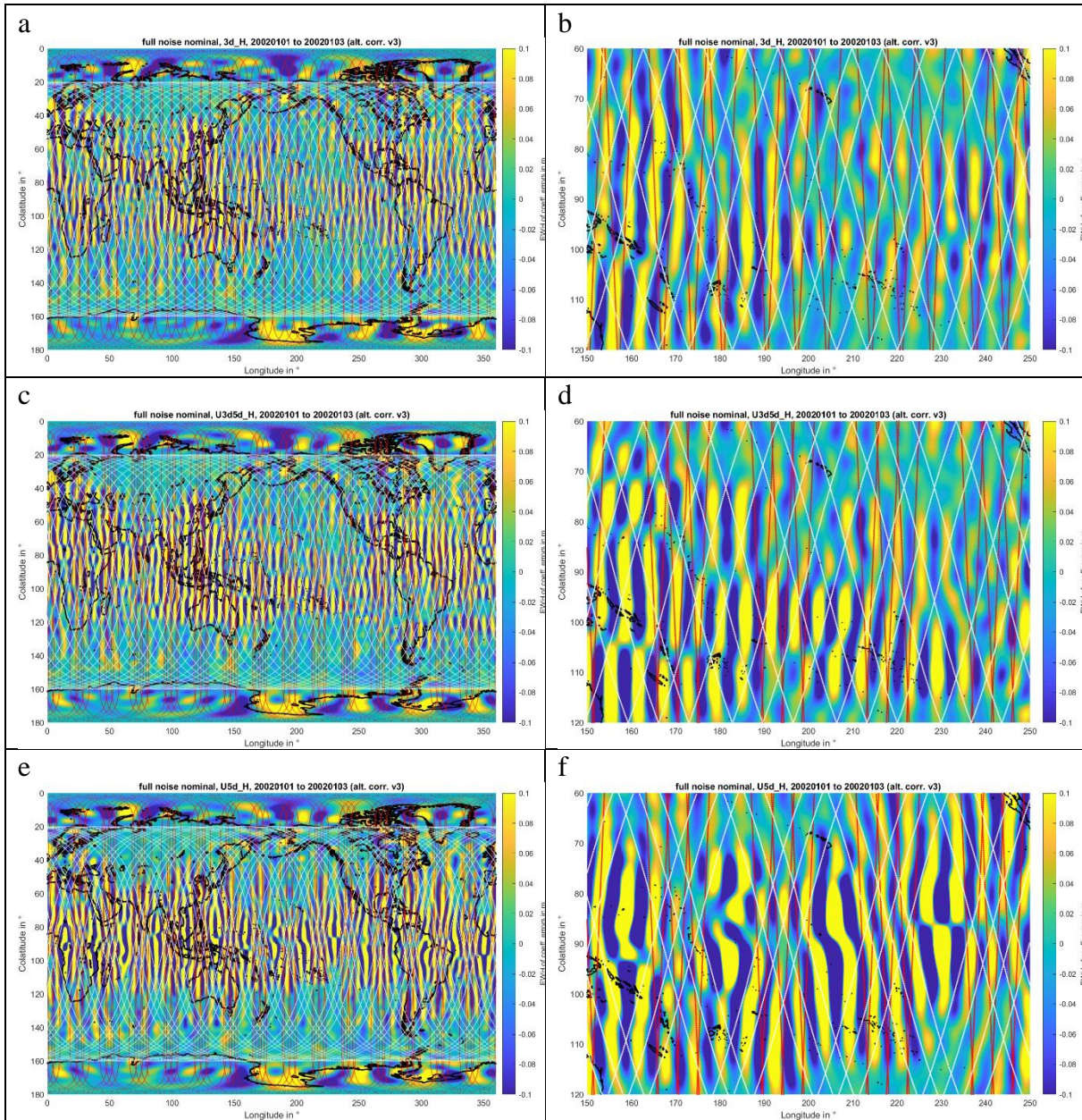
Figure 13-3 EWH error grids of the first d/o 70 full noise nominal 3-day solution of the scenario 2_pIg_iIn using the orbit scenario 3d_H (panels a, b), U3d5d_H (panels c, d) and U5d_H (panels e, f). The left column shows global maps while the right column shows a selected regional section at the equator. [Path: Deliverables/D1/simulation_results/full_scale_simulator_v009/1_by_sqrt(10)_noise_scaling/full_noise_no minal/]
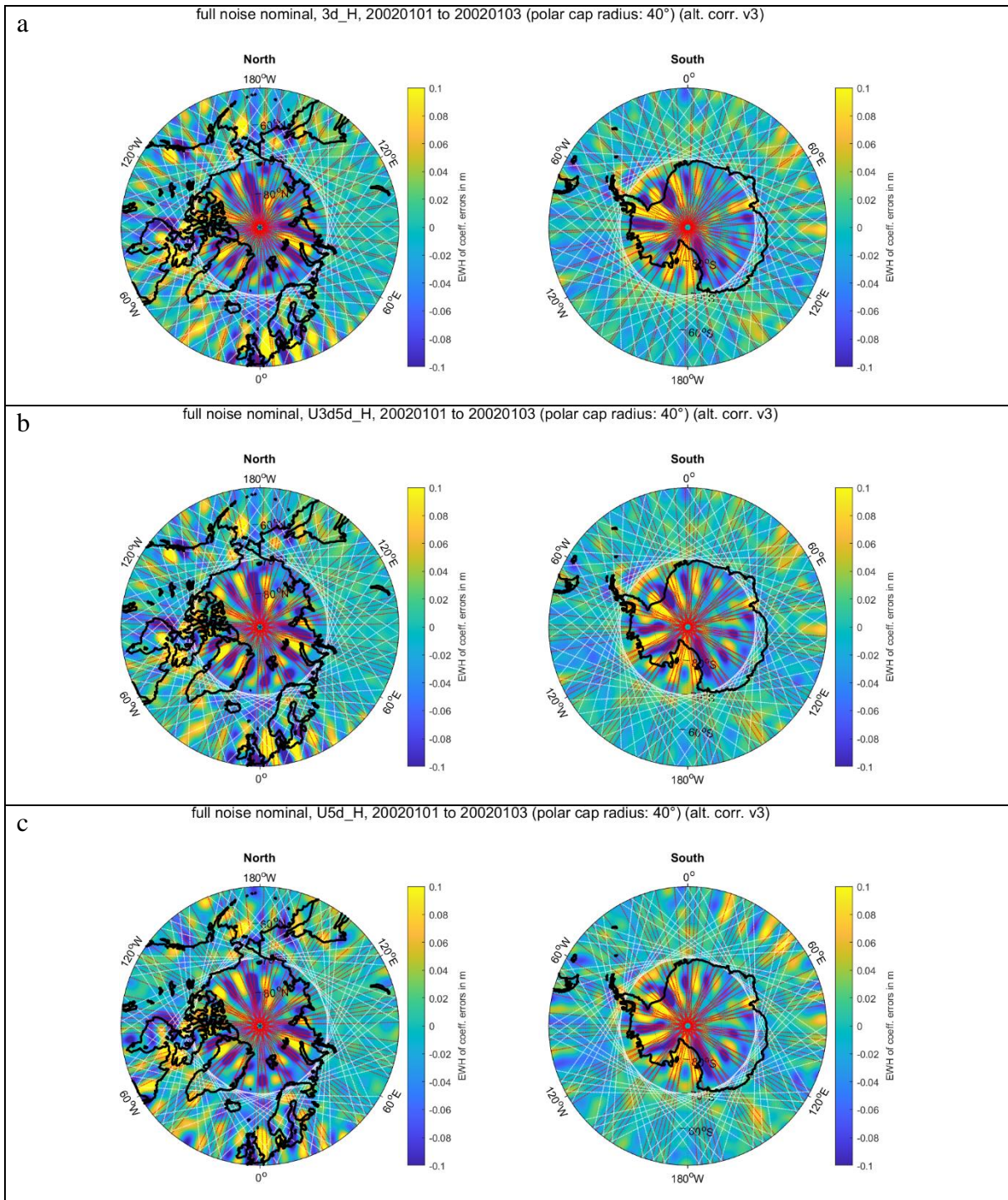
Figure 13-4 EWH error grids of the first d/o 70 full noise nominal 3-day solution of the scenario 2_pIg_iIn using the orbit scenario 3d_H (panel a), U3d5d_H (panels b) and U5d_H (panels c). Shown are stereographic projections with a radius of 40° in latitude, centred about the north pole (left column) and the south pole (right column). [Path: Deliverables/D1/simulation_results/full_scale_simulator_v009/1_by_sqrt(10)_noise_scaling/full_noise_nominal/]
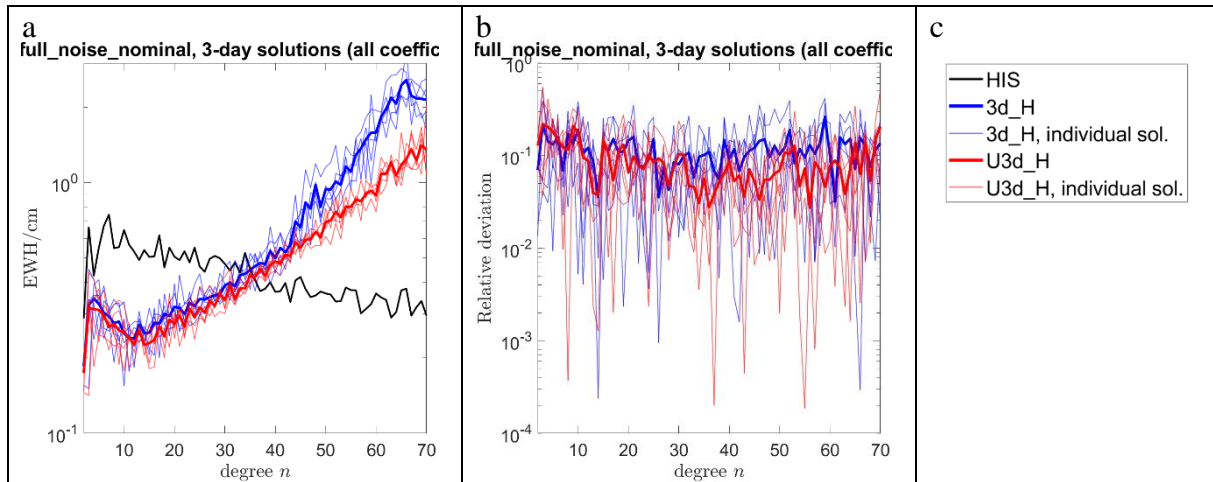
Figure 13-5 Thin curves in panel a: Degree amplitude curves of five subsequent d/o 70 3-day full noise nominal solutions for the scenario 2_pIg_iIn (3d_H and U3d_H). Thin curves in panel b: ratio of the error curves of the five individual curves divided by their mean curve. The thick curves in both panels show the mean curve of the thin curves in the respective panel. Panel c shows the legend valid for both panel a and b. [Path: Deliverables/D1/simulation_results/full_scale_simulator_v009/1_by_sqrt(10)_noise_scaling/full_noise_nominal/]

14 1-DAY GRAVITY RETRIEVAL

As described in Section 5.4, the retrieval errors of 3-day, 5-day, 7-day and 31-day solutions for the scenario 2_pIn_iIn (3d_H) scale with their retrieval period, such that the retrieval error of a 31-day solution can be multiplied by sqrt(x/31) to find the error level of the corresponding x-day solution. In this section, our aim is to investigate 1-day full noise solutions for the same scenario.

To this end, we compare three cases of 1-day solutions, in all of which we assemble and solve the respective NEQs up to SH d/o 15:

1. 1-day solutions using gravity signals up to d/o 120 in the forward calculation, as has been done for the 3-, 5-, 7- and 31-day solutions presented in Section 5.4. This is the "worst case", as the retrieval errors will contain the full spectral leakage effect of high-degree errors leaking to the solution.
2. 1-day solutions using gravity signals up to d/o 15 in the forward calculation. This is the "best case", as spectral leakage errors are excluded from the retrieval error budget.
3. Daily Wiese solutions (DWS), which already have been presented in Section 5.4. These are computed along with 31-day d/o 120 full noise Wiese solutions.

As done in Section 5.4, for all cases solutions for the 2-month simulation period starting on 01.01.2002 are computed, and the mean of the degree amplitude curves of the individual solutions are plotted in Figure 14-1. This Figure also includes the solutions shown by Figure 5-21 b.

By comparing the relative differences of the curves shown by panels a and b of Figure 14-1, it can be observed that the formal errors only reflect the number of observations in the retrieval period, which is why all curves referring to 1-day solutions coincide. The coefficient errors shown by panel a, however, do not only include the retrieval period effect, but also the temporal aliasing and spectral leakage errors affecting the specific solutions. For example, it can be seen that for shorter retrieval periods, the temporal aliasing errors are reduced, which is the reason why the up-scaled retrieval error of the 31-day solution overestimates the retrieval errors of the 1-day solutions.

Comparing the coefficient errors of the 1-day solutions of the first two cases, we see that the spectral leakage effect manifests itself as an error increase towards the large-degree end of the parametrized SH spectrum in the case 1 solutions. Comparing the performance of the DWS to the best-case scenario 2 shows that the DWS outperform the best-case solution for degrees < 10, which we interpret as an effect of the co-estimation of 31-day solutions which absorb part of the temporal aliasing errors. For degrees > 10, however, the effect of spectral leakage that is excluded in the best-case solutions but included in the DWS starts to dominate and leads to a worse performance of the DWS compared to the best case.

Figure 14-2 shows the EWH error grids and the coefficient error triangles for the first of the computed 1-day solutions for case 1 (panels a, b), case 2 (panels c, d) and case 3 (panels e, f). Panels g and h additionally show the first 31-day solution up-scaled by the factor sqrt(31) and cut at $N_{max} = 15$. It is visible how the effect of spectral leakage degrades the case 1 compared

to the case 2 solution, the DWS is better for small degrees, and the up-scaled retrieval errors of the 31-day solution over-estimates the temporal aliasing errors present in the 1-day solutions.

In order to visualize the effect of spectral leakage if choosing a too low maximum SH d/o in the gravity retrieval, we compute 3-, 5-, 7- and 31-day solutions parametrized up to d/o 15 (by stacking the daily NEQ systems of case 1 accordingly). The results can be seen in Figure 14-3. As for the case 1 solutions, the spectral leakage effect of large-degree signals contained in the data degrades the retrieved solution towards the large-degree end of the resolved spectrum. This visualizes the importance of parametrizing a solution up to the largest SH degree that is allowed by the ground track density in the respective retrieval period in order to avoid spectral leakage effects.

Summarizing our findings on the choice of retrieval period and maximum SH degree parametrized, we firstly found that the shorter the retrieval period, the smaller the temporal aliasing errors degrading the retrieval performance, as the maximum temporal period that causes temporal aliasing is reduced. In the case of 1-day solutions, the reduction of temporal aliasing errors is that large such that an up-scaling of 31-day solution retrieval errors to find the performance of daily gravity retrieval is not possible. Secondly, the smaller the parametrized maximum SH d/o N_{max}, the larger the effect of $n > N_{max}$ signals leaking into the solution. This effect however has only been observed to dominate the retrieval errors of d/o 15 1-day solutions. For retrieval periods of ≥ 3 days, temporal aliasing errors are dominating the error budget (assumed that the maximum possible N_{max} for the individual retrieval period has been used). Thirdly, we note that the maximum retrieved SH d/o is limited by the ground track density within the retrieval period.
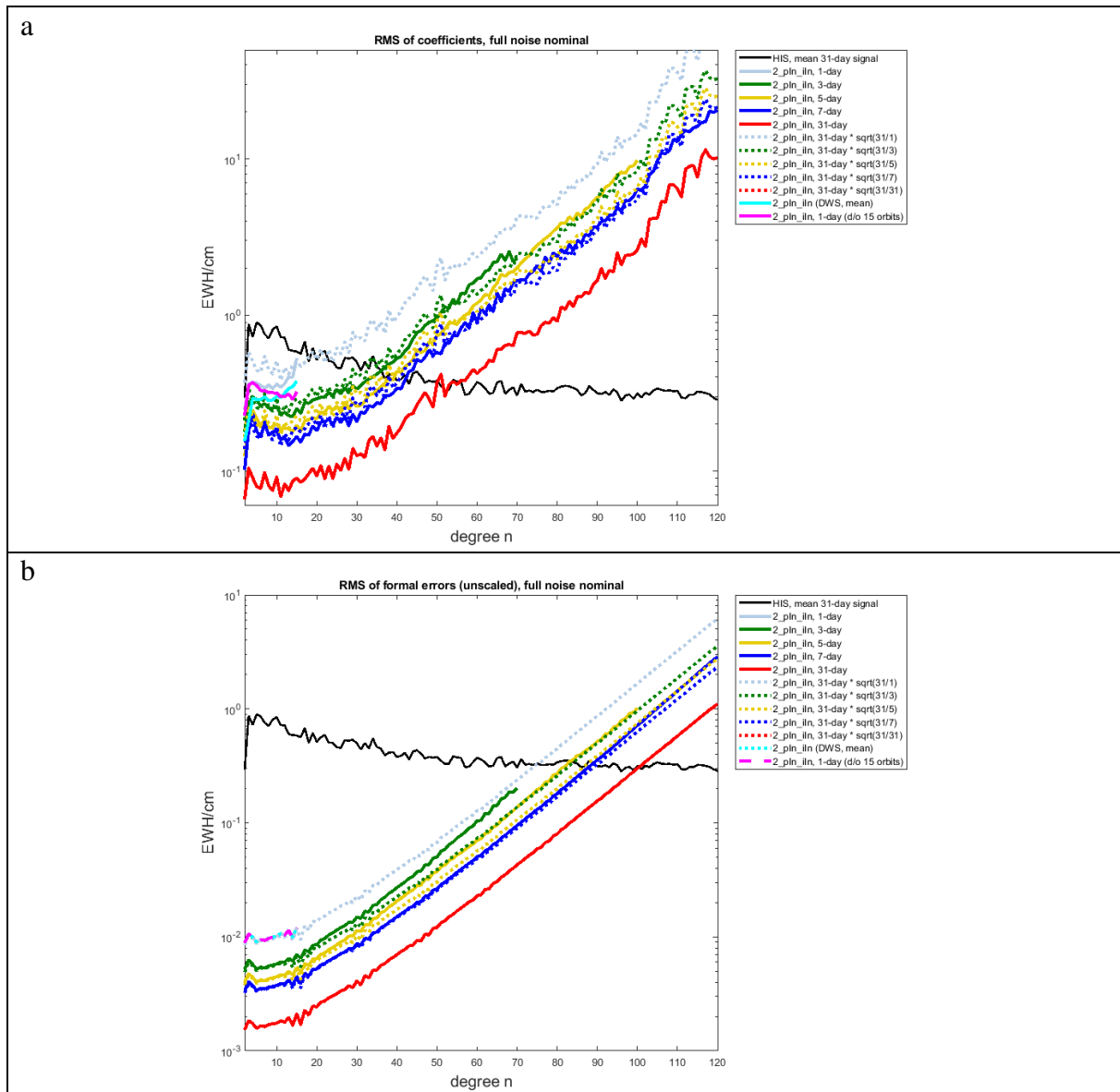
Figure 14-1 Degree amplitudes of full noise nominal simulations for the scenario 2_pIn_iIn. The solid lines are computed based on the respective coefficient errors (panel a) and formal errors (panel b) of 1-day d/o 15, 3-day d/o 70, 7-day d/o 100 and 31-day d/o 120 solutions, while the dotted lines show the 31-day curve upscaled by a factor of sqrt(31/x) to approximate the x-day curve. The three cases for the 1-day solutions are described in the text. [Path: Deliverables/D1/simulation_results/ful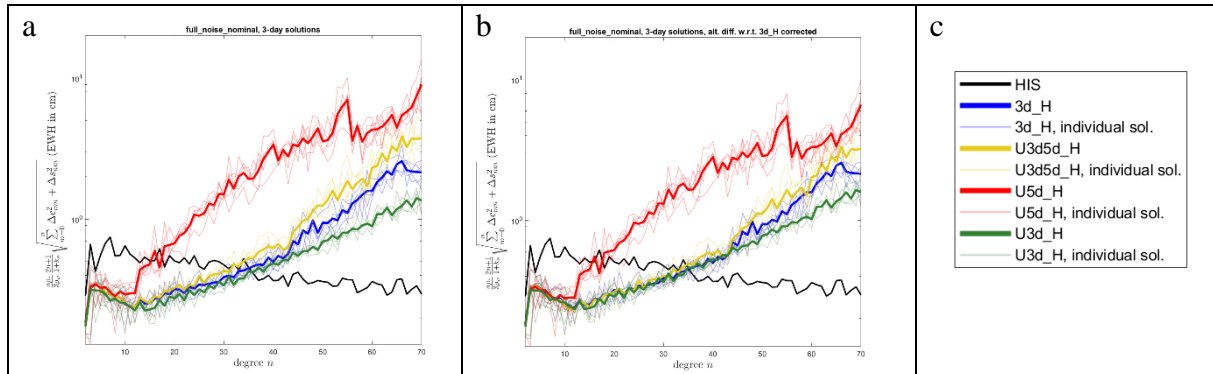l_scale_simulator_v009/old_noise_scaling/full_noise_nominal/2_pIn_iIn/ and Deliverables/D1/simulation_results/full_scale_simulator_v009/old_noise_scaling/full_noise_wiese/2_pIn_iIn/31d/]
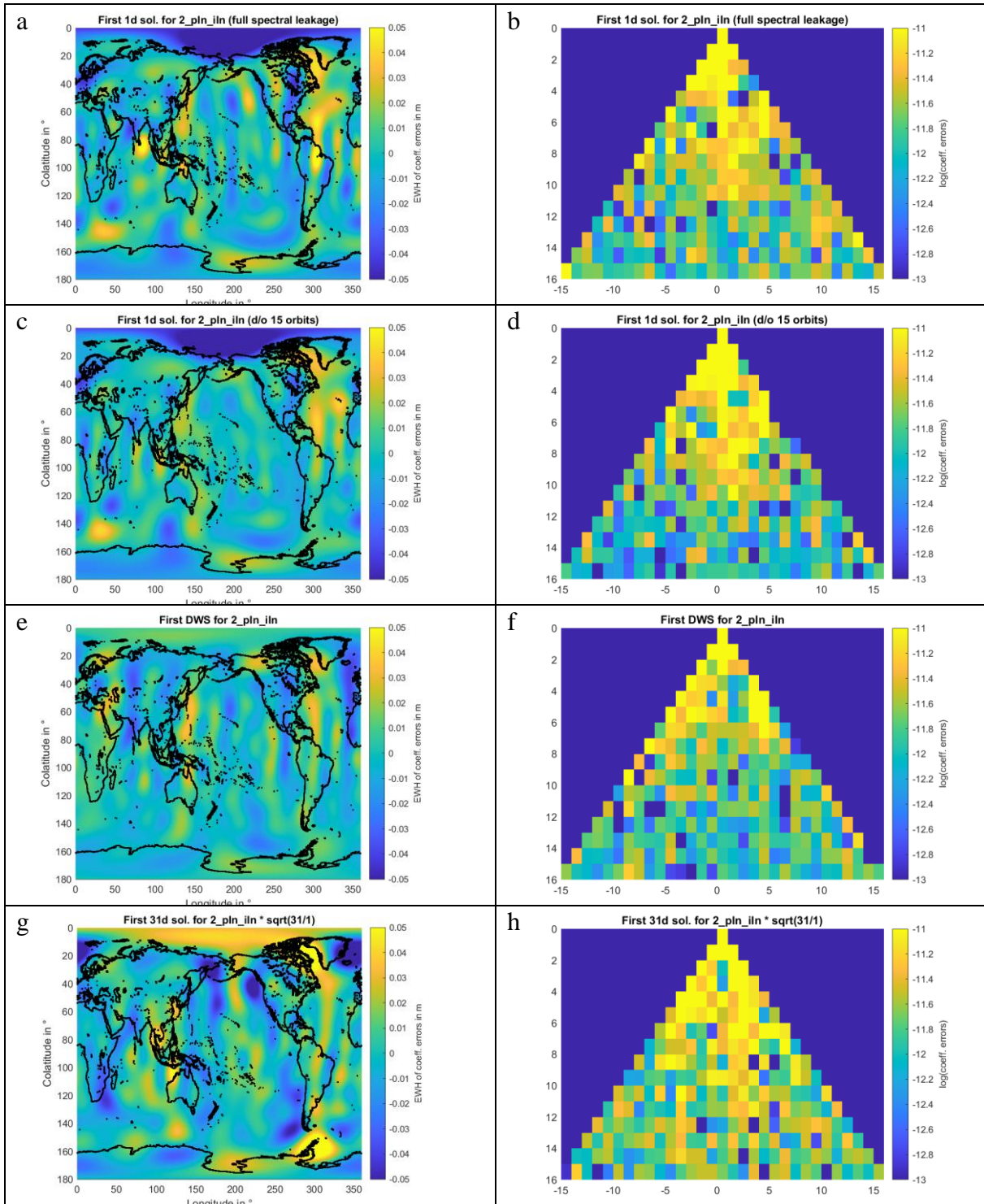
Figure 14-2 EWH grids (left column) and coefficient triangles (right column) showing the retrieval errors of the first daily solutions of case 1 (panels a, b), case 2 (panels c, d) and case 3 (panels e, f) as well as the first 31-day solution scaled by sqrt(31) and cut at SH degree 15 (panels g, h). The three cases for the daily solutions are described in the text. [Path: Deliverables/D1/simulation_results/full_scale_simulator_v009/old_noise_scaling/full_noise_nominal/2_pIn _iIn/ and Deliverables/D1/simulation_results/full_scale_simulator_v009/old_noise_scaling/full_noise_wiese/2_pIn_iI n/31d/]
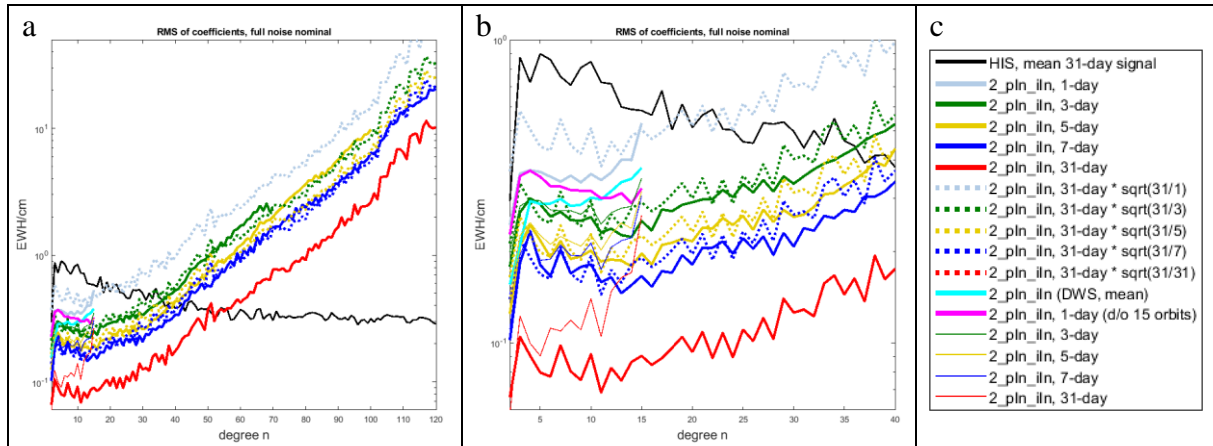
Figure 14-3 Degree amplitude plot as shown by Figure 14-1 a, additionally including d/o 15 3-, 5-, 7- and 31-day solutions to visualize the effect of spectral leakage to the solutions if not parametrized to a large-enough maximum SH degree and order. Panel b shows the section of panel a up to SH degree 40. [Path: Deliverables/D1/simulation_results/full_scale_simulator_v009/old_noise_scaling/full_noise_nominal/2_pIn _iIn/ and
Deliverables/D1/simulation_results/full_scale_simulator_v009/old_noise_scaling/full_noise_wiese/2_pIn_iI n/31d/]

15   IMPACT OF NOISE SCALING FACTOR ON RESULTS

15.1   IMPACT ON RESULTS OF 1_PIG (3D_H)

The aim of this section is to evaluate the impact of scaling the instrument (ACC, LRI and orbit) noise by a factor of 1/sqrt(10) (implying a scaling of the used P matrices by a factor of 10) on the retrieval errors of instrument only and full noise nominal results.

To this end, we analyze the scenario 1_pIg (3d_H). As can be seen by comparing the curves shown by Figure 15-1 a, scaling the instrument noise used or scaling the retrieval errors of instrument only simulations by the same factor give the same results. That means that for instrument only results that contain un-scaled instrument noise time series, it is possible to directly derive the results that would be obtained in the case of a scaled instrument noise by applying the factor of 1/sqrt(10) to the retrieval errors. As shown by the green curve in panel a, the impact of scaling the orbit noise on the results is negligible, i.e. for new simulations that use the scaled instrument noise, it is possible to use the already computed orbit data. The reason for this is that the orbit noise is only introduced to the high-low satellite-to-satellite tracking NEQ systems which are dominated by the low-low satellite-to-satellite tracking NEQ systems.

As shown by Figure 15-1 b, the impact of scaling the instrument noise by a factor of 1/sqrt(10) on the full noise results is very small, since in this case the much larger temporal aliasing errors are dominating the error budget.
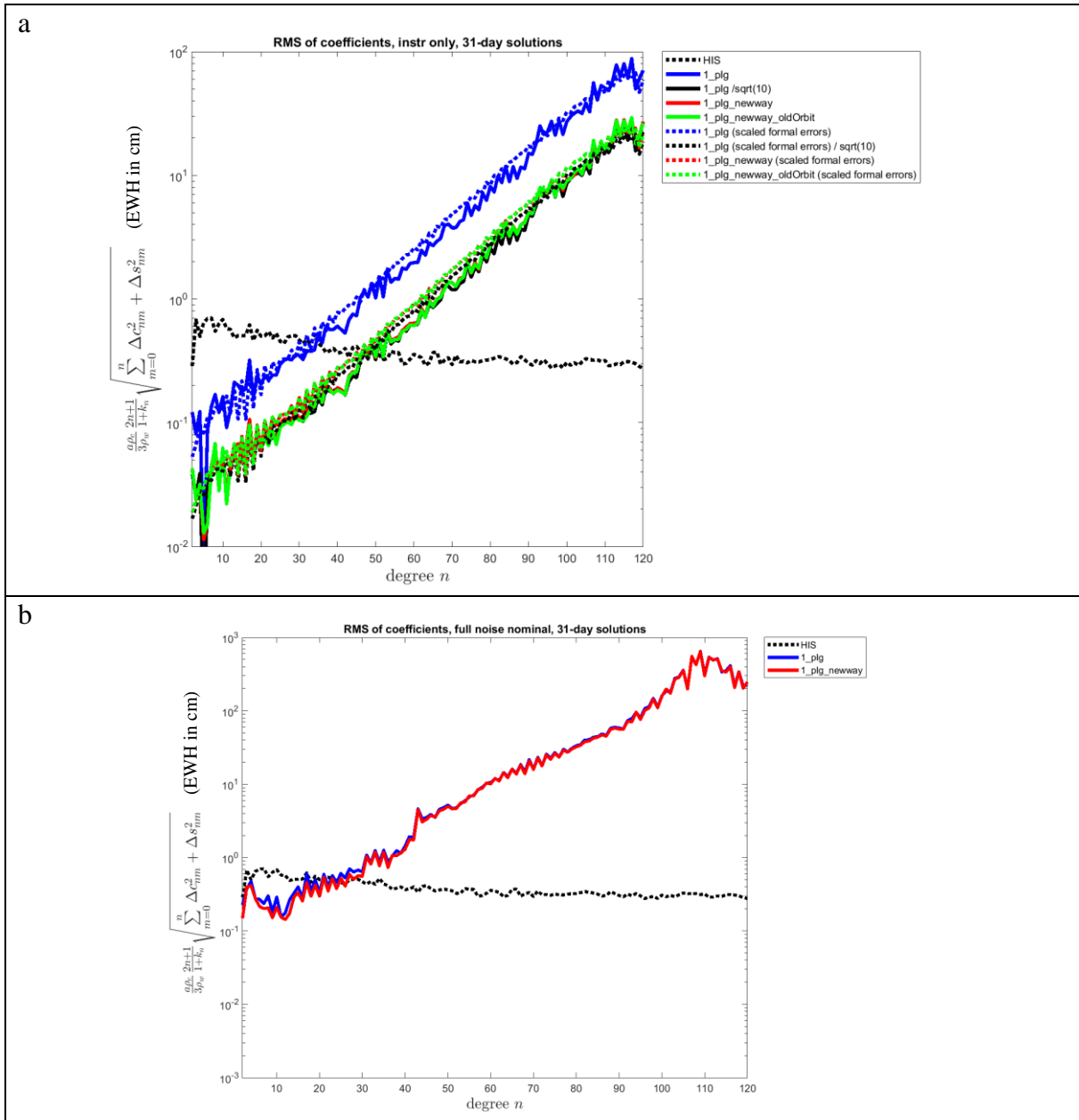
Figure 15-1 Degree amplitudes of instrument-only (panel a) and full noise nominal (panel b) solutions for the scenario 1_pIg (3d_H). In panel a, the solid lines show the coefficient errors while the dotted lines show the formal errors. In both panels, the blue curves show the original results while the red curves show the results where the instrument noise has been scaled by a factor of 1/sqrt(10). In panel a, the black curves shows the blue curves multiplied by 1/sqrt(10) and the green curves show the results if only the ACC and LRI noise is scaled by 1/sqrt(10) but the same (un-scaled) orbit noise is used. [Path: Deliverables/D1/simulation_results/full_scale_simulator_v009/old_noise_scaling/ and Deliverables/D1/simulation_results/full_scale_simulator_v009/1_by_sqrt(10)_noise_scaling/]

15.2 IMPACT ON RESULTS OF 2_PIG_IIG (3D_H)

In addition to the analysis given by Section 15.1, we investigate the impact of scaling the noise time series by a factor of 1/sqrt(10) on the analysis performed earlier in Section 8.1 where the 3d_H scenarios 2_pIg_iIn and 2_pIg_iIg are compared.

As shown by Figure 15-2, the error reduction due to the noise scaling is smaller for 2_pIg_iIn than for 2_pIg_iIg. The reason for this are the numerical errors that dominate the error budget if using NGGM/MAGIC-type instrument noise specifications in the instrument only simulations performed using the old version of the full scale simulator. Therefore, the difference between the scenarios, which is produced by the improved ACC instrument on the satellites of the inclined pair, is more strongly masked by numerical errors when down-scaling the instrument noise by 1/sqrt(10).

Figure 15-3 shows the corresponding full noise results. Here, as before, the instrument noise is dominated by the much larger temporal aliasing errors which mask the impact of the improved ACC instrument on the satellites of the inclined pair completely.
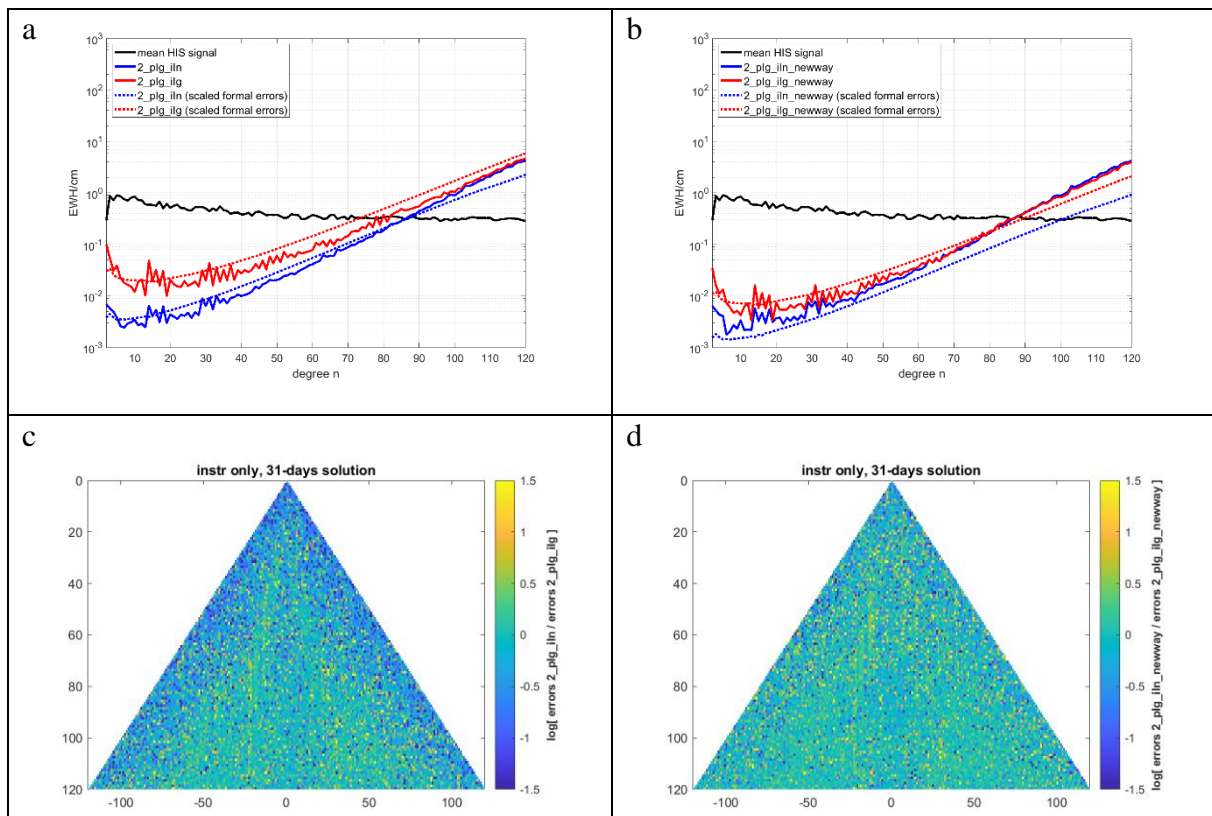
Figure 15-2 Retrieval errors of d/o 120 31-day instrument-only simulations for the scenarios 2_pIg_iIn (3d_H) and 2_pIg_iIg (3d_H). Left: original results (without scaling factor included in the instrument noise), right: results when a scaling factor of 1/sqrt(10) is applied to the instrument noise. Top: degree amplitude curves. Bottom: ratio of coefficient errors of 2_pIg_iIn divided by 2_pIg_iIg, on a logarithmic scale. [Path: Deliverables/D1/simulation_results/full_scale_simulator_v009/old_noise_scaling/instrument_only/ and Deliverables/D1/simulation_results/full_scale_simulator_v009/1_by_sqrt(10)_noise_scaling/instrument_only/]
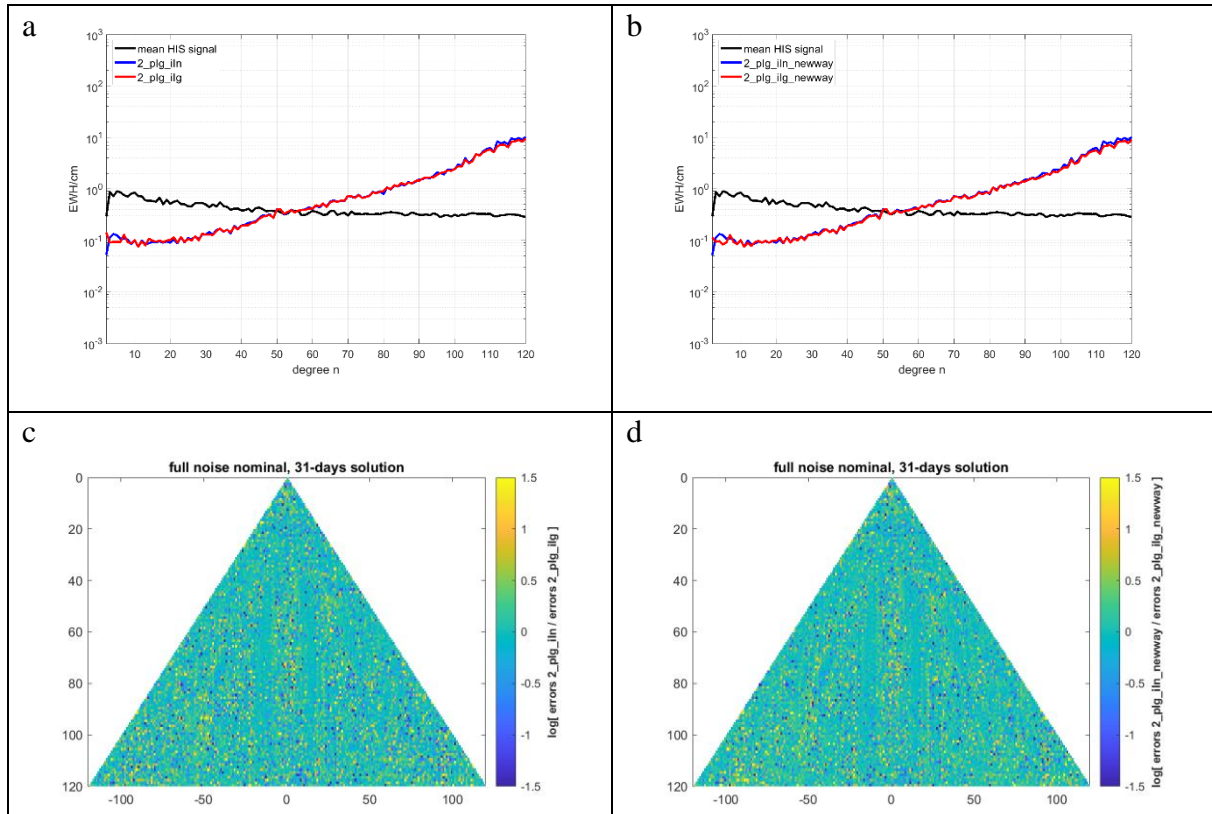
Figure 15-3 Retrieval errors of d/o 120 31-day full noise nominal simulations for the scenarios 2_pIg_iIn (3d_H) and 2_pIg_iIg (3d_H). Left: original results (without scaling factor included in the instrument noise), right: results when a scaling factor of 1/sqrt(10) is applied to the instrument noise. [Path: Deliverables/D1/simulation_results/full_scale_simulator_v009/old_noise_scaling/full_noise_nominal/ and Deliverables/D1/simulation_results/full_scale_simulator_v009/1_by_sqrt(10)_noise_scaling/full_noise_nominal/]

16 FURTHER ANALYSIS ON ANOMALIES IN FULL NOISE WIESE SOLUTIONS

16.1 EFFECT OF P MATRICES AND NUMERICAL STABILITY

In this section, we continue our investigations regarding the anomalies in the full noise wise solutions given in Section 5.3, in which we found that the anomalies can be avoided by either decreasing the maximum d/o of the daily wiese solutions (DWS) or by using a different P matrix (the latter, however, led to overall larger errors in the solution). Therefore, the anomalies in the full noise wiese solutions were interpreted as an effect of a numerically unstable inversion of the NEQs.

In order to understand the role of the P matrix in the formation of the bump-shaped structures in the degree amplitude curves of the full noise wiese solutions, we compute d/o 120 7-day solutions for the scenario 2_pIg_iIn (5d_LH) in which the instrument noise and/or the P matrices are turned on or off (turning off the P matrix means to insert a unit matrix instead of the P matrix that fits the instrument noise characteristics). Figure 16-1 shows the results: The red curve (instrument noise off, P matrices off) shows the retrieval error level due to the (un-weighted) temporal aliasing errors. If turning on the P matrices, the bump-shaped structures appear (independently of turning on or off the instrument noise). This indicates that the P matrices seem to introduce numerical instability to the system.

The orange curves in Figure 16-1 show the results if instead of the P matrices corresponding to the used instrument noise, a different P matrix (as also tested in Section 5.3) is applied in the NEQ systems of both satellite pairs. These solutions have a much larger error level, but do not show the artefacts. For this reason, as a next step, we investigate the numerical stability of the 3 P matrices involved in this analysis so far in Figure 16-2. Indeed, the inverse P matrices for the MAGIC and the GRACE noise show longer correlations in time domain compared to the other P matrix, and also the higher condition numbers imply a numerically more unstable behavior.

Figure 16-3 shows the results of further tests, in which we apply numerically stabilized P matrices. These are computed by

$$P_{stab} = P + factor \cdot I$$

where we insert values between 10^{14} and 10^{17} for $factor$. As can be seen in Figure 16-3, this numerical stabilization of the main diagonal of the MAGIC and GRACE P matrices indeed leads to a reduction of the bump-shaped artefacts. However, the decorrelation performance of the stabilized P matrices is decreased by changing the main diagonal of the P matrices, by which the retrieval errors are increased.

This shows that numerical stabilizing the main diagonal of the P matrices does not solve the problem, as this increases the retrieval errors significantly.

Pursuing the goal of numerically stabilizing the full noise wiese NEQ systems, an extensive analysis of the numerical stability of individual NEQ matrix parts has been performed to find

out where the bad conditioning of the used P matrices maps to. Thereby, the condition numbers of the individual NEQ matrix parts that are inverted in the course of the wiese processing have been computed. This, however, did not give conclusive results as the condition numbers of both the case using the MAGIC/GRACE noise P matrices and the case using the different P matrix are comparable. Also externally solving the NEQ systems using MATLAB without applying the parameter elimination algorithm used by the full scale simulation software was performed, which gave the same results as output by the full scale simulator.
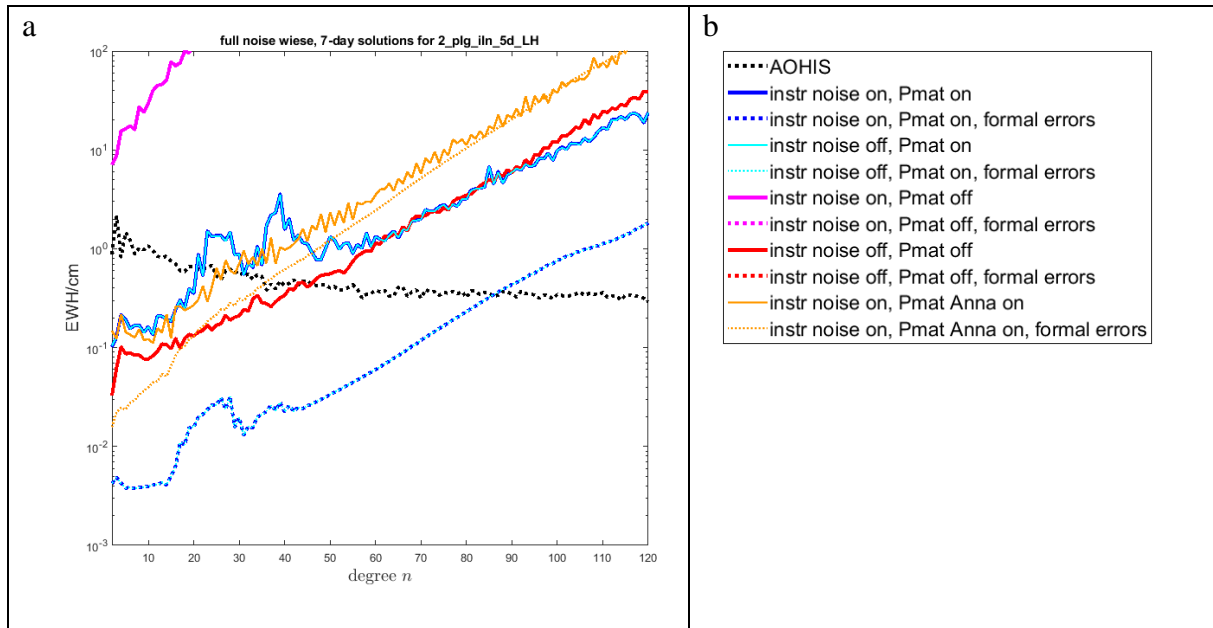
Figure 16-1 Degree amplitude curves of d/o 120 full noise wiese solutions (d/o of DWS is 15) for scenario 2_pIg_iIn (5d_LH) if applying varying P matrices and turning on or off the instrument noise.

	„102" P matrix cond(P) = 93	MAGIC noise P matrix cond(P) = 6.6e4	GRACE noise P matrix cond(P) = 1.9e7
P	a	b	c
P^{-1}	d	e	f
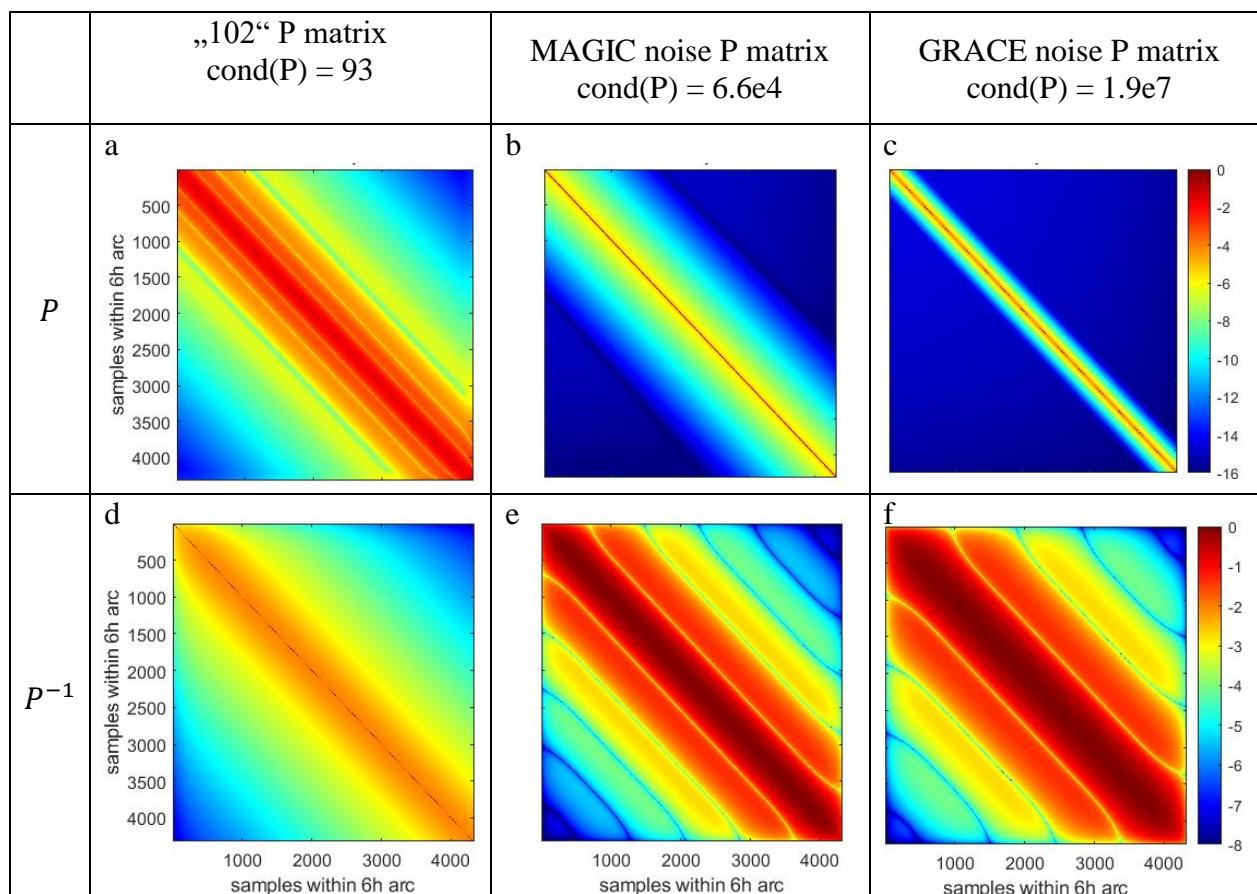
Figure 16-2 Analysis of the P matrices involved in the investigation on the artefacts in the full noise wiese simulation results. The values of the P matrices are normalized by their maximum values and visualized by the colour coding. All panels use the same axes and panels of the same row use the same colour bar. The values on the colour bars are the base-10 logarithms of the visualized matrix values. Left column: P matrix used for both the polar and the inclined pair's NEQ systems for the solution visualized by the orange curve in Figure 16-1. Middle and right columns: P matrices used for the inclined (middle) and polar (right) pair's NEQ systems for the "regular" 2_pIg_iIn (5d_LH) simulations. At the top, the condition numbers computed as the ratio of the maximum divided by the minimum eigenvalue of the considered matrix are given. The top panels show the P (weighting) matrices, the bottom panels show the inverse P matrices (corresponding to the VCV matrices of the noise).
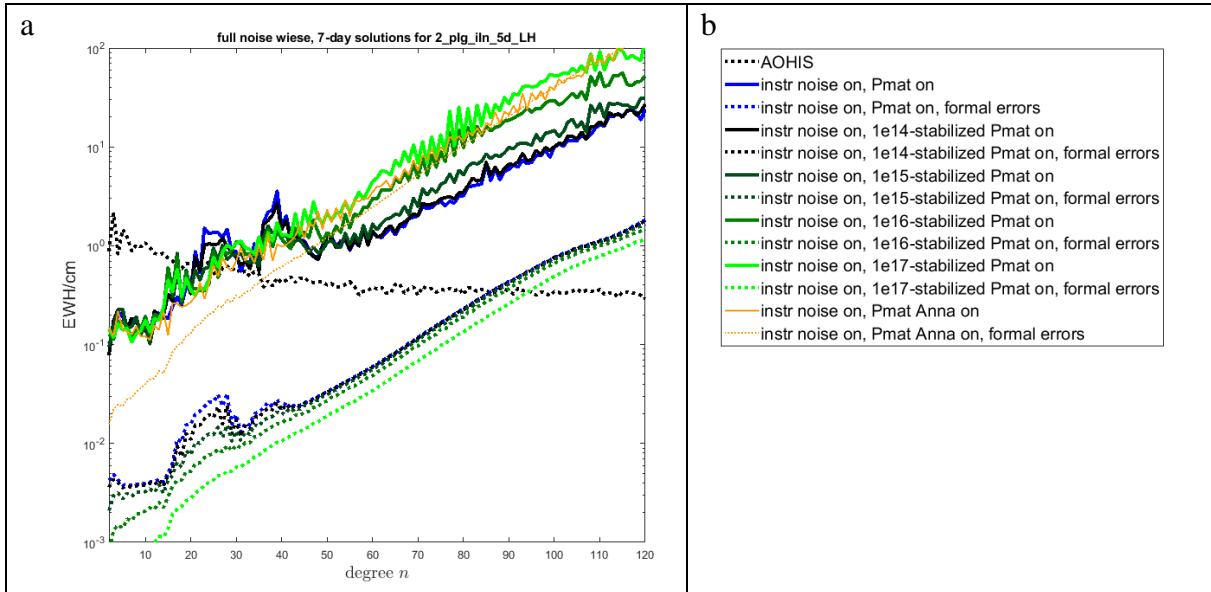
Figure 16-3 Degree amplitude curves of d/o 120 7-day full noise wiese (d/o of DWS: 15) simulations for the scenario 2_pIg_iIn (5d_LH), applying various P matrices, as described in the text.

16.2 CHANGING THE RELATIVE WEIGHTING OF THE POLAR AND INCLINED PAIRS' NEQ SYSTEMS

In this section, we show how a change of the relative weighting of the NEQ systems of the polar and the inclined pair in a double-pair formation can decrease the artefacts observed before in full noise wiese solutions. To this end, we again consider d/o 120 7-day solutions for the scenario 2_pIg_iIn (5d_LH), as this is the scenario that showed the strongest artefacts compared to the other scenarios, as can be observed in panels c and d of Figure 5-3.

As shown by Table 16-1, the orbit scenario 5d_LH is the scenario combining the smallest orbit height of the inclined pair with the largest orbit height of the polar pair. The effect of this difference in orbital height is a lower weight of the NEQ system of the polar pair (NEQ_p) relative to the NEQ system of the inclined pair (NEQ_i) in the double-pair NEQ system. This strong weighting of NEQ_i relative to NEQ_p could become problematic because of the polar gaps of the inclined pair's orbit. Although in the double-pair solution, the polar gaps of the data of the inclined pair are "filled" by the data of the polar pair, correlations of the coefficients in NEQ_i could lead to a degradation of the double-pair solution if NEQ_i is given a too high weight.

Besides the orbital heights of the two pairs, also the instrument noise introduced to the NEQs of the two pairs leads (by the usage of P matrices fitting the individual noise characteristics) to a relative weighting of the two NEQ systems. In the so far considered scenario 2_pIg_iIn, NEQ_p is down-weighted relative to NEQ_i due to the larger ACC noise amplitudes introduced to NEQ_p. As shown by the blue curves in Figure 16-4, replacing the MAGIC-type ACC noise for the inclined pair by the higher-amplitude GRACE-type ACC noise leads to larger formal errors, but decreases the coefficient errors as well as the amplitudes of the bump-shaped artefacts in the full noise wiese results. We interpret this observation in the way that in the case of the scenario 2_pIg_iIg, NEQ_p is given a larger weight relative to NEQ_i than in the scenario 2_pIg_iIn which helps to reduce the effects introduced by the polar gaps of NEQ_i to the double-pair NEQs.

To test if it is possible to improve the full noise wiese results of the scenario 2_pIg_iIn (5d_LH) without changing the noise assumptions for the two satellite pairs, we compute double-pair solutions by solving the modified NEQ system

$$NEQ_p = \frac{w_p \cdot NEQ_p + w_i \cdot NEQ_i}{w_p + w_i}$$

Varying the weights w_p and w_i between 10^0 and 10^3, we found that the best-performing double-pair solution in terms of small coefficient errors can be found using $\frac{w_p}{w_i} = 100$. As shown by Figure 16-5, while the formal errors of the new solution are larger than for the original results, the coefficient errors and especially the bump-shaped artefacts are significantly reduced using the new weighting. This is also the case for the associated DWS. EWH grids of the retrieval errors as well as a visualization of the improvement of the double-pair solution are given by Figure 16-6.

Concluding the so-far-made analysis on the bump-shaped artefacts in the degree amplitude curves of full noise Wiese solutions, we found that these artefacts especially show up if the NEQ system of the inclined pair obtains a much larger weight relative to the NEQ system of the polar pair. It is possible to reduce the artefacts and also globally improve the double-pair solution if giving the polar pair's NEQs a higher weight.

Table 16-1 Orbit scenarios as defined in Massotti et al. (2021)

ID	Sats 1 (IP)		Sats 2 (PP)		h_{l1} [-]	h_{l2} [-]	$\lambda_{shift,1}$ [deg]	$\lambda_{shift,2}$ [deg]	Sub-cycles [days]
	Alt. [km]	Incl. [deg]	Alt. [km]	Incl. [deg]					
3d_M	409	70	440	89	1.368	1.383	2.308	2.384	2, 3, 8, 11, 30
3d_H	432	70	463	89	1.451	1.449	-3.076	-3.067	3, 7, 31
5d_Ma	396	65	434	89	1.397	1.383	-1.499	-1.458	2, 3, 5, 13, 18, 31
5d_Mb	397	70	425	87	1.168	1.167	0.736	0.733	2, 5, 27, 32
5d_H	465	75	488	89	1.185	1.190	0.762	0.781	4, 5, 29
7d_M	389	70	417	87	1.238	1.253	0.743	0.786	2, 7, 30
7d_H	432	70	463	89	1.218	1.226	0.672	0.692	3, 7, 31
SSO for 3d_H	477	97	463	89	1.454	1.449	-3.097	-3.067	3, 7, 31
SSO for 7d_H	477	97	463	89	1.201	1.226	0.622	0.692	3, 7, 31
5d_LL	344	70	376	89	1.423	1.410	-1.671	-1.628	1, 2, 5, 12, 29
5d_LH	344	71.5	492	89	1.169	1.172	-0.732	-0.790	5, (32-31)

Figure 16-4 Degree amplitude curves of d/o 120 7-day full noise wiese (d/o of the DWS is 15) solutions for the 5d_LH scenarios 2_pIg_iIn (Test 1, cyan curves), 2_pIn_iIn (Test 3, black curves) and 2_pIg_iIg Test 5, blue curves).
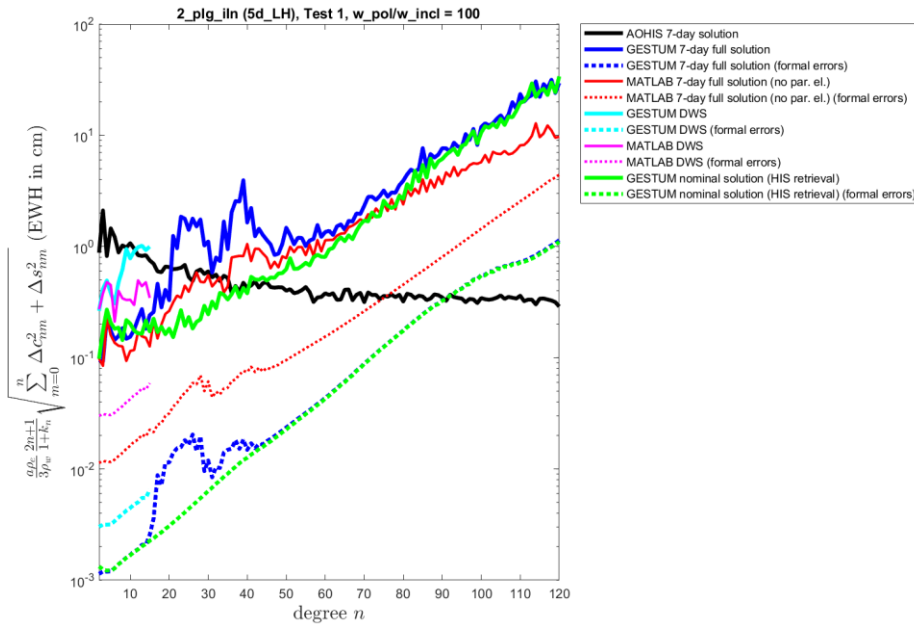
Figure 16-5 Degree amplitude curves of d/o 120 7-day full noise wiese (d/o of the DWS is 15) solutions for the scenario 2_pIg_iIn (5d_LH). The blue curves show the previous results (corresponding DWS are shown by the cyan curves) and the red curves the results if an up-weighting of NEQ_p relative to NEQ_i by a factor of 100 is applied (corresponding DWS are shown by the magenta curves). The green curves show the previous results of the corresponding full noise nominal solution, as a reference.
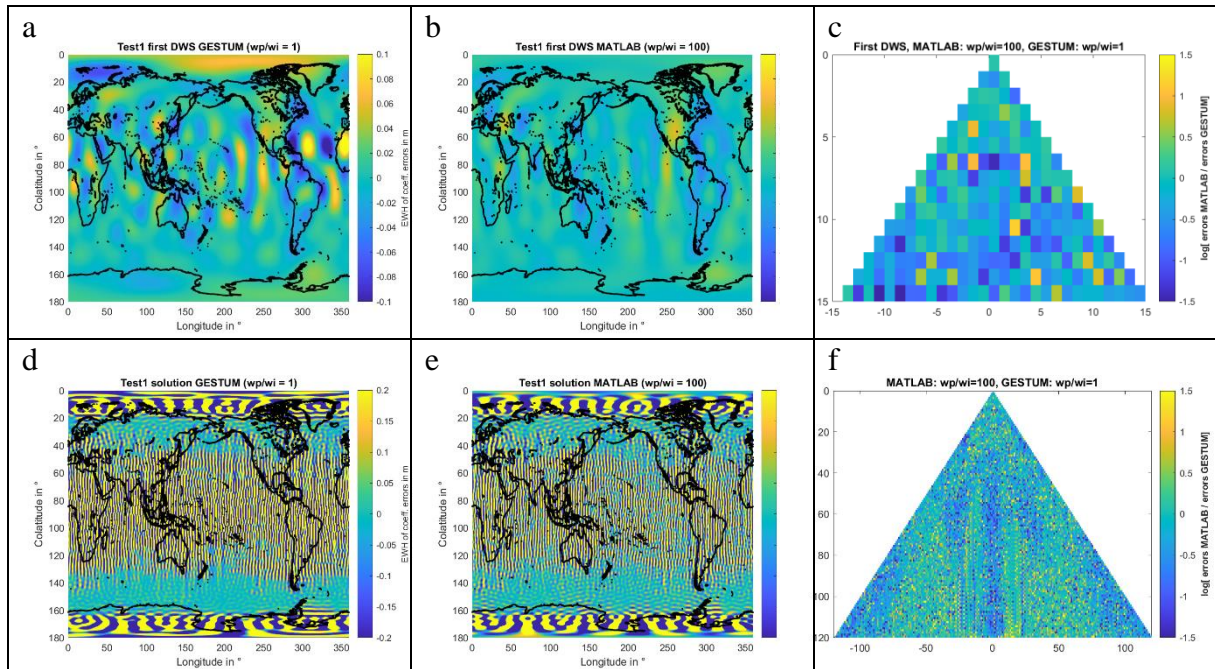
Figure 16-6 Retrieval errors of d/o 120 7-day full noise wiese (d/o of DWS: 15) simulations for the scenario 2_pIg_iIn (5d_LH). The top row refers to the first d/o 15 DWS, the bottom row to the d/o 120 7-day solution. Panels a and d show the previously computed results, panels b and e the results if an up-weighting of NEQ_p relative to NEQ_i by a factor of 100 is applied. Panels c and f show the ratio of the corresponding retrieval errors of the two solutions on a logarithmic scale (blue colors indicate an improvement by the up-weighting).

16.3 ORIGIN OF ARTEFACTS IN FULL NOISE WIESE SOLUTIONS

In this section, we show how correlations between certain groups of sectorial coefficients of the multi-day solution and the coefficients of the DWS originating from the inclined pair's NEQ system lead to the artefacts in the full noise wiese solutions described in the preceding subsections. To this end, we investigate a d/o 100 7-day solution for the scenario 2_pIg_iIn (5d_LH) with maximum d/o 15 for the DWS.

Firstly, we identify the coefficient groups that lead to the increased full noise wiese retrieval errors of the coefficients around degrees 26 and 39 which have been observed in the degree amplitude plots of the full noise wiese solutions (see e.g. Figure 16-5). Comparing the coefficient errors of the nominal (Figure 16-10 e) and the wiese (Figure 16-11 e) double-pair solutions reveals increased retrieval errors for the near-sectorial coefficients around d/o 26 and 39 in the wiese solution that are not present in the nominal solution. This specific error pattern seems to stem from the inclined pair's NEQ system, since it is also shown by the corresponding single-inclined pair solution (cf. Figure 16-11 c). The fact that the corresponding DWS of the single-inclined pair solution (cf. Figure 16-12 e) shows large errors for the near-zonal, polar-gap related coefficients is a hint that the observed error pattern in the 7-day solution could be related to the co-estimation of the DWS in the wiese processing.

As a side note, we compare the performance of the single-inclined pair's DWS (cf. Figure 16-12 d to f) to the performance of corresponding d/o 15 stand-alone 1-day solutions (cf. Figure 16-13 d to f). The fact that the large near-zonal errors observed in the DWS are not present in the stand-alone 1-day solution suggests that the missing data over the poles in the inclined pair's system only lead to large near-zonal errors in the low degrees if the overall NEQ system is parametrized up to a larger (here: d/o 100) maximum degree. Also this observation suggests large correlations between the 7-day solution and the DWS in the NEQ system of the inclined pair.

As a second step, to further investigate our before-made observations indicating large correlations between the coefficients of the 7-day solution and the DWS in the case of an inclined-pair dominated double-pair system, we plot the correlation matrix of the full wiese NEQ system in Figure 16-7 c. Indeed, increased correlation values between the sectorial coefficients around d/o 26 and 39 and the DWS can be observed. I.e., we indeed observe larger correlations between the worse-performing sectorial coefficient groups that produce the bump-shaped artefacts in the degree and order amplitude curves (cf. Figure 16-7 b and d) and the coefficients of the DWS.

To confirm the hypothesis that these correlations are the reason for the error structure in the wiese solutions, we solve the same NEQ system in which we now set the entries representing the correlations between the DWS and the 7-day solution coefficients to zero in the NEQ matrix (cf. Figure 16-9 a), which leads to a block-diagonal structure of the corresponding coefficient correlation matrix (cf. Figure 16-9 c). Indeed, the bump-shaped artefacts in the degree and order amplitude curves of the retrieval errors of the modified NEQ system disappear (however, on the cost of the solution's performance in the low and high degrees, as shown by Figure 16-9 b and d).

As shown by Figure 16-5, it is possible to improve the full noise wiese double-pair solution of the investigated scenario by increasing the relative weight of the polar pair's NEQ system by a factor of 100. For completeness, we show the NEQ matrix as well as the corresponding correlation matrix of this modified double-pair system in Figure 16-8. As expected, given the before-shown reduction of the bump-shaped artefacts in the degree amplitude curves, the correlation matrix of this modified system (Figure 16-8 c) shows smaller correlations between the 7-day solution and the DWS compared to the original system (Figure 16-7 c).

To summarize, we could identify the origin of the bump-shaped artefacts that we observed in the degree amplitude curves of full noise wiese solutions for double-pair scenarios that are dominated by the NEQ system of the inclined pair: These artefacts correspond to larger retrieval errors of certain groups of near-sectorial coefficients, which are produced by correlations between these coefficient groups and the coefficients of the co-estimated DWS. These correlations are introduced by the instability of the inclined pair's NEQ system due to the inclined pair's polar gap. A mitigation of this problem is possible either in the processing, by slightly increasing the weight of the polar pair's NEQ system (see Figure 16-5) or by decreasing the maximum d/o of the co-estimated DWS (see Figure 5-19). Or, in the mission design, by preventing a large performance difference between the polar and the inclined pair, which can be done by an appropriate choice of the orbits and the instrument performance of both pairs.

Improving the numerical stability of the NEQs for the investigated double-pair scenario 2_pIg_iIn (5d_LH) by applying a "polar gap" regularization (pushing the solution to zero or to the single-polar pair solution over the poles/in the near-zonal coefficients) has been tested. It yields a slight improvement of the double-pair solution, however does not reduce the above-described artefacts in full noise Wiese solutions. As shown by Figure 16-14, applying a polar gap regularization to the single inclined pair scenario 1_iIn (5d_LH) does not remove the artefacts in the Wiese solution.
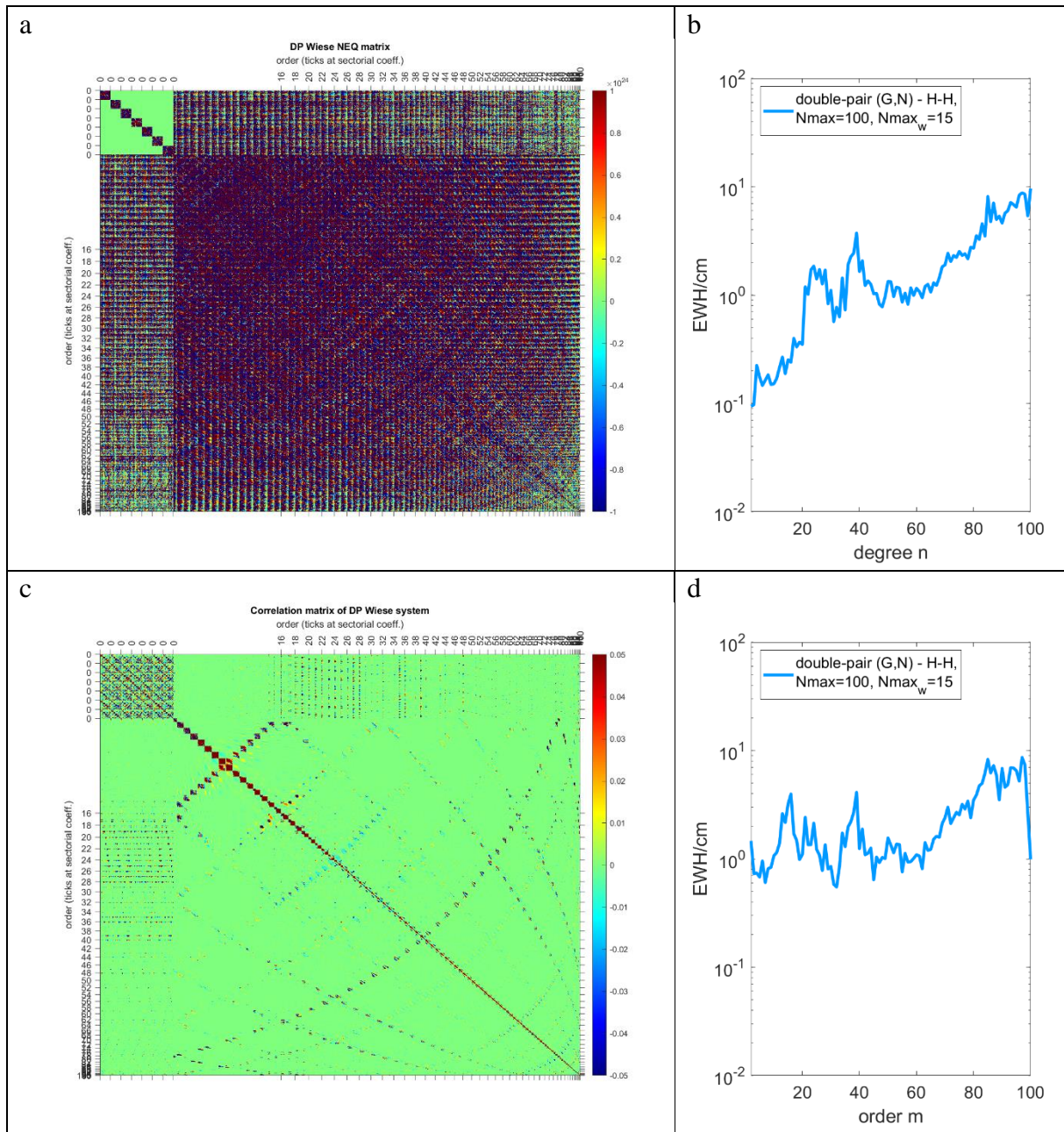
Figure 16-7 d/o 100 7-day full noise wiese (d/o of DWS: 15) simulation for the scenario 2_pIg_iIn (5d_LH). Panel a shows the full Wiese NEQ matrix with the entries corresponding to the degree 0 to 15 coefficients of the 7 DWS in the top left blocks, and the entries corresponding to the degree 16 to 100 coefficients of the 7-day solution in the bottom right block. Within each block, the coefficients are sorted by order, then by degree, then by Cnm/Snm. Panel c shows the corresponding correlation matrix. Panels b and d show the retrieval errors of the simulation in terms of degree and order amplitudes, respectively.

NGGM/MAGIC – Science Support Study During Phase A	Final Report	
	Doc. Nr:	MAGIC_FR
	Issue:	1.0
	Date:	15.11.2022
	Page:	184 of 466

a

b

c

d
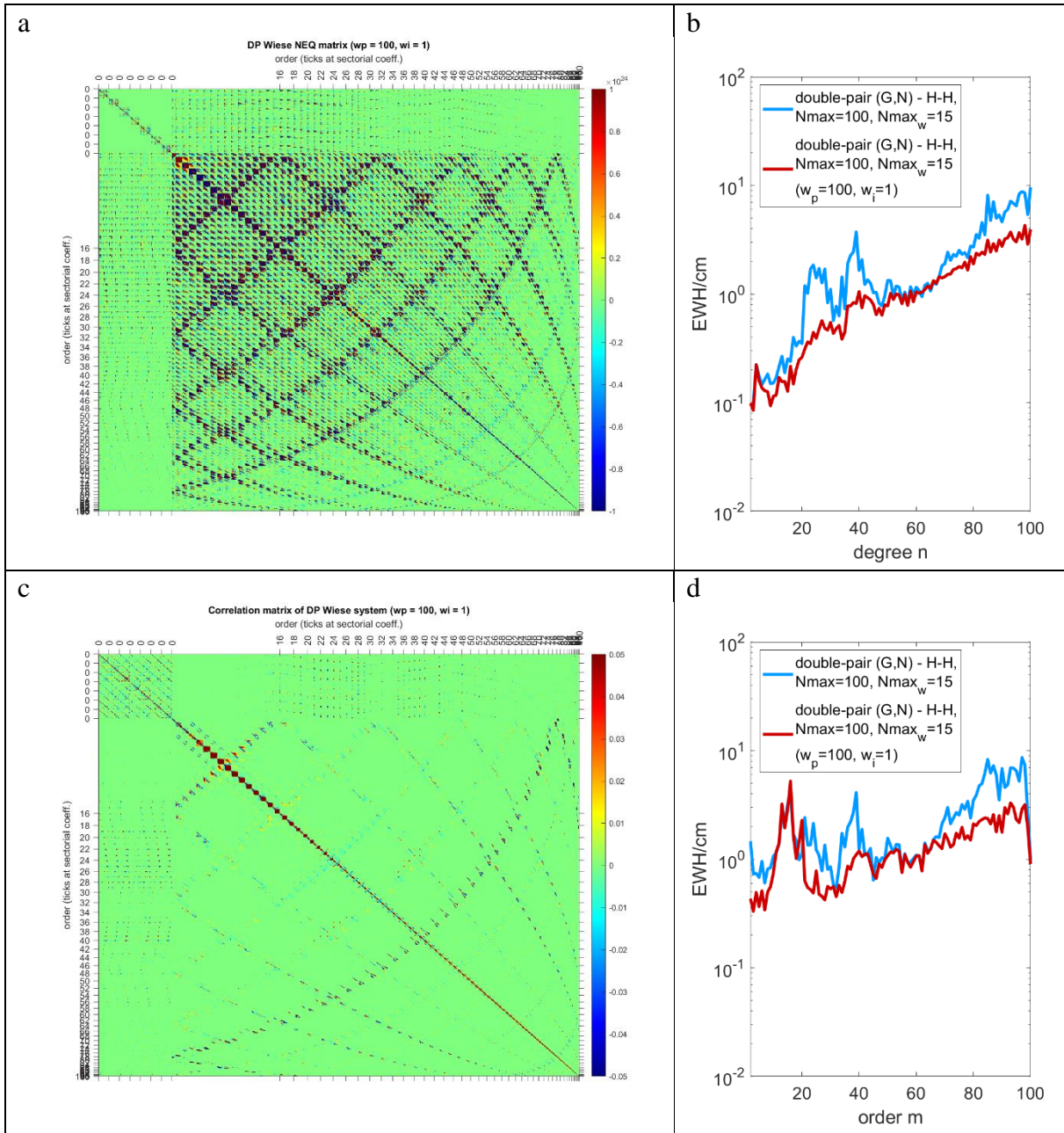
Figure 16-8 Same as Figure 16-7, but for the modified scenario from 2_pIg_iIn (5d_LH) where the weight of the NEQ system of the polar pair is increased by a factor of 100. Panels b and d show the retrieval errors of this modified scenario as the red curves, while the blue curves are the same as shown by Figure 16-7, for reference.

a

b

c

d
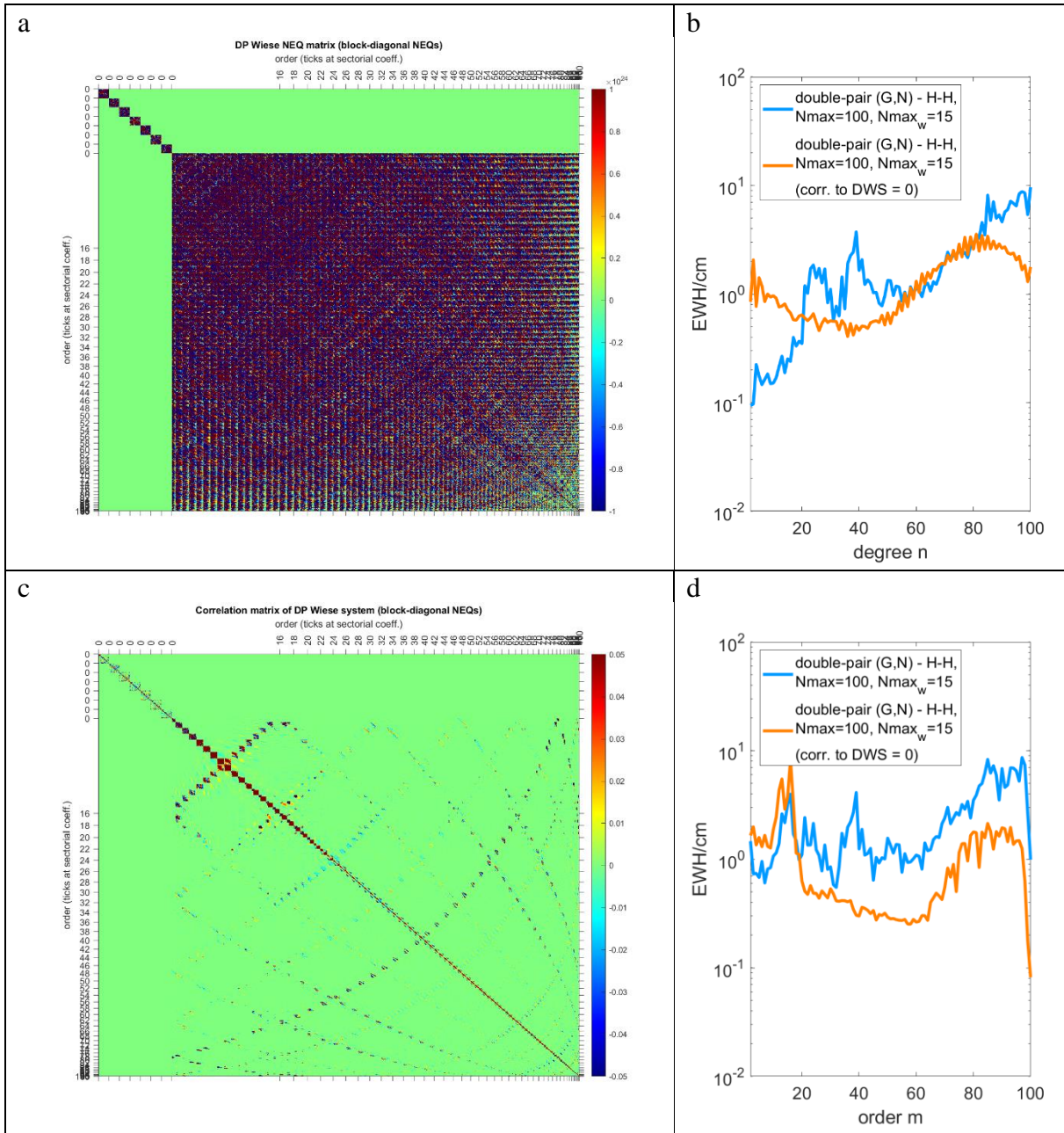
Figure 16-9 Same as Figure 16-7, but for the modified scenario from 2_pIg_iIn (5d_LH) where the off-diagonal entries of the NEQ system (panel a) representing the correlations between the coefficients of the 7-day solution and the DWS are set to zero, resulting in a block-diagonal correlation matrix (panel c). Panels b and d show the retrieval errors of this modified scenario as the orange curves, while the blue curves are the same as shown by Figure 16-7, for reference.
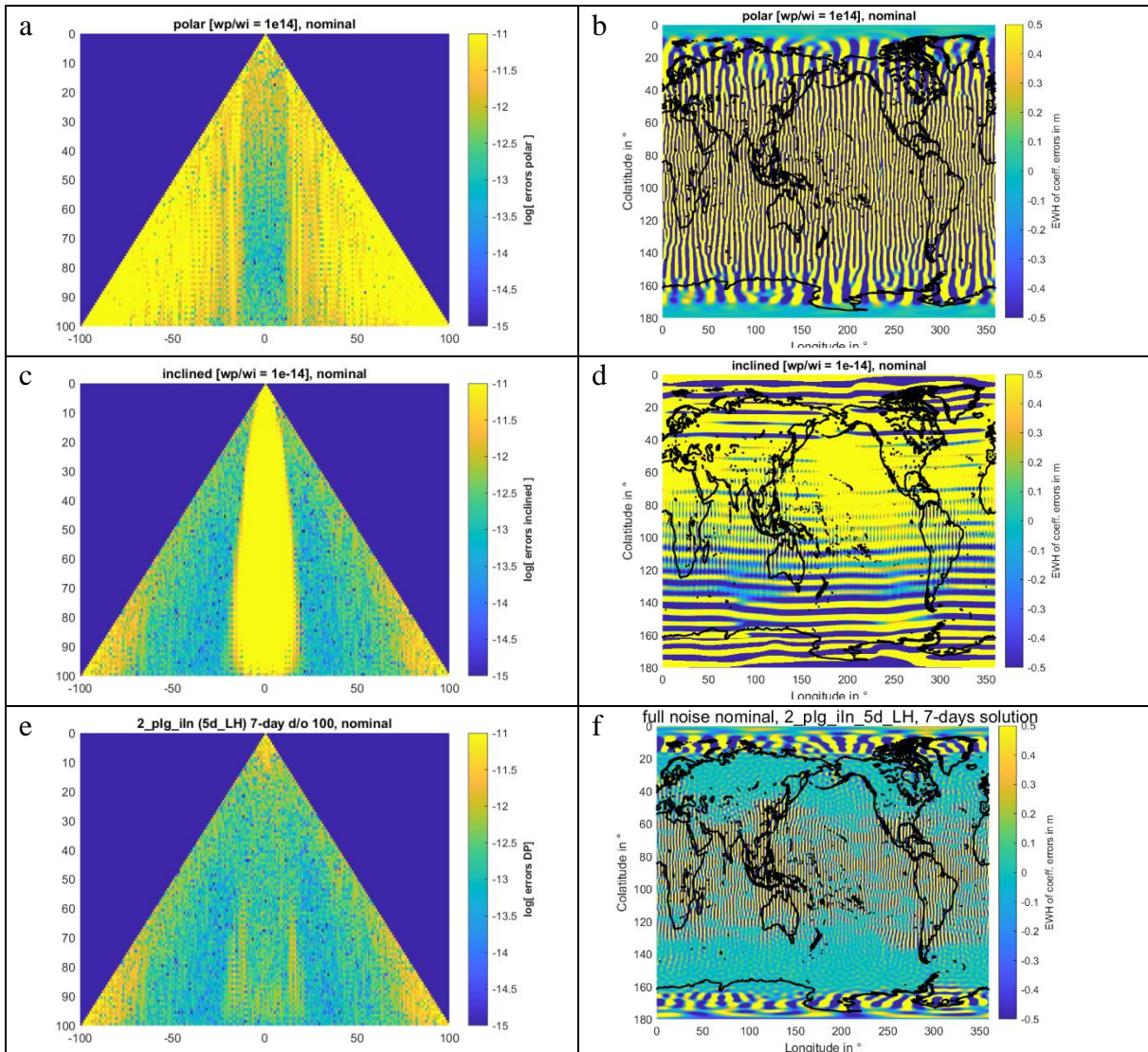
Figure 16-10 Retrieval errors of the d/o 100 7-day full noise nominal simulation for the scenario 2_pIg_iIn (5d_LH). Panels e and f show the original double-pair solution. Panels a and b (c and d) show the modified double-pair solution in which the relative weight of the NEQ system of the polar pair (inclined pair) is increased by a factor of 1e14, which approximates the performance of the respective single-polar (single-inclined) pair scenario.
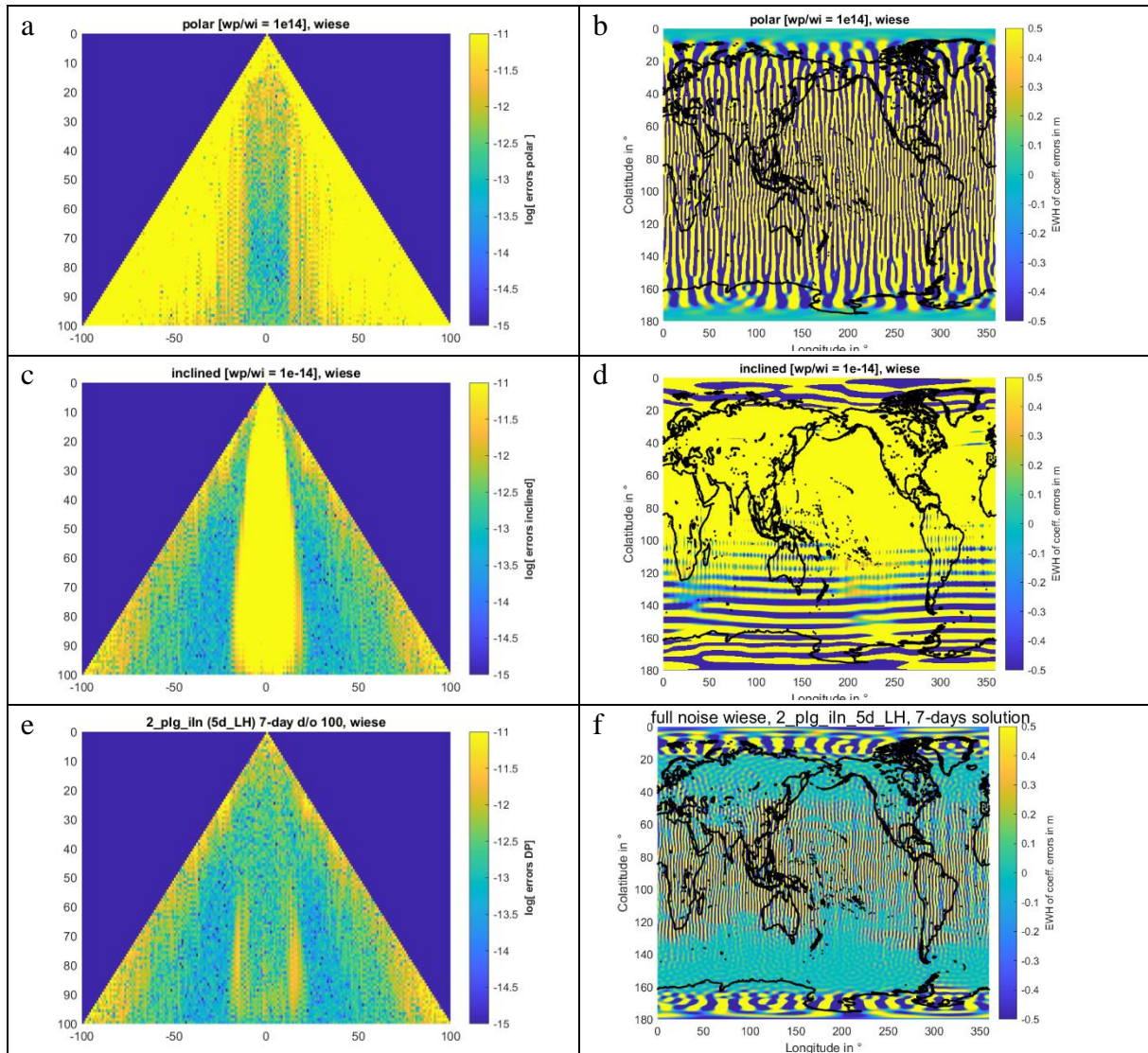
Figure 16-11 Retrieval errors of the d/o 100 7-day full noise wiese simulation (d/o of DWS: 15) for the scenario 2_pIg_iIn (5d_LH). Panels e and f show the original double-pair solution. Panels a and b (c and d) show the modified double-pair solution in which the relative weight of the NEQ system of the polar pair (inclined pair) is increased by a factor of 1e14, which approximates the performance of the respective single-polar (single-inclined) pair scenario.
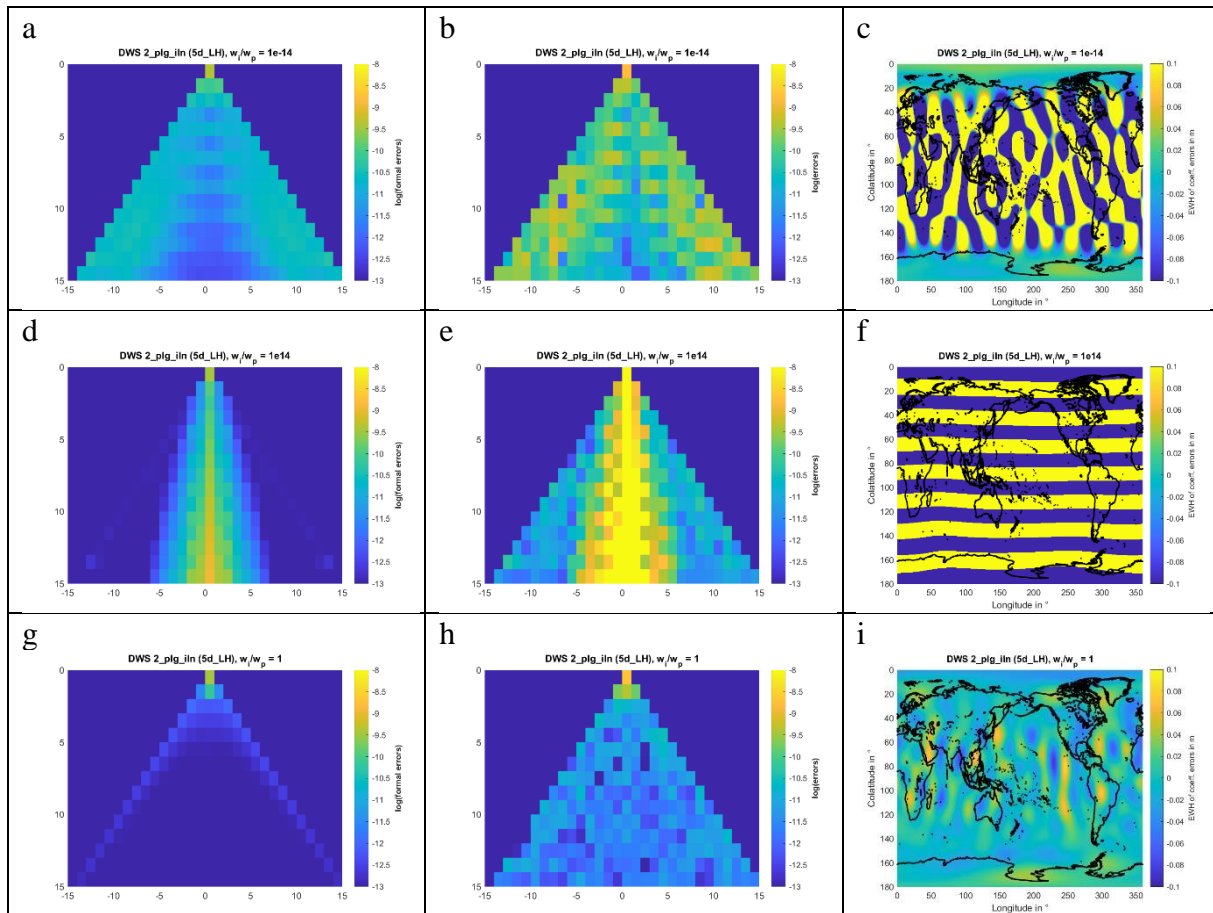
Figure 16-12 Retrieval errors of the d/o 15 DWS of the d/o 100 7-day full noise wiese simulation for the scenario 2_pIg_iIn (5d_LH). Left column shows the formal errors, middle column the coefficient errors and right column the spatial plots computed based on the coefficient errors. Panels g, h and i show the original double-pair solution. Panels a, b and c (d, e and f) show the modified double-pair solution in which the relative weight of the NEQ system of the polar pair (inclined pair) is increased by a factor of 1e14, which approximates the performance of the respective single-polar (single-inclined) pair scenario.
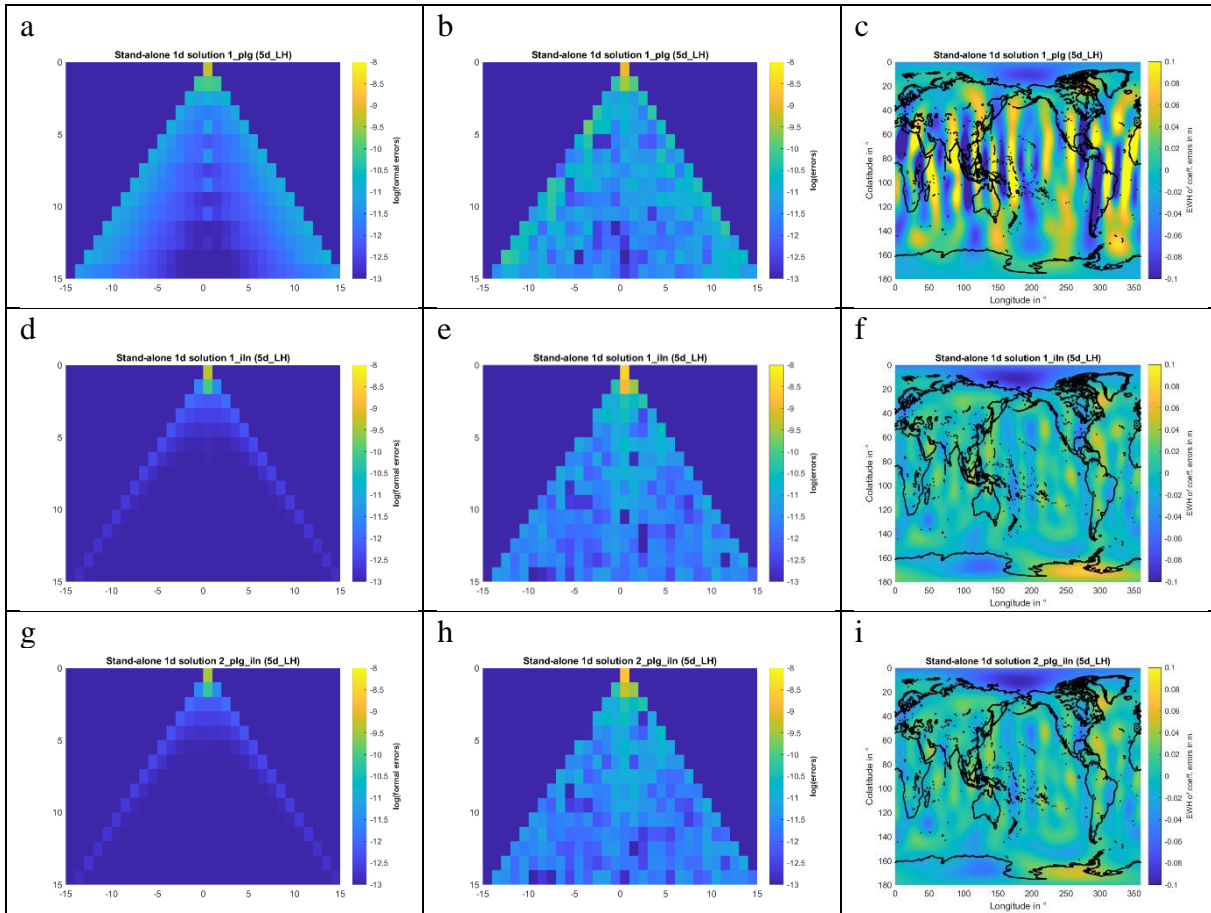
Figure 16-13 Stand-alone full noise nominal d/o 15 1-day simulation for the scenario 2_pIg_iIn (5d_LH). Left column shows the formal errors, middle column the coefficient errors and right column the spatial plots computed based on the coefficient errors. Panels g, h and i show the original double-pair solution. Panels a, b and c (d, e and f) show the modified double-pair solution in which the relative weight of the NEQ system of the polar pair (inclined pair) is increased by a factor of 1e14, which approximates the performance of the respective single-polar (single-inclined) pair scenario.
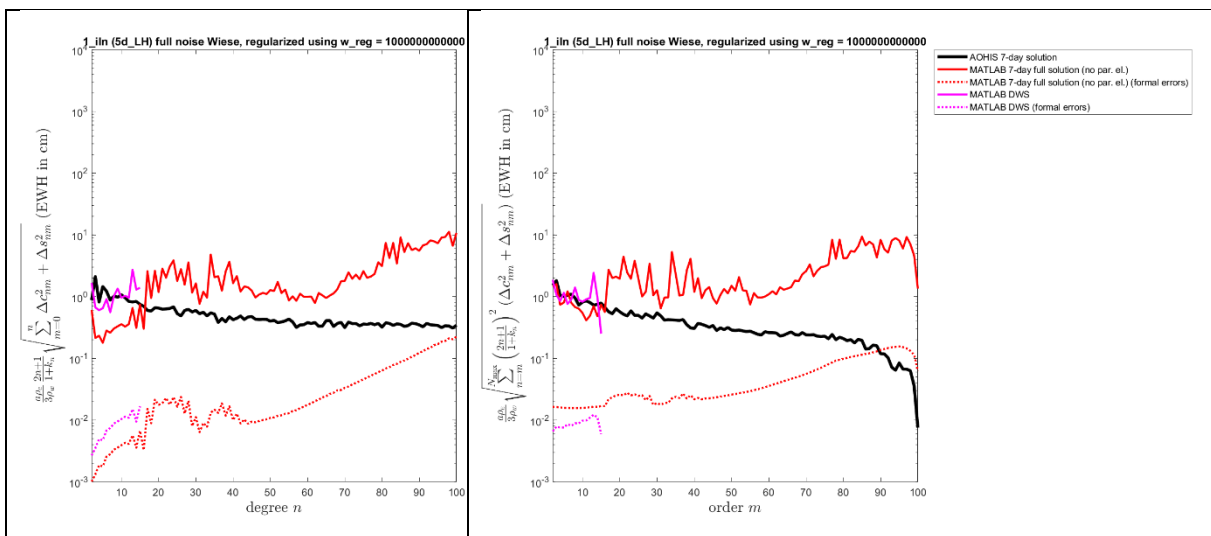
Figure 16-14 Degree (left) and order (right) amplitude plots for 7-day full noise Wiese simulations for the single-inclined pair scenario 1_iIn (5d_LH) using maximum degrees of 100 and 15 for the 7-day solutions and the DWS, respectively. A polar gap regularization has been applied that constrains the solution towards zero over the poles.

17 SCENARIOS U5D5D_HL AND COMPARISON OF SIMULATOR VERSIONS

In this section, the scenario U5d5d_HL is investigated. This is a Bender-type double-pair scenario in which the polar pair is in the 5d_LH orbit (492 km orbit height, 89° inclination) and the inclined pair in the 5d_Ma orbit (396 km orbit height, 65° inclination), see Table 17-1 which is repeated here for convenience. For the polar pair, GRACE-like ACC noise is used, while for the inclined pair, either the before-used NGGM/MAGIC-like ACC noise (for U5d5d_HL_ref) or a MicroSTAR (MS) ACC noise time series delivered by TASI (for U5d5d_HL_ms) is used. For each of the two scenarios U5d5d_HL_ref and U5d5d_HL_ms, we compute one d/o 120 7-day solution. The aim is to compare the retrieval errors of the two scenarios, i.e. see the effect of using either the theoretical MAGIC ACC noise or the simulated MS ACC noise time series delivered by TASI for the second pair.

Figure 17-1 visualizes how the used types of instrument noise compare in the spectral domain. In particular, it can be seen that the MS noise follows the analytical specifications for the MAGIC ACC and LRI noise very closely.

Figure 17-2 shows the ll-sst prefit residuals of the instrument-only simulations of the two scenarios. The blue curves show the prefit residuals of the polar pair, while the red and green curves show the prefit residuals of the inclined pair in the U5d5d_HL_ref and U5d5d_HL_ms scenario, respectively.

For the instrument-only simulations of the two scenarios investigated in this section, we apply an updated version (v010) of the full-scale simulation software for the first time. In this software version, the numerical errors are much smaller compared to the software version used so far (v009), such that the numerical errors are not any more the limiting factor for some of the instrument-only simulations, which has been the case before. The software update strongly affects instrument-only solutions in which rather small noise amplitudes are assumed for the instruments, which in our project is mainly the case for the MAGIC-type ACC noise, but also for the GRACE-type ACC noise if the 1/sqrt(10)-downscaled version of it is used, as it is the case for the simulations in this section.

Figure 17-2 visualizes how the software update affects the instrument-only prefit residuals relevant for the U5d5d_HL_ref and U5d5d_HL_ms scenarios. Comparing the data between the old and the new software versions shows the strong impact of the software update. With respect to the present scenarios, it can be seen that only by using the new software version, a small deviation between the MAGIC noise and the MS noise becomes visible.

Figure 17-3 shows the retrieval errors of the instrument-only simulations for the two scenarios. It can be observed that the results obtained by the new software show much smaller retrieval errors compared to the results obtained using the old software. As a reference, we also included the results obtained for the same scenarios using the reduced-scale simulation software. As shown by panel a, the retrieval errors obtained using v010 of the full-scale software or using the reduced-scale software are very similar, as are the results obtained for the two scenarios. This observation can also be made by considering Figure 17-4 and Figure 17-5.

As the retrieval errors are very similar between the scenarios already when excluding temporal gravity signals, it is expected that also the retrieval errors of the full noise simulations for the scenarios U5d5d_HL_ref and U5d5d_HL_ms will be very similar to each other. This is confirmed by the plots shown in Figure 17-6 and Figure 17-7.

From this, we can conclude that both in the instrument-only and the full-noise simulations, replacing the MAGIC ACC noise by the MS noise time series delivered by TASI does not change the retrieval errors of the simulation results significantly.

Table 17-1 Orbit scenarios.

ID	Sats 1 (IP)		Sats 2 (PP)		h_{l1} [-]	h_{l2} [-]	$\lambda_{shift,1}$ [deg]	$\lambda_{shift,2}$ [deg]	Sub-cycles [days]
	Alt. [km]	Incl. [deg]	Alt. [km]	Incl. [deg]					
3d_M	409	70	440	89	1.368	1.383	2.308	2.384	2, 3, 8, 11, 30
3d_H	432	70	463	89	1.451	1.449	-3.076	-3.067	3, 7, 31
5d_Ma	396	65	434	89	1.397	1.383	-1.499	-1.458	2, 3, 5, 13, 18, 31
5d_Mb	397	70	425	87	1.168	1.167	0.736	0.733	2, 5, 27, 32
5d_H	465	75	488	89	1.185	1.190	0.762	0.781	4, 5, 29
7d_M	389	70	417	87	1.238	1.253	0.743	0.786	2, 7, 30
7d_H	432	70	463	89	1.218	1.226	0.672	0.692	3, 7, 31
SSO for 3d_H	477	97	463	89	1.454	1.449	-3.097	-3.067	3, 7, 31
SSO for 7d_H	477	97	463	89	1.201	1.226	0.622	0.692	3, 7, 31
5d_LL	344	70	376	89	1.423	1.410	-1.671	-1.628	1, 2, 5, 12, 29
5d_LH	344	71.5	492	89	1.169	1.172	-0.732	-0.790	5, (32-31)

Figure 17-1 Amplitude spectral densities of the instrument noise used in the simulations. The magenta curve shows the combination of the MicroSTAR ACC noise delivered by TASI and the LRI noise, which is used for the inclined pair in the scenario U5d5d_HL_ms.
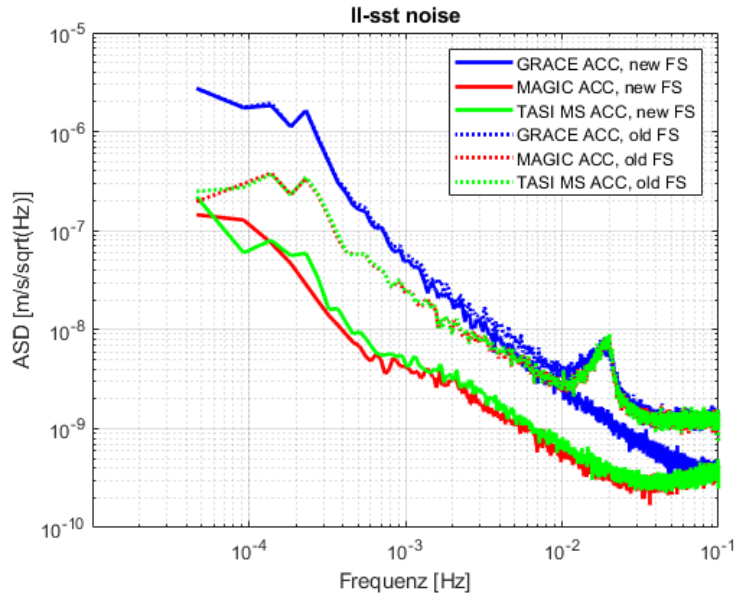
Figure 17-2 Amplitude spectral densities of the instrument-only pre-fit residuals obtained using the full-scale simulator. The solid (dotted) curves show the data obtained using the new (old) version of the software. Figure 17-3 shows the retrieval errors of the associated instrument-only simulations.
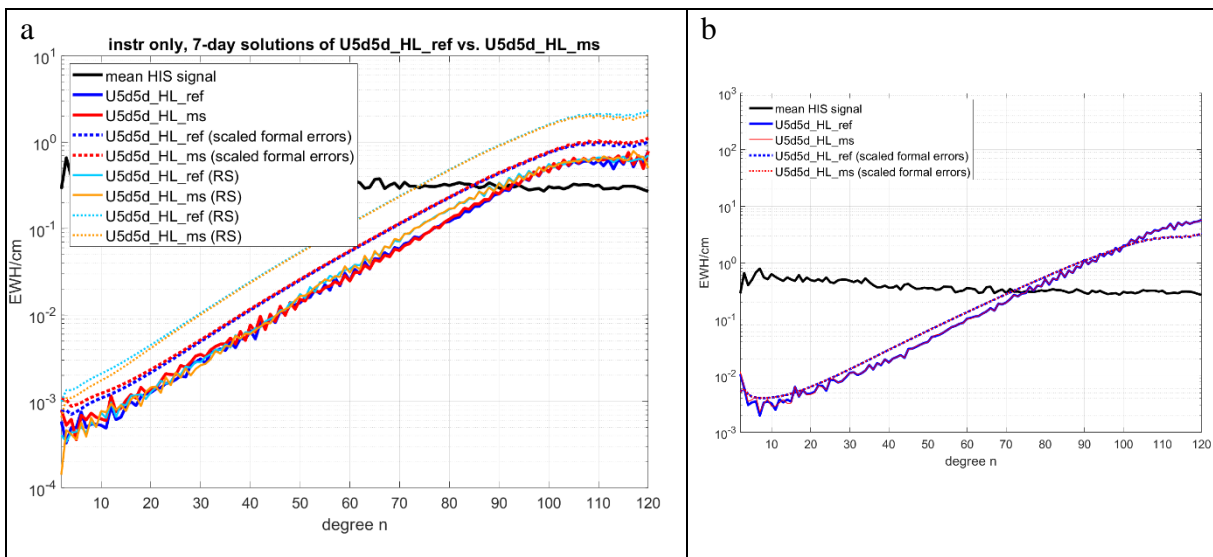
Figure 17-3 Degree amplitude curves for the d/o 120 7-day instrument-only retrieval errors for the scenarios U5d5d_HL_ref and U5d5d_LH_ms (see text). Panel a: The blue and red curves show the results obtained by the new version of the full-scale simulator, the light-blue and orange curves show the results obtained using the reduced-scale simulator. Panel b: Results obtained using the old version of the full-scale simulator, for comparison. Note the different y axis limits between the panels. [Paths: Deliverables/D1/simulation_results/full_scale_simulator_v010/1_by_sqrt(10)_noise_scaling/instrument_only/, Deliverables/D1/simulation_results/full_scale_simulator_v009/1_by_sqrt(10)_noise_scaling/instrument_only/ and Deliverables/D1/simulation_results/reduced_scale_simulator/1_by_sqrt(10)_noise_scaling/instrument_only/]
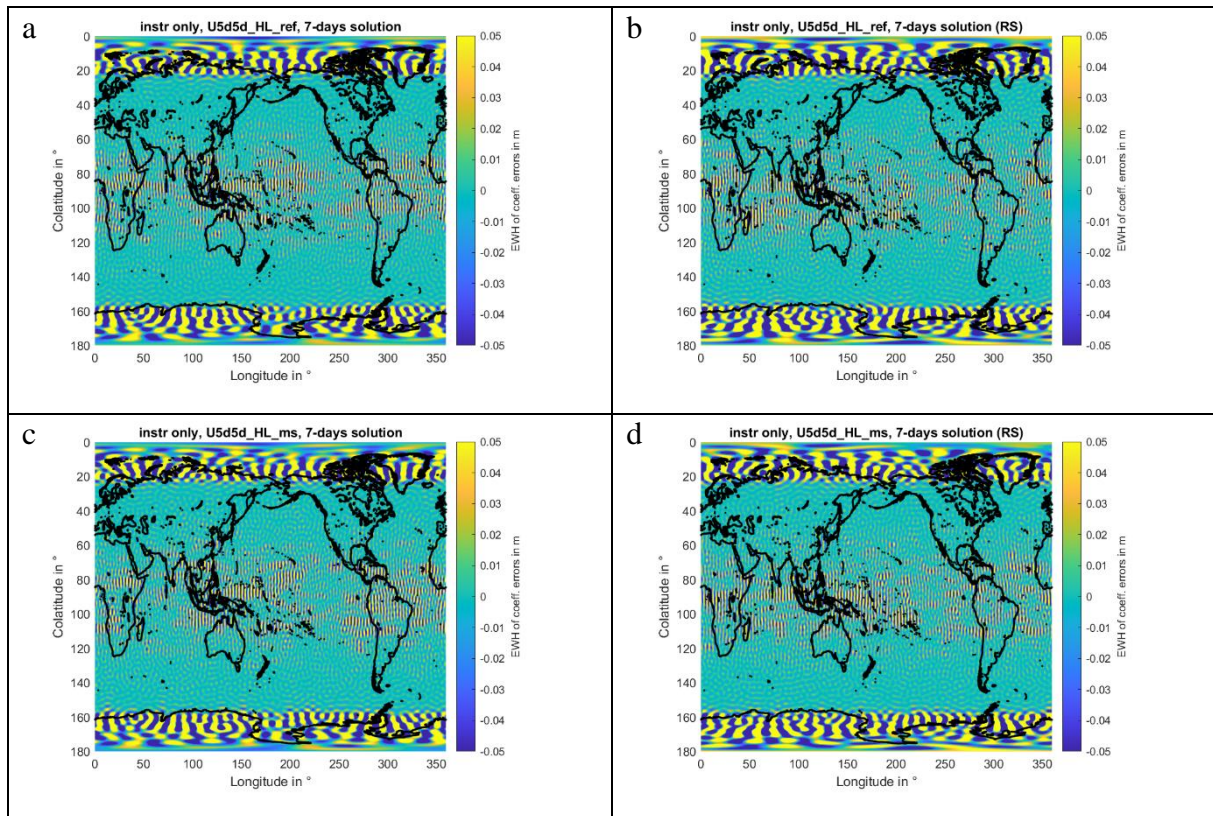
Figure 17-4 EWH error grids of the d/o 120 7-day instrument-only solutions of the scenarios U5d5d_HL_ref (panels a, b) and U5d5d_HL_ms (panels c, d). The panels in the left (right) column show the results obtained using the new version of the full-scale simulator (using the reduced-scale simulator). [Paths:
Deliverables/D1/simulation_results/full_scale_simulator_v010/1_by_sqrt(10)_noise_scaling/instrument_only/ and
Deliverables/D1/simulation_results/reduced_scale_simulator/1_by_sqrt(10)_noise_scaling/instrument_only/]
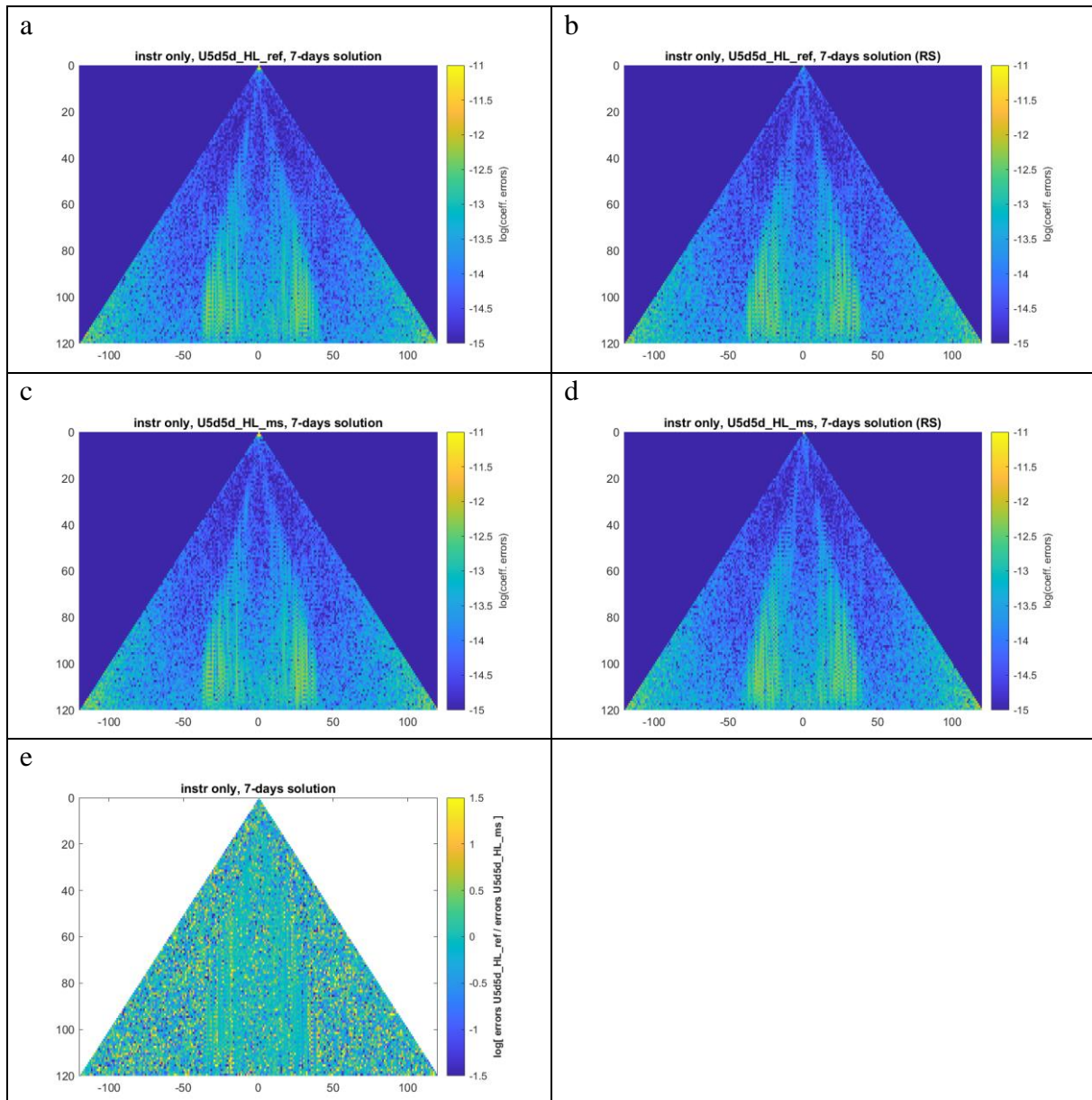
Figure 17-5 Retrieval errors of the d/o 120 7-day instrument-only results for the scenarios U5d5d_HL_ref (panels a, b) and U5d5d_HL_ms (panels c,d) obtained using the new version of the full-scale simulator (a, c) or the reduced-scale simulator (c, d). Panel e shows the ratio of the retrieval errors shown in panels a and c. [Paths: Deliverables/D1/simulation_results/full_scale_simulator_v010/1_by_sqrt(10)_noise_scaling/instrument_only/ and Deliverables/D1/simulation_results/reduced_scale_simulator/1_by_sqrt(10)_noise_scaling/instrument_only/]
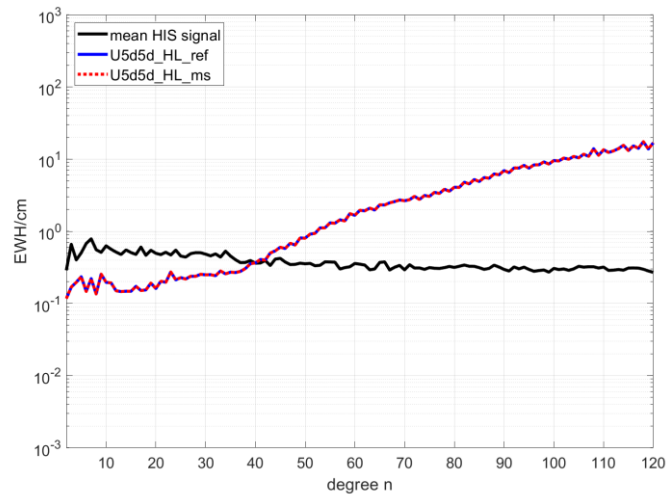
Figure 17-6 Degree amplitudes of the retrieval errors of the d/o 120 7-day full noise nominal solutions for the scenarios U5d5d_HL_ref and U5d5d_HL_ms described in the text. [Path: Deliverables/D1/simulation_results/full_scale_simulator_v009/1_by_sqrt(10)_noise_scaling/full_noise_nominal/]
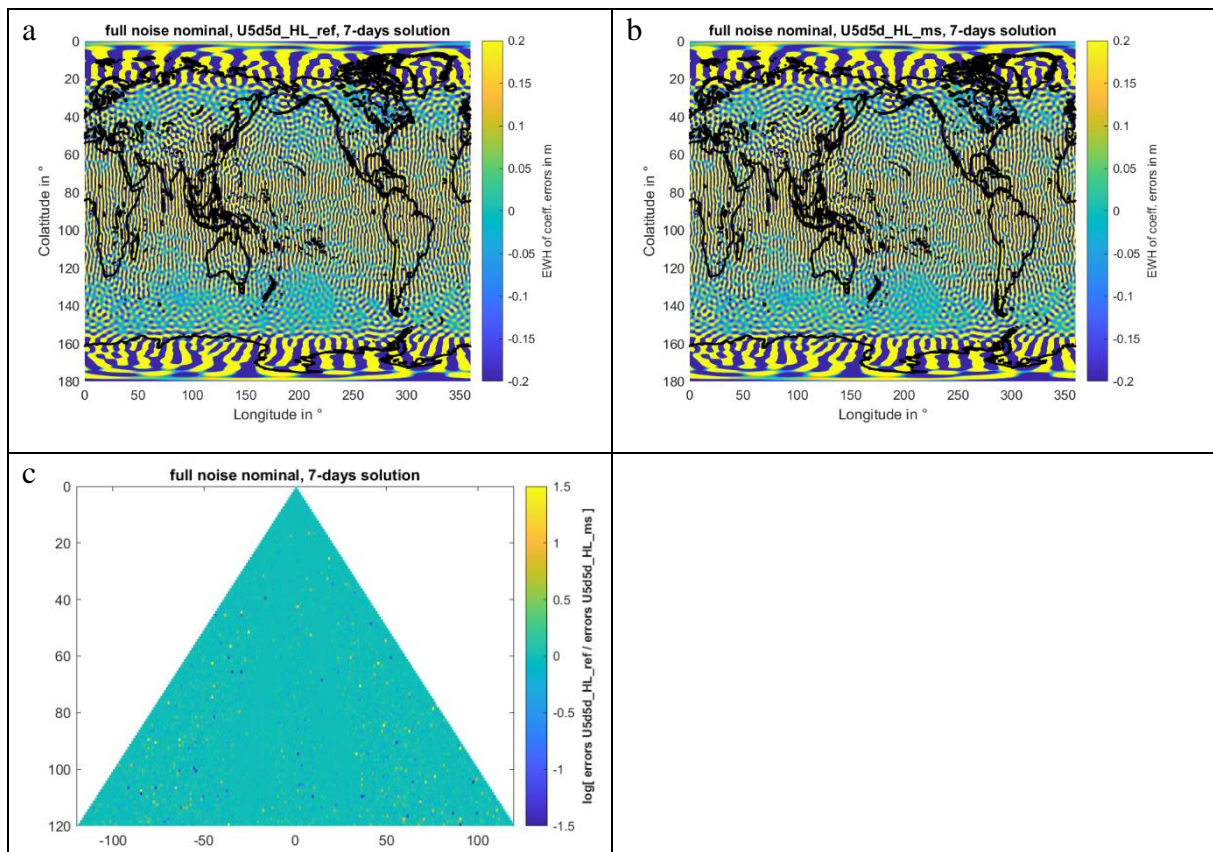
Figure 17-7 Top row: EWH error grids of the d/o 120 7-day full noise nominal solutions for the scenarios U5d5d_HL_ref (panel a) and U5d5d_HL_ms (panel b) described in the text. Panel c shows the ratio of the retrieval errors. [Path: Deliverables/D1/simulation_results/full_scale_simulator_v009/1_by_sqrt(10)_noise_scaling/full_noise_nominal/]

18 APPLICABLE DOCUMENTS, REFERENCE DOCUMENTS, AND PUBLICATIONS TO PART 1

18.1 APPLICABLE DOCUMENTS

[AD-1] Mission Requirements Document, Next Generation Gravity Mission as a Mass-change And Geosciences International Constellation (MAGIC) - A joint ESA/NASA double-pair mission based on NASA's MCDO and ESA's NGGM studies (2020). ESA-EOPSM-FMCC-MRD-3785

[AD-2] Scientific Readiness Levels (SRL) Handbook, Issue 1, Revision 0, 05-08-2015

[AD-3] Statement of Work - ESA Express Procurement - EXPRO NGGM/MAGIC science support study during Phase A, Issue 1, Revision 0, 18/01/2021 Ref ESA-EOPSM-FUTM-SOW-3813

18.2 REFERENCE DOCUMENTS

[RD-1]   Statement of Work, ESA Express Procurement EXPRO, NGGM/MAGIC science support study during Phase A, Ref ESA-EOPSM-FUTM-SOW-3813, Date 18/01/2021

[RD-2]   Assessment of a Next Generation Mission for Monitoring the Variations of Earth's Gravity. Final Report, ESTEC Contract No. 22643/09/NL/AF, Issue 2, Date: 22.12.2010

[RD-3]   Assessment of a Next Generation Gravity Mission to Monitor the Variations of Earth's Gravity Field. Final Report, ESTEC Contract No. 22672/09/NL/AF, Issue 1, Date: 10.10.2011.

[RD-4]   Assessment of Satellite Constellations for Monitoring the Variations in Earth Gravity Field "SC4MGV", ESA Contract No 4000108663/13/NL/MV, Final Report, 04 November 2015

[RD-5]   P.N.A.M. Visser, E.J.O. Schrama, N. Sneeuw, and M. Weigelt, Dependency of resolvable gravitational spatial resolution on space-borne observation techniques, International Association of Geodesy Symposia, DOI 10.1007/978-3-642-20338-1_45, Vol. 136, Springer Verlag, pp. 373-379

[RD-6]   GOCO, Gravity observation combination (GOCO), www.goco.eu, accessed 23 September 2021

[RD-7]   D.E. Pavlis, S. Poulouse, J.J. McCarthy, GEODYN operations manual, Contractor report, SGT Inc. Greenbelt, 2006

[RD-8]   Lemoine, F.G., S.C. Kenyon, and J.K. Factor et al. (1998), The Development of the Joint NASA GSFC and the National Imagery and Mapping Agency (NIMA) Geopotential Model EGM96, NASA/TP--1998--206861.

[RD-9]   TU Munich LRZ server (https://syncandshare.lrz.de/).

PART 2:

GENERATION OF 2ND BASELINE IMPLEMENTATION FOR CLOSED-LOOP SIMULATIONS

19 INTRODUCTION

This Part 2 refers to Task 2 of the SoW and covers the work performed under WP 200 of the WBS. It refers to the deliverable document TN D4 "Generation of a 2nd baseline implementation for closed-loop simulations.

The main purpose is to set-up a second independent implementation of the numerical simulation environment based on the EPOS software package for validating the results of the TUM numerical simulators.

20 2ND NUMERICAL SIMULATION ENVIRONMENT

In this chapter the 2nd numerical simulation environment is introduced and compared with the first environment used by TUM, denoted as full-scale simulator. This was done theoretically as well as based on simulated data. The second simulation software is defined by the Earth Parameter and Orbit System (EPOS) software package (https://www.gfz-potsdam.de/en/section/global-geomonitoring-and-gravity-field/topics/ earth-system-parameters-and-orbit-dynamics/earth-parameter-and-orbit-system-software-epos/) also applied for GRACE and GRACE-FO real data analysis.

GFZ routinely processes monthly gravity fields as part of the Science Data System (SDS) by using the latest RL06 processing strategy. A detailed description of the GFZ RL06 gravity field processing can be found in [RD-1]. The processing of the simulations within this project is based on the GRACE-FO RL06 method, making use of some smaller adaptions in order to increase the speed of processing and to consider the corresponding mission specific preconditions. A complete description of the simulation processing with EPOS is addressed in D8 of the ESA TPM study. All the background models as well as instrument noise assumptions are described in D8. If diverging data was used, it is addressed in this document.

20.1 SOFTWARE DEVELOPMENT

At first, both simulation software packages, and in particular their differences, are evaluated on the theoretical point of view. The main individual processing steps and its differences are addressed in the following:

- Orbit integration: The TUM full-scale simulator uses a multistep method which applies a modified divided difference form of the Adams-Bashford-Moulton-Predict-Evaluate-Correct-Evaluate formulas and local extrapolation. The integration is performed in a 5 sec step size integrating step-wise arcs of 6 hours length. EPOS uses a multistep method applying a symmetric, 2-times summed up Cowell approach of 8th order. The integration step size is 5 sec and the integration is performed as one continuous run without interruptions.

- Generation of observations: The TUM full-scale simulator generates differential hl-SST observations which are derived geometrically from the integrated erroneous orbit positions/velocities, i.e. the positions/velocities are taken directly as hl-SST observations. Additionally, white noise of 1 cm was added on top of these observations. They can be also described as dynamic orbits. The ll-SST observations are computed geometrically by projecting orbit error free positions/velocities onto the line-of-sight.

Before the projection, instrument errors due to the accelerometer (ACC) and star camera is added. The satellite-to-satellite tracking (SST) noise of the inter-satellite ranging instrument is added after the projection. The observable is range-rate. The GFZ EPOS software uses hl-SST observations in an absolute sense by generating code and phase observations from a real GPS constellation. The uncertainty was assumed with 40 cm for the code observations and 0.3 cm for the phase observations. The ll-SST observations are computed geometrically by projecting error free positions/velocities onto the line-of-sight and adding the noise of the inter-satellite ranging instrument. In contrast to the TUM full-scale simulator, EPOS generates non-gravitational observations from background models which are affected by the noise of the ACC as well as the influence of the attitude uncertainty. As all simulations within this study were simulated drag-free, the non-gravitational observations express the noise of the ACC and the additional coupling effect of the attitude noise, exclusively.

- Stochastic modelling: At the TUM full-scale simulator, weighting matrices are set up explicitly for hl-SST and ll-SST, by approximating sensor noise contributions with digital filter models based on pre-fit residuals. In that case, the pre-fits contain instrument noise, exclusively. The filter matrix F is chosen in such a way that F^TF approximates the weighting matrix P. At EPOS, one weighting matrix for the ll-SST component is set up explicitly, by computing the covariance function of the combined product noise (ACC+SST) and deriving a variance-covariance matrix. The matrix is then inverted and decomposed via Cholesky decomposition and forms a triangular filter matrix. The stochastic modelling of the hl-SST component is done by setting up unit matrices according to the standard deviations of code and phase measurements.

- Approach for gravity field retrieval: TUM full-scale simulator is based on the integral equation approach by dividing orbits into continuous short arcs of 6 hours length. The EPOS software is based on the variation equation approach or dynamic approach using arcs of 24 hours.

- Parameterization: The parameterization at the TUM full-scale simulator was chosen to estimate the state vector (position/velocity) per arc as well as the gravity field coefficients up to degree and order (d/o) 120. The software at GFZ estimates the state vector per arc, ACC bias parameters in three directions per arc as well as gravity field coefficients up to d/o 120. GPS clock parameters and phase ambiguities are getting pre-eliminated.

The test scenario for the software comparison was chosen to be scenario 13 of the ESA ADDCON project (see D10 of the ADDCON study) by focussing only on the polar pair flying at an altitude of 355 km. The background models are identical to the ones applied for all other simulations in this study. Differences in the instrument uncertainties are addressed in chapter 20.3.2.
At first, the integrated orbits of this test scenario were compared against each other. The evaluation of the integrated orbits can be found in chapter 20.3.1. Closed-loop simulations were performed for the test scenario including gravity field signals, separately, in order to check the consistency between GFZ und TUM solutions wrt. individual error sources. Simulations were done for the product noise case, the product noise + AOHIS case (where an AO de-aliasing model was applied), the product noise + ocean tides case, and the full noise case. The evaluation of the corresponding results can be found in chapter 20.3.2.

20.2 SIMULATION OF SELETED SCENARIOS

Next to the test scenario, selected scenarios were simulated as well which were chosen to be the 3d_H (2_plg_iln) Bender scenario and the 3d_H Advanced Pendulum (AP) scenario with a 45° deviation angle where the latter includes the same polar pair as the Bender scenario. These scenarios refer to scenarios No. 1 and No. 2 of the ESA TPM study (see D8). The simulation assumptions are described in D2 of this study as well as in D8 of the ESA TPM study. The AP scenario was further simulated by CNES/GRGS and JPL. The Bender scenario was simulated by JPL as well. Therefore, both selected scenarios can serve as further validation wrt. consistency among simulated gravity fields from TUM and GFZ. Results are presented in chapter 20.4.

20.3 COMPARISON OF TUM AND GFZ RESULTS

The integrated orbits as well as the simulated gravity fields of the ADDCON test scenario were evaluated in 20.3.1 and in 20.3.2. In 20.3.3, the selected scenarios were assessed.

20.3.1 EVALUATION OF THE INTEGRATED ORBITS OF THE TEST SCENARIO

The orbit integration as part of the forward modelling defines the first main step in the gravity field simulation processing scheme. As all observations are computed from these orbits afterwards, the integrated orbits of both software packages should match to a certain extend in order to guarantee consistent satellite gravity field observations, especially with regard to the geographical position of the satellites.

Figure 20-1 shows the differences among the integrated positions in three directions after 2 months of integration time in the Earth-centered-Earth-fixed frame (ECEF). It is seen that the coordinate differences in the y and z direction (y points towards the cross-track axis, z points towards the radial axis) increase in time up to a value of about 1000 m after 2 months. For the x direction (x points towards the along-track axis) the difference reaches 8000 m after 2 months. The differences arise due to different integration software on the one hand but mainly due to the uninterrupted integration of the GFZ orbit over 2 months on the other hand. The TUM full-scale simulator performs the orbit integration arc-wise, stopping and starting again, according to the arc length of 6 hours. This keeps the integration error at a certain level while for the EPOS software the error of integration increases along with the time. However, the differences after 2 months are small in y and z direction. The slightly larger difference in x direction can be considered as uncritical as it affects the along-track component and the polar orbit geometry is maintained.

In Figure 20-2 the difference in the geocentric distance of the TUM and GFZ orbit wrt. the mean Earth radius is displayed. It shows a change in the altitude between both orbits by about 20 m after 2 months indicating that both orbits behave almost identical.

Further, the separation of the polar pair is displayed in Figure 20-3 (left), respectively. The plot shows a slightly larger change of about 100 m in the inter-satellite-separation for the GFZ orbit compared to the TUM orbit after 2 months which is due to the larger integration error of the EPOS software. However, both pairs behave stable over time. On the right of Figure 20-3 the inter-satellite-separation of TUM satellite A wrt. GFZ satellite A is displayed. It changes up to

about 8 km after 2 months and is closely related to the x coordinate difference shown in Figure 20-1.
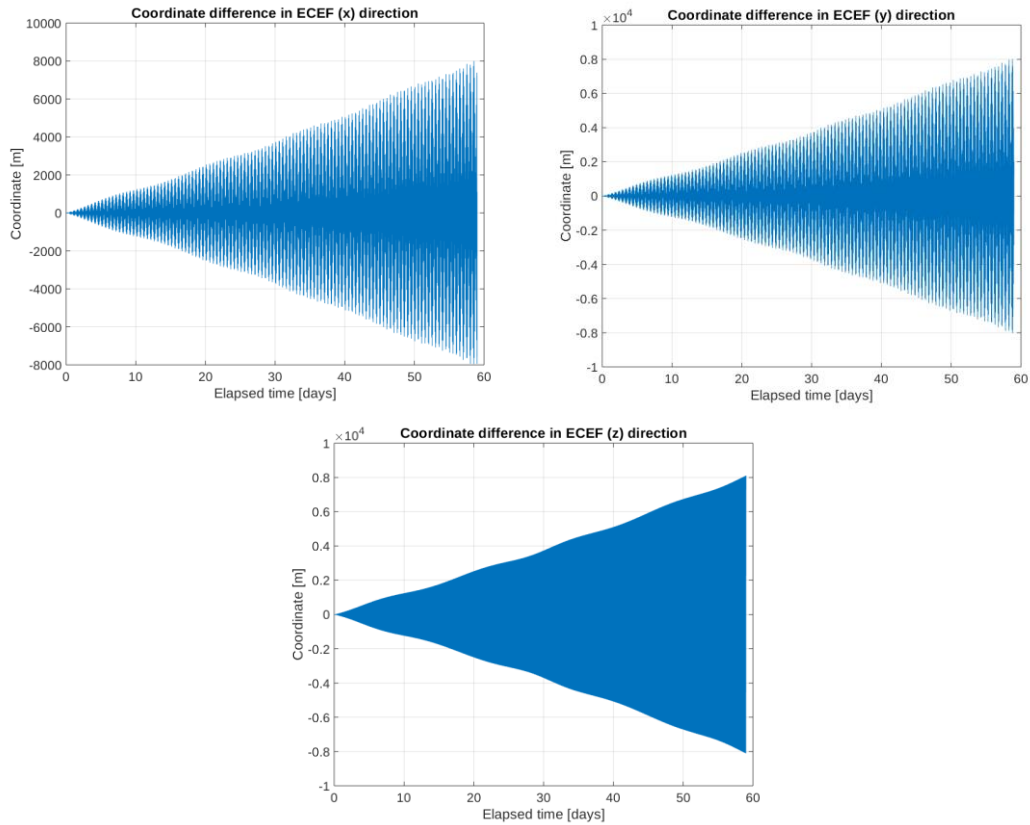
Figure 20-1: Coordinate differences after 2 months of integration for the polar pair of the ADDCON test scenario in x (top left), y (top right) and z (bottom) direction in terms of meters.
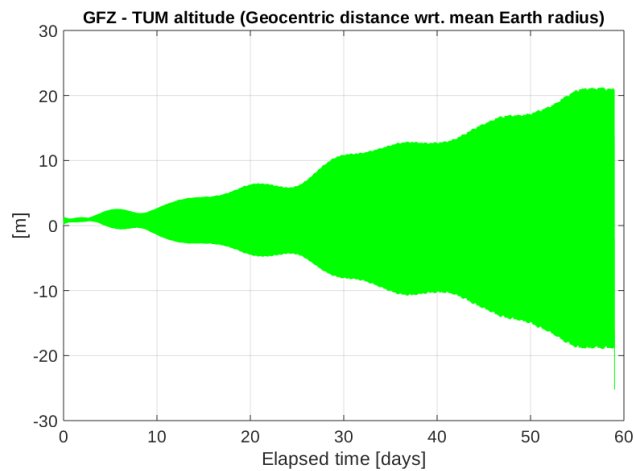
Figure 20-2: Difference in the geocentric distance between the TUM ang GFZ orbits of the polar pair of ADDCON test scenario in terms of meters.
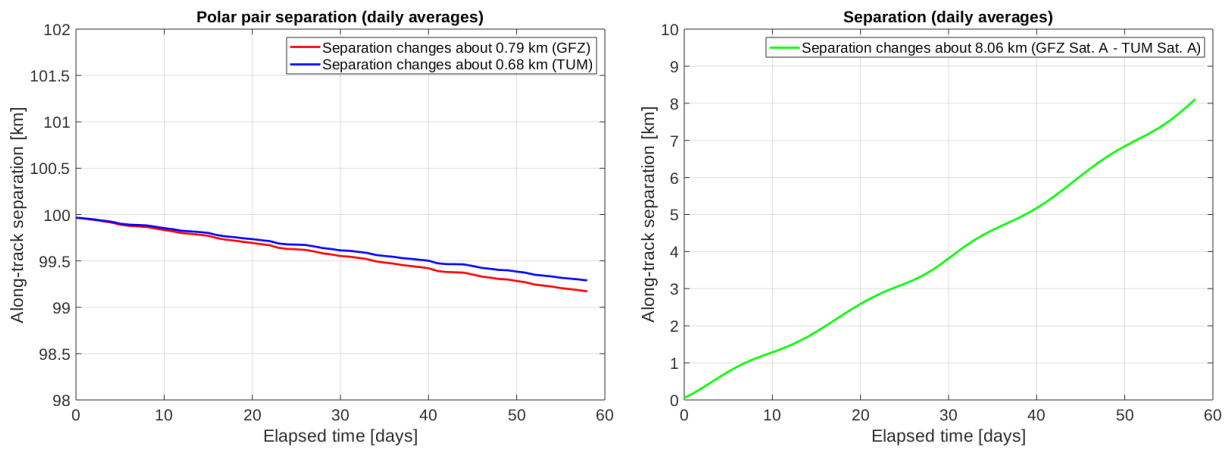
Figure 20-3: Left: Polar pair separation for the GFZ orbit (red) and the TUM orbit (blue) after 2 months. Right: Inter-satellite-separation between the satellites A of GFZ and TUM orbit after 2 months.
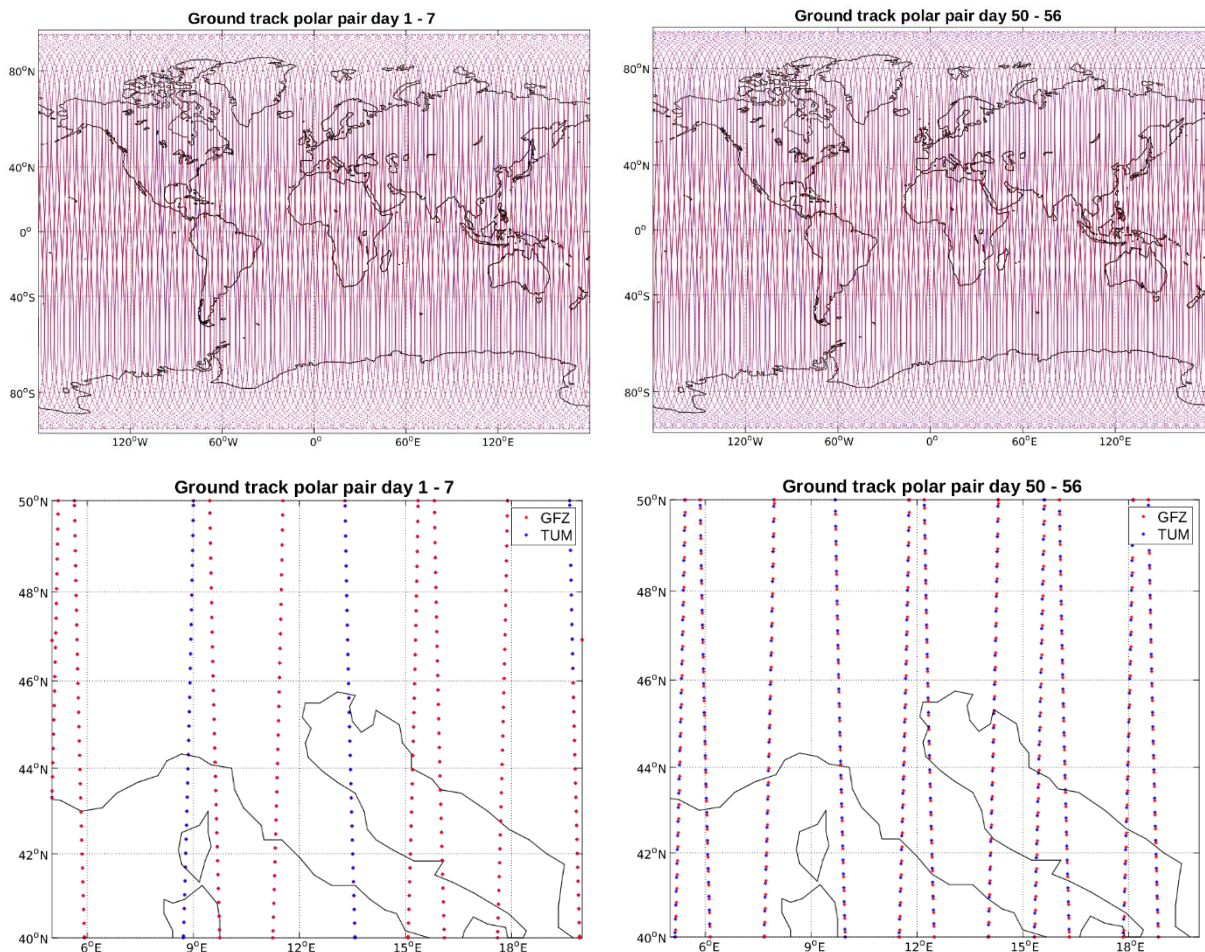
Figure 20-4: Ground track of satellite A of the polar pair for the TUM orbit (blue) and the GFZ orbit (red) displayed on a global scale (top) and for a chosen geographical region (bottom) for the first 7 days (left) and the last 7 days (right) of the integration period.

Figure 20-4 shows the ground tracks of the TUM and GFZ orbits on a global grid as well as for a chosen geographical region for the first 7 days and the last 7 days of the integration period. Differences among both orbits are hardly visible on a global scale but can be seen for the last 7 days of the integration period at smaller geographical scales. Here, the orbits diverge slightly in along-track direction as it was already visible in the inter-satellite-separation presented in Figure 20-3. However, the general picture of the integrated orbits demonstrates consistency among both software and as gravity field retrieval is done in terms of an adjustment process, smaller differences in the integrated orbits should not account for the estimated gravity fields.

20.3.2 EVALUATION OF THE GRAVITY FIELD RETRIEVAL OF THE TEST SCENARIO

In contrast to all other simulation scenarios executed within this study, the test scenario is based on the ADDCON scenario 13. Therefore, the underlying instrument noise assumptions according to the ADDCON study were used for this test scenario. The background models remain identical for all simulation scenarios, including the test scenario. The analytical noise model for the SST instrument noise assumed for the test scenario, given in terms of amplitude spectral density (ASD), reads

$$\mathrm{SST_{ADDCON}} = 2 \cdot 10^{-8} \sqrt{1 + \left(\frac{10^{-2}\mathrm{Hz}}{f}\right)^2} \quad \frac{\mathrm{m}}{\sqrt{\mathrm{Hz}}}$$

The consideration of the uncertainty of the ACC instrument was assumed with

$$\mathrm{ACC(x,z)_{ADDCON}} = 10^{-11} \sqrt{\frac{\left(\frac{10^{-3}\ \mathrm{Hz}}{f}\right)^4}{\left(\left(\frac{10^{-5}\ \mathrm{Hz}}{f}\right)^4 + 1\right)} + 1 + \left(\frac{f}{10^{-1}\mathrm{Hz}}\right)^4} \quad \frac{\mathrm{m}}{\mathrm{s}^2/\sqrt{\mathrm{Hz}}}$$

$$\mathrm{ACC(y)_{ADDCON}} = 10 \cdot \mathrm{ACC(x,z)_{ADDCON}}$$

It is to mention that the noise model of the ACC includes a steep rise ($1/f^2$) of the noise signal for frequencies smaller than 1e-3 Hz. From the previous ADDCON study it is known that this effect causes a degradation of the retrieved gravity field solution by propagating additional erroneous signal into the observations and the resulting product noise solution (all time-varying gravity field signals were excluded) showed unrealistic high signal error amplitudes. This phenomenon could be somehow avoided by high-pass-filtering the ACC noise time series for frequencies below 1e-4 Hz without having an impact on the measurement bandwidth for the time-varying gravity field whose signal starts at the orbital frequency (~1.8e-4 Hz). The situation is demonstrated in Figure 20-5, showing the nominal ACC noise model and the high-pass-filtered version of it. Consequently, the ACC noise assumptions for the test scenario were taken into account according to the high-pass-filtered version.
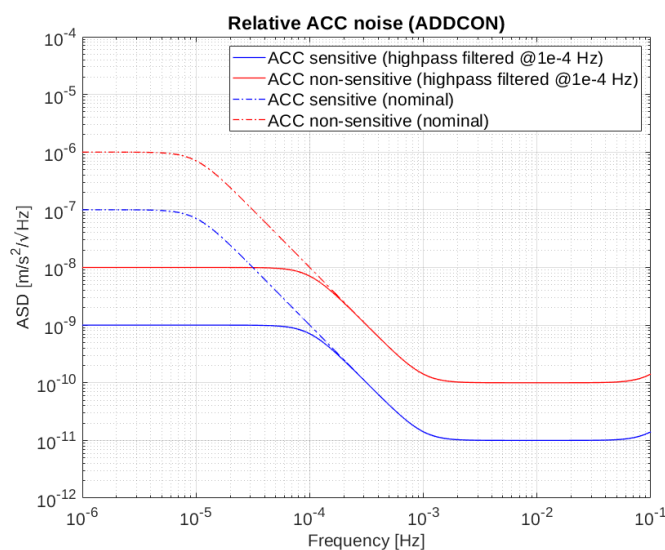
Figure 20-5: ASD of the nominal ADDCON ACC noise model (dashed lines) and the high-pass-filtered version (solid lines) for the sensitive axes (blue) and the non-sensitive axis (red).

In the following, the estimated gravity field solutions are evaluated in terms of retrieval errors in the form of degree error amplitudes as well as cumulated errors. All results are presented in EWH unit. The results are related to a monthly gravity field retrieval covering the first 30 days of January 2002.

In Figure 20-6 the gravity field retrieval error is displayed in terms of degree error amplitudes and cumulated errors for the product noise case. Results demonstrate consistency over the whole spectrum. However, the formal errors displayed in terms of degree amplitudes show an offset among each other where the GFZ related formal errors are assumed to be too optimistic. It is assumed that this is caused by the fact that no covariance information has been used for the GPS observations at the EPOS software so far. Figure 20-7 depicts the corresponding coefficient triangles in terms of residual unitless coefficients as well as the spatial representation of the results resolved up to d/o 50. The triangles show similar error pattern of the estimated coefficients with slightly increased error signals at the very high degrees for the TUM solution. The spatial plots show a similar amount of error pattern as well.

A further consistency check can be made by comparing the pre-fit residuals for the product noise case. Figure 20-8 displays the pre-fit residuals in terms of ASD of the TUM and GFZ data (blue and red). In case of simulating only product noise, the pre-fit residuals should approximate the behavior of the assumed instrument uncertainties (mainly ACC and SST), ideally. The plot shows that the pre-fit residuals follow the behavior of the SST noise (green dashed line) at the high frequencies and follow the behavior of the sensitive ACC axis (black dashed line) at the lower frequency band. An offset is visible between the TUM and GFZ residuals for frequencies between $7e^{-4}$ Hz and $7e^{-3}$ Hz. A test simulation assuming 3 sensitive ACC axes (orange line) demonstrates that this effect is not caused by the inclusion of the non-sensitive cross-track axis. It is rather due to the numerical accuracy reached for the TUM solution for these frequencies, which can be seen from the pre-fit residuals based on a noise free simulation (purple line). However, the retrieved gravity field solutions for the product noise case discussed before show similar error performance indicating that the differences in the pre-fit residuals do not have an impact on the final solution in that case.

Figure 20-6: Product noise solutions of the test scenario simulated by GFZ (red) and TUM (blue) in terms of SH degree error amplitudes (left) and cumulated errors (right). The monthly averaged HIS signal is displayed in black.
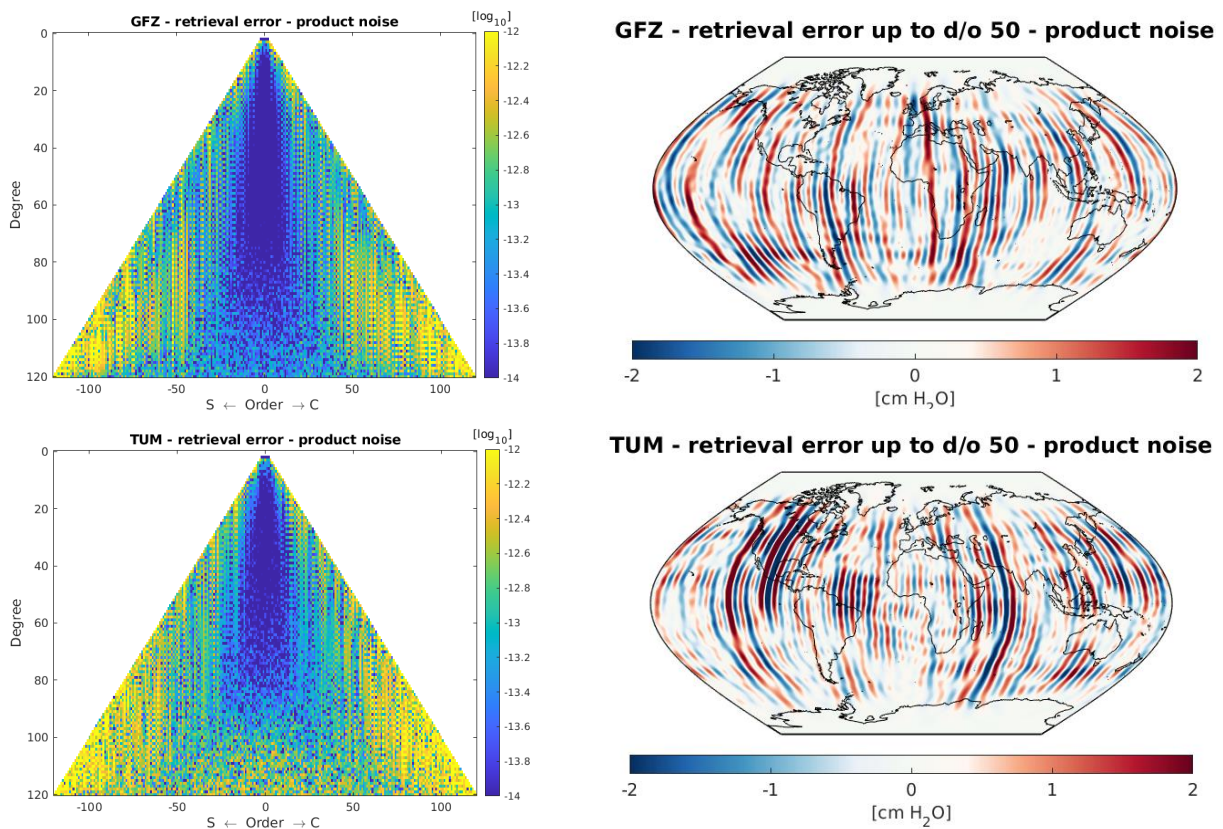
Figure 20-7: Residual coefficient triangles of unit-less coefficients case in a logarithmic scale (left) and global grids of gravity field retrieval errors resolved up to d/o 50 (right) simulated by GFZ (top) and TUM (bottom) for the product noise case.
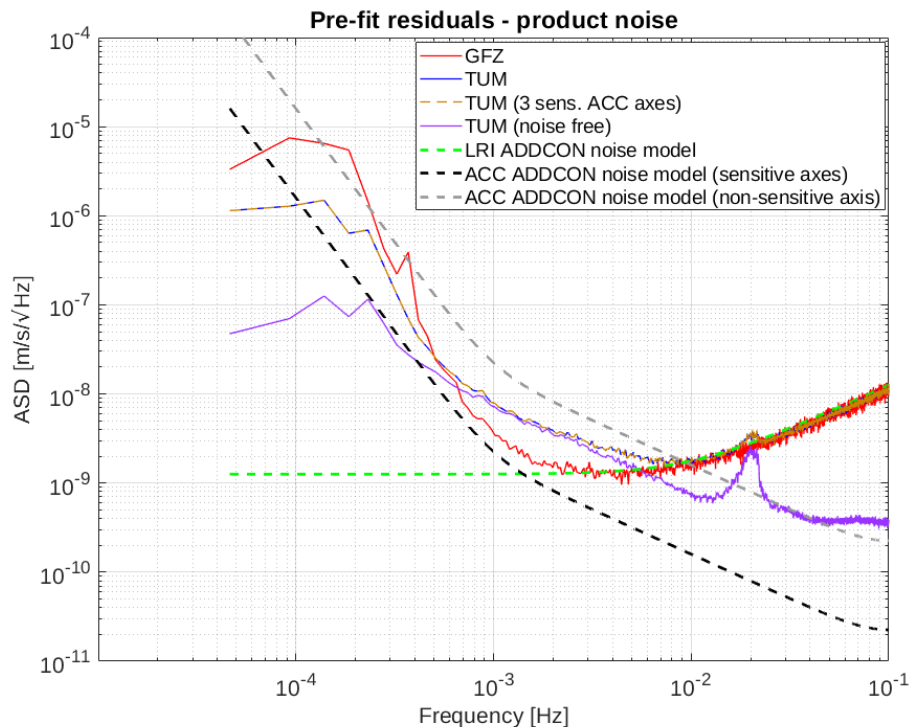
Figure 20-8: Arc-wise averaged ASD of pre-fit residuals of the test scenario in terms of range-rates for the product noise case simulated by GFZ (red) and TUM (blue). Pre-fit residuals based on a simulation done by TUM, assuming 3 sensitive ACC axes on the one hand (orange) and assuming no noise sources on the other hand (purple), are displayed as well. The analytical instrument noise models are displayed for SST (green dashed), ACC sensitive axes (black dashed) and ACC non-sensitive axis (grey dashed).

The second simulation case includes the product noise and the signals from the non-tidal time-varying gravity field, AOHIS. As an AO-de-aliasing model was applied during gravity field recovery, the recovered field contains mainly errors due to mismodelling of AO signals as well as hydrological errors, expressed in terms of temporal aliasing. Figure 20-9 displays the retrieval error of the TUM and GFZ simulated gravity fields in the spectral domain per degree and in a cumulated sense. Results demonstrate consistency over the whole spectrum. The GFZ solution shows a peak at degree 2 which is somehow caused by degraded estimation performance of the C20 coefficient. Simulations done with EPOS have shown that this effect arises for different satellite configurations and different signals included into the simulations (see also results of the TPM study) and is not related to a dedicated satellite configuration or to dedicated signals included. It is actually not clear where this effect comes from. Usually, the estimation of the very long wavelength signals is supported by measurements from SLR which improve the estimation performance of C20 as well. In the simulations SLR observations were not used. For the computation of the cumulative errors information of degree 2 coefficients were not included as the performance of the C20 coefficient would give a wrong picture of the overall cumulated retrieval error.

Figure 20-10 shows the residual coefficients as well as the spatial grids of the product noise + AO case. The triangles of both solutions have the typical structure of a polar single-pair configuration showing well determined zonal and near-zonal coefficients and less well determined coefficients for dedicated order bands. The global grids of both solutions show similar error pattern with slightly increased errors for the GFZ solution. The signals are

dominated by temporal aliasing errors due to mismodelling of AO error signals as well as hydrological signals.
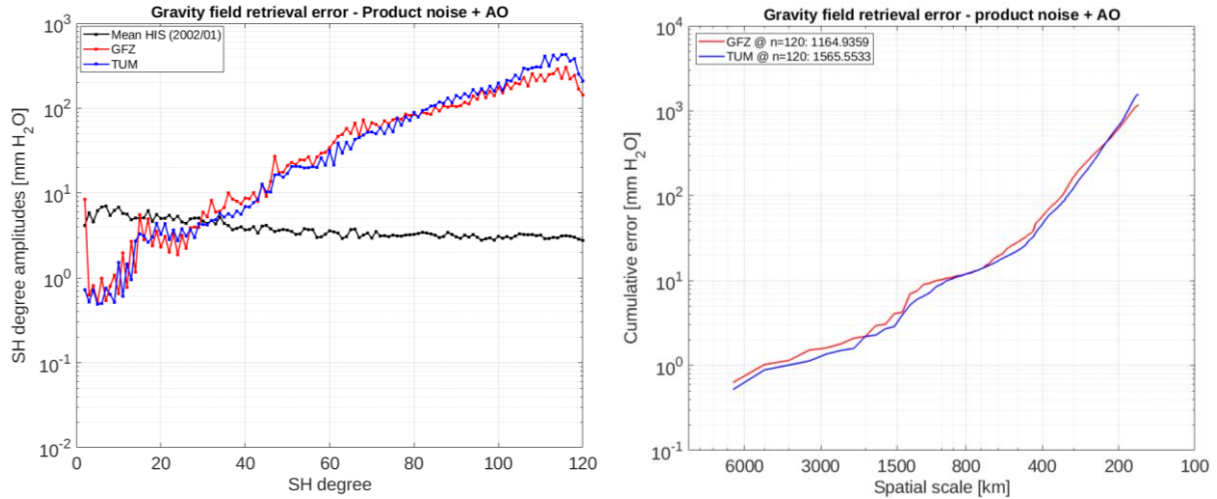
Figure 20-9: Product noise + AO solutions of the test scenario simulated by GFZ (red) and TUM (blue) in terms of SH degree error amplitudes (left) and cumulated errors (right). The monthly averaged HIS signal is displayed in black.
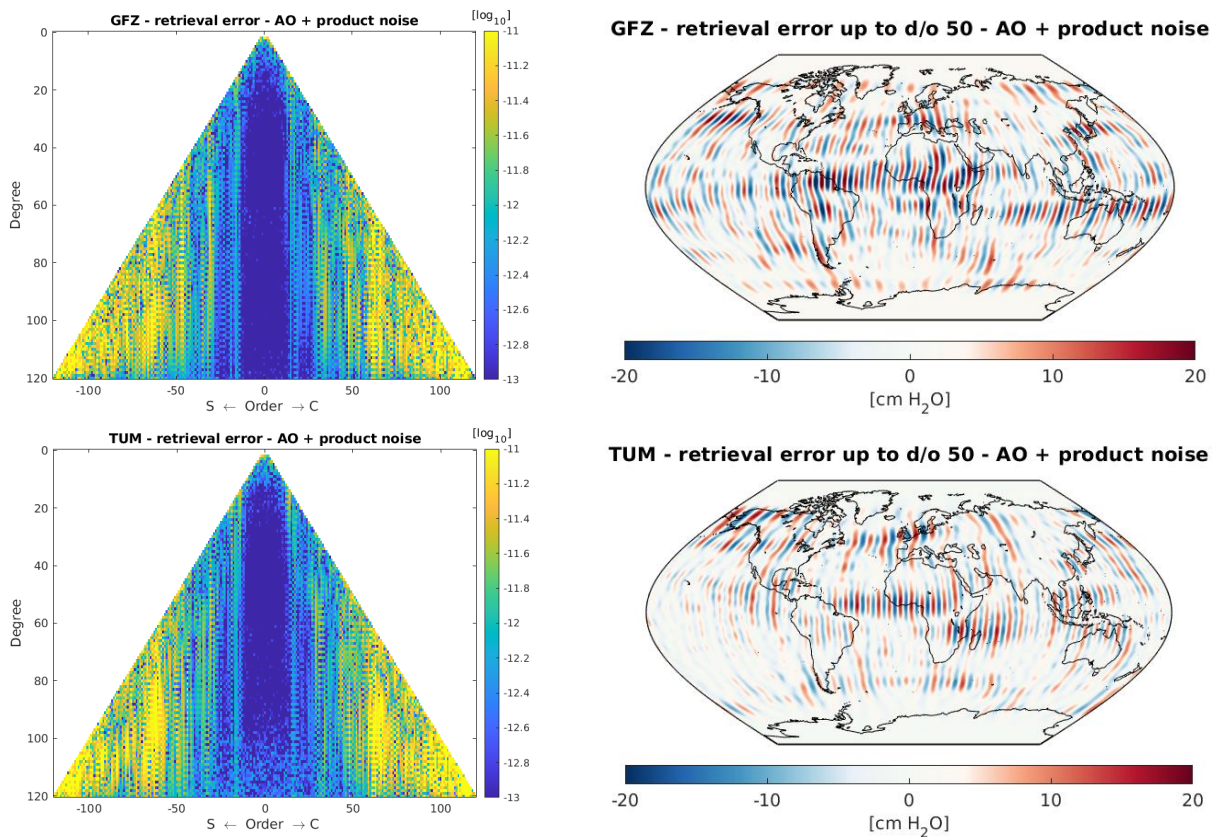
Figure 20-10: Residual coefficient triangles of unit-less coefficients case in a logarithmic scale (left) and global grids of gravity field retrieval errors resolved up to d/o 50 (right) simulated by GFZ (top) and TUM (bottom) for the product noise + AO case.

The third case describes the simulation of the product noise and ocean tide signals. The recovered gravity field contains mainly aliasing errors due to imperfect ocean tide modelling. Figure 20-11 displays the degree amplitudes and the cumulated errors for this case. In contrast to the previous results, the retrieval errors do not perform consistently, especially for the lower and mid degrees where the GFZ solution shows larger amplitudes. However, the very short wavelength signals show similar performances and the cumulative errors have consistent values at the very small spatial scales, therefore. The triangle plots and spatial grids displayed in Figure 20-12 confirm the performances of the solutions seen in Figure 20-11. The residual coefficients of the GFZ solution show some larger aliasing errors for dedicated order bands. This is reflected by an increased striping pattern in the spatial representation. As such a difference between the GFZ and TUM solutions was not seen for the product noise plus AO case, we assume that tidal aliasing signals are propagated in a somehow increased sense into the recovered gravity field at EPOS, compared to the TUM full-scale simulator. The reason for that could be the arc length of 24 hours, so that daily and half-daily tidal signal errors alias stronger into the solution than the signals at the full-scale simulator, which uses arcs of 6 hours. The daily arc length is related to about 15-16 orbit revolutions. These numbers and its multiples are known as resonance order bands arising for polar orbits at altitudes between 300 and 500 km. Figure 20-13 depicts the order amplitudes for both solutions. The GFZ solution shows increased amplitudes at the mentioned order bands, especially at orders 30-31, 46-47 and 61-62, indicating that the tidal error signals are propagated stronger into dedicated resonance order bands due to the daily arc length.

In order to investigate whether forces from ocean tides are propagated correctly into the observation component of both processing software, the pre-fit residuals of both solutions were plotted globally using the underlying position information of the satellite orbits. Additionally, the pre-fit residuals were bandpass-filtered beforehand (frequencies below 0.3 mHz and above 18 mHz were filtered out) in order to see the gravity related high frequency signals. Figure 20-14 shows the spatial representation of the pre-fit residuals demonstrating consistent tidal error signals wrt. the geographical location after 1 month as well as wrt. the signal amplitudes. The standard deviation is given with 0.321 nm/s^2 for the GFZ solution and with 0.339 nm/s^2 for the TUM solution. As a reference, the difference between the two tide models used for the simulations is displayed for a dedicated epoch being representative for the tidal errors. The comparison among these differential signals and the pre-fit residuals shows consistent distribution of tidal signal errors, globally, indicating a correct propagation of signal into the observations at both software packages. Differences among the GFZ and TUM pre-fit residuals can be seen only at smaller scales. The differential plot shows few larger differences in terms of error signal along the orbit ground track originating from the TUM residuals but mainly noise.

From this we conclude that the difference in the performance of the retrieved gravity fields is not related to incorrect implementation of tide model signals but rather to systematic reasons propagating tidal signal errors into the gravity field solution, differently.
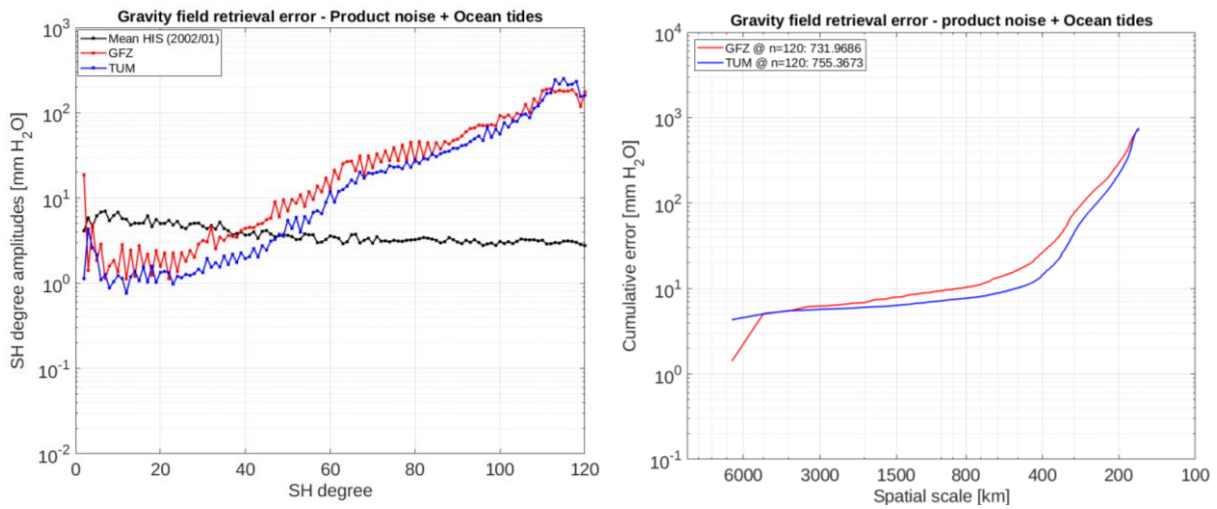
Figure 20-11: Product noise + ocean tide solutions of the test scenario simulated by GFZ (red) and TUM (blue) in terms of SH degree error amplitudes (left) and cumulated errors (right). The monthly averaged HIS signal is displayed in black.
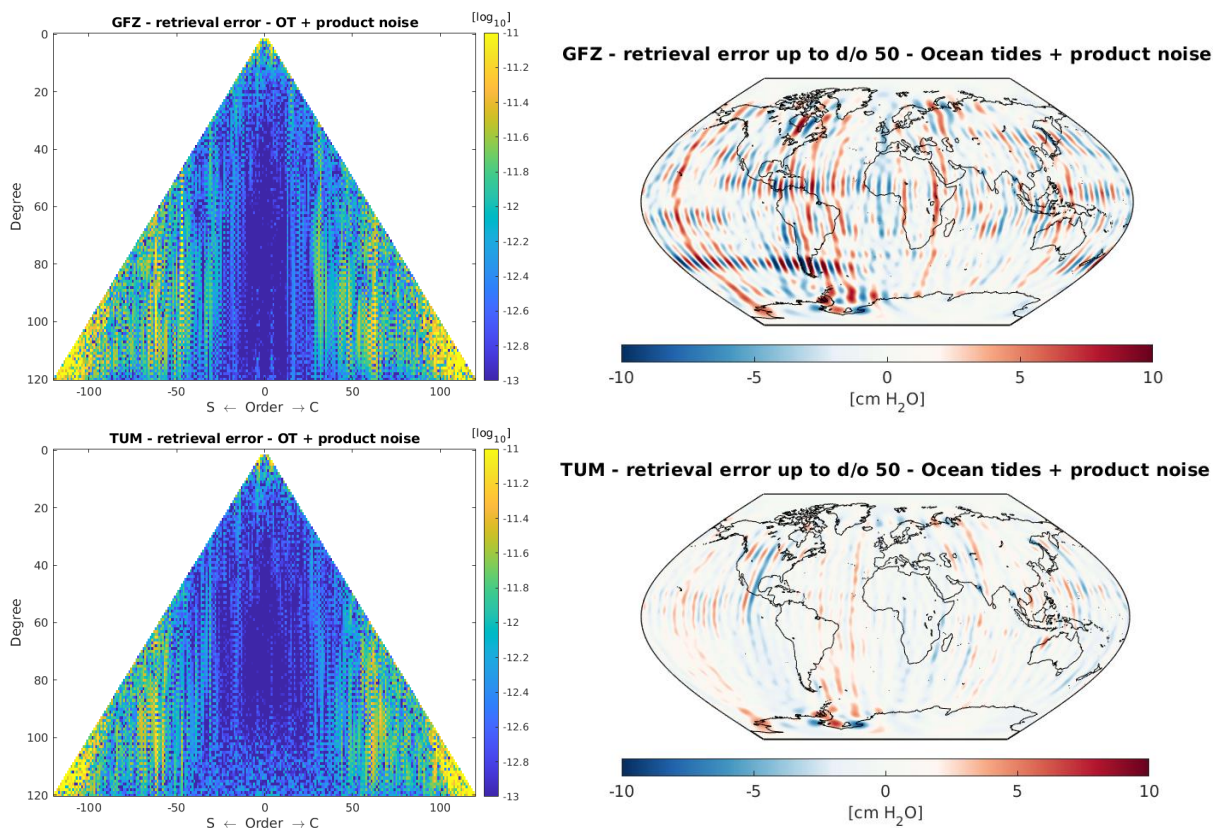
Figure 20-12: Residual coefficient triangles of unit-less coefficients case in a logarithmic scale (left) and global grids of gravity field retrieval errors resolved up to d/o 50 (right) simulated by GFZ (top) and TUM (bottom) for the product noise + ocean tide case.
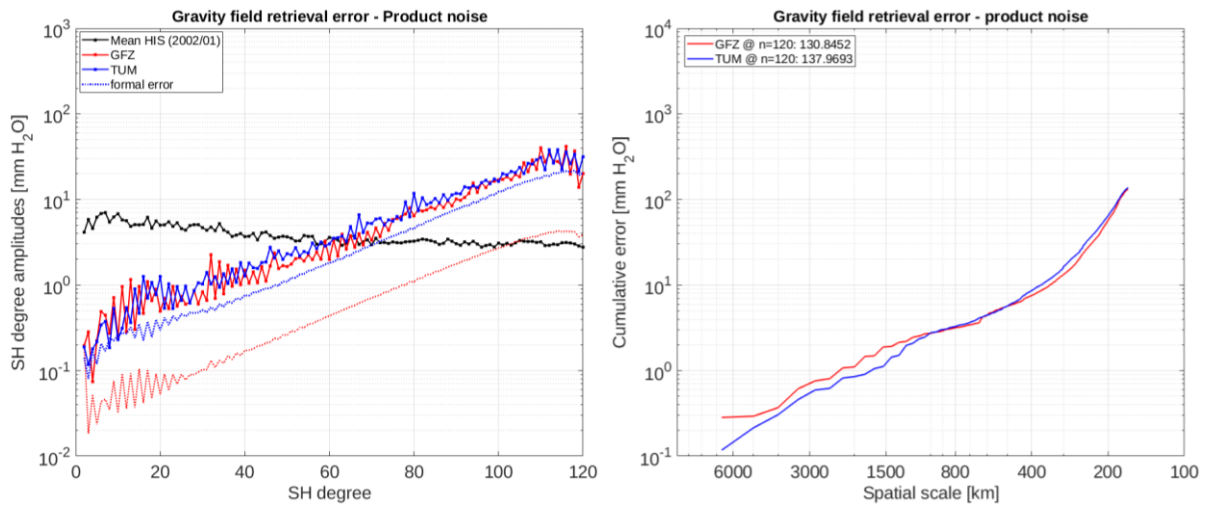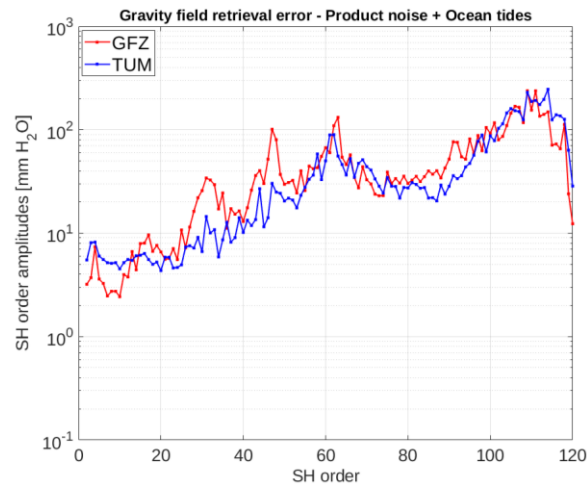
Figure 20-13: Product noise + ocean tide solutions of the test scenario simulated by GFZ (red) and TUM (blue) in terms of SH order error amplitudes.
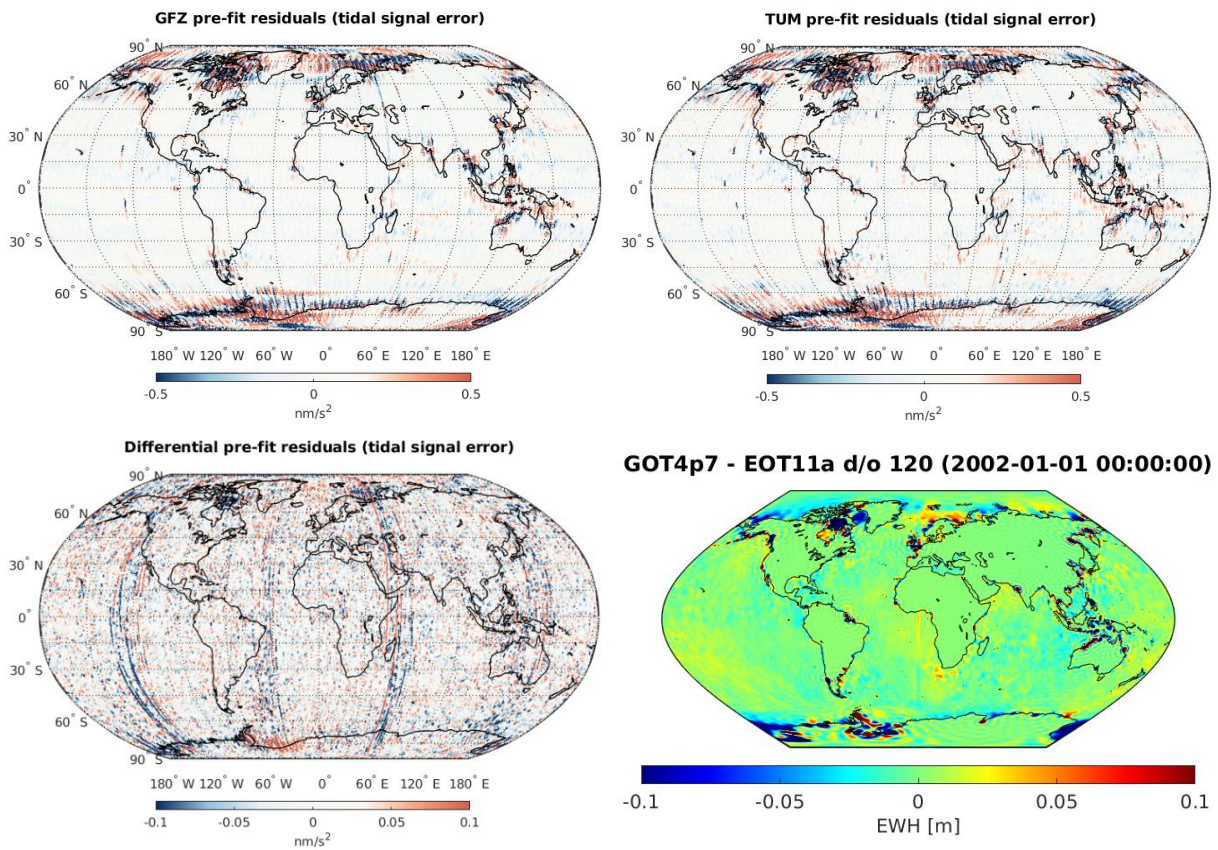
Figure 20-14: Bandpass-filtered pre-fit residuals in terms of nm/s^2 for the product noise + ocean tide case simulated by GFZ (top left) and by TUM (top right) together with the difference among both data sets (bottom left). As a reference, the difference between the GOT4.7 model and the EOT11a model is displayed for the first epoch in January 2002 in terms of m EWH.

NGGM/MAGIC – Science Support Study During Phase A	*Final Report*	
	Doc. Nr:	MAGIC_FR
	Issue:	1.0
	Date:	15.11.2022
	Page:	211 of 466

The combination of all error sources was simulated in the full noise case representing the most realistic picture of the retrieved gravity field. The degree error amplitudes and cumulative errors displayed in Figure 20-15 show consistent performances for both solutions with slightly increased amplitudes for the GFZ solution at the mid degrees. The full noise solutions are dominated mainly by the aliasing error from the AO error signal so that the differences seen for the product noise + ocean tides case play only a subordinate role at the full noise case. Figure 20-16 displays the coefficient triangles and spatial representations for the full noise case showing consistent error behavior for both solutions. The slightly increased striping pattern at the GFZ solution is related to somehow larger error amplitudes for the mid degree and order coefficients.

A quantitative assessment of the results was done by computing the latitude dependent weighted RMS up to two different maximum resolutions, listed in Table 20-1. The values confirm the previously made conclusions. For the full noise case, the solutions of TUM and GFZ diverge only about 1.5% when considering signals up to d/o 100.

The results related to the test scenario have shown that consistency in terms of gravity retrieval error performance was reached to a certain extent for the TUM and GFZ simulations. This indicates that similar performances of recovered gravity field solutions can be expected for both software packages when identical simulation assumptions are met.
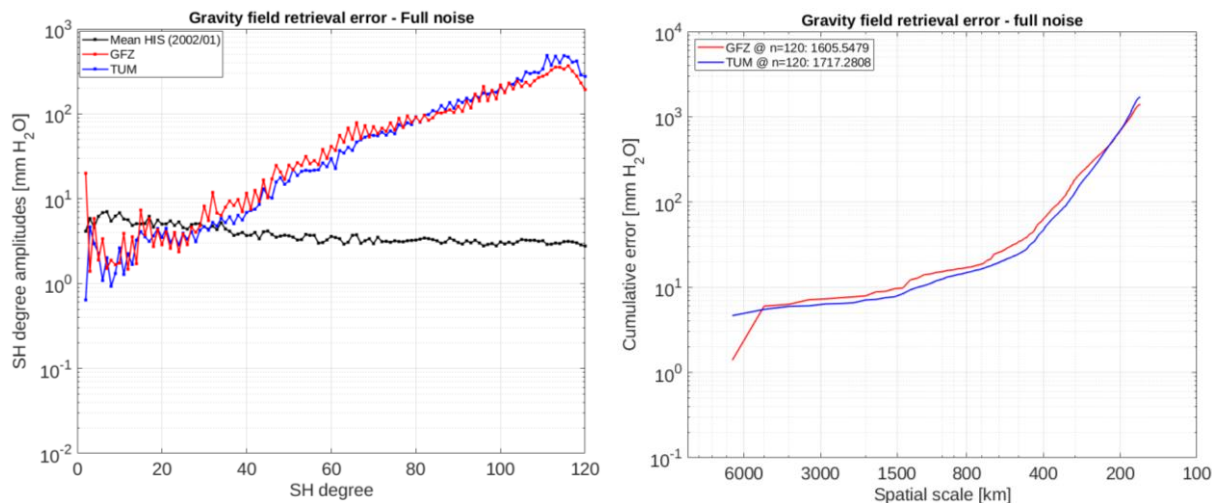
Figure 20-15: Full noise solutions of the test scenario simulated by GFZ (red) and TUM (blue) in terms of SH degree error amplitudes (left) and cumulated errors (right). The monthly averaged HIS signal is displayed in black.
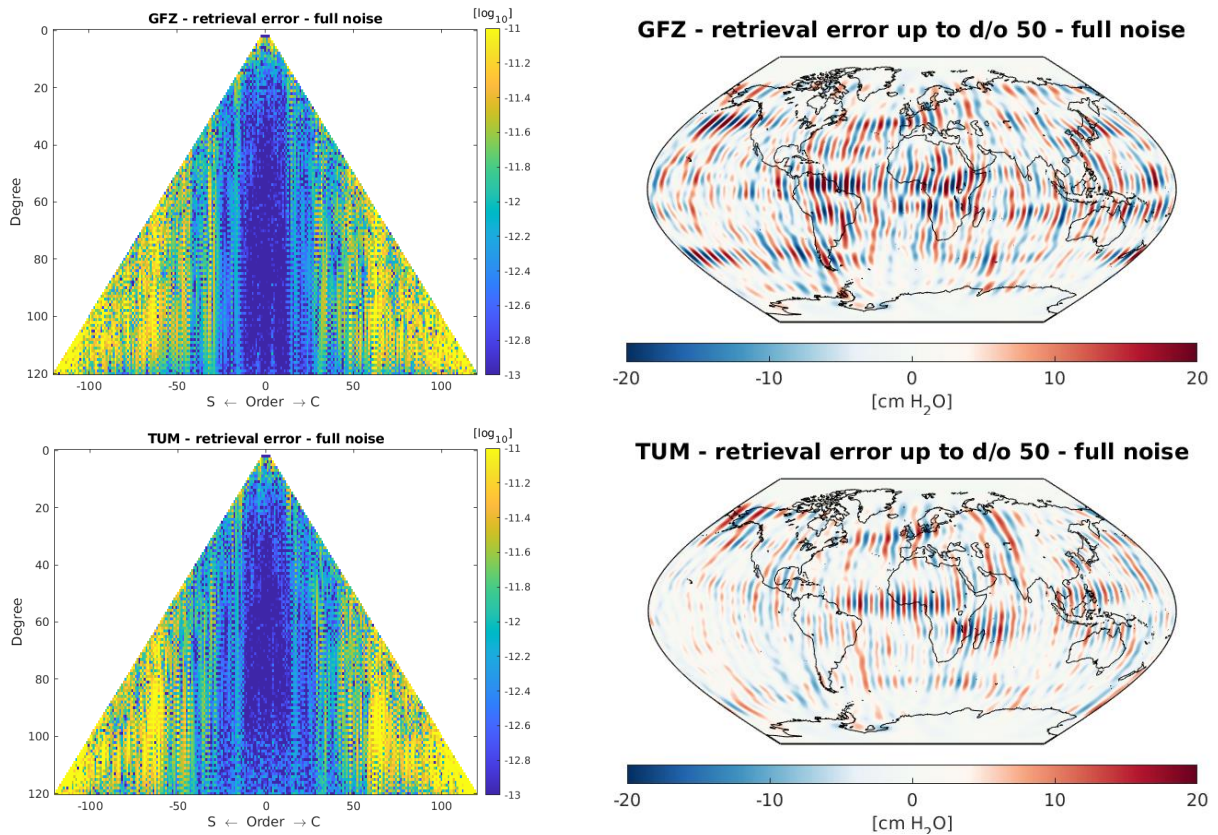
Figure 20-16: Residual coefficient triangles of unit-less coefficients case in a logarithmic scale (left) and global grids of gravity field retrieval errors resolved up to d/o 50 (right) simulated by GFZ (top) and TUM (bottom) for the full noise case.

Table 20-1: Latitude dependent weighted RMS computed up to d/o 50 and 100 for the different simulation cases of the test scenario.

Test scenario	wRMS up to d/o 50 [cm EWH]	wRMS up to d/o 100 [cm EWH]
TUM (prod. noise)	0.09	0.65
GFZ (prod. noise)	0.08	0.58
TUM (prod. + AO error)	0.47	6.84
GFZ (prod. + AO error)	0.59	6.32
TUM (prod. + OT error)	0.15	2.22
GFZ (prod. + OT error)	0.27	3.01
TUM (full noise)	0.48	7.13
GFZ (full noise)	0.65	7.02

20.3.3 EVALUATION OF THE GRAVITY FIELD RETRIEVAL OF THE POLAR PAIR OF THE 3DH BENDER SCENARIO

The ADDCON test scenario for software comparison purposes has shown some discrepancies among TUM and GFZ solutions for the simulation of the product noise and ocean tide signals. In order to check if this effect is present in other simulation configurations using different simulation assumptions, simulations were performed for the Bender 3dH case using the polar pair, exclusively. Further, the generation of the instrument noise time series has not been done consistently thus showing an offset of a factor of $1/\sqrt{2}$. Therefore, the instrument noise has been re-scaled on TUM side. The simulation assumptions are described in D2 of this study as well as in D8 of the ESA TPM study. The setup between the ADDCON test scenario and the 3dH polar pair differs mainly by the orbits (now flying about 100 km higher), the instrument noise assumptions and the stochastic modelling.

Figure 20-17 displays the degree amplitudes, the order amplitudes and the cumulated errors for this case for a 30-day retrieval.
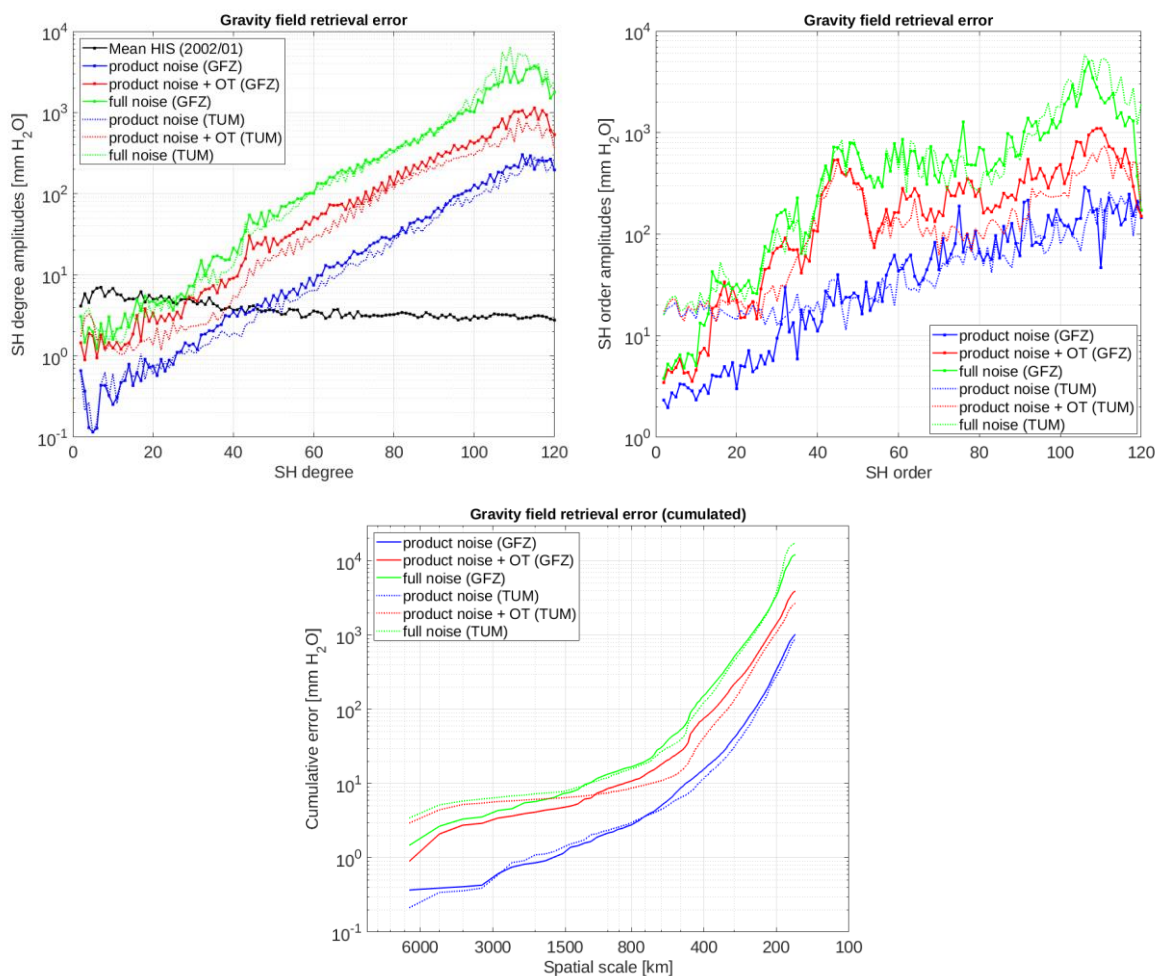
Figure 20-17: Degree error amplitudes (top left), order error amplitudes (top right) and cumulated errors (bottom) simulated by GFZ (solid) and TUM (dotted) for the product noise case (blue), the product noise + ocean tides case (red) and the full noise case (green). The monthly averaged HIS signal is displayed in black.

The corresponding coefficient- and spatial representations are shown in Figure 20-19 and Figure 20-20. A quantitative assessment has been made in terms of cumulated errors, listed in Table 20-2. Simulations have been performed for the product noise case, the product noise + ocean tides case, and for the full noise case. The full noise and product noise solutions of TUM and GFZ show consistency among each other, respectively. The order amplitudes and coefficient triangles related to the product noise solutions reveal slightly larger error signals for TUM for coefficients of lower orders and high degrees due to numerical accuracy issues. This phenomenon is still visible in the full noise solution. However, consistency is reached for the product noise case as the assumed ACC noise is larger than the numerical accuracy of the TUM full-scale simulator and dominates the majority of the spectrum. Figure 20-18 shows the pre-fit residuals for the product noise case demonstrating consistent performance, except for the high frequency spectrum, which causes larger retrieval errors at the high degree coefficients, and for the very low frequency spectrum. The product noise + ocean tides results show somehow larger discrepancies with larger error signals on GFZ side related to coefficients of specific resonance orders (e.g. around 30, 62, 76) and close to them. These coefficients cause additional error signals visible in the spatial grid of the GFZ related solution.
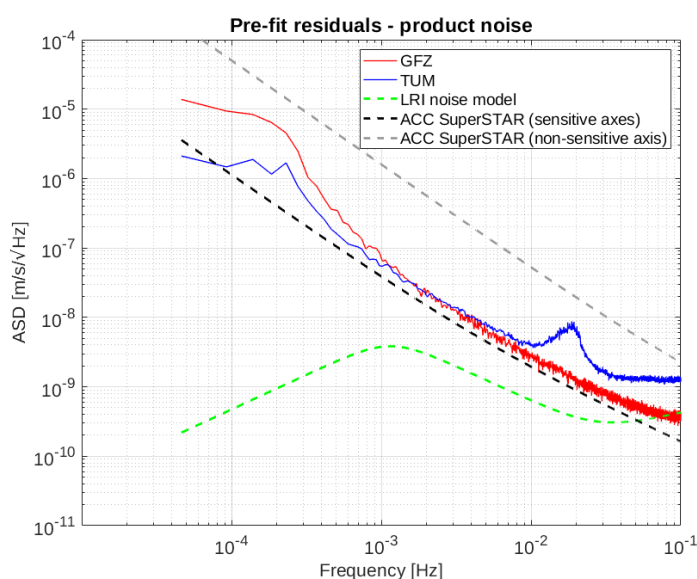
Figure 20-18: Arc-wise averaged ASD of pre-fit residuals of the 3dH (polar pair) scenario in terms of range-rates for the product noise case simulated by GFZ (red) and TUM (blue). The analytical instrument noise models are displayed for SST (green dashed), ACC sensitive axes (black dashed) and ACC non-sensitive axis (grey dashed).

Table 20-2: Cumulated error computed up to d/o 100 for the different simulation cases of the 3dH (polar pair) scenario.

Scenario 3dH (polar pair)	Cumulated error up to d/o 100 [cm EWH]
TUM (prod. noise)	28
TUM (prod. noise + OT)	108
TUM (full noise)	376
GFZ (prod. noise)	34
GFZ (prod. noise + OT)	141
GFZ (full noise)	336
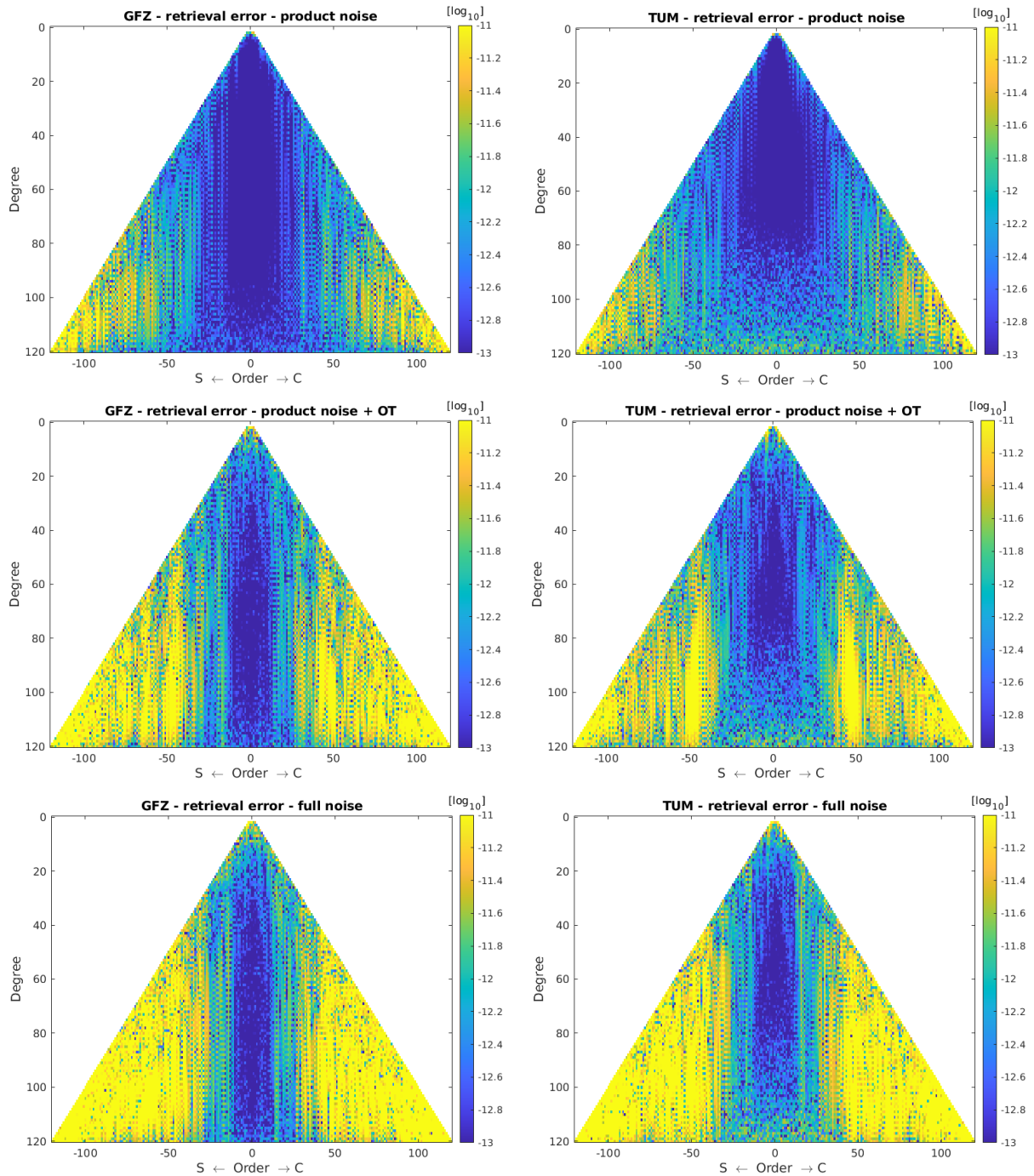
Figure 20-19: Residual coefficient triangles of unit-less coefficients case in a logarithmic scale simulated by GFZ (left) and TUM (right) for the product noise case (top), the product noise + ocean tides case (center) and the full noise case (bottom).
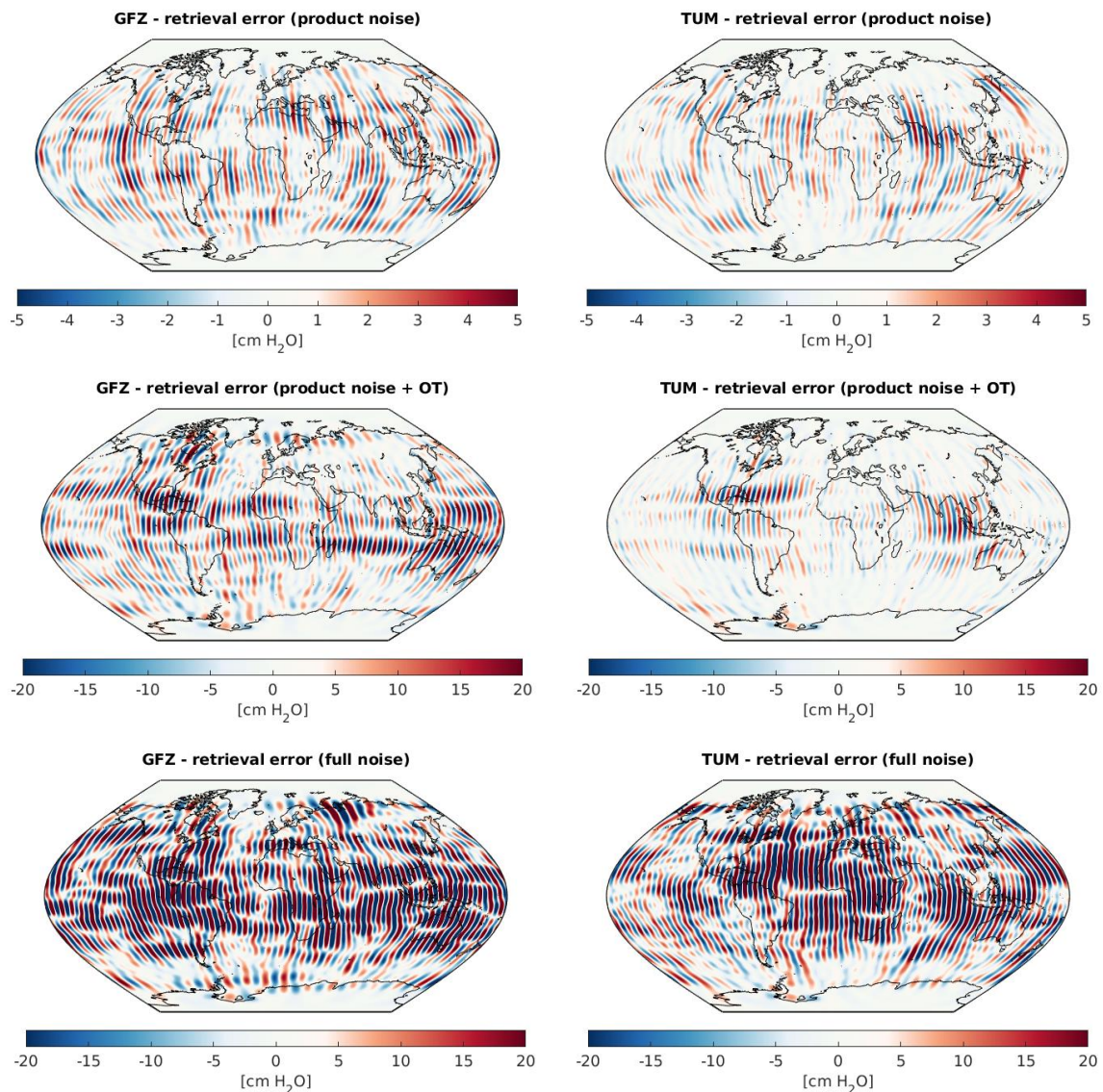
Figure 20-20: Global grids of gravity field retrieval errors solved up to d/o 50 simulated by GFZ (left) and TUM (right) for the product noise case (top), the product noise + ocean tides case (center) and the full noise case (bottom).

In order to investigate the differences among the product noise + ocean tides result further, tidal signals were included, exclusively, when setting up the pre-fit residuals. Figure 20-21 shows the pre-fit residuals for this case for both simulation groups. The spectrum demonstrates consistency for the majority of the frequencies but reveals a large offset of more than factor 100 at the very short wavelengths caused by the limitations of numerical accuracy at the TUM software. Furthermore, the pre-fits residuals are displayed in the time domain for the first 24 hours showing similar signal amplitudes for both, TUM and GFZ. The residuals can be evaluated in the spatial domain as well where the signals are plotted against the respective trajectory. Figure 20-22 shows the spatially distributes signals in terms of accelerations demonstrating equally distributed signals sof tidal errors. The difference (TUM minus GFZ) plotted in an absolute sense reveals a slightly larger signal error level for TUM compared to

GFZ. This is further confirmed by the standard deviations given with 0.40 nm/s^2 for GFZ and 0.43 nm/s^2 for TUM.
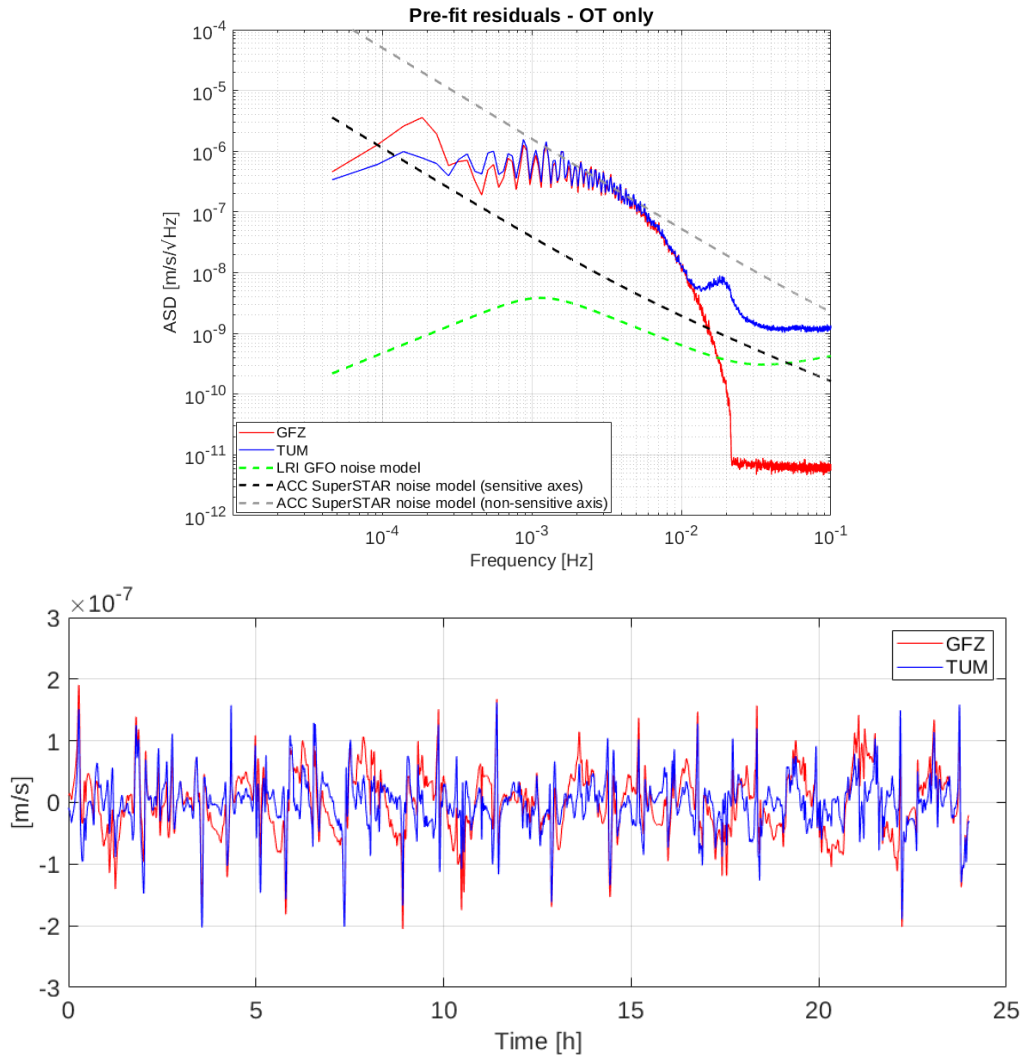
Figure 20-21: Top: Arc-wise averaged ASD of pre-fit residuals of the 3dH (polar pair) scenario in terms of range-rates for the ocean tides only case simulated by GFZ (red) and TUM (blue). The analytical instrument noise models are displayed for SST (green dashed), ACC sensitive axes (black dashed) and ACC non-sensitive axis (grey dashed). Bottom: Pre-fit residuals in the time domain for the first 24 hours.
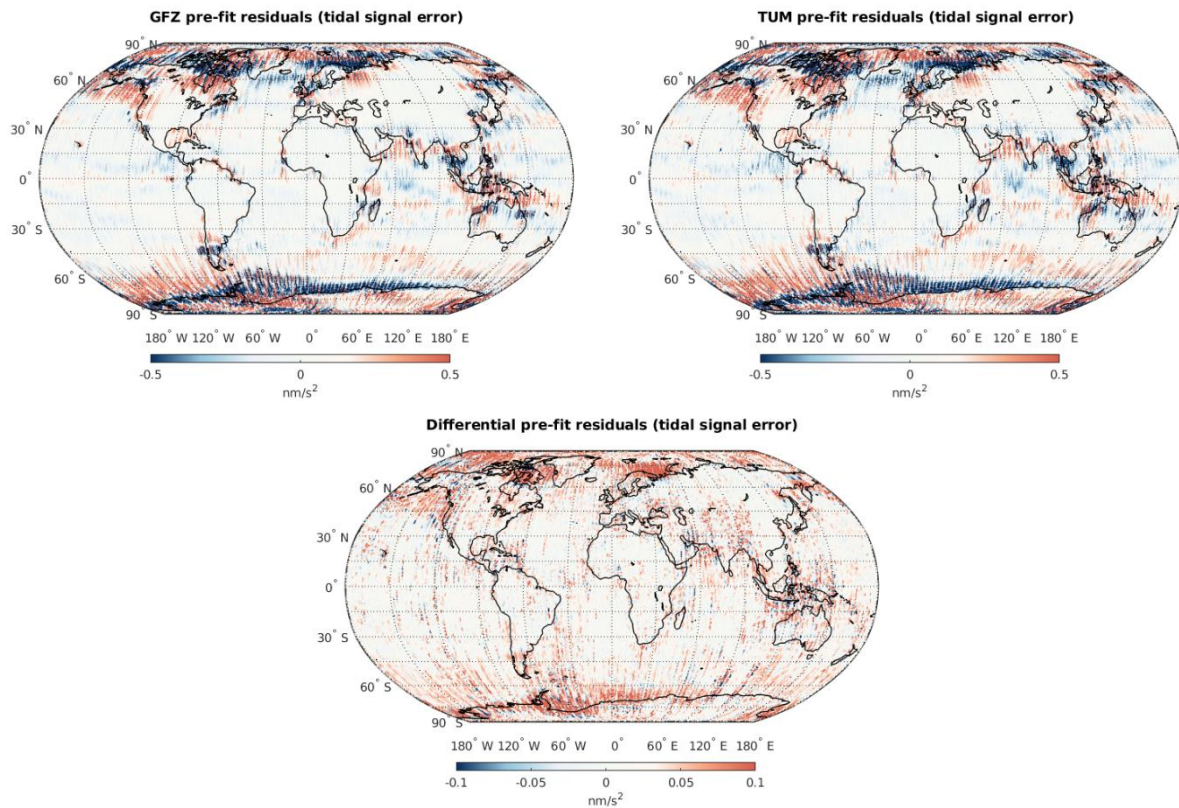
Figure 20-22: Bandpass-filtered pre-fit residuals (passband between 0.15 and 18 mHz) in terms of nm/s^2 for the ocean tide only case simulated by GFZ (top left) and by TUM (top right) together with the absolute difference among both data sets (bottom).

Next to the pre-fit residuals, the disturbing potential due to ocean tides generated during gravity field processing by means of tide models was evaluated in order to check possible differences in the computation of tidal signals for both simulation groups. For this purpose, dimensionless potential coefficients including ocean tide signals originating from the GOT4.7 model, exclusively, were outputted by the simulation software for a specific date. Figure 20-23 depicts the tidal signal for both groups together with the corresponding difference. While the full signal results do not show differences, as expected, the differential plots reveal smaller differences among both groups. This might be caused by different conventions for the computation of SH potential from ocean tide models implemented in both software packages. The difference plotted in an absolute sense shows that the signal amplitude of ocean tides generated by the TUM full-scale simulator is slightly larger compared to the one computed by EPOS. However, these differences are more than a factor of 10 smaller than the tidal error signals (difference between two tide models) shown in Figure 20-14 (bottom right) and are not assumed to have an impact on the final gravity field solution, therefore.

The analysis of the output of ocean tide signal from the software as well as the pre-fit analysis indicate correctly propagated tidal signals during gravity field processing for both simulation environments.
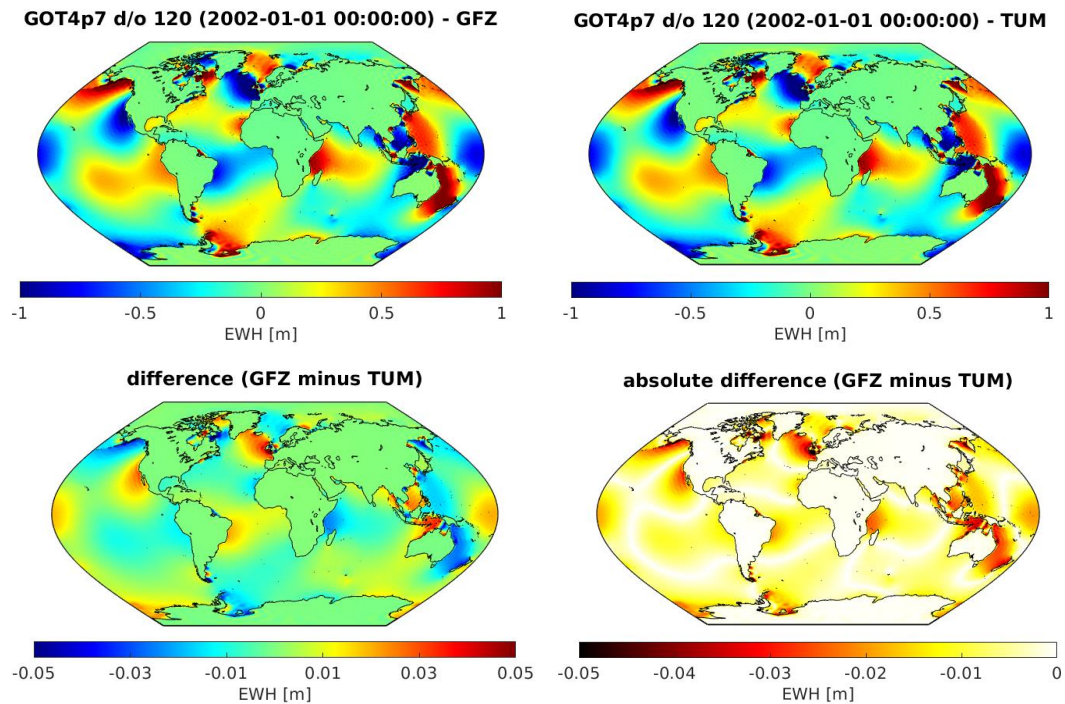
Figure 20-23: Software output of SH potential due to the ocean tide model GOT4.7 in terms of EWH (top) together with the relative difference (bottom left) and the difference in an absolute sense (bottom right).

From Figure 20-18, it can be seen that the very long wavelength signals (around once the orbital frequency and twice) have larger amplitudes in case of GFZ for the product noise case in the frequency domain. The corresponding pre-fit residuals in the time domain, shown in Figure Figure 20-24 (top), show larger signal amplitudes for GFZ, therefore. This is further confirmed in the spatial domain as shown in Figure 20-25 (top). The signal in the very low frequency band is dominated by the noise of the ACC, which is even larger than the tidal error signal. This can be seen when comparing the very low frequency band in Figure 20-18 and Figure 20-21 (top). We assume that the larger signal amplitudes due to the ACC for GFZ in the very low frequency spectrum compared to TUM is related to a longer arc length (24 h for GFZ vs. 6 h for TUM). Longer arcs lead to the inclusion of more information at the longer wavelength spectrum. For GFZ, the larger signal amplitudes due to ACC lead to increased amplitudes for the ocean tides + product noise case due to superposition, as it can be seen in Figure 20-24 (bottom). Therefore, Figure 20-25 (bottom) shows larger randomly distributed signals for GFZ compared to TUM.
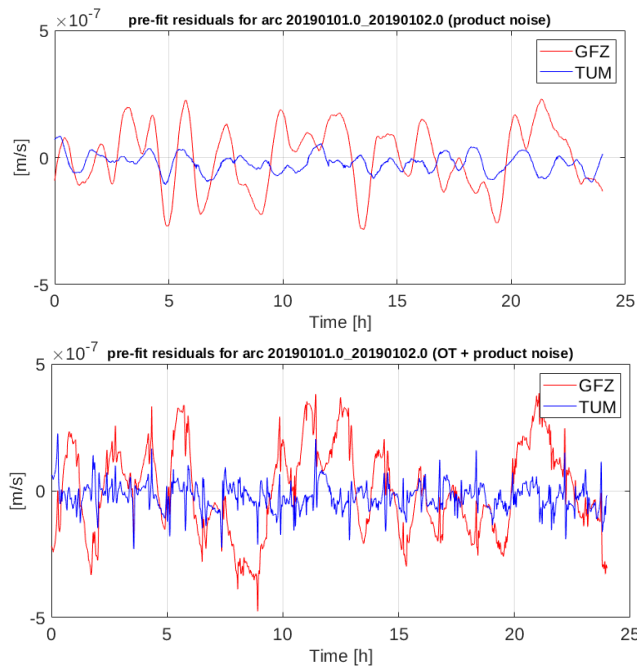
Figure 20-24: Pre-fit residuals in the time domain for the first 24 hours for the product noise case (top) and the ocean tides + product noise case (bottom).
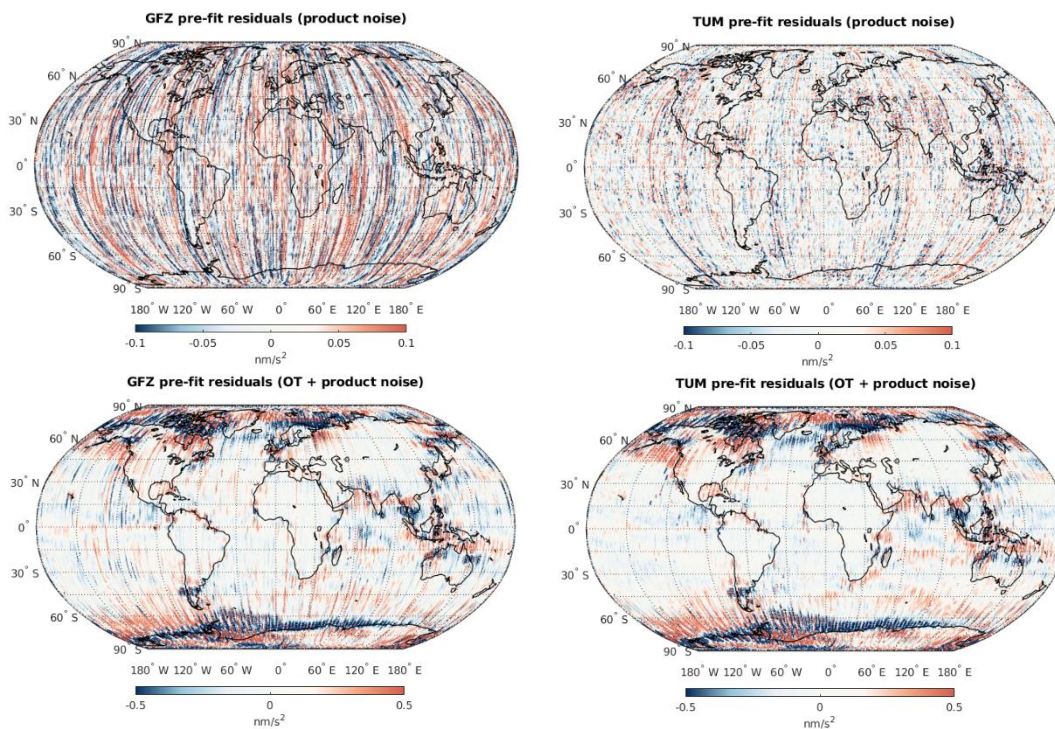
Figure 20-25: Bandpass-filtered pre-fit residuals (passband between 0.15 and 18 mHz) in terms of nm/s² for the product noise case (top) and the ocean tides + product noise case (bottom) simulated by GFZ (left) and by TUM (right).

Despite the fact of larger signal amplitudes due to ACC on GFZ side, the resulting gravity field solutions of TUM and GFZ are relatively similar for the product noise case with only slightly larger errors for the GFZ result. In order to better understand this issue, pre-fit residuals were filtered or weighted with the corresponding weighted matrices, according to the underlying stochastic model, similar to what is done in the simulation. Figure 20-26 depicts the filtered residuals in the time domain for the product noise case and the ocean tides + product noise case. After filtering, residuals show similar amplitudes for both, GFZ and TUM, for the product noise case, in general. However, GFZ signals reveal larger amplitudes at the beginning of specific arcs which are assumed to be caused by filter warming effects affecting additional consecutive epochs after the first epoch of a dedicated arc. Large amplitudes for TUM signals are related to filter warming effects at the beginning of each 6 hour arc (6, 12, 18 and 24 h). The filtered residuals for the ocean tides + product noise case show larger amplitudes for GFZ compared to TUM. It is assumed that the larger signal amplitudes for GFZ already visible at the unfiltered residuals (cf. Figure 20-24) ,which are caused by superposition of larger instrument noise with ocean tide signals, mirrors in the filtered case as well.
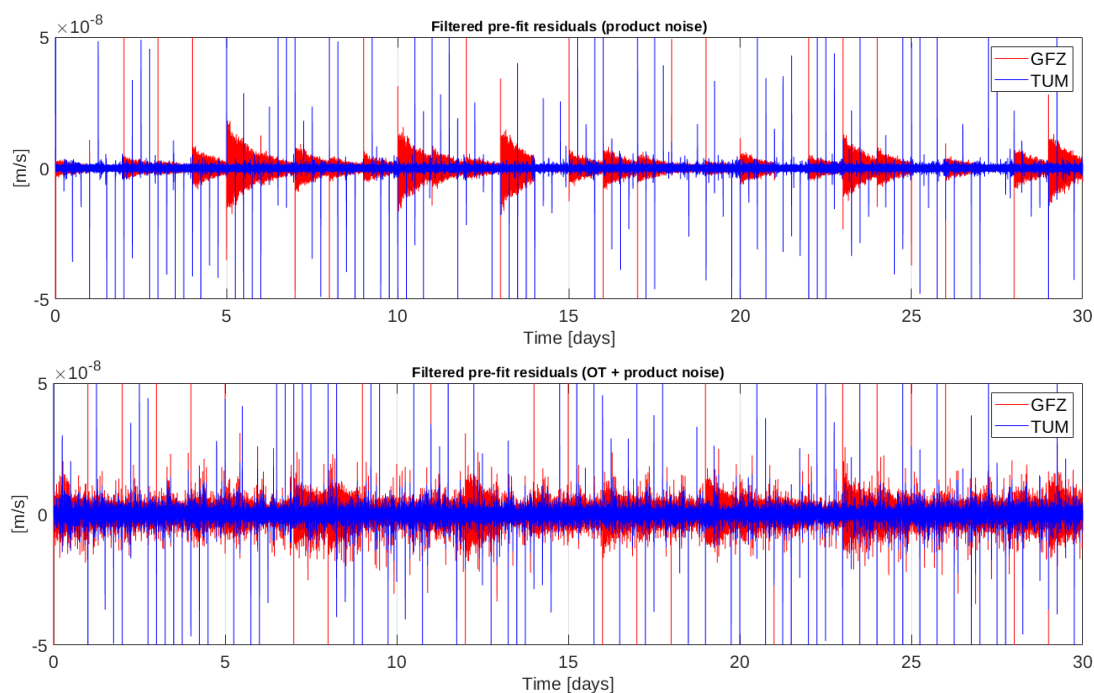
Figure 20-26: Filtered pre-fit residuals in the time domain for 30 days for the product noise case (top) and the ocean tides + product noise case (bottom).

Figure 20-27 shows the unfiltered versus the filtered signal in the frequency domain. In case of product noise, the GFZ and TUM filtered signals show an almost white noise performance which can be expected, as the stochastic model approximates the noise of ACC and LRI. The ASD for the ocean tides + product noise case. Now, no noise whitening is expected as tidal signals are included, additionally. Both spectra, product noise and OT + product noise, show a larger signal amplitude level for the filtered residuals in case of GFZ confirming the larger signal amplitudes in the time domain.
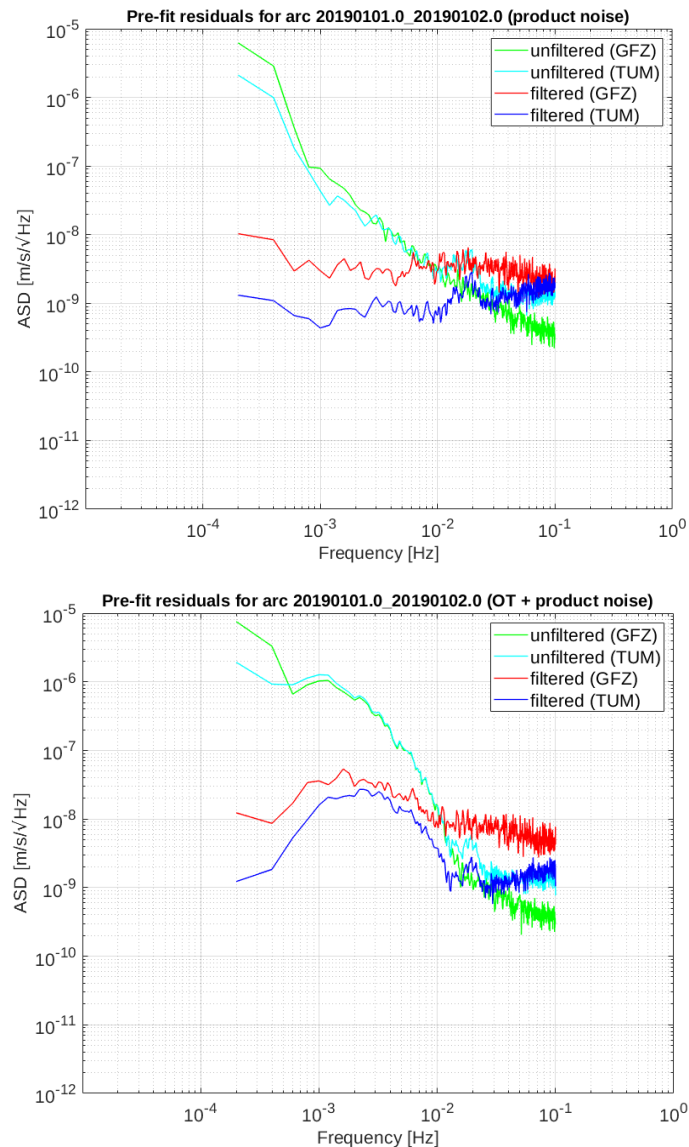
Figure 20-27: ASD of unfiltered (green and cyan) and filtered (red and blue) pre-fit residuals of the 3dH (polar pair) scenario in terms of range-rates for the product noise case (top) and the ocean tides + product noise case (bottom).

Based on this analysis, we assume that the larger signal amplitudes for GFZ at the very low frequency spectrum originating from the ACC noise increase the signal amplitudes of the ocean tides in a greater extent than it is happening for the signals at TUM software, when simulating the case ocean tides + product noise. This might be the reason for the differences in the retrieval errors for the ocean tides + product noise case. The similar results for TUM and GFZ for the product noise case indicate that the filter functions applied at both software packages are not causing a larger discrepancy in the recovered gravity field solution. In case of full noise simulations, aliasing errors due to non-tidal signals dominate the spectrum so that the impact of the increased instrument noise amplitudes caused by a longer arc length is negligible.

20.4 EVALUATION OF SELECTED SCENARIOS

The selected scenarios described in chapter 20.2 were further validated against simulations executed by other groups. The inter-comparison should demonstrate that consistent simulation results can be achieved assuming identical satellite orbits, background models and instrument noise characterization. At the same time, the comparison should show that the simulations that have been presented in this study are plausible. The comparison is restricted to degree error amplitudes.

Figure 20-28 displays the retrieval error for the 3dH Bender case simulated for 7-day and 30/31-day retrieval by TUM and GFZ. The results show a consistent performance over the whole spectrum. Slightly larger errors are visible for the GFZ solutions, as already seen for the ADDCON test scenario.

In Figure 20-29 the monthly gravity field retrieval error of the AP configuration is displayed. The comparison among the CNES (red) and GFZ (dark blue) solutions shows consistency from d/o 40 and up but shows an offset at the lower degrees. This is caused by the fact that the simulated polar in-line pair of CNES has a significantly degraded performance compared to the GFZ solution (result not shown here). The corresponding TUM solution (grey) suffers from the less-sensitive ACC cross-track axis due to a sub-optimal implementation of the ACC coordinate system in the software. Therefore, simulations were run by assuming three sensitive ACC axes where the resulting solutions of TUM and GFZ (green and orange) demonstrate consistency over the whole spectrum. Next to the AP configuration, the 3dH Bender case is displayed as well (identical to results shown in Figure 20-28) due to reasons of comparison wrt. the AP configuration.

Figure 20-30 displays the comparison among GFZ and JPL simulated solutions. It is to mention that the simulation results of JPL are based on a different observation period (January 2006 instead of January 2002) as well as different background models and instrument noise assumptions. This should be considered during comparison. The largest differences are the following ones:

- Static gravity field: ggm05c
- Ocean tide models: GOT4.7 and FES2014
- Non-tidal atmosphere and ocean: AOD RL05 and DEAL + AOerr (ESA Earth system model)
- Hydrology and ice: ESA Earth system model
- ACC noise for polar pair and pendulum: sensitive axes perform about a factor of 2 better (in terms of ASD m/s/sqrt(Hz)) than assumed in this study. Non-sensitive axis performs about a factor of 5 better (in terms of ASD m/s/sqrt(Hz)) than assumed in this study.
- ACC noise for inclined pair: MicroSTAR was assumed where axes perform about a factor of 5 better (in terms of ASD m/s/sqrt(Hz)) than assumed in this study.

Simulated AP solutions from JPL and GFZ match against each other for a large part of the spectrum in terms of course. This is valid for both ACC noise assumptions, considering one less-sensitive cross-track axis (green and blue solutions) as well as three sensitive axes (orange and yellow solutions). However, a small offset is visible among the corresponding AP simulations of GFZ and JPL which is assumed to be caused by the discussed differences in the simulation assumptions. The very low degrees of the JPL solutions suffer from sub-optimal balancing of hl-SST and ll-SST observations and should therefore considered with care. Additionally, the 3dH Bender case solutions of GFZ and JPL were compared against each other showing consistency over the largest part of the spectrum.

The inter-comparison among different groups demonstrates that simulation results match against each other, generally. Therefore, results, which have been presented in this study so far, can be considered as realistic.
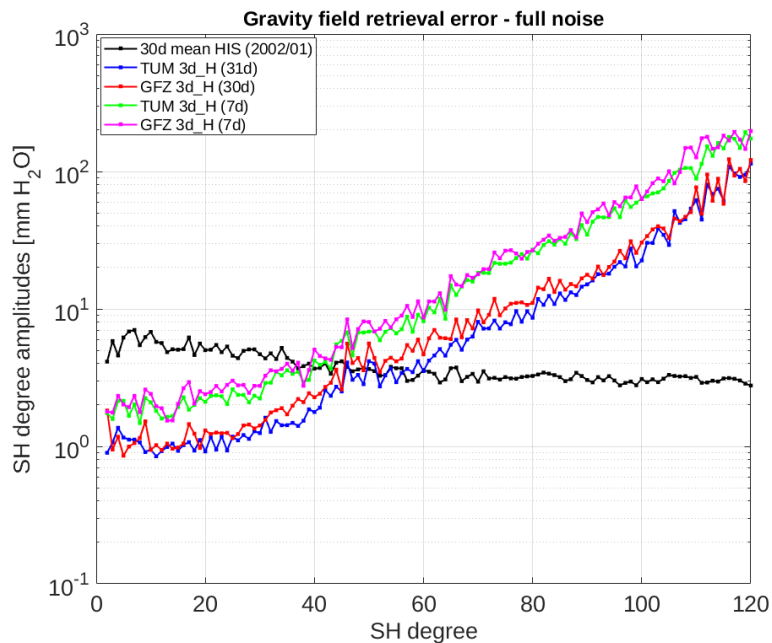
Figure 20-28: Full noise solutions of the 3d_H Bender scenario simulated by GFZ (red and magenta) and TUM (blue and green) in terms of SH degree error amplitudes. The monthly averaged HIS signal is displayed in black.
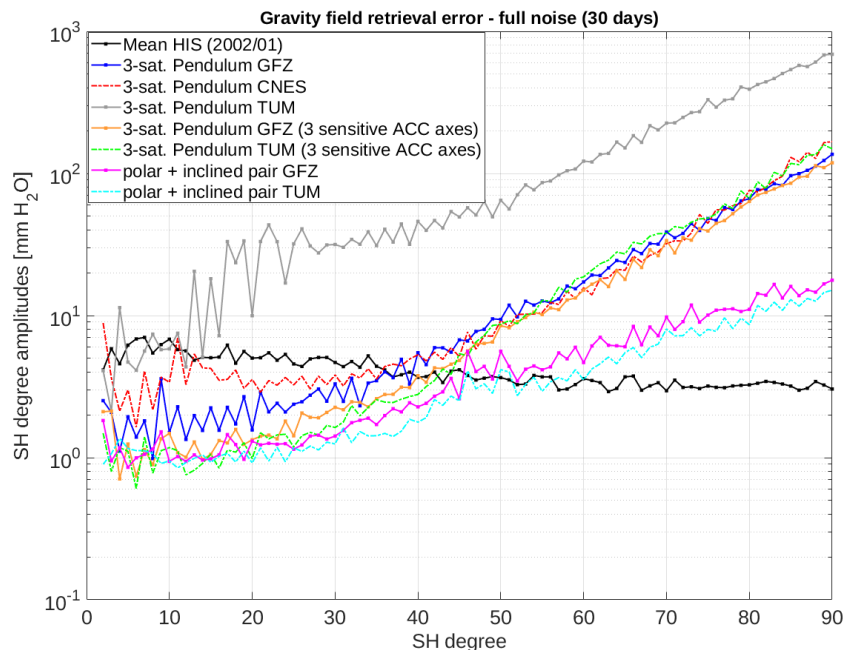
Figure 20-29: SH degree amplitudes of the AP configuration simulated by GFZ (blue), CNES (red) and TUM (grey) and assuming 3 sensitive ACC axes, simulated by GFZ (orange) and TUM (green). Additionally, solutions of the 3d_H Bender case are displayed, simulated by GFZ (magenta) and TUM (cyan). The 30-day averaged HIS signal is displayed in black.
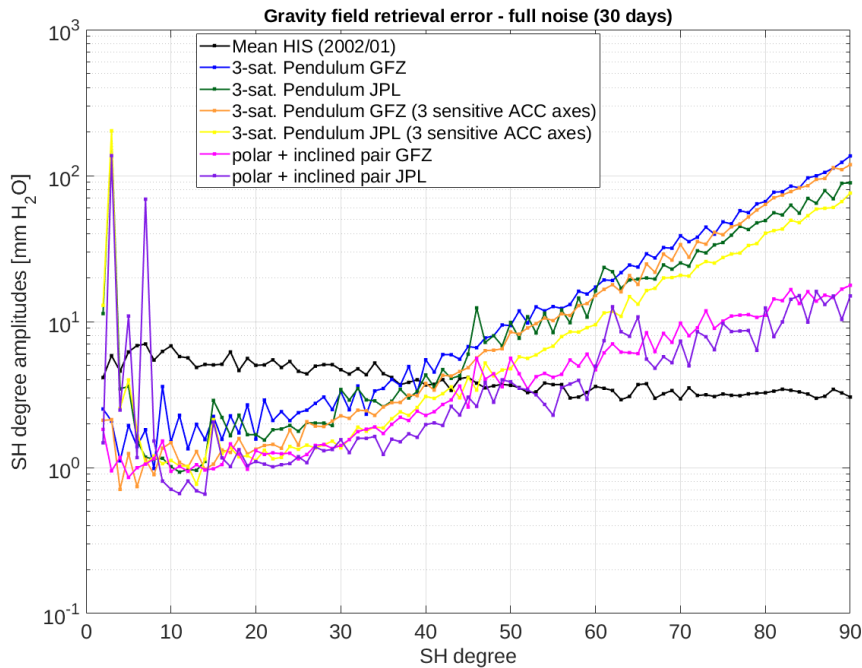
Figure 20-30: SH degree amplitudes of the AP configuration simulated by GFZ (blue) and JPL (green) and assuming 3 sensitive ACC axes, simulated by GFZ (orange) and JPL (yellow). Additionally, solutions of the 3d_H Bender case are displayed, simulated by GFZ (magenta) and JPL (purple). The 30-day averaged HIS signal is displayed in black.

All results presented in section 20.3 are related to the nominal processing scheme. As it is planned to apply advanced processing strategies, such as the Wiese approach, an inter-comparison among such solutions produced by TUM and GFZ software packages shall be done before starting the simulations of dedicated scenarios. The comparison was executed at the example of the 3d_H Bender scenario applying the co-estimation of short-term gravity field parameters together with the long-term gravity field coefficients (Wiese approach).

Figure 20-31 shows the long-term 30-day solutions generated by the TUM full-scale simulator and the GFZ EPOS software. The corresponding short-term parameters were set up on a daily basis up to a maximum d/o 15. During processing no AO de-aliasing product has been used thus the full AOHIS signal is included in the estimated gravity field parameters. Results demonstrate consistency over the whole spectrum with slightly larger error for the GFZ solution at shorter wavelengths. In Figure 20-32 results are displayed for two chosen 7-day retrieval blocks of the 3d_H scenario, demonstrating even larger consistency. Dedicated short-term solutions are shown in Figure 20-33 at the example of the 30-day retrieval. Again, consistency is reached for both software packages.
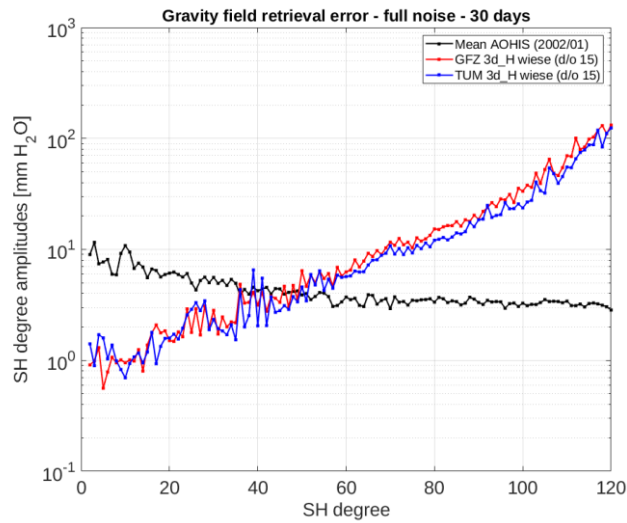
Figure 20-31: Long-term Wiese solutions for a 30-day retrieval of the 3d_H Bender scenario simulated by GFZ (red) and TUM (blue) in terms of SH degree error amplitudes. The monthly averaged AOHIS signal is displayed in black.
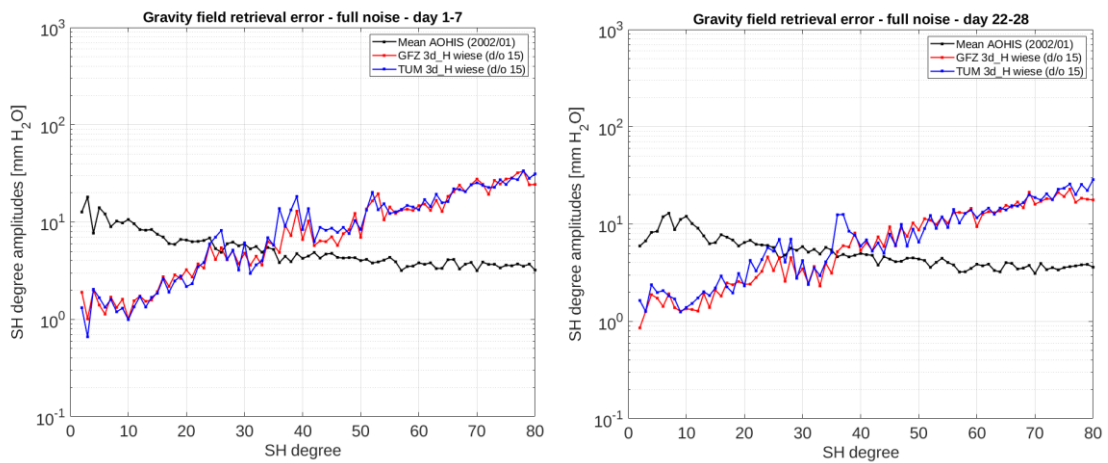
Figure 20-32: Long-term Wiese solutions for two 7-day retrieval periods (left: day 1-7, right: day 22-28) of the 3d_H Bender scenario simulated by GFZ (red) and TUM (blue) in terms of SH degree error amplitudes. The averaged AOHIS signal is displayed in black.
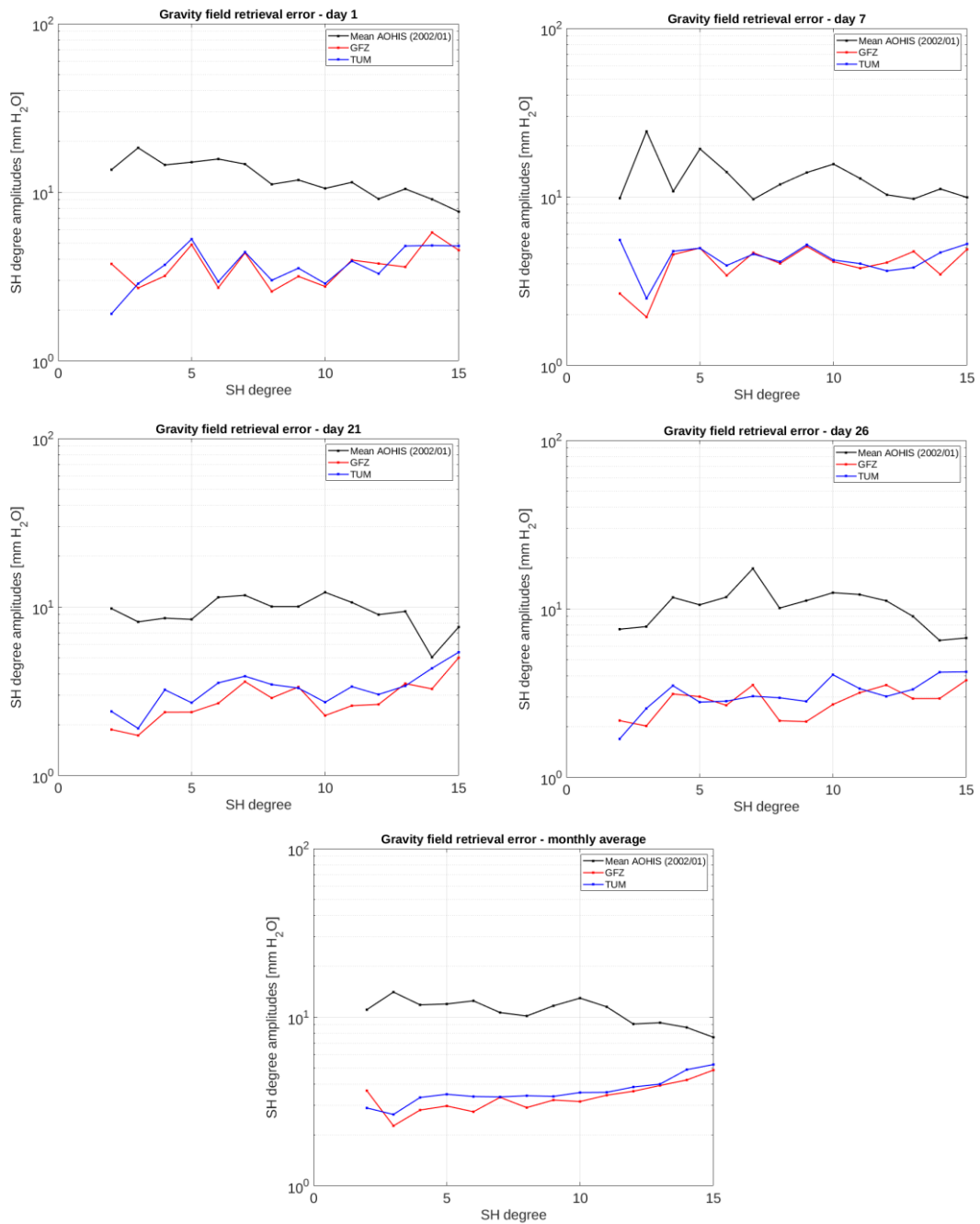
Figure 20-33: Short-term Wiese solutions for a 30-day retrieval period (top left: day 1, top right: day 7, center left: day 21, center right: day 26, bottom: 30-day average) of the 3d_H Bender scenario simulated by GFZ (red) and TUM (blue) in terms of SH degree error amplitudes. The averaged AOHIS signal is displayed in black.

21 APPLICABLE DOCUMENTS, REFERENCE DOCUMENTS, AND PUBLICATIONS TO PART 2

21.1 APPLICABLE DOCUMENTS

[AD-1] Mission Requirements Document, Next Generation Gravity Mission as a Mass-change And Geosciences International Constellation (MAGIC) - A joint ESA/NASA double-pair mission based on NASA's MCDO and ESA's NGGM studies (2020). ESA-EOPSM-FMCC-MRD-3785

[AD-2] Scientific Readiness Levels (SRL) Handbook, Issue 1, Revision 0, 05-08-2015

[AD-3] Statement of Work - ESA Express Procurement - EXPRO NGGM/MAGIC science support study during Phase A, Issue 1, Revision 0, 18/01/2021 Ref ESA-EOPSM-FUTM-SOW-3813

21.2 REFERENCE DOCUMENTS

[RD-1] Dahle C., Murboeck M., Flechtner F., Dobslaw H., Michalak G., Neumayer KH., Abrykosov O., Reinhold A., Koenig R., Sulzbach R., Foerste C. (2019) The GFZ GRACE RL06 Monthly Gravity Field Time Series: Processing Details and Quality Assessment. Remote Sensing, 11(8), 2116. https://doi.org/10.3390/rs11182116

PART 3:

DORIS AIDED ORBIT AND GRAVITY FIELD DETERMINATION

22 INTRODUCTION

This Part 3 refers to Task 3 of the SoW and covers the work performed under WP 300 of the WBS. It refers to the deliverable document TN D7 "DORIS aided orbit and gravity field determination".

The main purpose is to study DORIS aided precise orbit determination and related impacts on gravity field determination and to evaluate and quantify the added value of DORIS.

23   EMBARKING DORIS RECEIVERS – CNES

In order to study the impact of embarking DORIS receivers on board of the gravity field satellites, gravity field retrieval (Section 23.3) have been conducted for the scenario 3d_H as outlined in [RD-1].
It will be assessed if DORIS, in addition to precise cm-level kinematic orbit solutions derived from GNSS observations, has the capability to enhance the quality of retrieved temporal gravity field models and to enhance the calibration of accelerometers. The use of satellite tandems allows to form differential DORIS observations, which mitigates some common errors such as tropospheric delay correction errors. Therefore, the gravity field retrieval and accelerometer calibration simulations will include solutions based on both absolute and differential DORIS observations.
Section 23.3 presents an analysis of Sentinel 3A/B DORIS residuals while in the tandem phase, which enables analysis of a real case of differential DORIS residuals even if at the altitude of 800 km. Section 23.4 describes the gravity field retrieval simulations and the results.

23.1 DORIS PROCESSING FOR SATELLITES IN TANDEM ORBIT

The general objective of this study is to improve the Doris processing for satellites in tandem flight. When two satellites are sufficiently close, it may be possible to constrain some common measurement parameters between the two satellites. For example, the beacon frequency or the vertical troposphere delay is common to the measurements acquired simultaneously on both satellites.

This approach is widely used in GNSS processing: the clocks contributions can be removed by constructing single differences (SD) or double differences (DD). For Doris it may be not so simple because for low orbits, the common views may be not so frequent as between two GNSS receivers. The two satellites must be close enough (less than a few hundred kilometers) to measure the same beacon, and due to the low altitude, simultaneous view of two beacons by the same satellite may be not very frequent.

A publication [RD-13] proposed to process directly the measurements in a dedicated receiver. Nominally this could remove the effect of the on board oscillator (USO) by processing two beacons which are in common view. However, the proposed approach has some limitations:
    - this allows only the on board frequency contribution elimination (SD between beacons for one satellite), this imposes also a new hardware, or at least a new instrument processing.

- it is not suited for two receivers (for close satellites) to remove the beacon frequency contribution, because the signal processing cannot be performed directly on the received signals by the two satellites.

Thus we propose to use directly the phase measurements which are now available in the Doris measurements files and test the differential processing characteristics, in a similar way as the GNSS measurements. This means that if a good synchronization is achieved, the SD or DD processing can be performed using the standard Doris phase measurements. There are multiple advantages to process this way:

- a new hardware development is not needed, and the differential processing can be extended on SD between satellites,
- this can be tested/validated on flight measurements (for example using the Sentinel 3A and 3B tandem phase),
- new formulations can be easily tested.

23.2 DIFFERENTIAL DORIS PROCESSING

The objective of differential processing is to remove the contributions of common errors between two measurements. This is very interesting when no model is available for such errors, like clocks errors. This approach is widely used in GNSS processing (double differences eliminate both transmitter and receiver clocks).

But other effects can be removed, for example in GNSS when we have a short baseline, the common ionosphere propagation effect can also be eliminated, because the GNSS satellite is very far from the GNSS receivers, and the propagation paths through the ionosphere are very close. However, in the Doris case, the baselines between the satellites or the beacons are too important to have sufficiently close propagation paths.

Figure 23-1 shows shows the geometry of the Sentinel satellites 3A and 3B tandem phase. The two beacons A and B are usually not very close. The two satellites are flying 30 s apart on the same ground track.

In this configuration there is a significant overlap between S3a and S3b measurements on a single beacon. A single pass can have a duration of 600 s (60 measurements), the sampling is 10 s, and the distance between the satellites corresponds to 3 samples: in this case there will be 57 common measurements epochs. This SD processing between S3A and S3B measurements can be performed continuously along the orbit. This removes the beacon frequency contribution.
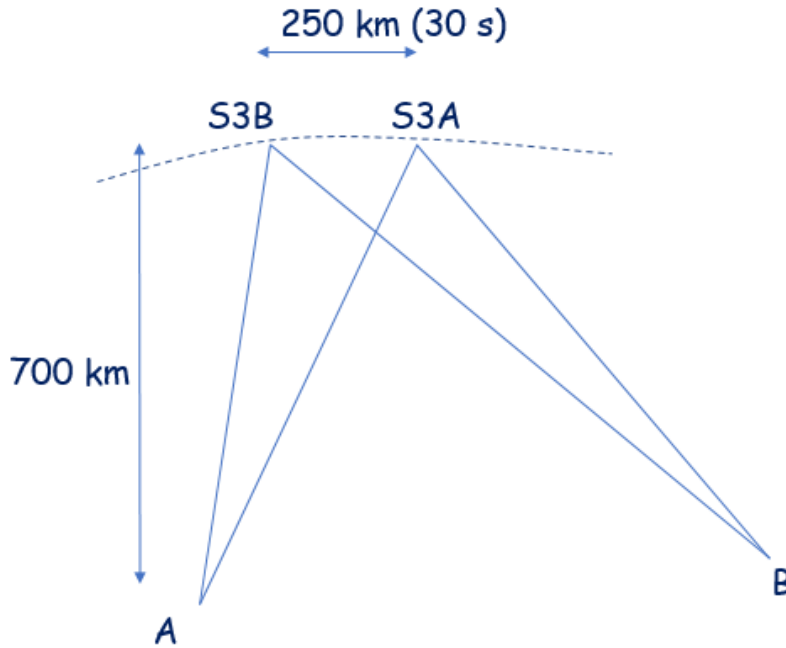
Figure 23-1 Sentinel 3A and 3B geometry during tandem phase.

Due to the distances between the beacons, the overlap between different beacons are usually small, however in some areas these overlaps allow to remove also the satellite frequency contributions. Figure 23-2 shows the Doris network. Common views between beacons are possible in Europe (some very close stations, like Toulouse and Grasse), or in the polar regions.

Figure 23-2 The Doris Network (IGN data).

23.3 DATA PREPARATION

The different steps of the initial data preparation are described for the application on Sentinel 3A and 3B. For these satellites, precise GNSS orbits are available with a 3D precision of a few centimeters (order of magnitude: 1 cm RMS in the radial direction and 5 cm in the tangential direction).

The objective is to investigate the characteristics of the different relative processing which can be performed using the Doris phase measurements. So we first construct the phase residuals for each satellite using the standard Doris processing:

- the timing alignment is performed independently on both satellites using the standard processing (polynomial clock adjusted on the pseudo-range measurements)

- the beacon frequency and zenith troposphere delay (ZTD) are adjusted per pass, independently for the two satellites.

- the elevation threshold is 8 degrees.

- an elimination of some outliers is performed to remove possible cycle slips. This is necessary because all available phase measurements are used in this residuals computation, without any a priori elimination from, for example, the Doris orbits processing.

After this preparation step, it is important to notice that some inconsistencies are present. The timing is independent between the two satellites, so it is necessary to verify that the measurement epochs are sufficiently close to obtain a correct SD processing between both satellites.

Figure 23-3 shows the timing characteristics for cycle 04 (7-day arcs). These are the measurement epochs in TAI. The measurement epochs are slightly drifting due to the on board USO frequency biases, which are different for both satellites. When the time offset is too important, the instrument performs a correction in order to remain close to the reference time. We observe on Figure 23-3 that the measurement events have a 0.015 s difference between both satellites. This means that a SD processing will have a remaining error for the beacon clock corresponding to his variation during this duration. This should be negligible (millimeters).
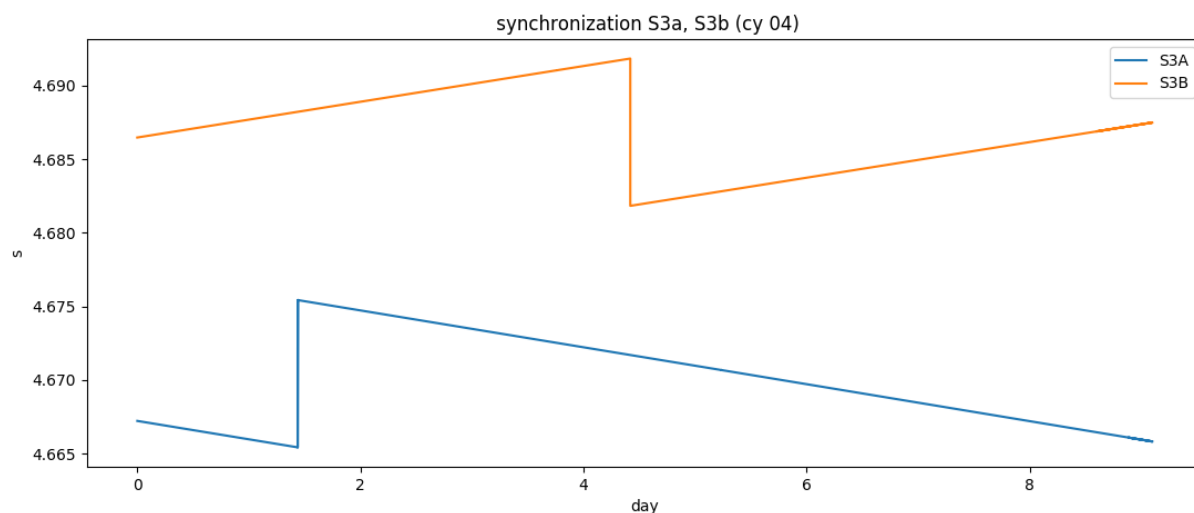
Figure 23-3 TAI measurement epochs for both satellites, cycle 04.

Also, the Tropospheric delay (ZTD) and beacon frequency must be corrected to have identical values on both satellites. The residuals are corrected to have a common ZTD value using the average of the adjusted ZTD on both satellites.

23.4 RESULTS

SD1 and SD2 single differences formulations

Figure 23-4 shows the residuals obtained for both satellites, and the single differences between the two satellites. There is one color for each beacon. A continuous phase measurement is shown by a continuous line.

The two top frames are the independent residuals obtained for S3A and S3B. The two bottom frames show single difference results. There are two cases:

  - common epoch: the difference is directly the difference of the S3B and S3A measurements performed at the same epoch: $r\_SD1 = r\_S3B(t) – r\_S3A(t)$. This is named SD1 (third frame).

  - common orbit position: for the Sentinel 3A,3B tandem phase, the two satellites are flying with 30 s (3 measurement samples) delay on the same ground track. So if the residuals are shifted by 3 samples, we have another interesting single difference processing, which does not remove completely the beacon clock contribution, but may remove efficiently some other effects related to the relative geometry between the satellite and the beacon (environment effects like multipath …): $r\_SD2 = r\_S3B(t) – r\_S3A(t+30 s)$. This is named SD2 (fourth frame).
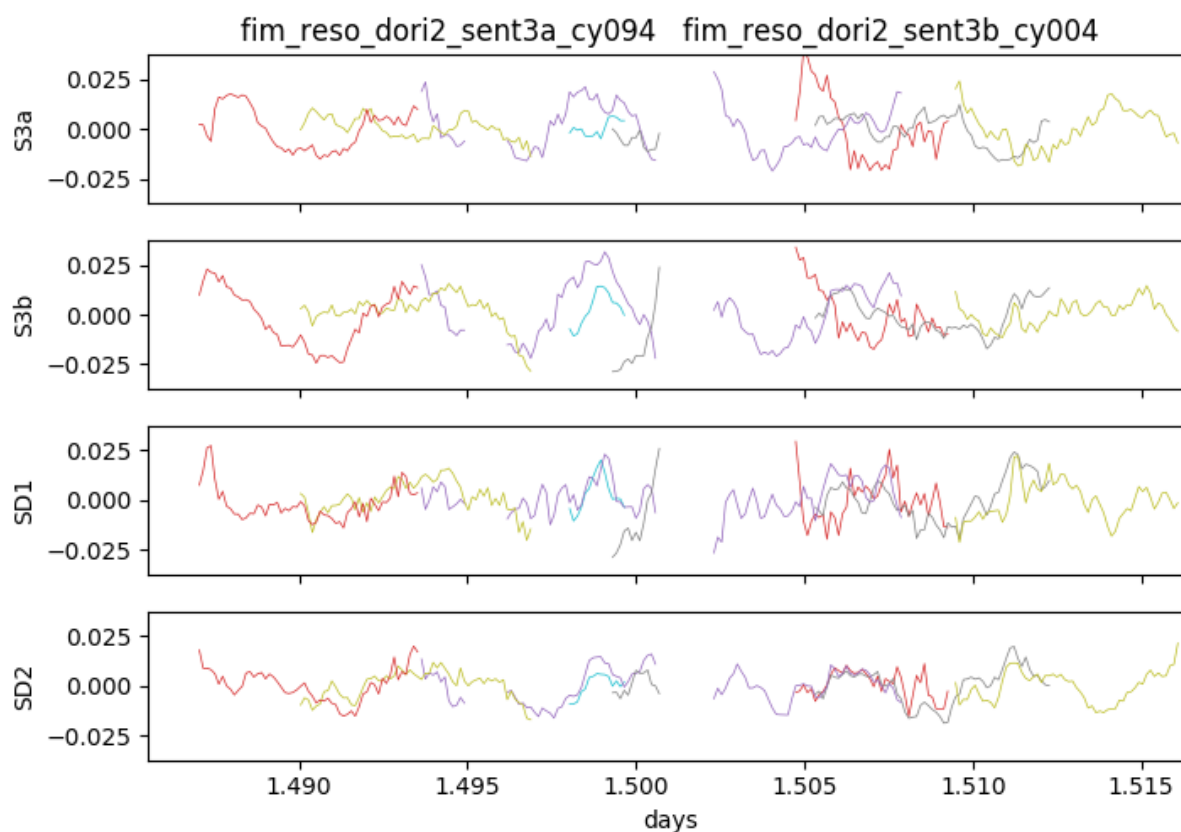
Figure 23-4 S3A and S3B dual frequency phase residuals, and two single differences SD1 (common epochs), and SD2 (common geometry).

In Figure 23-4, we can observe the following properties:

  - on the individual residuals, the residuals may be different between different beacons. This is due to the beacon frequencies which behave independently. The satellite frequency is common to all beacons, so the satellite frequency contribution will produce common variations in the beacons residuals.

  - for the SD1 processing, the beacons frequency effects are clearly removed, the different beacons have a clear common variation, which corresponds to the difference of the S3B and S3A clocks.

  - for the SD2 processing, the important observation is that the short term noise in the residuals is significantly lower than the noise observed on the SD1 case. The overlapping between different beacons residuals is clearly better. For example, if we look at the three passes between the epochs 1.505 and 1.510 the residuals are quasi identical for case SD2, and reflect the S3B and S3A oscillators differences, with a 30 s shift.

Global SD1 and SD2 results on the network

The residuals shown on Figure 23-5 are now analyzed in a global way, a RMS value is computed for each beacon. This is shown in Figure 23-5, for the S3A and S3B independent phase residuals, and for the SD1 and SD2 processing.
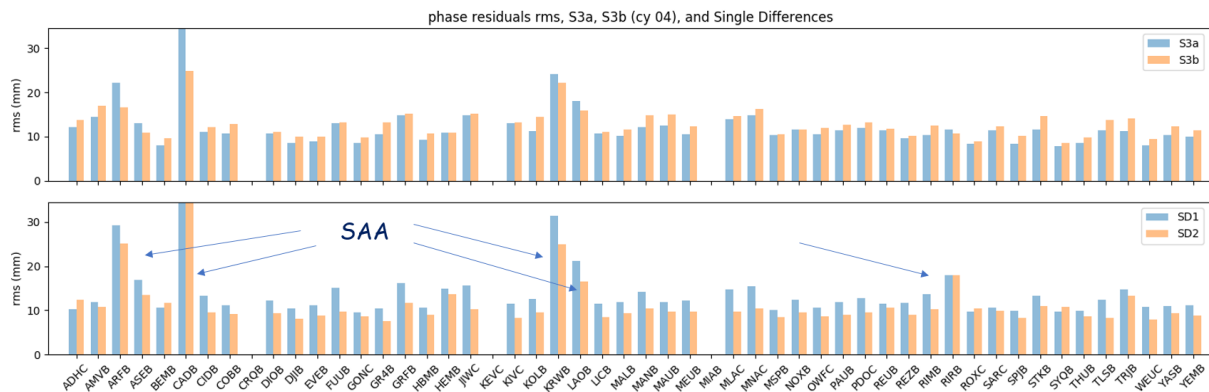
Figure 23-5 S3A and S3B dual frequency phase residuals, and two single differences SD1 (common epochs), and SD2 (common geometry), rms for each beacon.

In Figure 23-5, top frame, the RMS values are similar for both satellites. Some beacons have higher results on both satellites, they correspond to stations located under the south Atlantic anomaly (SAA). The increase of the RMS is due to rapid variations of the on board USO frequency. S3A has a slightly better performance than S3B for almost all beacons, except on the SAA beacons, where the RMS for S3A is significantly higher. The S3A USO is probably more affected by the SAA.

The bottom frame shows the results for the SD1 and SD2 processing cases. This confirms the observation made in Figure 23-5 that the noise in the SD2 residuals is significantly lower than the noise on the SD1 residuals. Now the SAA beacons are clearly visible, and the RMS values are higher than in the top frame due to the contribution of the SAA USO effects from the two satellites. For the beacons outside SAA, the RMS values for SD2 processing are very stable around 9 - 10 mm.

So we can conclude that removing the common geometry effect (SD2 case) is more efficient event if there is a more important contribution of the beacon clocks errors than in the SD1 case.

Double differences

Now it is possible to study the double differences (DD) for the overlapping passes (Figure 23-4). To have realistic comparisons between the DD1 (corresponding to SD1) and DD2 cases, the SAA stations (ARFB, ASEB, CADB, KRWB, LAOB, RIRB) are removed from the data set. Normally the DD1 processing should remove efficiently the contribution of these stations, this was not studied here.

The DD processing is performed by constructing for each beacon the differences of the SD results with all other beacons. Only the DD passes with more than 6 measurements (60 s) are used. Figure 23-6 shows the RMS of these double differences for all passes corresponding to a given beacon, from the SD1 case (DD1). Figure 23-7 shows the same results for the SD2 case (DD2).
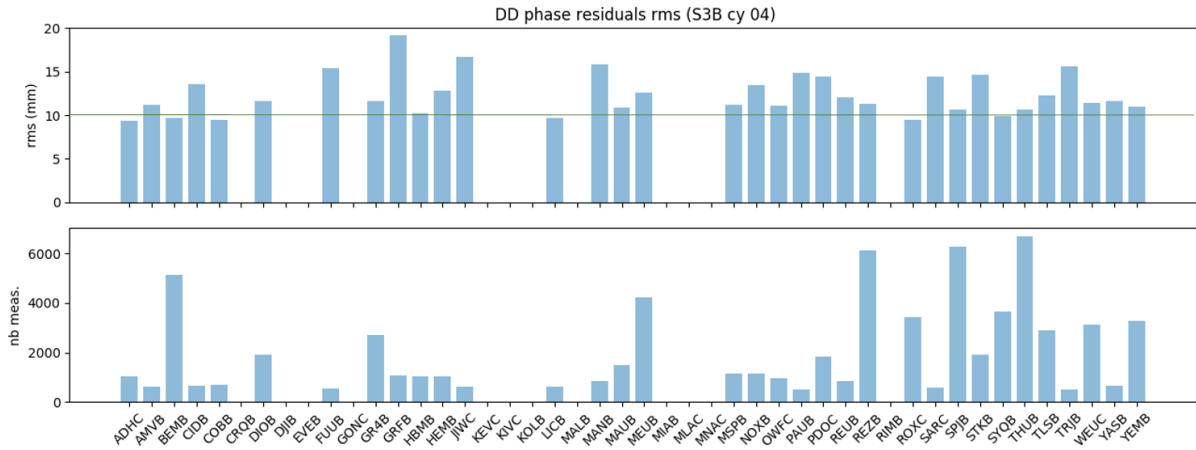
Figure 23-6 double differences results for the common time case (SD1 --> DD1).
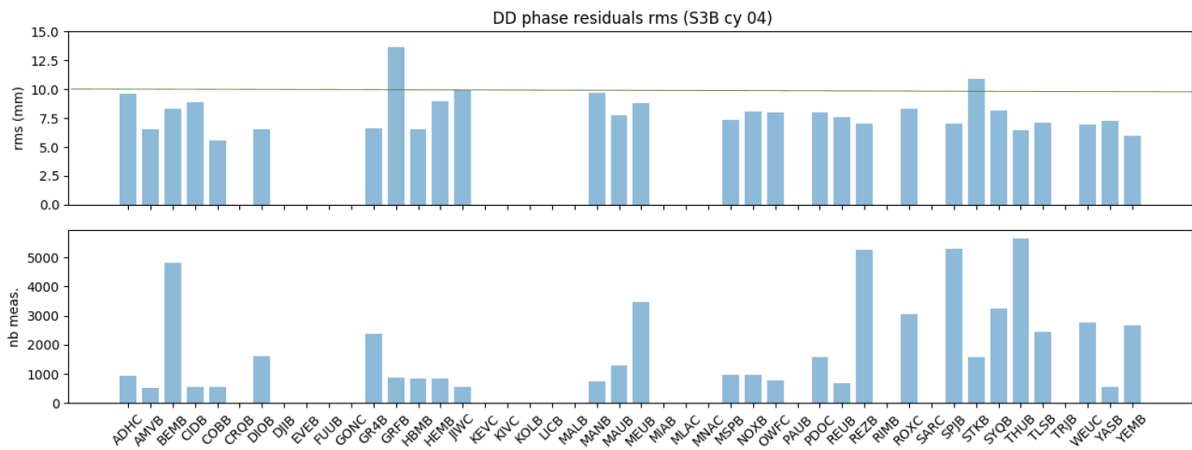
Figure 23-7 double differences results for the common geometry case (SD2 --> DD2).

In Figure 23-6the RMS values are between 9 and 15 mm. There are only few beacons that have a significant number of DD measurements (BEMB, MEUB, REZB, SPJB, THUB, see Figure 23-2). For these beacons the RMS values are around 11-12 mm.

For the order of magnitude of the orbit errors contributions, the following estimation can be done: for a 1 cm periodic error, this corresponds to a velocity error of 10^{-5} m/s (error supposed at orbital period). For a duration of 500 s (most DD passes are shorter than that) this produces a 5 mm error. We have to sum the errors of the two satellites, and also the local orbit error may be at higher frequencies, and maybe higher also than the RMS performance of 1 cm. So a small part of these residuals can be due to the orbit errors (worst case).

23.5 CONCLUSIONS SENTINEL STUDY

Using the Sentinel 3A and 3B tandem phase, and the Doris phase measurements, it was possible to investigate the possible performances (for dual frequency phase measurements) of different single differences (SD) and double differences (DD) processing.

The initial objective of the differential processing is to remove clock contributions as in GNSS processing. Due to the particular geometry of the problem (close satellites, low orbits, distant beacons), the satellite-satellite single differences have first been studied. This single difference processing shows an efficient removal of the beacon clock variations (same time difference).

Another possibility (thanks to the specific geometry of the S3B-S3A tandem phase), is to construct the differences between measurements obtained at the same ground track location (performed at different times, here 30 s delay). This single difference processing (same geometry difference) shows better results than the classical case. The errors due to remaining environmental effects (troposphere, ionosphere, multipath…) are efficiently removed by this approach, and the increased contribution of the clocks errors (that is the beacon clock variation during 30 s) is not so important. This should be studied more in details using the characteristics of the Doris USOs.

These results are confirmed by the corresponding double differences processing (same time double difference, same geometry double difference). The double difference processing allows the elimination of the on board clock error contribution. However, due to the network repartition (distant beacons), only few beacons are sufficiently close to produce a correct number of double-differences observations. This processing remains interesting to check some performances at few points of the orbit.

24 CNES GRAVITY FIELD RETRIEVAL SIMULATIONS

The gravity field simulation, presented in Table 24-1, was setup nearly identically to the TU Delft setup, but the observation noise is different. The ll-SST time series for MAGIC provided by TUM was used, which contains all noise due to ll-SST, accelerometer and star trackers. TU Delft has employed the individual noise series for ll-SST, accelerometer and star tracker instead. Secondly, the tropospheric scale factor error and the DORIS station coordinate errors were not used.

Table 24-1 Simulation set-up for scenario **3d_H**. In addition, the error models and estimated parameters are specified.

Period 1-31 January 2002	Period 1-31 January 2002
True force model	• GOCO05s 120x120 • AOHIS 120x120 • Solid-earth tides (IERS) • Ocean tides: EOT11a (120x120) • 3rd body perturbations (JPL ephemeris)
Reference force model = true force model except for:	• AO+AOerr (120x120) [RD-9] • Ocean tides: GOT4.7 (120x120)
Observables generated for 31 days:	• ll-SST @ 5 s • DORIS @ 10 s (10° elevation cut-off) • X,Y,Z position coordinates @ 30 s
Observation noise/errors	• ll-SST: as provided by TUM • DORIS: 0.03 mm/s • X,Y,Z position coordinates: 1 cm
Estimated parameters	• Daily state vector per satellite • Hourly piece-wise linear accelerations along-track/crosstrack/radial (constrained 1e-7 m/s^2) • 50x50 gravity spherical harmonic coefficients
Observation weights	• ll-SST: 10 nm/s • X,Y,Z position coordinates: 1 cm • DORIS: 0.3 mm/s

The PSDs of the datasets LRI_GRACE_AB_TUM and LRI_GRACE_CD_TUM is shown in Figure 24-1.
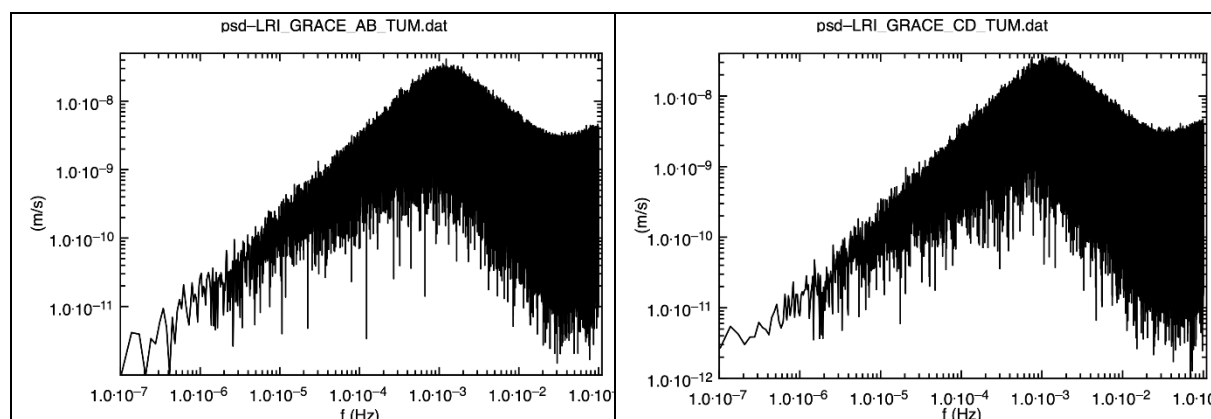
Figure 24-1. The PSDs of the LRI used in the simulations.

The gravity field retrievals were done using the adopted full error model. In order to obtain comparable simulation results, all measurement types (ll-SST, DORIS, X,Y,Z positions) were used and the full error model, and the same parameter estimation scheme as in Section 23.4 was adopted here:
• One set of spherical harmonic gravity field coefficients (50x50) per retrieval period +daily initial position and velocity for each satellite
• Hourly piecewise-linear (PWL) accelerations in the radial, along-track and cross-track directions for each satellite (including identical constraints).

The result of the retrievals of the complete model with all observations for TU Delft and CNES is shown in Figure 24-2, and they are very close. The slightly higher differences of TU Delft (red curve) can be explained by the use of individual noise per sensor, which is based on GRACE noise. For NGGM, an all sources combined LRI noise was applied, and then the CNES (pink curve) and TU Delft (blue curve) results are very close. This result demonstrates that comparable simulation results are obtained with both software in case of a similar setup.
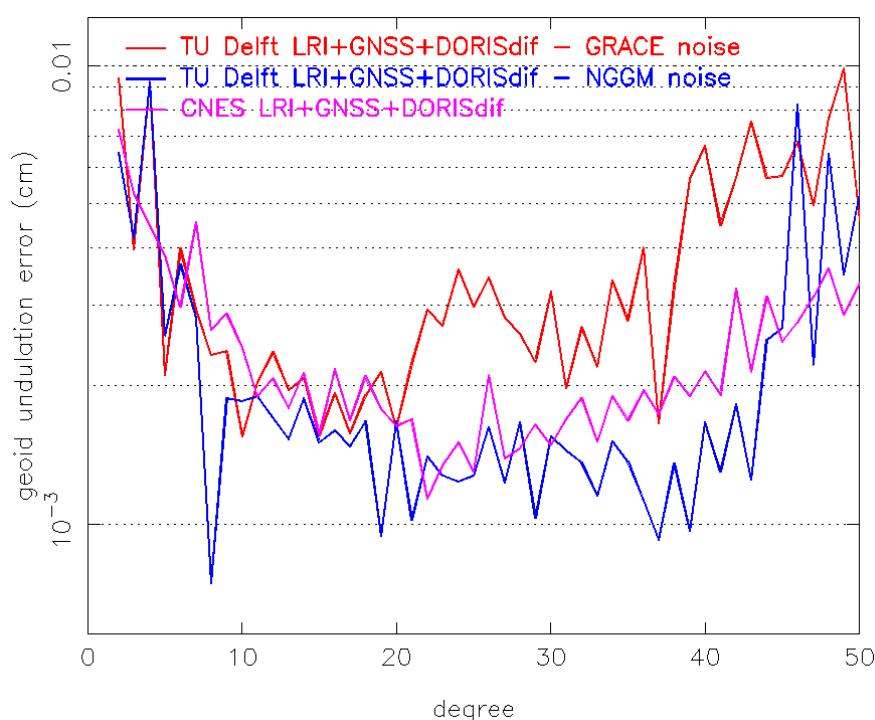
Figure 24-2. The geoid undulation error for the complete simulation of a monthly solution to d/o 50 using all observation types.

Additional simulations with this full error model were performed to quantify the importance of the empirical PWL accelerations. A first test showed the impact of the number of PWL estimated on the quality of the retrieval. When only one bias per day is estimated in the three directions, the error increases by about a factor 3 (red curve). This is displayed in Figure 24-3.
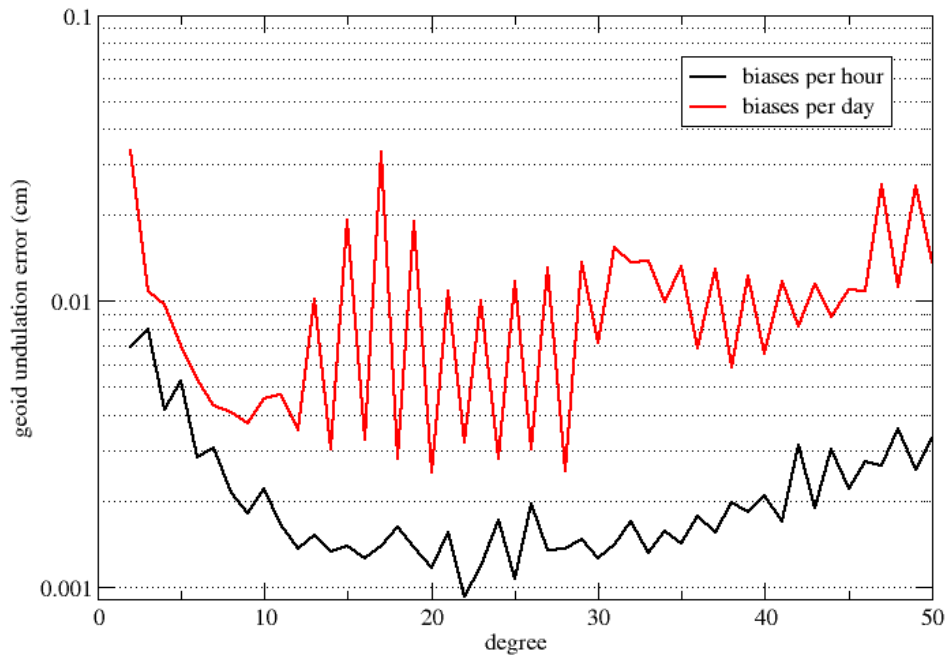
Figure 24-3. The geoid undulation error for the complete simulation of a monthly solution to d/o 50 using all observation types: effect of the cadence of the estimation of empirical PWL accelerations and constraints.

A third test was done to evaluate the importance of the accelerations with respect to their direction. To that purpose, the gravity field retrieval was done estimating PWL accelerations per hour but along one axis only, or estimating along the axes of the couples T-N, R-N and R-T. The results are presented in Figure 24-4. It is clear, and as expected, that the tangential component is most important, followed by R, and that the normal component is not contributing to error reduction significantly (the black curve and the T-R curve are superposed).
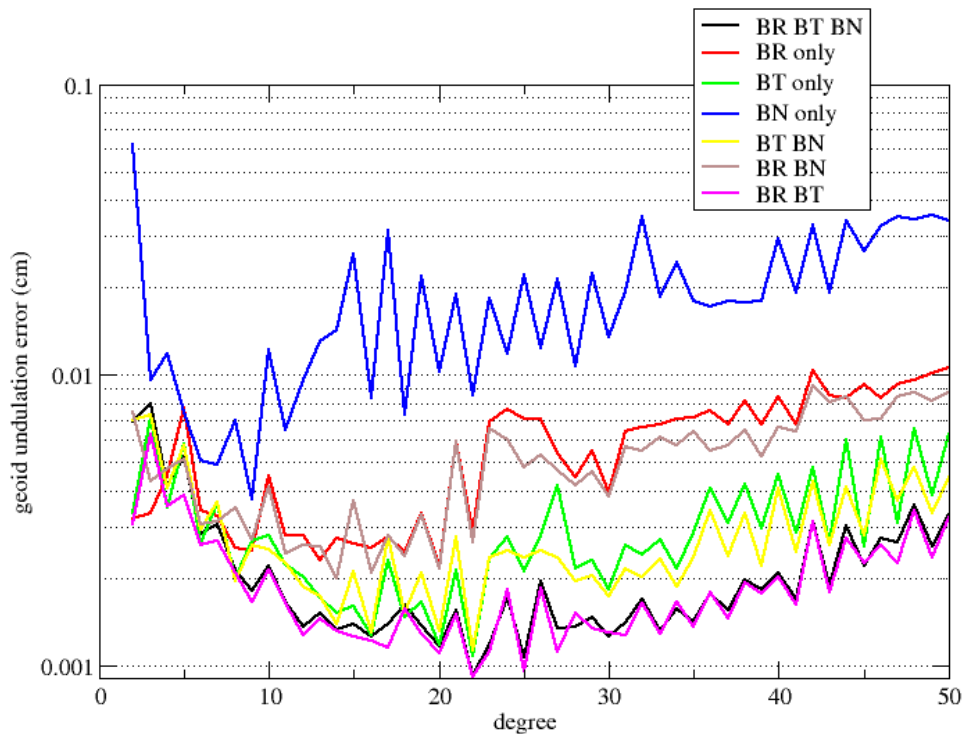
Figure 24-4. The geoid undulation error for the complete simulation of a monthly solution to d/o 50 using all observation types: effect of the axes selected for empirical PWL accelerations estimation.

Finally, it is shown in Figure 24-5 that adding differential DORIS measurements does not improve the gravity field retrieval compared with a GNSS+LRI solution. In fact, the best solution is obtained using LRI plus GNSS. Adding the DORIS measurements slightly deteriorates the quality, less so with the differential measurements than with the Doppler measurements. There is a very small positive contribution for degrees 2-5, but this simulation is very optimistic in view of the results obtained with Sentinel 3A/B.

Simulations without measurement noise were also performed at the beginning of the project for internal verifications. These are without interest for the NGGM/MAGIC study and are not shown.
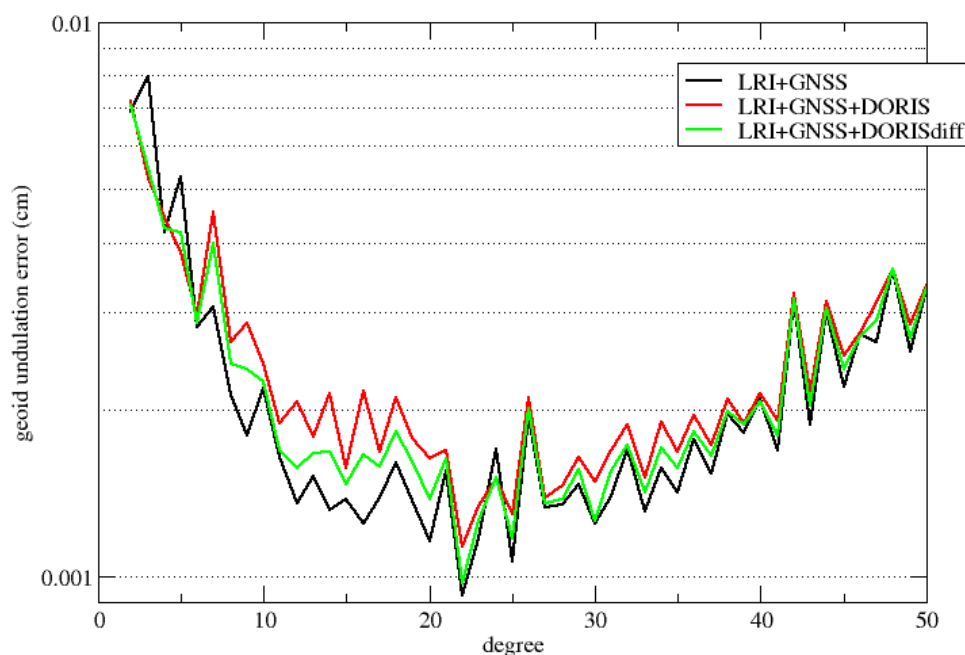
Figure 24-5. The geoid undulation error for the complete simulation of a monthly solution to d/o 50 using LRI plus GNSS, plus GNSS and differential DORIS, or plus GNSS and DORIS Doppler.

25 EMBARKING DORIS RECEIVERS – TUD

In order to study the impact of embarking DORIS receivers on board of the gravity field satellites, gravity field retrieval simulations (Section 26) simulations have been conducted for the scenario **3d_H** as outlined in [RD-1]. This scenario has a repeat cycle of 31 days with 3- and 7-day sub-cycles. The end-to-end simulator as used in precursor NGGM studies [RD-2][RD-3][RD-4] includes the DORIS observable type and is in fact also capable of processing real DORIS observations, as is done for, e.g., CryoSat-2 [RD-12]. DORIS has a proven capability of providing precise orbit solutions for Low Earth Orbiting satellites at the sub-decimeter level in terms of 3-dimensional position, and approaching the cm-level for the radial direction (see again, e.g., [RD-12]).

It will be assessed if DORIS, in addition to precise cm-level kinematic orbit solutions derived from GNSS observations, has the capability to enhance the quality of retrieved temporal gravity field models. The use of satellite tandems allows to form differential DORIS observations, which mitigates (largely) common errors such as tropospheric delay correction errors. Therefore, the gravity field retrieval simulations will include solutions based on both absolute and differential DORIS observations.

Section 26 introduces the gravity field retrieval scheme and simulation setup, and also includes the gravity field retrieval results. This Technical Note is summarized and concluded by Section 27.

26 IMPACT OF ADDING DORIS ON GRAVITY FIELD RETRIEVAL

26.1 INTRODUCTION

The nominal observations for gravity field retrieval by NGGM consist of low-low satellite-to-satellite tracking (ll-SST) and GNSS-based precise kinematic orbit coordinates (typically Cartesian coordinates in ITRF). These observations are supported by accelerometer observations for observing the non-gravitational accelerations and star tracker observations for precisely describing the attitude motion of the satellites (and accelerometers). For the simulations described in this Technical Note, DORIS observations will be added with the option to form differential DORIS observations for the associated satellite pairs or tandems.

Section 26.2 provides the information of the gravity field retrieval scheme. Section 26.3 includes the adopted simulation setup. Section 26.4 provides the results of the gravity field retrieval simulations.

26.2 GRAVITY FIELD RETRIEVAL SCHEME

The procedure for gravity field retrieval simulations is identical to the one used in previous studies to a Next Generation Gravity Mission (NGGM) [RD-2][RD-3][RD-4]. A brief summary is included below. For more details is referred to these previous studies.

A TU-Delft tailored version of the GEODYN software [RD-8] was used, based on version 0712, which included the capability to expand ocean tide models above degree and order 99, and also allows to estimate for example piecewise linear empirical accelerations (see Section 26.3).

The real-world gravity field was compiled by taking into account the static background model GOCO05S [RD-7], truncated at SH degree and order 120. Time-varying mass changes caused by hydrology, oceanography, atmosphere, solid-earth and ice are added, i.e., also the part complete to SH degree and order 120. Use was made of the 6-hourly piecewise-linear harmonic (SH) expansions from the European Space Agency (ESA) Earth System Model study. In addition, the time-varying gravity field due to ocean tides was taken into account, again complete to SH degree and order 120. The real-world model includes furthermore models for solid earth tides, 3rd body perturbations, polar motion, etc. (for more details, see [RD-4]). It is assumed that the satellites are flying largely "drag-free", i.e., non-gravitational force models were not taken into account, but assumptions about residual drag can be made if so required.

The closed-loop gravity field retrieval approach is outlined in more detail in [RD-4]. For reference, the associated flow chart is displayed in Figure 26-1. The closed-loop approach allows for the assessment of the impact of different choices for mission scenarios, different sensors and in association sensor noise levels/profiles, errors in the modeling of specific gravity field sources, etc.
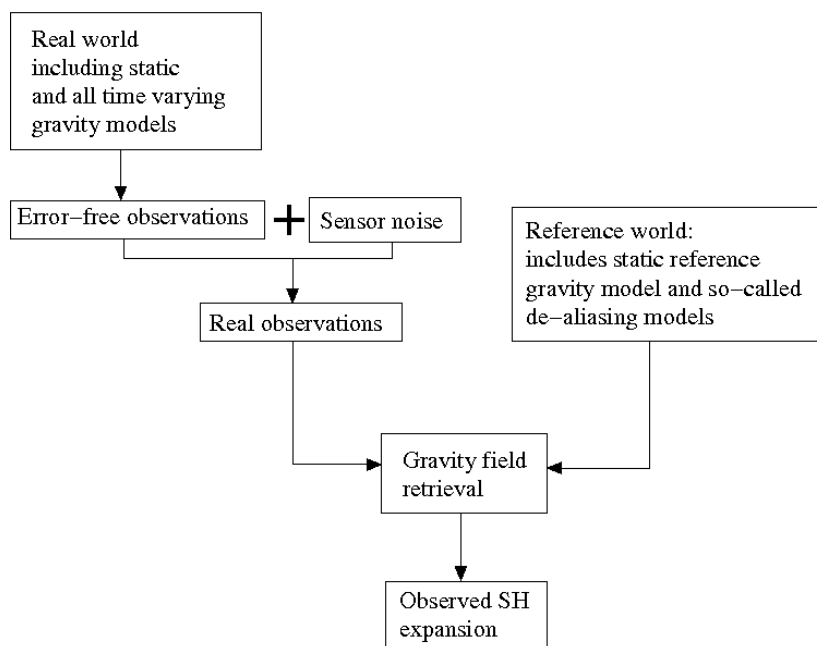
Figure 26-1 Flow chart for closed-loop gravity field retrieval.

26.3 GRAVITY FIELD SIMULATION SETUP

First, a 31-day data set of observations is simulated, covering 1-31 January 2002 (i.e. a full repat cycle for scenario **3d_H**). Each satellite constellation consists of tandems of in-line pairs of satellites with a nominal inter-satellite distance of 220 km. The observations consist of ll-SST range-rate observations with a time interval of 5 s, DORIS observations with a time interval of 10 s, and time series of satellite position coordinates (inertial X, Y and Z axes assumed to be derived from GNSS tracking) with a time interval of 30 s (Table 26-1). This results in 17280 ll-SST observations and 17280 position coordinates per satellite tandem per day. The time series of ll-SST and position coordinates are continuous. The availability of DORIS observations depends on the visibility of satellites by the associated tracking stations. For DORIS an elevation cut-off angle of 10º above the local horizon is applied. A typical daily coverage for a polar satellite is displayed in Figure 26-2. It can be observed that although a large part of the world is covered, relatively large gaps can be observed in, e.g., the South Pacific.

DORIS Satellite 1
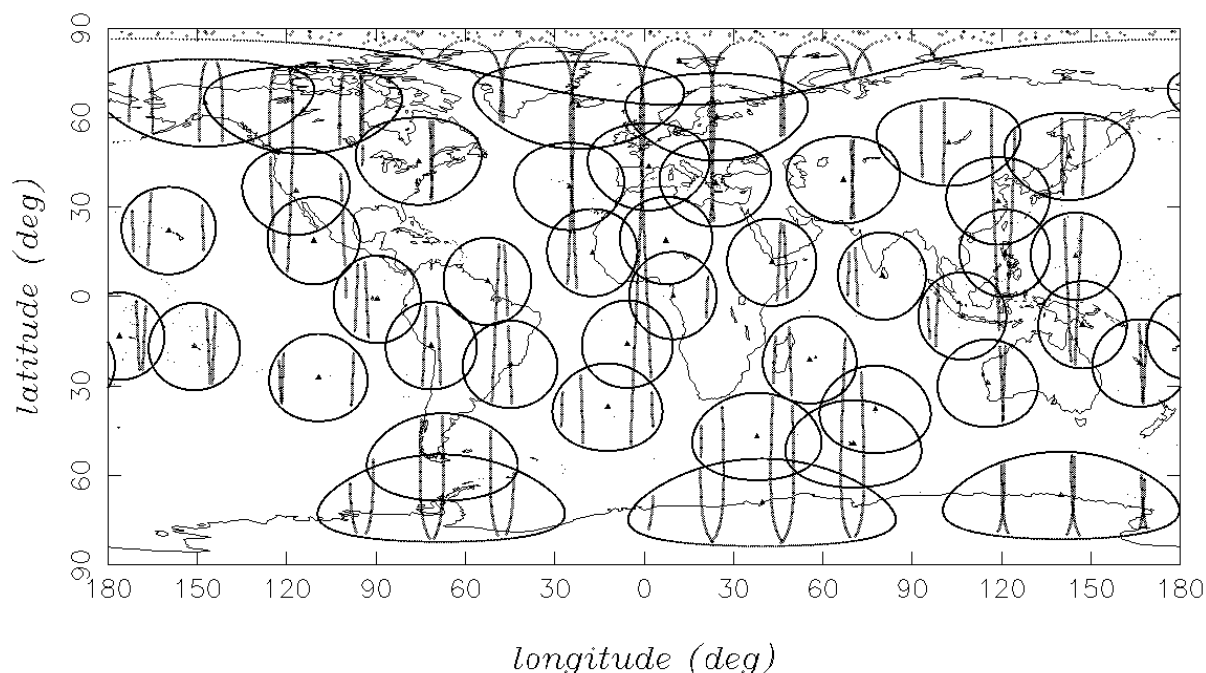
Figure 26-2 Selected DORIS network, polar satellite coverage with 10^0 elevation cut-off (scenario **3d_H**).

The force model includes a *true* static gravity field model, represented by the 120x120 part of GOCO05S [RD-7]. The *true* ocean tide model is represented by a 120x120 spherical harmonic expansion of the EOT11a model. In addition, the ESA Earth System Model (ESA/ESM) is taken into account, referred to as *AOHIS*. Moreover, the force model includes solid-earth tides and 3rd body perturbations. Finally, it is assumed that the satellites fly drag free down to a level of the order of 10 nm/s^2 [RD-4].

Table 26-1 Simulation set-up for scenario 3d_H. In addition, the error models and estimated parameters are specified.

Period	1-31 January 2002
True force model	• GOCO05s 120x120 • AOHIS 120x120 • Solid-earth tides (IERS) • Ocean tides: EOT11a (120x120) • 3rd body perturbations (JPL ephemeris) • Drag-free (residual drag ≈ 10 nm/s^2) [RD-4]
Reference force model = true force model except for:	• AO+AOerr (120x120) [RD-11] • Ocean tides: GOT4.7 (120x120)
Observables generated in daily batches:	• ll-SST @ 5 s • DORIS @ 10 s (10° elevation cut-off) • X,Y,Z position coordinates @ 30 s

	Final Report	
NGGM/MAGIC – Science Support Study During Phase A	Doc. Nr:	MAGIC_FR
	Issue:	1.0
	Date:	15.11.2022
	Page:	247 of 466

Observation noise/errors	• ll-SST: colored GRACE-type noise, RMS ≈ 0.67 nm/s [RD-11] • Accelerometer: colored GRACE-type noise, RMS ≈ 0.12-0.17 nm/s^2 [RD-11] • DORIS: 0.03 mm/s + 0.5% tropospheric scale factor • X,Y,Z position coordinates: 1 cm • Star tracker: 5 arcsec Gaussian for roll, pitch and yaw
DORIS station coordinates	• X,Y,Z: 1 cm Gaussian

Estimated parameters	• Daily epoch position & velocity for each satellite (2x2x6=24 per day)
	• Hourly piece-wise linear accelerations along-track/cross-track/radial:
	  ▪ Constraints orbit fit: 10/10/0 nm/s^2
	  ▪ Constraints gravity retrieval: 100/100/100 nm/s^2
	• 31-day =50x50 gravity spherical harmonic coefficients (2600)

Nominal observation weights	• ll-SST: 1 μm/s • X,Y,Z position coordinates: 1 m • DORIS undifferenced/differenced: 1/1 mm/s
Optimal weights (based on observation fits)	• ll-SST: 0.2 μm/s • X,Y,Z position coordinates: 0.02 m • DORIS undifferenced/differenced: 0.3/0.1 mm/s

26.4 GRAVITY FIELD RETRIEVALS

This Section includes the gravity field retrieval results. The gravity field retrievals were done using the adopted full error model, except for a benchmark test (see below). The adopted error models are specified in Table 26-1 and include force model errors due to the differences between the *true* EOT11a and *reference* GOT4.7 model. Furthermore, the retrievals aim at retrieving the *HIS* part of the *AOHIS* ESA/ESM. This means that the reference temporal gravity field model consists of the *AO* part, in general referred to as the de-aliasing product. Since in reality the *AO* part is not perfectly know, errors in this part are included as well, referred to as *AOerr*. These errors were carefully modelled in the framework of the ESA/ESM modelling efforts. In addition, observation errors include so-called GRACE-type colored ll-SST and accelerometer errors [RD-11], 1-cm Gaussian noise for the GNSS-based kinematic position coordinates, 0.03-mm/s Gaussian DORIS noise, and 5 arcsec Gaussian noise for the roll, pitch and yaw angles. Moreover, DORIS observations are affected by the troposphere and a Gaussian uncertainty of 0.5% was assumed for the pass-dependent tropospheric scale factors. Note that the latter are mitigated by differential DORIS, since the DORIS signals travel through predominantly the same part of the atmosphere for two satellites that together form a tandem. Finally, an accuracy level of 1 cm for the DORIS station coordinates was assumed.

Based on the simulations conducted in earlier studies [RD-2][RD-3][RD-4], the following parameter estimation scheme was adopted:

- One set of spherical harmonic gravity field coefficients (50x50) per retrieval period + daily initial position and velocity for each satellite (Note: since a possible impact of

DORIS is expected to be predominantly at the low degrees, the retrievals were limited to a maximum degree of 50);

- Hourly piecewise-linear (PWL) empirical accelerations in the radial, along-track and cross-track directions for each satellite.

The nominal retrieval includes one set of 50x50 SH coefficients for the full 31-day period, whereas for the Wiese approach, for each day a 10x10 set of SH coefficients are estimates which are then 31-day averaged. The retrieved gravity field models are then compared with the *true* averaged HIS model for the associated 31-day period.

The design matrix (which includes the partial derivatives of the observations to the estimated parameters) are computed with nominal weights as specified in Table 26-1. Optimal weights for estimating the gravity field SH coefficients are based on the a posteriori fit of the observations, which resulted in specifying an accuracy level of 2 cm for the 1-dimensional satellite position coordinates, 0.3/0.1 mm/s for the absolute/differential DORIS observations, and 0.2 μm/s for the ll-SST range-rate observations.

The estimated method is Bayesian least-squares, where constraints for estimated parameters are added as specified in Table 26-1. The gravity field retrieval consists of two estimation steps. In the first step, for each day all parameters as indicated in Table 26-1 are estimated except for the gravity field coefficients to arrive at a best orbit fit, where after convergence the normal equations are set up (with nominal observation weights). When computing these normal equations, the gravity field coefficients are included. In the second step, the daily normal equations are combined for the gravity field coefficients (with optimal observation weights), using a partitioning and back-substitution method for obtaining consistent values for the other estimated parameters.

Gravity field solutions have been generated for several combinations of tracking observations:

- kinematic orbit positions (in the Figures below indicated by GNSS);
- ll-SST observations (LRI);
- absolute DORIS observations (DORIS undif);
- differential DORIS observations (DORIS dif).

26.4.1 BENCHMARK

As stated above, a benchmark gravity field retrieval was simulated. In this benchmark, no error sources were included, i.e., all observations are error-free and the *true* tides model was used. Also, for the benchmark, the objective was to retrieve the HIS signal complete to degree and order 50. The temporal gravity field signal was modeled by the *120x120* AOHIS model, except for the 50x50 part for which only the *AO* signal was used. Thus, the benchmark gravity field retrieval aimed at observing the 50x50 *HIS* part. Differences between the retrieved gravity field and the 31-day averaged 50x50 *HIS* source signal are then due to temporal aliasing.

Figure 26-3 shows the results for the error-free observations case in terms of the RMS of retrieved gravity field coefficient errors as a function of SH degree. The retrieval is for 1 31-day period using the **3d_H** Bender constellation. This figure shows the impact of adding DORIS is marginal at best, be it absolute or differential DORIS observations. Also, compared to GNSS, the contribution is very small. It is interesting to compare for example the green and purple curves. It can be concluded that in case of error-free DORIS observations, differencing leads to a significantly larger impact of temporal aliasing for the DORIS-only solutions. This is due to the weaker observing geometry that results from the differencing. However, when adding DORIS to GNSS+LRI the differencing appears to improve the solution, possibly because of the

inherent lower weight that results by the differencing when added to the strong GNSS+LRI combination. Because of the non-homogeneous global coverage by DORIS, it thus also appears less straightforward to combine with LRI and GNSS observations, which provide true global coverage.
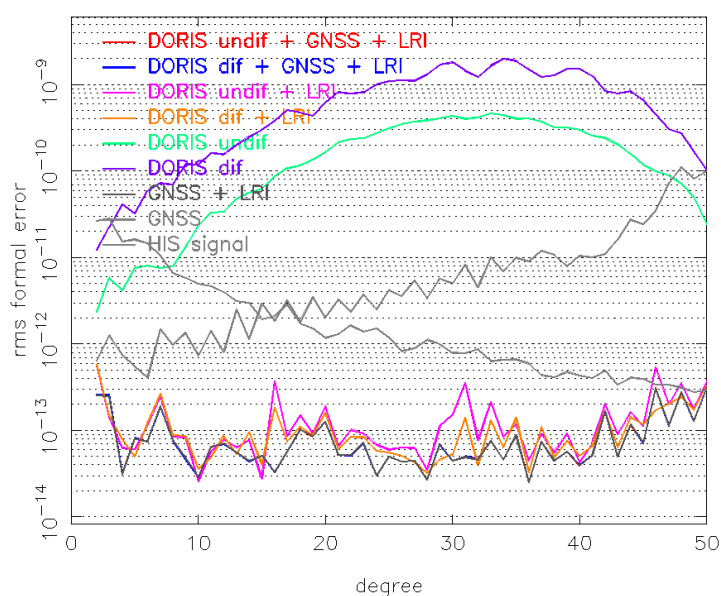
Figure 26-3 RMS spherical harmonic coefficient retrieval errors as a function of spherical harmonic degree due to temporal aliasing of the 50x50 HIS signal only (31-day period covering 1-31 January 2002). The decaying gray curve represents the 31-day averaged HIS signal. Bender constellation 3d_H. Optimal weighting.

26.4.2 FULL ERROR MODEL

The quality of the retrieved 31-day temporal gravity field is displayed for each individual observation type and for several combinations of observation types in Figure 26-4 and Figure 26-5 in terms of the RMS of gravity field coefficient errors as a function of SH degree. It can be clearly observed that the ll-SST observations are crucial for observing temporal gravity. However, at the same time it can be observed that the kinematic position coordinates (GNSS) are essential for stabilizing the solution at the very long wavelengths (e.g., SH degree 2 cannot be retrieved with sufficient precision by ll-SST observations only).
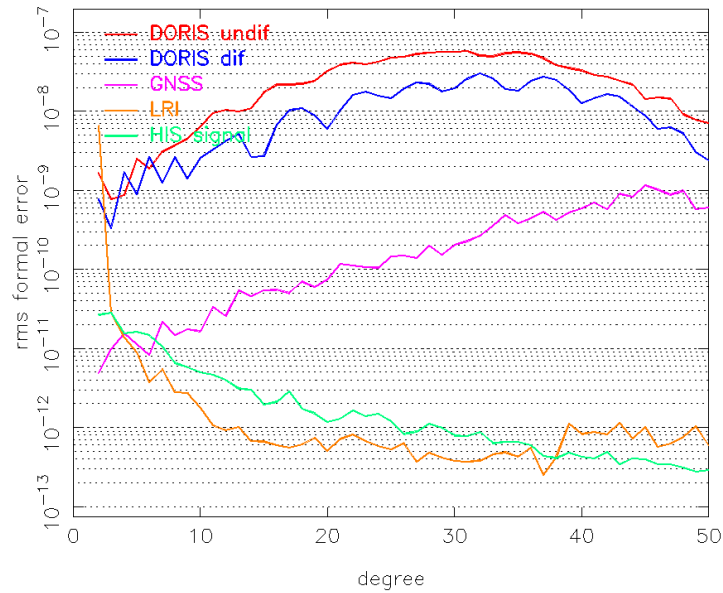
Figure 26-4 RMS spherical harmonic coefficient retrieval errors as a function of spherical harmonic degree due to the sum of all modeled errors sources (31-day period covering 1-31 January 2002). The green curve represents the 31-day averaged HIS signal. Bender constellation 3d_H. Optimal weighting – Part I.

It is interesting to note, that although temporal gravity field variations can hardly be observed by DORIS observations alone, the retrieval errors are smaller when using differential DORIS observations. This can be explained by the mitigation by a factor of 3 of the 0.5% tropospheric scale uncertainties.
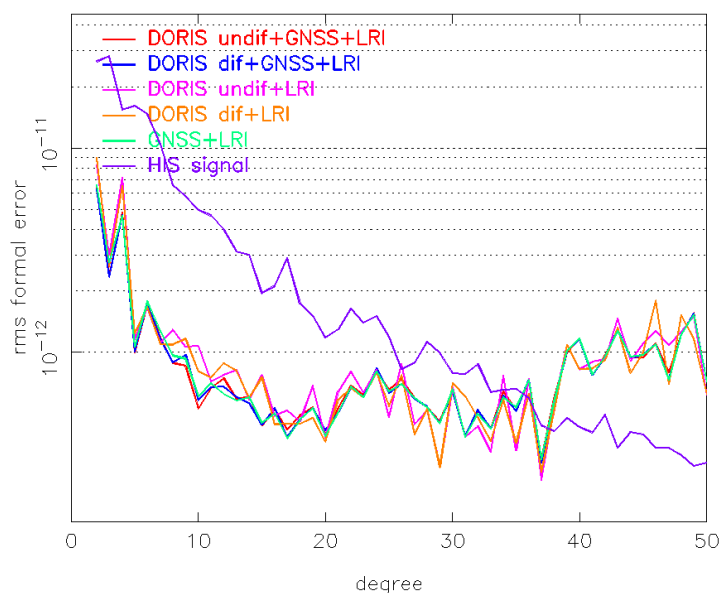
Figure 26-5 RMS spherical harmonic coefficient retrieval errors as a function of spherical harmonic degree due to the sum of all modeled errors sources (31-day period covering 1-31 January 2002). The purple curve represents the 31-day averaged HIS signal. Bender constellation 3d_H. Optimal weighting – Part II.

The curves in Figure 26-5 indicate that DORIS can serve to a large extent as backup for GNSS in terms of RMS coefficient error as a function of SH degree. The RMS degree error curves are very similar for all ll-SST/GNSS, ll-SST/DORIS and ll-SST/GNSS/DORIS combinations. Also, for the combinations a slight improvement can be observed when using differential instead of absolute DORIS observations.

The retrieval error in terms of geoid is displayed in Figure 26-6 for several combinations of observation types. The errors are almost identical for the combinations including and excluding DORIS observations, whether undifferenced (or absolute) or differential. This shows the marginal impact of adding DORIS observations. The global RMS of geoid errors is equal to 0.191, 0.185, and 0.187 mm for respectively the combination of (1) absolute DORIS, GNSS and LRI, (2) differential DORIS, GNSS and LRI, and (3) GNSS and LRI observations, compared to the HIS signal of 0.672 mm (see also Table 26-2), when applying a 20° spherical cap smoothing (close to a spatial resolution of 2,000 km). A slight improvement is obtained by adding differential DORIS observations.
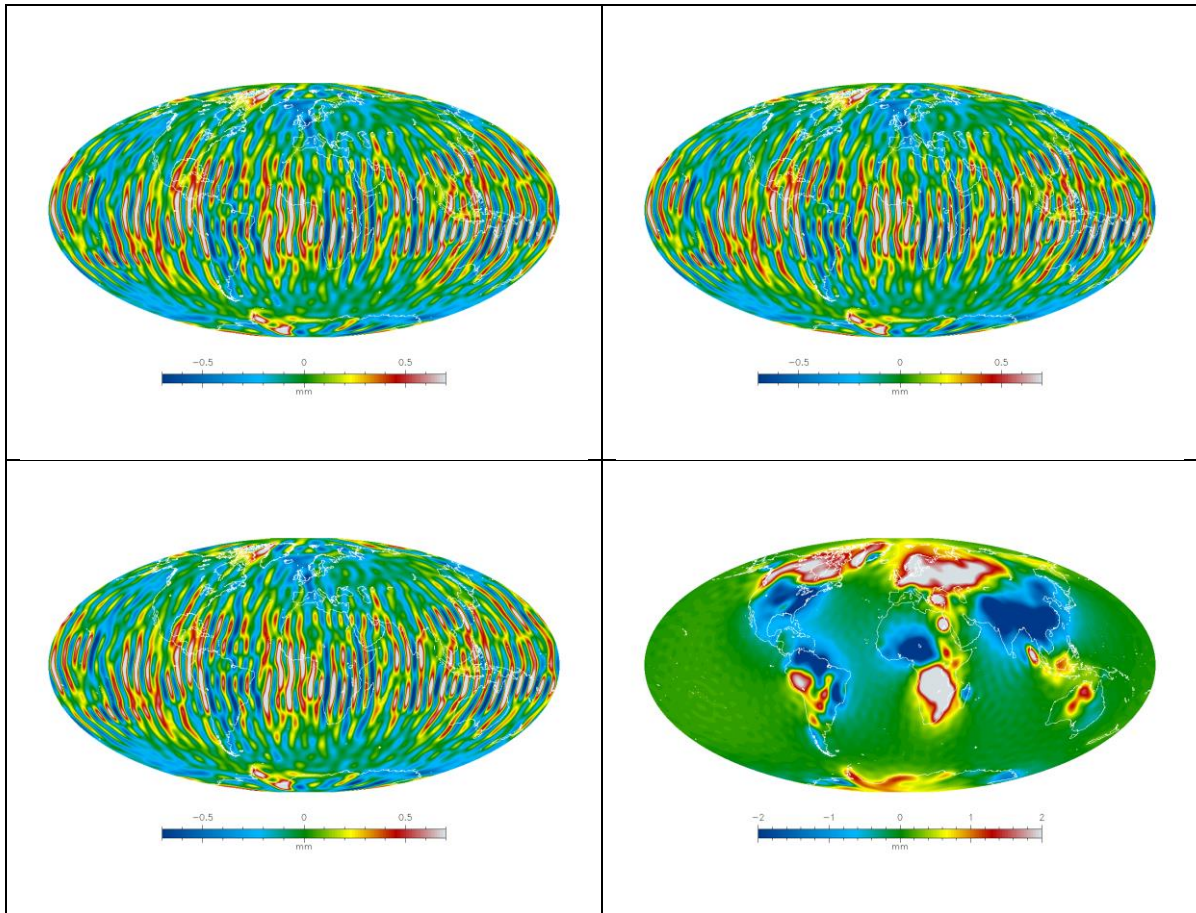
Figure 26-6 Geoid error for several combinations: (1) absolute DORIS, GNSS and LRI (top left), (2) differential DORIS, GNSS and LRI (top right), and (3) GNSS and LRI (bottom left). Bender constellation 3d_H. Optimal weighting for 50x50 SH expansion. The 50x50 HIS source geoid signal is included for reference (bottom right).

In addition, the retrieval error in terms of 20^0 spherical cap smoothed equivalent water height (EWH) is displayed in Figure 26-7 for the same combinations of observation types. Also in terms of EWH, the errors are almost identical for the combinations including and excluding DORIS observations. This again shows the marginal impact of adding DORIS observations. The global RMS of 20^0 spherical cap smoothed EWH errors is equal to 3.151, 3.120 and 3.152 mm, for respectively the combination of (1) absolute DORIS, GNSS and LRI, (2) differential DORIS, GNSS and LRI, and (3) GNSS and LRI observations, compared to the HIS signal of 0.672 mm (Table 26-2). Also here, a slight improvement is obtained by adding differential DORIS observations.
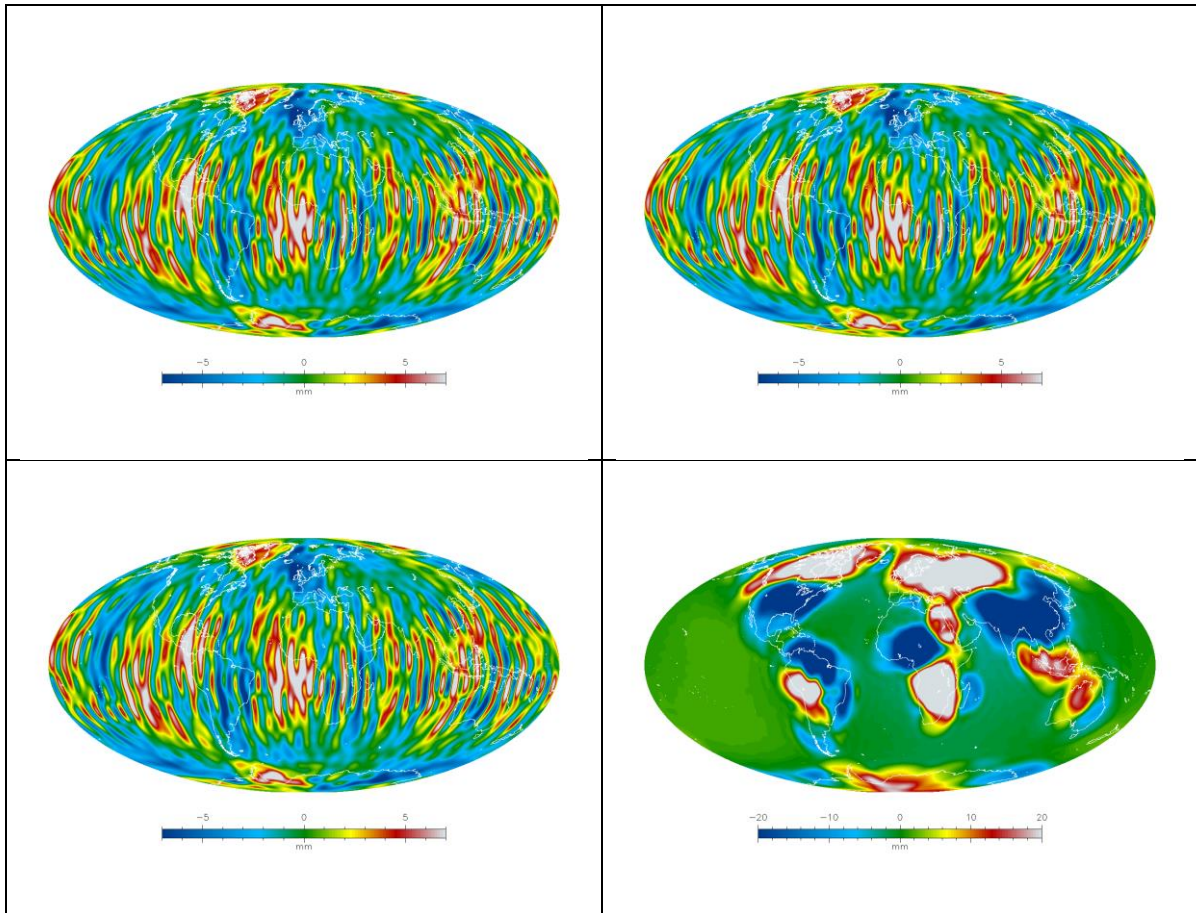
Figure 26-7 Equivalent Water Height (EWH) error, 20^0 spherical cap smoothed, for several combinations: (1) absolute DORIS, GNSS and LRI (top left), (2) differential DORIS, GNSS and LRI (top right), and (3) GNSS and LRI (bottom left). Bender constellation 3d_H. Optimal weighting for 50x50 SH expansion. The 50x50 HIS source geoid signal is included for reference (bottom right).

Table 26-2 Global RMS retrieval error in terms of geoid and equivalent water height (EWH) for a number of combinations of observations. 20^0 spherical cap (with "undif" for absolute and "dif" for differential DORIS observations. Optimal weighting for 50x50 SH expansion.

Geoid global RMS	mm
HIS source	0.676
Bender	
DORIS undif+GNSS+LRI	0.114
DORIS dif+GNSS+LRI	0.110
GNSS+LRI	0.115
Polar pair	
DORIS undif+GNSS+LRI	0.189
DORIS dif+GNSS+LRI	0.184
GNSS+LRI	0.185

EWH global RMS	**mm**
HIS source	14.655
Bender	
DORIS undif+GNSS+LRI	3.079
DORIS dif+GNSS+LRI	3.048
GNSS+LRI	3.080
Polar pair	
DORIS undif+GNSS+LRI	5.816
DORIS dif+GNSS+LRI	5.717
GNSS+LRI	5.716

The impact on the gravity field retrieval of adding DORIS to the combination of ll-SST (LRI) and kinematic position coordinates (GNSS) was also assessed by computing geoid differences between solutions with and without either absolute or differential DORIS observations. For the 50x50 gravity field retrievals, the impact showed to be very small, of the order of less than 0.05 mm in terms of geoid compared to a signal size of a few mm (Figure 26-8). Adding DORIS to the combination of LRI and kinematic orbits (GNSS) thus indeed has a low impact on the quality of the gravity field retrievals. For undifferenced or absolute DORIS observations, the quality might even slightly deteriorate in case of tropospheric model errors. The latter is mitigated when using differential DORIS observations in which case the retrieval might slightly improve. However, by differencing the DORIS observations, the geometric contribution becomes smaller as well.

GNSS+DORIS+LRI vs. GNSS+LRI (50x50) – weighted   GNSS+DORIS+LRI vs. GNSS+LRI (50x50) – 20° smoothed – weighted
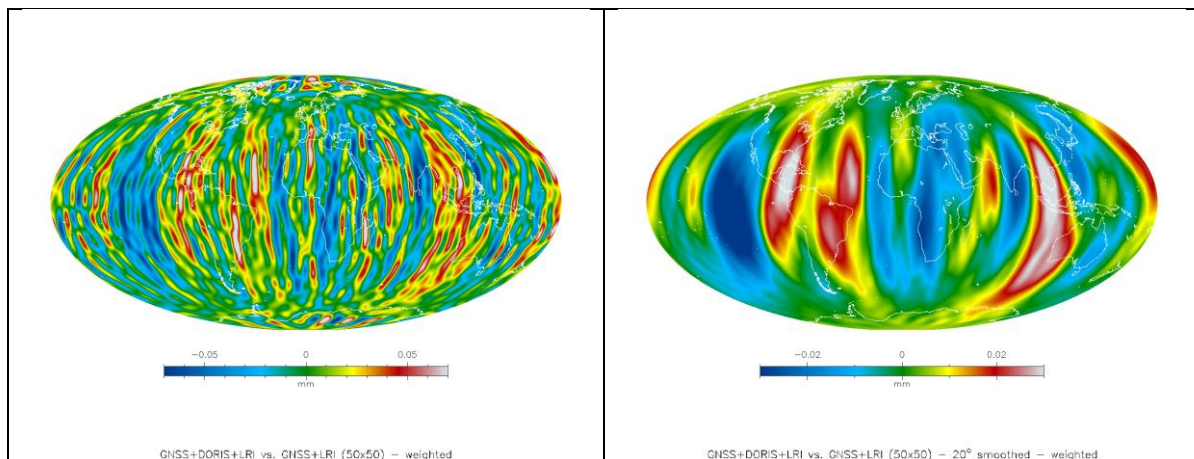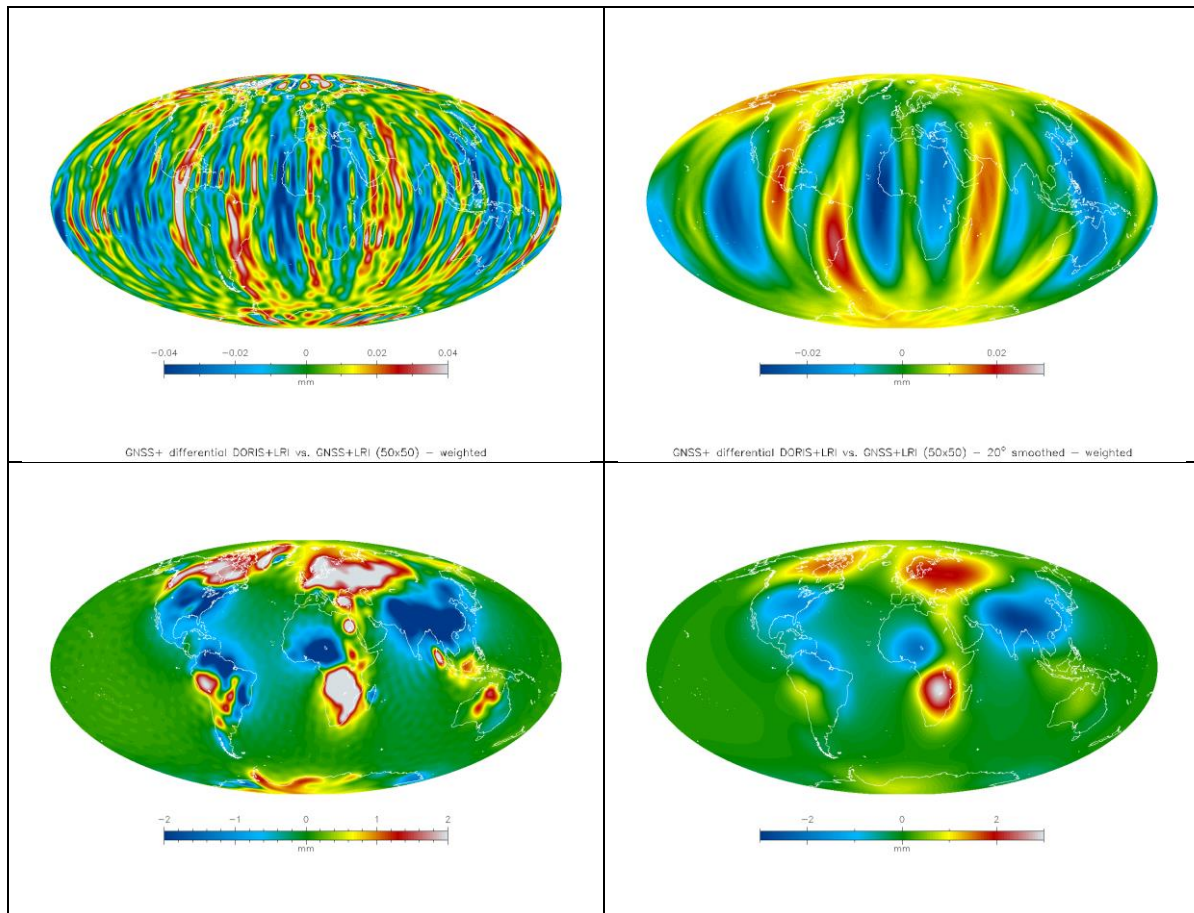
Figure 26-8 Impact of adding DORIS in terms of geoid: undifferenced (top) and differenced (middle), unsmoothed (left) and 20^0 spherical cap smoothed (right). The HIS source is included (bottom). Bender constellation 3d_H. Optimal weighting for 50x50 SH expansion.

The latter can be shown as well by computing the so-called contribution measure of a certain set of observations to the overall solution. Figure 26-9 and Figure 26-10 show the contribution measures of a certain observation type in case a retrieval is based on the weighted combination of all the available observation types (i.e., GNSS+LRI+DORIS undif or GNSS+LRI+DORIS dif).

The contribution measure is computed using the following equation:

$$C_o = N_o \, N_t^{-1}$$

where C_o represents the contribution matrix for a certain observation type o, with o indicating DORIS (absolute or differential), kinematic orbit coordinates, or ll-SST observations. The normal equations for the observation type o is represented by N_o. The inverse of the combined normal equations is given by N_t^{-1} with t indicating that the combination of ll-SST, kinematic orbit coordinates and DORIS observations (absolute or differential) is used.
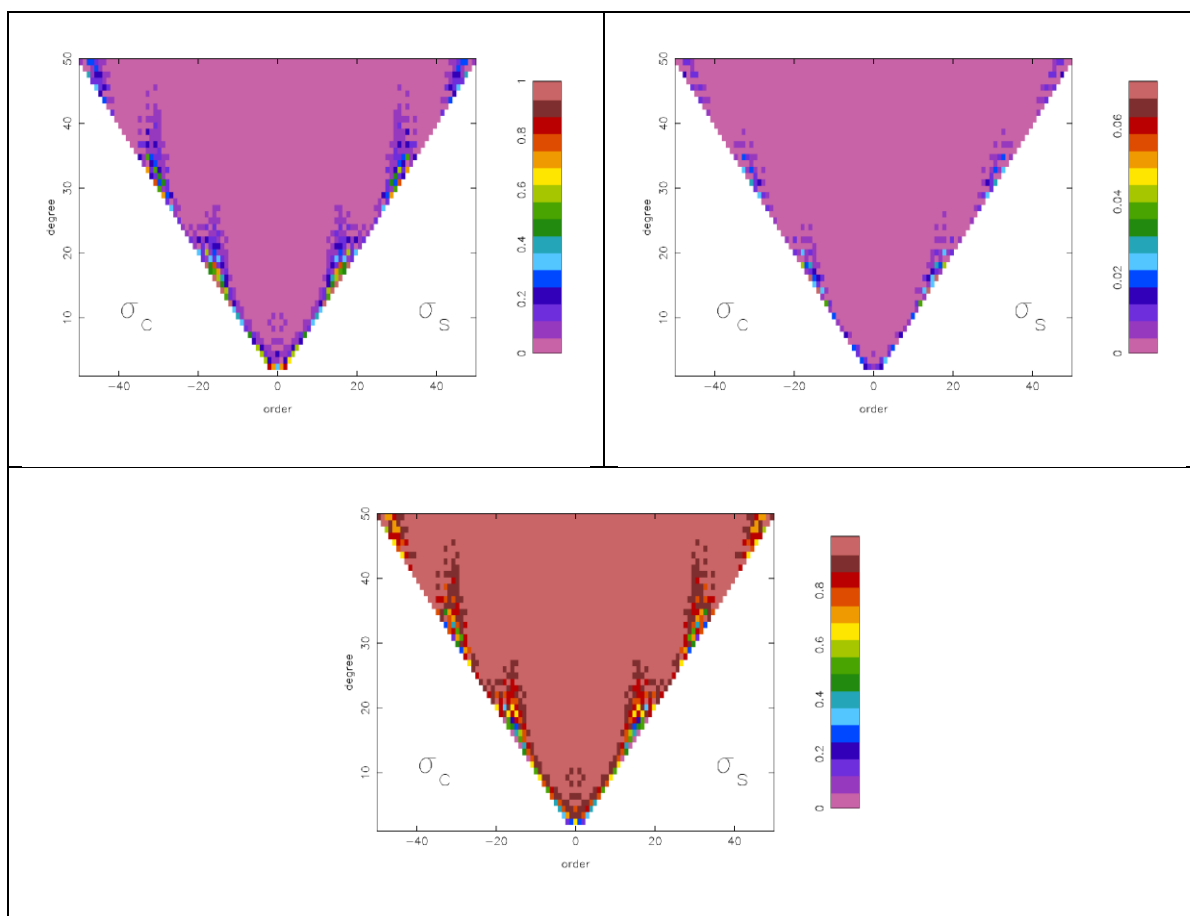
Figure 26-9 Contribution of observation types to estimated spherical harmonic coefficients: kinematic orbits (GNNS, top left), differential DORIS (top right), and LRI (bottom). Bender constellation 3d_H. Optimal weighting.

Figure 26-9 and Figure 26-10 show the contribution as a fraction, thus per definition values between 0 and 1. Please note the difference in scales for especially the plots showing the contribution of the differential DORIS observations. It can be seen that the contribution of the differential DORIS observations is in general negligible with a maximum of 0.06 (or 6%) for the **3d_H** Bender constellation for a few (near-)sectorial coefficients.

It is interesting to assess if the impact would be more significant in case only a polar pair would be available, which provides a more inhomogeneous and anisotropic geometry for observing temporal gravity variations. For the polar pair solution, if was found that the DORIS contribution increases to a maximum of 0.4 (or 40%) for a few (near-)sectorial coefficients. Thus, as can be expected, the impact for the polar pair only solution increases a bit, but is still marginal. Also, a marginal impact can be observed for a few spherical harmonic coefficients at the resonance orders (around 16 and 32).
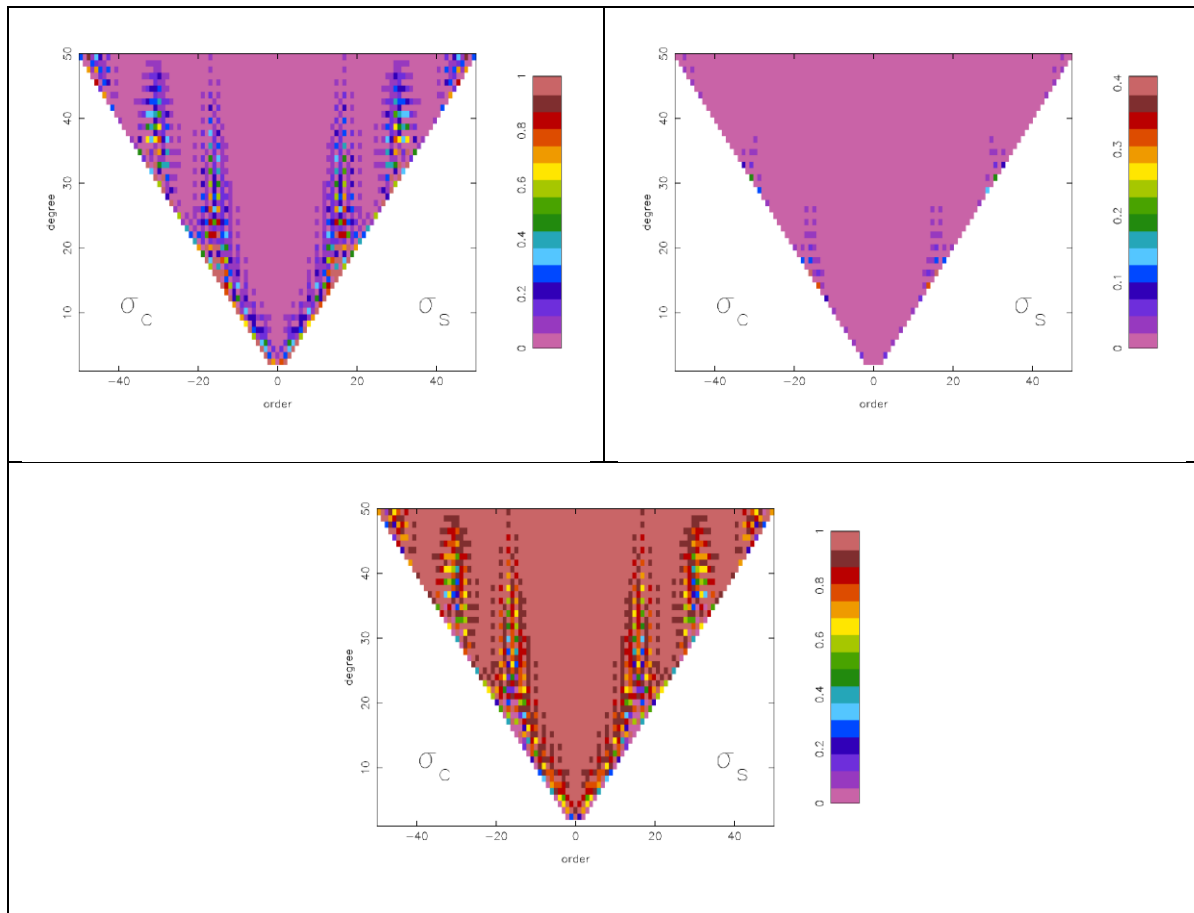
Figure 26-10 Contribution of observation types to estimated spherical harmonic coefficients: kinematic orbits (GNNS, top left), differential DORIS (top right), and LRI (bottom). Polar pair only from 3d_H. Optimal weighting.

It can also be observed that the GNSS plays a crucial rule with much larger contribution measures for a few (near-)sectorial terms, but even more so for coefficients at resonant orders. Also, here it can be seen that the impact is bigger for the polar pair only solution. The LRI as expected contributes the most for the vast majority of the spherical harmonic coefficients, even more so for the Bender than for the polar pair only solution.

In addition to the results described above, formal error propagations were conducted based on the optimal weighted covariance matrices. These propagations in general display consistent results between predicted formal and real errors of the retrieved SH coefficient coefficients (see Figure 28-1, Figure 28-2 and Figure 28-3, in Annex 28). For the solution based on only absolute DORIS observations, it can be observed that the real errors are significantly above the predicted formal errors (Figure 28-3, bottom left), which is due to the non-random 0.5% tropospheric scale factor errors (formal errors are typically optimistic in the presence of systematic errors). Finally, predicted formal geoid errors confirm the relative contributions of the several observation types (Figure 28-4 and Figure 28-5). For DORIS, these predictions display the partly inhomogeneous global coverage by ground stations (Figure 28-5).

27 CONCLUSIONS

It is verified that TU Delft and CNES software lead to comparable gravity field retrieval simulation results.

Full-scale gravity field retrieval simulations show that in terms of gravity field performance, the addition of DORIS observations to the complement of LRI and GNSS observations hardly have a significant impact. The simulations also show that the combination of LRI and DORIS leads to stable gravity field retrievals. Thus, DORIS can serve as a backup for GNSS. In fact, stable solutions can be obtained when using either absolute or differential DORIS observations, where the differencing is done between observations that are taken at the same time for DORIS beacons that are in view of both satellites that form a tandem. The differencing helps to mitigate errors due to for example errors in the tropospheric corrections leading to slightly improved gravity field retrievals.

Contribution measures confirm the limited and often negligible impact of adding DORIS observations. Based on these contribution measures, it can be predicted that the contribution of differential DORIS observations is in general negligible with a maximum of 0.06 (or 6%) for the Bender constellation for a few (near-)sectorial coefficients. Interesting is that for the polar pair solution, this contribution increases to a maximum of 0.4 (or 40%) for a few (near-)sectorial coefficients. Thus, as can be expected, the impact for the polar pair only solution increases a bit, but is still marginal. Also, a marginal impact can be observed for a few spherical harmonic coefficients at the resonance orders (around 16 and 32).

It can also be observed that the GNSS plays a crucial rule with much larger contribution measures for a few (near-)sectorial terms, but even more so for coefficients at resonant orders. In addition, it can be seen that the impact is bigger for the polar pair only solution. The LRI as expected contributes the most for the vast majority of the spherical harmonic coefficients, even more so for the Bender than for the polar pair only solution.

28 ERROR PROPAGATION: FORMAL VS. RETRIEVAL ERRORS
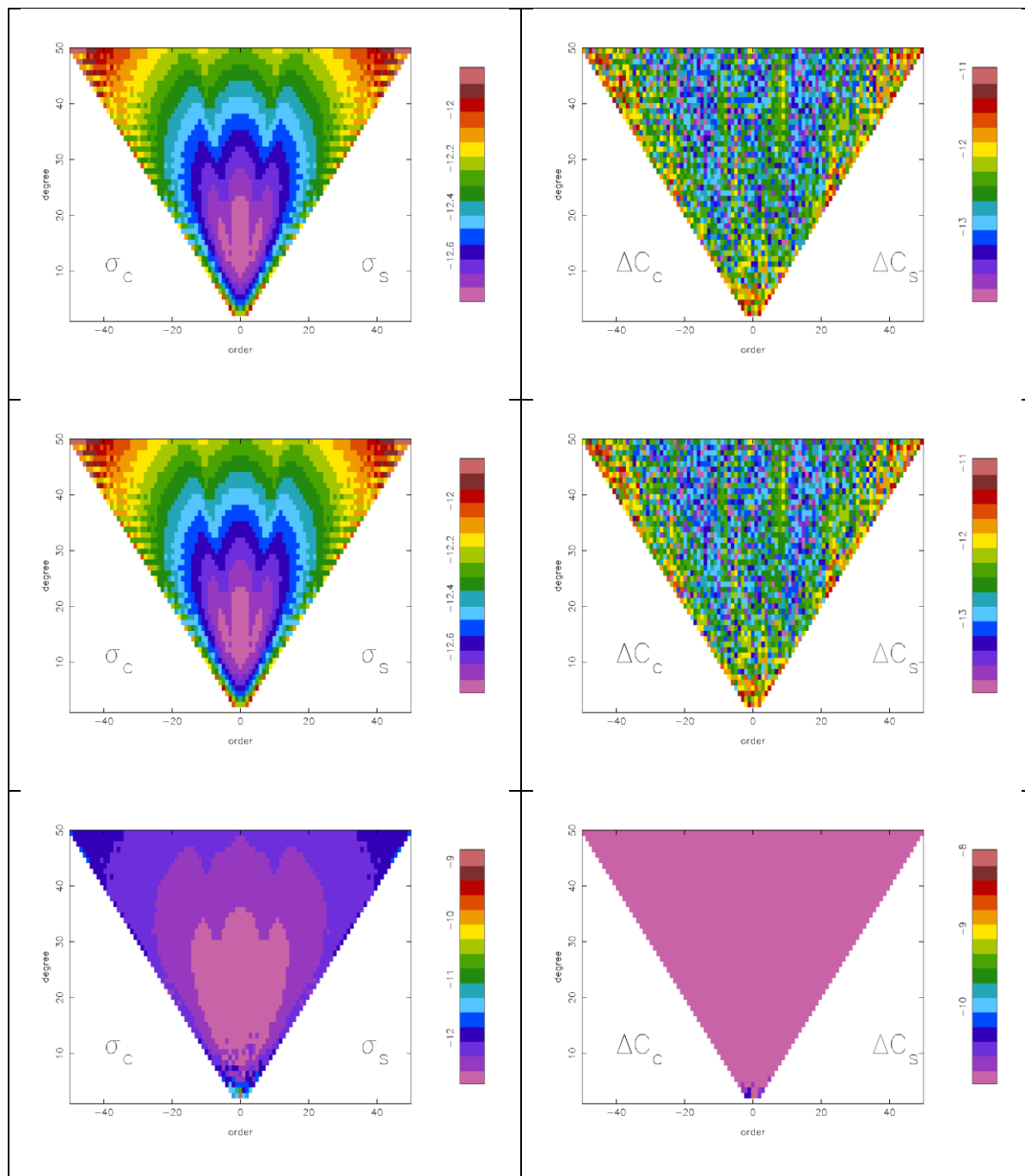
Figure 28-1 Formal (left) and real (right) SH gravity field coefficient errors for 30-day gravity field retrieval (1-31 January 2002) with the Bender constellation 3d_H. Optimal weighting. From top to bottom: (1) DORIS undif+GNSS+LRI, (2) DORIS dif+GNSS+LRI, and (3) LRI only. Note the differences in logarithmic scales.
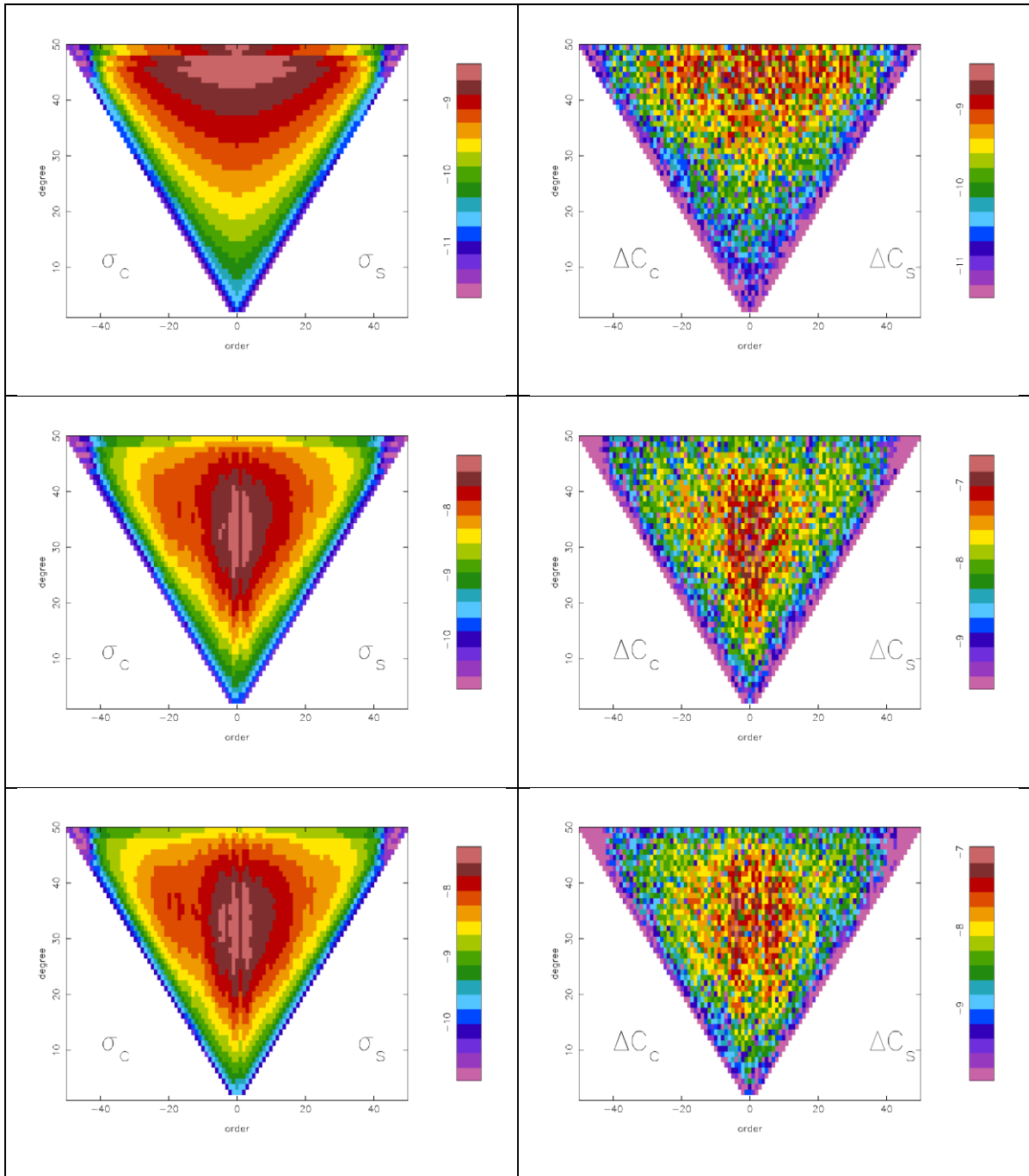
Figure 28-2 Formal (left) and real (right) SH gravity field coefficient errors for 30-day gravity field retrieval (1-31 January 2002) with the Bender constellation 3d_H. Optimal weighting. From top to bottom: (1) GNSS, (2) DORIS undif, and (3) DORIS dif. Note the differences in logarithmic scales.
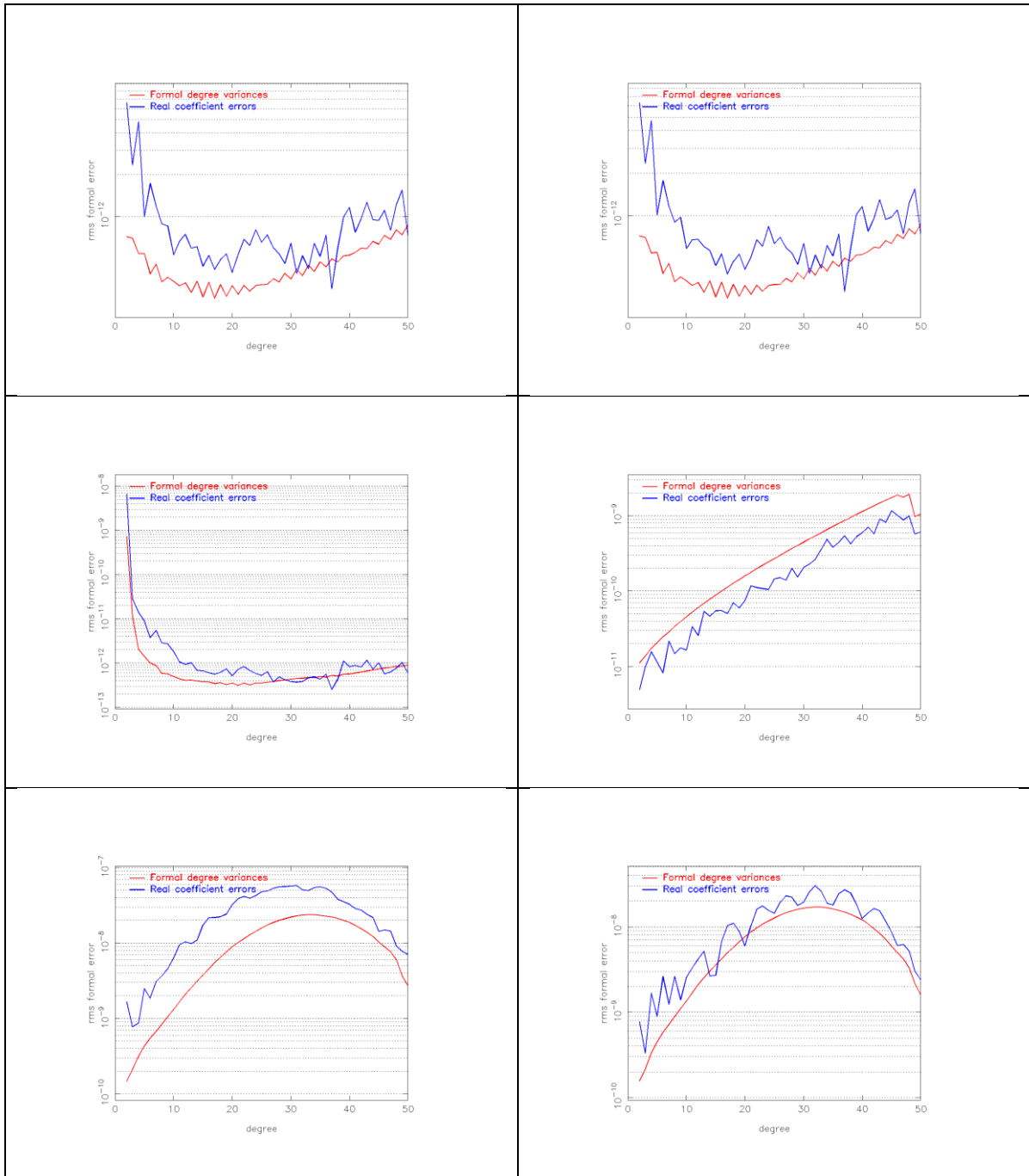
Figure 28-3 Formal and real RMS coefficient errors as a function of SH degree error for 30-day gravity field retrieval (1-31 January 2002) with the Bender constellation 3d_H. Optimal weighting for the following combinations: (1) DORIS undif+GNSS+LRI (top left), (2) DORIS dif+GNSS+LRI (top right), (3) LRI only (middle left), (4) GNSS (middle right), (5) DORIS undif (bottom left), and (6) DORIS dif (bottom right). Optimal weighting.
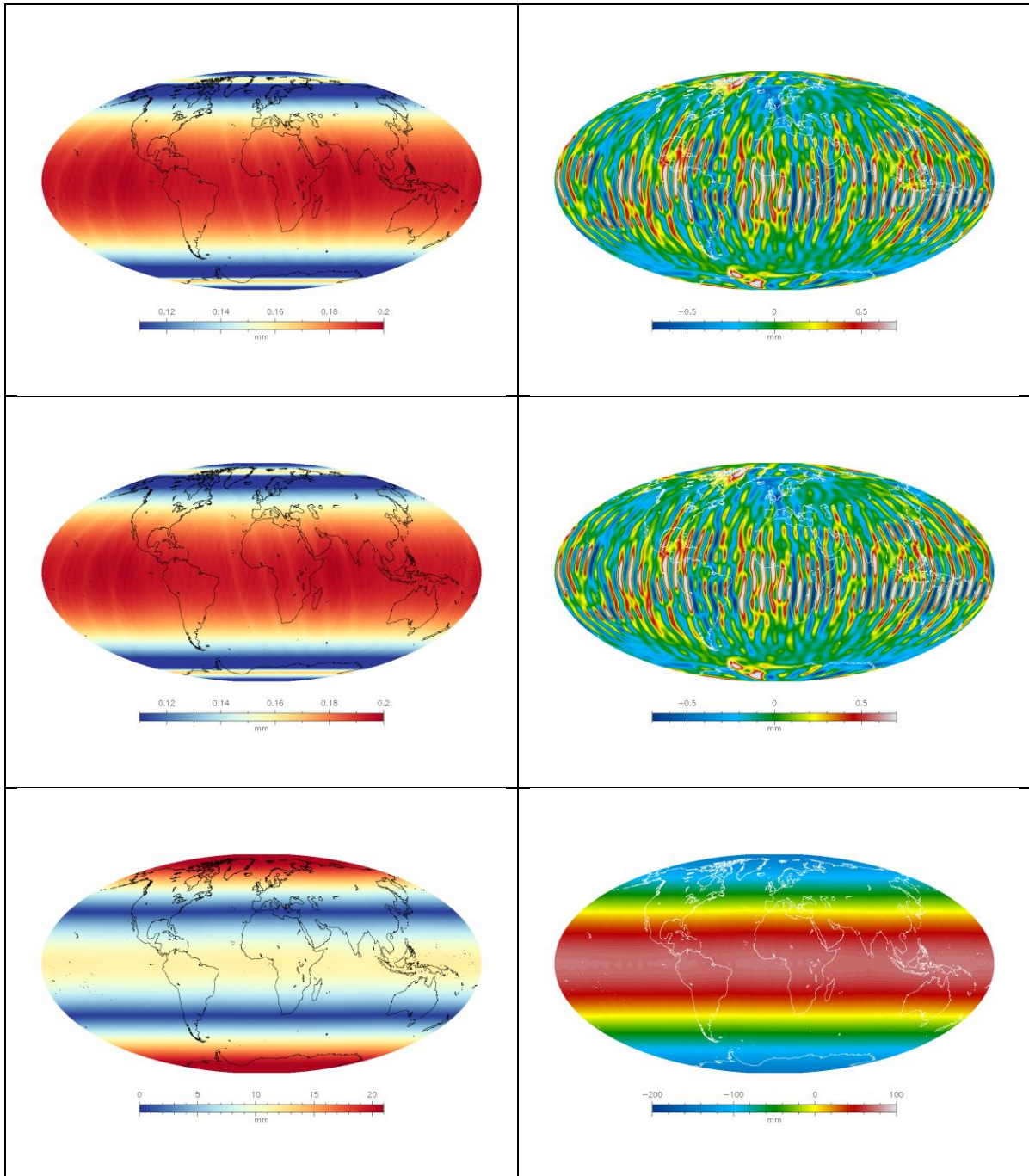
Figure 28-4 Formal (left) and real (right) geoid error for 31-day gravity field retrievals (1-31 January 2002) with the Bender constellation 3d_H. Optimal weighting for the following combinations: (1) DORIS undif+GNSS+LRI (top), (2) DORIS dif+GNSS+LRI (middle), (3) LRI only (bottom). Optimal weighting. Note the differences in scale.
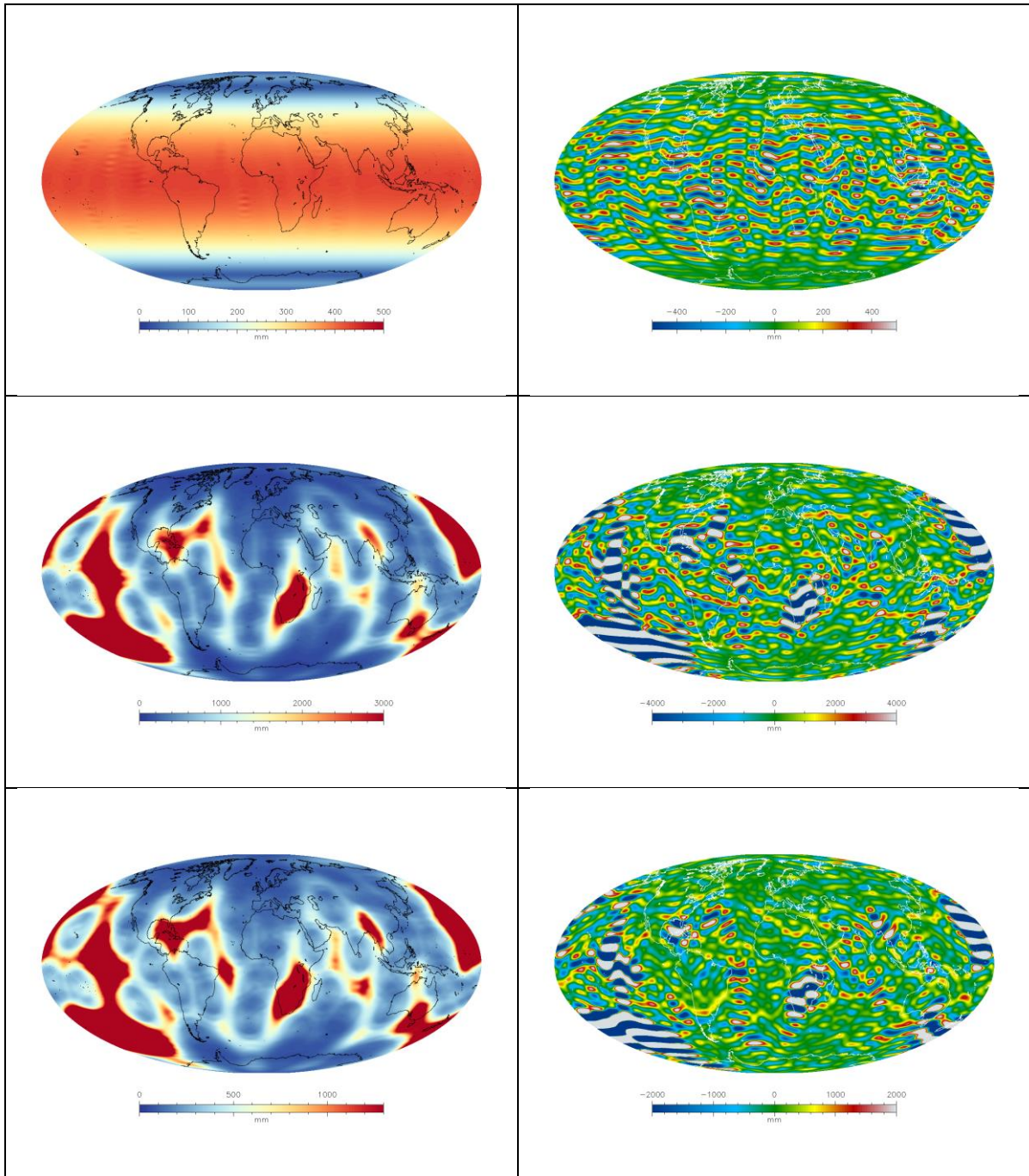
Figure 28-5 Formal (left) and real (right) geoid error for 31-day gravity field retrievals (1-31 January 2002) with the Bender constellation 3d_H. Optimal weighting for the following combinations: (1) GNSS (top), (2) DORIS undif (middle), and (3) DORIS dif (bottom). Optimal weighting. Note the differences in scale.

29   APPLICABLE DOCUMENTS, REFERENCE DOCUMENTS, AND PUBLICATIONS TO PART 3

29.1 APPLICABLE DOCUMENTS

[AD-1]   NGGM/MAGIC – SCIENCE SUPPORT STUDY DURING PHASE A – EXPRO, RFP Proposal No. TUM/2021-MAGIC-Science, ESA RFP/3-17035/20/NL/FF/tfd, 16-03-2021

29.2 REFERENCE DOCUMENTS

[RD-1]   Statement of Work, ESA Express Procurement EXPRO+, Additional Constellation & Scientific Analysis Studies of the Next Generation Gravity Mission Concept, EOP-SM/2974, Issue 1, Revision 0, 19/04/2016

[RD-2]   Assessment of a Next Generation Mission for Monitoring the Variations of Earth's Gravity. Final Report, ESTEC Contract No. 22643/09/NL/AF, Issue 2, Date: 22.12.2010

[RD-3]   Assessment of a Next Generation Gravity Mission to Monitor the Variations of Earth's Gravity Field. Final Report, ESTEC Contract No. 22672/09/NL/AF, Issue 1, Date: 10.10.2011.

[RD-4]   Assessment of Satellite Constellations for Monitoring the Variations in Earth Gravity Field "SC4MGV", ESA Contract No 4000108663/13/NL/MV, Final Report, 04 November 2015

[RD-5]   R.D. Ray, Precise comparisons of bottom-pressure and altimetric ocean tides, J. Geophys. Res.: Oceans, Vol. 118, pp. 4870-4584, doi: 10.1002/jgrc.20336, 2013

[RD-6]   Savcenko, R. and Bosch, W. (2012): EOT11A - Empirical Ocean Tide Model from Multi-Mission Satellite Altimetry, München, Deutsches Geodätisches Forschungsinstitut (DGFI), hdl:10013/epic.43894

[RD-7]   GOCO, Gravity observation combination (GOCO), www.goco.eu, accessed 23 September 2021

[RD-8]   D.E . Pavlis, S. Poulouse, J.J. McCarthy, GEODYN operations manual, Contractor report, SGT Inc. Greenbelt, 2006

[RD-9]   ESA Earth System Model for Mass Distribution and Transport, https://isdc.gfz-potsdam.de/esmdata/esaesm/, last accessed 23 September 2021

[RD-10]   D.N. Wiese, P. Visser, R.S. Nerem, Estimating Low Resolution/High Frequency Gravity Fields to Reduce Temporal Aliasing Errors, Adv. Space Res., 48(6), pp. 1094-1107, doi: 10.1016/j.asr.2011.05.027, 2011

[RD-11]   TU Munich LRZ server (https://syncandshare.lrz.de/).

[RD-12]   E Schrama, Precision orbit determination performance for CryoSat-2, Advances in Space Research 61 (1), pp. 235-247, doi: 10.1016/j.asr.2017.11.001, 2018

[RD-13] E. Weinstein, Measurement of the differential Doppler shift. IEEE Transactions on Acoustics, Speech, and Signal Processing, 30(1), 112-117, 1982, doi: 10.1109/TASSP.1982.1163849

PART 4:

CLOSED-LOOP SIMULATOR IMPROVEMENT AND ANALYSIS

30 INTRODUCTION

This Part 4 refers to Task 4 of the SoW and covers the work performed under WP 400 of the WBS. It refers to the deliverable document TN D8 "Closed-loop simulator improvement and analysis".

We discuss improved data processing strategies that could be implemented into the closed-loop full-scale simulator's processing chain, which include
- Alternative orbit scenarios and optimal application of de-aliasing models (WP 410 to 430);
- Treatment of ocean tides in NRT analysis and post-processing (WP440);
- Optimal signal parametrization with respect to space and time in terms of multi-period estimation (WP 450);
- Analysis of need for long-term trend estimation (WP 460);
- Analysis of need for post-processing (WP 470).

31 ORBIT GENERATION FOR ALTERNATIVE SCENARIOS (WP 410)

It it was decided to use the simulation scenarios described in chapter 32. Alternative scenarios have not been generated, therefore.

32 ALTERNATIVE ORBIT SCENARIOS (WP 420)

In the following, the choice of optimized orbits for short-term intervals with respect to the high frequency signals in ocean and atmosphere is listed. As starting point, already existing orbits were used which were optimized regarding a dedicated retrieval period or repeat orbit cycle. The orbits are listed in Table 32-1. For a detailed discussion, please refer to chapter 41 and TN D9.

NGGM/MAGIC – Science Support Study During Phase A	*Final Report*	
	Doc. Nr:	MAGIC_FR
	Issue:	1.0
	Date:	15.11.2022
	Page:	268 of 466

Table 32-1: Orbit scenarios for an optimal application of de-aliasing models.

Scenario		Alti-tude [km]	Inc. [deg]	Defl. [deg]	Avg. sep. [km]	Repeat orbit period [days]	Drag. comp.	ACC noise	ATT noise	SST noise
3d_H	pol	463	89		220	3/7/31	Yes	SuperStar	GFO	LRI
	inc	432	70		220	3/7/31	Yes	MAGIC		LRI
5d_H	pol	488	89		220	5	Yes	SuperStar	GFO	LRI
	inc	465	75		220	5	Yes	MAGIC		LRI
7d_M	pol	417	87		220	7	Yes	SuperStar	GFO	LRI
	inc	389	70		220	7	Yes	MAGIC		LRI
5d_HL	pol	487	89		220	5	Yes	SuperStar	GFO	LRI
	inc	343	71		220	5	Yes	MAGIC		LRI

The maximum d/o of resolution of the retrieved gravity field solutions was chosen to be 120 for the long-term (monthly) retrieval periods. For the sub-monthly periods the maximum d/o of resolution was chosen in dependency of the largest distance of adjacent ground tracks at the equator after one repeat orbit cycle. This value was set in relation to the half of the circumference of the sphere (180°). Table 32-2 shows the derived values for the different scenarios.

Table 32-2: Maximum distance in longitude between adjacent ground tracks at the equator after a certain repeat orbit cycle together with the derived maximum d/o of resolution.

Simulation	Max. delta longitude [degree]	Max. d/o of resolution
3d_H (3 days)	3.48	50
3d_H (7 days)	2.38	80
5d_H (5 days)	2.45	80
7d_M (7 days)	1.82	100
5d_HL (5 days)	2.51	80

The scenarios are evaluated in chapter 33.

33 OPTIMAL APPLICATION OF DE-ALIASING MODELS (WP 430)

33.1 INDIVIDUALLY ASSESSMENT OF TIDAL AND NON-TIDAL ALIASING ERRORS

For a more optimized assessment of the non-tidal high frequency signals, the ocean tides were excluded for dedicated simulations. On the other side, non-tidal mass signals were excluded in order to investigate the performance due to tidal error signals. In order to get a complete picture of the error system of space-time aliasing, all time-varying signals were included in the simulations, finally. The noise assumptions for the instruments are included in all simulations.

First, the different Bender-type scenarios shall be evaluated wrt. errors due to non-tidal signals. Results presented in the following do not contain ocean tide signals, therefore. An atmosphere and ocean de-aliasing (AOD) model was applied during the processing in order to mitigate temporal aliasing due to AO signals. The remaining retrieved signal is mainly HIS.

Figure 33-1 displays the 30-day retrieval error for the Bender-type scenarios for January 2002 in terms of degree amplitudes as well as in terms of order amplitudes in mm EWH. The signal is affected mainly by error due to mismodelling of AO (AOerr). Results show a degraded performance for the 5dH scenario compared to the other scenarios caused by higher flying satellites. The degree amplitudes reveal larger errors due to AO even at low degrees for the 5dH scenario while the three other scenarios show similar performances up to d/o 60. The performance of the 7dM scenario is improved in a range between degree 60 and 100 due to lower flying spacecraft, however, the 5dHL scenario outperforms the 7dM scenario a the very high degrees due to a significantly lower flying inclined pair. The order amplitudes show increased signal amplitudes for orders between 10 and 30. These signals represent aliasing errors at polar regions caused by the polar pair, respectively. The higher order spectrum behaves similar to the spectrum of the higher degrees in the degree amplitudes.
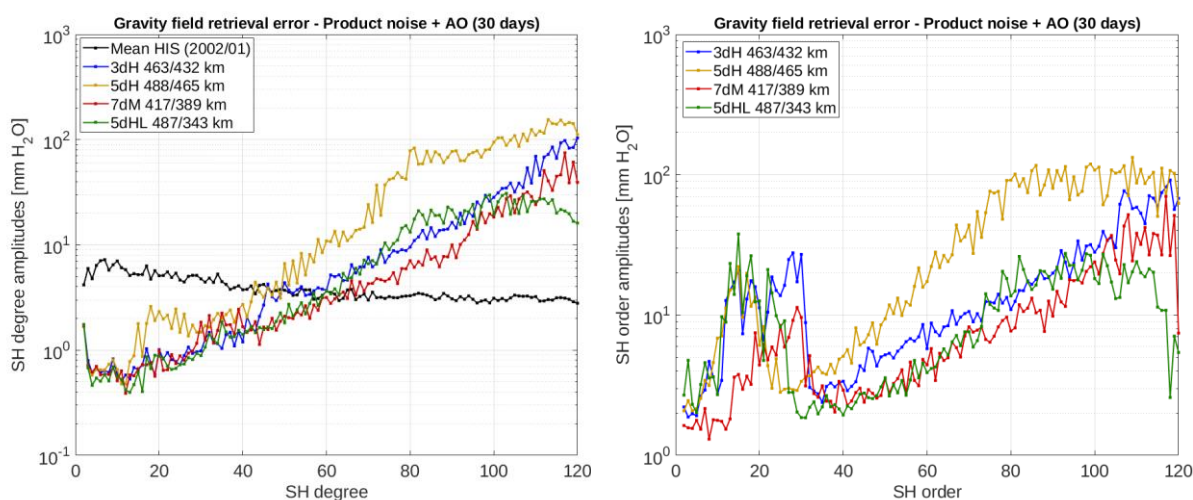
Figure 33-1: Left: degree error amplitudes im mm EWH for a 30-day retrieval including product noise and AOHIS for the 3dH scenario (blue), 5dH (orange), 7dM (red) and 5dHL (green). The reference HIS signal is plotted in black. Right: order error amplitudes in mm EWH.

For a more detailed analysis of the effects at lower orders it is worth to analyse the corresponding coefficient triangles displayed in Figure 33-2. All triangles contain larger signals for dedicated lower orders and degrees larger than about 50. The higher the degree the more order are affected by this phenomenon. This effect reflects the performances seen at the order amplitudes and is caused by larger errors at the polar regions due to signal originating from the polar pairs which aliases into the gravity field retrieval. Figure 33-3 shows a version of the spatially distributed gravity field retrieval error of the 3dH case where all signals included in coefficients lower than order 10 and larger than order 30 as well as coefficients lower than degree 50 have been excluded. At the same time, the right plot shows the signal distribution for coefficients larger than d/o 80, exclusively. The left plot reveals the error at polar areas while the right plot displays error signals at mid- and low latitude areas. The fully synthesized signal can be seen in Figure 33-4. Comparing scenarios 3dH and 5dH, the latter shows increased error for mid- and low latitude areas due to higher altitudes while it shows decreased errors at the polar regions due to a higher inclination (75° instead of 70°). Further, the 5dHL scenario shows decreased error for mid- and low latitude areas due to the lower altitude of the inclined pair but shows larger errors at polar areas due to a lower inclination (71° instead of 75°) compared to the 5dH scenario. Additional reduction of error at the high latitude areas can be reached when lowering the altitude of the polar pair, as it can be seen for the 7dM scenario.

Figure 33-2: Triangles of unitless coefficients in a logarithmic scale for a 30-day retrieval including product noise and AOHIS for the scenarios 3dH (top left), 5dH (top right), 7dM (bottom left) and 5dHL (bottom right).
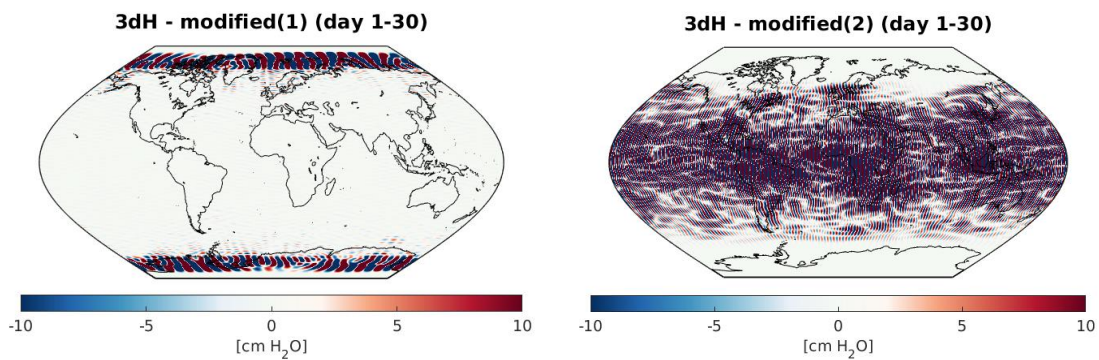
Figure 33-3: Spatial distribution of the 30-day retrieval error including product noise and AOHIS of the 3dH case including only coefficients between orders 10 and 30 as well as degrees larger than 50 (left) and including only coefficients larger than d/o 80 (right).
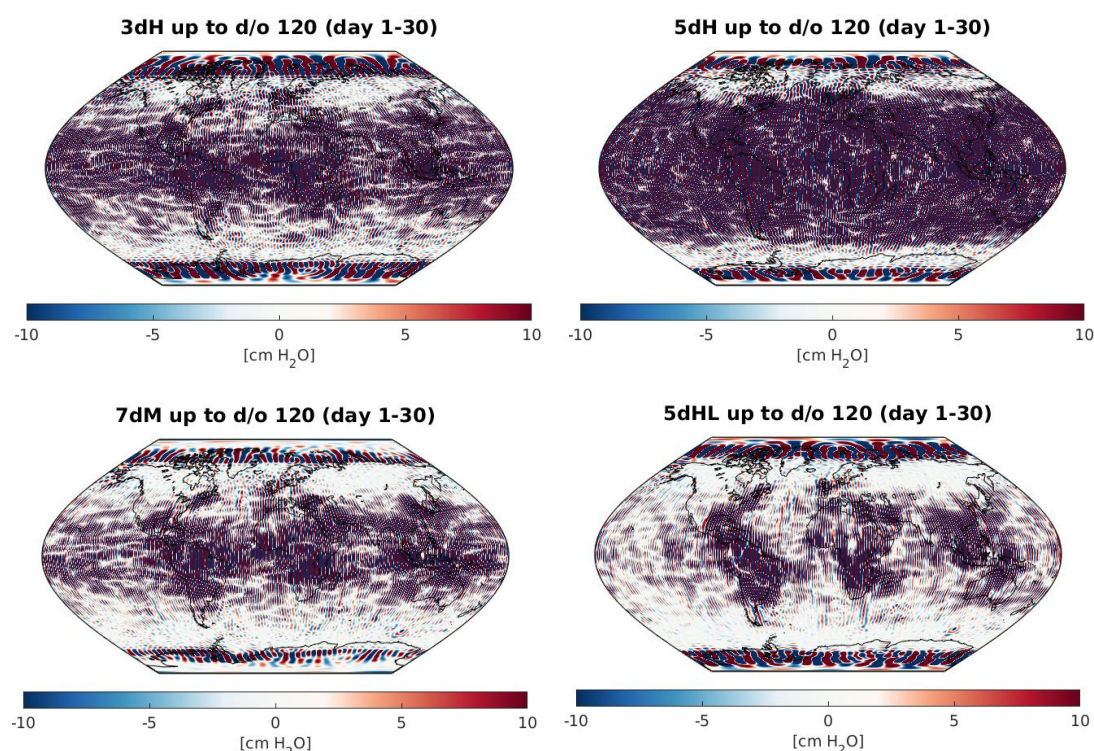
Figure 33-4: Spatial distribution of the 30-day retrieval error including product noise and AOHIS solved up to d/o 120 for the scenarios 3dH (top left), 5dH (top right), 7dM (bottom left) and 5dHL (bottom right).

The sub-monthly retrieval errors are displayed in Figure 33-5 in terms of degree and order amplitudes averaged for one month. In contrast to the monthly retrieval, the degree amplitudes for the sub-monthly retrieval show a retrieval period dependent performance for the very low degrees (~ up to d/o 16). The performance of the 5dH scenario is again degraded compared to the other scenarios due to the higher orbit altitudes. Despite the fact that the 3dH (3d) scenario solution is based on 3-daily retrieval periods, the performance is improved compared to the 5dH scenario, which is based on a 5-daily retrieval, due to lower altitudes. The performance of the 3dH (7d), 7dM and 5dHL scenarios is relatively similar to each other for the whole spectrum. The order amplitudes show again increased error signals for orders between 10 and 30 but in a somehow reduced format compared to the monthly retrieval errors. It is seen that this effect affects more orders for the 7dM scenario as it has been resolved up to a higher maximum d/o (100) compared to the other scenarios (50 and 80). The strongly reduced order amplitudes for the 3dH (3d) scenario at the very last three orders is caused by the fact that the corresponding solutions do only contain signals up to d/o 50. The coefficient triangles displayed in Figure 33-6 show reduced error signals along dedicated low orders compared to the monthly solutions due to a smaller maximum d/o of resolution confirming the lower order error amplitudes in Figure 33-5. The spatial retrieval error representation in Figure 33-7 confirms the lower aliasing error phenomenon at the polar areas. The larger part of the aliasing error is concentrated at the mid- and low latitude areas. As it was already seen in the degree amplitudes the error performance of the 3dH (7d), 7dM and 5dHL scenarios is relatively similar and shows improved behavior compared to the 3dH (3d) scenario due to a larger retrieval period. The the 5dH scenario suffers from higher altitudes and shows a degraded performance, therefore.
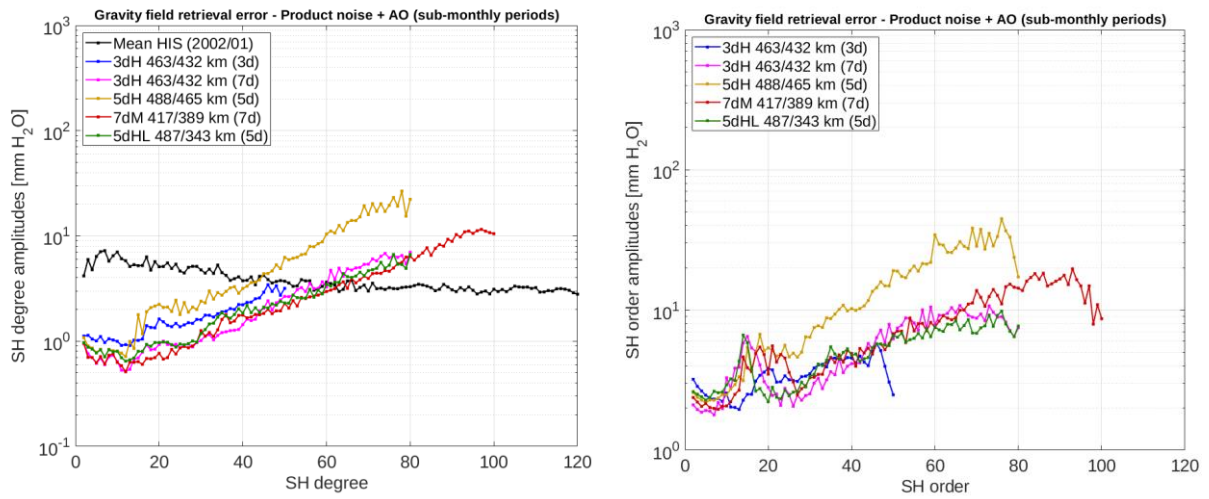
Figure 33-5: Left: degree error amplitudes im mm EWH for averaged sub-monthly retrieval including product noise and AOHIS for the 3dH (3d) scenario (blue), 3dH (7d) (magenta), 5dH (orange), 7dM (red) and 5dHL (green). The reference HIS signal is plotted in black. Right: order error amplitudes in mm EWH.
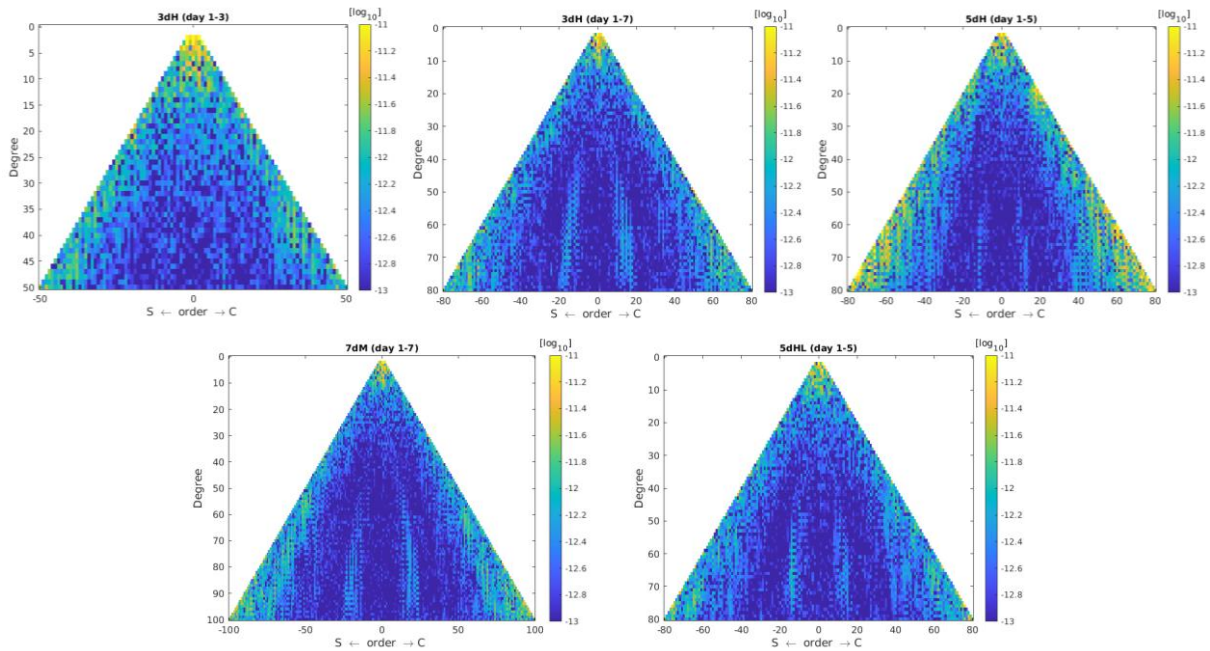
Figure 33-6: Triangles of unitless coefficients in a logarithmic scale for sub-monthly retrieval including product noise and AOHIS for the scenarios 3dH - 3 days (top left), 3dH - 7 days (top center), 5dH – 5 days (top right), 7dM – 7 days (bottom left) and 5dHL – 5 days (bottom right).
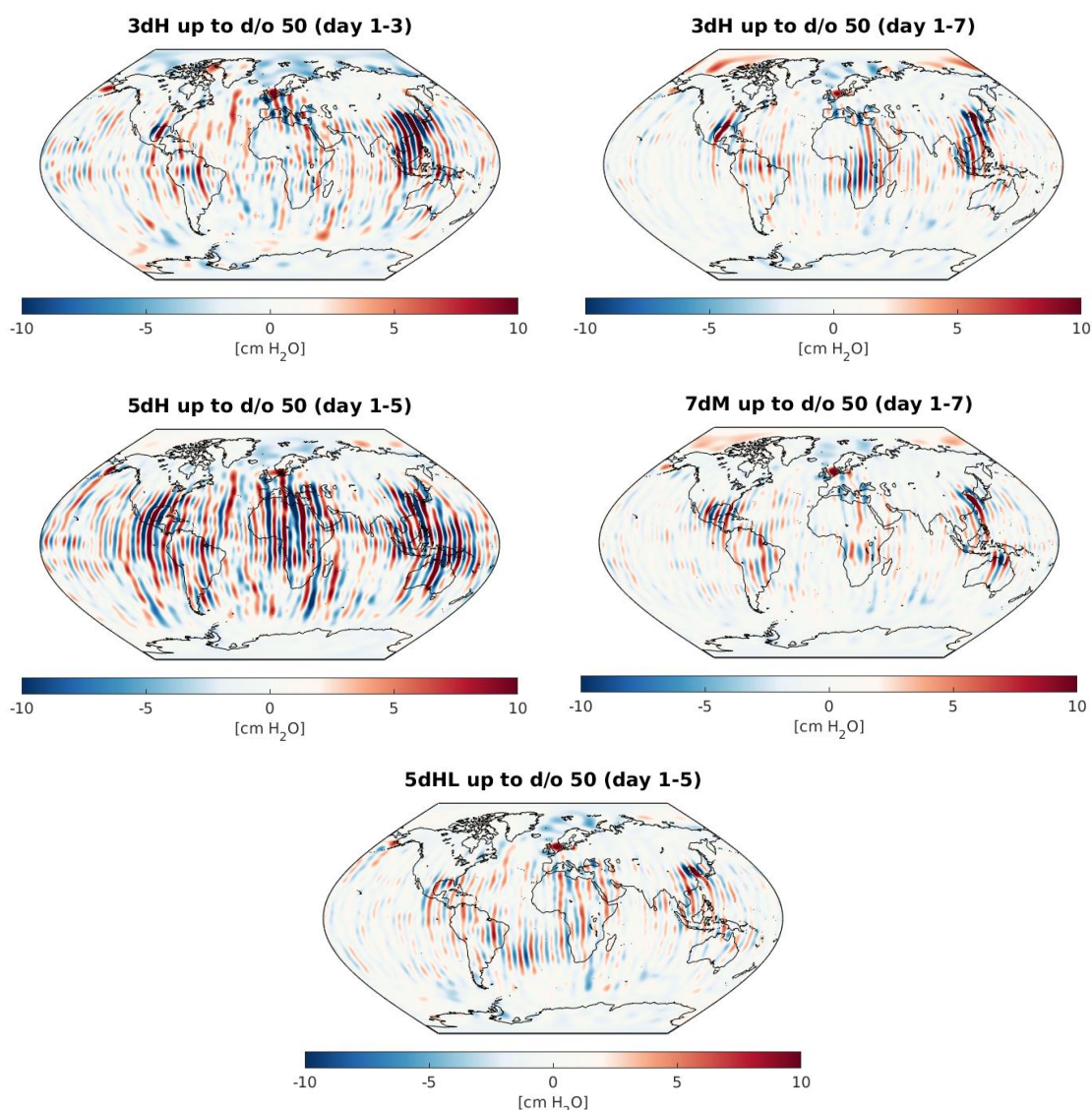
Figure 33-7: Spatial distribution of the sub-monthly retrieval error solved up to d/o 50 including product noise and AOHIS for the scenarios 3dH - 3 days (top left), 3dH - 7 days (top right), 5dH – 5 days (center left), 7dM – 7 days (center right) and 5dHL – 5 days (bottom).

In the following, the Bender-type scenarios were analysed wrt. tidal aliasing errors, i.e. no AOHIS signal has been included during processing. The related degree error and order error amplitudes for a 30-day retrieval are displayed in Figure 33-8, the corresponding triangles are shown in Figure 33-9and the spatial signal distribution is displayed in Figure 33-10. The degree amplitudes show similar performances up to d/o 40 for all scenarios. Compared to the simulation case including non-tidal signals and excluding tidal signals, now the 5dH scenario shows an improved performance at the longer wavelength spectrum. Thus, tidal aliasing impacts the low degree performance less when simulating scenarios with different orbit altitudes. However, the error performance at the shorter wavelengths is driven by the orbit altitude, again. The order amplitudes at the very low orders show that the 7dM scenario benefits from the low flying polar pair. Furthermore, the 3dH and 7dM scenarios show increased error signals between orders 20 and 30 due to larger error signals at high degree coefficients >80

which can be seen from the corresponding triangle plots in Figure 33-9. In contrast, the 5dH and 5dHL scenarios show decreased order error amplitudes at this range due to smaller error signals at high degree coefficients.
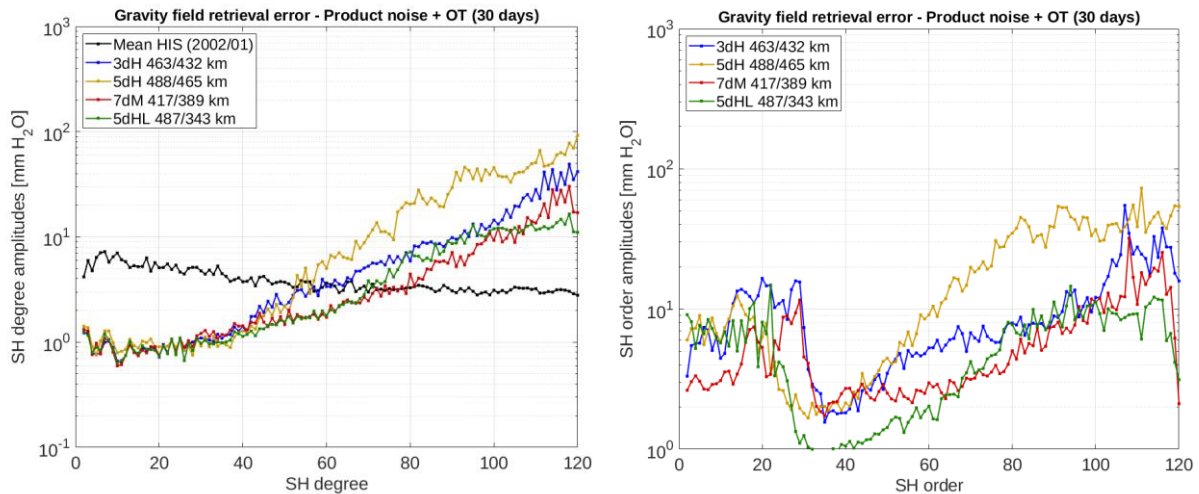
Figure 33-8: Left: degree error amplitudes im mm EWH for a 30-day retrieval including product noise and ocean tides for the 3dH scenario (blue), 5dH (orange), 7dM (red) and 5dHL (green). The reference HIS signal is plotted in black. Right: order error amplitudes in mm EWH.
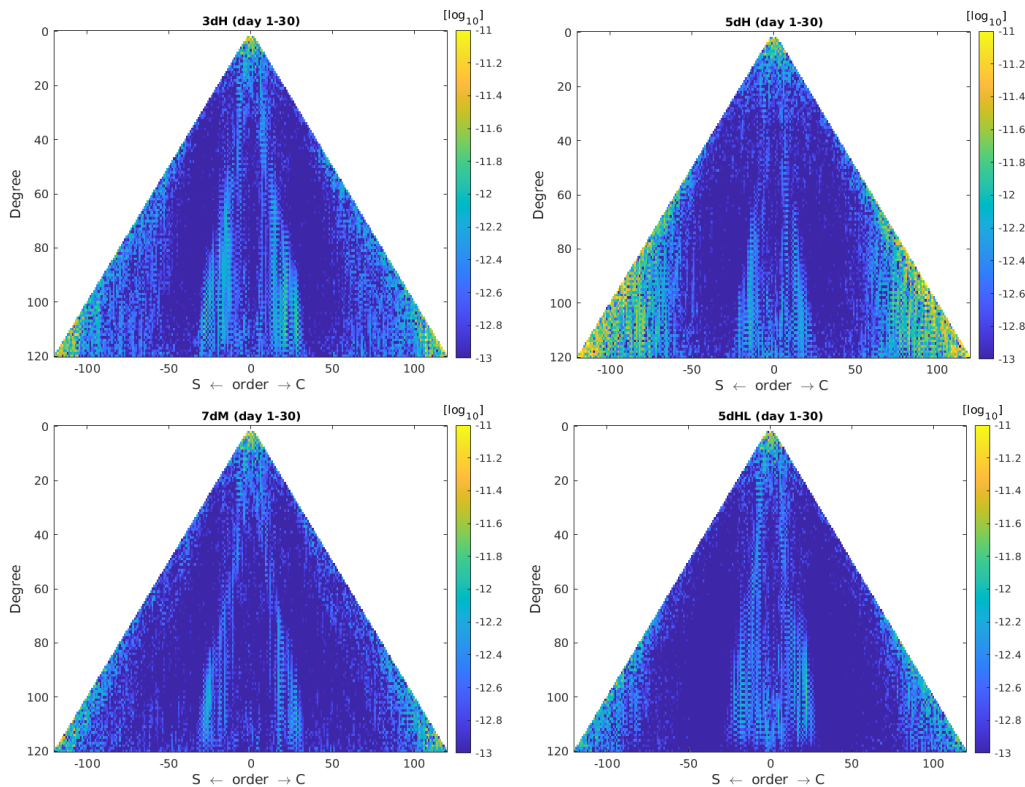
Figure 33-9: Triangles of unitless coefficients in a logarithmic scale for a 30-day retrieval including product noise and ocean tides for the scenarios 3dH (top left), 5dH (top right), 7dM (bottom left) and 5dHL (bottom right).
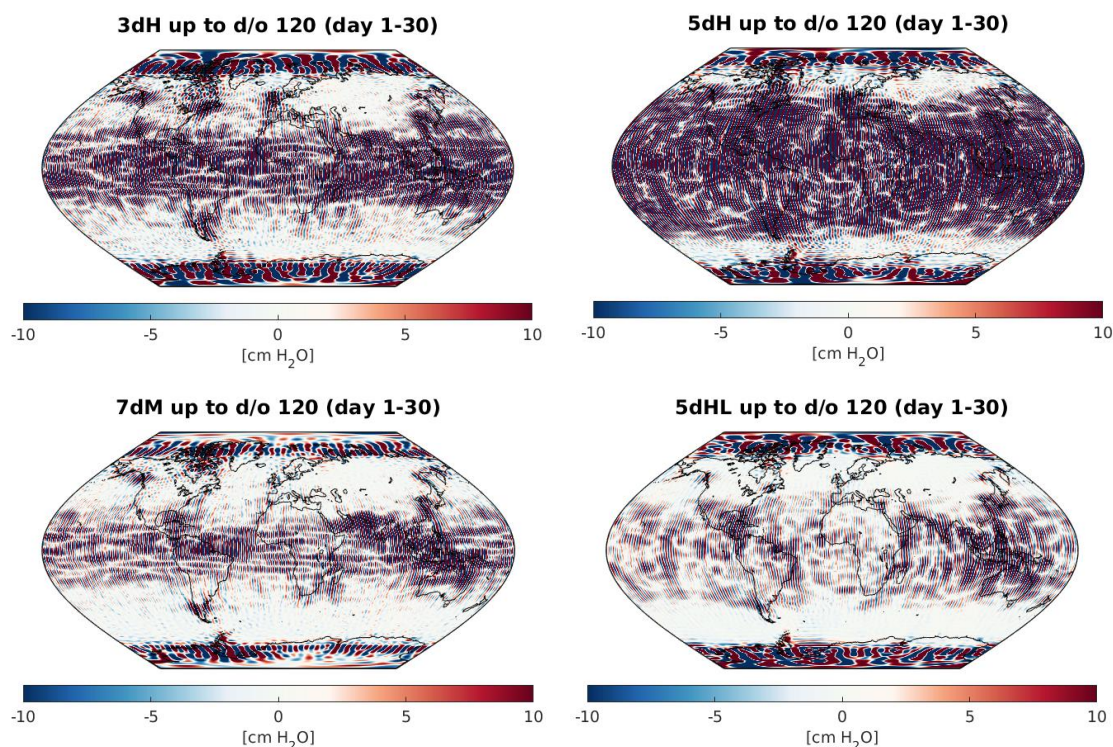
Figure 33-10: Spatial distribution of the 30-day retrieval error including product noise and ocean tides solved up to d/o 120 for the scenarios 3dH (top left), 5dH (top right), 7dM (bottom left) and 5dHL (bottom right).

The analysis of the sub-monthly results of the product noise + ocean tides simulation case is shown in Figure 33-11 in terms of degree and order error amplitudes as well as in terms of coefficient triangles in Figure 33-12. The spatial analysis can be found in Figure 33-13. From the degree error amplitudes it can be seen that for the low degrees the performance is related to the length of the retrieval period, i.e. the 7dM and 3dH (7d) scenarios show reduced errors. The higher degree error performance is dominated by the orbit altitudes, respectively. Similar to the product noise + AOHIS simulation case, the order amplitudes show a larger error performance for the 7dM scenario between orders 15 to 25 due to a higher maximum d/o of resolution compared to the other scenarios.

From this analysis and based on the previous results of the product noise + AOHIS case, it can be stated that temporal aliasing errors at polar regions can be reduced by solving the gravity fields only up to ~maximum d/o 80 for sub-monthly retrieval. Errors at polar regions can be further reduced by lowering the altitude of the polar pair or increasing the inclination of the inclined pair, in general. High frequency temporal aliasing errors at mid- and low latitude areas are highly related to the altitude of the inclined pair and can be reduced by flying at lower orbits. The monthly retrieval error performance is highly related to the orbit altitude, especially for the shorter wavelength spectrum. The sub-monthly retrieval error performance is related to both, the length of the retrieval period and the altitude. Especially at the longer wavelength spectrum, the retrieval period is more dominant so that longer periods lead to improved performances, more for reducing AO de-aliasing errors than for reducing tidal aliasing errors.
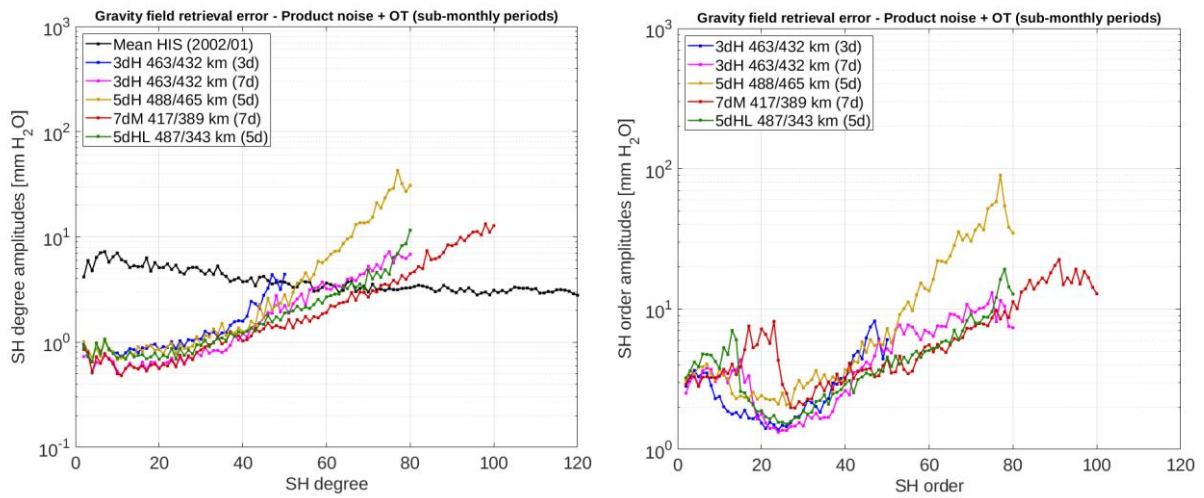
Figure 33-11: Left: degree error amplitudes im mm EWH for averaged sub-monthly retrieval including product noise and ocean tides for the 3dH (3d) scenario (blue), 3dH (7d) (magenta), 5dH (orange), 7dM (red) and 5dHL (green). The reference HIS signal is plotted in black. Right: order error amplitudes in mm EWH.
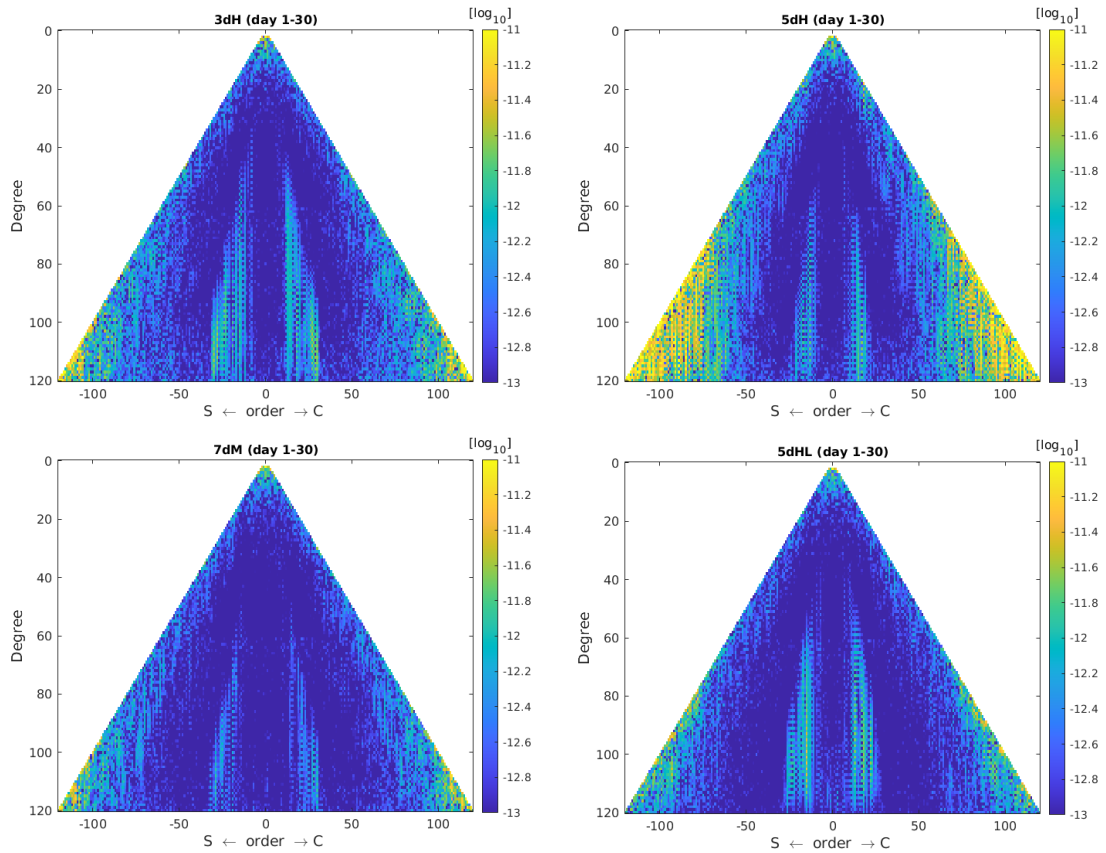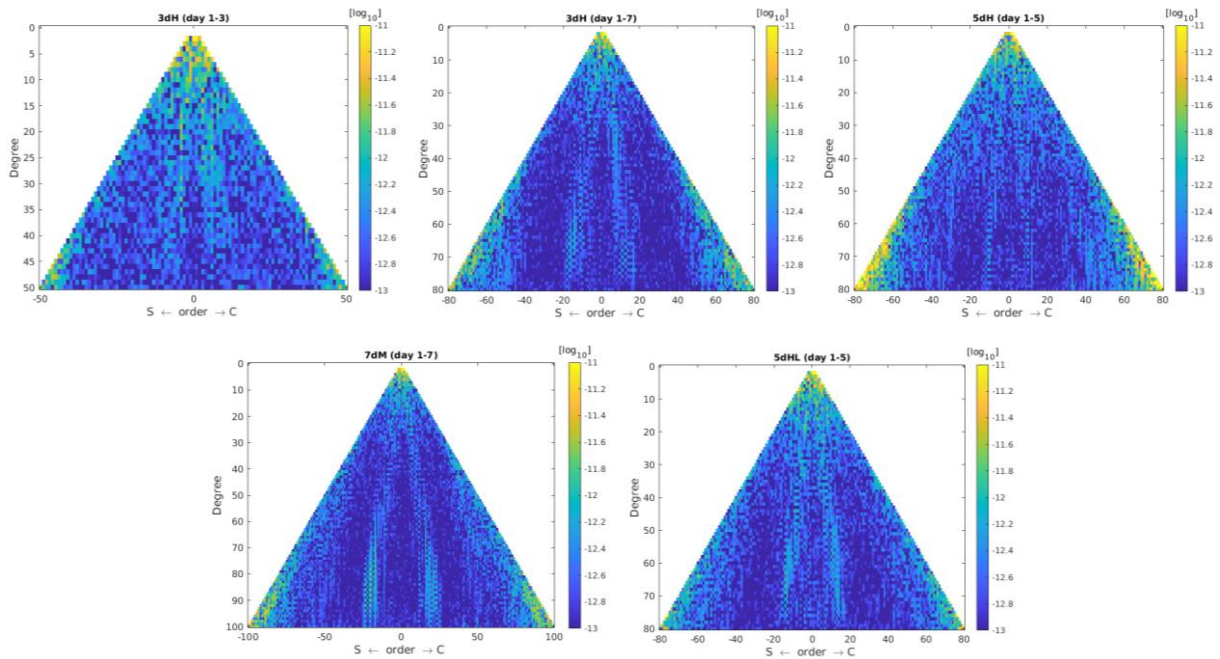

Figure 33-12: Triangles of unitless coefficients in a logarithmic scale for sub-monthly retrieval including product noise and ocean tides for the scenarios 3dH - 3 days (top left), 3dH - 7 days (top center), 5dH – 5 days (top right), 7dM – 7 days (bottom left) and 5dHL – 5 days (bottom right).
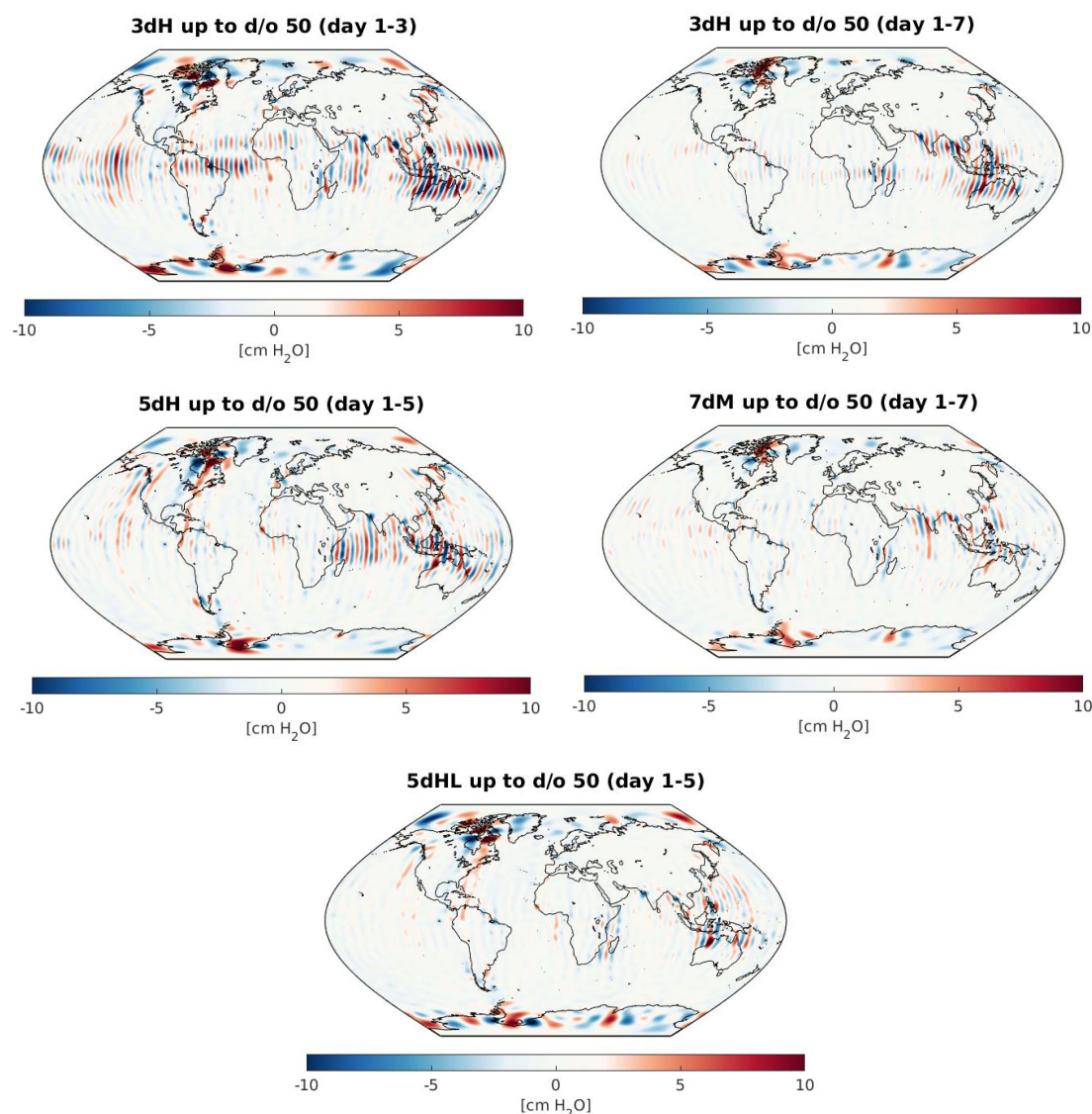
Figure 33-13: Spatial distribution of the sub-monthly retrieval error solved up to d/o 50 including product noise and ocean tides for the scenarios 3dH - 3 days (top left), 3dH - 7 days (top right), 5dH – 5 days (center left), 7dM – 7 days (center right) and 5dHL – 5 days (bottom).

Finally, full noise simulations have been performed for a two-month time span including product noise, AOHIS and ocean tide signals. Figure 33-14 shows the degree error amplitudes for the monthly and sub-monthly retrieval. The error performances are dominated by errors due to AO de-aliasing and show a similar performance as for the simulation case when excluding ocean tides. Figure 33-15 displays the cumulated errors for the monthly and sub-monthly retrieval wrt. the target and threshold requirements. In case of the monthly retrieval, threshold requirements can only be fulfilled at 200 km spatial scale for all Bender-type scenarios except for the 5dH scenario. The target requirements cannot be met. In case of the sub-monthly retrieval, all threshold requirements can be fulfilled by all simulation scenarios, except for the 5dH scenario at 800 km spatial scale. Target requirements cannot be met either. A quantitative assessment of the full noise based retrieval errors in a cumulated sense is given in Table 33-1.
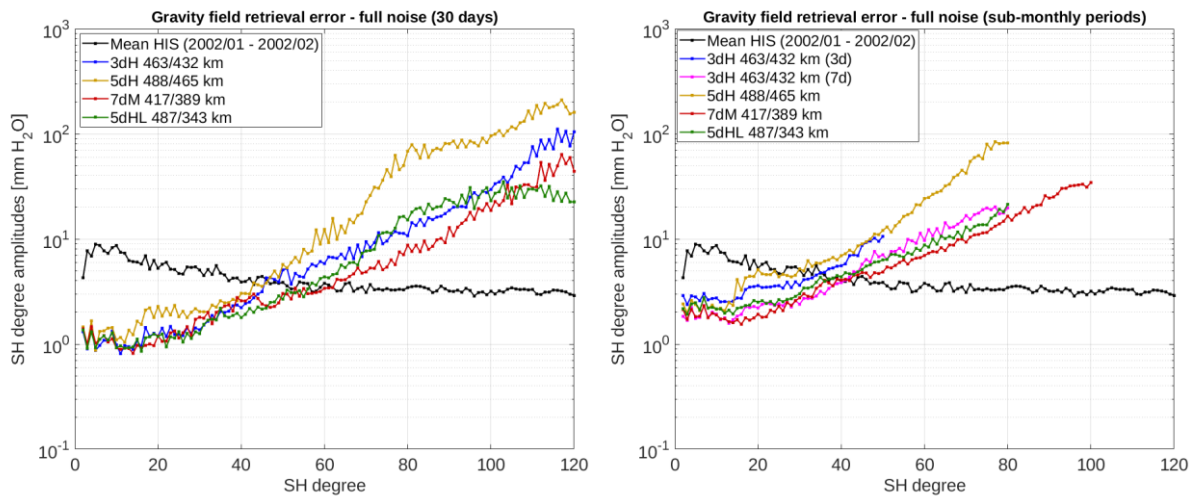
Figure 33-14: Left: degree error amplitudes im mm EWH for a 30-day two-monthly average retrieval including full noise for the 3dH scenario (blue), 5dH (orange), 7dM (red) and 5dHL (green). The reference HIS signal is plotted in black. Right: degree error amplitudes in mm EWH for a sub-monthly average retrieval.
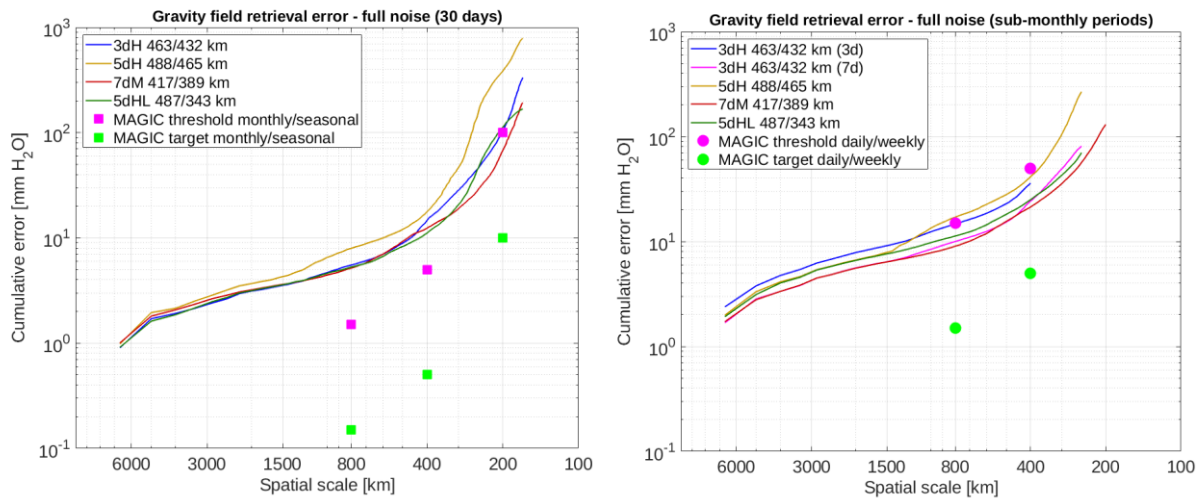
Figure 33-15: Left: cumulative error im mm EWH for a 30-day two-monthly average retrieval including full noise for the 3dH scenario (blue), 5dH (orange), 7dM (red) and 5dHL (green). Right: cumulative error in mm EWH for a sub-monthly average retrieval. The threshold and target requirements are displayed in magenta and light green.

Table 33-1: Cumulative error in mm EWH for different retrieval periods averaged over two months for specific maximum d/o of resolution.

Scenario	Cumul. error d/o 50 [mm EWH]	Cumul. error d/o 80 [mm EWH]	Cumul. error d/o 120 [mm EWH]
3d_H (3 days)	36	-	-
3d_H (7 days)	24	81	-
3d_H (30 days)	15	46	334
5d_H (5 days)	41	267	-
5d_H (30 days)	18	158	790
7d_M (7 days)	21	57	-
7d_M (30 days)	12	29	192
5d_HL (5 days)	25	70	-
5d_HL (30 days)	11	47	168

33.2 APPLICATION OF "CLASSIC" WIESE PARAMETERIZATION

In this chapter the so called 'Wiese' parameterization has been applied when estimating gravity field parameters with the goal to reduce temporal aliasing errors (mainly due to high frequency AO signals) by setting up short-term gravity field parameters (e.g. daily) in addition to the long-term gravity field parameters (e.g. one month). More background information about this approach can be found in chapter 35.1.

The Wiese parameterization has been applied based on two different processing strategies: gravity field retrieval without using an AOD model and retrieval including an AOD model. The approach has been tested on the 3dH and 7dM scenarios as they operate at different orbit altitudes. The short-term parameters were set up on a daily basis up to a maximum d/o of 15.

The results of the monthly retrieval are displayed in Figure 33-16. In case of not using an AOD model, retrieval errors are dominated by temporal aliasing errors due to high frequency AO signals, especially at the very low degrees where the signal content of AO is strongest. In that case, the Wiese parameterization helps to reduce the temporal aliasing error from AO leading to improved error performances at the long wavelength spectrum. The improvement is restricted mainly up to few degrees above the maximum d/o of parameterization of the short-term gravity fields. At the very high degrees some reduced error behaviour can be seen as well. However, some coefficients at the mid degrees (between 20 and 50) show a degraded performance compared to the nominal retrieval. This effect is present for both, the 3dH and the 7dM scenario and indicates an overparameterization of the system. In case of including an AOD model, the Wiese solutions do not show an improved performance compared to the nominal solutions. Again, increased error signals are visible for some mid degrees. The results indicate that, the signal amplitude of the remaining aliasing error due to mismodelling of AO signals (if an AOD model is applied) is too small in order to further de-alias it by applying the Wiese parameterization when using the current Bender-type configurations. In Figure 33-17 the discussed simulation cases are plotted against each other at the example of the 3dH scenario. It is seen that the nominal solution based on the AOD model applied performs similar to the solution processed via Wiese without applying an AOD model at the very low degrees. Results

demonstrate that the Wiese parameterization does not further improve the gravity field retrieval when an AOD model is applied.
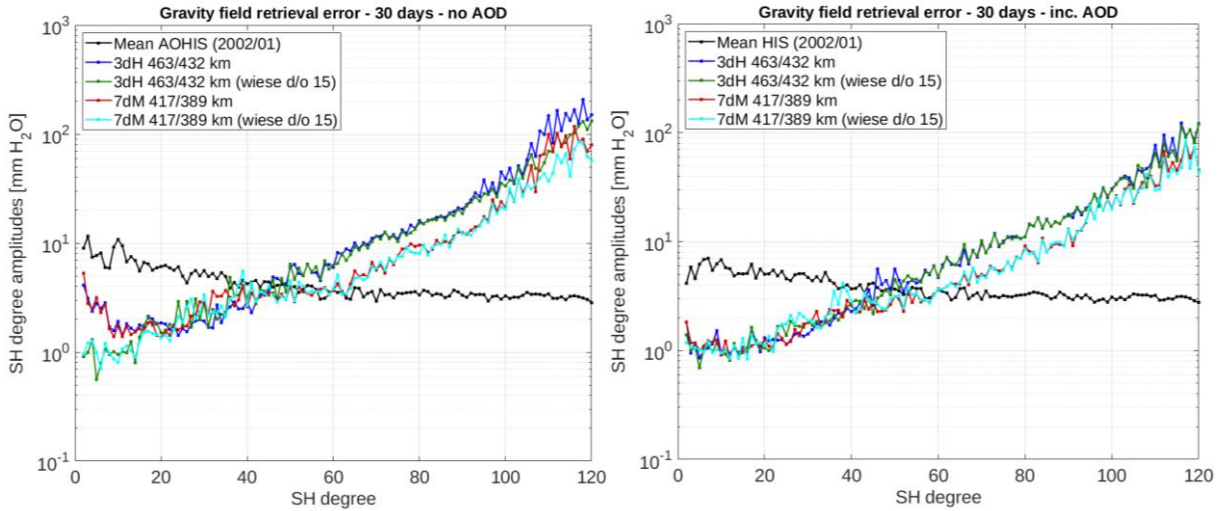
Figure 33-16: Left: degree error amplitudes in mm EWH of scenarios 3dH and 7dM for a 30-day retrieval when performing the nominal processing (blue and red) and when applying the Wiese approach (green and cyan) without using an AOD model. Right: corresponding degree error amplitudes when using an AOD model. The reference AOHIS/HIS signal is plotted in black.
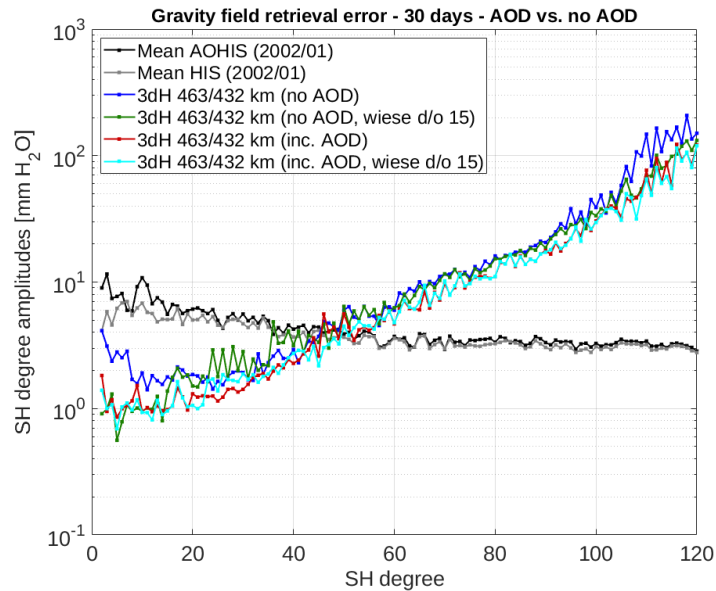
Figure 33-17: degree error amplitudes in mm EWH of scenario 3dH for a 30-day retrieval when performing the nominal processing without using an AOD model (blue) and including an AOD model (red) and when applying the Wiese approach without using an AOD model (green) and including an AOD model (cyan). The reference AOHIS signal is plotted in black, the reference HIS signal is plotted in grey.

The results related to sub-monthly retrieval show a similar picture compared to the results of the monthly retrieval. Figure 33-18 displays the situation for a 7-day retrieval period (January 8-14). Reduced aliasing errors at the low degrees can be seen when applying the Wiese parameterization if no AOD model is used. At the same time, increased error signals arise for specific coefficients of mid degrees. In case of using an AOD model, no further error reduction can be seen. It is to mention that the retrieval error performance of the long-term Wiese solutions varies with the retrieval period. Other periods show only small improvements or even do not show an improved behaviour for the Wiese solutions at the very low degrees when no AOD model is applied.
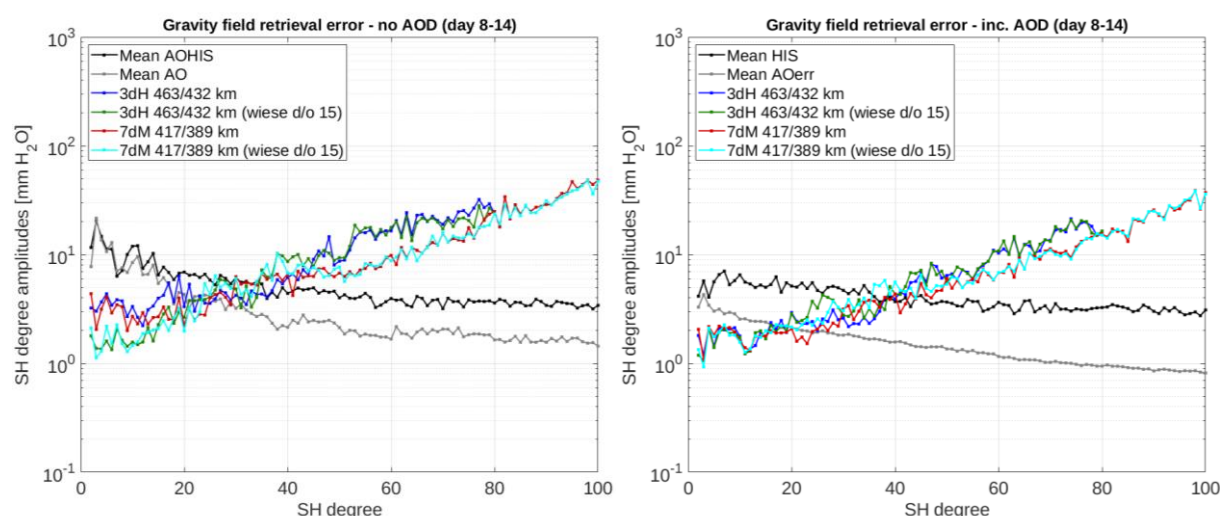
Figure 33-18: Left: degree error amplitudes in mm EWH of scenarios 3dH and 7dM for a sub-monthly retrieval when performing the nominal processing (blue and red) and when applying the Wiese approach (green and cyan) without using an AOD model. Right: corresponding degree error amplitudes when using an AOD model. The reference AOHIS/HIS signal is plotted in black. The mean AO signal (left) and the mean AOerr signal (right) are plotted in grey.

In order to investigate the effect of degraded coefficients at the mid degrees when applying the Wiese parameterization, coefficient triangles can be used. Figure 33-19 shows the coefficients for the nominal and Wiese case when no AOD model is applied at the example of a 7-day retrieval (day 8-14) of scenario 3dH. Additionally, the difference among both solutions is displayed together with the relative improvement of the Wiese solution wrt. the nominal solution. The differential plots reveal larger differences for low degrees and orders as well as for the sectorial and near-sectorial coefficients. The former is related to the reduction of aliasing errors at the low degrees when applying the Wiese approach, the latter is related to the degraded performance of dedicated coefficients between degree 20 and 50.

The situation might become clearer when looking at the spatial signal distribution in Figure 33-20 and Figure 33-21. The former shows the error signal resolved up to d/o 15 with significantly reduced error signals for the Wiese solution. The latter shows the error signal resolved only for coefficients between d/o 20 and 50 with significantly larger errors signals at some mid- and low latitude areas for the Wiese solution. This leads to the conclusion that temporal aliasing signal, which is not captured by the Wiese parameters, aliases with larger amplitudes into the long-term solution and causes a degraded estimation performance for especially mid degree coefficients due to overparameterization.
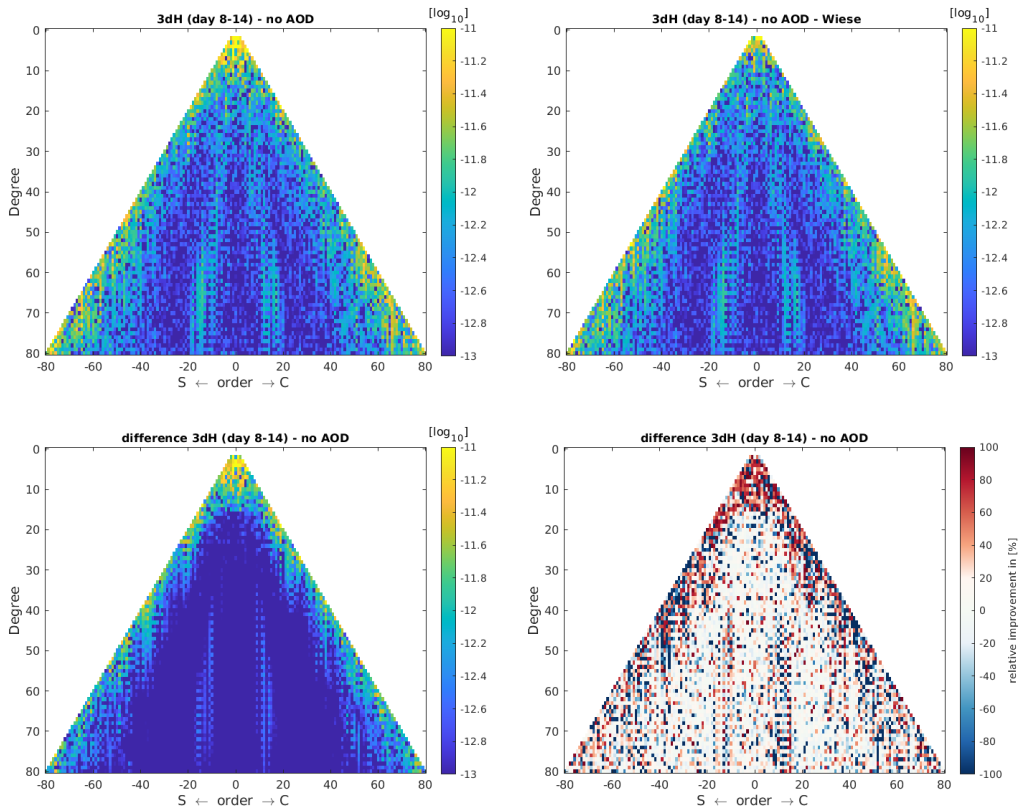
Figure 33-19: Triangles of unitless coefficients in a logarithmic scale of scenario 3dH for a 7-day retrieval error without using an AOD model. Top left: nominal solution. Top right: Wiese parameterization applied. Bottom left: difference between Wiese- and nominal processed solutions. Bottom right: relative improvement of Wiese solution wrt. the nominal solution in terms of percentages.
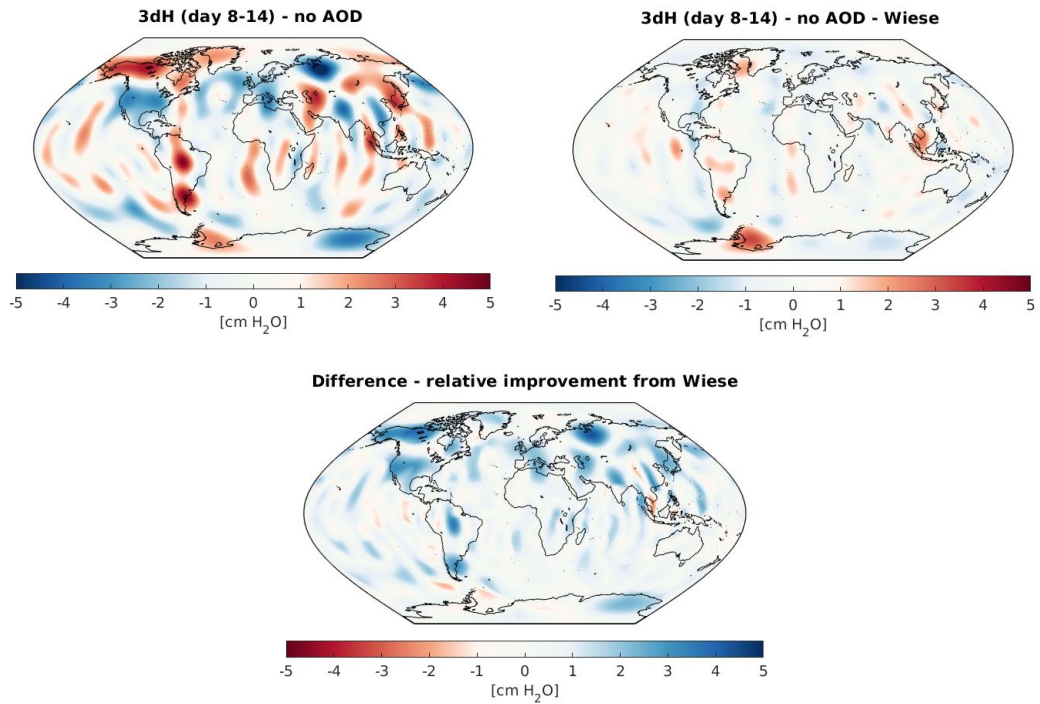
Figure 33-20: Spatial distribution of the 7-day retrieval of scenario 3dH without using an AOD model resolved up to d/o 15. Top left: nominal solution. Top right: Wiese parameterization applied. Bottom left: relative improvement of Wiese solution wrt. the nominal solution in terms of cm EWH.
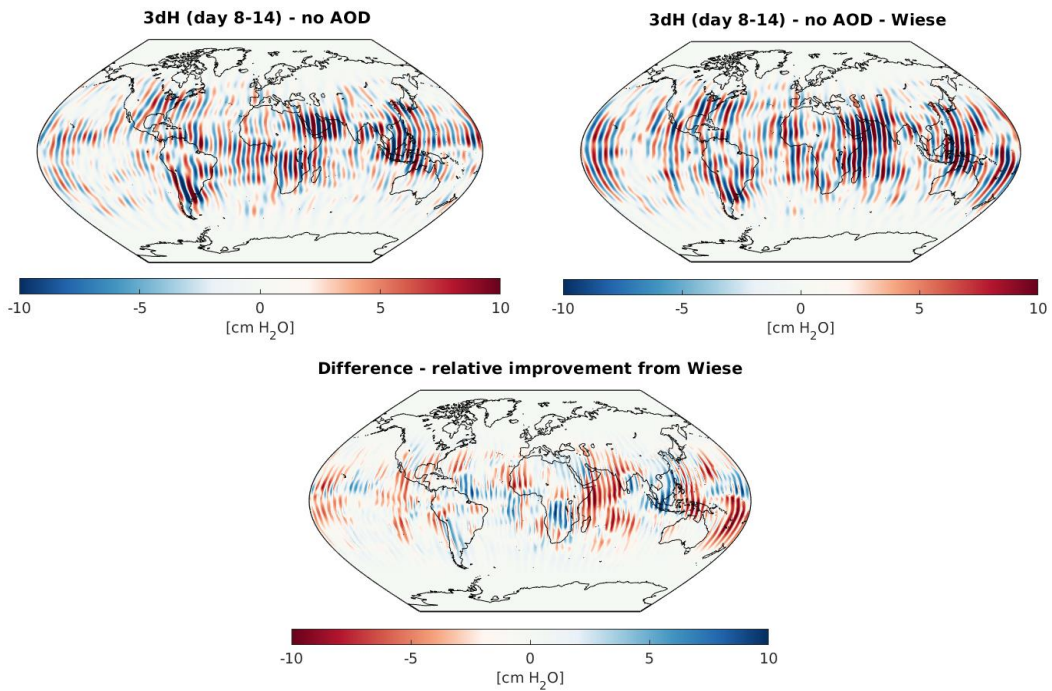
Figure 33-21: Spatial distribution of the 7-day retrieval of scenario 3dH without using an AOD model resolved for coefficients between d/o 20 and 50. Top left: nominal solution. Top right: Wiese parameterization applied. Bottom left: relative improvement of Wiese solution wrt. the nominal solution in terms of cm EWH.

Performance of Wiese solution when omitting ocean tides and product noise

In order to check a possible impact of tidal signal error and noise due to instruments (ACC, LRI) on the estimation performance of Wiese parameterized gravity field solutions, simulations have been done at the example of the 3dH scenario excluding both types of errors.

Figure 33-22 shows the degree amplitudes excluded for a monthly and sub-monthly retrieval period as a comparison among the full noise results and the results where ocean tides and product noise have been excluded. The processing has been executed without applying an AOD model for de-aliasing. The graphs representing the solutions without including tides and instrument errors show a slightly reduced error level compared to the full noise solutions due to less signal included. This is especially visible at the very low degree spectrum where tidal errors have usually a larger impact in terms of temporal aliasing error. This fact leads to further improved Wiese solutions for the low degree spectrum up to d/o 15. However, the peaky structure of the solutions at mid degrees caused by over parameterization remains, equal to the full noise solutions. This indicates that the estimation performance of Wiese parameterized solutions is mainly dependent on the error signal of A and O.
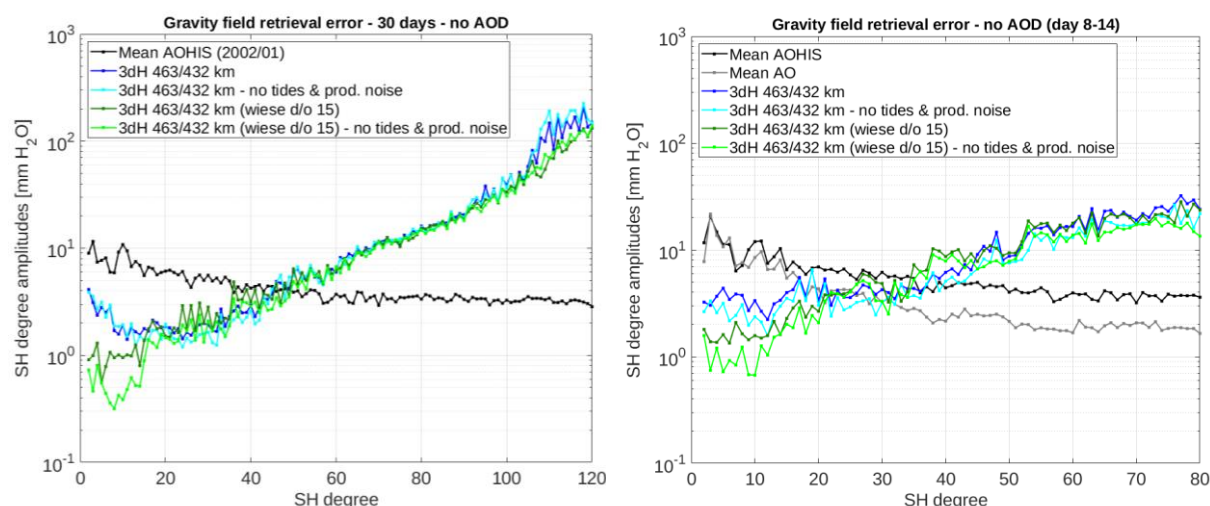
Figure 33-22: Degree error amplitudes in mm EWH of scenario 3dH for a 30-day retrieval (left) and a 7-day retrieval (right) without using an AOD model when performing the nominal processing including full noise (blue) and omitting ocean tides and product noise (cyan) and when performing the Wiese processing including full noise (dark green) and omitting ocean tides and product noise (light green). The reference AOHIS/AO signal is plotted in black and grey.

The findings are further confirmed by the coefficient triangles for a 7-day retrieval when omitting ocean tides and product noise, shown in Figure 33-23. Main differences among the nominal and the Wiese solutions are visible at the very low degree spectrum. The spatial representations are displayed in Figure 33-24 showing the error signal resolved only for coefficients between d/o 20 and 50 with significantly larger errors signals at some mid- and low latitude areas for the Wiese solution.
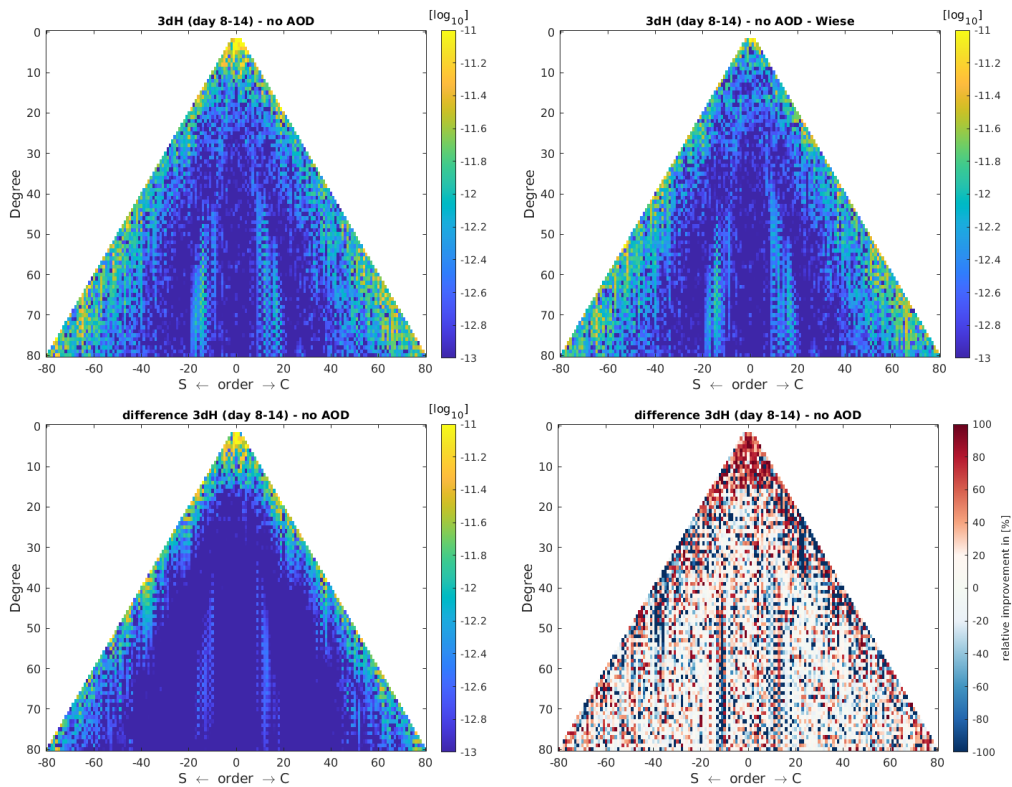
Figure 33-23: Triangles of unitless coefficients in a logarithmic scale of scenario 3dH for a 7-day retrieval error without using an AOD model and omitting ocean tides and product noise. Top left: nominal solution. Top right: Wiese parameterization applied. Bottom left: difference between Wiese- and nominal processed solutions. Bottom right: relative improvement of Wiese solution wrt. the nominal solution in terms of percentages.
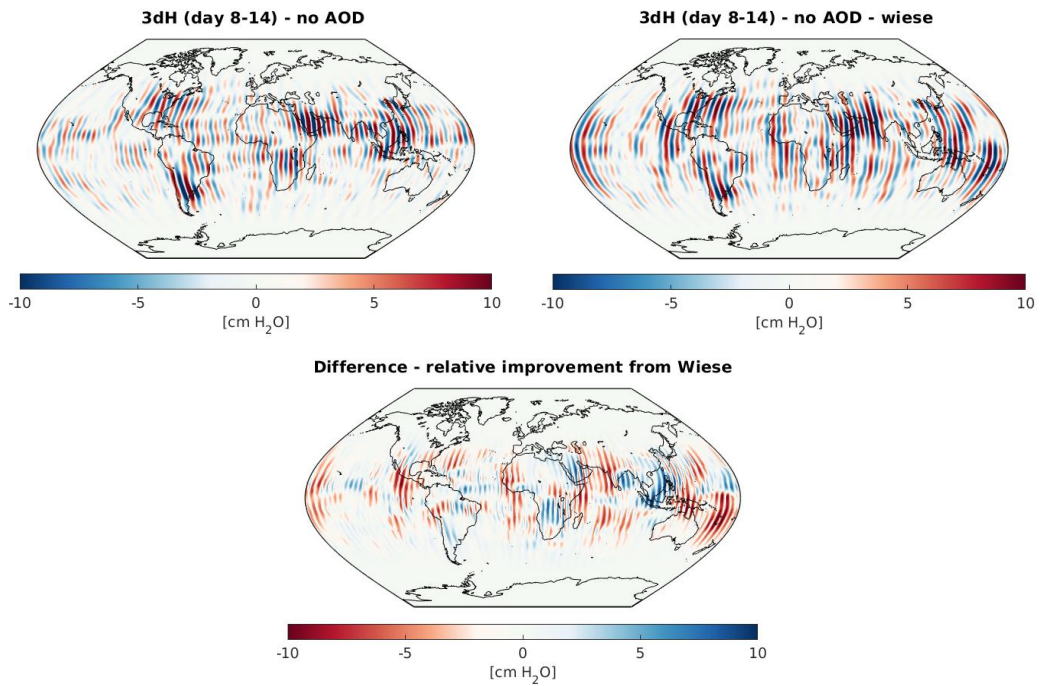
Figure 33-24: Spatial distribution of the 7-day retrieval of scenario 3dH without using an AOD model and omitting ocean tides and product noise resolved for coefficients between d/o 20 and 50. Top left: nominal solution. Top right: Wiese parameterization applied. Bottom: relative improvement of Wiese solution wrt. the nominal solution in terms of cm EWH.

NGGM/MAGIC – Science Support Study During Phase A	*Final Report*	
	Doc. Nr:	MAGIC_FR
	Issue:	1.0
	Date:	15.11.2022
	Page:	288 of 466

34 TREATMENT OF OCEAN TIDES IN NRT ANALYSIS AND POST-PROCESSING (WP 440)

The AO- and OT-based de-aliasing errors stemming from uncertainties within geophysical BMs are currently the single-most limiting factor for satellite-based gravity retrieval performance. Especially for NRT-based applications where the retrieval is carried out over short time intervals of a few days (c.f. RD-6) for a comparatively low spatial resolution, classic post-processing techniques may not be applicable. Instead, one should aim to mitigate the errors directly in the data processing chain itself.

In case of OT, an approach aiming to co-estimate tidal constituents alongside the actual retrieved gravity field and to apply them as corrections to the OT de-aliasing model has been proven beneficial RD-5. However, this processing technique requires the processing of long time intervals of multiple years (at least twice the longest aliasing period of a tidal constituent) in order to function properly, and while the OT de-aliasing model could in principle be improved by co-estimating OT corrections based on the GRACE mission as well as its successors and then be applied in the NRT-type processing, it somewhat contradicts the idea of short-periodic data processing. Instead, we propose the stochastic modelling of OT BM errors analogously to [RD- **7**]. The basis for this approach is the fact that OT models feature a time-invariant spatial error pattern – low error level in open waters and high error level in high latitudes (above $|\varphi|=60°$) as well as in shallow waters, i.e. coastal regions. Consequently, if such error information is accounted for (e.g. in terms of co-variance matrices of the underlying in-phase and quadrature coefficients) and propagated onto the level of observations, then observations carried out in "problematic" regions receive a lower weight within the parameter estimation which results in the reduction of aliasing effects.

In a first iteration the OT BM error weighting method is not incorporated into the NRT processing scheme as presented in [RD- 6], but is instead simply applied to a short-term retrieval in closed-loop simulations carried out with the RSS. The reason for choosing this approach is on one hand the fact that the error propagation scheme is not yet implemented in the FSS, but the performance of RSS and FSS simulations has been proven to be consistent in a relative sense in multiple previous scientific studies. On the other hand, the benefit of an improved stochastic modelling is not bound to any specific parametrization as long as it is done correctly, and can thus be directly translated between the 'nominal' short-period simulation scenario and one using an enhanced parametrization such as the NRT processing.
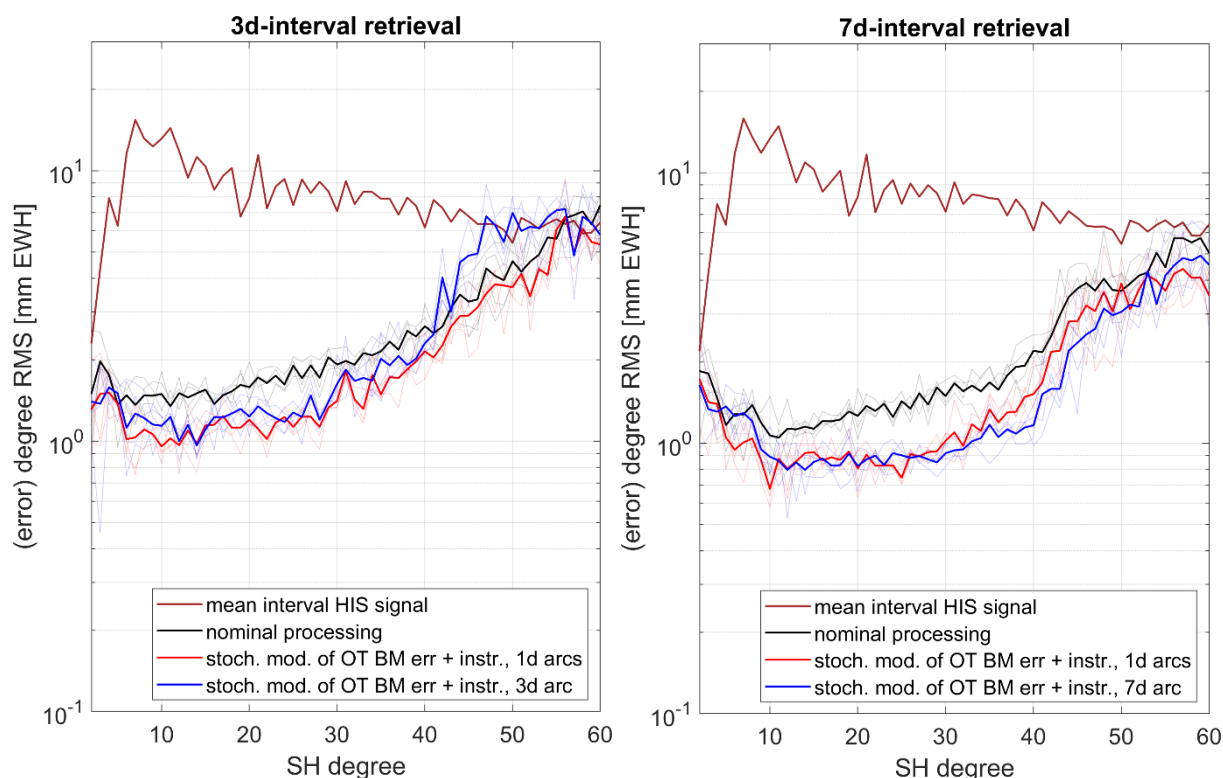
Figure 34-1: Retrieval performance of 3d- (left) and 7d-solutions (right) in case of the nominal processing as well as stochastic modelling of OT BM errors and instrument noise employing various arc lengths. Thin lines indicate the retrieval error of the respective interval field while the thick lines of the respective colour represent the corresponding mean.

For the purpose at hand the simulations are based on a Bender-type satellite formation using the orbits of the 3d_H scenario (c.f. Table 32-1), and the retrieval periods are chosen in accord with the underlying sub-cycles of 3 and 7 days, which are also in accord with the NRT retrieval periods presented in [RD- 6]. For the gravity signal, in this study limited to d/o 60, we consider the OT de-aliasing error of the eight principal tidal constituents in terms of differences between the GOT4.7 and EOT11a OT models, the AO de-aliasing error as 10% of the true AO signal in addition to the full HIS signal as well as the static field GOCO05s. On the instrument side we consider the NGGM-type ACC and the LRI (cf. D2 for instrument specifications). Stochastic modelling is done for the instruments as well as for the OT models. For the latter, we apply the full co-variance matrices of the eight major tidal constituents up to d/o 60 which have also been applied in [RD- 7]. In order to maintain consistency, the retrieval is also carried out up to d/o 60.

The results are presented in Figure 34-1 in terms of degree RMS. As expected, the additional stochastic modelling of OT BM errors yields an improved retrieval performance in comparison to the nominal processing where only the sensor noise is weighted. In case of the 7d-solutions it is evident that a substantial improvement of up to more than 40% can be reached when the data is processed based on daily arcs, while a processing based on a full VCM of observations, i.e. using a single full-interval arc, yields up to nearly 50%. What is interesting, however, is that in case of the 3d-retrieval the best results can be achieved by using daily arcs, whereas using a full VCM of observations seems to even degrade the retrieval performance in the spectrum

above d/o 40. It is assumed that this issue arises from the interaction between the OT BM error weighting and the non-tidal observation components, although the exact reason for this behaviour is not yet understood. Further, as can be deduced from Figure 34-2, it is of major importance to apply stochastic modelling for both the instrument noise and the OT components, since only weighting OT BM errors will greatly degrade the retrieval performance
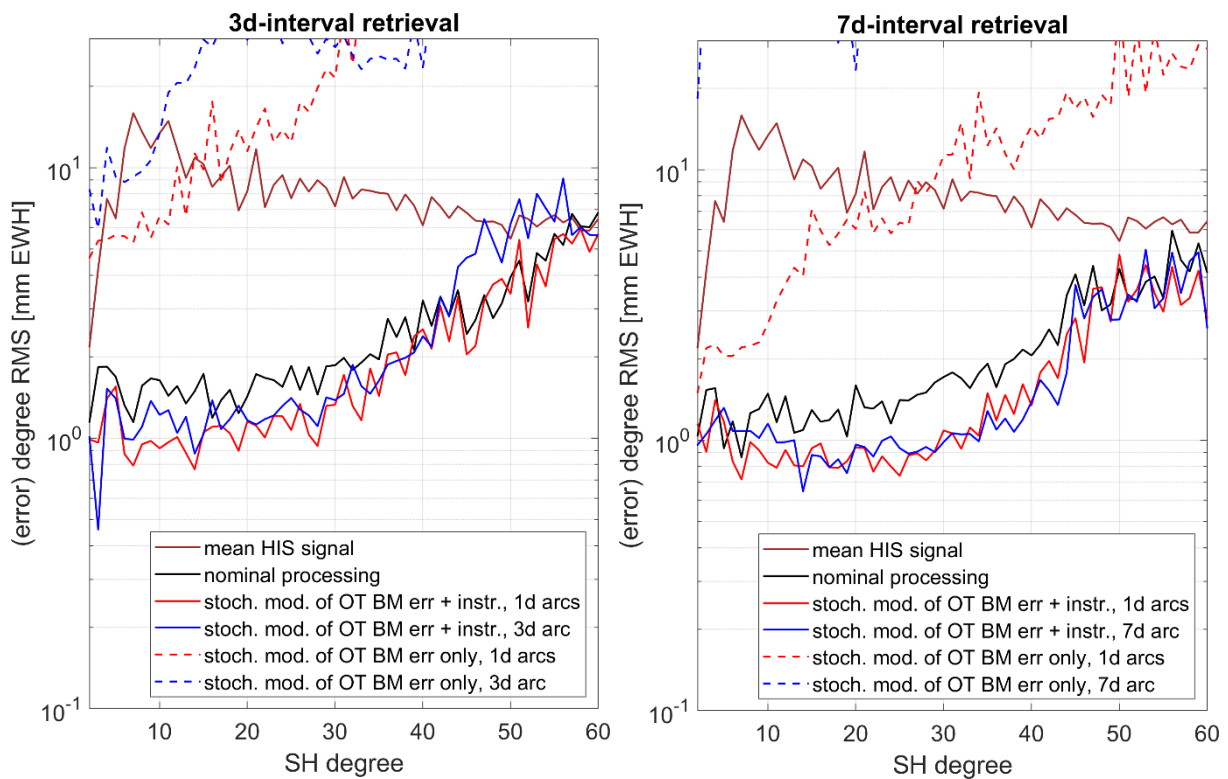
Figure 34-2: Retrieval performance of scenarios including tidal and non-tidal gravity signal as well as instrument noise where stochastic modelling is applied for OT BM errors only, OT BM errors and instrument noise or no stochastic modelling is applied at all. Retrieval period is set to 3 (left) and 7 days (right).

Overall, it can be concluded that the stochastic modelling of OT BM errors can be applied not only to the retrieval of long-term, e.g. monthly, solutions, but also to the retrieval of short-interval fields. It thus poses a valid processing strategy for estimating NRT-type gravity field solutions. It can be stated that applying processing based on longer arcs seems to be favourable for the 7d-fields (although the difference to the processing based on shorter arcs is rather small), while shorter arcs seem to be beneficial for the 3d-retrieval. This finding is exceptionally valuable as it shows that results of high quality can be achieved even through reduced computational efforts (smaller VCMs of observations).

It is planned to process 5d-solutions in order to further validate the retrieval performance based on various arc lengths. The interaction between the weighting and the various signal components shall also subject of future investigations. Although the presented RSS results already give a good indication towards the expected level of retrieval performance enhancement in a full-fledged simulation, future work of this WP shall encompass the implementation treatment of OT BM errors treatment in the FSS. In this sense, the performance of this method shall also be explicitly tested in the scope of actual NRT-type processing according to [RD- 6].

35 OPTIMIZED SPACE-TIME PARAMETRZATION IN TERMS OF MULTI-PERIOD ESTIMATION (WP450)

The discussion presented here is based on simulation results obtained with the reduced-scale simulator. While this simulation tool encompasses some major simplifications compared to the real data processing scheme (c.f. [RD- 2], [RD- 3]) in favour of improved computational performance, these results nevertheless pose a good approximation of corresponding full-scale closed-loop simulations. The simulations were carried out using a polar and an inclined satellite pair (c.f. Table 35-1) for a retrieval period of 30 days.

Table 35-1: Orbit parameters

	Altitude [km]	Inclination [°]	Rev/nodal day	Ascending node [°]	Mean anomaly difference [°]
GRACE-A GRACE-B	475.14	89	457/30	0	- 1.674
GRACE-C GRACE-D	475.13	70	439/29		- 1.674

35.1 VALIDATION OF "CLASSIC" WIESE PARAMETRIZATION

Wiese et al. (c.f. [RD- 1]) have established a self-de-aliasing method which includes the co-estimation of low-degree (e.g. d/o 15) fields over short time intervals (e.g. daily) in addition to the high degrees which are estimated over the entire retrieval period (e.g. one month) up to a certain maximum d/o. This so-called Wiese approach aims to explicitly parametrize the short-periodic atmosphere and ocean (AO) signals by means of the short-interval fields, and thus to prevent them from manifesting themselves within the long-term gravity field solution as temporal aliasing (striping). Therefore, one should ideally be able to retrieve the full AOHIS signal without the need for a priori geophysical background models In previous works (c.f. [RD- 4], [RD- 6]), it was assumed that by this procedure the parameter model is able to soak up all signals with a longer period than twice the period of the short-interval fields, e.g., 2 days in case of daily Wiese parameterization.
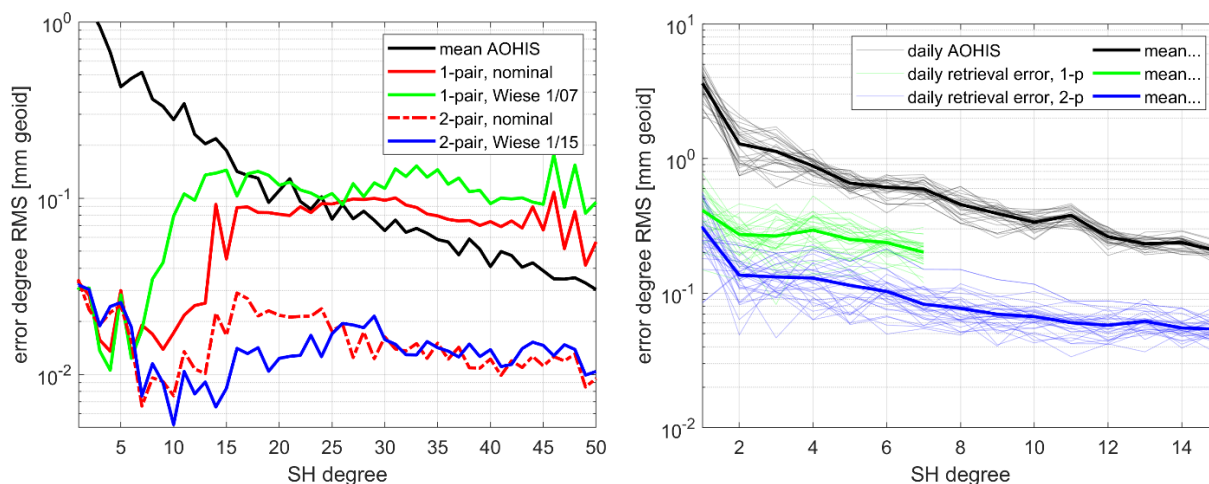
Figure 35-1: Left: Retrieval error of the 30-day field from a single- as well as a double-pair mission scenario with and without applying Wiese parametrization (daily fields up to d/o 7 in case of the single pair, daily fields up to d/o 15 in case of the double pair). Right: Retrieval error of corresponding daily fields.

This method has been proven to work well for double-pair mission scenarios in numerous simulation studies. Now, its functionality is additionally investigated for a single-pair mission. Figure 35-1 shows the AOHIS retrieval error for a single- as well as a double-pair mission scenario when using the Wiese approach. Here we assume perfect instrument performance, i.e. no instrument noise is included, and perfect ocean tide de-aliasing, i.e. the only remaining error source in the closed-loop simulation is the temporal aliasing of non-tidal temporal gravity signals based on AOHIS. In case of the double-pair scenario daily fields up to d/o 15 are co-estimated, while in case of the single-pair the maximum d/o of the daily fields is lowered to 7 (maximum theoretical d/o based on the spatial distribution of the ground tracks resulting from the number of revolutions). While in both scenarios the daily fields seem quite reliable (the retrieval error RMS curve lies well below the signal RMS curve), the Wiese solution is heavily degraded in the spectrum above d/o 7 in case of the single-pair mission. On the other hand, the Wiese-based solution notably outperforms the nominal one between degree 10 and 25 in case of the double-pair scenario.

In order to understand the reason for this behaviour the correlation matrices of the estimated coefficients are investigated (c.f. Figure 35-2). It becomes evident in case of a double-pair scenario there are barely any correlation coefficients above an absolute value of 10%. In case of a single-pair mission, however, significantly more and larger correlations occur specifically between the daily coefficient groups. This indicates that the adjustment system is not able to properly separate the long- from the short-wavelength signal within the given time intervals, and thus, the overall estimation becomes flawed. Additional tests have been carried out, and it turned out that the classic Wiese parametrization at best yields no benefit over the nominal solution in case for a single-pair-based retrieval.
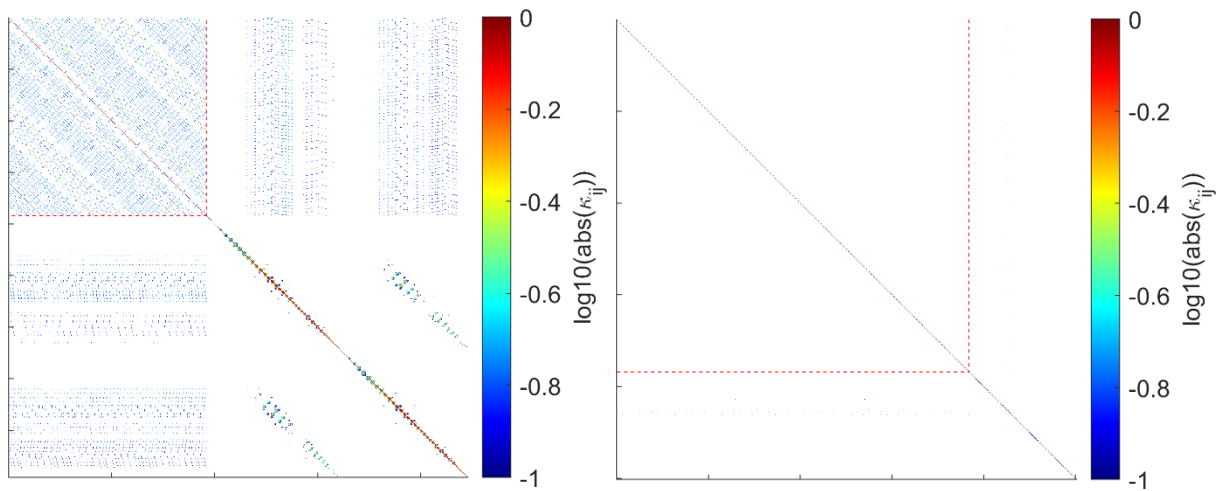
Figure 35-2: Correlation matrices of coefficients retrieved with Wiese in case of a single-pair mission scenario (daily fields up to d/o 7, left) as well as in case of a double-pair mission (daily fields up to d/o 15, right). The square marked with dashed red lines indicates the coefficients of the interval fields.

Further on, explicit investigation of the underlying signal observed by the satellite reveals that the core idea on which Wiese is based, i.e. that all signal components with excitation frequencies lower than twice the frequency at which the interval fields are estimated, is in fact not true. In order to further investigate this matter, additional simulations were carried out with a 10-day low-pass filtered AO signal (i.e. the time series of each AO coefficient has been treated with a low-pass filter) as signal input. Figure 35-3 shows the projection of the observation time series onto the globe based on the true AO signal (left column) as well as on the 10-day low-pass filtered AO signal (right column). Although all signal components with periods of less than 10 days have indeed been cancelled for any given observation point throughout the entire time interval in the latter scenario, the overall observation time series barely changes compared to the true AO case. This is quite logical, because each observation point (or, more generally, its vicinity) features a widely unique signal evolution throughout the observation period, and the fact that each of these unique signals is observed at very different phases fully contradicts the central postulate of the Wiese approach. This is also true if only the signals up to d/o 7, which should be fully captured by the daily Wiese parameterization, are used as in input signal (second row of Figure 35-3). Using the complementary signal of d/o 8 to 50 as input shows a similar behaviour (last row of Figure 35-3).
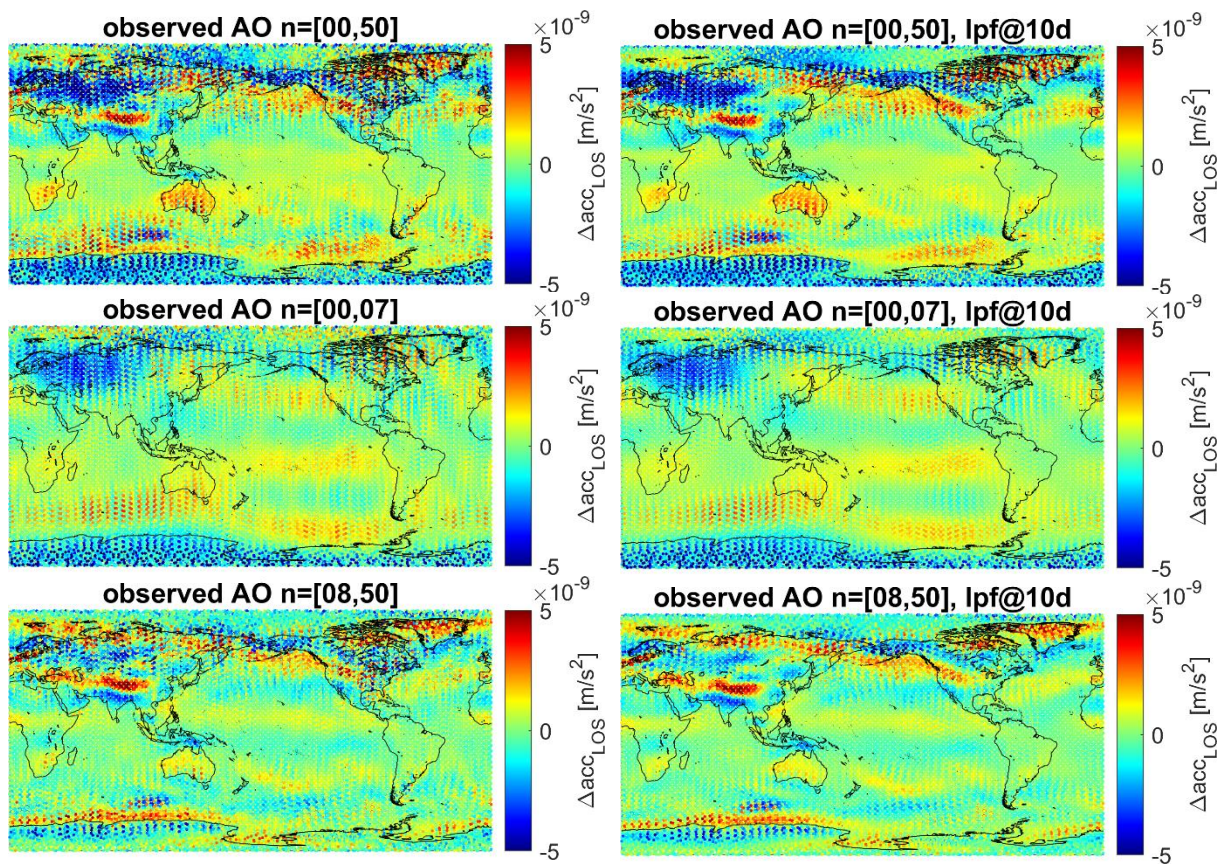
Figure 35-3: The polar pair's observation time series plotted along the ground track based on the true AO signal (top left) and the 10-day low-pass-filtered AO signal (top right) up to d/o 50. In addition, the contributions of degrees 0 to 7 as well as 8 to 50 are shown separately for both cases.
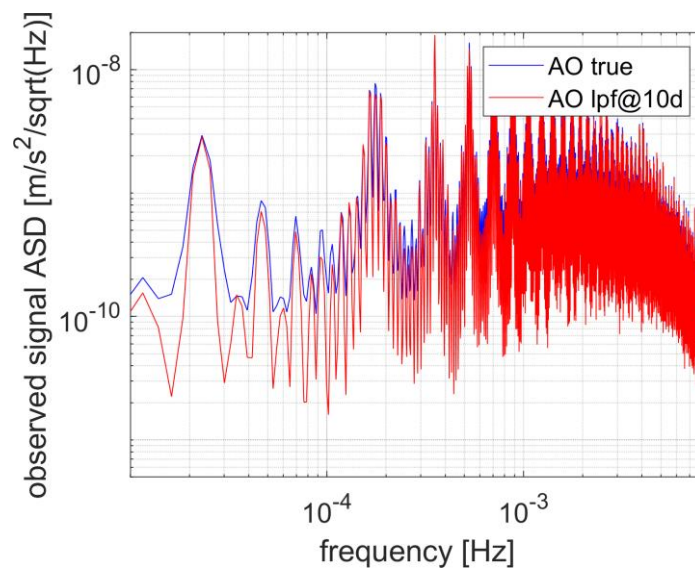
Figure 35-4: ASD of observation time series based on the true AO signal and the 10-day low-pass-filtered AO signal up to d/o 50.

This matter can also be clearly seen in the respective time series' ASD. It is evident that the time series based on the filtered AO signal features a near-identical spectral behaviour as the one based on the true AO signal, further confirming that the idea behind the Wiese approach cannot be fulfilled. The Wiese approach can only work as intended if filtering the AO signal with respect to time would also result in an observation time series with the same pass- and stop-bands defined by the filter.

In summary, it seems that although the idea behind Wiese is not fully correct, the approach can still contribute to increasing the AOHIS retrieval performance in case of a double-pair mission. This behaviour can be attributed to the optimized observation geometry stemming from the additional inclined satellite pair. The improved observation coverage mitigates the striping by generating a significantly more isotropic observation pattern, as can be seen in Figure 35-5. The correlations between the long- and the short-wavelength spectrum arising due to the high-frequency nature of the AO signal are thus implicitly removed (or at least weakened), which in turn allows more of the AO signal to be – correctly – captured in the short-interval fields. In contrast, in case of the single-pair scenario the striping pattern inducing erroneous high-degree signal fully remains within the observations. Thus, the various spatial-temporal signal components cannot be properly separated (as already demonstrated in Figure 35-2), which consequently degrades the retrieval.
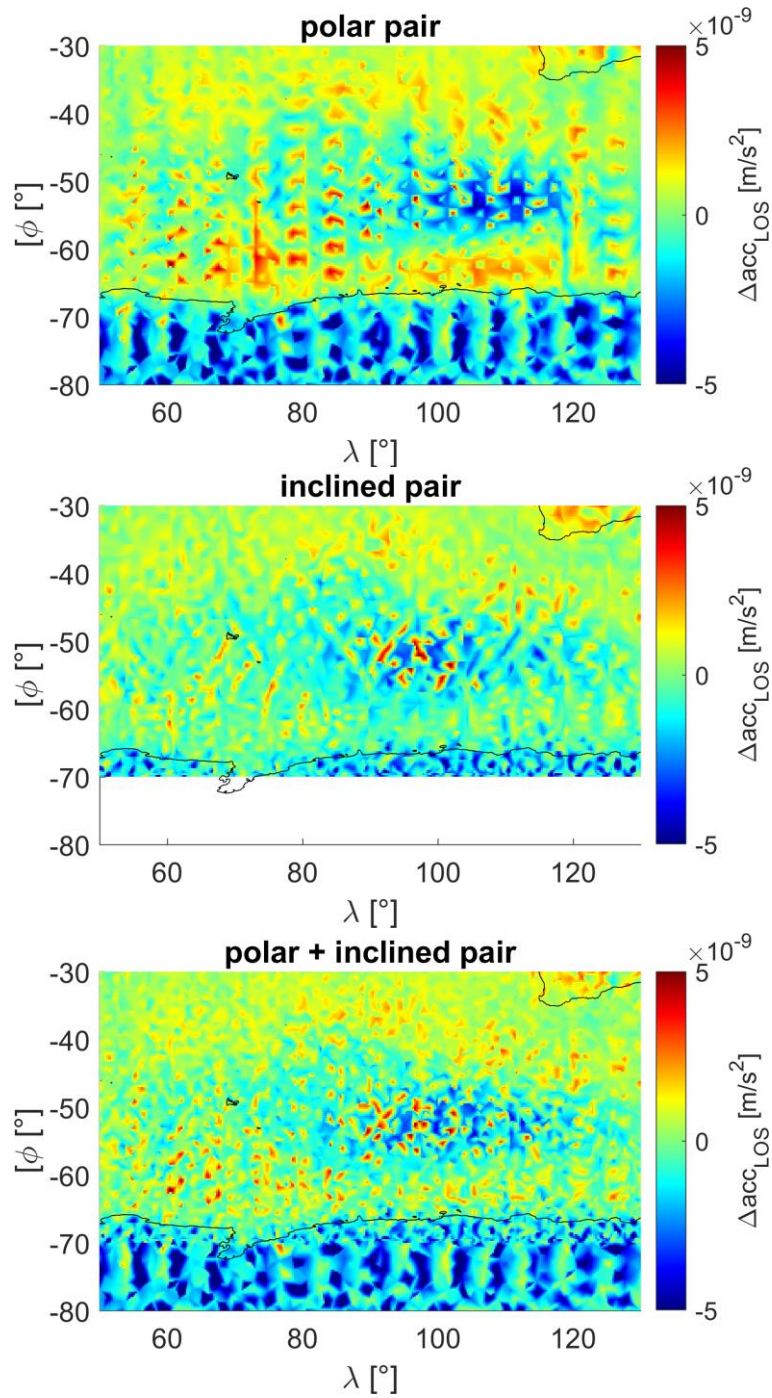
Figure 35-5: The observations based on the true AO signal interpolated from the polar pair (top), the inclined pair (middle) and their combination (bottom) for a selected region in the southern Indian Ocean.

35.2 VALIDATION OF "MULTI" WIESE PARAMETRIZATION

It was originally planned to investigate a "multi" Wiese approach where in addition to the high-temporal, low-spatial resolution fields up to a certain maximum degree $n_{max,1}$ fields of lower temporal resolution are estimated for the spectrum between $n_{max,1}+1$ and $n_{max,2}$ ($n_{max,2} < n_{max, monthly}$). By doing so, one would hope to be able to explicitly parametrize signal components of shorter spatial wavelengths which feature lower underlying temporal excitation frequencies. In principle, an arbitrary amount of such intermediate steps (resp. fields) can be introduced, but such an approach would only yield a benefit if the formerly discussed basic assumption of Wiese was correct. Because this base assumption is proven to be invalid, the multi-Wiese approach cannot be expected to yield any additional benefit. Moreover, such a system would be more prone to errors, as it would have more freedom to erroneously parametrize signal components.

Figure 35-6 shows some selected results obtained with various multi-Wiese schemes and supports this hypothesis: in case of the single-pair scenario the nominal solution shows a better performance than any of the Wiese-based solutions. For the double pair one can see that the classic Wiese approach where daily fields are co-estimated up to d/o 15 yields the best result, while the retrieval may become significantly degraded in the higher degrees when additional Wiese-type steps are introduced.

Please note that the multi-Wiese simulation results presented here were performed based on orbits which do not feature short sub-cycles. While it is generally reasonable to assume that estimating fields over a period aligned with that of a sub-cycle would yields a slightly better result due to the more homogenous observation coverage, the results presented in Figure 35-6 do not indicate that multi-Wiese yields any improvement whatsoever. Therefore, no additional orbits with short sub-cycles are used for the multi-Wiese tests.

Nevertheless, for the sake of completeness, it is attempted to execute the multi-period Wiese approach for a Bender-type scenario using orbits with fixed sub-cycles. For this test, the orbits of the 3d_H scenario are chosen (cf. Table 32-1) which feature sub-cycles of 3 and 7 days and, consequently, the additional sub-period for the co-estimation is chosen accordingly. In alignment with the expectations following the discussion above, the exemplary results presented in Figure 35-7 clearly prove that an additional co-estimation of higher degrees over longer time intervals, even if they correspond to underlying orbital sub-cycles, does not improve the retrieval performance in any way
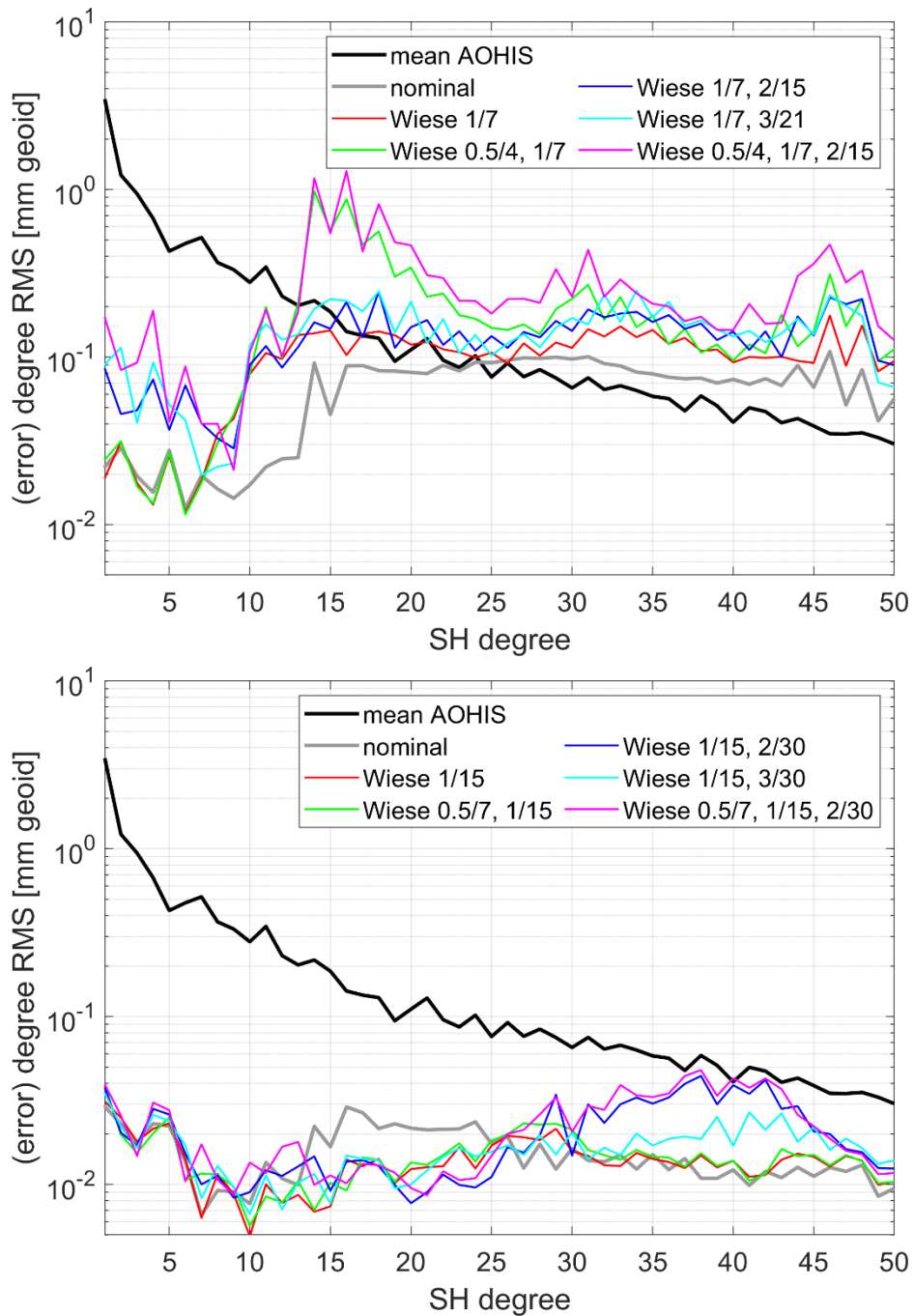
Figure 35-6: Retrieval error of the 30-day field from a single- (top) as well as a double-pair mission scenario (bottom) based on multi-Wiese parametrization. Note that the nomenclature X/Y used in the legend indicates that short-term fields up to d/o Y were co-estimated over intervals of the length X (in days).
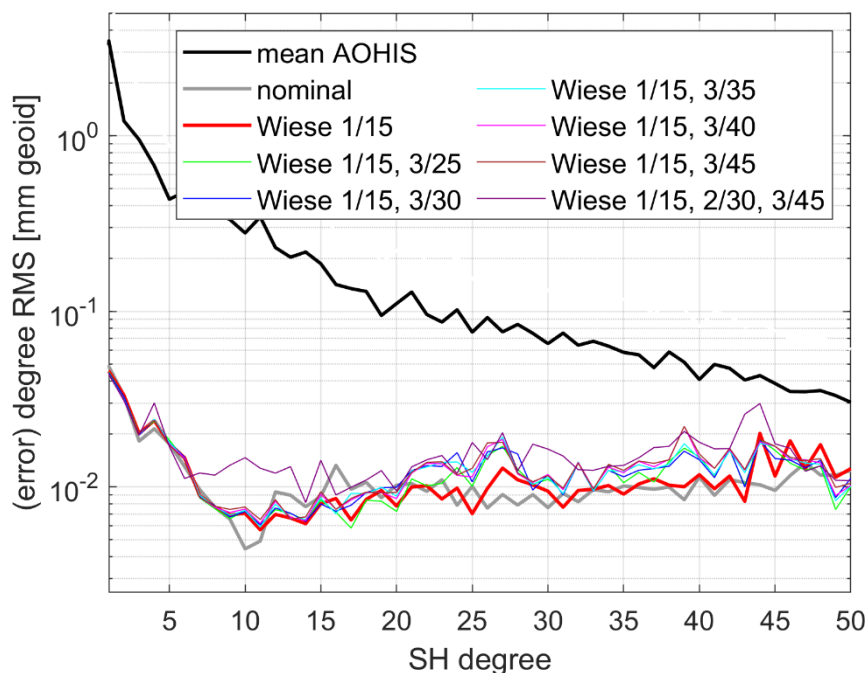
Figure 35-7: Retrieval error of the 30-day field from a double-pair mission scenario based on 3d_H repeat orbits employing multi-Wiese in alignment with the 3d-sub-cycle. Note that the nomenclature X/Y used in the legend indicates that short-term fields up to d/o Y were co-estimated over intervals of the length X (in days).

35.3 DATA-DRIVEN MULTI-STEP SELF-DE-ALIASING (DMD)

In the previous sections it was shown that short-interval, low-resolution fields can be estimated with an acceptable accuracy within the scope of the Wiese parametrization even in case of a single-pair scenario. It was also simultaneously shown that retaining correlations between the low- and the high-degree spectrum degrades the overall retrieval performance. Therefore, the question arises whether it would be beneficial to separately estimate low-resolution fields over short intervals and to use them as a de-aliasing product in a follow-up step. While neglecting correlations between coefficients of different degrees may generally be seen as unfavourable, it is absolutely justifiable from a geophysical perspective – the single-most dominant signal components over short, e.g. (sub)daily, periods are primarily related to AO (if ocean tides are neglected), whose strongest signals are in turn of a long-wavelength nature. Thus, by estimating e.g. daily low-resolution fields from the "full" observations (i.e. the ones stemming from the AO signal up to some n_{max}) one should be able to capture (predominantly) these signal components in the corresponding part of the spectrum. Subtracting the observations related to these daily fields from the "full" observations should then yield observations related mostly to signal components with longer periods. The mean, e.g. monthly, field can then be estimated from the reduced observations, hereby preventing temporal aliasing in the higher degrees. Finally, since one aims to retrieve the full AOHIS field, the mean of the short-term solutions is restored to the monthly field. Alternatively, instead of restoring the mean of the interval fields at the end it is also valid to first reduce the mean from the interval fields before reducing the observations. In this way, the mean signal remains in the long-term solution and the interval estimates represent variations with respect to this mean. Further, just as shown above for the

classic Wiese approach, this method can be extended by additional steps, e.g., one could estimate daily fields up to d/o 7 as well as in a following step two-day fields up to d/o 15 before estimating the full-resolution monthly field. The primary goal of this approach is, just like in case of Wiese, to improve the long-term (monthly) solution while simultaneously retrieving reliable interval estimates that can be used as stand-alone products. The overall processing scheme is summarized in Figure 35-8.
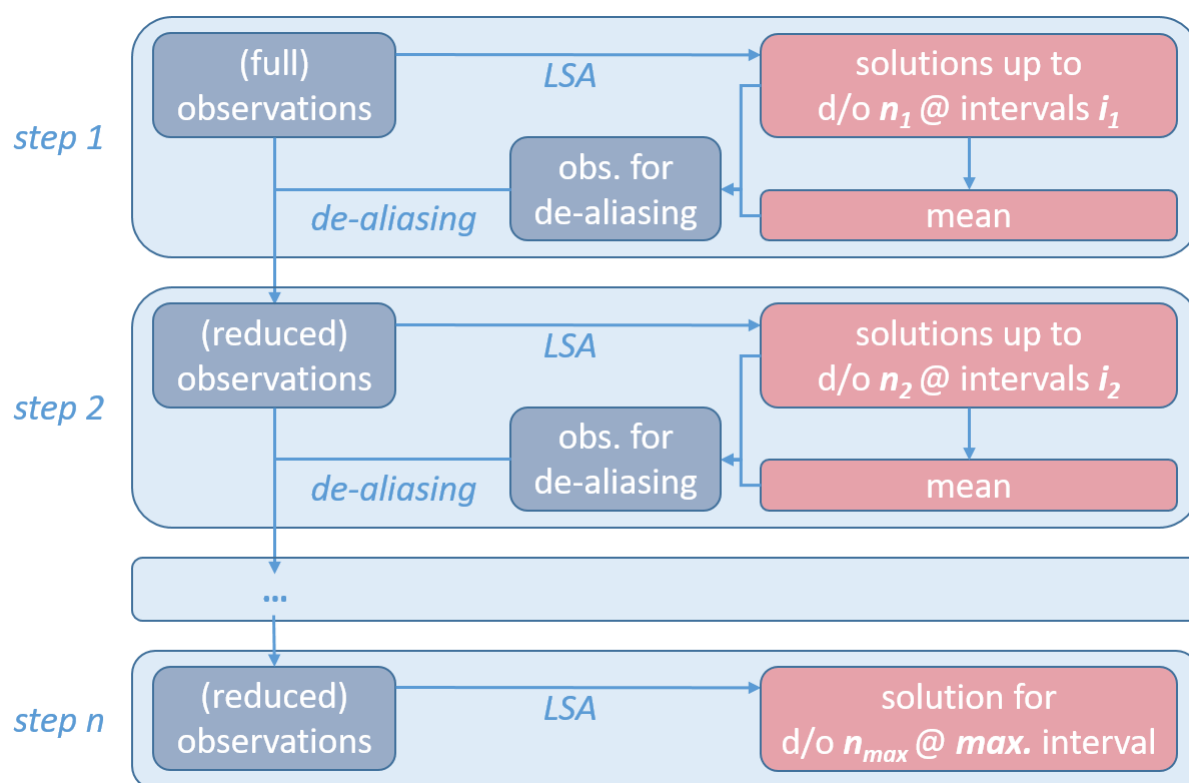
Figure 35-8: DMD processing scheme.

In summary, the procedure is somewhat equivalent to the classic Wiese approach. However, while Wiese only alters the left-hand side of the LSA compared to a standard parameterization, the approach presented above affects the observation vector, i.e. the right-hand side of the LSA. This is in fact nothing other than de-aliasing, similar to what is done with background models in the GRACE data processing. However, this de-aliasing does not require any background models and is thus exclusively data-driven, which generally makes it preferable to the background-model-based approach.
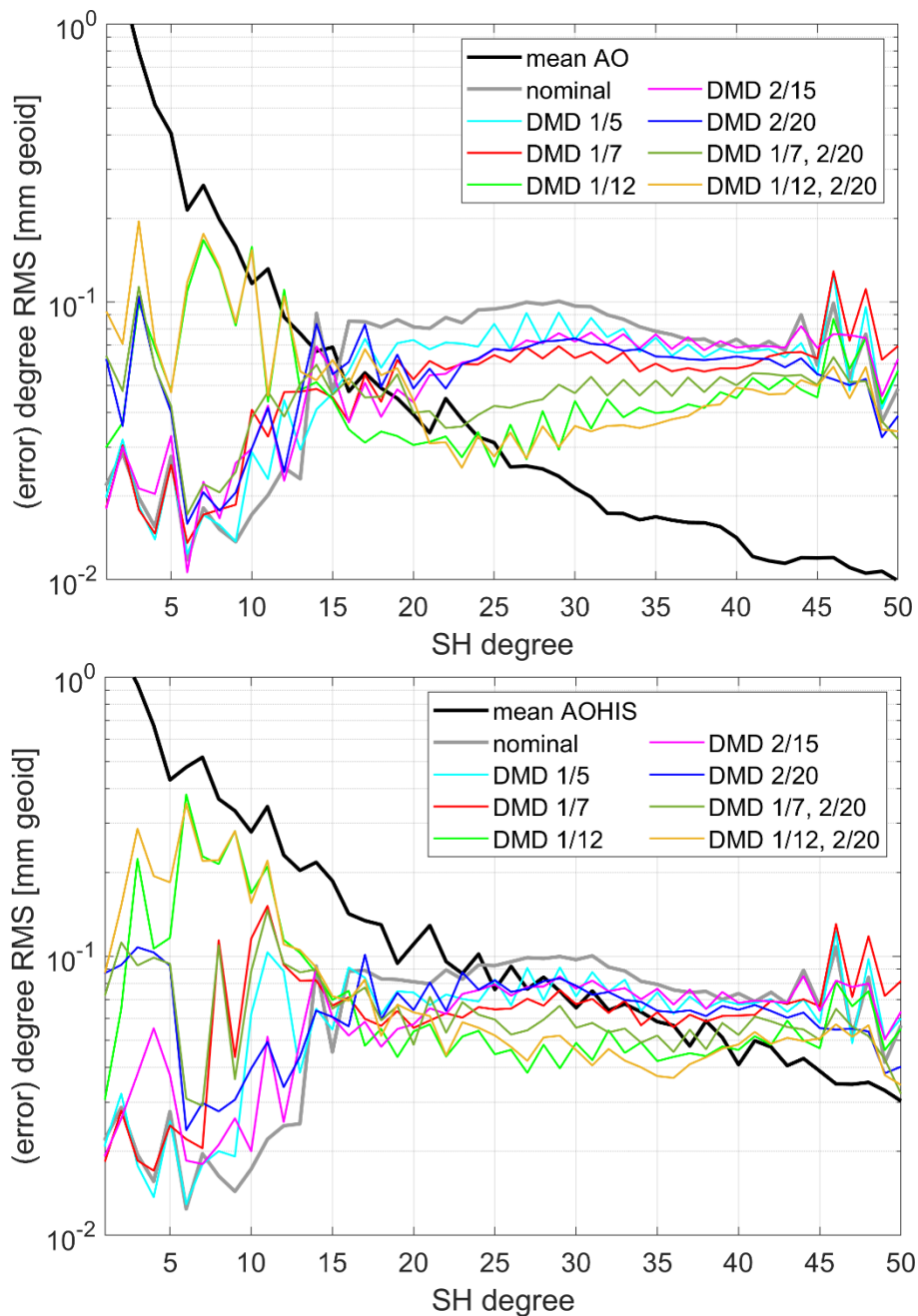
Figure 35-9: Retrieval error of the 30-day field for a single-pair mission scenario based the AO (top) and AOHIS signal (bottom) using DMD. Note that the nomenclature X/Y used in the legend indicates that short-term fields up to d/o Y were estimated over intervals of the length X (in days).

In the following we present some preliminary reduced-scale simulation results obtained with the approach discussed above. Figure 35-9 illustrates the AO and the AOHIS retrieval performance for a single-pair mission. It is evident that the DMD approach yields an improved retrieval performance in the higher degrees in comparison to the nominal solution. This improvement increases when the interval fields' spatial resolution is increased, but, unfortunately, at the cost of a degraded retrieval performance in the low-degree spectrum. Also, unlike for Wiese, applying DMD with multiple consecutive de-aliasing steps seems to be

beneficial. This can be explained as follows. On one hand, the stability of the interval fields decreases with increasing degree of resolution. On the other hand, spectral leakage inevitably occurs, because the interval field estimation is free to parametrize any given signal components it deems fit into the low-degree spectrum. The daily fields are thus naturally prone to errors, but it seems that the majority of the signals can nevertheless be parametrized correctly, as the interval fields they can still be retrieved with sufficient quality (as long as a reasonable maximum resolution is chosen, c.f. Figure 35-11). These signal components are then prevented from being erroneously estimated into the high-degree spectrum of the long-term field. The results presented above clearly indicate that the striping constitutes the major error contributor in the high degrees and greatly supersedes the drawback of spectral leakage, even in case of AOHIS.

The logical next step is now to attempt retaining the gain in the high-degree spectrum while simultaneously reducing the degradation in the low degrees. For the reasons stated above it is clear that the DMD-based low-degree spectrum of the monthly solution is always inferior to the one obtained with the nominal approach. It is therefore reasonable to constrain the interval fields, e.g. by forcing their mean to equal the corresponding spectrum of the nominal solution:

$$\frac{1}{n_{intervals}} \sum_{i=1}^{n_{intervals}} \begin{Bmatrix} C_{nm} \\ S_{nm} \end{Bmatrix}_i = \begin{Bmatrix} C_{nm} \\ S_{nm} \end{Bmatrix}_{nominal} \qquad [7\text{-}1]$$

Note that this constraint is also exclusively data-driven. It enters the estimation of the interval fields in terms of pseudo-observations, and is thus equivalent to a regularization of the NEQ system. Figure 35-10 indicates that the constraint indeed helps to stabilizing the monthly field's low degrees. Furthermore, as can be seen in combination with Figure 35-11, it apparently also yields an improvement in the retrieved interval solutions, and its effect logically becomes more pronounced the higher one sets their maximum resolution. Here can also be seen that the constraint has a significantly larger impact in case of AOHIS. A possible explanation for this behaviour is that in case of AO the signal components are already correctly parametrized for the most part due to their high-frequency nature. The HIS signal components, on the other hand, feature over the course of one month a near-static, from a spatial perspective rather short-wavelength behaviour, so observing only certain selected parts of these signals (which essentially happens in DMD) may degrade the interval solutions, since they are misinterpreted as contributors to the variations within each interval. Constraining the intervals to the nominal solution which correctly parametrizes the HIS components to the high-degree spectrum therefore remedies this to some extent.
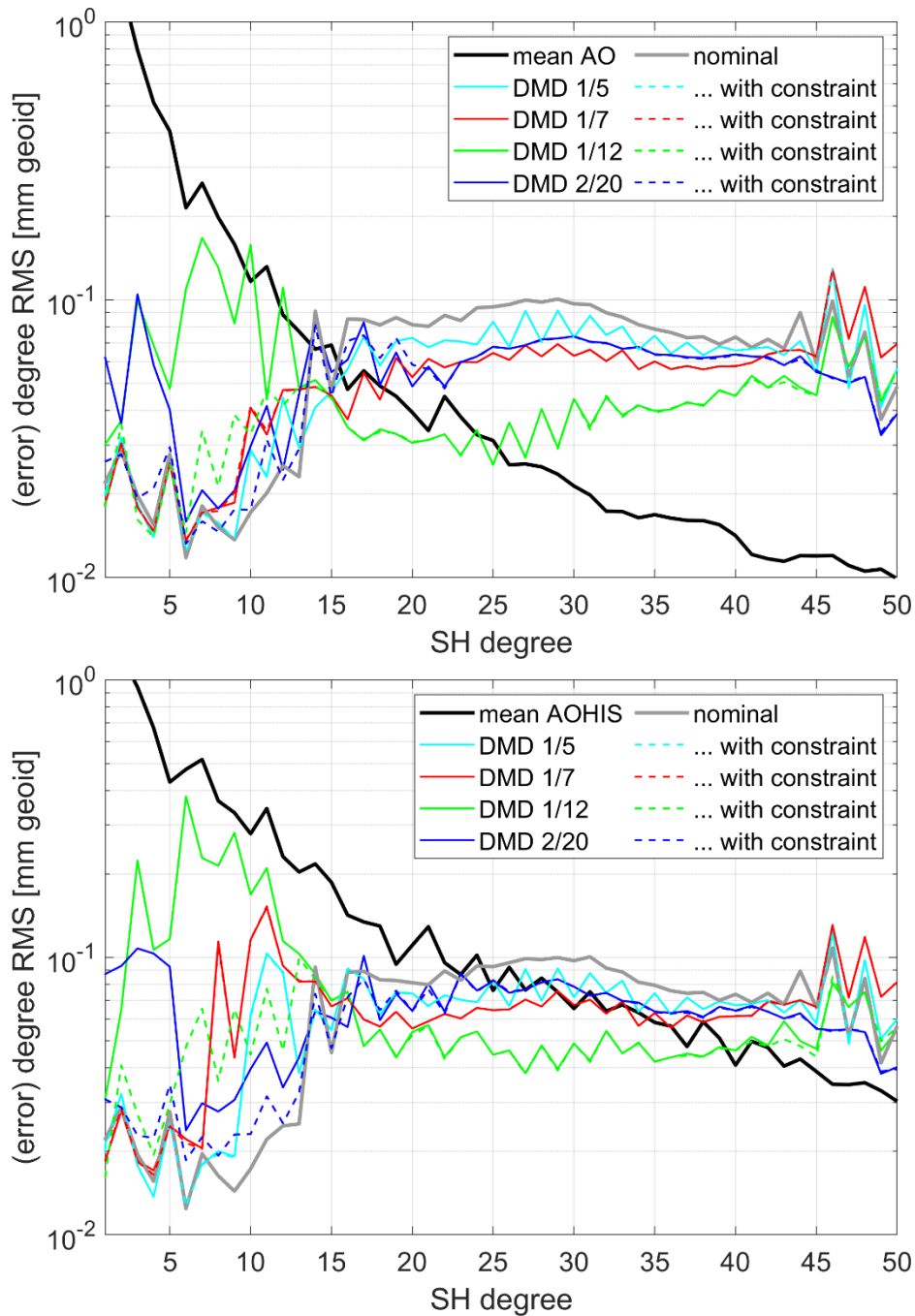
Figure 35-10: Retrieval error of the 30-day field for a single-pair mission scenario based the AO (top) and AOHIS signal (bottom) using DMD with and without the constraint. Note that the nomenclature X/Y used in the legend indicates that short-term fields up to d/o Y were estimated over intervals of the length X (in days).
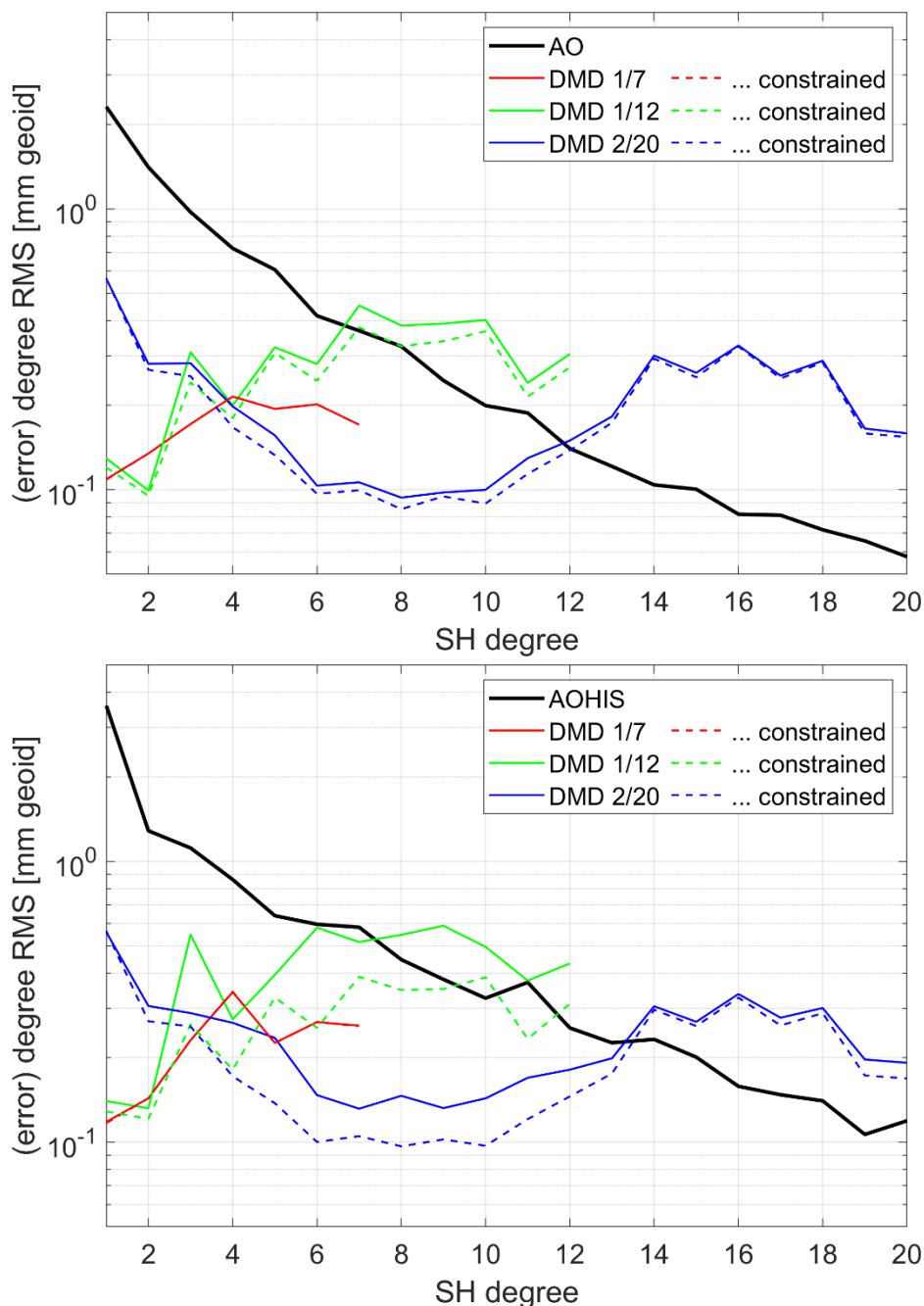
Figure 35-11: Mean degree RMS of the interval solutions based on the AO (top) and AOHIS signal (bottom) obtained through DMD. Note that the nomenclature X/Y used in the legend indicates that short-term fields up to d/o Y were estimated over intervals of the length X (in days).

For the sake of completeness, Figure 35-12 depicts the retrieval error of the 30-day nominal solution as well as the ones obtained with DMD employing daily fields up to d/o 12 with and without applying constraint in terms of global EWH grids. The added value of DMD is clearly distinguishable both in case of AO and AOHIS, where the erroneous stripes over northern Asia and North America are notably reduced in comparison to the nominal solution. The value of the constraint becomes evident primarily in case of AOHIS. Here, additional reduction of the

striping can be established over South America as well as south of the equator in the Pacific and the Atlantic Oceans.
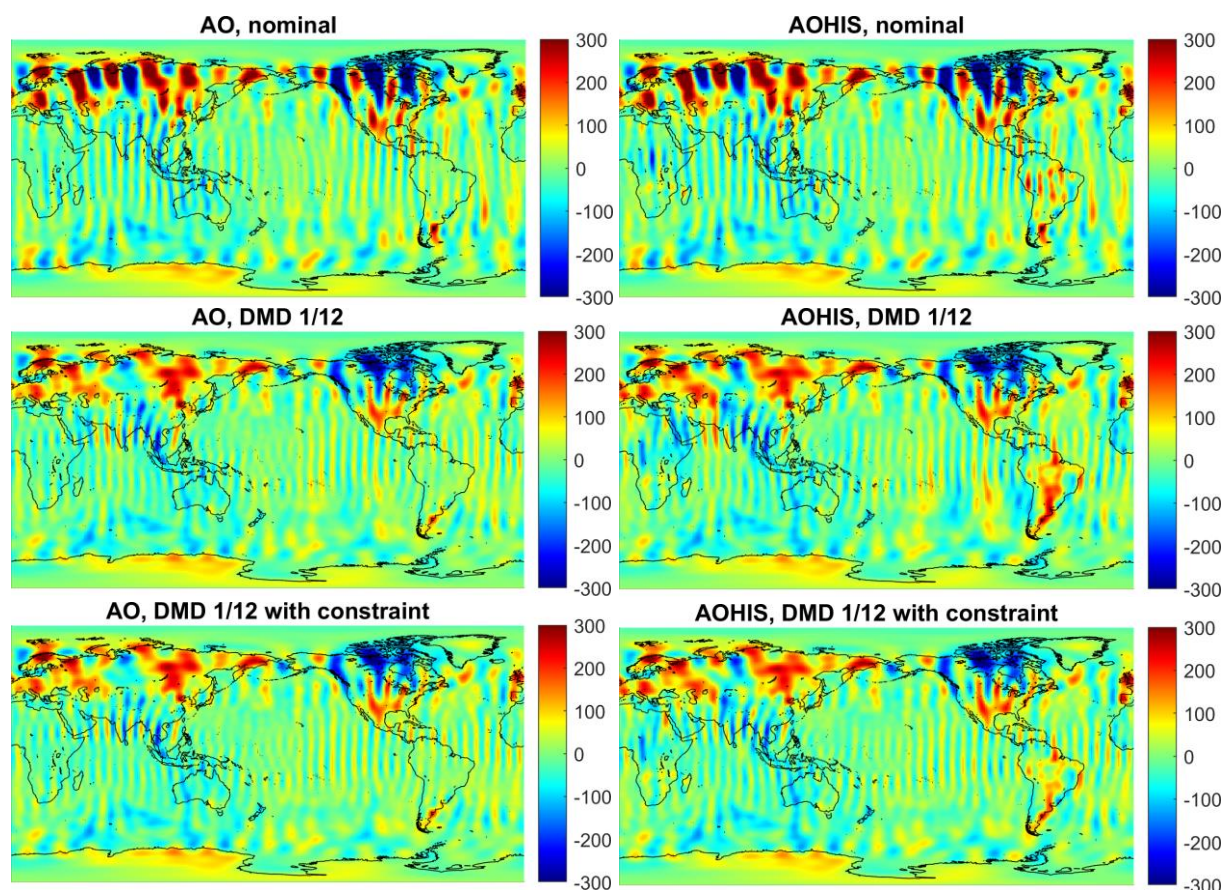
Figure 35-12: Retrieval error of the monthly solution (in terms of mm EWH) based on the AO (left column) and the AOHIS signal (right column) using the nominal processing (top row), DMD 1/12 (middle row) as well as DMD 1/12 with constraint (bottom row).

In the following we present some selected results obtained with DMD in case of a double-pair constellation. Figure 35-13 clearly shows that nearly all DMD-based solutions significantly outperform the nominal one in case of AO-only. On the other hand, while some improvements can be established in the spectral band between d/o 12 and 25, from d/o 25 onwards the nominal solution shows the best overall performance in case of AOHIS. Only the solution where daily fields are estimated up to d/o 15 yields a consistently lower retrieval error than the nominal one. However, this solution is still inferior to its counterpart obtained with the classic Wiese approach (daily fields co-estimated up to d/o 15, c.f. Figure 35-1 & Figure 35-6). In combination with the results obtained for the single-pair scenario, this behaviour suggests that the temporal aliasing problem is significantly less pronounced here. Consequently, this means that the faulty parametrization (leakage) of high-degree HIS signal components into the interval fields has a notable impact on the monthly solution's high degrees. In case of AO-only, on the other hand, the dominant long-wavelength components can be resolved close to perfectly and, thus, also properly confined to the interval fields, whereas the high-frequency signals are correctly left to be estimated in the monthly solution.

In this regard, it could theoretically be attempted to use the interval fields co-estimated during the course of Wiese for the de-aliasing step of DMD. However, the correctness of such a "mixed" approach would first need to be validated.
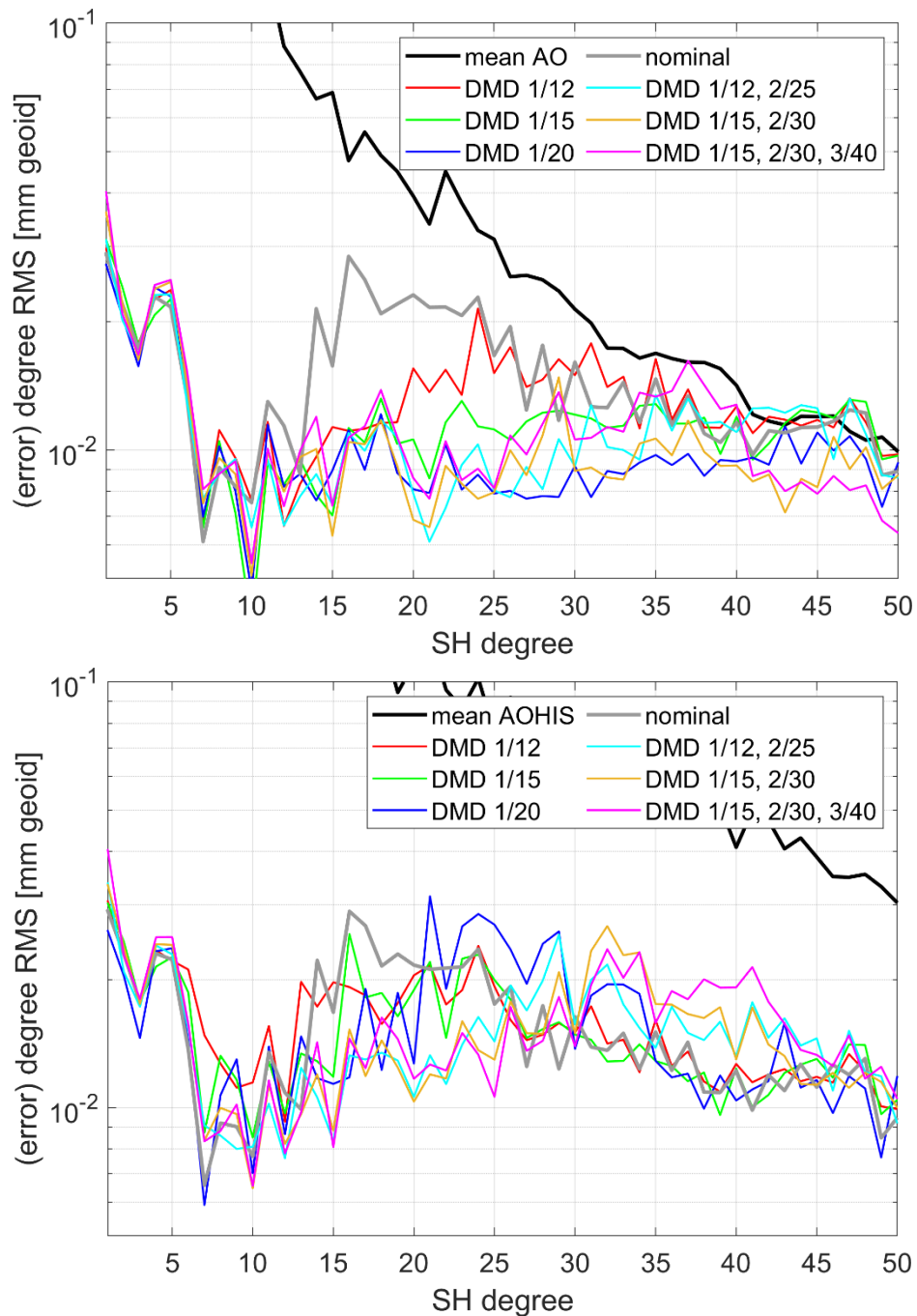
Figure 35-13: Retrieval error of the 30-day field for a double-pair mission scenario based the AO (top) and AOHIS signal (bottom) using DMD. Note that the nomenclature X/Y used in the legend indicates that short-term fields up to d/o Y were estimated over intervals of the length X (in days).

As a final test, the DMD approach is applied to selected double-pair based retrieval scenarios in combination with the previously discussed constraint for low degrees. Figure 35-14 demonstrates that the Wiese-type co-estimation employing daily fields up to d/o 15 which so far has yielded the best overall results is now being slightly outperformed by the DMD approach. As expected, this behaviour is primarily notable in the AO-only scenario, where practically the entire spectrum upwards from d/o 23 is improved by up to 60%. Nevertheless, the impact of the constrained multi-period DMD is also visible in case of the full AOHIS signal, although here the improvement is mostly limited to the spectrum between d/o 25 and 30. Evidently, the multi-period de-aliasing combined with the constraint allows one to further refine the spectral mapping of the time-variable gravity field's signal components and should thus be seen as a valid equivalent to the Wiese-type parametrization for multi-pair scenarios
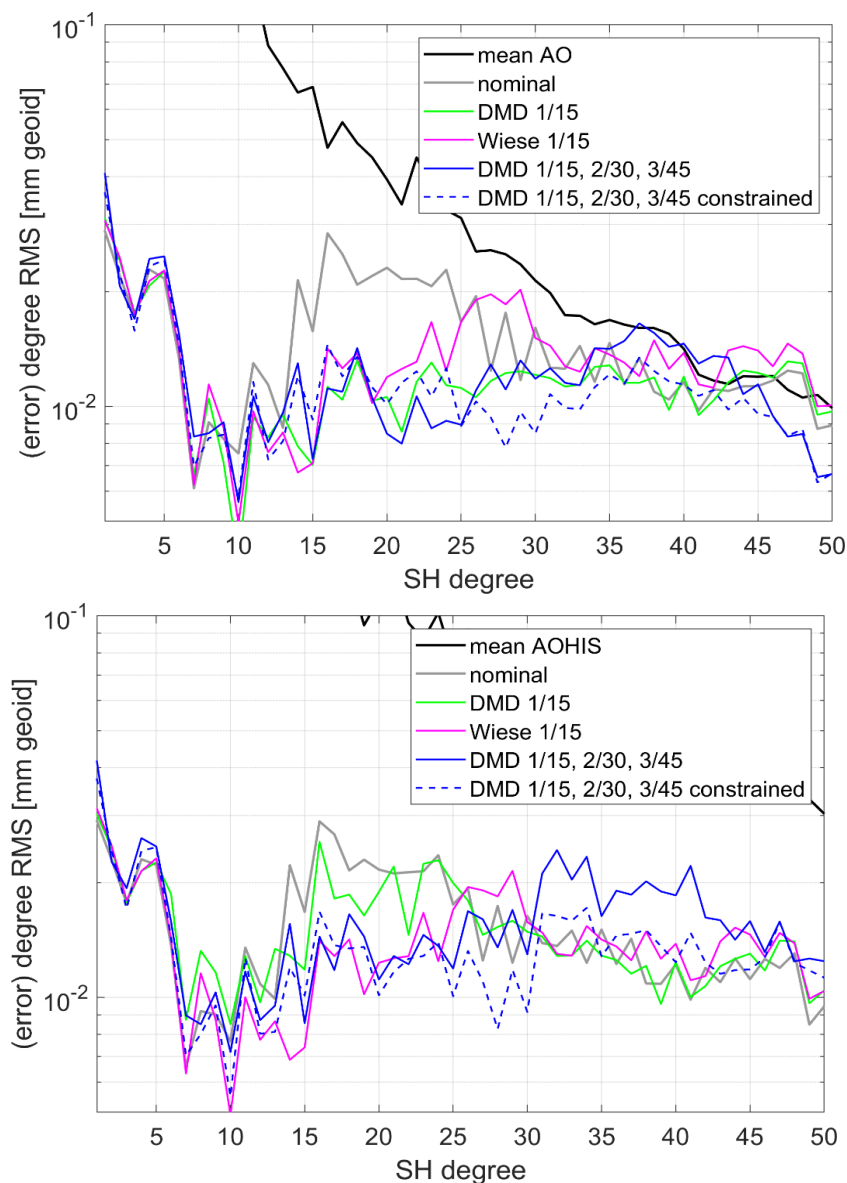
Figure 35-14: Retrieval error of the 30-day field for a double-pair mission scenario based the AO (top) and AOHIS signal (bottom) using multi-period DMD and the low-degree constraint. Note that the nomenclature X/Y used in the legend indicates that short-term fields up to d/o Y were estimated over intervals of the length X (in days).

35.4 SUMMARY AND CONCLUSIONS

Firstly, it was shown that the underlying hypothesis of the classic Wiese parametrization is flawed. It was demonstrated that especially in case of a single-pair scenario the adjustment system cannot recognize long-wavelength, high-amplitude signal components predominantly related to AO as such and instead maps them into other spectral bands, thus (in parts greatly) degrading the retrieval performance. In case of a double-pair constellation Wiese still yields reasonable results, although only due to the fact that temporal aliasing effects are greatly reduced and, therefore, the adjustment system is able to properly parametrize the dominant AO components into the low degrees (implicit constraint). Expanding the classic Wiese approach with additional intermediate steps has been shown to be of little to no use at best. In the worst case such a parametrization scheme significantly decreases the retrieval performance.

Instead, we propose a data-driven self-de-aliasing method which due to their underlying spatial-temporal nature primarily targets AO signal constituents. This approach is found to be of primary benefit for a single-pair mission scenario, where faulty parametrization of high-degree signals (predominantly related to HIS) into the low-degree spectrum is counterbalanced by the immense reduction of temporal aliasing in the short-wavelength spectrum of the monthly solution. In addition, a data-driven constraint which allows to retain the gains in the high degrees while also minimizing the mis-parametrization-related performance degradation in the low degrees has been introduced and validated. It is further shown that the self-de-aliasing approach features a worse performance in comparison to classic Wiese in case of a double-pair mission scenario.

More generally, the spatial-temporal parameterization scheme has to be optimized as a compromise between temporal aliasing reduction and avoidance of leakage effects. Since in a single-pair scenario the first error contributor is the dominant one, DMD outperforms both the nominal solution as well as the classic Wiese parameterization. In contrast, due to the added inclined pair of a Bender scenario the temporal aliasing error itself is already reduced, so that spectral leakage may dominate if the DMD is applied.

The implementation of the self-de-aliasing approach as described in this TN is thus recommended for implementation in the full-scale simulator, as it can be expected to yield a significant increase in retrieval performance for a single-pair mission. Its value should also be validated for single-pair based NRT applications, as it potentially allows a reliable estimation of gravity fields over short time spans. Additional investigations shall be carried out towards the definition of optimal multi-period estimations as well as towards an optimal constraint in this case. Although it was demonstrated that the classic Wiese approach does not perfectly fulfil the original assumption, it is nevertheless recommended for double pair scenarios, because it outperforms all other spatial-temporal parameterisation strategies investigated so far. In this regard it may also be valuable to apply the de-aliasing part of DMD based on the short-interval fields co-estimated with Wiese.

36 ANALYSIS OF NEED FOR LONG-TERM TREND ESTIMATION (WP460)

In this WP is shall be evaluated if the co-estimation of long-term parameters such as linear trends can improve the quality of temporal gravity solutions.

For this purpose, an extended parameter model was implemented in the reduced-scale simulator, where monthly solutions can be estimated together with a long-term linear trend, and optionally also annual signals. The extended observation equation (with annual parameters) reads:

$$f(x) = x_{offset} + x_{monthly} + x_{long-term\ trend} * t$$

Since this might result in a very large number of parameters, technically this problem is solved by a parameter elimination and re-substitution scheme for the monthly parameters.

For the numerical analysis, the test period was 10 years with a 50 s sampling. As input temporal gravity field the terrestrial water storage, i.e. the sum of the parameters soil moisture and snow cover, of the GFDL climate model 4 was used up to d/o 10 (in order to reduce the computational load). Figure 36-1 shows the results evaluated for the EWH change in the Danube hydrological catchment, for the parameter groups (monthly estimates [red dotted curve] and trend [red solid curve]) separately, and the total signal (red dashed curved). As a reference, the input hydrological signal is shown in blue. While the total signal can be recovered almost perfectly, it is evident that the monthly estimates soak up a significant part of the trend signal. In this respect, an important choice is also the reference epoch of the trend, in order to avoid or at least minimize leverage effects.
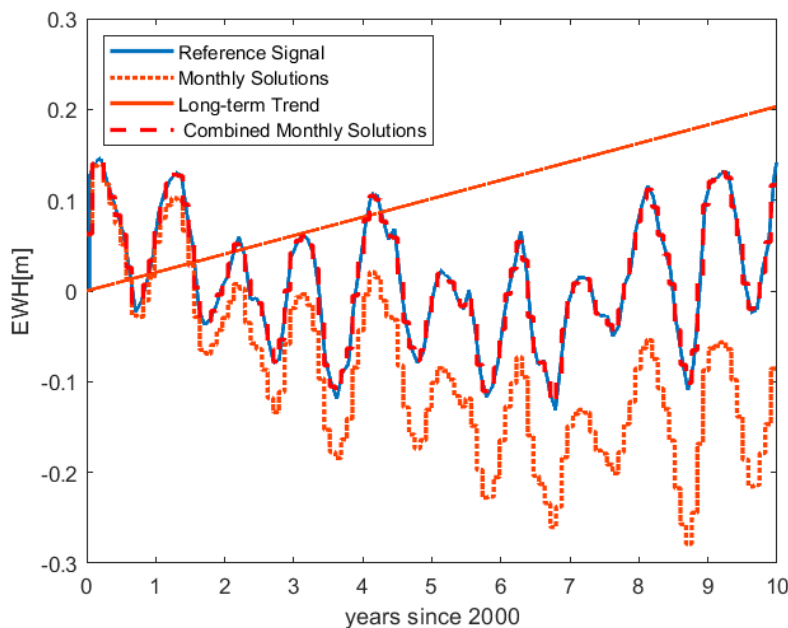
Figure 36-1: Monthly and trend estimates (unconstrained) of EWH [m] for Danube hydrological catchment.

In order to avoid trend signal leaking into the monthly solutions, they have been constrained by an additional condition, stating that no trend is allowed among the monthly solution. Figure 36-2 shows the results of this constrained parameter estimation. As intended, the monthly solutions are now free of any linear trend.
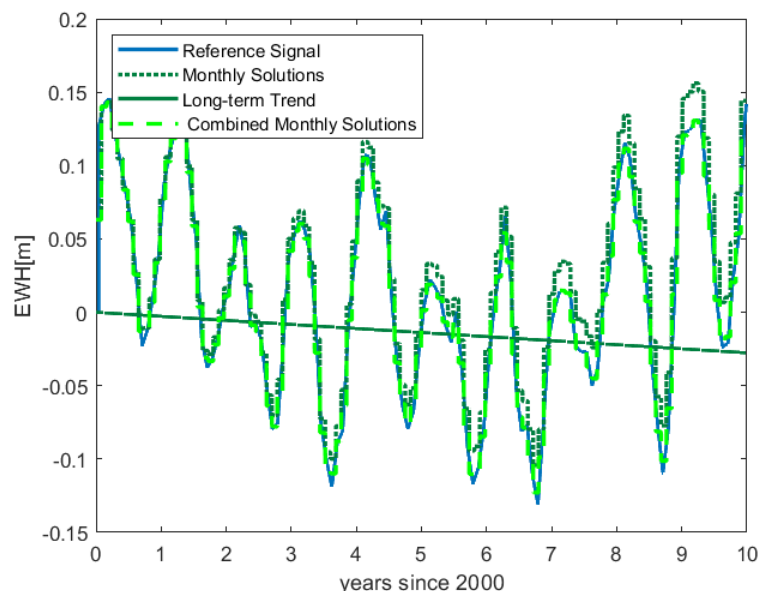
Figure 36-2: Monthly and trend estimates (constrained) of EWH [m] for Danube hydrological catchment.

As a next step, it is investigated if there is a significant difference between the monthly estimates without/with co-estimation of the long-term trend. Figure 36-3 shows EWH deviations from the input reference signal in terms of spatial grids, and Figure 36-4 the corresponding SH degree standard deviations. Evidently, the difference is very small, and there is no indication of a benefit for monthly solutions when the long-term trend is co-estimated.

Vice versa, the long-term trend estimation tends to suffer from a leverage effect, so that a single trend estimation (without co-estimation of monthly solutions) might be more accurate. The main advantage of deriving trends directly from a long time series instead from a sequences of monthly solution is the fact, that a much higher spatial resolution (maximum degree/order) of the trend estimate can be achieved.

a)

b)

c)

d)

e)

f)
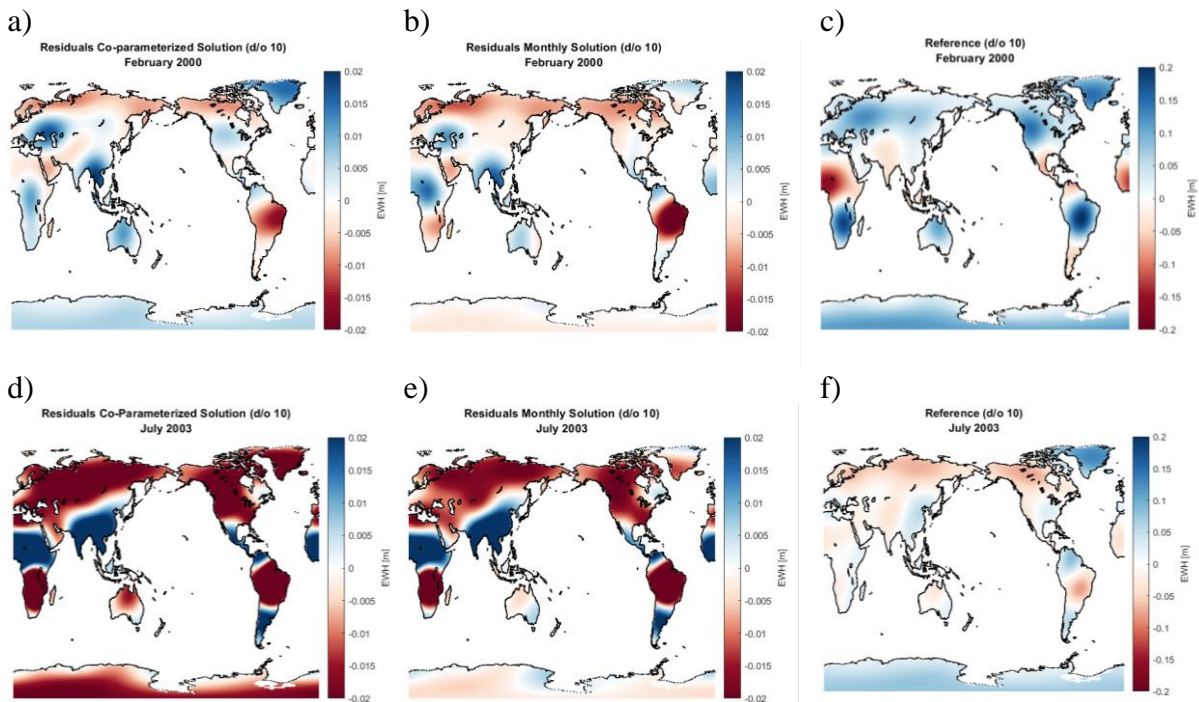
Figure 36-3: EWH differences [m] to input reference signal (c and f) for February 2000 (first row) and July 2003 (second row). a) and d) are results with co-parametrization of linear trend, b) and e) without co-parameterization.
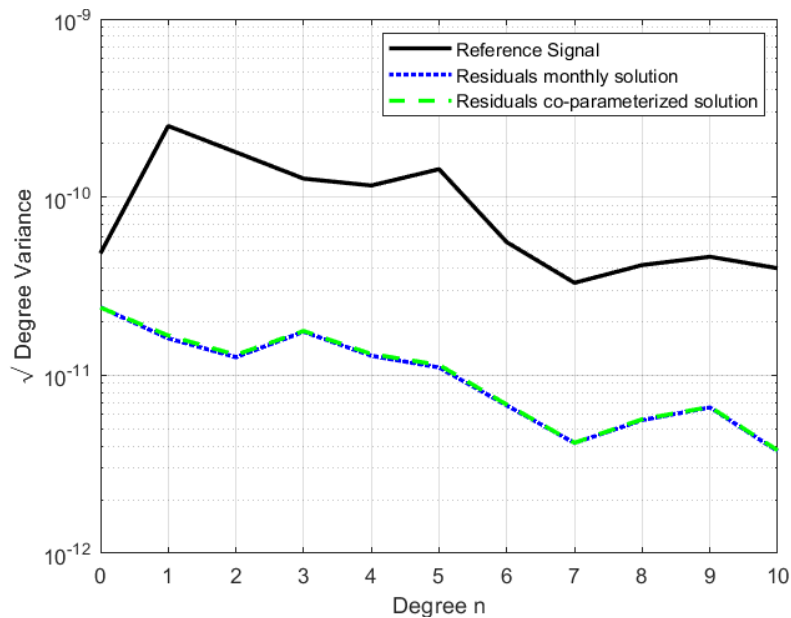
Figure 36-4: Degree standard deviations of EWH signal and EWH differences without/with co-parameterization of trend.

37 ANALYSIS OF NEED FOR POST-PROCESSING (WP470)

In this chapter the derivation of an optimal filter technique for post-processing of Bender-type gravity field solutions is described. The filtered gravity fields are then further evaluated against the true reference signal as well as unfiltered fields at the example of river basins and ice sheets.

37.1 ASSESSMENT OF AN OPTIMAL FILTER TECHNIQUE FOR BENDER-TYPE FORMATIONS

Unconstrained simulated gravity field solutions, in terms of equivalent water height (EWH), from four Bender constellations for monthly and sub-monthly retrieval periods are shown in Figure 37-1 and Figure 37-2, respectively.

From the monthly anomalous gravity field solutions, shown in Figure 37-1, it appears as though striping over mid-latitudes decreases with lower inclined pair altitudes whereas striping over the polar regions decreases with lower polar pair altitudes.

Due to ill-conditioned normal equations the 3dH (3-days)-scenario, shown in the top-left of Figure 37-2, was solved only up to degree- and order 50. In doing so, increasing noise in the higher frequencies, which are responsible for the striping, were omitted from the solution and this scenario therefore shows the least striping. Vertical error patterns are however still visible in the East for the first 3-daily solution and this pattern shifts as the timeframe progresses. The remaining sub-monthly scenarios were solved up to degree- and order 80 or 100 and therefore exhibit increased striping.

All monthly and sub-monthly scenarios display significant striping and cannot be used to their full spectral extent without modification. Methods to reduce striping were therefore investigated

NGGM/MAGIC – Science Support Study During Phase A	*Final Report*	
	Doc. Nr:	MAGIC_FR
	Issue:	1.0
	Date:	15.11.2022
	Page:	313 of 466
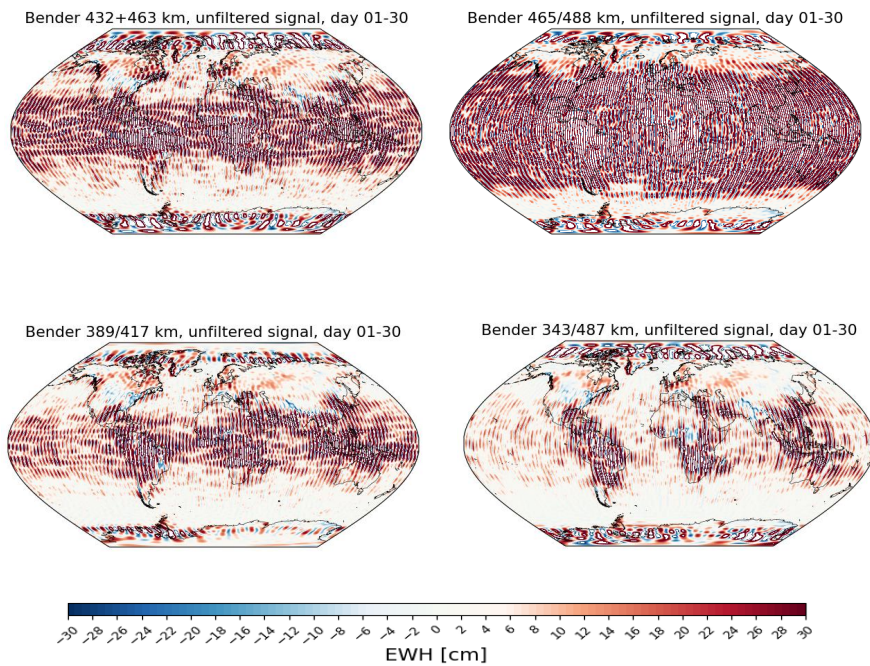
Figure 37-1: Unconstrained anomalous gravity field signal for monthly retrieval for scenarios 3dH (top left), 5dH (top right), 7dM (bottom left) and 5dHL (bottom right).
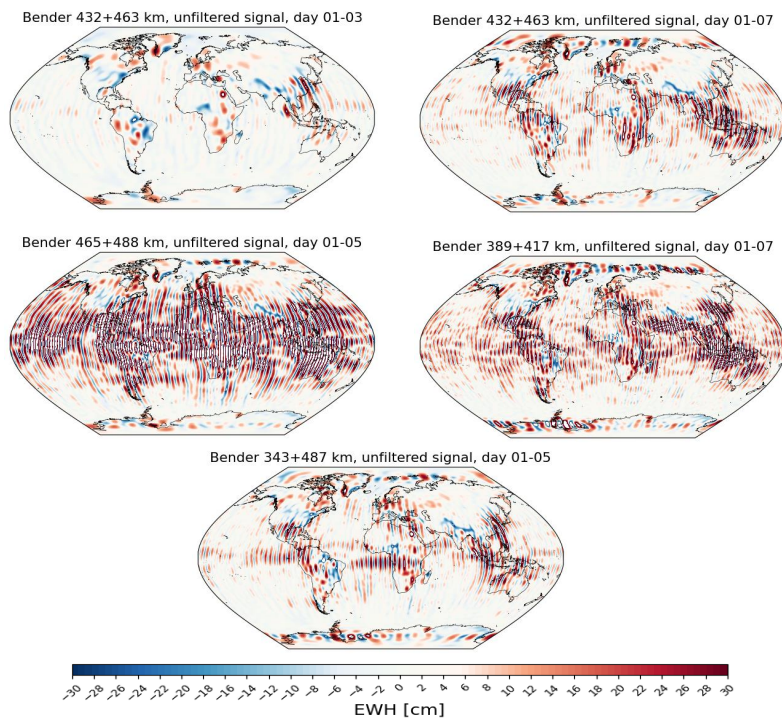
Figure 37-2: Unconstrained anomalous gravity field signal for sub-monthly retrieval for scenarios 3dH – 3d (top left), 3dH – 7d (top right), 5dH (center left). 7dM (center right) and 5dHL (bottom).

Popular methods to reduce striping include Gaussian smoothing [RD-11], a combination of decorrelation and Gaussian smoothing [RD-10], non-isotropic smoothing by approximate decorrelation and regularization i.e., DDK [RD-9], and time variable decorrelation i.e., VADER/VDK filters [RD-8]. In this work package DDK and VDK filters of various strengths were applied to monthly- and sub-monthly retrieval period solutions.

The VDK filtering approach regularises the normal equations. The main relation between unfiltered x and filtered x_α, gravity field solutions, represented by vectors of spherical harmonic coefficients, is given by

$$x_\alpha = (N + \alpha M)^{-1} N, \tag{9.1}$$

where N is the normal equation matrix and M is the signal variance matrix. The signal variance matrix is dependent only on the degree l:

$$\sigma_M(l) = a \cdot l^b, \tag{9.2}$$

where $a = 1.0$ and $b = -4.0$ are constants derived from 143 months of real GRACE data, filtered with the DDK4 filter (Horvath, Murboeck, Pail, & Horwath, 2018).

The DDK filter functions similarly to the VDK filter but, instead of using the actual normal equation and signal variance, it uses approximations to estimate these values. The benefit being that it can be applied by users that have access only to the normal equation solutions and not the normal equations themselves. For a detailed overview of how these approximations are made the reader is referred to Section 3 of Kusche, 2007.

Each of the scenarios was filtered with 6 DDK and 4 VDK filters. VDK filters were applied to the normal equations and DDK filters were applied to the normal equation solutions. The filtered spatial signal, in terms of equivalent water height, was calculated over a 180x360 grid and subtracted from Earth system model derived HIS values to obtain absolute differences. For each filter, the standard deviation of these differences was then used as a measure to determine the best global filter i.e., the filter that delivered an error (difference) with the smallest standard deviation was considered optimal. This was also verified by visual inspection of the spatial signals for each of the filters and cumulative degree-variance error graphs.

The unfiltered monthly spatial signals and error distributions are shown in Figure 37-1 and Figure 37-3, respectively, whereas the unfiltered sub-monthly spatial signals and error distributions are shown in Figure 37-2 and Figure 37-4, respectively. The standard deviation of the filtered signal error distributions for ten filters (4 VDK and 6 DDK) are listed in Table 37-1.
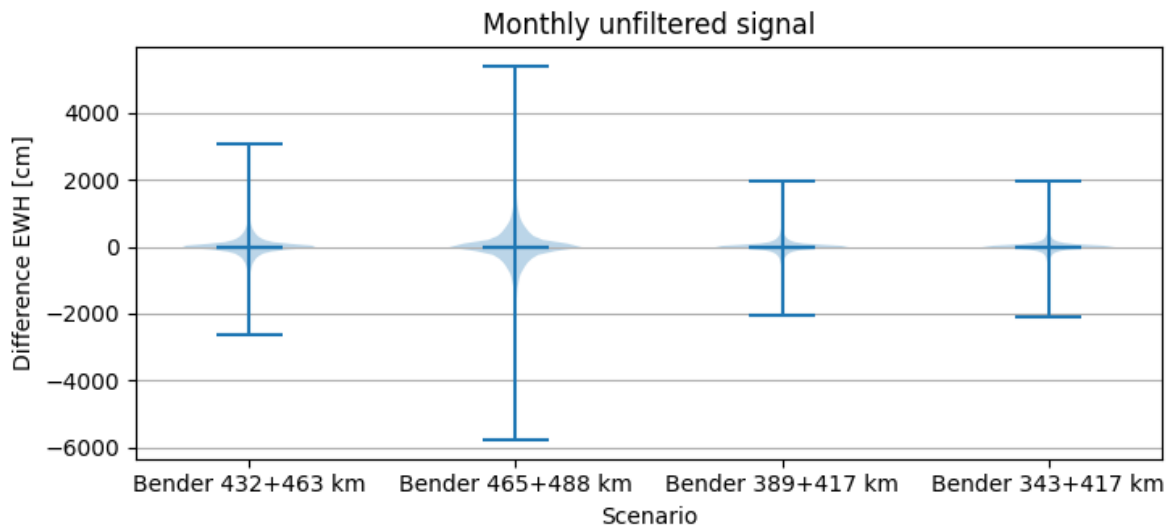
Figure 37-3: Unfiltered monthly error distributions.
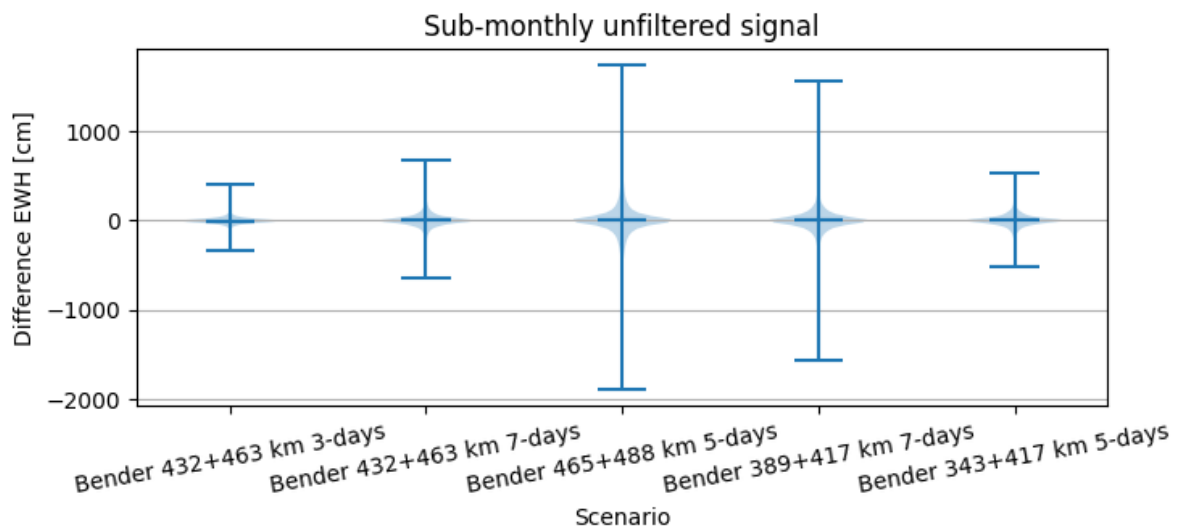
Figure 37-4: Unfiltered sub-monthly error distributions.

	Final Report	
NGGM/MAGIC – Science Support Study During Phase A	Doc. Nr:	MAGIC_FR
	Issue:	1.0
	Date:	15.11.2022
	Page:	316 of 466

Table 37-1: Standard deviation for monthly and sub-monthly scenarios. Values shown in red indicate the minimum standard deviation.

Scenario/ std	DDK3	DDK4	DDK5	DDK6	DDK7	DDK8	VDK α=1e23	VDK α=1e23	VDK α=1e23	VDK α=1e23
3dH (3d)	22.5	22.6	23.8	24.7	27.4	28.8	20.9	22.1	27.6	32.8
3dH (7d)	26.3	25.8	25.2	25.3	27.2	29.0	24.3	23.8	31.3	50.7
3dH (30d)	30.2	29.5	28.3	27.9	27.9	28.6	27.0	25.0	28.0	43.0
5dH (5 days)	27.3	27.4	28.7	29.8	34.1	37.1	26.2	26.1	32.2	52.4
5dH (30d)	30.4	29.8	28.5	28.1	27.9	28.4	28.2	26.5	28.9	50.5
7dM (7d)	28.6	28.0	29.9	26.8	27.4	28.3	26.8	25.5	31.2	50.6
7dM (30d)	30.2	29.5	27.9	27.4	26.5	26.3	26.6	24.6	26.0	37.1
5dHL (5d)	26.4	26.0	26.0	26.4	29.4	31.7	24.4	23.9	31.5	49.0
5dHL (30d)	30.2	29.5	28.2	27.8	27.8	28.4	26.0	23.8	27.8	56.2

The best performing filters are highlighted in red. For all scenarios, except 3dH (3-days), a VDK filter with a scaling factor of $\alpha = 1e22$ resulted in the smallest standard deviation value. The VDK filter always outperformed the DDK filter and monthly- and sub-monthly filtered error distributions are shown in Figure 37-5 and Figure 37-6, respectively
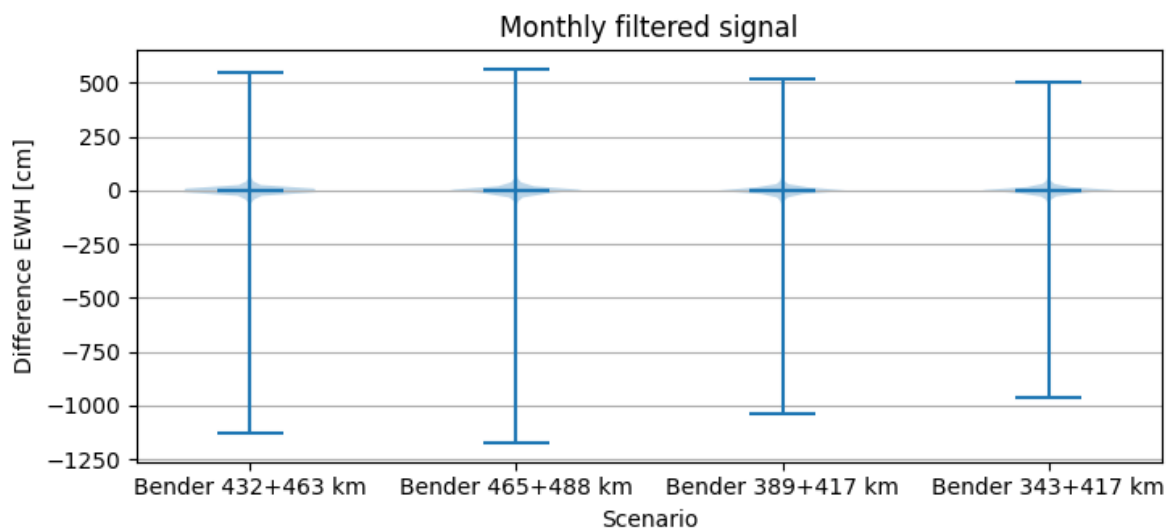
Figure 37-5: Filtered monthly error distributions.
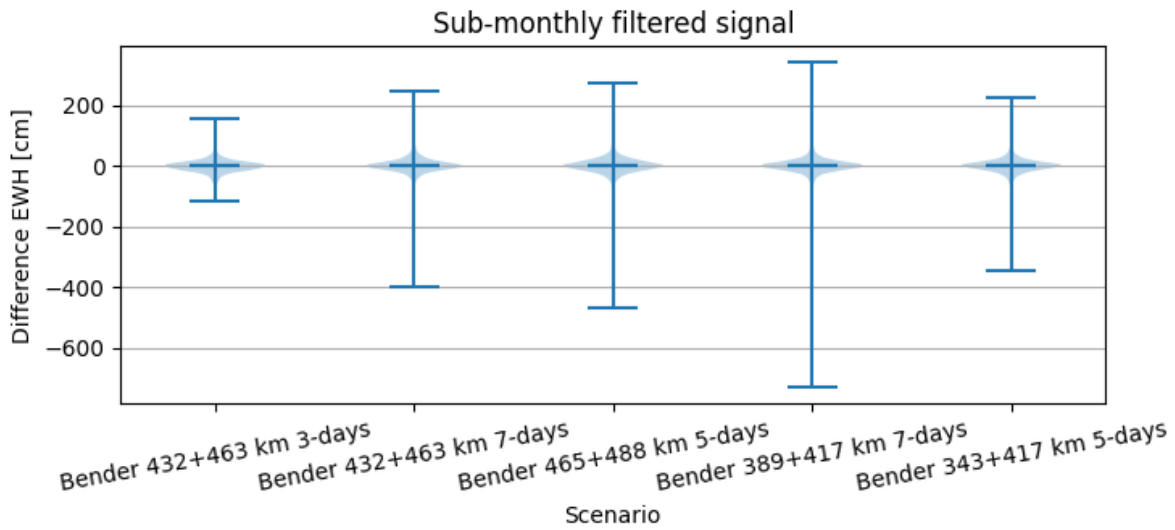
Figure 37-6: Filtered sub-monthly error distributions.

The unfiltered- and filtered cumulative errors in terms of EWH are shown in Figure 37-7 and Figure 37-8, respectively. Before filtering, the monthly 7dM scenario comes closest to satisfying the user requirements, however, after filtering, the 5dHL scenario performs best when compared to the user requirements. For the sub-monthly retrieval periods the requirements are best satisfied by the 7dM scenario, for both filtered and unfiltered scenarios as shown in Figure 37-8.
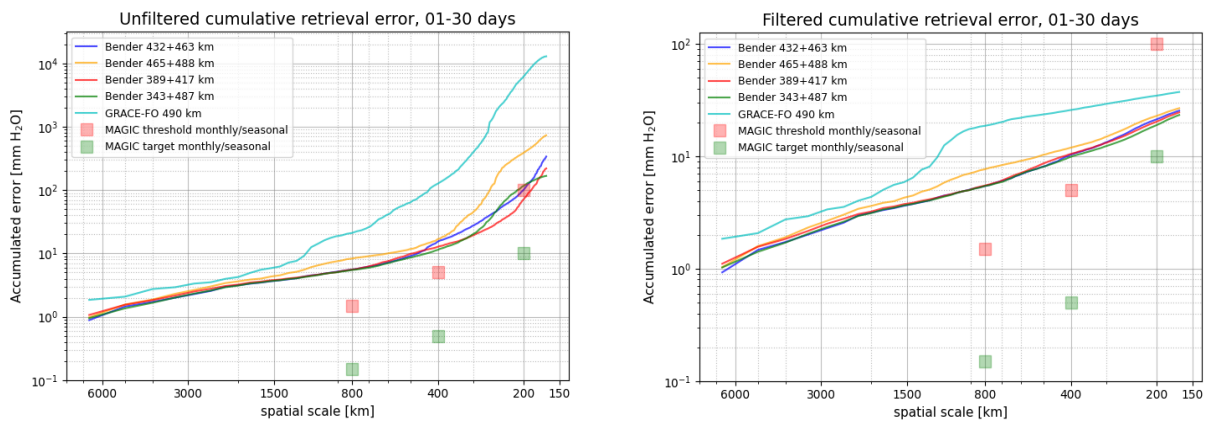
Figure 37-7: Cumulative error for unfiltered (left) and VDK filtered (right) monthly retrieval signals in terms of mm EWH.
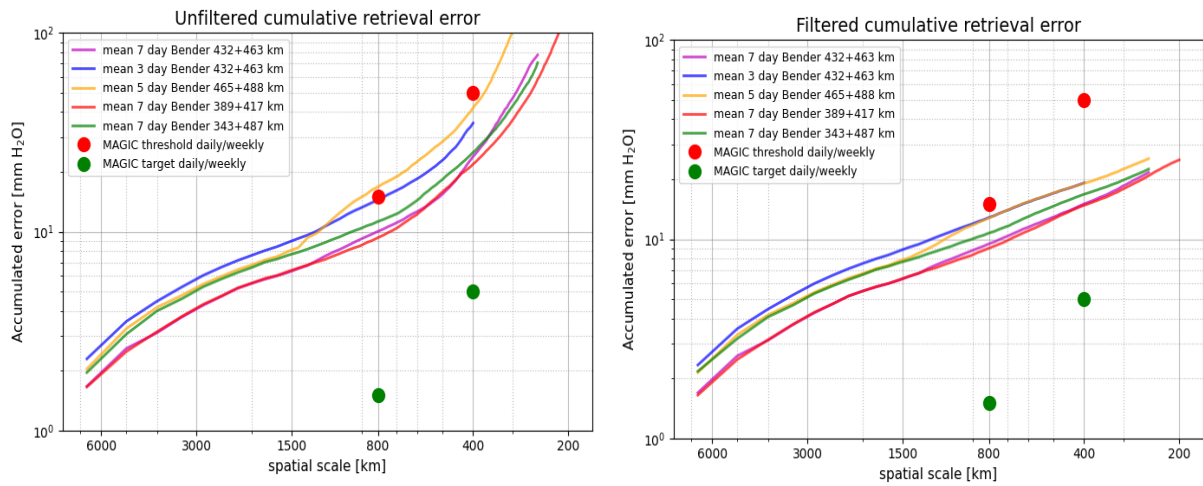
Figure 37-8: Cumulative error for unfiltered (left) and filtered (right) sub-monthly retrieval signals in terms of EWH.

Spatial comparisons of the monthly unfiltered and filtered gravity signals in terms of EWH are shown in Figure 37-9 and Figure 37-10 and verifies that the VDK filter successfully reduced noise in the higher frequencies.
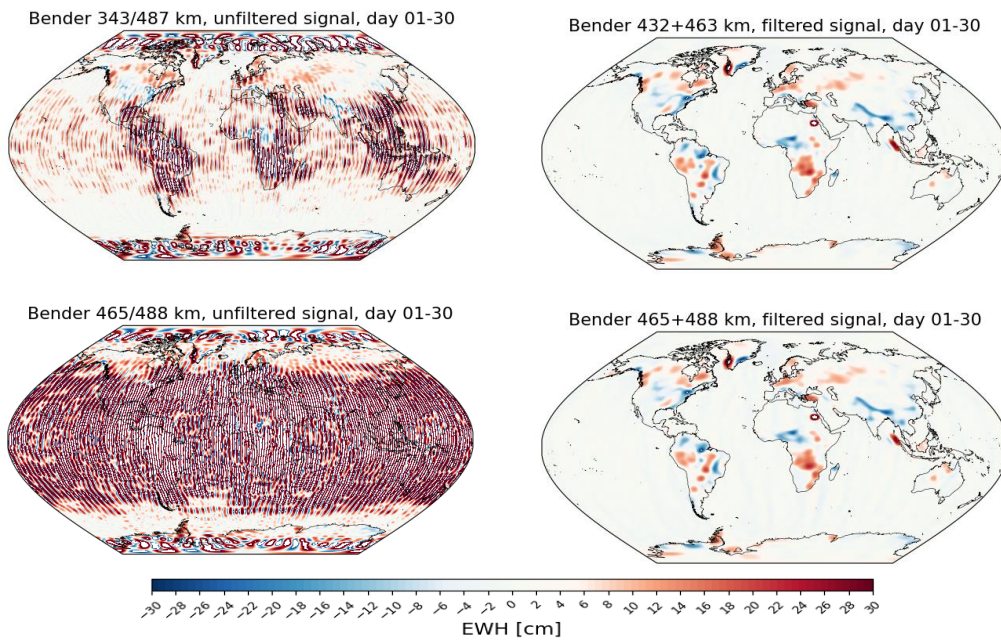
Figure 37-9: Spatial comparison for filtered and unfiltered monthly retrieval periods for 3dH and 5dH.
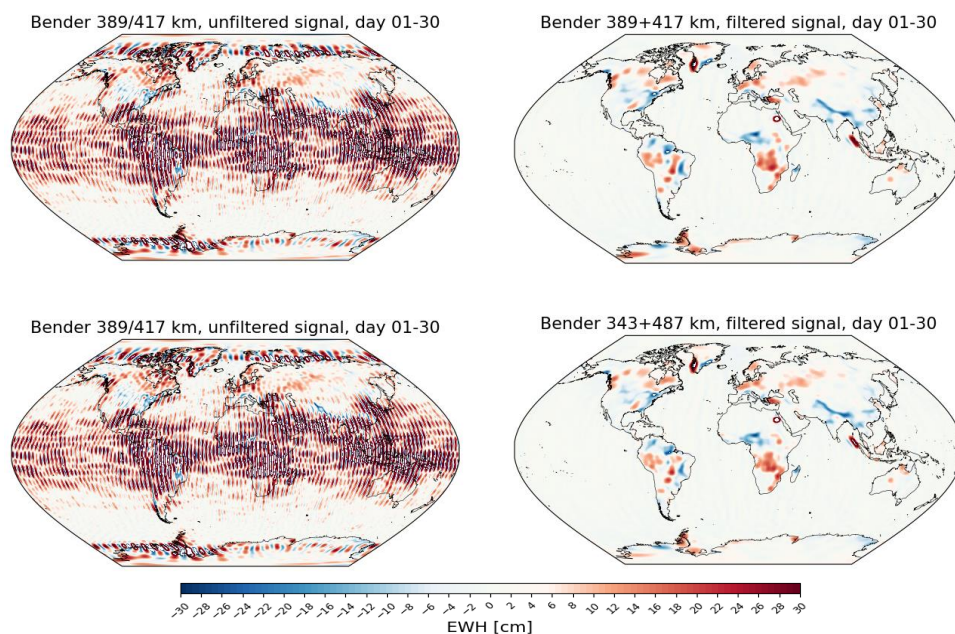
Figure 37-10: Spatial comparison of unfiltered (left) and filtered (right) monthly retrieval periods for 7dM and 5dHL.

Similarly, spatial comparisons for the sub-monthly retrieval periods, shown in Figure 37-11, Figure 37-12 and Figure 37-13, show that the short wavelength (i.e. high frequency) errors were also successfully reduced for these scenarios.
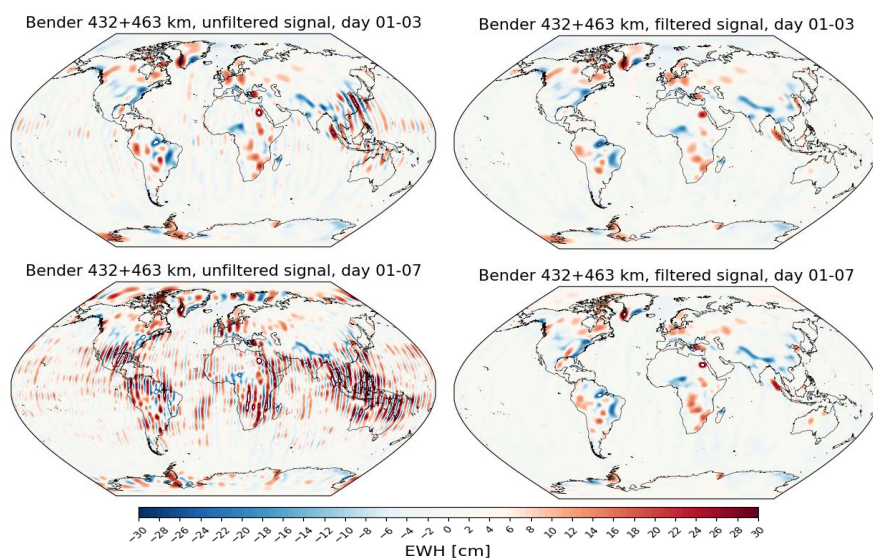
Figure 37-11: Spatial comparison for filtered and unfiltered sub-monthly retrieval periods for 3dH (3d) and 3dH (7d).
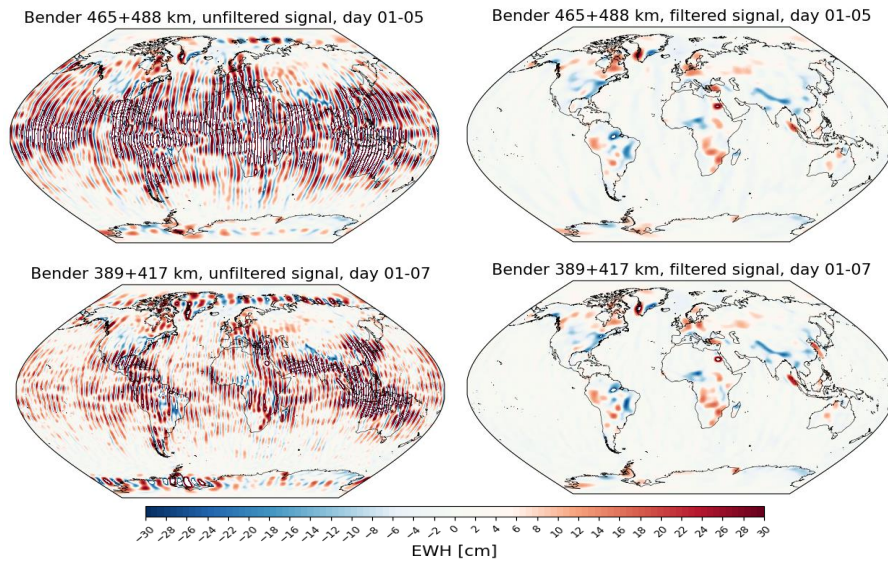
Figure 37-12: Spatial comparison for filtered and unfiltered sub-monthly retrieval periods for 5dH and 7dM.
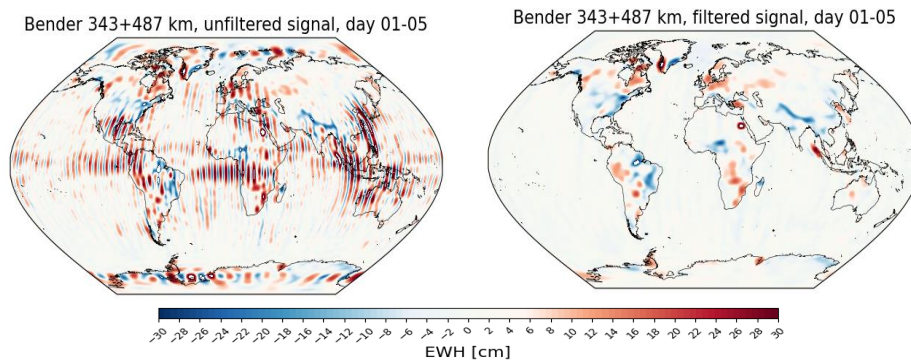
Figure 37-13: Spatial comparison for filtered and unfiltered sub-monthly retrieval periods for 5dHL.

37.2 EVALUATION OF NEED FOR POST-PROCESSING AT THE EXAMPLE OF RIVER BASINS AND ICE SHEETS

From several plots representing spatial signal distribution of gravity field retrieval from Bender-type configurations it can be seen that temporal aliasing errors are present in terms of varying amplitudes at different locations on Earth. In order to assess whether filtering is necessary or not, retrieved gravity fields were investigated quantitatively wrt. the truth HIS signal at specific river basins (Amazon, Congo and Malaysian Peninsula) and ice sheets (Greenland and Antarctica). In this context, the 'raw' gravity field retrieval and the VDK filtered retrieval were compared against the reference HIS signal in terms of a latitude dependent mean for the locations mentioned above.

Figure 37-14 displays the sub-monthly retrieved signal up to d/o 50 for three river basins. It is seen that filtering is not needed for basins which are not affected by stripes (Amazon, Congo). In that cases the raw retrieval mirrors the truth quite well so that the application of a VDK filter does not lead to further improvement, in contrast, it even leads to a very slightly falsification of the retrieved signal for some retrieval periods. However, filtering can be useful for regions affected stronger by aliasing errors, such as the Malaysian Peninsula basin. This is especially visible at the 3-day retrieval of the 3dH scenario.

The evaluation up to d/o 80 shown in Figure 37-15 reveals larger error signals for the raw retrievals, especially for the 5dH scenario. Here filtering is necessary in any case. The other scenarios show low-to-moderate displacement wrt. the truth HS signal but filtering helps to approximate reality, though.

Figure 37-16 displays the situation for Greenland and Antarctica ice sheets up to a maximum d/o of 50. In case of scenarios 3dH, 7dM and 5dHL, filtering helps to approximate reality. The inclined pair of scenario 5dH has a higher inclination (75 degrees) compared to the other scenarios resulting in reduced errors at high latitude areas for the 5dH scenario. In this case, for Greenland, filtering is not necessary, at least for specific retrieval periods. As Antarctica is located at very high latitudes, the effect of a slightly higher inclination for the 5dH scenario disappears and filtering is required. Solving the retrieval up to d/o 80, shown in Figure 37-17, leads to similar conclusions.
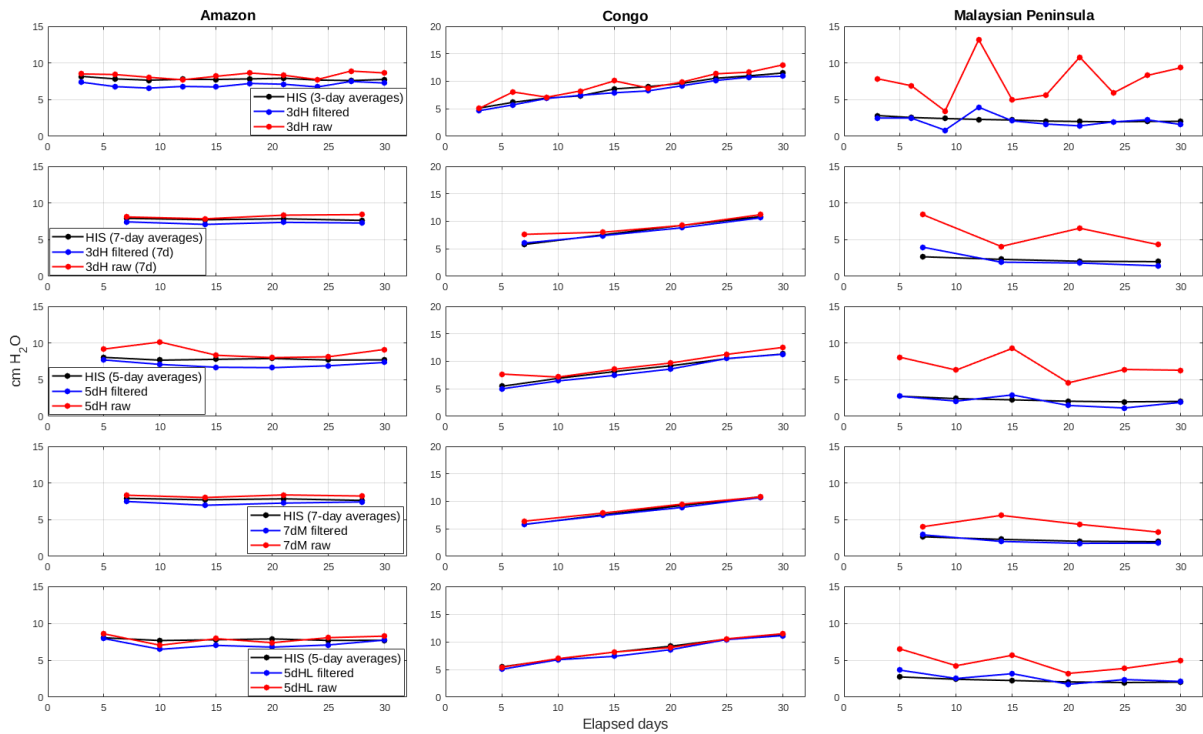
Figure 37-14: Latitude dependent mean in terms of cm EWH computed up to d/o 50 for Amazon (left), Congo (center) and Malaysian Peninsula (right) basins for sub-monthly retrievals of scenarios 3dH (first (3d) and second (7d) row), 5dH (third row), 7dM (fourth row) and 5dHL (fifth row). The reference HIS signal is displayed in black, the raw retrieval is displayed in red and the filtered retrieval is displayed in blue.
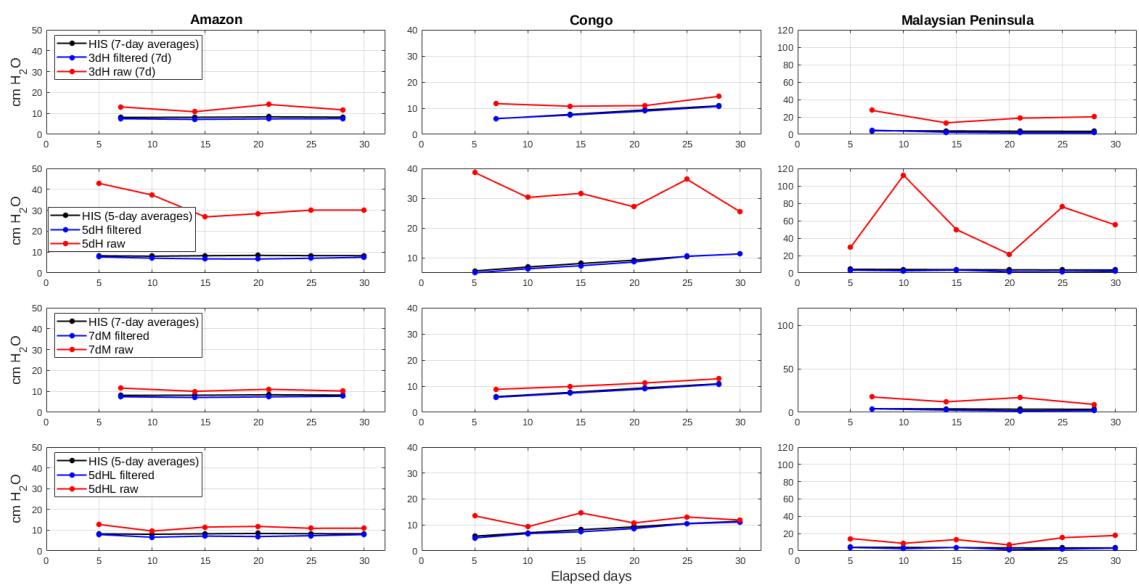
Figure 37-15: Latitude dependent mean in terms of cm EWH computed up to d/o 80 for Amazon (left), Congo (center) and Malaysian Peninsula (right) basins for sub-monthly retrievals of scenarios 3dH (first row), 5dH (second row), 7dM (third row) and 5dHL (fourth row). The reference HIS signal is displayed in black, the raw retrieval is displayed in red and the filtered retrieval is displayed in blue.
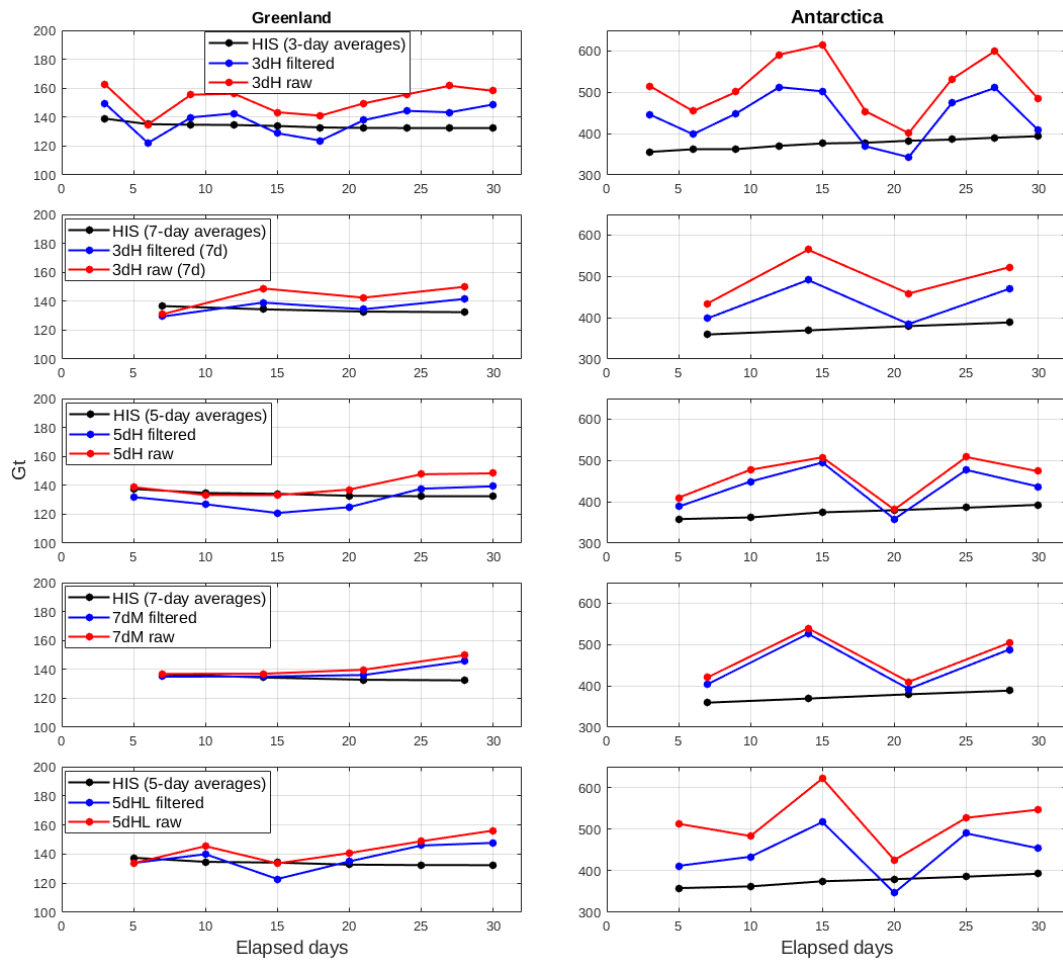
Figure 37-16: Latitude dependent mean in terms of Gigatons computed up to d/o 50 for Greenland (left) and Antarctica (right) for sub-monthly retrievals of scenarios 3dH (first (3d) and second (7d) row), 5dH (third row), 7dM (fourth row) and 5dHL (fifth row). The reference HIS signal is displayed in black, the raw retrieval is displayed in red and the filtered retrieval is displayed in blue.
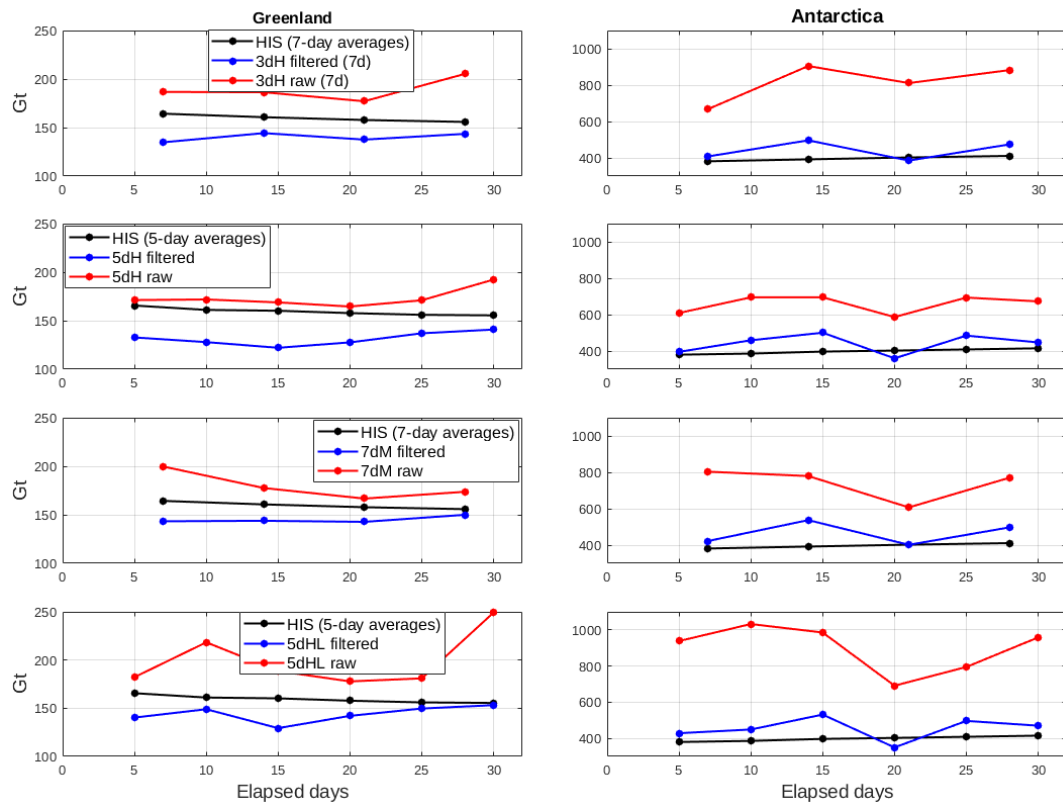
Figure 37-17: Latitude dependent mean in terms of Gigatons computed up to d/o 80 for Greenland (left) and Antarctica (right) for sub-monthly retrievals of scenarios 3dH (first row), 5dH (second row), 7dM (third row) and 5dHL (fourth row). The reference HIS signal is displayed in black, the raw retrieval is displayed in red and the filtered retrieval is displayed in blue.

Figure 37-18 shows the monthly retrieval solved up to d/o 50 for the three river basins and the two ice sheets. Results indicate that post-processing by filtering is not necessary for river basins which are not affected by striping errors (Amazon, Congo). For basins being affected stronger (Malaysian Peninsula) filtering helps to approximate the truth signal. In contrast to Greenland, Antarctica is affected stronger by striping errors as the inclined pair cannot contribute to this region. Therefore, filtering can help to approximate the real signal. In Figure 37-19 the situation is displayed for signals solved up to d/o 120. The high resolution implies larger aliasing errors due to high frequency signals. Filtering is necessary in order to approximate the truth, in any case.

Results demonstrate that filtering of Bender-type gravity fields via VDK can be useful in order to extract the signal of interest in such a way that errors due to temporal aliasing are significantly reduced. However, the observation geometry of a Bender-type formation leads to an inhomogeneous error signal distribution, compared to a single polar pair formation, so that some regions are affected more by aliasing errors and some are almost free of errors. Depending on the region to be investigated, it is advisable to look at the error distribution of the 'raw' retrieval on a spatial scale first and then decide which type of gravity field (filtered or unfiltered) to be used.
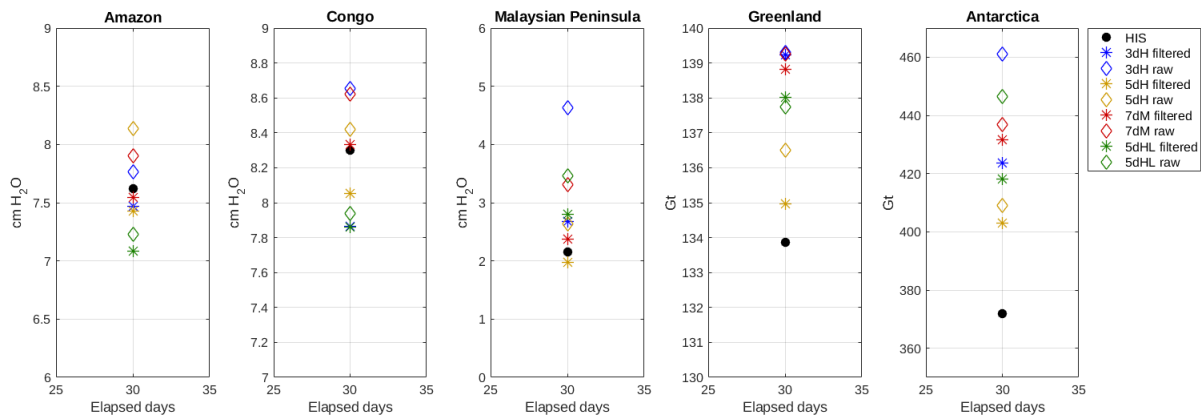
Figure 37-18: Latitude dependent mean computed up to d/o 50 for Amazon (first column), Congo (second column) and Malaysian Peninsula (third column) basins as well as for Greenland (fourth column) and Antarctica (fifth column) for monthly retrievals of scenarios 3dH (blue), 5dH (orange), 7dM (red) and 5dHL (green). The raw retrieval is displayed as asterisk, the filtered retrieval is displayed as diamond. The reference HIS signal is displayed in black.
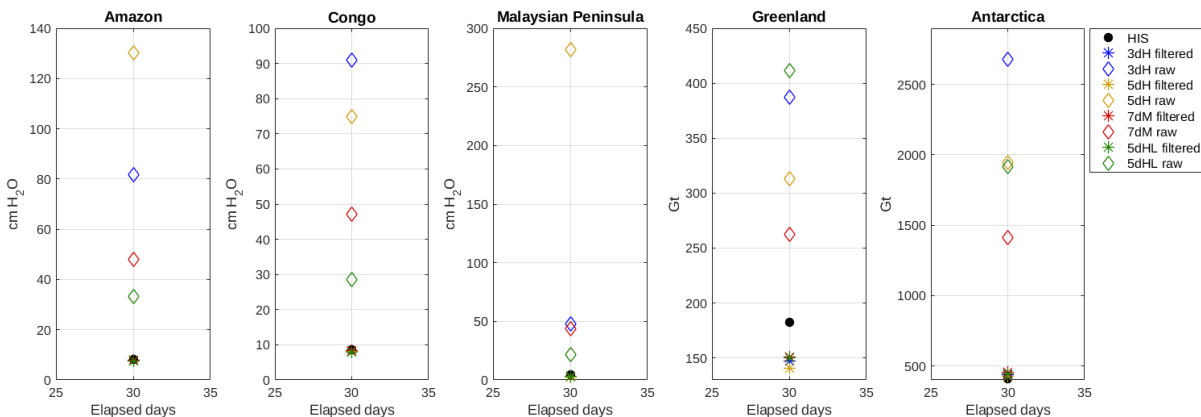
Figure 37-19: Latitude dependent mean computed up to d/o 120 for Amazon (first column), Congo (second column) and Malaysian Peninsula (third column) basins as well as for Greenland (fourth column) and Antarctica (fifth column) for monthly retrievals of scenarios 3dH (blue), 5dH (orange), 7dM (red) and 5dHL (green). The raw retrieval is displayed as asterisk, the filtered retrieval is displayed as diamond. The reference HIS signal is displayed in black.

38   COMBINING METHODOLOGY UPDATES

38.1 DMD WITH STOCHASTIC MODELLING OF OCEAN TIDE BACKGROUND MODEL ERRORS

Based on the findings of WP400 two promising improvements with regard to processing strategy could be identified – on the one hand the data-driven multi-step self-de-aliasing approach (DMD) which primarily targets the non-tidal AO signal components and on the other hand the stochastic modelling of OT background model errors (c.f. Abrykosov et al. 2021). In the following we attempt to combine these two methods in order evaluate their collective value. It is noted that the evaluation is once again based on results obtained with the reduced-scale simulation software.

As has been shown in the framework of WP400 and in external scientific studies, the DMD scheme shows the most benefit for single-pair-based gravity retrieval and especially in case one attempts to retrieve the full AO signal in addition to the HIS components. However, notable improvements in retrieval performance could also be established with HIS as the target signal, i.e. when applying BM-based a priori AO de-aliasing. In case of a double-pair scenario the DMD's overall impact was shown to be far less pronounced due to the observation geometry's intrinsic de-aliasing capabilities.
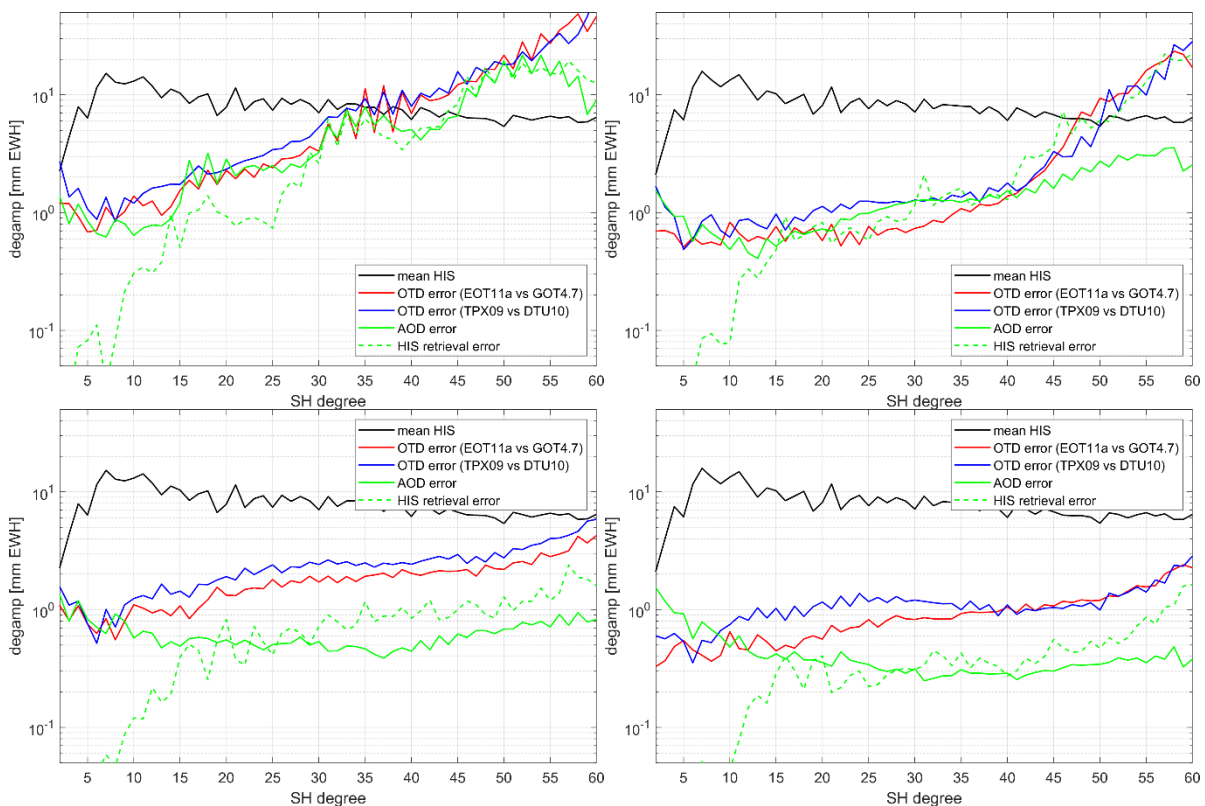
Figure 38-1: Individual contributions of the OT de-aliasing error, AO de-aliasing error and HIS to the gravity retrieval in case of a single- (top row) and double-pair scenario. The retrieval period of 7 days (left column) and 30 days (right column) is investigated. Note that two scenarios for the OT de-aliasing error are investigated – in the blue scenario, the OT de-aliasing error is taken as the difference between the models TPX09 and DTU10, while in the red scenario EOT11a and GOT4.7 are used (which is the standard for the MAGIC study).

On the other hand, the OT error weighting has been shown to show the largest improvements for a double-pair-based retrieval, as the OT aliasing greatly supersedes that of the residual AO. The added value is significantly reduced in case of a single-pair-based retrieval, as the AO de-aliasing error (and also the naturally occurring HIS-induced aliasing) features very similar amplitudes in the low-degree spectrum and significantly larger ones in the high degrees than the OT de-aliasing error. This behaviour is visualized in Fig. 38-1 in terms of degree amplitudes of the retrieval error.
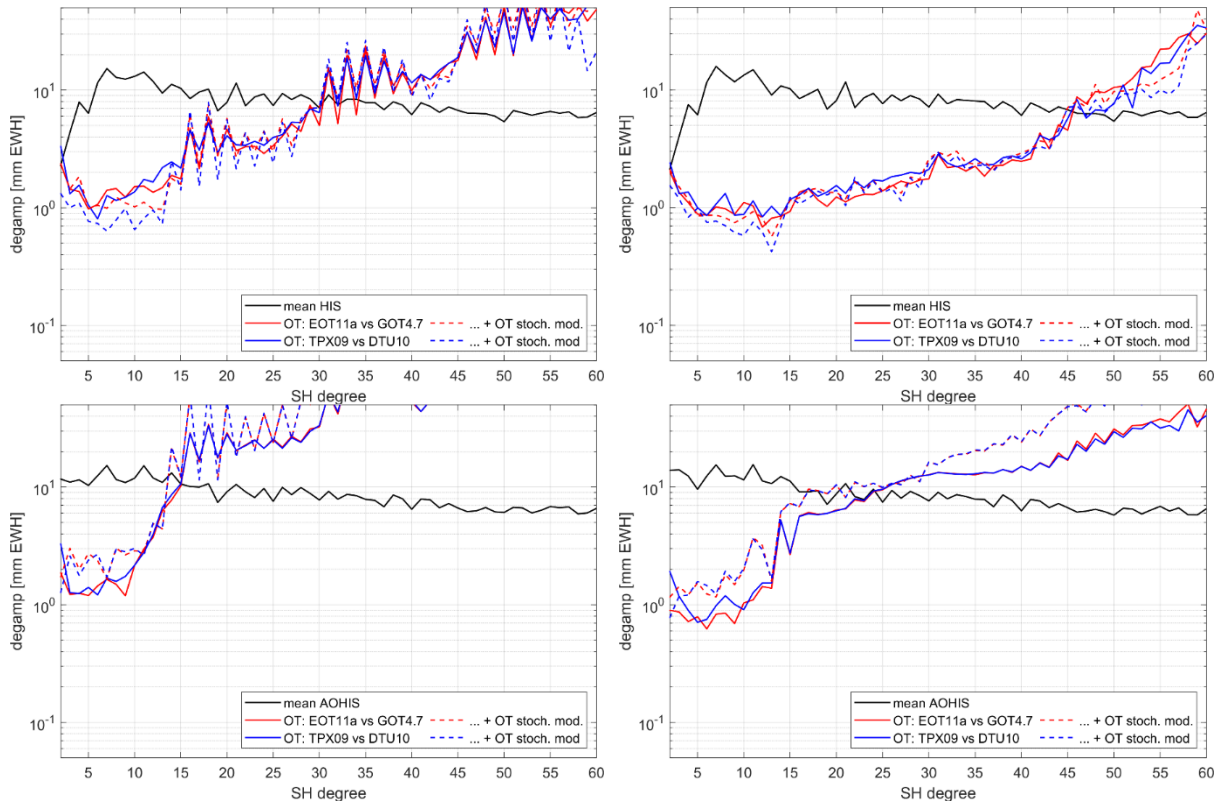
Figure 38-2: Gravity retrieval error of a single-pair based 7-day (left col.) and 30-day (right col.) solution with and without applying stochastic modelling of OT BM errors. The non-tidal time-variable signal is assumed to be HIS incl. an a priori AO de-aliasing error constituting 10% of the full AO signal (top row) as well as the full AOHIS signal (bottom row).

From these findings alone it is already evident that the DMD and the OT error weighting are rather contrasting approaches rather than complementary ones. Nevertheless, in order to better understand the interactions between the signal components and the stochastic modelling of OT errors, the latter is applied in various simulation scenarios. In a first step this is done without additionally employing the DMD, i.e. the nominal processing scheme is retained. Fig. 38-2 and 38-3 show the retrieval errors in case of a 7- and 30- day retrieval based on the observations of a single- and a double-pair mission, respectively. Here, the OT de-aliasing error is simulated based on the difference of either EOT11a and GOT4.7 (which is the standard in the study at hand, but GOT4.7 is not part of the model ensemble used to derive the OT error VCMs, see Abrykosov et al. 2021) or TPX09 and DTU10 (both models are part of the model ensemble used to derive OT error VCMs). It is noted that since full OT error VCMs are provided up to d/o 60, the simulations analogously include gravity signals up to d/o 60 and the gravity retrieval is also carried up to d/o 60 in order to guarantee full consistency.
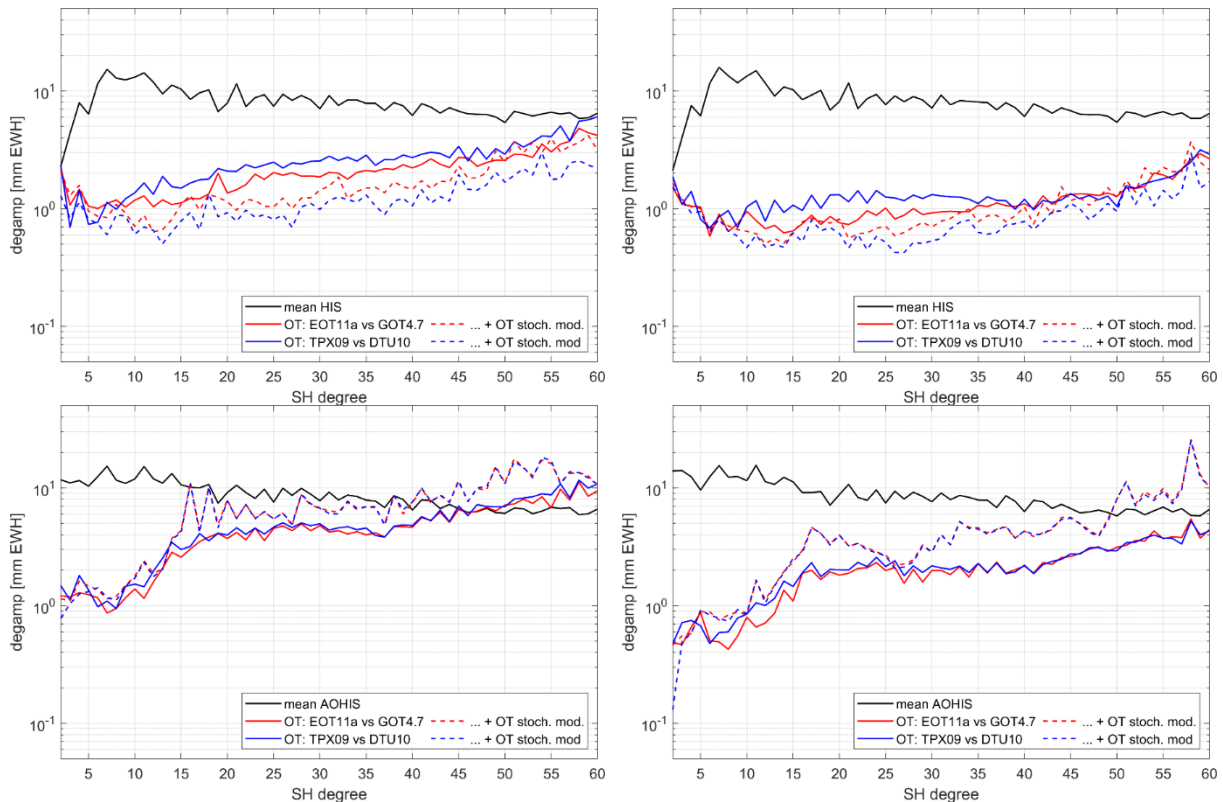
Figure 38-3: Gravity retrieval error of a double-pair based 7-day (left col.) and 30-day (right col.) solution with and without applying stochastic modelling of OT BM errors. The non-tidal time-variable signal is assumed to be HIS incl. an a priori AO de-aliasing error constituting 10% of the full AO signal (top row) as well as the full AOHIS signal (bottom row).

In case of the single pair (c.f. Fig. 38-2) it is evident that once the full AOHIS signal is included in addition to the OT de-aliasing errors, the application of OT error weighting completely degrades the retrieval performance. This was to be expected, since in this case the AO signal features the strongest amplitudes and the stochastic modelling is thus applied exclusively to this component. On the other hand, in case a priori AO de-aliasing is applied and only residual AO signals remain within the system, the OT error weighting does indeed contribute to an improved retrieval performance in certain spectral bands. A comparison to Fig. 38.1 reveals that these spectral bands are also the ones in which the de-aliasing errors induced by the OT components are dominant. However, since the discrepancies between the de-aliasing errors induced by tidal and non-tidal (i.e., AO de-aliasing and naturally occurring retrieval error of HIS) components are comparatively small, the improvements facilitated by the OT error weighting are also rather small. However, it should be noted that simulation scenario employing TPX09 vs DTU10 to simulate the OT de-aliasing error features larger overall improvements when applying OT error weighting. On one hand, this is of course due to the fact that the overall discrepancies between these two models are larger than in case of EOT11a vs GOT4.7 and there is more room for improvement. On the other hand, the representation of the spatial error pattern through the OT error VCMs shows a better fit to the simulated signal since, as mentioned above, both TPX09 and DUT10 were part of the model ensemble that the OT error VCMs were derived from, while GOT4.7 was not. In other words, the employed OT error VCMs do not optimally represent the spatial errors present with the difference of EOT11a and GOT4.7 which limits potential improvements in retrieval performance.

In case of the double-pair scenario (c.f. Fig. 38-3), once again no improvements can be established through the OT error weighting when the full AOHIS signal is included. However, due to the fact that the OT de-aliasing errors show significantly higher amplitudes than the ones related to AO de-aliasing, notable gains of up to ca. 15% can be established in case a priori AO de-aliasing is applied (if the OT de-aliasing error is taken from EOT11a vs GOT4.7). These findings are in line with the ones presented within the framework of WP400. Similarly to the single-pair case, the improvements are largest in the spectral bands where the OT de-aliasing errors outweigh their AO-induced counterpart. Also, larger overall gains can be established in case of TPX09 vs DTU10, i.e. when the error VCMs represent the true error patterns as closely as possible.
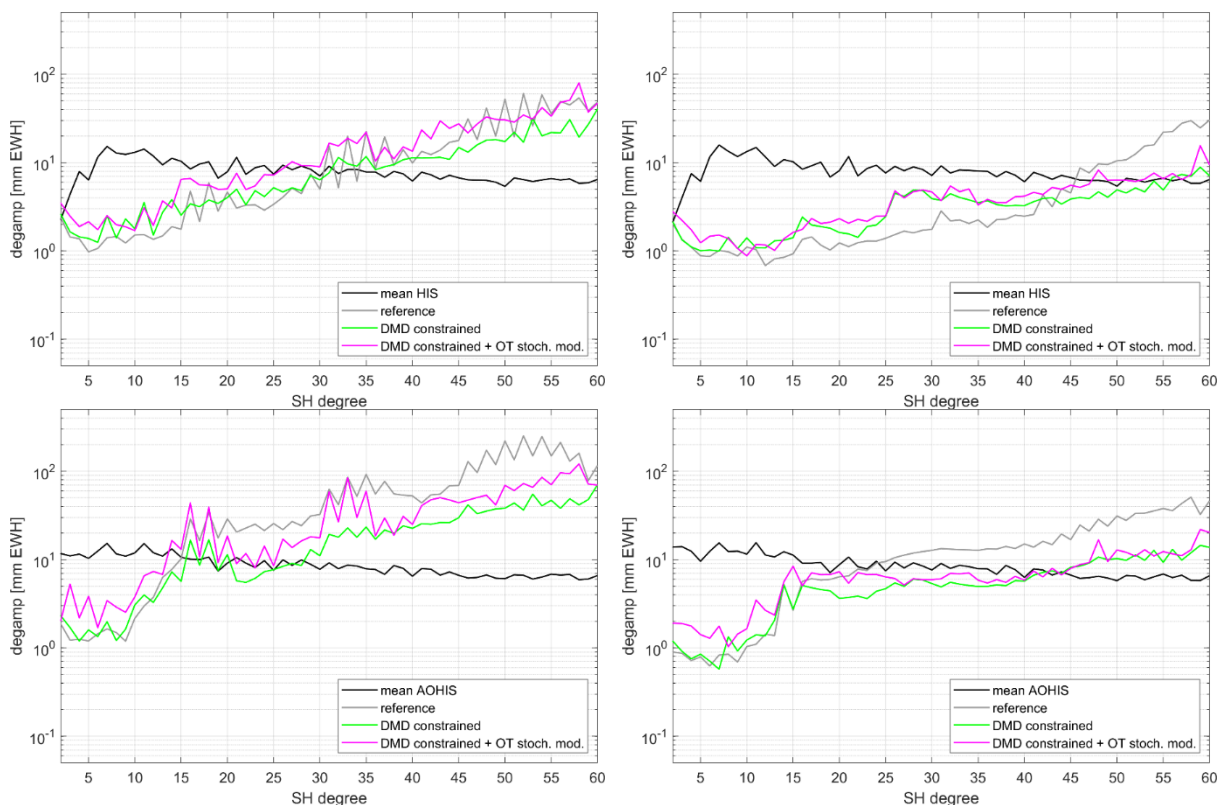
Figure 38-4: Gravity retrieval error of a single-pair based 7-day (left col.) and 30-day (right col.) solution with and without applying a combination of constrained DMD and stochastic modelling of OT BM errors. The non-tidal time-variable signal is assumed to be HIS incl. an a priori AO de-aliasing error constituting 10% of the full AO signal (top row) as well as the full AOHIS signal (bottom row).

Overall, the OT error weighting shows the most benefit in case of a double-pair scenario and only in case a priori AO de-aliasing is applied. As already mentioned earlier, this somewhat contradicts a combination with the DMD which shows the most benefit in case of a single-pair mission where the retrieval of the full AOHIS signal is sought. Fig. 38-4 indeed underlines that the combination of the two processing methods yields no benefit (or rather, degrades the overall retrieval performance) in the single-pair case both when the full and the de-aliasing AO signal are present in the observations. The most likely reason for this deterioration is the fact that the DMD constraint matrix which is used to enhance the interval estimates and in this way to stabilize the performance in the low degrees is now in a sense "superimposed" by the OT error VCM and therefore (partially) loses its effect. This interaction is further demonstrated by the fact that the performance of the non-constrained DMD actually improves when the OT error VCM is applied. However, since the overall performance of the stand-alone constrained DMD

(i.e., without applying OT error weighting) is superior to that of the non-constrained DMD combined with OT error weighting, this approach is not further investigated and the results are also not shown in this report. It is noted that further investigations regarding the relative scaling of the DMD's constraint matrix and the OT error VCM can be carried out, but one can expect little benefit, since increasing the relative weight of the constraint will negate the impact of the OT error weighting and vice versa.

In case of the double pair, on the other hand, the results based on observations including the de-aliased AO signal indicate that the combination of the (constrained) DMD and the OT error weighting might indeed yield an improved solution. The corresponding results are presented in Figure 38-5. However, the improvements constitute only a few per cent and are also limited to certain spectral bands. Above all, however, the SNR of the retrieved signal is for the most part still well above 1 here, so these added gains are in any case negligible. In case the full AO signal is present, an overall degradation of the retrieval quality can be established similarly to the single-pair retrieval discussed above.
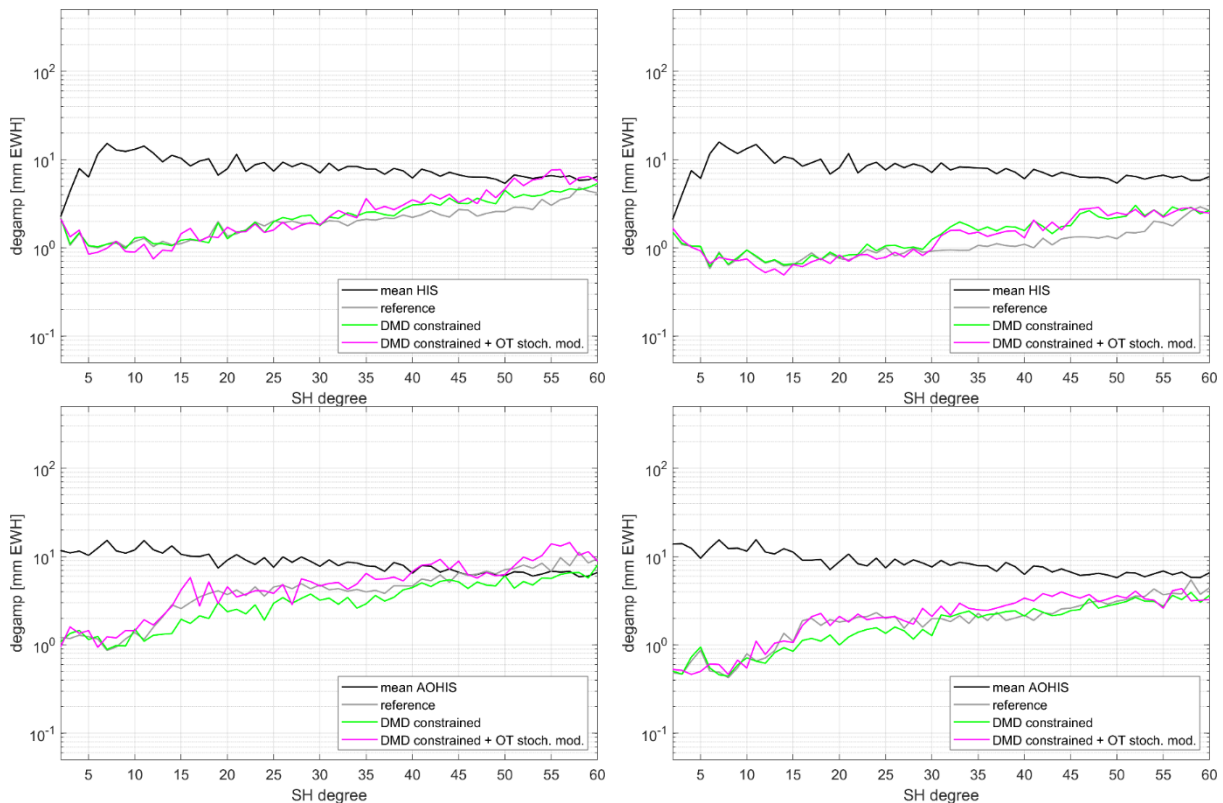
Figure 38-5: Gravity retrieval error of a double-pair based 7-day (left col.) and 30-day (right col.) solution with and without applying a combination of constrained DMD and stochastic modelling of OT BM errors. The non-tidal time-variable signal is assumed to be HIS incl. an a priori AO de-aliasing error constituting 10% of the full AO signal (top row) as well as the full AOHIS signal (bottom row).

In conclusion, it is evident that that the DMD and the OT error weighting are non-complementary processing strategies and therefore should be used separately. In case of the single-pair immense gains in retrieval performance can be asserted by applying a stand-alone DMD, while the benefit of the OT error weighting is negligible in comparison. On the other hand, the situation is reversed in case of the double-pair-based gravity retrieval. Here, overall very minor gains can be asserted with the stand-alone DMD, while improvements of up to 15%

can be established when applying stand-alone OT error weighting. It is therefore recommended to apply the stand-alone DMD for single-pair-based data processing, while the stand-alone OT error weighting is recommended for the double-pair case. However, it should be noted that the signals and retrieval in this study were limited to d/o 60 full OT error VCMs are only available to this d/o. The behaviour for higher degrees should be re-evaluated if higher-resolution error VCMs become available.

As a final aspect, we note that the impact of the OT error VCM is reduced in the single-pair scenario due to the fact that the retrieval error is assumed to be dominated by non-tidal aliasing. Should the AO de-aliasing performance increase (as is the case in the double-pair scenario) while the OT de-aliasing performance remains on a similar level, then it is well possible that the impact of the OT error VCM will also become more pronounced. In this case, the validity of the statements made above shall have to be re-evaluated. However, such a discrepancy in de-aliasing performance can be regarded as extremely unlikely, since improvements are continuously made in both tidal and non-tidal de-aliasing models.

38.2 ADD-ON: WIESE APPROACH WITH STOCHASTOC MODELLING OF OCEAN TIDE BACKGROUND MODEL ERRORS

In the following, we evaluate the added value of combining the classic Wiese parametrization with the OT error weighting in a double-pair-based retrieval scenario. The orbit parameters remain unchanged to subsection 38.1.

Fig. 38-6 shows the simulation results for a 30-day retrieval period. Here, the OT de-aliasing error is analogously to the previous section based on the difference between the models EOT11a and GOT4.7 (referred to as "sc1" in the following, left column) as well as TPX09 and DTU10 (referred to as "sc2" in the following, right column). To this signal we subsequently add the non-tidal HIS including an AO de-aliasing error (10% of full AO; center row) as well as the full AOHIS (bottom row). All scenarios are processed applying the nominal scheme (i.e., no stochastic modelling, to additional (co-)parametrization), the stochastic modelling of OT BM errors, the Wiese parametrization where daily fields up to d/o 15 are used as well as a combination of both.

It is evident that the Wiese parametrization does not yield any added value in case the temporal signal consists exclusively of the OT de-aliasing error, independently of the OT models used in the simulation. Here, the largest improvement stems from the stand-alone OT error weighting, while additionally applying the Wiese approach has next to no impact on the solution quality.

In case the full AOHIS signal is added to the simulation environment, an overall decrease in retrieval performance can be established for OT sc1 when OT error weighting is combined with the Wiese approach in comparison to stand-alone Wiese, while for OT sc2 some small-scale improvements can be asserted in the spectrum below d/o 15. In accord with the results presented in the previous chapter, the OT error weighting leads to a degradation in retrieval performance in comparison to the nominal processing. This holds for both OT sc1 and sc2.

If a priori AO de-aliasing is applied, the stand-alone Wiese processing once again shows no benefit in comparison to the nominal processing strategy. In case of the stand-alone OT error weighting the retrieval performance can be improved (as has already been shown). The magnitude of this improvement greatly depends on the "true" spatial error pattern (i.e., the
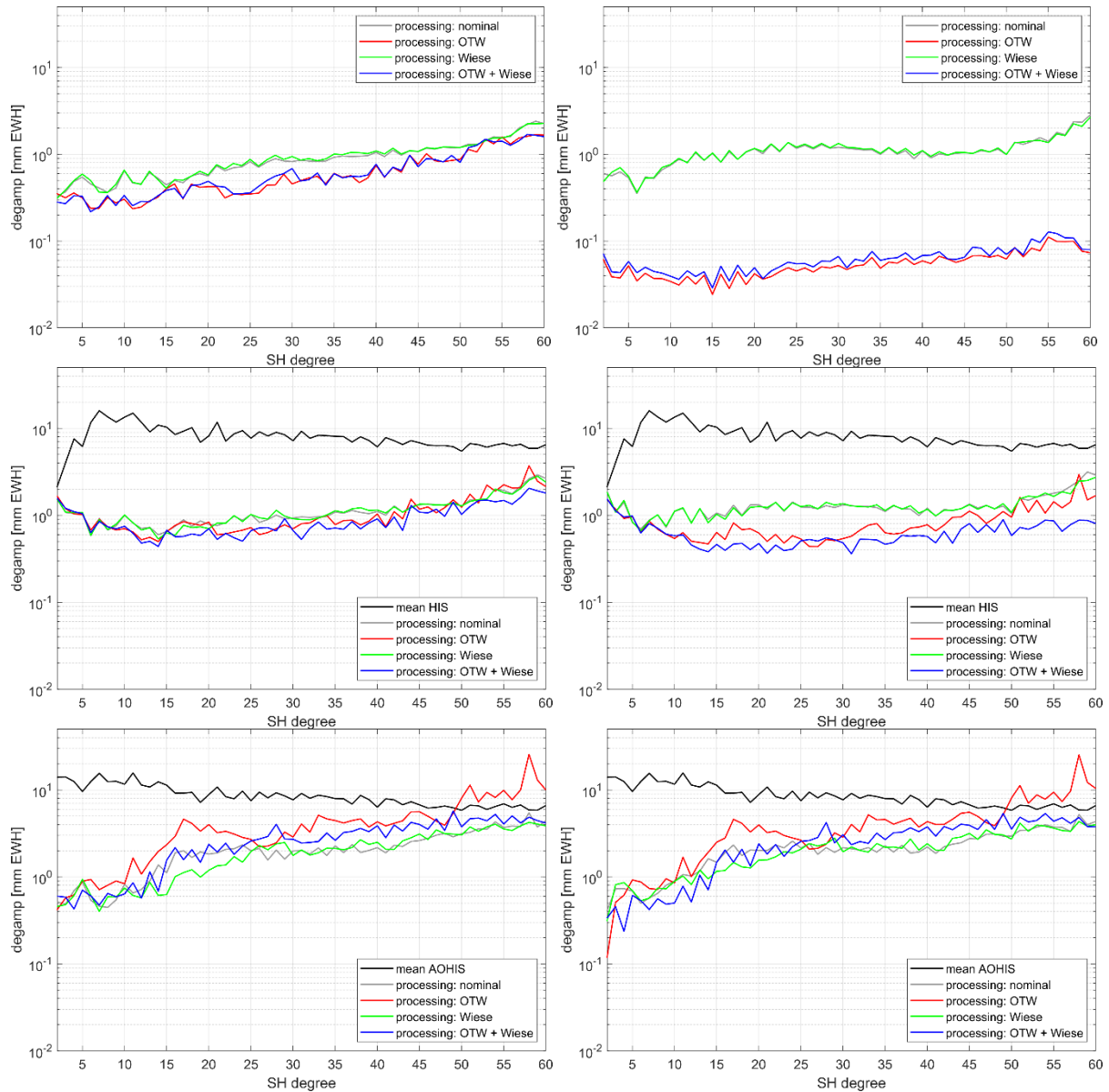
Figure 38-5: Gravity retrieval error of a double-pair based 30-day solution with and without applying a stand-alone Wiese approach, a stand-alone OT BM error weighting as well as a combination of both. The non-tidal time-variable signal is assumed to be HIS incl. an a priori AO de-aliasing error constituting 10% of the full AO signal (center row), the full AOHIS signal (bottom row) or not present at all (top row). The OT de-aliasing error is taken as the difference between the models EOT11a and GOT4.7 ("sc1", left column) as well as TPX09 and DTU10 ("sc2", right column).

discrepancies between the two OT models applied in the simulation) and the stochastically modelled one (i.e., the error pattern described by the underlying error VCMs). In this way, up to max. 15% improvement can be gained in certain spectral bands in case of sc1, while in case of sc2 this improvement may constitute up to 60%. It can further be established that in this simulation scenario a combination of the OT error weighting approach with Wiese seems to additionally enhance the retrieval performance. While in case of sc1 only minor additional improvements of a few per cent with respect to the nominal processing can be achieved in this way, in case of sc2 they can constitute up to 20% depending on the spectral bands.

In conclusion, it seems that combining OT error weighting with the Wiese approach may be beneficial for a double-pair based retrieval if a priori AO de-aliasing is applied. A definitive explanation of the observed improvements cannot be given at this point and would require further in-depth studies. For now, however, we assume that this behaviour originates from the fact that the amplitudes of the OT-related retrieval error are reduced through the OT error weighting to a point where the contribution of the AO de-aliasing error and the HIS component become dominant. These can then be further improved by means of the Wiese approach. This thesis is supported by the fact that the added value of combining the two methods is larger in case of sc1 than sc2, as in sc1 the OT-related errors cannot be reduced enough to fully make the non-tidal gravity signal the dominant error contributor.

39 APPLICABLE DOCUMENTS, REFERENCE DOCUMENTS, AND PUBLICATIONS TO PART 4

39.1 APPLICABLE DOCUMENTS

[AD-1] Mission Requirements Document, Next Generation Gravity Mission as a Mass-change And Geosciences International Constellation (MAGIC) - A joint ESA/NASA double-pair mission based on NASA's MCDO and ESA's NGGM studies (2020). ESA-EOPSM-FMCC-MRD-3785

[AD-2] Scientific Readiness Levels (SRL) Handbook, Issue 1, Revision 0, 05-08-2015

[AD-3] Statement of Work - ESA Express Procurement - EXPRO NGGM/MAGIC science support study during Phase A, Issue 1, Revision 0, 18/01/2021 Ref ESA-EOPSM-FUTM-SOW-3813

39.2 REFERENCE DOCUMENTS

[RD- 1] Wiese DN, Visser P, Nerem RS (2011): Estimating low resolution gravity fields at short time itnervals to reduce temporal aliasing errors. Advances in Space Research 48 (2011), 1094-1107, doi:10.1016/j.asr.2011.05.027

[RD- 2] Murböck M, Pail R, Daras I, Gruber T (2014) Optimal orbits for temporal gravity recovery regarding temporal aliasing. Journal of Geodesy, 88 (2), 113-126. https://doi.org/10.1007/s00190-013-0671-y

[RD- 3] Murböck M (2015) Virtual Constellations of Next Generation Gravity Missions. Deutsche Geodätische Kommission der Bayerischen Akademie der Wissenschaften, Reihe C, Dissertationen, Heft 750, Verlag der Bayerischen Akademie der Wissenschaften, ISBN(Print) 978-3-7696-5162-1, ISSN 0065-5325, 2016.

[RD- 4] Daras, I., Pail, R. (2017) Treatment of temporal aliasing effects in the context of next generation satellite gravimetry missions. J. Geophys. Res. Solid Earth 122 (9), 7343–7362. https://doi.org/10.1002/2017JB014250.

[RD- 5] Hauk M, Pail R (2018): Treatment of ocean tide aliasing in the context of a next generation gravity field mission. Geophysical Journal International 214, 345-365, doi: 10.1093/gji/ggy145

[RD- 6] Purkhauser, A., Pail, R. (2019) Next generation gravity missions: near-real time gravity field retrieval strategy. Geophys. J. Int., 17(2):1314–1333, https://doi.org/10.1093/gji/ggz084

[RD- 7] Abrykosov P, Sulzbach R, Pail R, Dobslaw H, Thomas M (2020): Treatment of ocean tide background model errors in the context of GRACE/GRACE-FO data processing. Geophysical Journal International 228 (2022). 1850-1865, https://doi.org/10.1093/gji/ggab421

[RD- 8] Horvath, A, Murböck M, Pail R & Horwath M (2018). Decorrelation of GRACE Time Variable Gravity Field Solutions using Full Covariance Information. *Geosciences* 2018, *8*(9), 323; https://doi.org/10.3390/geosciences8090323

[RD- 9] Kusche J (2007) Approximate decorrelation and non-isotropic smoothing of time-variable GRACE-type gravity field models. J. Geod, pp. 733-749. DOI https://doi.org/10.1007/s00190-007-0143-3

[RD- 10] Swenson, S. & Wahr, J. (2006) Post-processing removal of correlated errors in GRACE data. Geophys. Res. Lett. Vol. 33(8) DOI https://doi.org/10.1029/2005GL025285

[RD- 11] Wahr, J., Molenaar, M. & Bryan, F. (1998) Time variability of the Earth's gravity field: hydrological and oceanic effects and their possible detection using GRACE. J. Geophys. Res., pp. 30205-30230. Vol 103 (B12) https://doi.org/10.1029/98JB02844

PART 5:

ELABORATED ALTERNATIVE ORBIT SCENARIOS

40 INTRODUCTION

This Part 5 refers to Task 4 of the SoW and covers the work performed under WP 420 of the WBS. It refers to the deliverable document TN D9 "Elaborated alternative orbit scenarios".

In this TN we discuss a compilation of simulation scenarios related to accelerometer noise assumptions provided by TASI, executed by means of the EPOS software at GFZ. Originally, these scenarios were supposed to be simulated by means of the TUM full-scale simulator. Due to numerical accuracy issues at the full-scale simulator, the simulations were done by GFZ.

41 ALTERNATIVE ORBIT SCENARIOS (WP 420)

Table 41-1 lists the orbit parameters and instrument noise assumptions for scenarios to be simulated in the scope of evaluating ACC instrument noise assumptions provided by TASI.

Table 41-1: Orbit scenarios for TASI simulations.

Scenario		Alti-tude [km]	Inc. [deg]	Avg. sep. [km]	Drag. comp.	ACC noise	SST noise
SR-1	pol	488	89	220	No	SuperStar coarse	LRI
SR-2	pol	488	89	220	No	SuperStar fine	LRI
SR-4	pol	488	89	220	No	SuperStar fine	LRI
	inc	488	75	220	No	SuperStar fine	LRI
SR-5	pol	488	89	220	No	SuperStar fine	LRI
	inc	465	75	220	1 axis	SuperStar fine	LRI
S-1	pol	488	89	220	No	MicroStar fine	LRI
S-2	pol	488	89	220	1 axis	MicroStar fine	LRI
S-3	pol	488	89	220	No	SuperStar fine	LRI
	inc	465	75	220	1 axis	MicroStar fine	LRI
S-4	pol	488	89	220	No	MicroStar fine	LRI
	inc	465	75	220	1 axis	MicroStar fine	LRI
S-5	pol	488	89	220	1 axis	MicroStar fine	LRI
	inc	465	75	220	1 axis	MicroStar fine	LRI
S-6	pol	463	89	220	No	MicroStar fine	LRI
	inc	432	70	220	1 axis	MicroStar fine	LRI
S-7	pol	463	89	220	1 axis	MicroStar fine	LRI
	inc	432	70	220	1 axis	MicroStar fine	LRI
S-8	pol	487	89	220	No	MicroStar fine	LRI
	inc	343	71	220	3 axes	MicroStar fine	LRI

The ACC noise assumptions were provided by TASI in terms of product noise (ACC noise + non-conservative forces along the line-of-sight). Some of the time series are already reduced from drag effects (1 axis or 3 axes). The EPOS simulation environment requires ACC instrument noise for all three axes separately. Therefore, the provided time series have been re-scaled by a factor of $1/\sqrt{2}$ in order to account for the coupling when projecting onto the line-of-sight. The time series generated in this way were assumed to be valid for all three axes, i.e. all axes show the same noise level.

Figure 41-1 shows the ASD of the different ACC noise time series together with the noise assumption for the LRI. MicroStar related time series show a lower noise level compared to time series based on the SuperStar assumption. Even lower noise levels can be observed for MicroStar if the drag assumption has been compensated for specific axes.
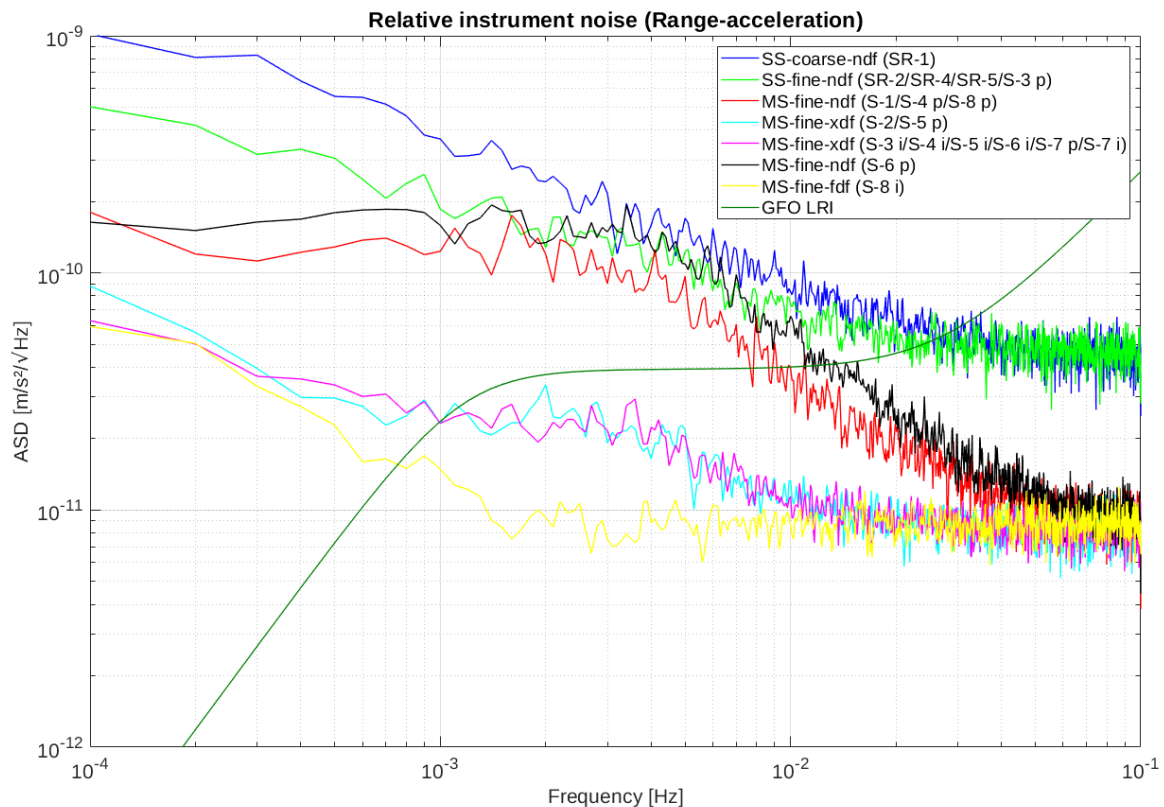
Figure 41-1: ASD in terms of accelerations of ACC noise time series for SuperStar (SS), MicroStar (MS) having a coarse or a fine pointing behaviour and are not drag compensated (ndf), drag compensated at one axis (xdf) or drag compensated at all axes (fdf). Scenarios related to a specific time series are indicated in the legend with p = polar and i = inclined in case of a double pair constellation.

Simulations were performed at a monthly time scale for the product noise case and the full noise case.
Scenarios SR-1, SR-5 and S-5 were simulated by TUM as well. Figure 41-2 displays the product noise solutions processed by TUM and GFZ for these three scenarios. SR-5 and S-5 show a lower noise level compared to SR-1 as they are double pair constellations. The slightly reduced noise level at SR-1 of the GFZ solution compared to TUM is somehow related to the limited numerical accuracy of the TUM full scale simulator. The S-5 GFZ solution shows a reduced error level due to a lower ACC noise assumption compared to SR-5. This is not visible at the

TUM related solutions and can be assumed as not realistic, therefore. This issue was the reason to repeat the TASI noise related simulations with the EPOS software and compare them with the results derived by TUM.

The double pair related full noise solutions shown in Figure 41-3 perform at a lower noise level compared to SR-1, as expected. Further, both double pair scenarios, SR-5 and S-5, perform similar despite the fact that S-5 includes a MicroStar ACC instead of a SuperStar ACC. The additional inclined pair compensates the benefit from an improved ACC by decorrelating the system due to the additional cross track observation component. At the full noise case, both simulation groups show consistent results.
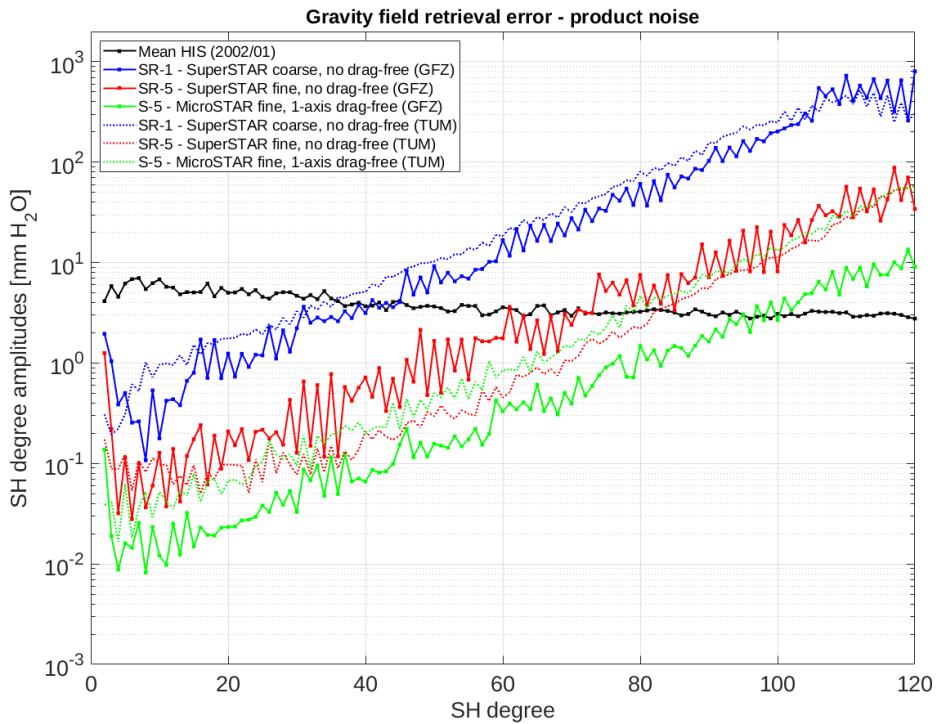
Figure 41-2: Degree error amplitudes im mm EWH for the product noise case of a 30-day retrieval for SR-1 (blue), SR-5 (red) and S-5 (green). GFZ related results are displayed in solid lines, TUM related results are displayed in dashed lines. The reference HIS signal is plotted in black.
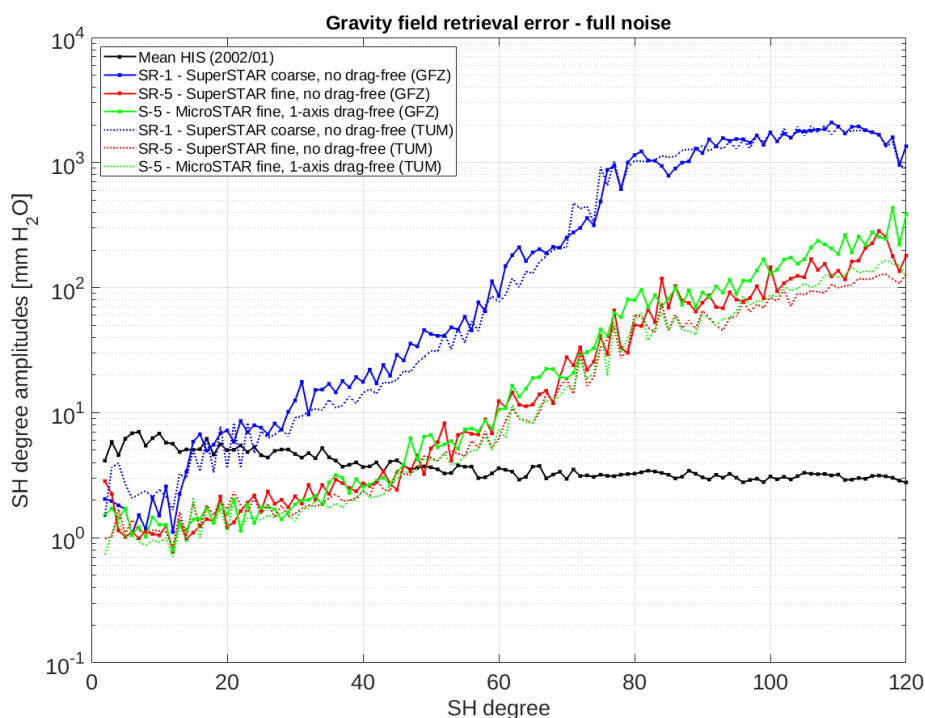
Figure 41-3: Degree error amplitudes im mm EWH for the full noise case of a 30-day retrieval for SR-1 (blue), SR-5 (red) and S-5 (green). GFZ related results are displayed in solid lines, TUM related results are displayed in dashed lines. The reference HIS signal is plotted in black.

Figure 41-4 displays the full list of scenarios simulated for the product noise case. The single pair scenario SR-2 shows an improved performance compared to SR-1 due to a lower ACC noise level. Further, the single pair S-1 scenario shows an improved behaviour due to the MicroStar noise assumption compared to SR-2, and S-2 shows an even further improved performance due to one drag compensated axis. The double pair scenarios SR-4 and SR-5 including the ACC SuperStar noise assumption perform similar. S-3, S-4 and S-5 perform similar as well flying all at the same altitude and do not show a dependency related to the ACC noise assumptions. S-6 shows a slightly lower error level at the high degree spectrum compared to the previous mentioned double pair scenarios due to lower flying satellites. Further, the performance of S-7 is slightly improved compared to S-6 due to a one axis drag compensation for both satellite pairs instead for only one pair at S-6. S-8 shows the best performance due to a very low flying inclined pair and drag free orbits for the inclined satellites.

The full noise results are displayed in Figure 41-5. All single pair scenarios show a similar performance independently from the ACC noise assumptions. Double pair scenarios SR-5, S-3, S-4 and S-5 perform relatively similar as well. SR-4 shows a slightly degraded performance between degree 20 and 50 due to the SuperStar ACC noise assumption for both pairs and shows a degraded performance at the very high degree spectrum due to the high-flying inclined pair compared to the other inclined pairs. Scenarios S-6 and S-7 show a reduced error behaviour compared to SR-5, S-3, S-4 and S-5 due to lower flying satellites. The lowest error signals can be seen for S-8 due to the low flying inclined pair and a drag free assumption. A quantitative assessment can be found in Table 41-2.
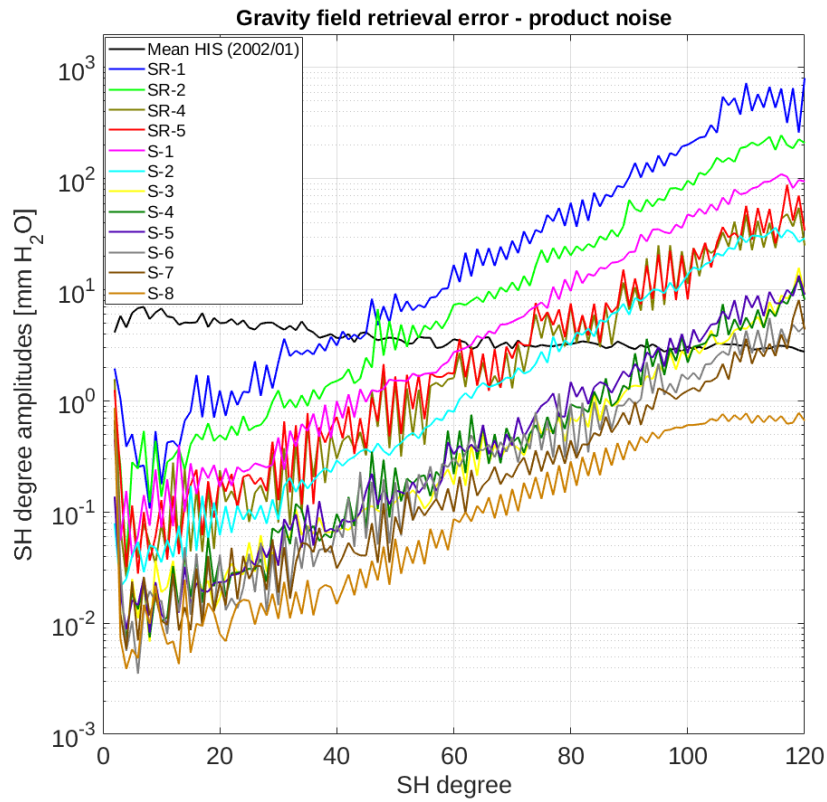
Figure 41-4: Degree error amplitudes im mm EWH for the product noise case of a 30-day retrieval for all scenarios listed in Table 3-1. The reference HIS signal is plotted in black.
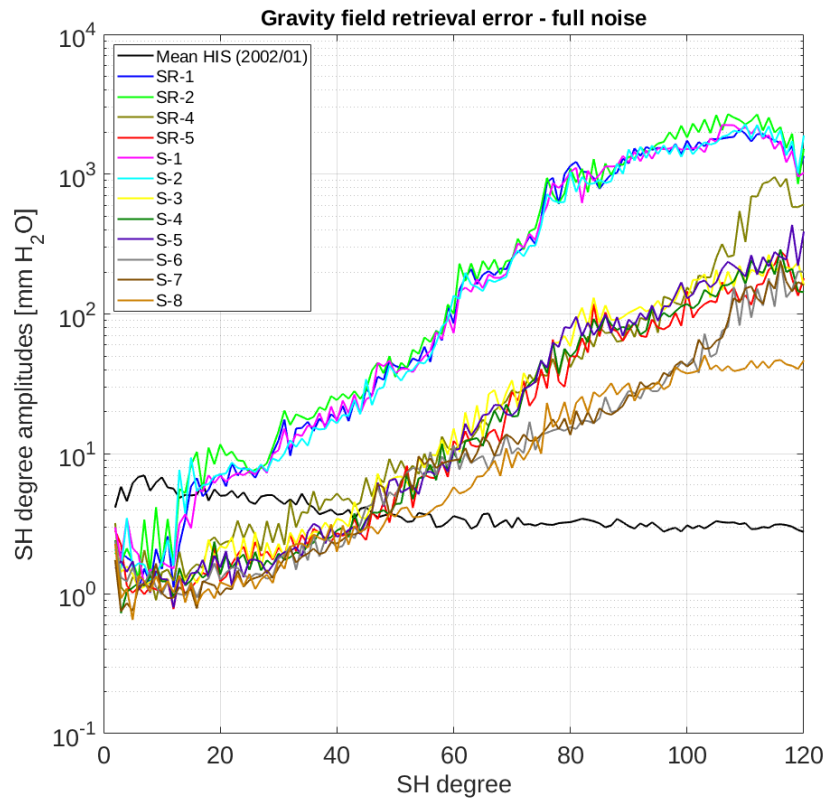
Figure 41-5: Degree error amplitudes im mm EWH for the full noise case of a 30-day retrieval for all scenarios listed in Table 41-1. The reference HIS signal is plotted in black.

Table 41-2: Cumulated errors for TASI simulations computed at d/o 120 for the product noise and the full noise case.

Scenario	Cumulative error @d/o 120 – product noise [mm EWH]	Cumulative error @d/o 120 – full noise [mm EWH]
SR-1	2.257	9.937
SR-2	854	11.963
SR-4	161	2.643
SR-5	197	849
S-1	380	10.061
S-2	126	10.088
S-3	31	1.024
S-4	30	928
S-5	35	1.186
S-6	17	613
S-7	15	613
S-8	4	241

42 APPLICABLE DOCUMENTS, REFERENCE DOCUMENTS, AND PUBLICATIONS TO PART 5

42.1 APPLICABLE DOCUMENTS

[AD-1] Mission Requirements Document, Next Generation Gravity Mission as a Mass-change And Geosciences International Constellation (MAGIC) - A joint ESA/NASA double-pair mission based on NASA's MCDO and ESA's NGGM studies (2020). ESA-EOPSM-FMCC-MRD-3785

[AD-2] Scientific Readiness Levels (SRL) Handbook, Issue 1, Revision 0, 05-08-2015

[AD-3] Statement of Work - ESA Express Procurement - EXPRO NGGM/MAGIC science support study during Phase A, Issue 1, Revision 0, 18/01/2021 Ref ESA-EOPSM-FUTM-SOW-3813

PART 6:

ANALYSIS OF RESULTS AND MATCH AGAINST REQUIREMENTS

43   INTRODUCTION

This Part 6 refers to Task 5 of the SoW and covers the work performed under

- WP 510: Match simulation results against requirements, and
- WP 520: Signal and noise content of co-estimated parameters

of the WBS. It refers to the deliverable document TN D13 "Analysis of results and match against requirements".

The purpose is to describe the detailed analysis of the simulation results and matching them against the science and mission requirements.

44   ANALYSIS OF RESULTS AND MATCH AGAINST REQUIREMENTS

44.1   MATCH SIMULATION RESULTS AGAINST REQUIREMENTS

In this section, we compare the retrieval errors of the 31-day full-scale gravity simulations presented in the document D2 to the user threshold and target requirements given by the IUGG. These requirements are given in terms of cumulative RMS errors, in cm EWH at four different spatial resolutions (SH degree 25, 50, 100 and 133), for a spatial resolution of one month.

Figure 44-1 shows the cumulative RMS error values for the 31-day instrument only coefficients. Additionally to the scenarios based on the 3d_H orbits (see D2, Table 3-1), we also show the results of some selected double pair scenarios based on the 5d_LL, 5d_LH, 5d_H and 7d_M orbits, for comparison. The comparison of the cumulative errors to the IUGG requirements shows that in order to meet the threshold requirements and come close to the target requirements, a double-pair mission is required. The errors of the single-pair scenarios are too high to meet the requirements; this also holds true for the single pendulum pair formations.

By comparing the performance of the double-pair scenarios among each other, we see that most of the double-pair configurations show a very similar performance. The factor having the largest impact on the performance of the double-pair scenarios is the orbit altitude: The scenarios using the 5d_H orbits (which have the highest satellite altitudes) perform worse compared to the corresponding 3d_H scenarios. The best performance is reached by the 7d_M and 5d_LL scenarios, in which the orbit altitude is lowest.

The relative behaviour of the individual scenarios is similar in the full noise results shown by Figure 44-2. As the retrieval errors are much higher there, only the double-pair scenarios even reach the threshold requirements.

However, we note that the IUGG requirements refer to post-processed (e.g. filtered) solutions, while we compare our raw simulation results to them. In order to obtain a more realistic assessment of the fulfilment of the requirements, one would have to filter the solutions, which would reduce the cumulative errors.

The Table 44-2 to Table 44-5 give the cumulative errors of the individual simulation results up to d/o 40, 80, 100 and 120. These values are extracted from the cumulative RMS curves as plotted in Figure 44-1 and Figure 44-2 as well as from similar curves for the respective 7-day solutions. Corresponding cumulative RMS values of the mean HIS signal are given by Table 44-1 for comparison.

Table 44-6 to Table 44-20 give the cumulative errors of additional simulation results, for reference. If not differently noted, the scenarios are based on 3d_H orbits.

The folder paths given in the table headings give the location of the simulation results in the sync&share folder "MAGIC", and contain the information about the software version the results have been computed with as well as the noise scaling convention that has been used for the set of simulations presented in the respective table.
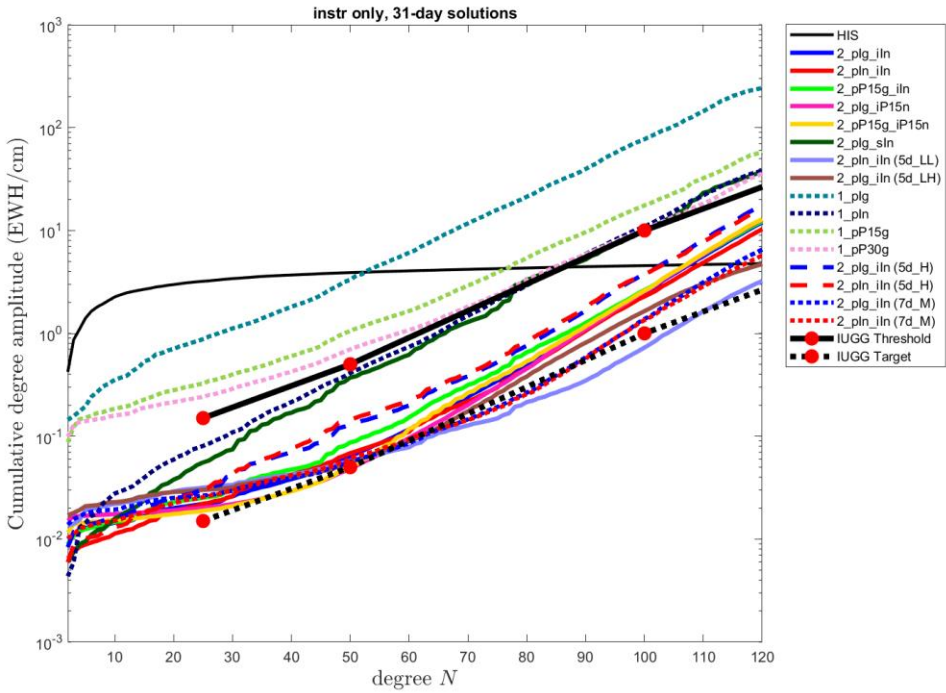
Figure 44-1 Cumulative RMS curves for the 31-day d/o 120 instrument only simulation results, compared to the IUGG threshold and target requirements. For each individual scenario, the mean curve of the cumulative RMS curves of two subsequent 31-day solutions is shown. [Path: Deliverables/D1/simulation_results/full_scale_simulator_v009/old_noise_scaling/instrument_only/]
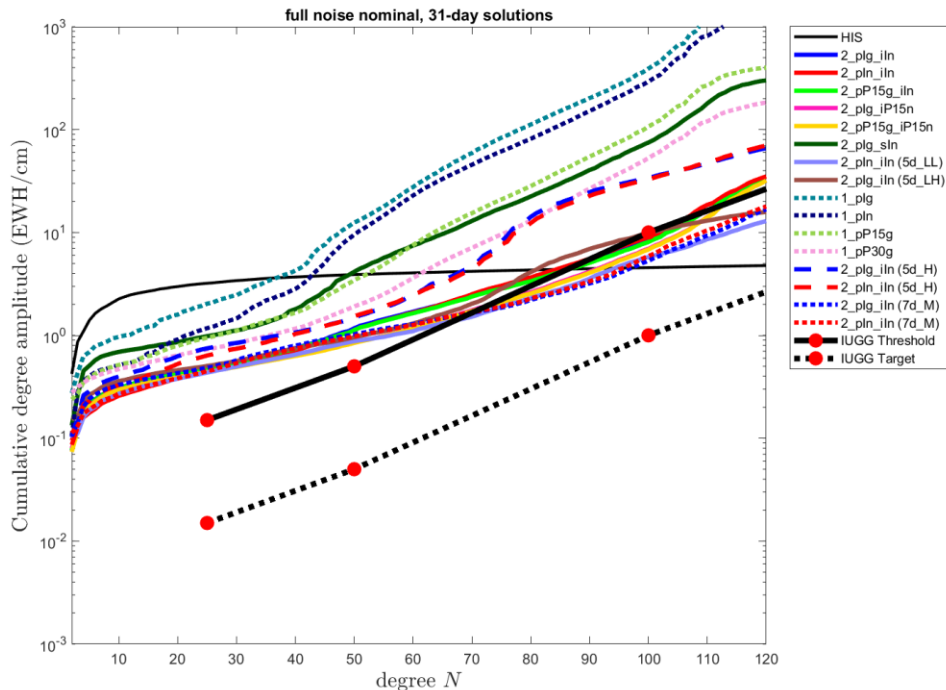
Figure 44-2 Cumulative RMS curves for the 31-day d/o 120 full noise nominal simulation results, compared to the IUGG threshold and target requirements. For each individual scenario, the mean curve of the cumulative RMS curves of two subsequent 31-day solutions is shown. [Path: Deliverables/D1/simulation_results/full_scale_simulator_v009/old_noise_scaling/full_noise_nominal/]

Table 44-1 Cumulative RMS signal values in units of cm EWH, for the 31-, 29-, 7-, 5- and 3-day mean HIS signal in the 2-month time period starting on 01.01.2002.

	d/o 20 (global)	d/o 40 (global)	d/o 60 (global)	d/o 80 (global)	d/o 100 (global)	d/o 120 (global)
HIS (31-day)	2,98	3,69	4,05	4,32	4,55	4,77
HIS (29-day)	2,92	3,63	3,99	4,26	4,5	4,71
HIS (7-day)	3,05	3,77	4,13	4,4	4,63	4,85
HIS (5-day)	3,08	3,8	4,16	4,43	4,66	4,88
HIS (3-day)	3,05	3,77	4,13	4,4	4,64	4,85

Table 44-2 Cumulative RMS errors in units of cm EWH, for the 31-day instrument only simulations. Both the single-pair and the double-pair solutions are resolved up to d/o 120. For each individual scenario, the error values read from the mean cumulative RMS curve of two subsequent solutions are given. [Path: Deliverables/D1/simulation_results/full_scale_simulator_v009/old_noise_scaling/instrument_only/]

	d/o 20 (global)	d/o 40 (global)	d/o 60 (global)	d/o 80 (global)	d/o 100 (global)	d/o 120 (global)
1_plg	0,71	1,82	6,08	21,32	77,00	242,96
1_pln	0,06	0,22	0,74	2,94	10,99	38,33
1_pP15g	0,28	0,60	1,65	5,40	17,52	57,77
1_pP30g	0,21	0,43	1,08	3,31	10,31	35,80

2_plg_iln	0,02	0,04	0,12	0,51	2,51	11,98
2_plg_iln (5d_LH)	0,03	0,04	0,09	0,38	1,64	4,72
2_plg_iln (5d_H)	0,03	0,07	0,20	0,76	3,75	17,77
2_plg_iln (7d_M)	0,03	0,04	0,09	0,27	1,38	6,53
2_pln_iln	0,02	0,04	0,11	0,46	2,28	10,32
2_pln_iln (5d_LL)	0,03	0,04	0,08	0,22	0,73	3,23
2_pln_iln (5d_H)	0,02	0,08	0,22	0,85	3,75	16,62
2_pln_iln (7d_M)	0,02	0,04	0,09	0,26	1,35	5,73
2_plg_sln	0,04	0,17	0,62	3,35	9,85	36,47
2_pP15g_iln	0,02	0,05	0,15	0,66	2,63	12,29
2_pP30g_iln	0,03	0,06	0,23	0,93	3,00	13,27
2_plg_iP15n	0,02	0,03	0,10	0,45	2,55	12,69
2_pP15g_iP15n	0,02	0,03	0,12	0,54	2,60	12,87
1_iln (5d_H) (sigma_polar = 0.1)	2,61	7,56	13,39	22,83	45,07	68,3
1_iln (7d_M) (sigma_polar = 0.1)	4,71	18,32	30,96	47,47	71,69	96,63
1_plg (5d_H)	0,55	1,99	7,68	30,2	108,43	287,45
1_plg (7d_M)	0,78	2,19	4,76	14,2	41,76	112,26
1_pln (5d_H)	0,06	0,25	0,99	4,08	15,82	56,12
1_pln (7d_M)	0,06	0,17	0,49	1,73	6,1	18,21
2_plg_ilg	0,18	0,22	0,33	0,94	3,26	13,29
2_plg_iln (5d_Ma)	0,02	0,03	0,12	0,46	1,99	8,16
2_plg_iln (5d_Mb)	0,03	0,04	0,08	0,28	1,5	7,1
2_pln_iln (ISD = 150 km)	0,02	0,04	0,13	0,49	2,57	11,85
2_pln_iln (ISD = 180 km)	0,01	0,04	0,11	0,44	2,42	11,25
2_pln_iln (ISD = 220 km)	0,01	0,03	0,09	0,41	2,26	10,41
2_sln_iln	0,14	1,5	7,28	19,7	31,68	36,12

Table 44-3 Cumulative RMS errors in units of cm EWH, for the 7-day instrument only simulations. The single-pair solutions are resolved up to d/o 100, the double-pair solutions up to d/o 120. For each individual scenario, the error values read from the mean cumulative RMS curve of nine subsequent solutions are given. [Path: Deliverables/D1/simulation_results/full_scale_simulator_v009/old_noise_scaling/instrument_only/]

	d/o 20 (global)	d/o 40 (global)	d/o 60 (global)	d/o 80 (global)	d/o 100 (global)	d/o 120 (global)
1_plg	1,49	5,72	18,23	99,10	228,04	-
1_pln	0,15	0,80	2,67	14,52	37,86	-
1_pP15g	0,41	1,35	6,13	19,53	39,19	-
1_pP30g	0,39	0,76	2,48	8,78	21,34	-
2_plg_iln	0,03	0,07	0,25	1,05	4,94	24,70
2_plg_iln (5d_LH)	0,03	0,07	0,25	0,97	3,49	11,12
2_plg_iln (5d_H)	0,04	0,15	0,51	2,63	13,11	54,31
2_plg_iln (7d_M)	0,03	0,07	0,17	0,57	2,58	12,13
2_pln_iln	0,03	0,07	0,21	0,83	3,95	18,66
2_pln_iln (5d_LL)	0,03	0,05	0,12	0,34	1,20	4,94
2_pln_iln (5d_H)	0,04	0,12	0,39	1,72	8,12	37,92
2_pln_iln (7d_M)	0,03	0,06	0,15	0,47	2,11	9,06
2_plg_sln	0,07	0,28	1,09	5,52	23,48	102,12
2_pP15g_iln	0,04	0,09	0,31	1,29	5,28	26,89
2_pP30g_iln	0,04	0,10	0,38	1,50	5,56	28,59
2_plg_iP15n	0,05	0,07	0,19	0,82	4,00	19,80
2_pP15g_iP15n	0,07	0,09	0,25	1,03	4,23	20,32
1_iln (5d_H) (sigma_polar = 0.1)	1,73	4,9	9,91	20,34	33,42	-
1_iln (7d_M) (sigma_polar = 0.1)	3,78	10,09	18,28	35,53	50,21	-
1_plg (5d_H)	2,26	7,4	33,19	207,49	598,1	-
1_plg (7d_M)	0,9	2,39	6,5	20,8	55,31	-
1_pln (5d_H)	0,31	0,98	4,72	38,75	123,91	-
1_pln (7d_M)	0,09	0,31	1	3,45	10,07	-
2_plg_ilg	0,32	0,39	0,66	1,93	6,82	27,86
2_pln_iln (ISD = 150 km)	0,03	0,08	0,27	0,99	4,55	20,93
2_pln_iln (ISD = 180 km)	0,03	0,07	0,23	0,88	4,18	19,95
2_pln_iln (ISD = 220 km)	0,02	0,06	0,19	0,8	3,91	18,74

Table 44-4 Cumulative RMS errors in units of cm EWH, for the 31-day full noise nominal simulations. Both the single-pair and the double-pair solutions are resolved up to d/o 120. For each individual scenario, the error values read from the mean cumulative RMS curve of two subsequent solutions are given. [Path: Deliverables/D1/simulation_results/full_scale_simulator_v009/old_noise_scaling/full_noise_nominal/]

	d/o 20 (global)	d/o 40 (global)	d/o 60 (global)	d/o 80 (global)	d/o 100 (global)	d/o 120 (global)
1_plg	1,59	4,26	27,66	112,16	392,75	1569,99
1_pln	0,91	2,83	22,91	81,51	293,44	1199,90
1_pP15g	0,79	1,66	7,56	28,25	106,90	400,90
1_pP30g	0,64	1,16	3,62	13,01	53,04	183,60
2_plg_iln	0,42	0,75	1,69	3,46	8,22	31,74
2_plg_iln (5d_LH)	0,46	0,75	1,30	4,12	9,84	15,82
2_plg_iln (5d_H)	0,63	1,07	2,43	14,21	33,98	65,94
2_plg_iln (7d_M)	0,43	0,79	1,29	2,21	5,30	16,72
2_pln_iln	0,38	0,72	1,66	3,65	9,00	35,04
2_pln_iln (5d_LL)	0,38	0,65	1,10	2,30	5,77	12,92
2_pln_iln (5d_H)	0,53	1,03	2,51	12,35	32,76	69,92
2_pln_iln (7d_M)	0,38	0,74	1,26	2,29	5,90	17,92
2_plg_sln	0,86	1,80	7,48	22,41	75,03	300,69
2_pP15g_iln	0,42	0,74	1,64	3,35	8,09	31,92
2_pP30g_iln	0,41	0,72	1,57	3,27	8,03	33,07
2_plg_iP15n	0,39	0,63	1,18	2,62	6,95	32,06
2_pP15g_iP15n	0,39	0,63	1,17	2,55	6,83	31,98
1_iln (5d_H) (sigma_polar = 0.1)	1,74	5,77	11,36	21,43	39,96	71,27
1_iln (7d_M) (sigma_polar = 0.1)	5,04	14,9	23,25	31,21	39,43	48,47
1_plg (5d_H)	1,78	4,92	20,6	221,45	631,49	1000,22
1_plg (7d_M)	1,53	4,89	15,36	51,72	156,59	438,03
1_pln (5d_H)	1,11	3,28	15,29	149,42	474,86	839,23
1_pln (7d_M)	0,88	2,94	10,35	35,71	113,05	361,39
2_plg_ilg	0,46	0,77	1,68	3,46	8,17	29,2
2_plg_iln (5d_Ma)	0,37	0,6	1,11	2,56	8,11	15,69
2_plg_iln (5d_Mb)	0,42	0,7	1,27	3,44	9,1	17,96
2_pln_iln (ISD = 150 km)	0,36	0,7	1,63	3,36	7,76	27,79
2_pln_iln (ISD = 180 km)	0,37	0,7	1,63	3,36	7,78	28,07
2_pln_iln (ISD = 220 km)	0,36	0,69	1,63	3,41	7,9	28,92
2_sln_iln	10,06	83,35	300,32	607,72	774,49	791,4

Table 44-5 Cumulative RMS errors in units of cm EWH, for the 7-day full noise nominal simulations. The single-pair solutions are resolved up to d/o 100, the double-pair solutions up to d/o 120. For each individual scenario, the error values read from the mean cumulative RMS curve of nine subsequent solutions are given. [Path: Deliverables/D1/simulation_results/full_scale_simulator_v009/old_noise_scaling/full_noise_nominal/]

	d/o 20 (global)	d/o 40 (global)	d/o 60 (global)	d/o 80 (global)	d/o 100 (global)	d/o 120 (global)
1_plg	4,02	14,05	77,19	353,99	675,24	-
1_pln	2,77	12,42	61,25	302,58	593,87	-
1_pP15g	1,34	4,05	19,88	69,34	152,44	-
1_pP30g	1,00	2,47	9,81	38,14	91,83	-
2_plg_iln	0,85	1,43	3,28	8,18	19,65	69,64
2_plg_iln (5d_LH)	0,86	1,50	2,91	7,90	24,60	66,70
2_plg_iln (5d_H)	1,17	2,18	5,60	21,81	85,83	266,89
2_plg_iln (7d_M)	0,82	1,47	2,60	5,06	12,94	39,50
2_pln_iln	0,76	1,35	3,27	8,45	20,38	66,88
2_pln_iln (5d_LL)	0,74	1,25	2,16	4,47	11,04	26,98
2_pln_iln (5d_H)	1,02	1,95	4,97	20,11	68,13	198,61
2_pln_iln (7d_M)	0,74	1,37	2,50	5,01	12,67	37,54
2_plg_sln	1,42	3,79	17,47	55,18	177,26	569,38
2_pP15g_iln	0,84	1,42	3,21	7,94	19,26	71,60
2_pP30g_iln	0,83	1,38	3,07	7,56	18,70	70,90
2_plg_iP15n	0,77	1,16	2,18	5,76	14,44	55,55
2_pP15g_iP15n	0,77	1,16	2,14	5,55	14,07	55,72
1_iln (5d_H) (sigma_polar = 0.1)	1,39	3,15	7,66	42,08	148,63	-
1_iln (7d_M) (sigma_polar = 0.1)	2,04	4,67	8,02	13,22	21,29	-
1_plg (5d_H)	8,11	22,29	96,48	556,64	1706,45	-
1_plg (7d_M)	2,82	12,14	34,69	120,55	290,79	-
1_pln (5d_H)	5,71	17,56	79,99	519,43	1645,91	-
1_pln (7d_M)	1,6	7,35	24,53	92,56	230,35	-
2_plg_ilg	0,87	1,47	3,32	8,24	19,62	64,21
2_pln_iln (ISD = 150 km)	0,76	1,35	3,2	7,96	18,36	57,9
2_pln_iln (ISD = 180 km)	0,76	1,35	3,21	7,99	18,58	58,61
2_pln_iln (ISD = 220 km)	0,76	1,35	3,23	8,13	18,99	60,63

NGGM/MAGIC – Science Support Study During Phase A	*Final Report*	
	Doc. Nr:	MAGIC_FR
	Issue:	1.0
	Date:	15.11.2022
	Page:	351 of 466

Table 44-6 Cumulative RMS errors in units of cm EWH, for 5-day instrument only simulations. The solutions for the first two scenarios are resolved up to d/o 100, the remaining solutions up to d/o 120. For each individual scenario, the error values read from the mean cumulative RMS curve of 13 subsequent solutions are given. [Path: Deliverables/D1/simulation_results/full_scale_simulator_v009/old_noise_scaling/instrument_only/]

	d/o 20 (global)	d/o 40 (global)	d/o 60 (global)	d/o 80 (global)	d/o 100 (global)	d/o 120 (global)
2_plg_iln (5d_Ma)	0,03	0,08	0,31	1,1	4,01	-
2_plg_iln (5d_Mb)	0,03	0,08	0,24	1,15	4,91	-
2_pln_iln (5d_LL) (ISD = 150 km)	0,03	0,07	0,18	0,54	1,95	7,5
2_pln_iln (5d_LL) (ISD = 180 km)	0,03	0,06	0,16	0,49	1,82	7,18
2_pln_iln (5d_LL) (ISD = 220 km)	0,02	0,05	0,14	0,45	1,72	6,84

Table 44-7 Cumulative RMS errors in units of cm EWH, for 5-day full noise nominal simulations. The solutions for the first two scenarios are resolved up to d/o 100, the remaining solutions up to d/o 120. For each individual scenario, the error values read from the mean cumulative RMS curve of 13 subsequent solutions are given. [Path: Deliverables/D1/simulation_results/full_scale_simulator_v009/old_noise_scaling/full_noise_nominal/]

	d/o 20 (global)	d/o 40 (global)	d/o 60 (global)	d/o 80 (global)	d/o 100 (global)	d/o 120 (global)
2_plg_iln (5d_Ma)	0,88	1,48	2,97	6,82	16,07	-
2_plg_iln (5d_Mb)	0,95	1,59	3,02	7,52	21,33	-
2_pln_iln (5d_LL) (ISD = 150 km)	0,86	1,49	2,63	5,58	13,7	32,57
2_pln_iln (5d_LL) (ISD = 180 km)	0,86	1,49	2,64	5,61	13,83	32,95
2_pln_iln (5d_LL) (ISD = 220 km)	0,86	1,49	2,65	5,67	14,09	33,86

Table 44-8 Cumulative RMS errors in units of cm EWH, for 29-day instrument only simulations. The solutions are resolved up to d/o 120. For each individual scenario, the error values read from the mean cumulative RMS curve of two subsequent solutions are given. [Path: Deliverables/D1/simulation_results/full_scale_simulator_v009/old_noise_scaling/instrument_only/]

	d/o 20 (global)	d/o 40 (global)	d/o 60 (global)	d/o 80 (global)	d/o 100 (global)	d/o 120 (global)
2_pln_iln (5d_LL) (ISD = 150 km)	0,01	0,03	0,06	0,17	0,75	3,57
2_pln_iln (5d_LL) (ISD = 180 km)	0,01	0,02	0,06	0,15	0,72	3,46
2_pln_iln (5d_LL) (ISD = 220 km)	0,01	0,02	0,05	0,14	0,67	3,24

Table 44-9 Cumulative RMS errors in units of cm EWH, for 29-day full noise nominal simulations. The solutions are resolved up to d/o 120. For each individual scenario, the error values read from the mean cumulative RMS curve of two subsequent solutions are given. [Path: Deliverables/D1/simulation_results/full_scale_simulator_v009/old_noise_scaling/full_noise_nominal/]

	d/o 20 (global)	d/o 40 (global)	d/o 60 (global)	d/o 80 (global)	d/o 100 (global)	d/o 120 (global)
2_pln_iln (5d_LL) (ISD = 150 km)	0,36	0,65	1,04	2,19	5,3	11,36
2_pln_iln (5d_LL) (ISD = 180 km)	0,36	0,65	1,04	2,21	5,34	11,5
2_pln_iln (5d_LL) (ISD = 220 km)	0,36	0,65	1,04	2,23	5,44	11,77

Table 44-10 Cumulative RMS errors in units of cm EWH, for 31-day instrument only simulations. Both the single-pair and the double-pair solutions are resolved up to d/o 120. For each individual scenario, the error values read from the cumulative RMS curve of one single solution is given. [Path: Deliverables/D1/simulation_results/full_scale_simulator_v009/1_by_sqrt(10)_noise_scaling/instrument_only/]

	d/o 20 (global)	d/o 40 (global)	d/o 60 (global)	d/o 80 (global)	d/o 100 (global)	d/o 120 (global)
1_plg	0,24	0,65	2,04	7,28	27,88	90,5
2_plg_ilg	0,06	0,08	0,13	0,46	2,32	10,65
2_plg_iln	0,02	0,03	0,1	0,42	2,39	11,65
SR1	0,47	1,59	5,48	20,42	78,65	184,06
SR5	0,04	0,07	0,16	0,66	3,22	15,88
S5	0,02	0,07	0,25	0,99	3,92	16,69

Table 44-11 Cumulative RMS errors in units of cm EWH, for 31-day full noise nominal simulations. Both the single-pair and the double-pair solutions are resolved up to d/o 120. For each individual scenario, the error values read from the cumulative RMS curve of one single solution is given. [Path: Deliverables/D1/simulation_results/full_scale_simulator_v009/1_by_sqrt(10)_noise_scaling/full_noise_nominal/]

	d/o 20 (global)	d/o 40 (global)	d/o 60 (global)	d/o 80 (global)	d/o 100 (global)	d/o 120 (global)
1_plg	1,21	3,86	26,72	98,52	374	1722,55
2_plg_ilg	0,44	0,74	1,59	3,46	8,24	28,19
2_plg_iln	0,45	0,75	1,64	3,51	8,29	31,27
SR1	1,58	4,57	19,25	236,56	628,9	974,81
SR5	0,6	1,03	2,24	11,89	29,35	55,17
S5	0,52	0,93	2,12	11,93	29,85	63,63

Table 44-12 Cumulative RMS errors in units of cm EWH, for 7-day d/o 120 instrument only simulations. For each individual scenario, the error values read from the cumulative RMS curve of one single solution is given. [Path: Deliverables/D1/simulation_results/full_scale_simulator_v009/1_by_sqrt(10)_noise_scaling/instrument_only/]

	d/o 20 (global)	d/o 40 (global)	d/o 60 (global)	d/o 80 (global)	d/o 100 (global)	d/o 120 (global)
U5d5d_HL_ms	0,02	0,06	0,25	1,2	5,28	19,22
U5d5d_HL_ref	0,02	0,06	0,25	1,2	5,27	19,24

Table 44-13 Cumulative RMS errors in units of cm EWH, for 7-day d/o 120 full noise nominal simulations. For each individual scenario, the error values read from the cumulative RMS curve of one single solution is given. [Path: Deliverables/D1/simulation_results/full_scale_simulator_v009/1_by_sqrt(10)_noise_scaling/full_noise_nominal/]

	d/o 20 (global)	d/o 40 (global)	d/o 60 (global)	d/o 80 (global)	d/o 100 (global)	d/o 120 (global)
U5d5d_HL_ms	0,77	1,4	4,81	13,69	33,89	67,65
U5d5d_HL_ref	0,77	1,4	4,81	13,7	33,89	67,64

Table 44-14 Cumulative RMS errors in units of cm EWH, for 7-day d/o 120 instrument only simulations. For each individual scenario, the error values read from the cumulative RMS curve of one single solution is given. [Path: Deliverables/D1/simulation_results/full_scale_simulator_v010/1_by_sqrt(10)_noise_scaling/instrument_only/]

	d/o 20 (global)	d/o 40 (global)	d/o 60 (global)	d/o 80 (global)	d/o 100 (global)	d/o 120 (global)
U5d5d_HL_ms	0	0,02	0,08	0,34	1,43	3,15
U5d5d_HL_ref	0	0,02	0,08	0,34	1,4	3,01

Table 44-15 Cumulative RMS errors in units of cm EWH, for 5-day d/o 70 instrument only simulations. For each individual scenario, the error values read from the mean cumulative RMS curve of three subsequent solutions are given. [Path: Deliverables/D1/simulation_results/full_scale_simulator_v009/1_by_sqrt(10)_noise_scaling/instrument_only/]

	d/o 20 (global)	d/o 40 (global)	d/o 60 (global)	d/o 80 (global)	d/o 100 (global)	d/o 120 (global)
3d_H	0,03	0,07	0,23	-	-	-
U3d_H	0,03	0,06	0,17	-	-	-
U3d5d_H	0,03	0,07	0,24	-	-	-
U5d_H	0,03	0,08	0,26	-	-	-

Table 44-16 Cumulative RMS errors in units of cm EWH, for 5-day d/o 70 full noise nominal simulations. For each individual scenario, the error values read from the mean cumulative RMS curve of three subsequent solutions are given. [Path: Deliverables/D1/simulation_results/full_scale_simulator_v009/1_by_sqrt(10)_noise_scaling/full_noise_nominal/]

	d/o 20 (global)	d/o 40 (global)	d/o 60 (global)	d/o 80 (global)	d/o 100 (global)	d/o 120 (global)
3d_H	0,99	1,75	3,97	-	-	-
U3d_H	0,9	1,53	3,01	-	-	-
U3d5d_H	0,99	1,77	4,04	-	-	-
U5d_H	1,06	1,87	3,46	-	-	-

Table 44-17 Cumulative RMS errors in units of cm EWH, for 3-day d/o 70 instrument only simulations. For each individual scenario, the error values read from the mean cumulative RMS curve of five subsequent solutions are given. [Path: Deliverables/D1/simulation_results/full_scale_simulator_v009/1_by_sqrt(10)_noise_scaling/instrument_only/]

	d/o 20 (global)	d/o 40 (global)	d/o 60 (global)	d/o 80 (global)	d/o 100 (global)	d/o 120 (global)
3d_H	0,04	0,12	0,46	-	-	-
U3d_H	0,03	0,08	0,29	-	-	-
U3d5d_H	0,04	0,17	0,7	-	-	-
U5d_H	0,18	1,07	2,55	-	-	-

Table 44-18 Cumulative RMS errors in units of cm EWH, for 3-day d/o 70 full noise nominal simulations. For each individual scenario, the error values read from the mean cumulative RMS curve of five subsequent solutions are given. [Path: Deliverables/D1/simulation_results/full_scale_simulator_v009/1_by_sqrt(10)_noise_scaling/full_noise_nominal/]

	d/o 20 (global)	d/o 40 (global)	d/o 60 (global)	d/o 80 (global)	d/o 100 (global)	d/o 120 (global)
3d_H	1,23	2,19	5,21	-	-	-
U3d_H	1,15	2,02	3,78	-	-	-
U3d5d_H	1,25	2,44	6,8	-	-	-
U5d_H	1,89	8,52	20,81	-	-	-

Table 44-19 Cumulative RMS errors in units of cm EWH, for 7-day full noise nominal simulations. The single-pair solution is resolved up to d/o 100, the double-pair solutions up to d/o 120. For each individual scenario, the error values read from the mean cumulative RMS curve of nine subsequent solutions are given. The top part of the table gives the results based on the unfiltered solutions, and the bottom part the results based on the VADER-filtered solutions, using a regularization parameter value of alpha = 100 that has been found to be optimal for the filtering. [Path: Deliverables/D1/simulation_results/full_scale_simulator_v009/old_noise_scaling/full_noise_nominal_1year_solutions/]

	d/o 20 (global)	d/o 40 (global)	d/o 60 (global)	d/o 80 (global)	d/o 100 (global)	d/o 120 (global)
Errors of unfiltered solutions:						
1_plg	4,02	14,05	77,19	353,99	675,24	-
2_pln_iln	0,76	1,35	3,27	8,45	20,38	66,88
2_pln_iln (5d_Ma)	0,7	1,16	2,56	6,79	22,81	44,75
2_pln_iln (5d_Mb)	0,73	1,26	2,33	5,92	17,65	56,4
Errors of VADER-filtered solutions (alpha = 100):						
1_plg	1,46	2,08	2,49	2,89	3,23	-
2_pln_iln	0,72	1,1	1,48	1,88	2,32	2,71
2_pln_iln (5d_Ma)	0,69	0,99	1,31	1,71	2,16	2,58
2_pln_iln (5d_Mb)	0,72	1,1	1,48	1,89	2,3	2,69

44.2 CUMULATIVE ERROR PLOTS FOR SUB-MONTHLY RETRIEVAL PERIODS

In this section, we visualize the cumulative errors of simulations using sub-monthly retrieval periods. In order to scale the monthly IUGG threshold and target requirements to the shorter retrieval periods, we multiply them by sqrt(31/retrvp), where retrvp is the considered retrieval period in days. Figure 44-3 is based on the same simulation results as Table 44-3 and Table 44-5. Figure 44-4 is based on the same results as Table 44-19 and Figure 44-5 on the same results as Table 44-15 to Table 44-18.
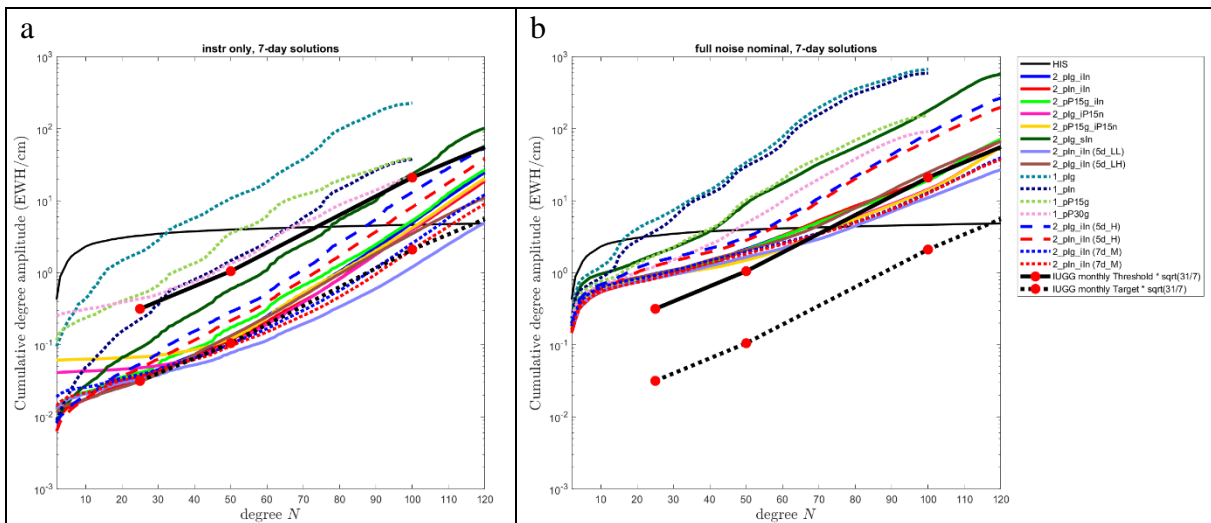
Figure 44-3 Cumulative RMS curves for the 7-day d/o 100 (120) single-(double-)pair simulation results (panel a: instrument only, panel b: full noise nominal), compared to the IUGG threshold and target requirements that have been up-scaled from monthly to weekly requirements. For each individual scenario, the mean curve of the cumulative RMS curves of nine subsequent 7-day solutions is shown. [Path: Deliverables/D1/simulation_results/full_scale_simulator_v009/old_noise_scaling/]
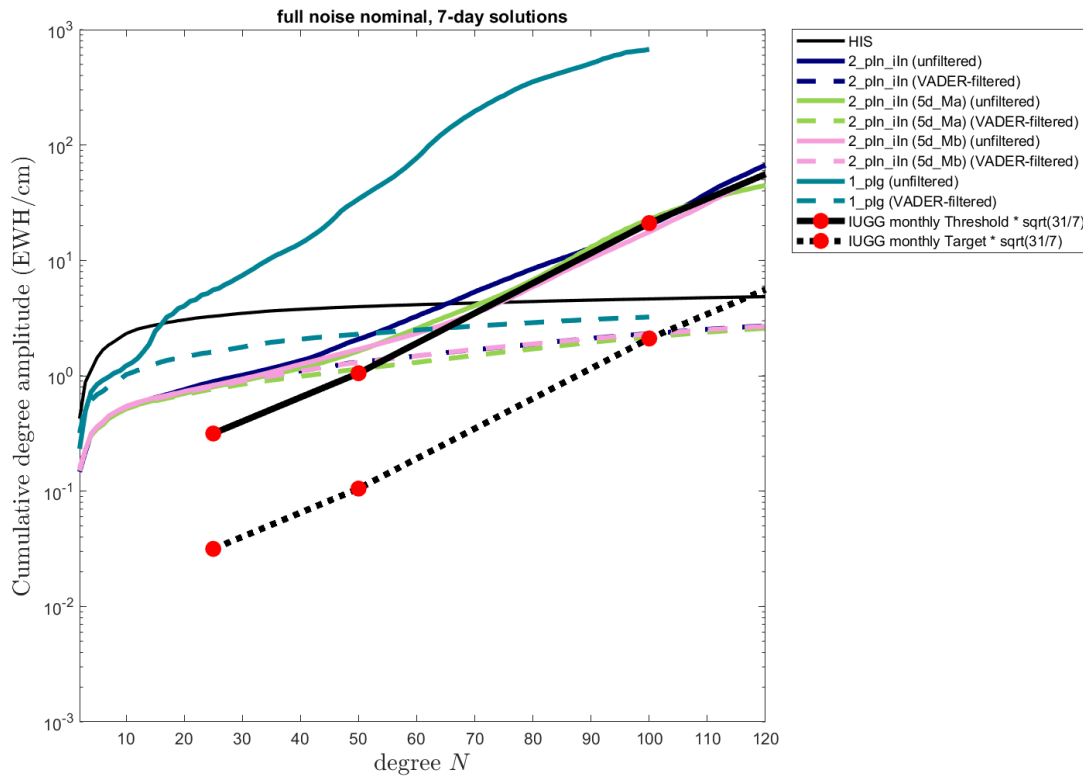
Figure 44-4 Cumulative RMS curves for the 7-day d/o 100 (120) single-(double-)pair full noise nominal simulation results (solid curves: retrieval errors of unfiltered solutions, dashed curves: retrieval errors of filtered solutions), compared to the IUGG threshold and target requirements that have been up-scaled from monthly to weekly requirements. For each individual scenario, the mean curve of the cumulative RMS curves of nine subsequent 7-day solutions is shown. [Path: Deliverables/D1/simulation_results/full_scale_simulator_v009/old_noise_scaling/full_noi se_nominal_1year_solutions/]
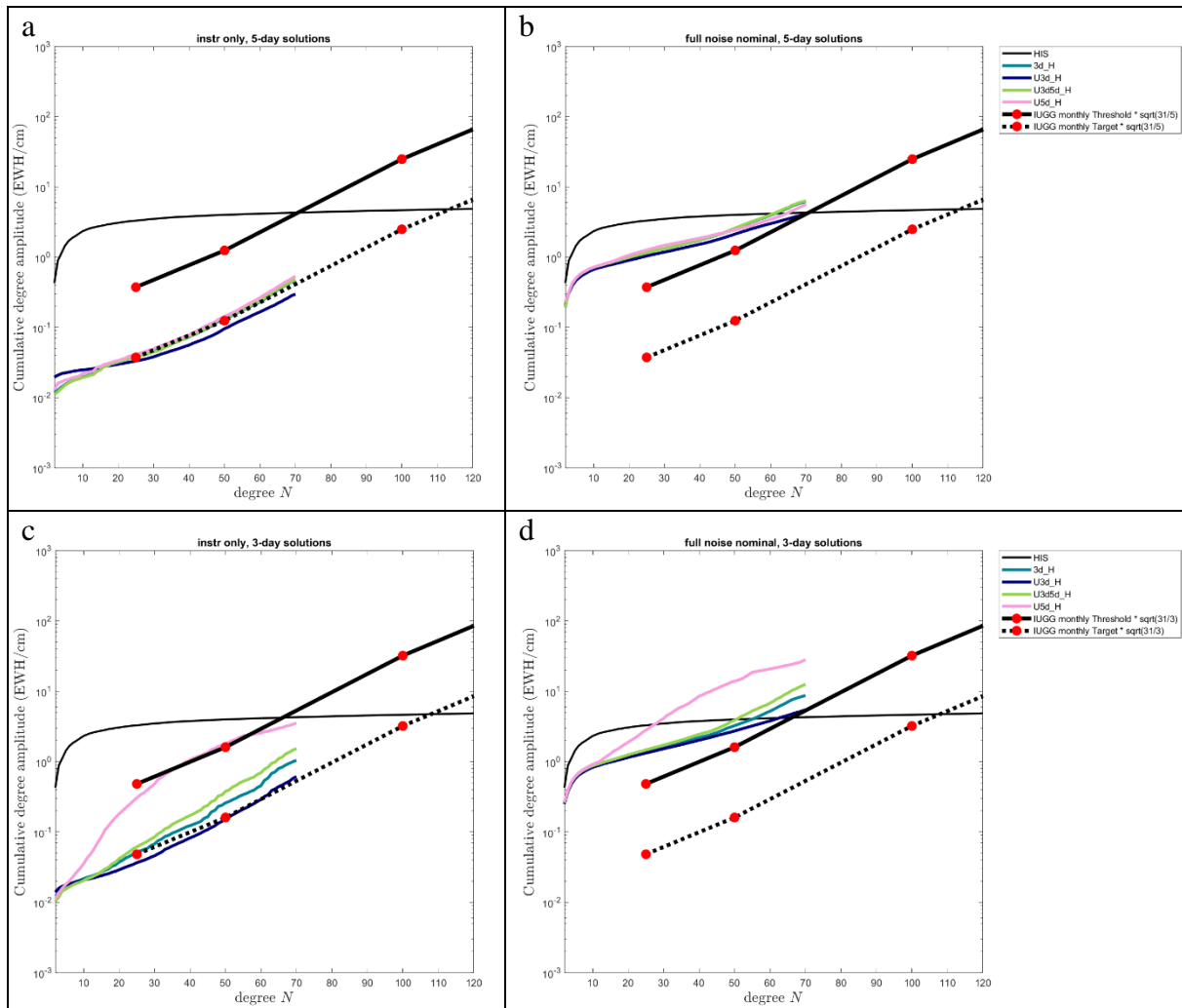
Figure 44-5 Cumulative RMS curves for the d/o 70 5-day (top row) and 3-day (bottom row) double-pair simulation results (panels a, c: instrument only, panels b, d: full noise nominal), compared to the IUGG threshold and target requirements that have been up-scaled from monthly to 5- and 3-day requirements, respectively. For each individual scenario, the mean curve of the cumulative RMS curves of three (top row) or five (bottom row) subsequent solutions is shown. [Path: Deliverables/D1/simulation_results/full_scale_simulator_v009/1_by_sqrt(10)_noise_scaling/]

44.3 IMPACT OF POST-PROCESSING ON THE CUMULATIVE MODEL ERRORS

In this section, we analyze the impact of post-processing of the retrieved gravity field models on the resulting cumulative error curves.

For the post-processing, we apply Gaussian filters in the spherical harmonics (SH) domain. As there is no 1:1 relation between the filter half width in the spatial and in the SH domain, the choice of the filter radius (defined in space domain) for a given maximum SH degree is not unique. For this reason, we use four possible definitions of the filter radius for a Gaussian degree-Nmax filter, as shown in Figure 44-6: For the filter Fx, the filter radius in space domain is computed as 20000 km/Nmax/x with x running from 1 to 4. As can be seen in Figure 44-6, the filter strength is decreasing from F1 to F4.
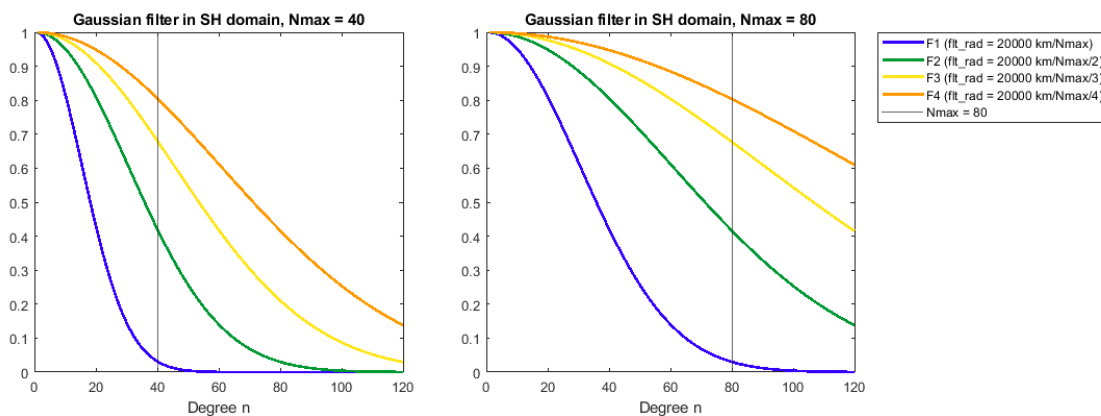
Figure 44-6 Four possible definitions for a Nmax=40 (left) and a Nmax=80 (right) Gaussian filter in spherical harmonics domain. The respective filter radii which are given in units of km in the spatial domain are specified in the legend.

As can be seen in Figure 44-6, applying a Gaussian filter (in contrast to a rectangular boxcar filter) in SH domain leads to

(1) a filtering out of parts of the long-wavelength (n < Nmax) signal contents of the model, resulting in a n < Nmax omission error in the filtered model.
(2) Also, as the filter values are not zero for degrees n > Nmax, the filters let pass parts of the short-wavelength (n > Nmax) noise of the retrieved model, resulting in a n > Nmax commission error in the filtered model.

Of course, the fact that the filter has values < 1 for n < Nmax also leads to a reduction in the n < Nmax commission error of the filtered model, as not only signal (as described in (1)) but also noise is filtered out for n < Nmax. Correspondingly, the fact that the filter has values > 1 for n > Nmax also leads to a reduction in the n > Nmax omission error of the filtered model, as not only noise (as described in (2)) but also signal is passed by the filter. However, in our case of HIS retrieval, for n < Nmax, the model mostly consists of signal and for n > Nmax, the model mostly consists of noise (the degree of validity of this statement of course depends on Nmax).

The stronger the chosen filter (the filter strength decreases from F1 to F4), the larger the above-mentioned contribution (1) to the omission error is and the smaller the above-mentioned contribution (2) to the commission error is. An optimum filter radius for the Nmax-Gaussian filter could be found by minimizing the sum of the two above-mentioned errors. As the amplitude of both errors depends on the wavelength-dependent signal and noise contents of the considered model, the optimum filter radius will be different for different models as well as be dependent on the value of Nmax. In the following, we will compare the results using the four filters F1 to F4 to see the impact that the choice for a specific filter radius definition has.

Figure 44-7 shows the degree error amplitudes of the Nmax=40 and Nmax=80-Gaussian-filtered 31-day 2_pIn_iIn (full noise nominal) model. It is visible that with increasing filter strength (F1 is the strongest filter), the short-wavelength noise in the model becomes reduced. However, if the chosen filter is too strong, significant HIS signal components remain in the difference between the filtered model and the (unfiltered) HIS reference model, as the above-mentioned omission error (1) becomes larger. This effect is especially visible for small n, where the application of the stronger filters leads to increasing error degree amplitudes. By comparing these effects between the two panels in Figure 44-7, we see that for Nmax=40, a good filter radius choice would e.g. be F3, and for Nmax=80, a good filter radius choice would e.g. be F2. This shows that because in our model, the signal is mainly concentrated in the low SH degrees and the noise is mainly concentrated in the high SH degrees, for large filter degrees Nmax, a stronger filter would be chosen, while for small filter degrees Nmax, a weaker filter would be chosen.

The above-described effects that the Gaussian filters F1 to F4 have on the model, the HIS reference as well as on their difference, can also be observed in Figure 44-8 and Figure 44-9 in the spatial domain.
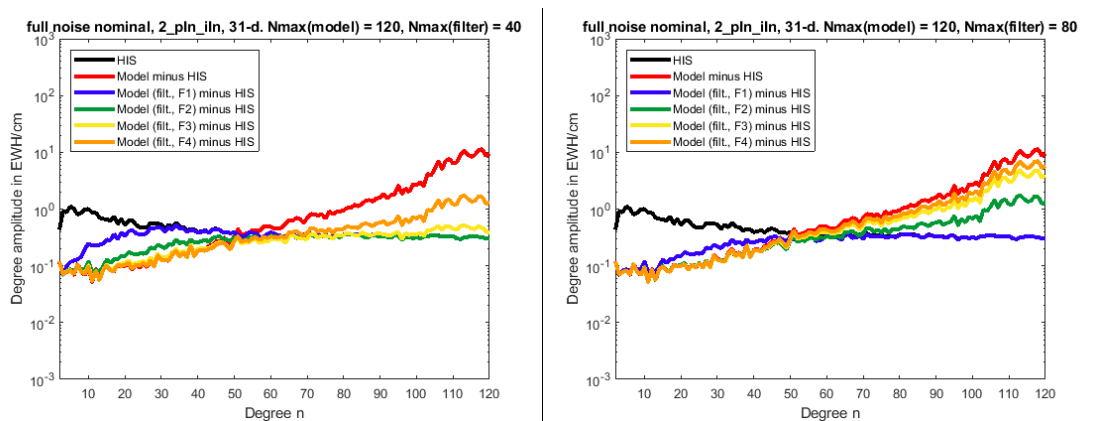
Figure 44-7 Error degree amplitudes of the d/o 120 31-day solution for the full noise scenario 2_pIn_iIn. Shown is the impact that a Gaussian degree-40 filter (left) and a Gaussian degree-80 filter (right) (applied as a post-processing step) has on the retrieval errors. The filters F1 to F4 differ by the definition of their filter radius in space domain (see the visualization of the four filters versions in Figure 44-6).

full noise nominal, 2_pIn_iIn, 31-days solution. Nmax(model) = 120, Nmax(filter) = 40
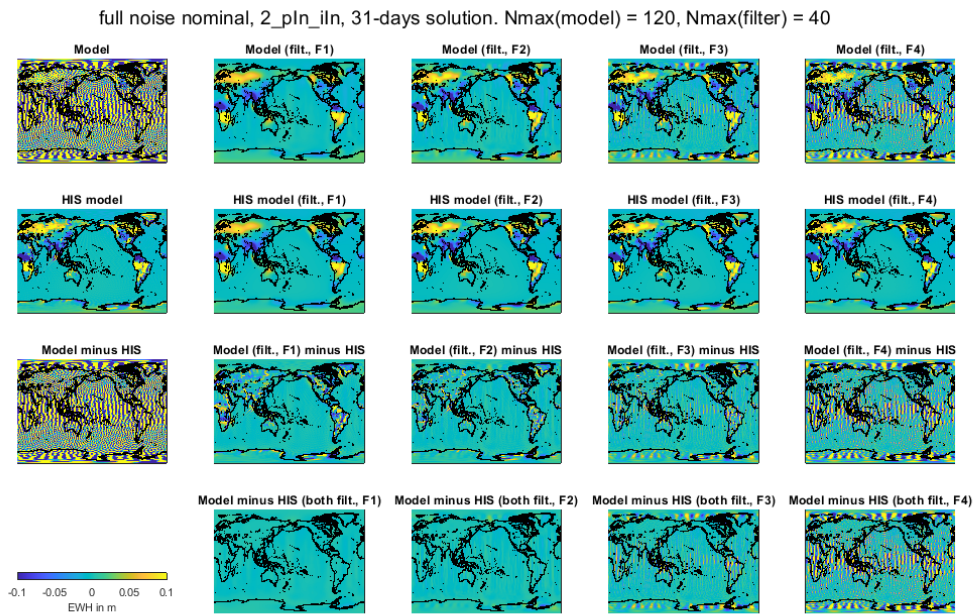
Figure 44-8 EWH grids of the retrieved d/o 120 31-day full noise model for the double-pair scenario 2_pIn_iIn as well as the HIS reference model used up to d/o 120. Shown is the impact that the application of a Nmax = 40 Gaussian filter has, on the full models as well as on their differences. The filter definitions F1 to F4 are given in the text and visualized in Figure 44-6 (left).

full noise nominal, 2_pIn_iIn, 31-days solution. Nmax(model) = 120, Nmax(filter) = 80
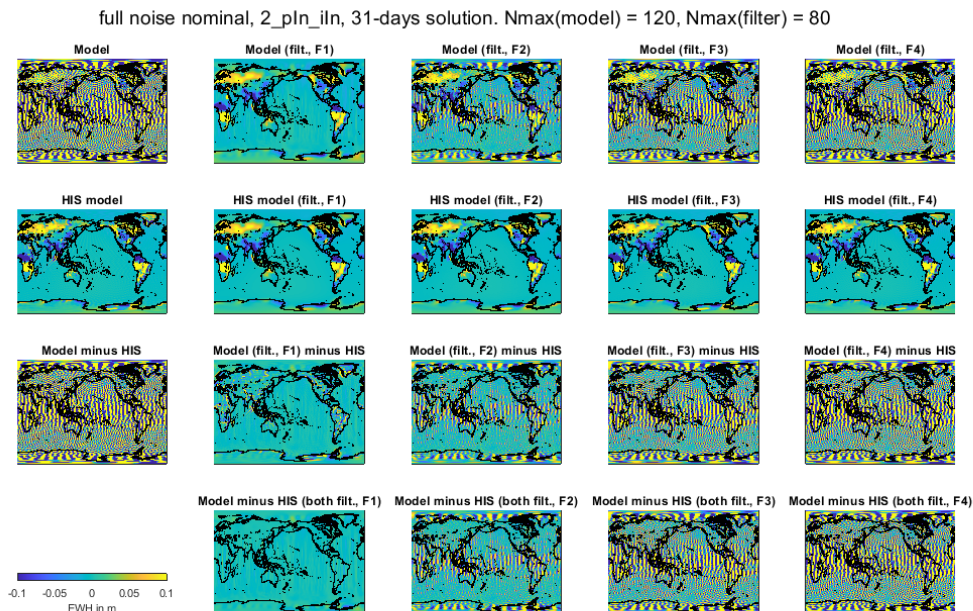
Figure 44-9 EWH grids of the retrieved d/o 120 31-day full noise model for the double-pair scenario 2_pIn_iIn as well as the HIS reference model used up to d/o 120. Shown is the impact that the application of a Nmax = 80 Gaussian filter has, on the full models as well as on their differences. The filter definitions F1 to F4 are given in the text and visualized in Figure 44-6 (right).

As noted in section 44.1, applying post-processing to the retrieved gravity field models will influence the computed cumulative errors and thereby also the match of the simulation results against the IUGG user requirements. To investigate the impact of the various filtering strategies on the cumulative error curves and their match to the IUGG requirements, we define the following possible ways to compute the cumulative error curves:

For a full noise nominal solution (HIS retrieval), the cumulative model error at degree N is computed using

$$cum.\,error(N) = \frac{a\,\rho_e}{3\,\rho_w}\sqrt{\sum_{n=2}^{120}\left(\frac{2n+1}{1+k_n}\right)^2\sum_{m=0}^{n}\left[\Delta c_{nm}^{(N)}\right]^2 + \left[\Delta s_{nm}^{(N)}\right]^2},$$

where 120 is the maximum degree of the retrieved model, and the coefficient errors are computed as

$$\Delta c_{nm}^{(N)} = c_{nm}^{(N)}(model) - c_{nm}^{(N)}(HIS)$$

and similarly for $\Delta s_{nm}^{(N)}$. Note that in this way, the cumulative error curves are constructed point-wise, i.e. for each degree N, the coefficient errors are computed for all degrees n and orders m up to d/o 120 and then summed up to n = 120 following the above formula.

In the following, we investigate five versions for computing the cumulative model error at degree N, depending on how the retrieved model and the HIS model are restricted to a maximum SH degree of N:

- cut models: $\bar{c}_{nm}^{(N)}(model) = \begin{cases} c_{nm}(model), n \leq N \\ 0 \qquad\quad, n > N \end{cases}$
- filtered models: $\tilde{c}_{nm}^{(N)}(model) = Fx^{(N)} \cdot c_{nm}(model)$
- filtered and cut models: $\hat{c}_{nm}^{(N)}(model) = \begin{cases} \tilde{c}_{nm}^{(N)}(model), n \leq N \\ 0 \qquad\qquad, n > N \end{cases}$

and similarly for $\bar{c}_{nm}^{(N)}(HIS)$, $\tilde{c}_{nm}^{(N)}(HIS)$ and $\hat{c}_{nm}^{(N)}(HIS)$ as well as the corresponding s_{nm} coefficients. Hereby, $Fx^{(N)}$ corresponds to the Gaussian filter coefficients in SH domain for the filter degree N and the filter definition $Fx = \{F1, F2, F3, F4\}$, as visualized in Figure 44-6 for $N = 40$ and $N = 80$.

The five versions to compute the cumulative error at degree N are defined as follows:

- v1: both model and HIS are cut at N:
$$c_{nm}^{(N)}(model) = \bar{c}_{nm}^{(N)}(model)$$
$$c_{nm}^{(N)}(HIS) = \bar{c}_{nm}^{(N)}(HIS)$$
- v2: model is filtered, HIS is cut at N:
$$c_{nm}^{(N)}(model) = \tilde{c}_{nm}^{(N)}(model)$$
$$c_{nm}^{(N)}(HIS) = \bar{c}_{nm}^{(N)}(HIS)$$

- v3: model is filtered and cut, HIS is cut at N:
$$c_{nm}^{(N)}(model) = \hat{c}_{nm}^{(N)}(model)$$

$$c_{nm}^{(N)}(HIS) = \bar{c}_{nm}^{(N)}(HIS)$$

- v4: model and HIS are filtered at N:

$$c_{nm}^{(N)}(model) = \tilde{c}_{nm}^{(N)}(model)$$
$$c_{nm}^{(N)}(HIS) = \tilde{c}_{nm}^{(N)}(HIS)$$
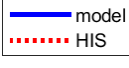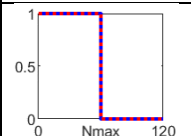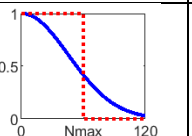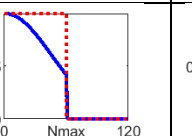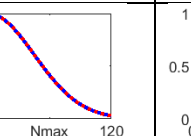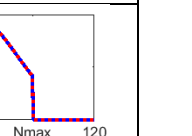
- v5: model and HIS are filtered and cut at N:

$$c_{nm}^{(N)}(model) = \hat{c}_{nm}^{(N)}(model)$$
$$c_{nm}^{(N)}(HIS) = \hat{c}_{nm}^{(N)}(HIS)$$

Table 44-20 gives a visualization of the version definitions by showing the "effective" filters in SH domain that are applied to the computed model and the HIS model. Furthermore, the table gives an overview of the effects that the cumulative errors computed using a specific definition include. Version v1 corresponds to the definition applied for the plots in section 44.1. In v1, the cumulative errors only include the n < Nmax model commission error, which is the noise contained in the model up to n = Nmax. This n < Nmax commission error becomes partly reduced by the filters in versions v2 to v5; this effect is strongest if using the (strong) F1 filter. If the model is Gaussian filtered (as in v2 and v4, no cutting at Nmax), part of the n > Nmax commission error contained in the model is passed by the filter; this effect is strongest if using the (weak) F4 filter. If for n < Nmax, the model is filtered and the HIS model is not filtered (as it is the case in v2 and v3), a n < Nmax omission error is introduced into the cumulative error curves. Finally, in version v2 signal parts in the model for n > Nmax that are passed by the Gaussian filter are contained in the cumulative error definition.

Table 44-20 Overview of the effects the five different cumulative error versions include. The Plots visualize the cutting, filtering or cutting and filtering of the model and the HIS reference in the individual versions. Filtering is done using a degree-Nmax Gaussian filter.

Version:	v1	v2	v3	v4	v5
n < Nmax commission error	full	slightly reduced by filter (strongest reduction for F1)	slightly reduced by filter (strongest reduction for F1)	slightly reduced by filter (strongest reduction for F1)	slightly reduced by filter (strongest reduction for F1)
n > Nmax commission error	-	partly passed by the filter (largest for F4)	-	partly passed by the filter (largest for F4)	-
n < Nmax omission error	-	yes (largest for F1)	yes (largest for F1)	-	-
n > Nmax signal contained in the model	-	yes (largest for F4)	-	-	-

Figure 44-10 shows the cumulative errors computed using the definitions v1 to v5 and the filter versions F1 to F4 for the 31-day full noise nominal model for the scenario 2_pIn_iIn. First of all, we note that the order of magnitude of the cumulative errors and consequently the match of the cumulative errors to the IUGG requirements strongly depends on both the method how the cumulative error curves are computed, as well as on the specific chosen Gaussian filter radius for each degree N.

The main effects governing the individual curves can be understood most easily if starting from version v5 (as this version contains the smallest number of effects, as can be seen in Table 44-20). Compared to v1, in v5 the n < Nmax commission error is reduced, the effect of which is strongest if using the F1 filter (see the magenta arrow and the associated textbox in Figure 44-10). Considering v4, the only difference to v5 is the additional n > Nmax commission error, which becomes passed strongest by F4 (see the upward-directed light blue arrow and the associated textbox in Figure 44-10). Considering v3, the only difference to v5 is the additional n < Nmax omission error, which is strongest if using the F1 filter and the impact of which is strongest for the low SH degrees (see the upward-directed green arrow and the associated textbox in Figure 44-10).

Assuming that we can neglect the impact of the n > Nmax signal contained in the model which is contained in the v2 curves, we can read from Table 44-20 that the difference between v2 and v4 is the n < Nmax omission error, and the difference between v2 and v3 is the n > Nmax commission error. Both of these effects are indicated by upward-directed red arrows in Figure 44-10.
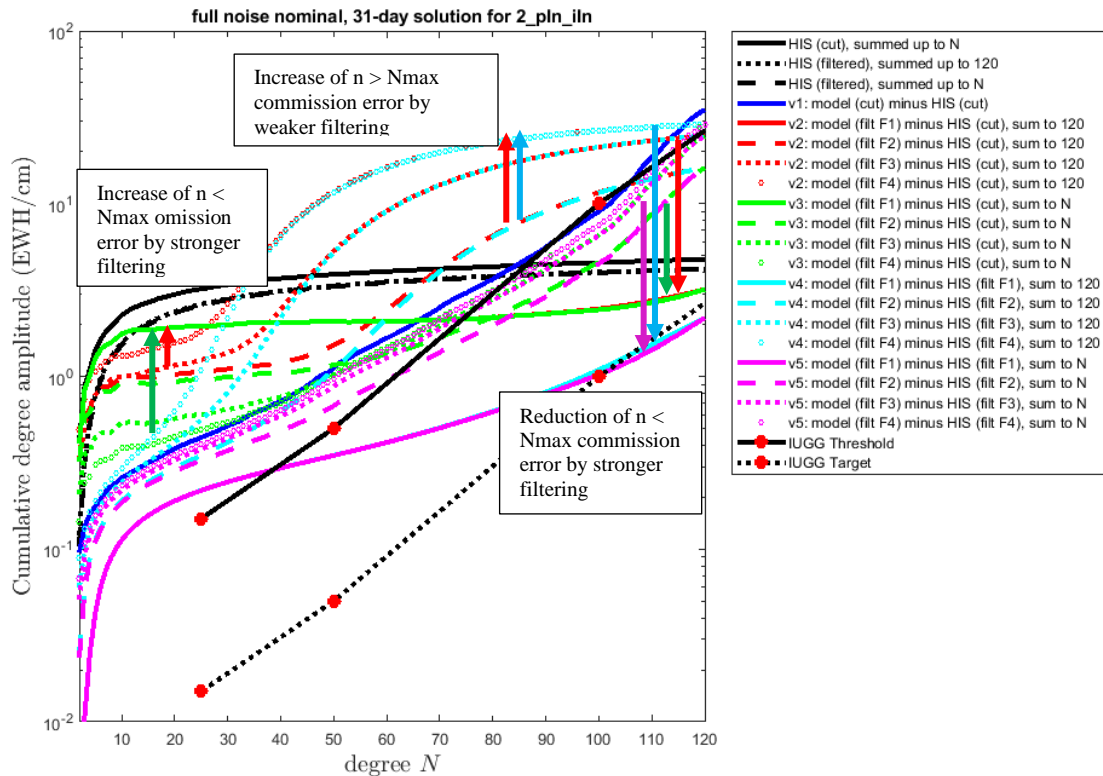
Figure 44-10 Cumulative error degree amplitudes for the d/o 120 31-day solution for the full noise scenario 2_pIn_iIn. Shown are five versions v1 to v5 to compute the cumulative error curve. v1 is the classical computation, as used in section 44.1; v2 to v5 involve a post-processing of the retrieved gravity field model using the Gaussian filter definitions F1 to F4 (see text). The main effects on the curves are indicated by the arrows and associated text boxes.

44.4 RELATIVE PERFORMANCE OF SCENARIOS

In this section, we present ideas on how the results shown in Section 44.1 could be visualized in different ways, especially with the aim to show the improvement of the gravity retrieval performance of the analysed scenarios w.r.t. the performance of the GRACE-like single pair scenario 1_pIg. Figure 44-11 and Figure 44-12 show two methods for this:

With the aim to visualize the error reduction w.r.t. the retrieval errors of scenario 1_pIg, we divide the cumulative errors of the considered scenario by the cumulative error of the scenario 1_pIg, which is done for each maximum degree N. The results are shown by Figure 44-11 and show an increasing improvement of the retrieval performance in terms of a larger reduction of errors.

The alternative to this is shown by Figure 44-12, where the cumulative errors of 1_pIg are divided by the cumulative errors of the respective considered scenario. With this method, an increasing improvement of the solution is shown by an increasing level of improvement w.r.t. 1_pIg.
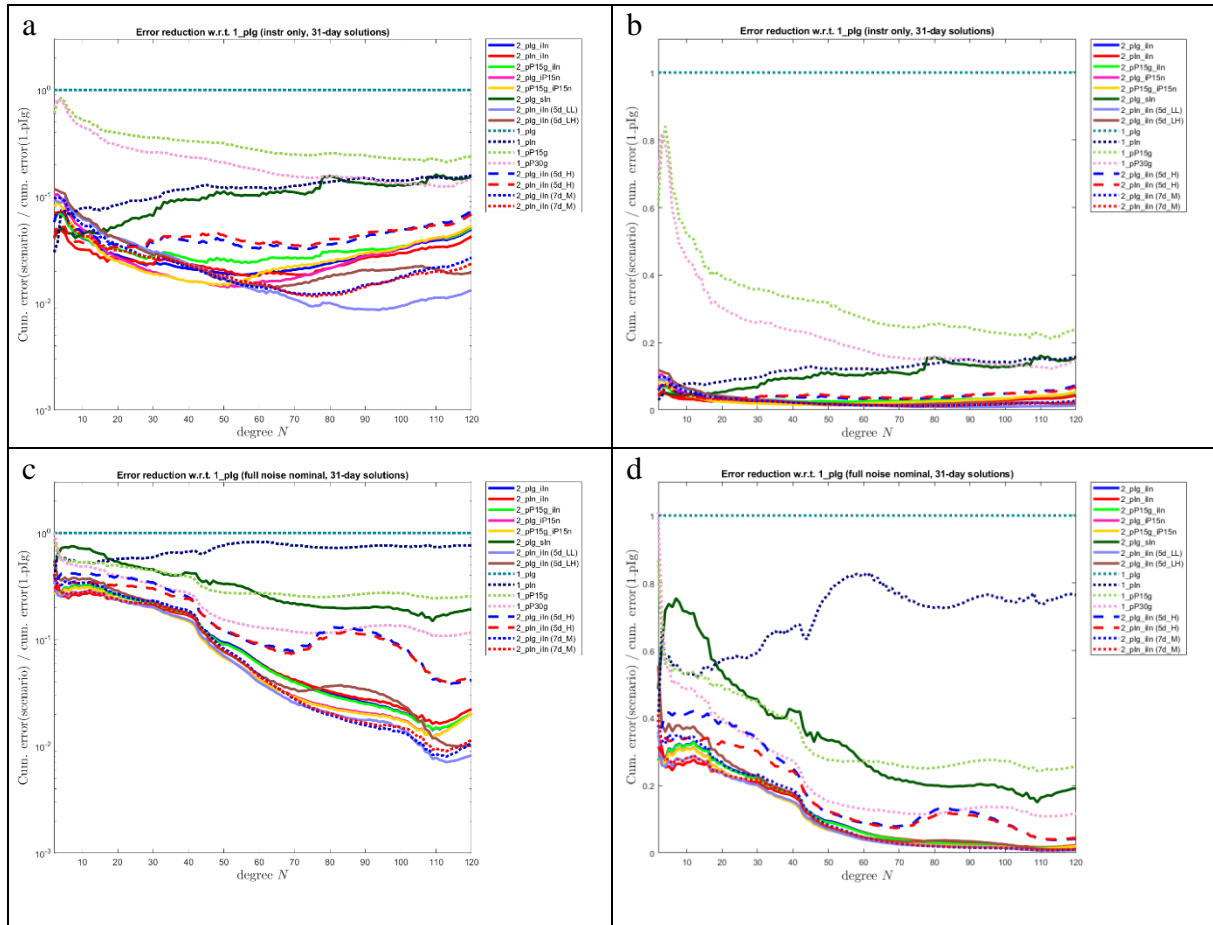
Figure 44-11 Ratio of the cumulative error curves of the individual scenarios shown by Figure 44-1 and Figure 44-2 by the cumulative error curve of the single-pair scenario 1_pIg, using a logarithmic y axis (left column) or a linear y axis (right column). Panels a and b show the curves corresponding to the instrument-only simulations, while panels c and d show the curves corresponding to the full noise simulations.
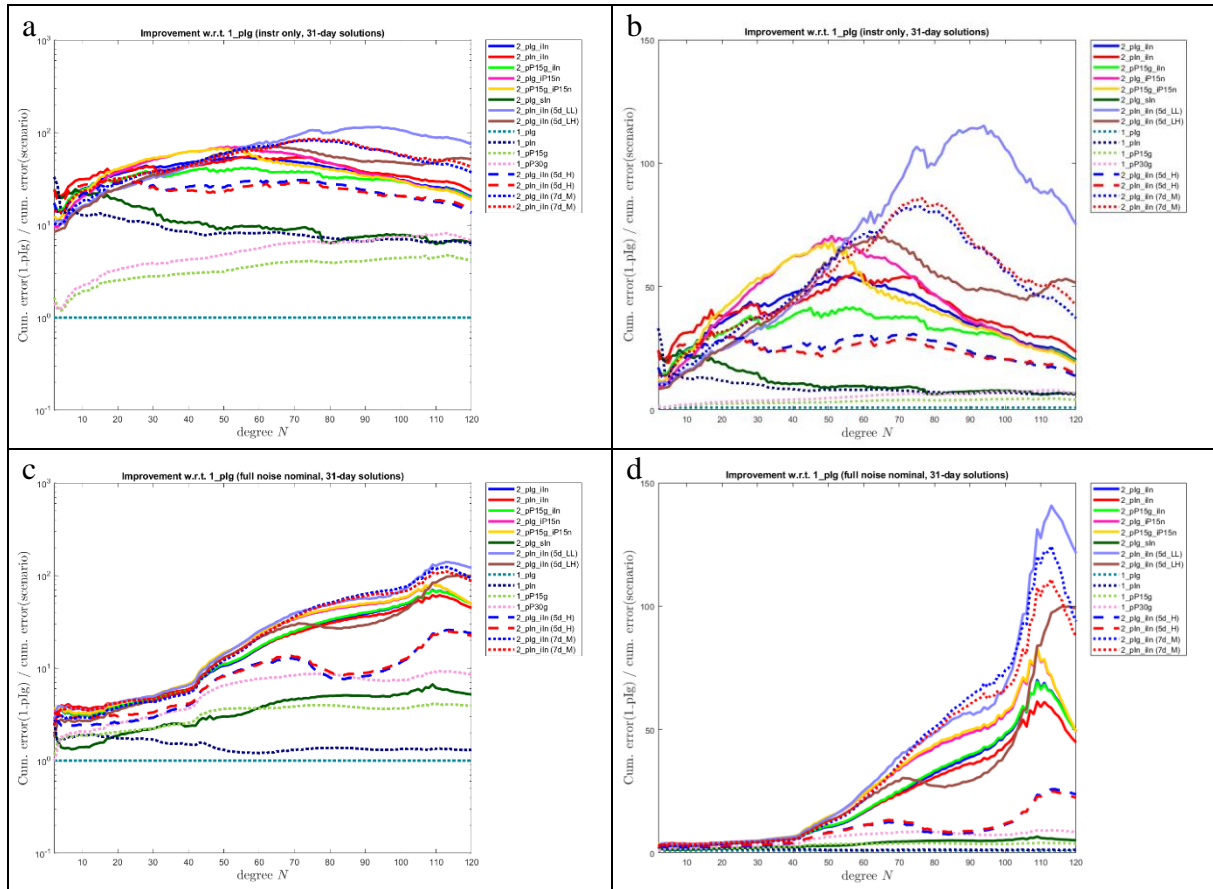
Figure 44-12 Ratio of the cumulative error curve of the single-pair scenario 1_pIg and the cumulative error curves of the individual scenarios shown by Figure 44-1 and Figure 44-2, using a logarithmic y axis (left column) or a linear y axis (right column). Panels a and b show the curves corresponding to the instrument-only simulations, while panels c and d show the curves corresponding to the full noise simulations.

44.5 SIGNAL AND NOISE CONTENT OF CO-ESTIMATED PARAMETERS (WP520)

In this chapter co-estimated parameters as part of the Level-2 processing are analysed. Parameters to be investigated are based on the four Bender-type simulation scenarios described in D8, which are 3dH, 5dH, 7dM and 5dHL. Within the EPOS simulation environment ACC calibration parameters are co-estimated, typically. As no non-gravitational forces (atmospheric drag, solar radiation pressure and Earth albedo) have been used for the simulations, no ACC scale factor parameters have been co-estimated because they would re-scale the ACC instrument noise into a false direction and would lead to falsified gravity field retrieval. ACC bias parameters have been co-estimated, which is necessary, in order to obtain gravity field solutions of adequate quality. In case of applying the Wiese approach, short-term gravity field parameters at low resolution are co-estimated, additionally. The setup of the short-term parameters was based on a daily period up to a maximum resolution d/o of 15. The Wiese approach has been applied to the 3dH and 7dM scenarios (see D8 for the corresponding long-term solutions). Additional parameters such as empirical accelerations have not been co-estimated.

In the following, the short-term gravity field parameters as well as the ACC bias parameters are assessed.

Figure 44-13 shows the degree error amplitudes of the co-estimated daily solutions for the 3dH and 7dM scenarios over a time span of 30 days. The underlying gravity field processing is based on a retrieval without using an AOD product. It is seen that both scenarios are able to resolve the daily gravity field significantly up to d/o 15 without being dominated by error signals, i.e. SNR>1. Further, both Bender-type scenarios provide similar quality of daily fields. The global RMS of averaged daily solutions is given with 12.6 mm EWH for 3dH and 12.9 mm EWH for 7dM.
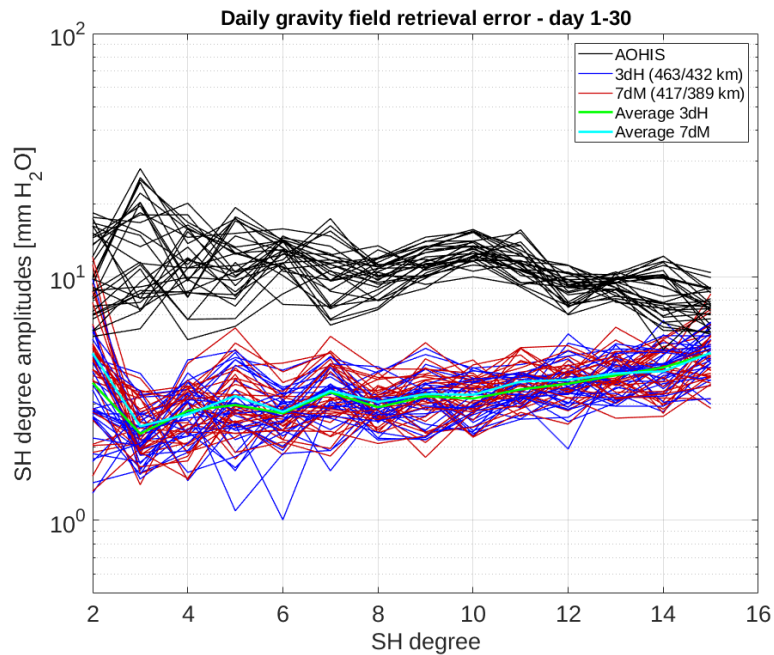
Figure 44-13: Degree error amplitudes in mm EWH for January 2002 of the scenarios 3dH (blue) and 7dM (red) including averages over 30 days (green and cyan). The reference mean daily AOHIS signal is displayed in black.

The almost 'error free' performance of the daily fields is confirmed by the spatial signal assessment in Figure 44-14. It shows the retrieved gravity field signal for specific days derived from 3dH wrt. the reference AOHIS signal. The comparison demonstrates a 'clear' gravity field recovery.
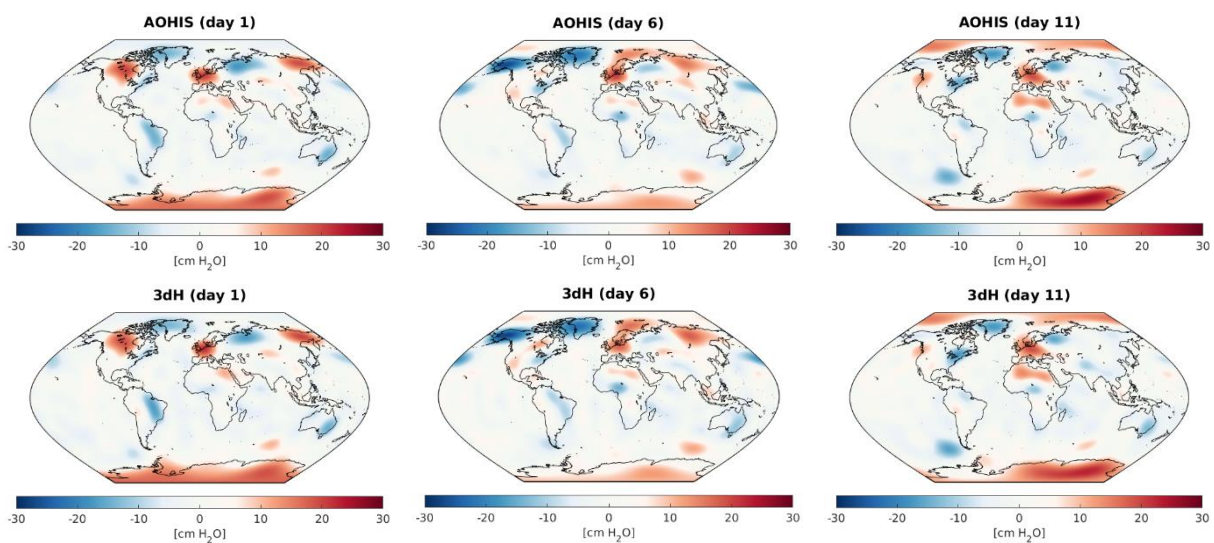
Figure 44-14: Spatial distribution of the retrieved signal by 3dH (bottom) vs. true AOHIS signal (top) for day 1 (left), day 6 (center) and day 11 (right) in cm EWH.

Next to the signal retrieved on a daily basis, the relative change between two consecutive days was analysed wrt. the changing reference signal. Figure 44-15 shows the relative changes in terms of retrieval errors for 3 different periods for the 3dH scenario. Results demonstrate that changes in the daily signal can be resolved significantly up to a maximum d/o of about 12 having a SNR>1. Figure 44-16 displays the spatial distribution of the retrieval as changing signal confirming the results of Figure 44-15.
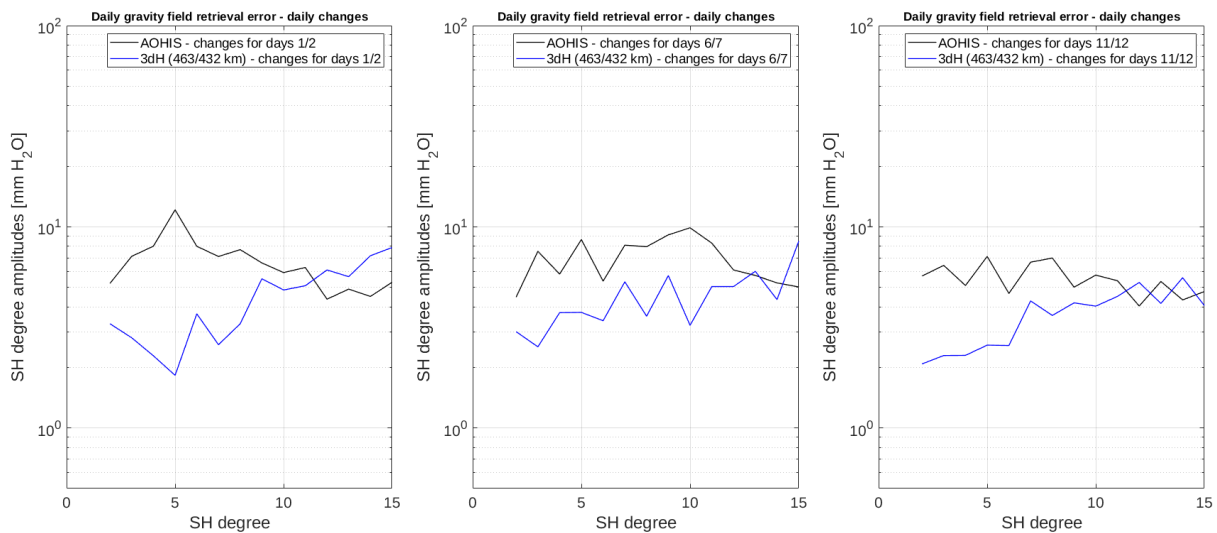
Figure 44-15: Degree error amplitudes in mm EWH of relative changes among days 1 and 2 (left), 6 and 7 (center) and 11 and 12 (right) based on daily Wiese solutions of the 3dH scenario. The relative changes of the reference AOHIS signal are displayed in black.
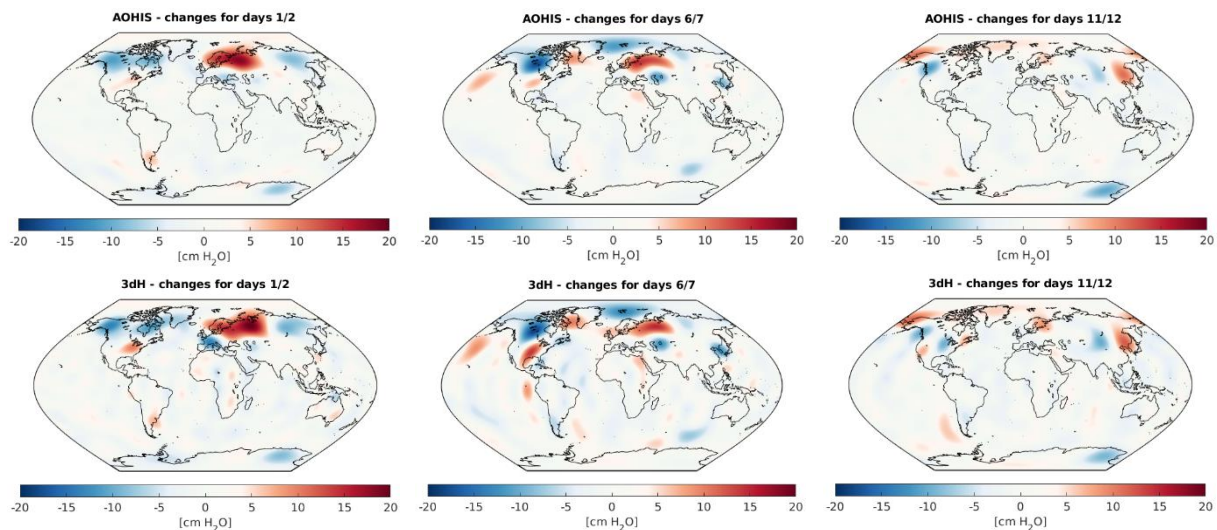
Figure 44-16: Spatial distribution of relative changes of the retrieved signal of two consecutive days from 3dH (bottom) vs. true AOHIS signal (top) for changes between days 1/2 (left), days 6/7 (center) and days 11/12 (right) in cm EWH.

The assessment of the co-estimated ACC bias parameters can be done wrt. the amount of signal amplitude and the stability within a dedicated retrieval period. In general, 3 bias parameters per satellite are co-estimated in radial and transversal direction, 9 parameters per satellite are co-estimated in normal direction as this is the non-sensitive ACC axis.

Figure 44-17shows the bias parameters for the four satellites of scenario 3dH for a 30-day retrieval. The biases for radial and normal directions show similar values, the biases in transversal direction are smallest. The biases show smaller values compared to biases derived from real GRACE-FO data analysis having values of about 1e-7 m/s² for radial and transversal directions and 1e-5 m/s² for normal direction. The larger values at the normal direction result from the non-sensitivity of the ACC. As already mentioned, in the simulation world, no non-gravitational forces have been introduced, consequently no ACC observations have been introduced as well, except for the ACC instrument noise. These facts lead to smaller values for bias parameters in the simulation world. Furthermore, Figure 44-17 shows that the values for the polar and inclined satellites are similar and the level of amplitude is stable over time. The small bias values as well as the stable performance are indicators of correctly derived bias parameters which have only marginal influence on the estimated gravity field parameters.

Figure 44-18 and Figure 44-19 show the estimated biases for a 7-day and a 3-day retrieval period. Compared to the 30-day retrieval, the bias values behave slightly smoother at a similar signal amplitude.

Finally, an inter-comparison among the co-estimated biases of one polar satellite of the four different Bender-type formations has been done, respectively. Results displayed in Figure 44-20 show similar values for all satellite formations indicating that the gravity field retrieval of each satellite formation does not suffer a disadvantage when co-estimating ACC bias parameters.
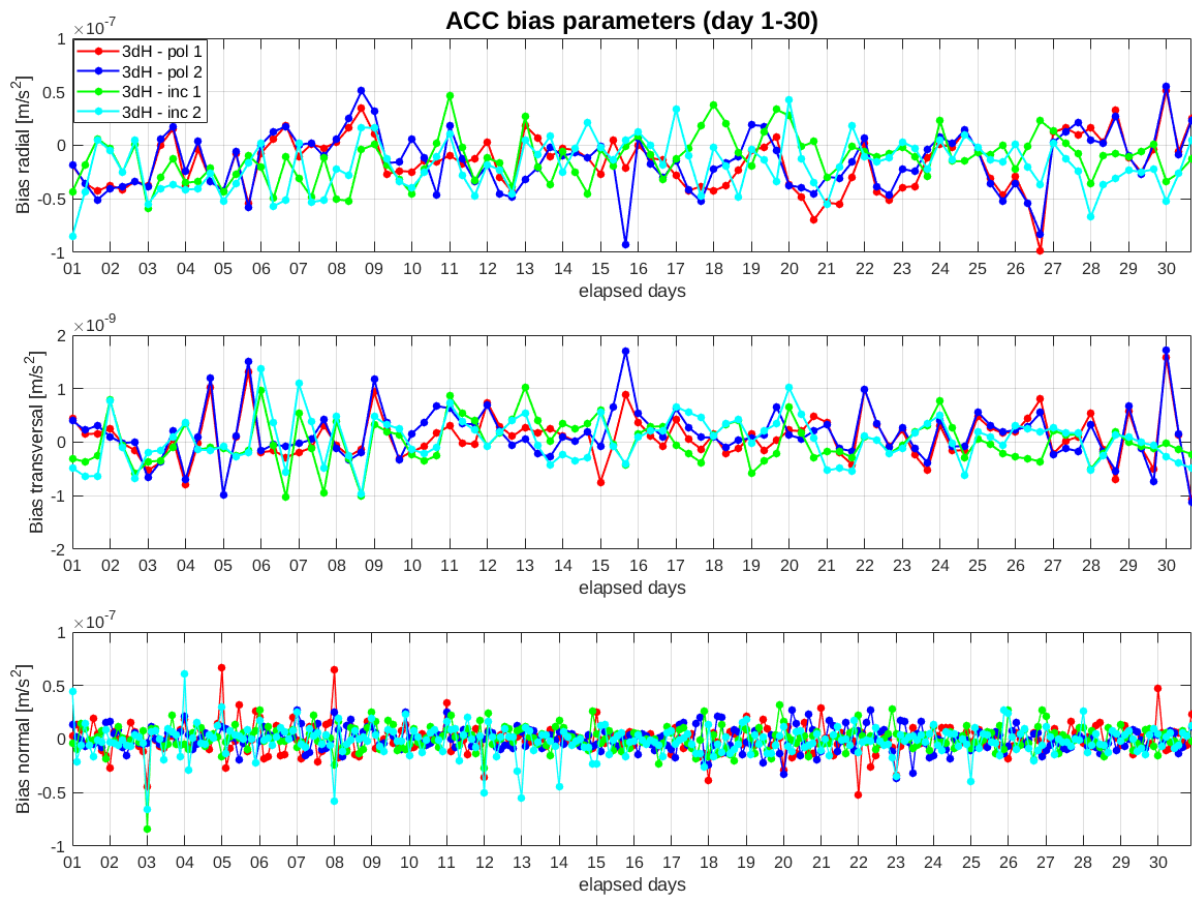
Figure 44-17: ACC bias parameters in radial (top), transversal (center) and normal (bottom) direction for a monthly retrieval of scenario 3dH. Parameters for the polar pair are displayed in red and blue, parameters for the inclined pair are displayed in green and cyan.
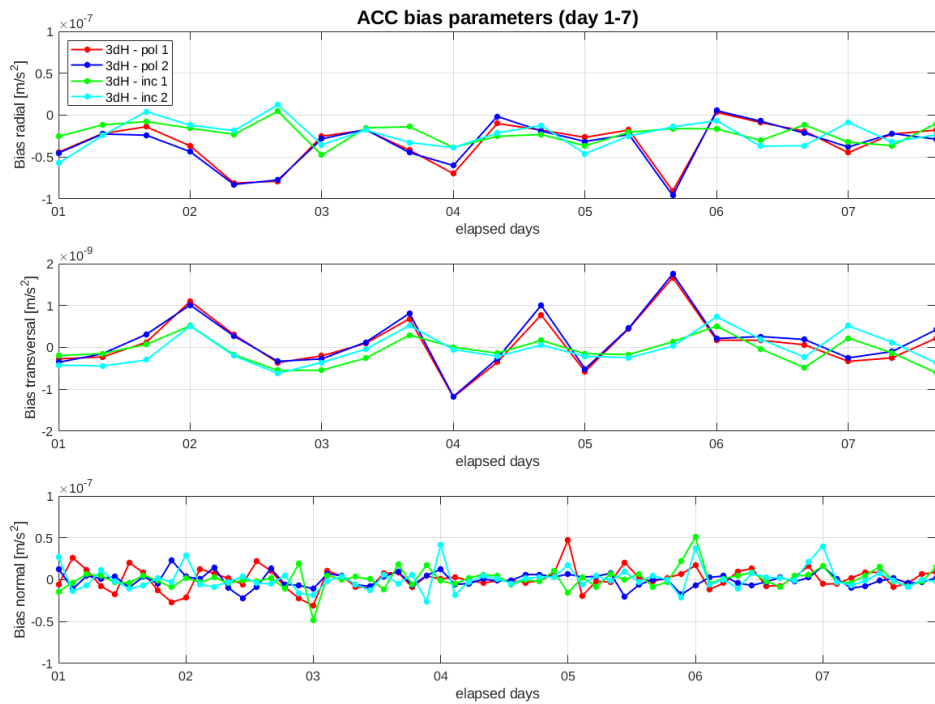
Figure 44-18: ACC bias parameters in radial (top), transversal (center) and normal (bottom) direction for a 7-day retrieval of scenario 3dH. Parameters for the polar pair are displayed in red and blue, parameters for the inclined pair are displayed in green and cyan.
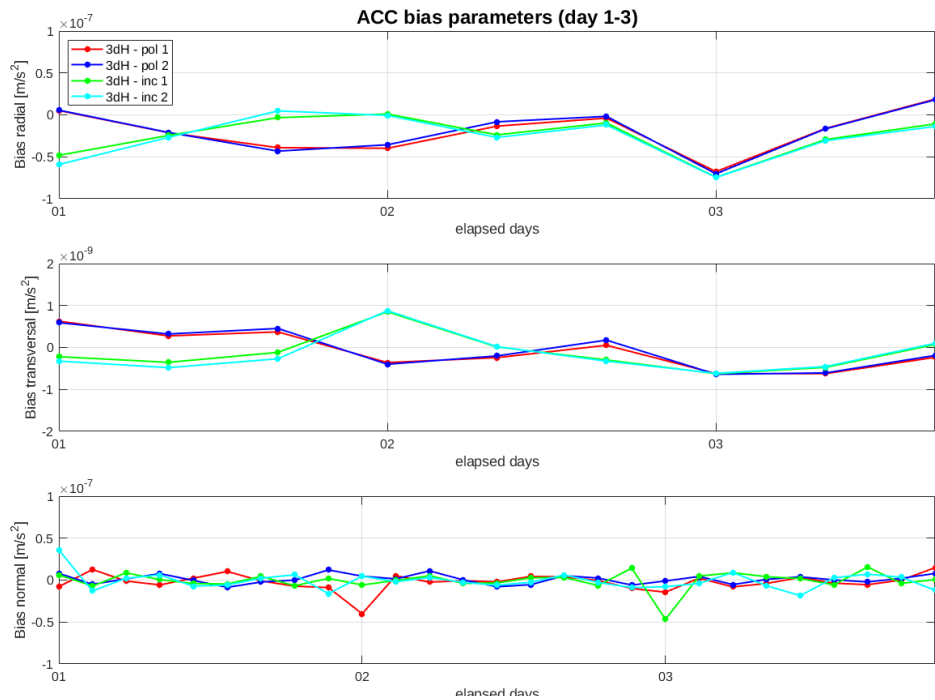
Figure 44-19: ACC bias parameters in radial (top), transversal (center) and normal (bottom) direction for a 3-day retrieval of scenario 3dH. Parameters for the polar pair are displayed in red and blue, parameters for the inclined pair are displayed in green and cyan.
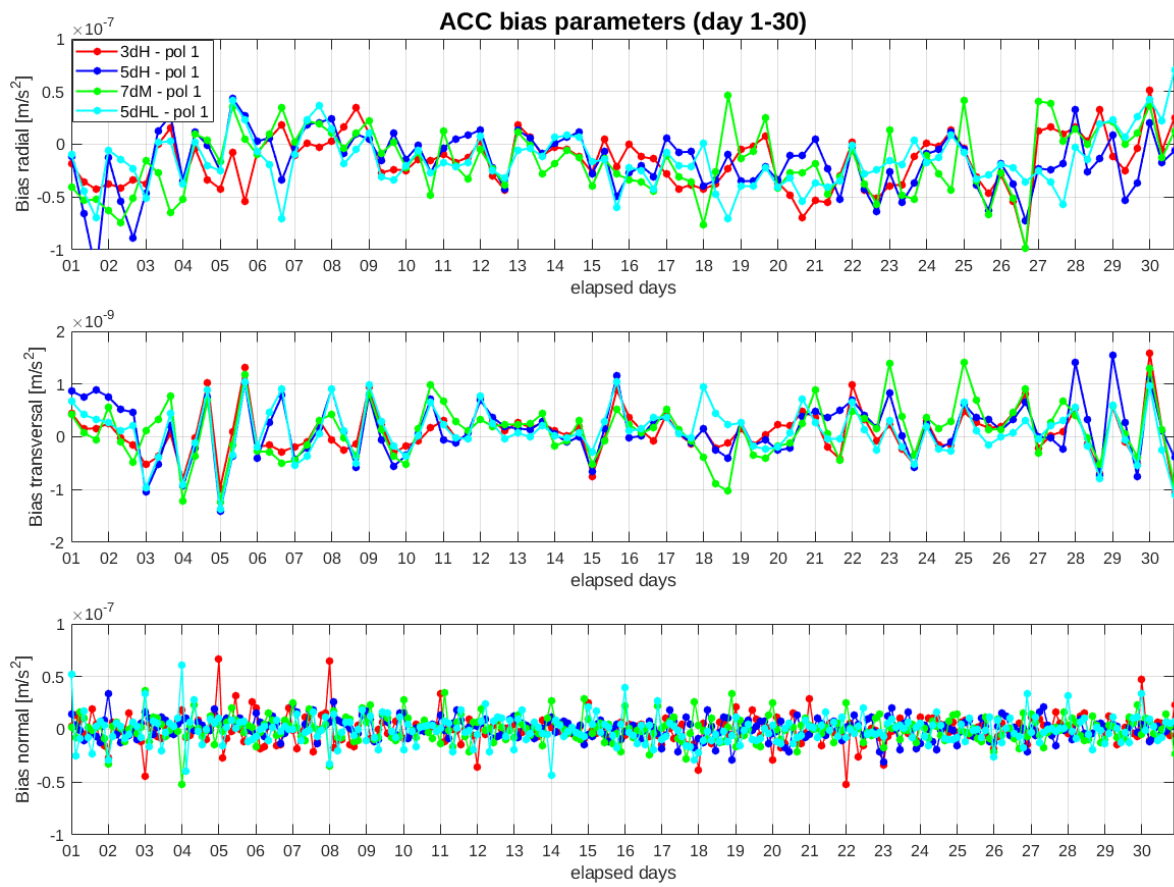
Figure 44-20: ACC bias parameters for the first polar satellite in radial (top), transversal (center) and normal (bottom) direction for a monthly retrieval of scenarios 3dH (red), 5dH (blue), 7dM (green) and 5dHL (cyan).

45 APPLICABLE DOCUMENTS, REFERENCE DOCUMENTS, AND PUBLICATIONS TO PART 5

45.1 APPLICABLE DOCUMENTS

[AD-1] Mission Requirements Document, Next Generation Gravity Mission as a Mass-change And Geosciences International Constellation (MAGIC) - A joint ESA/NASA double-pair mission based on NASA's MCDO and ESA's NGGM studies (2020). ESA-EOPSM-FMCC-MRD-3785

[AD-2] Scientific Readiness Levels (SRL) Handbook, Issue 1, Revision 0, 05-08-2015

[AD-3] Statement of Work - ESA Express Procurement - EXPRO NGGM/MAGIC science support study during Phase A, Issue 1, Revision 0, 18/01/2021 Ref ESA-EOPSM-FUTM-SOW-3813

PART 7:

SCIENCE IMPACT ANALYSIS

46 INTRODUCTION

This Part 7 refers to Task 6 of the SoW and covers the work performed under

- WP 530: Science expert review, and
- WP 600: Science impact analysis

of the WBS. It refers to the deliverable document TN D15 "Science impact analysis".

The purpose is to describe the science impact analyses of the relevant mission scenarios in different fields of applications of the mass change data in geosciences, in particular in the fields of hydrology, ocean science, cryosphere, solid Earth science and climate change. The goal is to provide an assessment of their science value with respect to the selected applications and to accordingly provide updates or rephrasing of science questions and objectives.

47 EVALUATION OF SIMULATION RESULTS AND TRANSFORMATION TO SCIENCE AND SERVICE RELATED PARAMETERS

47.1 HYDROLOGY - WATER STORAGE TIME SERIES IN HYDROLOGICAL UNITS

One of the most common applications of satellite gravimetry is the analysis of time series of water storage variations in hydrological units such as river basins or aquifers. To assess the benefit of the MAGIC mission for this purpose, the simulation results were assessed according to the following inputs to the computations:

- spherical harmonic coefficients of 52 weekly (7-days) simulation solutions from WP 100 up to degree/order N=120 for the Bender configuration (i.e. the MAGIC setup)
- spherical harmonic coefficients of 52 weekly (7-days) simulation solutions from WP 810 up to degree/order N=100 for a single pair configuration (i.e. the GRACE/GRACE-FO setup)
- spherical harmonics coefficients of the corresponding input signal (reference signal) from ESA ESM HIS fields

Time series of equivalent water heights were derived for the continental grid cells of a global 1° grid and for basin averages of 405 individual river basins defined by the Global Runoff Data Center (GRDC), representing the largest river basins worldwide. Figure 47-1 shows an exemplary time series for the Amazon basin.
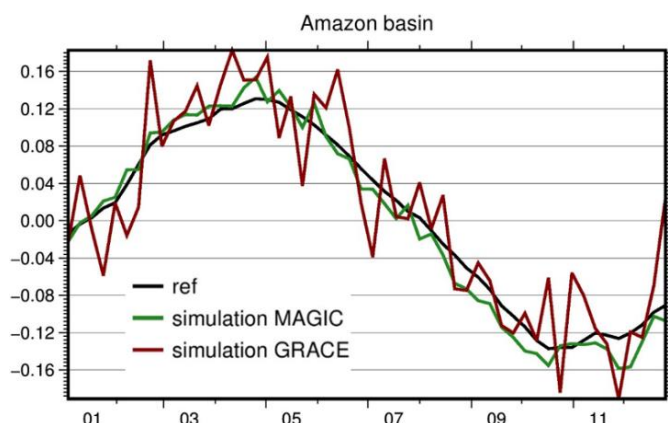
Figure 47-1: Basin average time series for the Amazon basin: reference signal (black), double-pair simulation (green) and single-pair simulation (red)

The temporal root-mean-square difference (RMSD) between the reference and the simulation time series was computed for each grid cell and each river basin to assess the accuracy of the simulation results.

The MRD lists target and threshold numbers to specify the envisaged accuracies for specific spatial resolutions, e.g. 600km and 300km for the "daily to weekly" time scale in the thematic field of hydrology. It still needs to be discussed how these spatial resolutions are best translated into specific applications, i.e. via filtering, via series truncation, and/or via averaging regions of a specific size. Here, following the suggestion made by the JMCMEG (meeting 2021/12/02), unfiltered solutions are used to mark the worst-case-scenario and the series expansions are truncated at the degree corresponding to the desired spatial resolution, i.e. 600km ≙ Nmax=33 and 300km ≙ Nmax=67.

Figure 47-2 displays the temporal RMSD for these two spatial resolutions for each grid cell and Figure 47-3 shows the RMSD for the basin average time series of the 405 selected river basins.
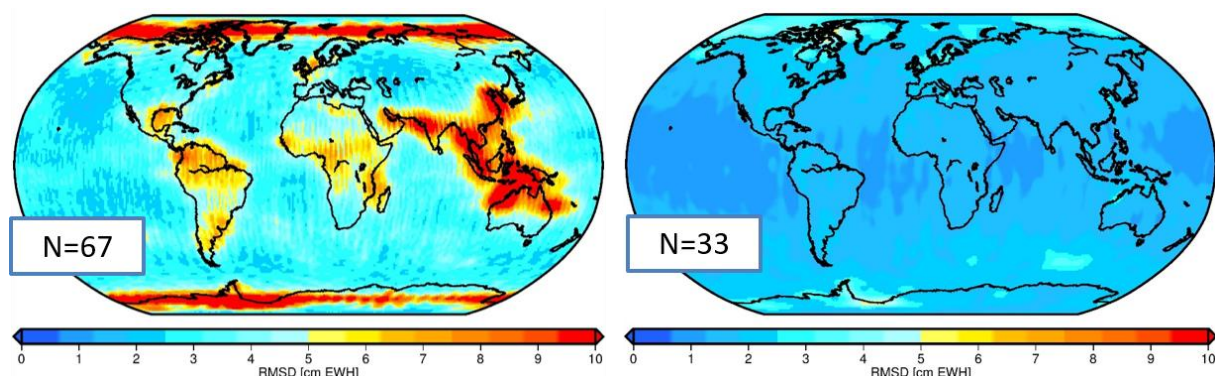
Figure 47-2: Temporal RMSD of 7-days simulation output (MAGIC constellation) and references solution.
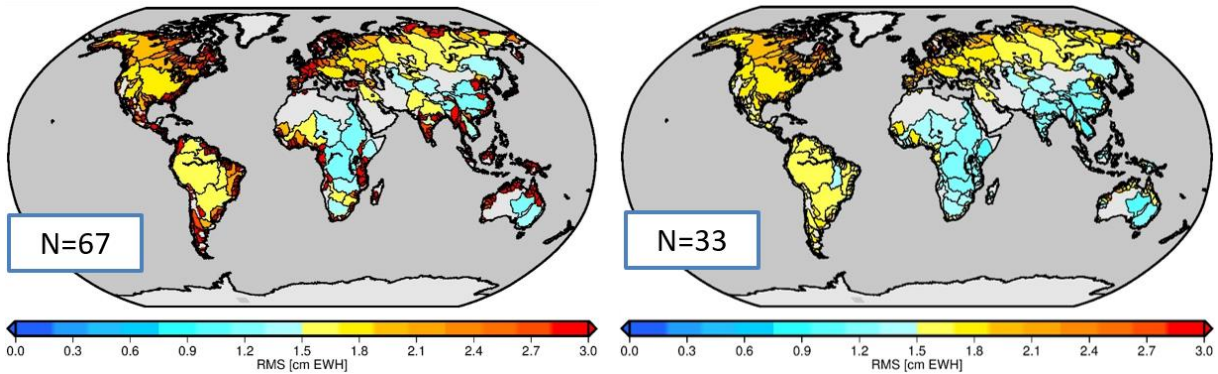
Figure 47-3: Temporal RMSD of 7-days simulation output (MAGIC constellation) and reference solution for basin averaged time series of 405 river basins defined by the Global Runoff Data Center (GRDC).

To assess the added benefit of the MAGIC mission for hydrological applications, the achieved accuracies of the MAGIC mission were compared to the simulation output obtained from a single-pair mission with GRACE-FO instrument accuracy. The ratio of the RMSD of the single-pair vs. the double-pair mission is shown in Figure 47-4 on grid cell level and in Figure 47-5 on the level of river basin averages. The polar regions in Figure 47-2 show an increase of the RMSD for MAGIC, all other regions exhibit a strong decrease with a mean ratio of 41 for N=67 (max=217) and 5.7 (max=13) for N=33.
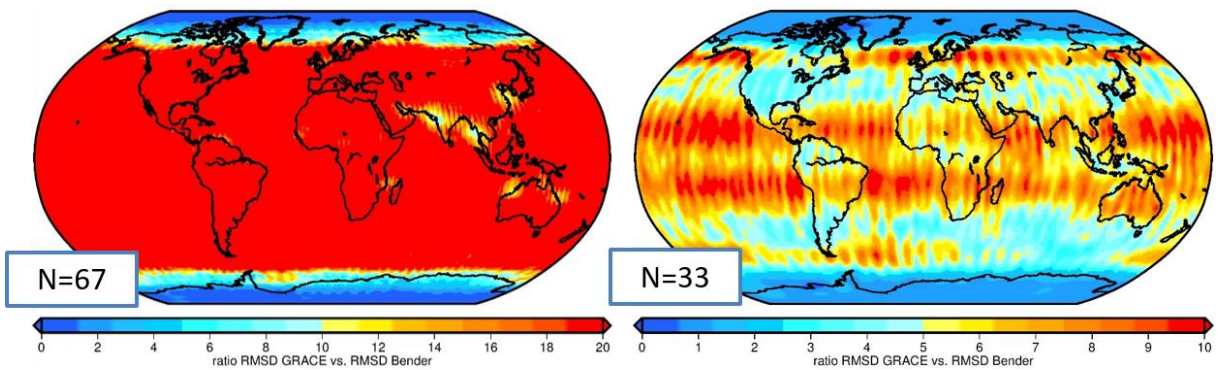
Figure 47-4: Ratio of RMSD of GRACE-like single-pair mission vs. RMSD of a MAGIC-like double pair mission for each grid cell.
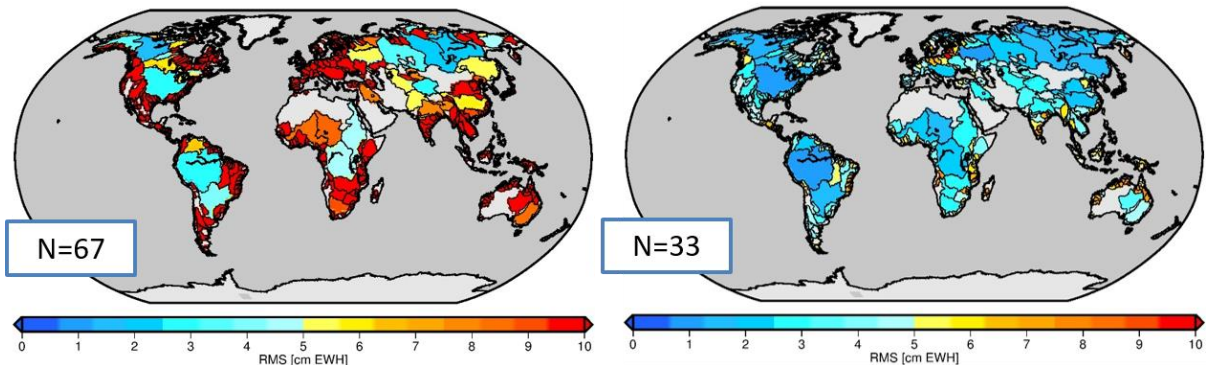
Figure 47-5: Ratio of RMSD of GRACE-like single-pair mission vs. RMSD of a MAGIC-like double pair mission for each river basin.

For a better overview of the numbers (RMSD and ratio of RMSD) computed for the individual basins, scatter plots were created in addition to the maps. Figure 47-6 (left) shows each of the RMSD values in relation to the size of the respective river basin for the different mission scenarios (GRACE vs. MAGIC) and for the two selected spatial resolutions of 600km (N=33) and 300km (N=67). A clear improvement is visible for the double-pair mission. To better quantify the improvement, the ratio of each RMSD value (GRACE vs. MAGIC) is shown in Figure 47-6 (right). For the lower spatial resolution, the RMSD is reduced by factors between 1.1 and 9.9 for the MAGIC constellation and for the higher spatial resolution, these factors are in the range between 10 and 60 for most basins. However, it should be noted that the unfiltered solutions are strongly corrupted by noise in the higher degrees.
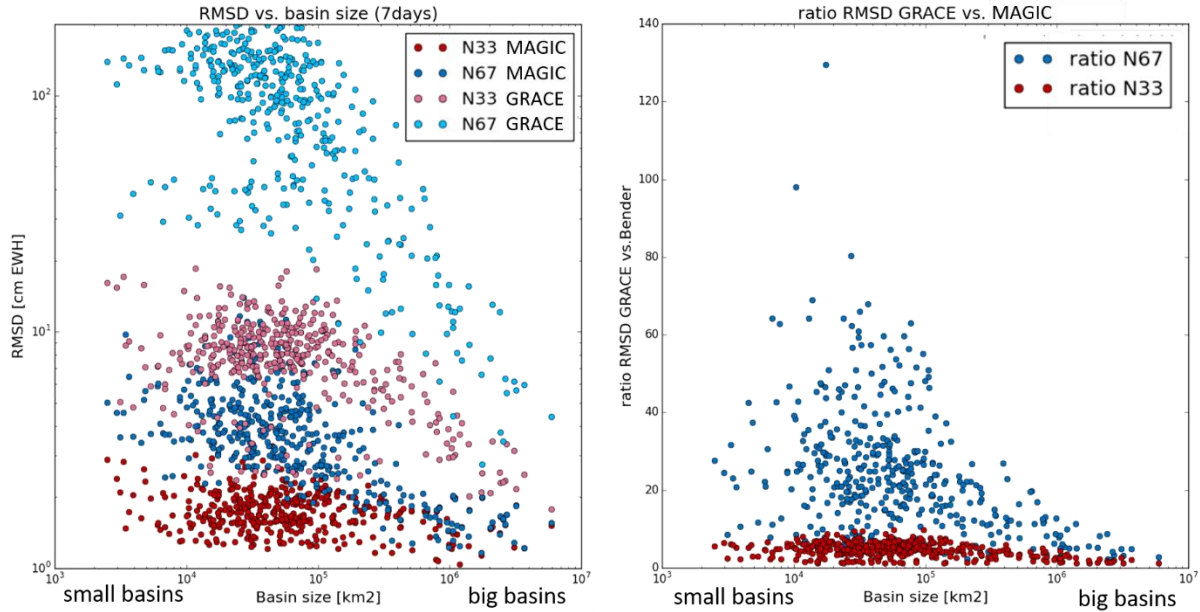
Figure 47-6: Scatter plot of RMSD of basin average time series vs. size of the river basin for different mission scenarios and spatial resolutions (left) and ratio of RMSD for each basin of GRACE constellation vs. MAGIC constellation.

In the results shown above, the envisaged spatial resolution of the provided 7-days solutions and the corresponding threshold accuracies were derived from the daily values given in the MRD (see below). In the meantime, it was decided for this project that deriving these quantities from the monthly accuracies is more reasonable. We thus compute 7-day accuracies via error propagation from the monthly values according to Figure 47-7.

Figure 47-7: Threshold for hydrological applications regarding different spatial resolutions (from MRD, Table 4) and the corresponding values derived for 7-days solutions by error propagation from the monthly values.

For the different spatial resolutions mentioned in the MRD for the monthly thresholds (400km corresponding to a truncation at spherical harmonics degree N=50 and 260km corresponding to truncation at N=77), the investigation of the error RMS (i.e., the temporal RMS of the difference between the unfiltered 7-days simulation result and the ESA-ESM model) was repeated both on grid cell level and for basin averages in the 405 largest river basins. Furthermore, the investigations were extended to cover the alternative orbit scenarios 5d_Ma and 5d_Mb in addition to the previously used 3d_H scenario.

Figure 47-8 shows the corresponding grid cell RMSD for the different scenarios. The improvement achieved by the MAGIC constellations compared to a GRACE-like mission is again strongly visible. Furthermore, the different error characteristics of the orbit constellations become evident. The 5d_Ma scenario (i.e., a lower inclination inclined pair compared to 3d_H) appears favorable for applications in continental hydrology (at least in lower to mid latitudes) as it shows the smallest residuals on large parts of the continents (but, of course, larger errors in the polar regions).
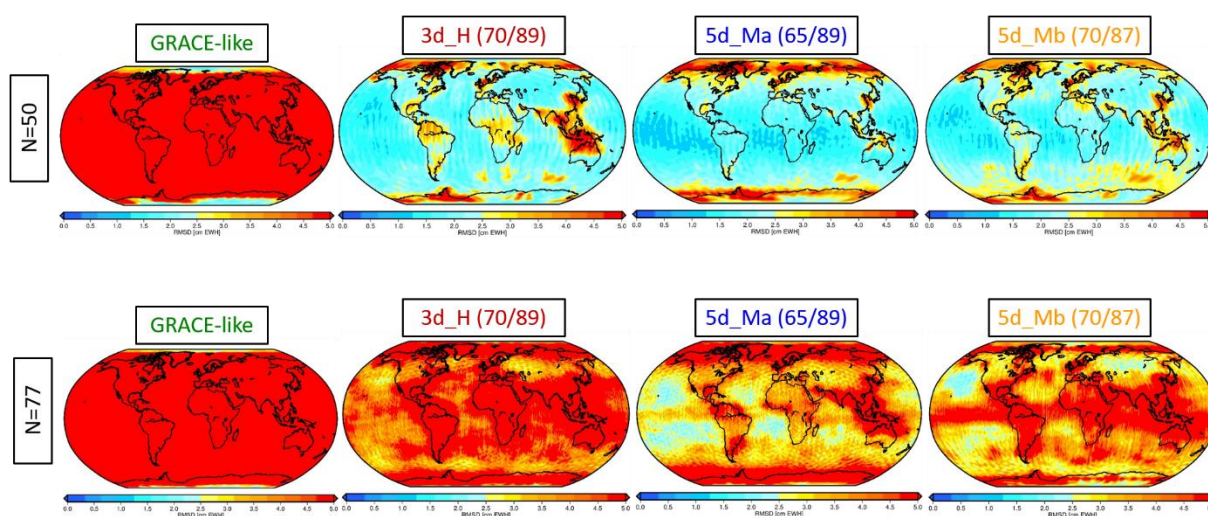
Figure 47-8: Temporal RMSD of 7-days simulation output (for different mission scenarios) and reference solution truncated at degree N=50 (i.e. 400 km spatial resolution, top) and N=77 (i.e. 260km spatial resolution, bottom).

	Final Report	
NGGM/MAGIC – Science Support Study During Phase A	Doc. Nr:	MAGIC_FR
	Issue:	1.0
	Date:	15.11.2022
	Page:	382 of 466

The conclusions derived on grid cell level are confirmed by the basin average analysis shown in Figure 47-9. Again 5d_Ma results in smaller errors in the lower to mid-latitude river basins with the drawback of an increase in the residuals towards higher latitudes.
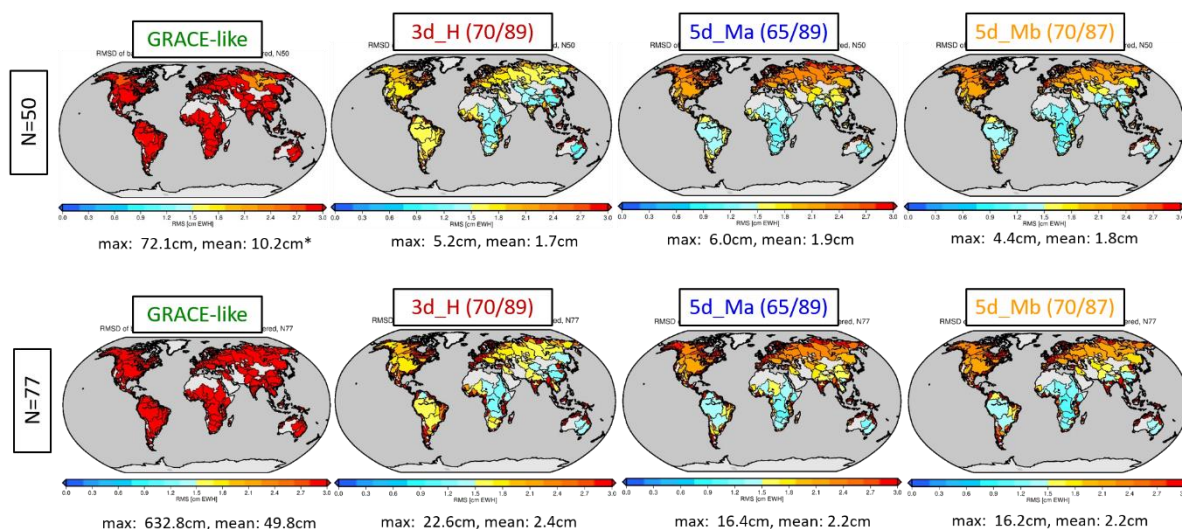
Figure 47-9: Temporal RMSD of 7-days simulation output (for different mission scenarios) and reference solution truncated at degree N=50 (i.e. 400 km spatial resolution, top) and N=77 (i.e. 260km spatial resolution, bottom) for GRDC basin averages.

A summary of the basin average RMSD values is presented in the scatter plot in Figure 47-10 for both spatial resolutions (400km => N=50 and 360km => N=77). A horizontal line representing the threshold accuracy of the respective spatial resolution (1.05cm for N=50 and 10.1cm for N=77) was added. The vertical blue line represents the size of a spherical cap with 400km diameter (i.e. ~125,600km^2) to very roughly indicate the size of a river basin of the same spatial resolution. It can be seen that for the lower resolution (400km, left plot of Figure 47-10) the accuracy demand of the MRD can hardly be fulfilled by the unfiltered 7-days solutions for any of the river basins. Signals in river basins below this threshold are difficult to isolate from the surroundings and for larger spatial units the computation of a basin average represents an additional spatial smoothing. Please note that this is only a rough indication since river basins can have strongly differing extend, e.g. elongated basins in north/south or east/west direction. However, even for the largest basins the RMSD is above the threshold accuracy. Nevertheless, also this scatter plot again stresses the strong improvement of MAGIC results over a GRACE-like mission, as the GRACE errors are an order of magnitude bigger compared to the different MAGIC scenarios. For the higher spatial resolution (right plot of Figure 47-10) the threshold accuracies appear to be more relaxed and therefore probably more realistic, as they can be reached by all the mission scenarios for most river basins. The only exceptions of RMSD values above the horizontal threshold line are basins with an area smaller than the one corresponding to a spherical cap of 260km diameter (i.e. ~53,100km^2) shown on the left of the vertical blue line in the right part of Figure 47-10.

Figure 47-10: RMSD of basin averages for GRDC river basins truncated at N= 50 (left) and N=77 (right). Threshold requirement for the corresponding spatial resolutions (400km and 260km, respectively) are indicated by the blue horizontal lines. Numbers below the figure indicate the number of basins with RMSD values below the threshold. The vertical blue lines represent the spatial extent of spherical caps with 400km and 260km diameter, respectively.

The results shown before are derived using the unfiltered 7-day solutions. However, in hydrological applications most likely filtered solutions will be applied. The comparison of filtered vs. non-filtered solutions is illustrated with the help of degree amplitude plots for an exemplary 7-days solution in Figure 47-11. The unfiltered solutions (left plot) are strongly dominated by noise, even when truncated at degree N=50 or (even more so) degree N=77. Even for N=50 the residuals of both the GRACE (dark green) and the MAGIC (dark red) simulations are above the signal line (black). For the filtered solutions (right plot, here shown for VADER filtered solutions optimized individually both for the GRACE and the MAGIC scenarios) the difference between input and simulation strongly depends on the filter omission error.
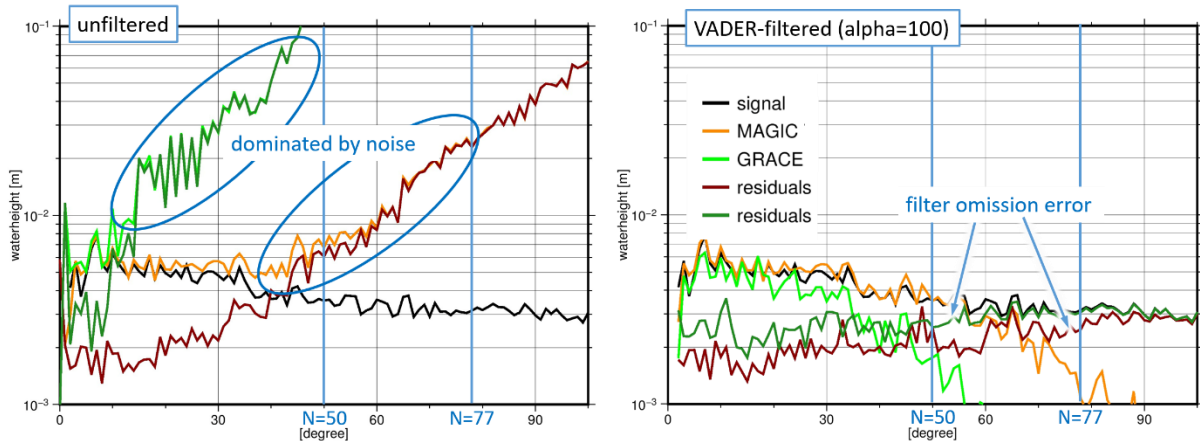
Figure 47-11: Degree amplitudes of one exemplary 7-days solution (January 1-7, 2002) for the unfiltered (left) and filtered (right) simulation output.

As filtered solutions will more likely be used by the hydrologic community, we additionally provide the RMSD values on grid cell and basin average level for the optimally VADER-filtered solutions (alpha=100, truncated at N=50) in Figure 47-12. The error made by smoothing also part of the signal in addition to reducing the noise is accounted for by the filter omission error. The filtered solutions are compared to the unfiltered reference signal. Since the differences between the different MAGIC scenarios are small (see above), here only the results for the 3d_H constellation are shown. These RMSD values include the filter omission error as the RMSD values are computed between the filtered simulation output and the unfiltered ESA-ESM input time series. A comparison with Figure 47-8, Figure 47-9, and Figure 47-10 shows the effect of the filtering.
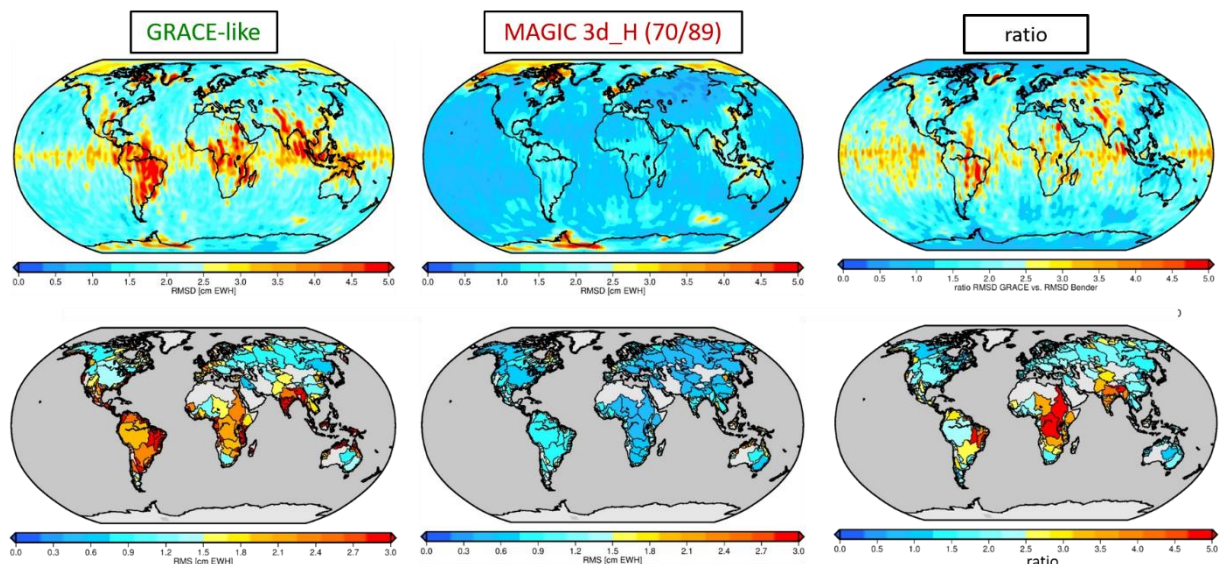
Figure 47-12: Temporal RMSD of 7-days simulation output and reference solution truncated at degree N=50 (i.e. 400 km spatial resolution) for VADER-filtered solutions for grid cells (top) and GRDC basin averages (bottom).
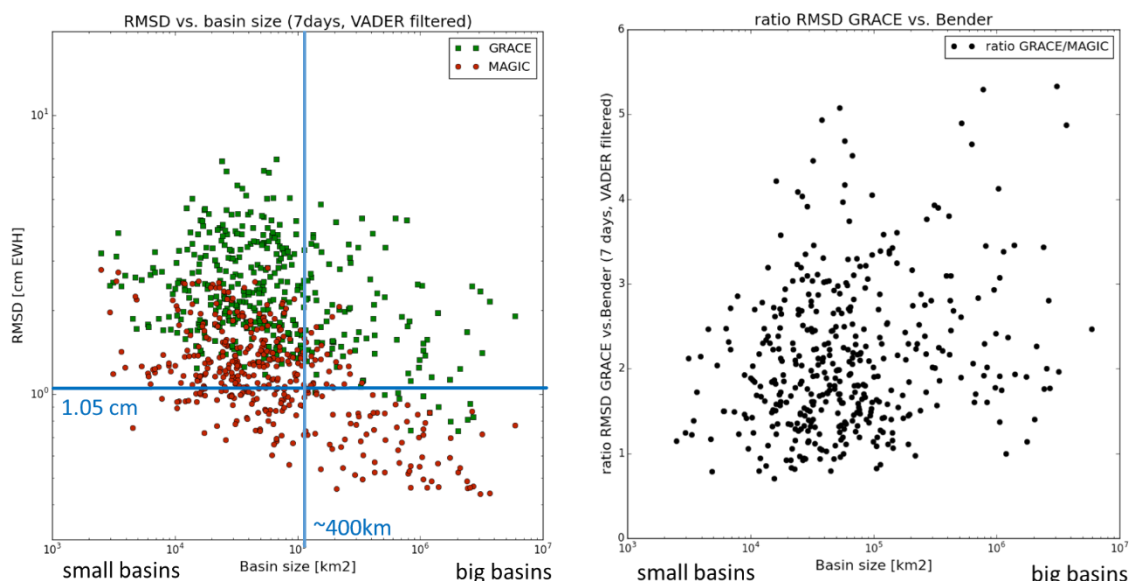
NGGM/MAGIC – Science Support Study During Phase A	Final Report	
	Doc. Nr:	MAGIC_FR
	Issue:	1.0
	Date:	15.11.2022
	Page:	385 of 466

Figure 47-13: RMSD of VADER-filtered solutions for basin averages for GRDC river basins truncated at N= 50 (left). The threshold requirement for the corresponding spatial resolution (400km) is indicated by the blue horizontal line. The vertical blue lines represent the spatial extent of spherical caps with 400km diameter. Additionally, the right plot shows the ratio of the GRACE vs. the MAGIC RMSD values.

The corresponding scatter plots for the river basins are shown for the filtered solutions in Figure 47-15 (left). Again, the blue horizontal line indicates the threshold requirement corresponding to a spatial resolution of N=50 and the vertical line a spherical cap with 400km diameter. For the MAGIC mission, a large number of basins (i.e. 150/405) meet the threshold requirements with most basins that do not have a size smaller than the one corresponding to a spherical cap with 400km diameter (vertical blue line). The histogram in Figure 47-14 summarizes the scatter plot and shows again the improvement of the MAGIC over the GRACE-like scenario. Figure 47-13 (right) additionally shows the ratio of the GRACE errors vs. the MAGIC errors, thus the factor of improvement of the RMSD for each river basin. For these optimally filtered solutions these improvements are by a factor of about 1.5-5.
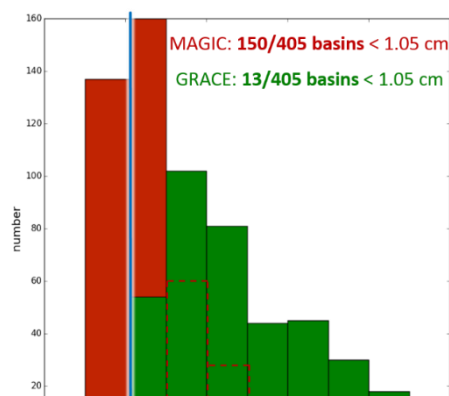
Figure 47-14: Histogram of RMSD of basin averages corresponding to the scatter plot in Figure 47-13: RMSD of VADER-filtered solutions for basin averages for GRDC river basins truncated at N= 50 (left). The threshold requirement for the corresponding spatial resolution (400km) is indicated by the blue horizontal line. The vertical blue lines represent the spatial extent of spherical caps with 400km diameter. Additionally, the right plot shows the ratio of the GRACE vs. the MAGIC RMSD values.

(left)

Conclusions

In conclusion, the MAGIC constellation will provide significant added value to hydrological applications because the number of hydrological units (here river basins) that can be analysed for water storage variations respecting certain accuracy requirements will markedly

increase compared to a GRACE-like mission (Table 47-1 and Figure 47-15). The threshold accuracy currently given in the MRD for hydrological applications at a comparatively high spatial resolution (10.1 cm at N=77) can be fulfilled by MAGIC 3d_H (and similarly for 5d_Ma and 5d_Mb) for more than 90% of the river basins worldwide when considering unfiltered solutions. Even higher accuracies that may be required for several hydrological applications can be met in a large number of basins (Table 47-1 right columns). In contrast, the current MRD at the lower spatial resolution of 400km cannot be met by MAGIC for any river basin. However, relaxing this threshold accuracy to 2.5 cm or 3.5 cm which can be expected to be still acceptable for many hydrological applications, will allow for resolving TWS variations in 67% and 90% of the river basins, respectively. Assuming error propagation according to the $\sqrt{n}$, the weekly numbers can be transformed into monthly values of threshold requirements of 1.2 cm and 1.7 cm, respectively. For filtered solutions, the improvement of MAGIC relative to GRACE in terms of RMSD errors of basin-average water storage variations worldwide amounts to a factor of 1.5 to 5 for the weekly simulations.

Table 47-1: Number of river basins that meet different accuracy thresholds for two spatial resolutions and the 7-day temporal resolution. The monthly threshold requirements of the current MRD converted into 7-day accuracies (following Figure 47-7) are given in the grey boxes.

N=50 (400 km)			N=77 (260 km)		
Threshold [cm]	Number of basins 3d_H	Number of basins GRACE	Threshold [cm]	Number of basins 3d_H	Number of basins GRACE
3.50	90% (366/405)	2.5% (10/405)	10.1	91% (370/405)	2.5% (10/405)
2.50	67% (270/405)	0.5% (2/405)	6.1	67% (273/405)	0.5% (2/405)
1.05	0% (0/405)	0% (0/405)	2.5	17% (69/405)	0% (0/405)
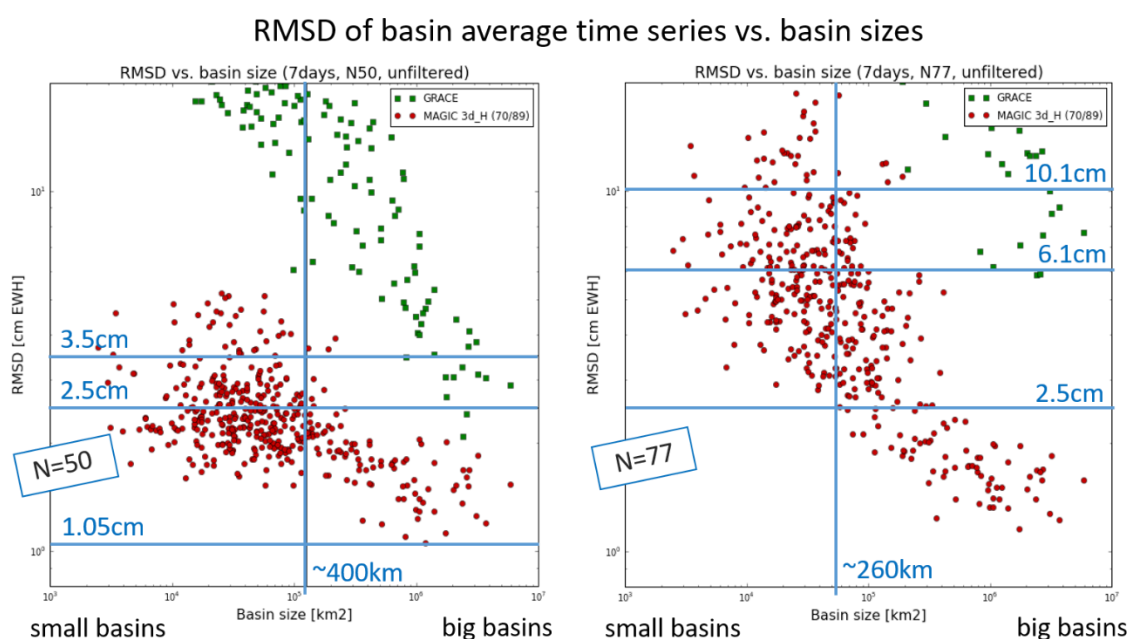
Figure 47-15: RMSD of basin averages for GRDC river basins truncated at N= 50 (left) and N=77 (right). The different accuracy requirements for the corresponding spatial resolutions (400km and 260km,

respectively) as given in Table 47-1 are indicated by the blue horizontal lines. The vertical blue lines represent the spatial extent of spherical caps with 400km and 260km diameter, respectively.

47.2 ICE MASS CHANGES

We assessed the performance of the different mission configurations in mass change applications related to the cryosphere. We focused on the ice sheets of Greenland (GrIS) and Antarctica (AIS), which were each subdivided into smaller regions, based on ice prominence, flow direction of the ice, and climatological settings. For Antarctica, the basin definition of [RD-19] was used, dividing the ice sheet into 27 regions; For Greenland, 6 regions were defined based on [RD-18]. These regions were further subdivided into the ablation and accumulation zone (see Figure 47-16). In the former, net mass loss occurs (typically because summer melt water runoff exceeds snow accumulation), whereas the latter exhibits a net mass gain. The dominant processes are very different from a physical point of view, and an improved retrieval of the mass changes in these two subregions is of high scientific relevance (e.g., [RD-17]). The division of the ablation/accumulation zone was approximated using the 2000-meter elevation contour. In Antarctica, surface melt contributes minimally to mass changes, hence, a similar subdivision of the regions was not made for this ice sheet.
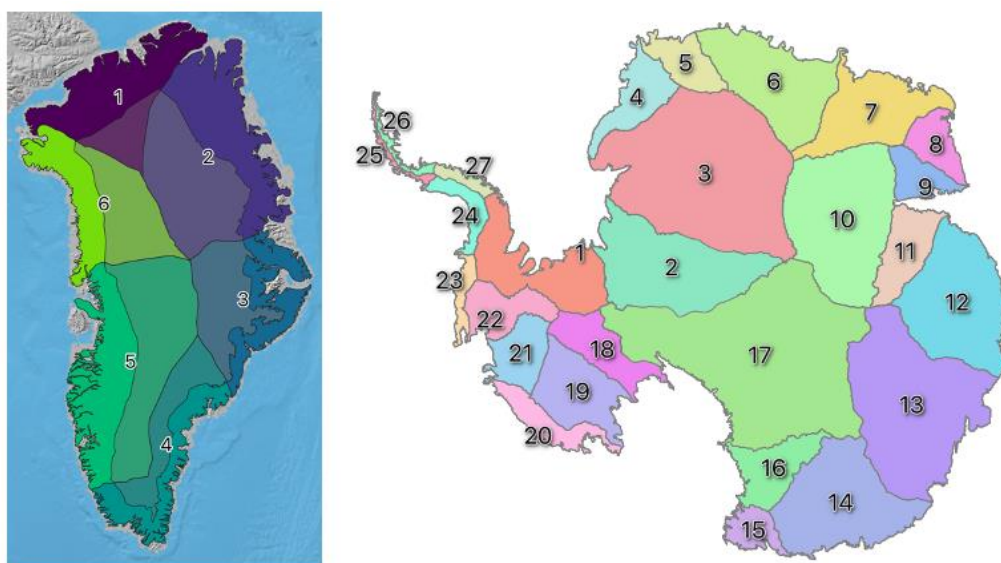
Figure 47-16: Basin definitions for Greenland (left) and Antarctica. For Greenland, each of the 6 basins was further divided in an accumulation and ablation zone.

The performance of four different mission configurations was studied: one GRACE/GRACE-FO-like, single-pair configuration, and three Bender double-pair configurations with varying altitudes and inclinations of the polar and inclined pair:

Table 47-2: Overview of dual-pair mission configurations considered in this scientific case study.

Configuration	Altitude inclined pair [km]	Inclination inclined pair [deg]	Altitude polar pair [km]	Inclination polar pair [deg]
3d_H	432	70	463	89

5d_Ma	396	65	434	89
5d_Mb	397	70	425	87

For each of the four scenarios, 52 weekly simulated solutions were provided in this project, based on the expected signal from the HIS model and a noise model. For the GRACE-like configuration spherical harmonic up to degree/order 100 were provided, for the dual pair configurations the maximum degree/order was set to 120. Furthermore, for all configurations spherical harmonics post-processed with the VADER-filter [RD-16] were made available as well. For the 5d_Ma and 5d_Mb configurations, solutions with a weak ($\alpha = 10$) and strong ($\alpha = 100$) VADER filtering were provided.

To retrieve the mass variations of the ice sheets and their (sub)regions, two approaches were used. First of all, the method of [RD-2], in which the spherical harmonics are transformed to surface mass loading anomalies. Subsequently, modelled mass anomalies in the (sub)regions are adjusted iteratively, until convergence is reached with the input mass anomalies from the simulation. Secondly, the mascon approach of [RD-3] synthesisis gravity disturbances at predefined points positioned at a specific satellite altitude, which are then converted into localized mass anomalies through a linear functional model which uses the variance-covariance matrix in its weighting. Since both methods yielded comparable results, it was decided to proceed with the method of [RD-2] for computational efficiency.

To assess the performance of the different mission configurations, the time series of mass variations retrieved from the simulations were compared to the *truth* signal, retrieved from the HIS model (i.e., without the noise component, provided up to degree/order 180). Time series for all basins were plotted for a qualitative assessment. For a quantitative analysis, the root-mean-square error was computed based on the difference between the simulated and *truth* time series.

The key question to be answered is if the proposed configurations meet the threshold and/or target accuracies specified in the Mission Requirements Document, listed in Table 47-3.

Table 47-3: User requirements for the cryosphere specified in the Mission Requirements Document

Thematic field	Time scale D: Daily to weekly; M: Monthly; L: Long-term trend	Threshold: Resolution & Accuracy [EWH]	Target: Resolution & Accuracy [EWH]
Cryosphere	D	Threshold-a: 400 km @ 5.0 cm; Threshold-b: 300 km @ 5.9 cm; Threshold-c: 250 km @ 6.3 cm	Target-a: 400 km @ 0.5 cm; Target-b: 300 km @ 0.6 cm; Target-c: 250 km @ 0.6 cm
	M	Threshold-a: 250 km @ 5.5 cm; Threshold-b: 150 km @ 50.0 cm	Target-a: 250 km @ 0.55 cm; Target-b: 150 km @ 5.0 cm
	L	Threshold-a: 170 km @ 2.6 cm/yr; Threshold-b: 130 km @ 15.0 cm/yr	Target-a: 170 km @ 0.26 cm/yr; Target-b: 130 km @ 1.5 cm/yr

In this study, we focused on the objectives for the monthly time scales. Since the simulated solutions were delivered at weekly intervals, we applied a scaling to the monthly

threshold/target accuracies, assuming that the noise in each weekly solution can be seen as an independent realization from a normal distribution with zero mean. In such a case, the monthly accuracies can be scaled by a factor of $\sqrt{31/7}{=}2.1$ to find the corresponding threshold/target accuracies at weekly time scales.

A can be seen from Table 47-3, the accuracy objectives are linked to varying spatial resolutions, which dictate the maximum degree and order of the spherical harmonics used in the mass retrieval algorithms. For example, for a spatial resolution of 250 km, the maximum degree/order was set at 80 (= 20 000 / 250). For spatial resolutions of 166 km or finer, the maximum degree/order was set to 120, since higher coefficients were not available in the simulations.

Results - Unfiltered solutions

The root-mean-square error (RMSE), based on the difference between the mass variations in the simulations and the HIS model are shown in Figure 47-17. At mid-latitudes, the bender configurations show an RMSE which is an order of magnitude lower than that of the GRACE-like configuration. At higher latitudes, both the 3d_H and 5d_Ma configuration display a pronounced band of increased RMSE, which exceeds that of the GRACE-like configuration substantially in many locations. Additional simulations have shown this to be an artefact of the Bender constellation at the transition zone between the two pairs, which can be treated by regularization. In the Southern Hemisphere, this band of increased RMSE parts of Antarctic Ice Sheet. In the north, overlap can be observed not only with the northernmost parts of the Greenland Ice Sheet, but also with important, large glacier regions such as the Canadian Arctic, Svalbard and the Russian Arctic.

Figure 47-18 is identical to Figure 47-17, with the exception that only coefficients up to degree/order 80 are used. The amplitude of the zonal band in the polar regions is markedly reduced in configuration 3d_H, and even more so in configuration 5d_Ma. This indicates that the zonal RMSE can be largely attributed to noise of the higher coefficients in these configurations.

From this visual interpretation, it can be expected that the 3d_H and 5d_Ma configurations will show a degraded performance in retrieving mass variations compared to the 5d_Mb configuration, especially at smaller spatial scales.
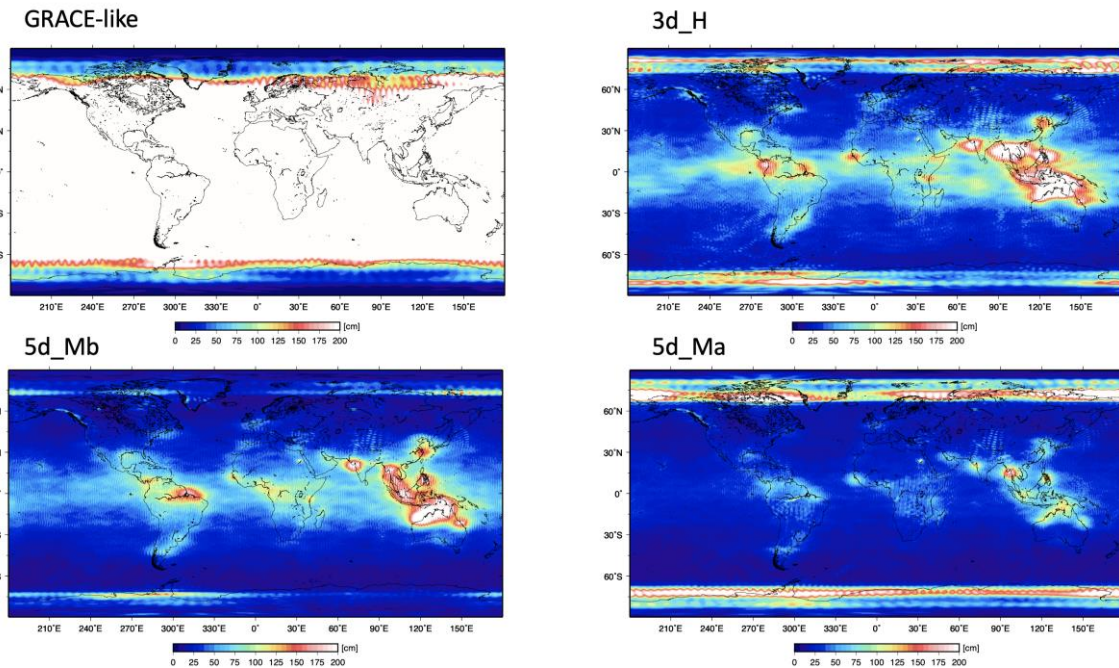
Figure 47-17: Root mean square of the difference between mass variations in the simulations and the HIS model, in cm equivalent water height, for the four different mission scenarios. Coefficients up to degree/order 120 were used in the simulations.
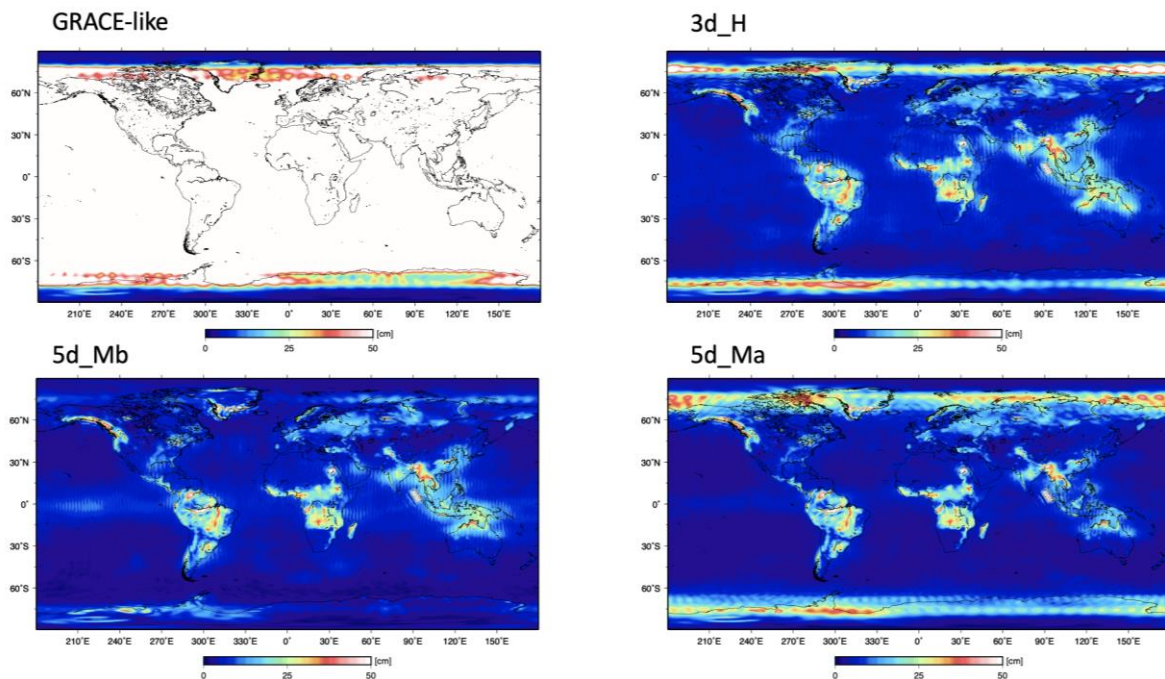
Figure 47-18: As in Figure 47-17, but using coefficients up to degree/order 80 in the simulations.

This is further illustrated in Figure 47-19, which shows the mass variations in the accumulation zone of Greenland basin 2. Independent of the maximum degree/order of the coefficients used, configuration 5d_Mb lies closest to the *truth* signal in the HIS model. For a maximum degree/order of 80, the 5d_Ma and 3d_H configurations perform marginally better than what can be achieved with a GRACE-like mission. Increasing the maximum degree/order to 120 results in an RMSE for these to configurations which is an order of magnitude larger than what

is found for the 5d_Mb configuration. Similar conclusions can be drawn for the Antarctic Ice Sheet, as illustrated in Figure 47-20 for the Northern Antarctic Peninsula (basins 25 & 26).
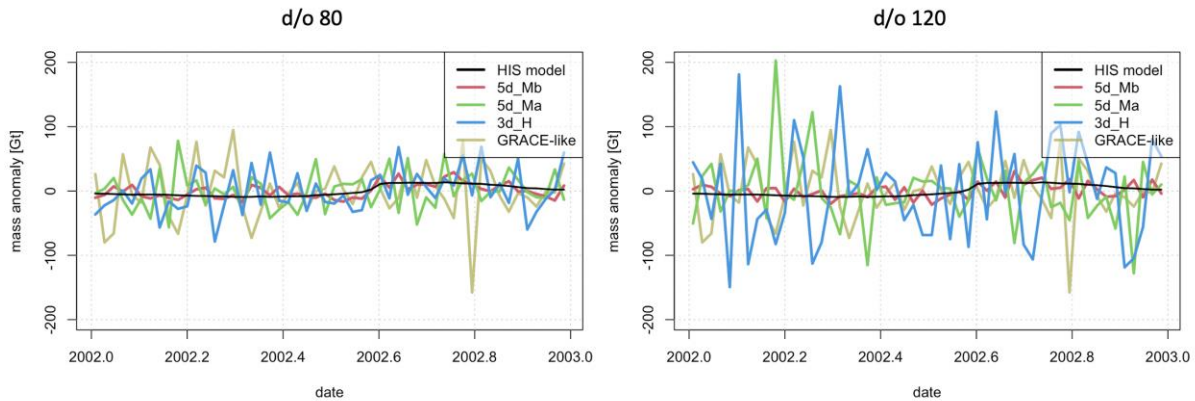
Figure 47-19: Mass variations in the accumulation zone of Greenland basin 2 simulated by the HIS model and retrieved from the 4 mission configurations simulations. Left figure shows results for maximum degree/order 80 (approx. 250 km resolution) and 120 (approx. 166 km resolution), respectively.
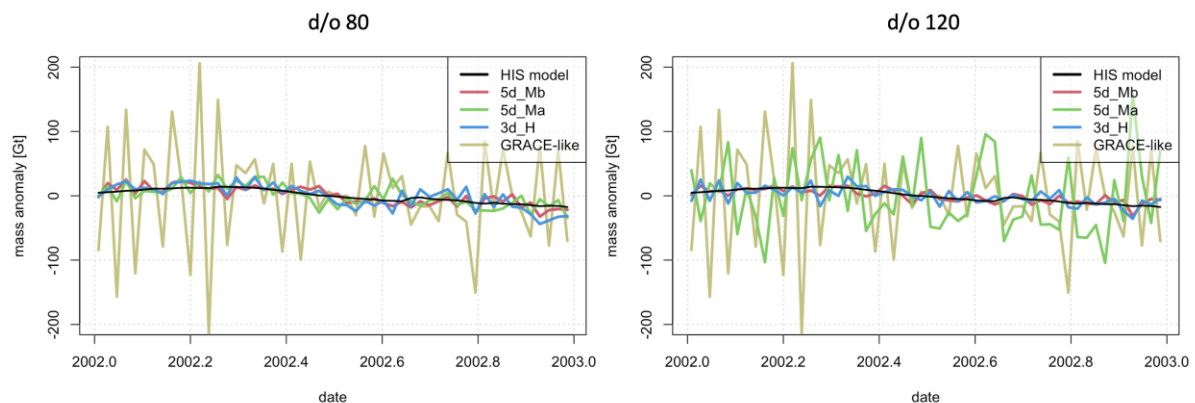
Figure 47-20: similar to Figure 47-19, but for the Northern Antarctic Peninsula (Antarctica basins 25 & 26)

Figure 47-21 and Table 47-4 summarize the performance of the four configurations with respect to the threshold and target criteria for a spatial resolution of 250 km at monthly time scales. For configuration 5d_Mb, the threshold of 5.5 cm RMSE is met for 40 out of the 45 basins. As can be seen in Figure 47-21, basins not passing the threshold for this configuration generally have areas smaller than approximately 62 500 (250 x 250) km^2. On Greenland, the 5.6 cm RMSE of the accumulation zone of region 1 is just above the threshold. In Antarctica, the basins exceeding the threshold are all located on the Peninsula (basin 24-27). For the 5d_Ma and 3d_H configurations, the threshold is exceeded for larger basins, at approximately 200 000 km^2. The 3d_H configuration performs slightly better than 5d_Ma, with basins 32 and 29 passing the criterion, respectively. Still, both outperform a single-pair configuration (20 basins). When considering the target criterion, very few basins pass. Again, the 5d_Mb configuration performs best, but even there 5 out of 45 basins meet the requirements.

Table 47-4: Number of basins for which the monthly threshold and target criteria are met for the four different configurations, using coefficients up to degree/order 80, corresponding to a spatial resolution of approximately 250 km.

Configuration	Threshold (5.5 cm RMSE)		Target (0.55 cm RMSE)	
	GrIS	AIS	GrIS	AIS
GRACE-like	5 /18	15 /27	0 /18	2 /27
5d_Mb (70/87 deg)	17 /18	23 /27	0 /18	5 /27
5d_Ma (65/89 deg)	10 /18	19 /27	0 /18	3 /27
3d_H (70/89 deg)	11 /18	21 /27	0 /18	3 /27

Figure 47-21: RMS difference for each of the GrIS (dots) and AIS (triangles) basins as a function of their area, for all four configurations. Only coefficients up to degree/order 80 were used, corresponding to a spatial resolution of approximately 250 km. The dotted and dashed-dotted line indicate the (scaled) target and threshold RMS criteria at monthly time scales, respectively.

When considering a higher spatial resolution of 166 km (maximum degree/order 120), similar conclusions hold. Again, the 5d_Mb configuration performs best, with all the basins meeting the (less stringent) threshold criterion of 50 cm RMSE. Configuration 3d_H performs almost equally well, whereas 5d_Ma and the single-pair configurations show a comparable performance, in terms of number of basins passing the criterion (Figure 47-22 and Table 47-5). Compared to the 250 km results discussed above, more of the basins also meet the target criterion, with 5d_Mb configuration again outperforming the other constellations.

RMSD vs basin size (7 days, d/o 120, no filter)
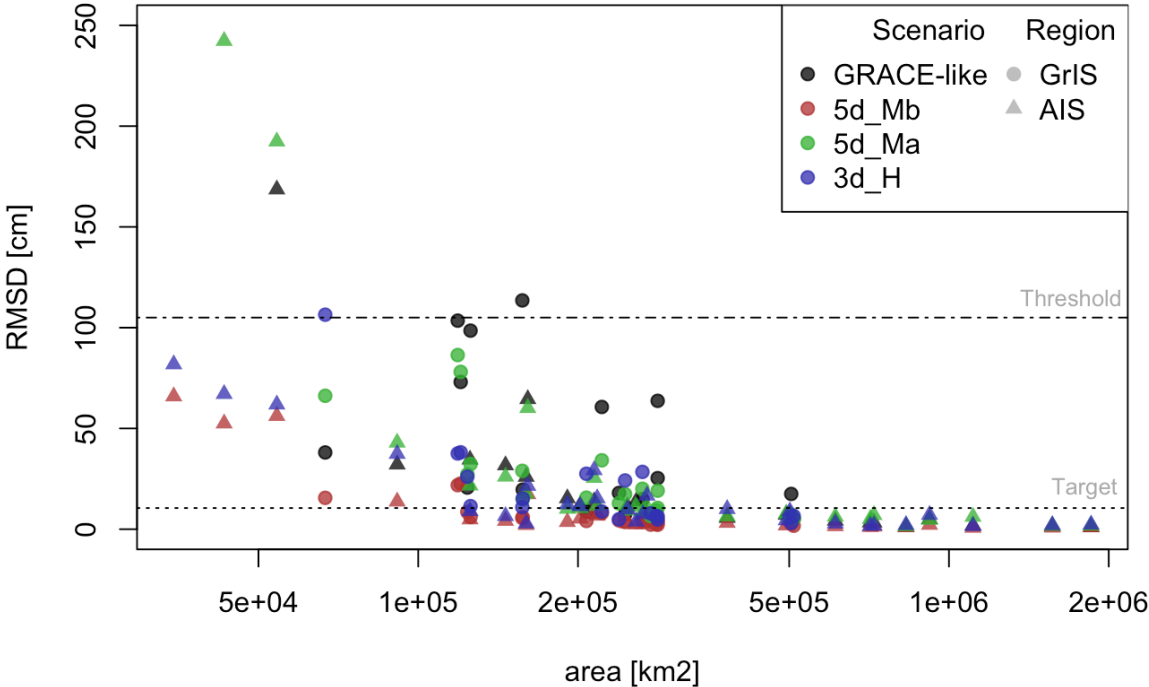
Figure 47-22: As Figure 47-21, but for a spatial resolution of 166 km (maximum degree/order 120).

Table 47-5: As Table 47-4, but for a spatial resolution of 166 km (maximum degree/order 120).

Configuration	Threshold (50 .0 cm RMSE)		Target (5.0 cm RMSE)	
	GrIS	AIS	GrIS	AIS
GRACE-like	17 /18	24 /27	5 /18	14 /27
5d_Mb (70/87 deg)	18 /18	27 /27	15 /18	22 /27
5d_Ma (65/89 deg)	18 /18	24 /27	4 /18	15 /27
3d_H (70/89 deg)	17 /18	27 /27	8 /18	17 /27

Results - Filtered solutions

Figure 47-23, Figure 47-24, Table 47-6 and Table 47-7 summarize the performance of the configurations, after applying a post-processing filter to the coefficients, as is general practice currently. Doing so drastically decreases the RMSE for all basins and configurations, including the single-pair constellation. In fact, at a 166 km resolution, the GRACE-like configuration performs better than the double-pair concepts. Furthermore, at a 250 km resolution, the RMSE for basins on the Antarctic Peninsula is significantly lower than in the other configurations (see triangles on the left side of Figure 47-23 and Figure 47-24). This may be due to the fact that the VADER filter was specifically optimized for the GRACE mission [RD-16]. It is recommended that further analysis is undertaken in optimizing the filter parameters for the double-pair

constellations. Overall, after filtering, the threshold criteria are met for all basins for the double-pair configurations, except for those on the Antarctic Peninsula.
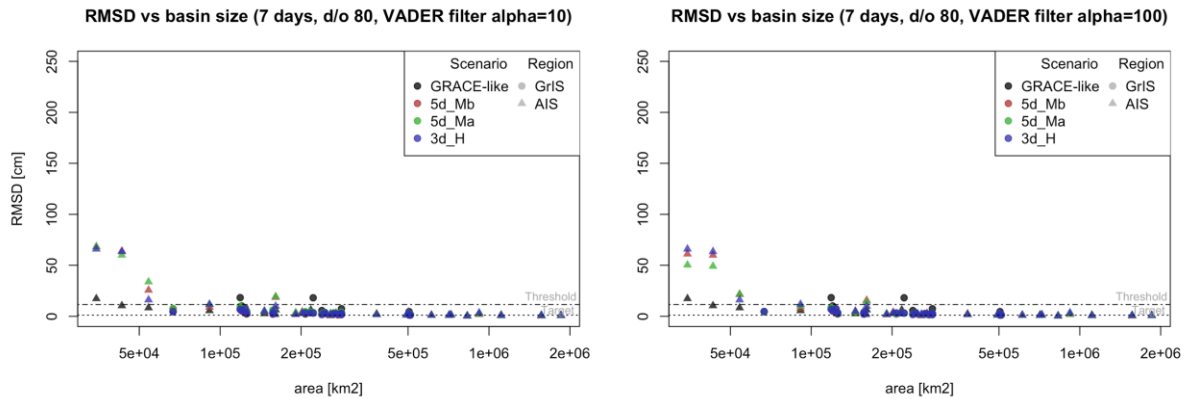
Figure 47-23: RMS difference for each of the GrIS (dots) and AIS (triangles) basins as a function of their area, for all four configurations, when filtering the solutions with the VADER filter (left: α = 10; right: α = 100). Only coefficients up to degree/order 80 were used, corresponding to a spatial resolution of approximately 250 km. The dotted and dashed-dotted line indicate the (scaled) target and threshold RMS criteria at monthly time scales, respectively.
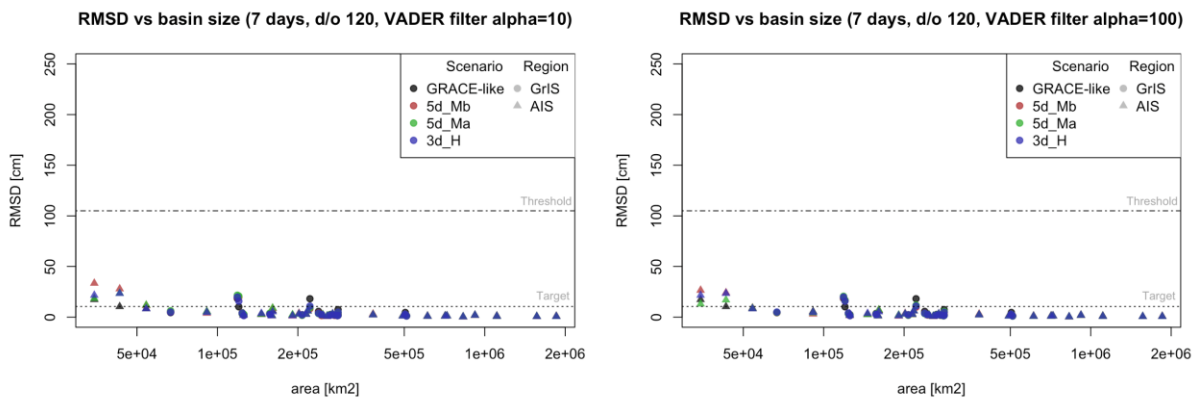
Figure 47-24: As Figure 47-23, but for a spatial resolution of 166 km (maximum degree/order 120).

Table 47-6: Number of basins for which the monthly threshold and target criteria are met for the four different configurations, when filtering the solutions with the VADER filter, using coefficients up to degree/order 80, corresponding to a spatial resolution of approximately 250 km.

Configuration	Threshold (5.5 cm RMSE)		Target (0.55 cm RMSE)	
	GrIS	AIS	GrIS	AIS
GRACE_like VADER	16 /18	26 /27	1 /18	5 /27
5d_Mb VADER α = 10 (70/87 deg)	18 /18	23 /27	0 /18	5 /27
5d_Ma VADER α = 10 (65/89 deg)	18 /18	23 /27	0 /18	5 /27
5d_Mb VADER α = 100 (70/87 deg)	18 /18	23 /27	0 /18	5 /27
5d_Ma VADER α = 100 (65/89 deg)	18 /18	23 /27	0 /18	6 /27
3d_H VADER (70/89 deg)	18 /18	23 /27	0 /18	6 /27

Table 47-7: As Table 47-6, but for a spatial resolution of 166 km (maximum degree/order 120).

Configuration	Threshold (50 cm RMSE)		Target (5 cm RMSE)	
	GrIS	AIS	GrIS	AIS
GRACE-like VADER	18 /18	27 /27	16 /18	26 /27
5d_Mb VADER α = 10 (70/87 deg)	18 /18	27 /27	16 /18	24 /27
5d_Ma VADER α = 10 (65/89 deg)	18 /18	27 /27	16 /18	24 /27
5d_Mb VADER α = 100 (70/87 deg)	18 /18	27 /27	16 /18	25 /27
5d_Ma VADER α = 100 (65/89 deg)	18 /18	27 /27	15 /18	25 /27
3d_H VADER α = (70/89 deg)	18 /18	27 /27	15 /18	25 /27
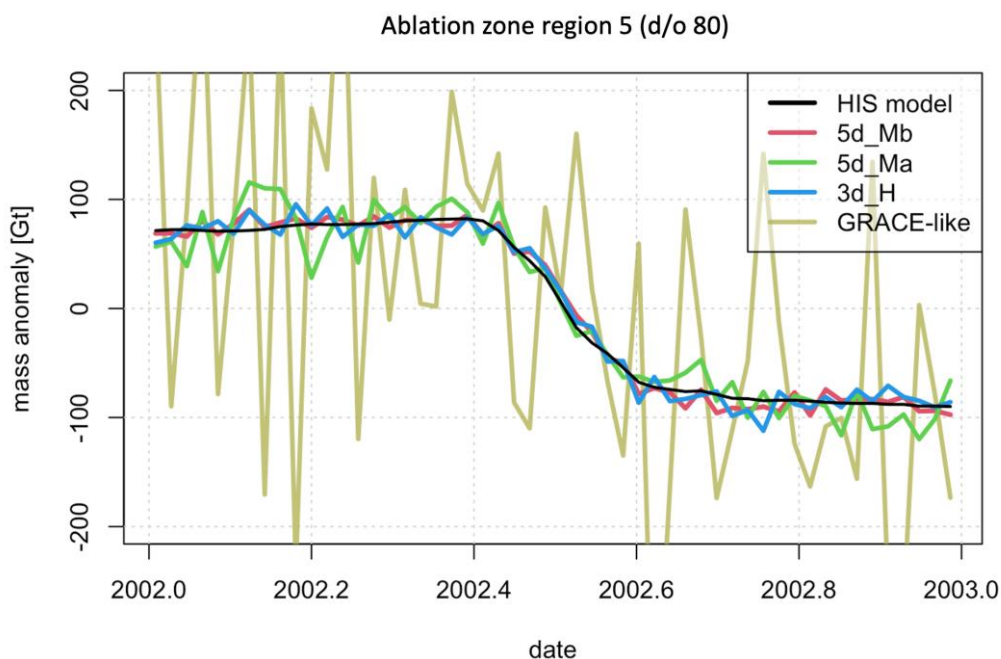
Figure 47-25: Mass variations in the ablation zone of Greenland basin 1 simulated by the HIS model and retrieved from the 4 mission configurations simulations.

Conclusions

Our analysis shows that the double-pair configurations proposed for a Next Generation Gravity Mission will drastically improve our ability to monitor mass displacements on the ice sheets compared to what is currently possible. For example, our results show that it should be feasible to separate mass signals in the interior from those in the coastal zones, which is of high scientific interest (see Figure 47-25). Overall, the 5d_Mb configuration shows the best performance, with the largest number of basins passing the threshold and target criteria and the lowest RMSE (see Table 47-3 and Table 47-4). This can be attributed to the altitude of the polar pair which is at 425km for 5d_Mb and 463km for 3d_H. At a 250 km resolution, the threshold accuracy for monthly time scales (5.5 cm RMSE) is met for 40 out of the 45 basins studied for this configuration, and at daily-to-weekly time scales (6.3 cm RMSE) still for 37 basins. For configurations 5d_Ma and 3d_H, this reduces to 29/21 (monthly/daily-to-weekly) and 32/24, respectively. Although the performance at lower resolutions at daily-to-weekly time scales were not evaluated in detail in this study, similar numbers can be expected. At 250 km resolution, configuration 5d_Mb already meets the most stringent threshold requirement of 5.0 cm RMSE for 400 km resolution in 34 basins (versus 17 and 21 basins for 5d_Ma and 3d_H, respectively).

Yet, irrespective of the chosen configuration, resolving mass redistribution in basins 25 and 26 on the Northern Antarctic Peninsula remains a challenge. These elongated geographical features have a typical width in the range of 50 – 100 km, well below the targeted resolution of a future mission. When retrieving mass changes, this will cause signal leakage from one basin to the other, thereby increasing the RMSE. However, when combining the two basins, this leakage cancels out and the RMSE drops to an order of magnitude lower than what is currently achievable with a single-pair mission. Given that the Antarctic Peninsula is a region of rapid ice loss, the added scientific value of a double-pair mission therefore is far-reaching.

47.3 OCEAN CIRCULATION CHANGES

There are a wide variety of possible signals to seek in the ocean, and GRACE data have already been used in a broad range of ways. Some of the larger bottom pressure signals at small length scales are associated with mesoscale (tens to a few hundred km) eddy variability penetrating to the seafloor, but the most oceanographically valuable information tends to be related to smaller amplitude signals which are highly spatially coherent [RD-15], but in many cases, that spatial coherence extends over narrow, convoluted regions such as the continental slope, rather than being extensive in a simple patch with a single well-defined length scale. To cover the two main possibilities, we here investigate two different types of region: the Caribbean Sea (a broad, localised region), and the signals near the western boundary of the North Atlantic associated with the Atlantic Meridional Overturning Circulation (AMOC). Two other signals were also investigated: the Caribbean Sea shelf region (both local and narrow), and the model localised to the Atlantic eastern boundary (highly coherent but in a narrow band, and with small amplitude). Neither of these produced useful outputs with any plausible noise model, so they are not considered further.

Results presented here are based on 54 years of data from a 1/12-degree resolution global ocean model. The data (described in more detail in a separate document for Deliverable 14) are

reduced to 7-day means to match the satellite simulation data provided, which is used to provide 1 year of noise estimates, added in repeated fashion to each year of model data. For the AMOC investigation, we use 54 annual means of model data, with the 52 weekly noise estimates (extended to 54 by repeating the first two at the end of the time series), scaled in various ways to estimate the noise in annual means.

Following [RD-14], the Caribbean Sea is known to have a highly coherent bottom pressure mode with (standard deviation) about 1.2 cm of water, and dominant period about 120 days. We define the Caribbean Sea as the area shown in red in the bottom left panel of Figure 47-26, enclosed by the 2000 m depth contour. Model bottom pressures were averaged over this region, and the resulting time series correlated with bottom pressures at each grid point (top left panel of Figure 47-26). It is clear that the mode is highly coherent inside the basin, and mostly localised, but there is a weaker very large-scale correlation across the Atlantic. Whether this is a genuine correlation or coincidental is hard to assess, and this highlights an important issue of interpretation: we can be certain that local signals are representing the mode we seek, but larger scales may produce skill (or interference) that gives an illusion of detection of local signals. It depends whether the teleconnections seen in model correlations are due to model physics, relationships between forcing fields in different parts of the world, or coincidence.
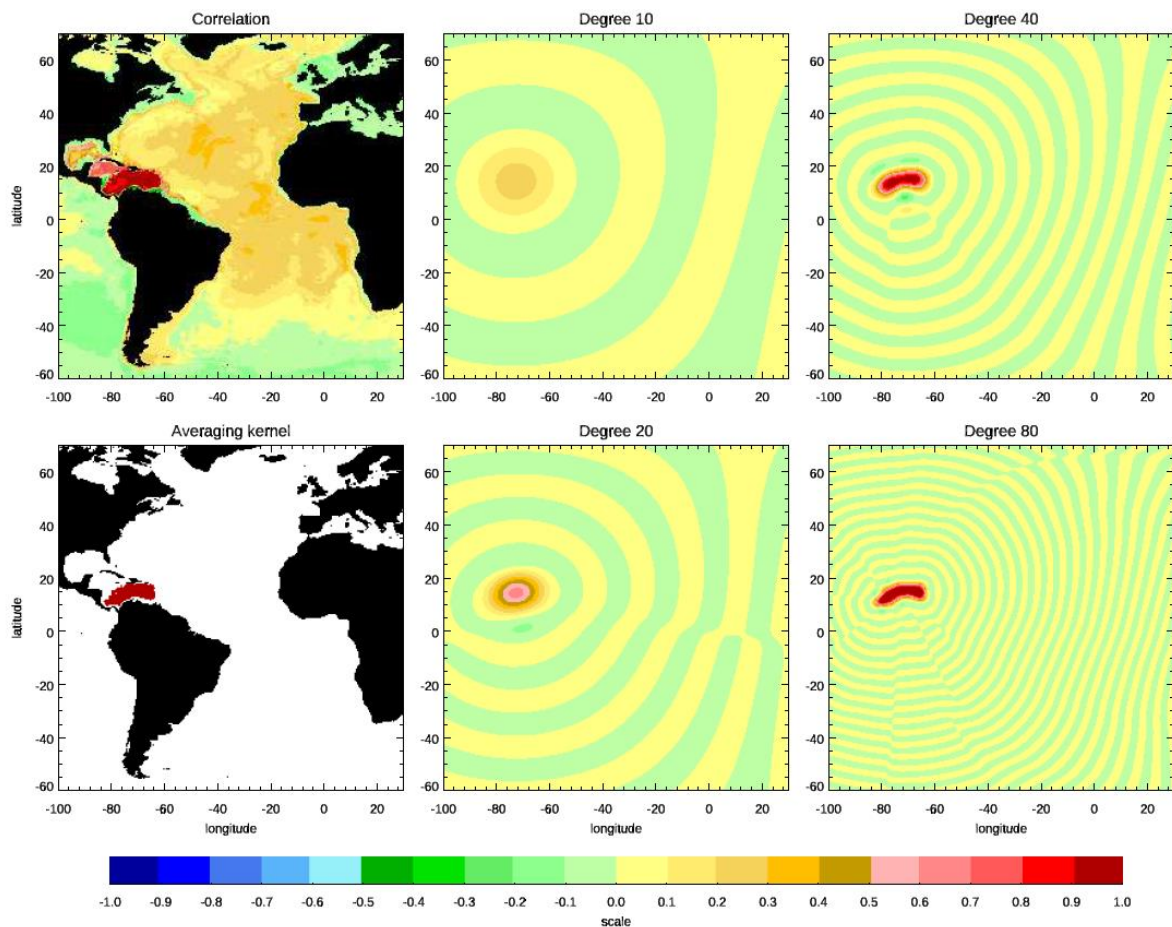
Figure 47-26: The Caribbean Sea Mode. Bottom left: the region averaged over. Top left: correlation between bottom pressure and that averaged over the Caribbean Sea. Other panels: the averaging kernel after truncation at various spherical harmonic degrees.

Calculating an average over the Caribbean Sea from data which is truncated at different spherical harmonic degrees is equivalent to using full resolution data, but a truncated averaging kernel. The other panels of Figure 47-26 show how truncation affects the localisation of this averaging kernel. It is only somewhere between degrees 20 and 40 that the kernel becomes well localised – a factor which should enter into our interpretations.

The full time series of basin-averaged pressure, together with a 5-year zoom, is shown in Figure 47-27. This confirms the expected dominant timescale, showing that there are a large number of degrees of freedom in this timeseries.

We now proceed to recalculate the basin-averaged timeseries using model plus (optionally) satellite simulation noise, truncated at different spherical harmonic degrees. For the noise, we use the baseline Bender-type configuration, and the single pair GRACE-type configuration.
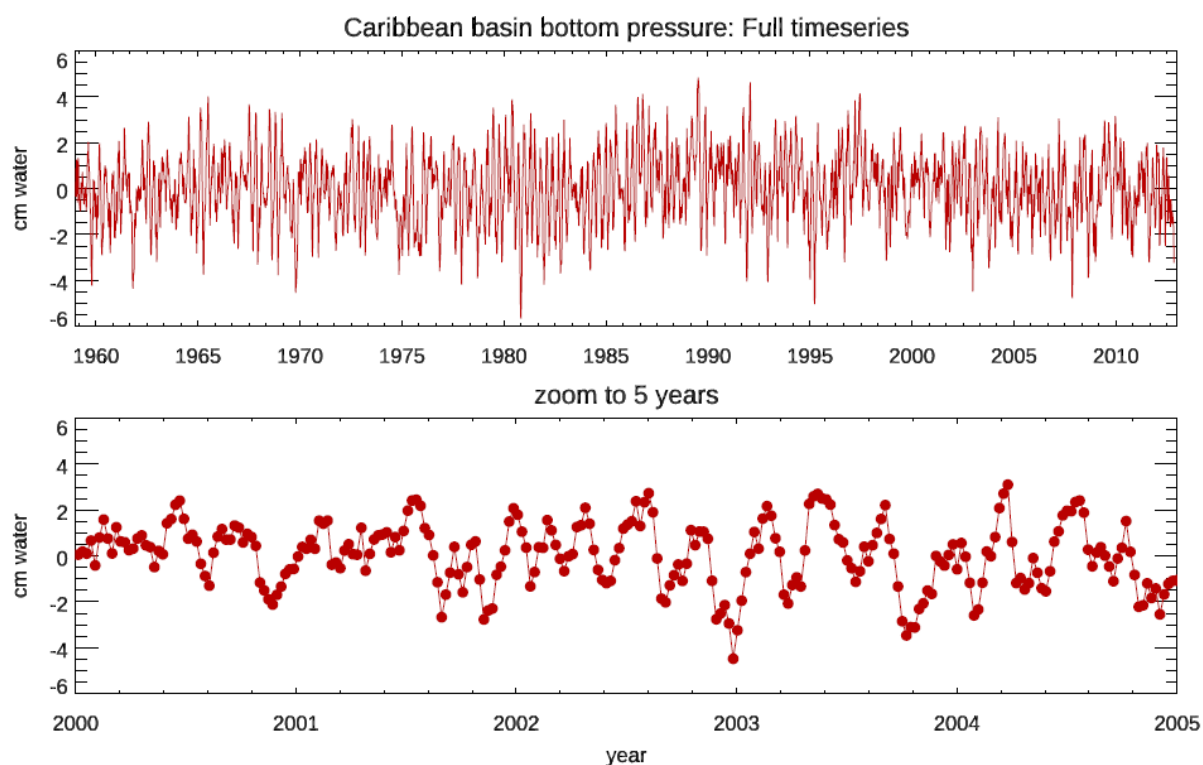
Figure 47-27: The Caribbean Sea basin-averaged bottom pressure timeseries.

We use this with weekly values for the noise, with weekly values divided by $\sqrt{4}$ to represent the expected noise for monthly means, and we also repeat the analysis with all data subsampled to 4-week means. We also run a case with no noise, just truncation of the model data. Time series are produced by convolving the model + noise fields with the averaging kernel shown in Fig. 26. Amplitudes of the timeseries produced by the convolution are rescaled by using the coefficient from a least-squares fit of the no-noise case on the exact result.

These results are summarised in Figure 47-28, in terms of the percentage of variance of the true timeseries which is explained by the timeseries calculated from truncated and noisy data. As expected, the "no noise" case is poor for low degree truncation, but as the truncation allows for a more localised signal it rapidly reaches over 90% variance explained. All three Bender cases

produce positive variance explained, but the weekly values only reach about 20%, with monthly values reaching about 50%, and almost 80% for weekly values with noise reduced by a factor of $\sqrt{4}$. The Bender smooth case, which is representative of monthly solutions, lies about half way between the Bender weekly and Bender 4 cases. GRACE results never produce positive variance explained. It is notable that in all cases, the low degrees interfere with the signal, and it is only as higher degrees enter in that the signal seems to be resolved. In the Bender case, the best compromise is at about degree 60 (resolution about 330 km half wavelength).

These results are probably too pessimistic. Straight truncation is a simplistic approach, and it may be helpful to down-weight certain harmonics. The results of [RD-14] suggest that, with processing designed to focus on localised signals, GRACE can in fact capture about 50% of the variance in this region. Nonetheless, it is clear that the Bender configuration represents a dramatic improvement over GRACE for this type of signal.

Figure 47-28: Percentage variance explained, of the Caribbean Sea basin-averaged bottom pressure, by the pressures truncated at different spherical harmonic degrees and with noise of different amplitudes added. "4" means noise has been reduced by a factor of square root of 4. "smooth" means 4-week averages were used instead of weekly data.

Some insight into the cause of the pessimism can be seen in Figure 47-29, which shows the typical noise to be expected at different truncations, due to instrumental and processing noise (commission, rather than omission error). We see that already at very low degree, the noise exceeds 1 cm of water for both GRACE and Bender weekly cases. Excluding just degrees 0 and 1 makes a significant difference to this (Figure 47-30), and highlights how much more slowly the Bender case errors grow with increasing degree than the GRACE case.

To conclude, for the Caribbean Sea, the Bender configuration represents a major improvement over GRACE, but an optimal exploitation of the data requires careful consideration to be given to the low degree harmonics. Given how much deeper into the high spherical harmonics the Bender configuration can penetrate than GRACE, before reaching 1 cm errors (circa degree 60 compared to degree 15, for 4-week averages, in Figure 47-30), it is reasonable to expect that

this would result in well over 50% of variance explained, but further work is needed to confirm this.

Moving on to the AMOC, this is a mode of Atlantic Ocean circulation in which the water flows northwards above about 1200 m depth, sinks in the subpolar and polar North Atlantic, and returns to the south between about 1200 m and 3200 m. On long time scales it is coherent throughout the Atlantic, but at periods shorter than 10-20 years the variations can be more localised. Both aspects can be seen in Figure 47-31, which shows timeseries of the northward flow above the depth which produces maximum northward flow in the time mean, at three different latitudes, and averaged over the Atlantic from 35°S to 43°N (the latter at 1200 m depth).
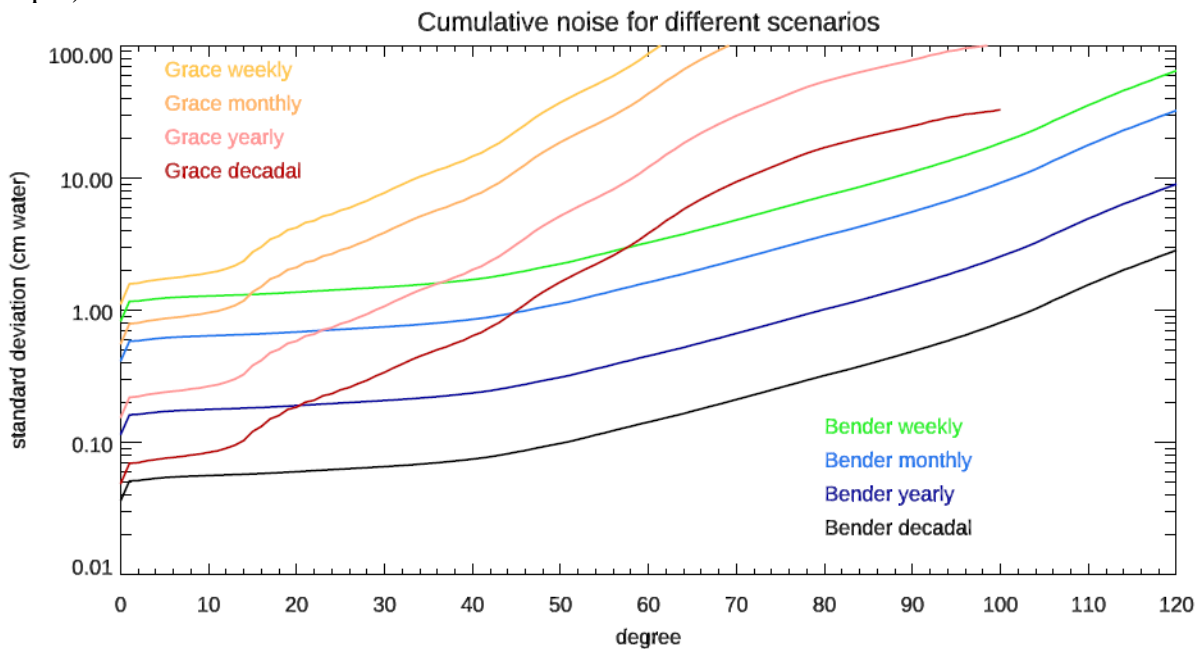
Figure 47-29: Noise for different scenarios and different time scales, as a function of spherical harmonic degree. Noise is given as the standard deviation of spurious bottom pressure variations averaged over the band 60°S to 60°N. All are based on weekly values, divided by the square root of the number of weeks in the time period considered. The validity of this is somewhat speculative for annual data, and highly so for decadal.
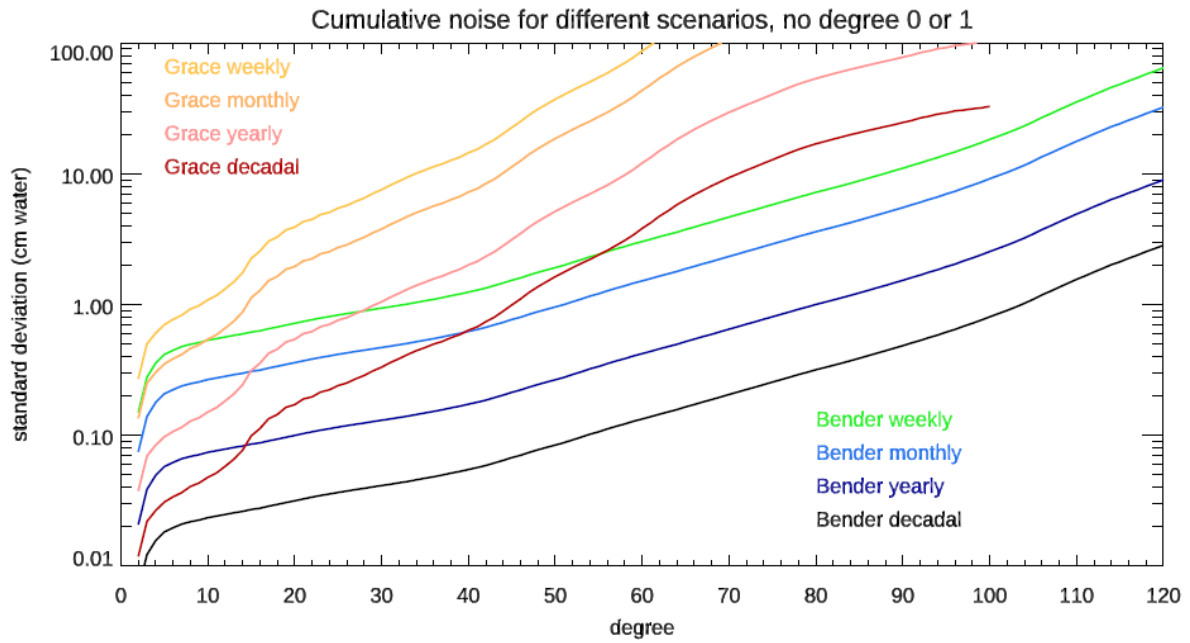
Figure 47-30: As for Figure 47-29, but with degree 0 and 1 noise set to zero.
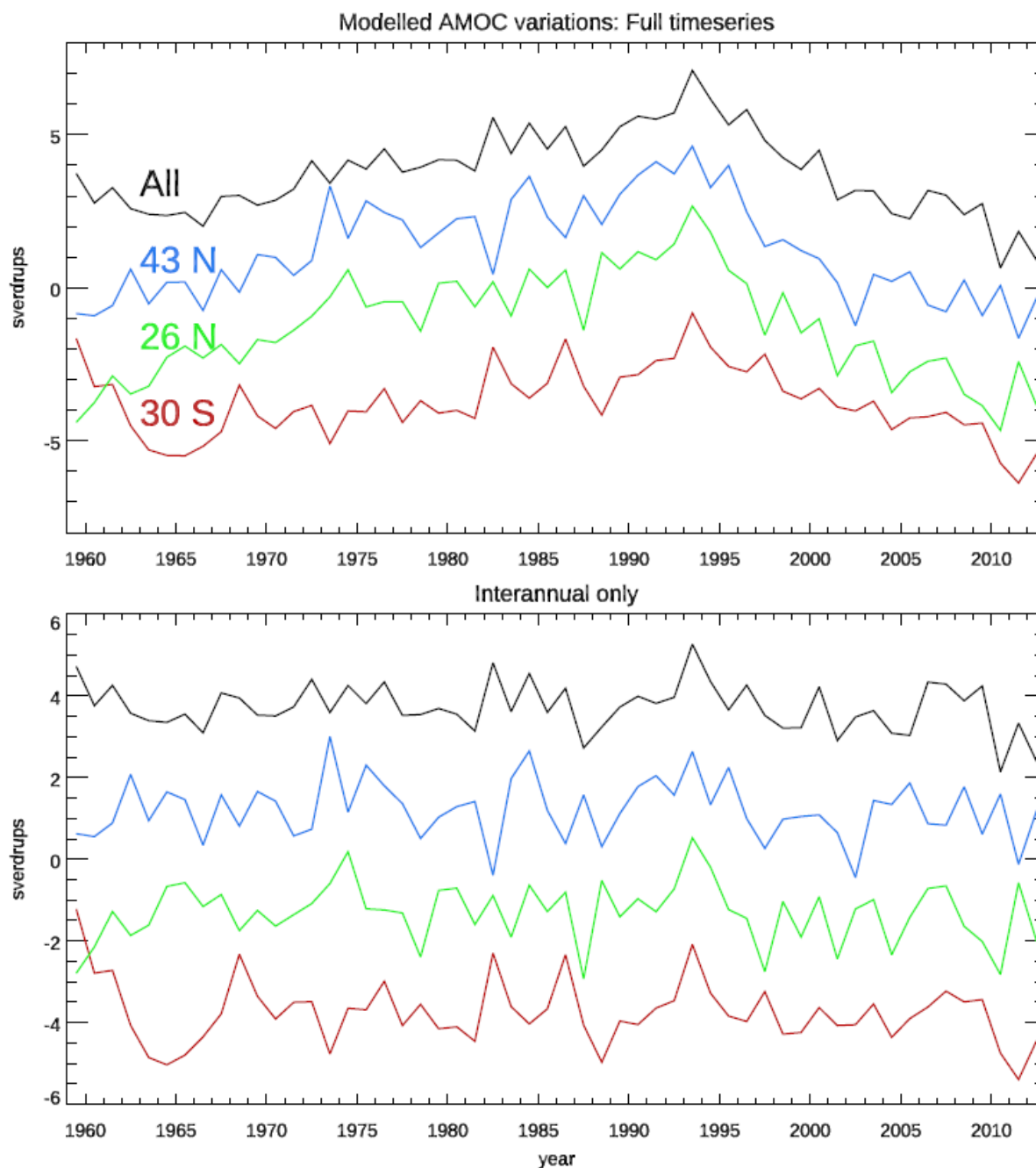
Figure 47-31: Annual mean Atlantic Meridional Overturning Circulation timeseries from different latitudes, and averaged from 35°S to 43°N. Units are sverdrups (10^3 m³/s). The lower panel has a running decadal mean subtracted off (extended as constant at each end).

The full timeseries is dominated by long timescales (and hence has few degrees of freedom), although less so at 30°S. The interannual timeseries is much less spatially coherent.

Simple physical arguments, verified within the model domain, show that the overturning at a particular latitude is reflected in bottom pressure on the western continental slope at the same latitude, with a negative pressure above the depth of peak overturning streamfunction, and positive below (signs are reversed in the southern hemisphere). For a particular latitude, this dipole across the slope is a very small-scale signal, so detection relies on the latitudinal

coherence of the variability. There may also be coherent signals off the slope, but the physics of any such relationship is not known, so for clarity of interpretation we need to restrict our measurements as closely as possible to the slope.

We use the 8 timeseries of Figure 47-31 as our targets, and construct weighting kernels designed to reproduce these timeseries from ocean bottom pressures. For physical interpretation, we restrict those weighting kernels to the west Atlantic continental slope at depths shallower than 3200 m. To retain some latitudinal resolution, we restrict the domain to the southern hemisphere for the 30°S section, to the range 0° to 43°N for the 26°N section, and to 30°N to 60°N for the 43°N section.

We start by calculating the correlations of the 8 AMOC timeseries with bottom pressure at each grid point (Figure 47-32).
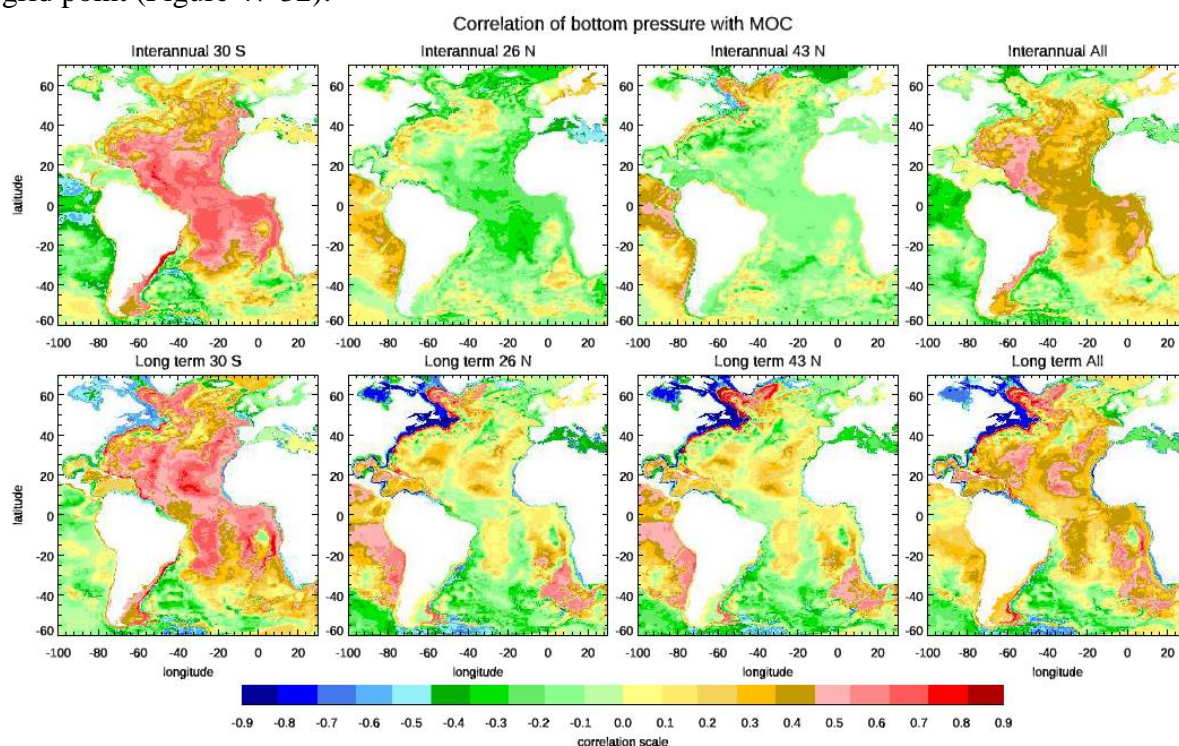
Figure 47-32: Correlations of annual mean AMOC at different latitudes with bottom pressure at each grid point. Top row has a running decadal mean subtracted off all timeseries to focus on interannual variability. The rightmost panels use AMOC averaged from 35°S to 43°N.

The correlations show the expected patterns over the west Atlantic continental slope: negative in shallow water turning positive in deeper water in the northern hemisphere, and the opposite in the south. These patterns are clearest and most spatially coherent when the full time series is used (bottom panel), despite the small number of degrees of freedom in this case. There are also correlations with the open Atlantic basin, especially in the 30°S case. Whether these are real or not is open to question, and reliance on such large spatial scale signals should be minimised if we are to have confidence in the results, hence the focus of the averaging kernels on the continental slope alone.

For each timeseries in Figure 47-31, and averaging kernel is created as follows: at each grid point, a linear fit of AMOC on bottom pressure is calculated, producing a scaling coefficient to convert bottom pressure to AMOC. Points are then weighted by this coefficient, multiplied by

the squared correlation coefficient, and by grid cell area. The resulting weighting function is then convolved with the model bottom pressure timeseries to obtain AMOC predictions. A fit of the AMOC on these predictions is then performed to produce an overall scaling factor, which is then applied to the weights to give the final averaging kernel. There is no claim that this produces the optimal kernel for monitoring the AMOC, but it should produce plausible bottom pressure target patterns for investigation.

The resulting kernels are shown in Figure 47-33 after truncation to degree 50, and in Figure 47-34 after truncation to degree 80. Some comments are in order:

- Although the relevant pressure signal is dipolar, it is expected to integrate to zero as a function of depth, not horizontal distance. This, together with different ocean dynamical noise at different positions, means that the kernel will not exactly cancel locally, and can contain large scale contributions. This is particularly clear in the case of 30°S, and interannual variability at 26°N, where only the shallow signal seems visible in most places.

- The picture when truncated at degree 80 is significantly more clear and physically meaningful than that with degree 50 truncation.

- Using an AMOC averaged over the entire Atlantic seems to be unhelpful in terms of identifying the physically meaningful mode.
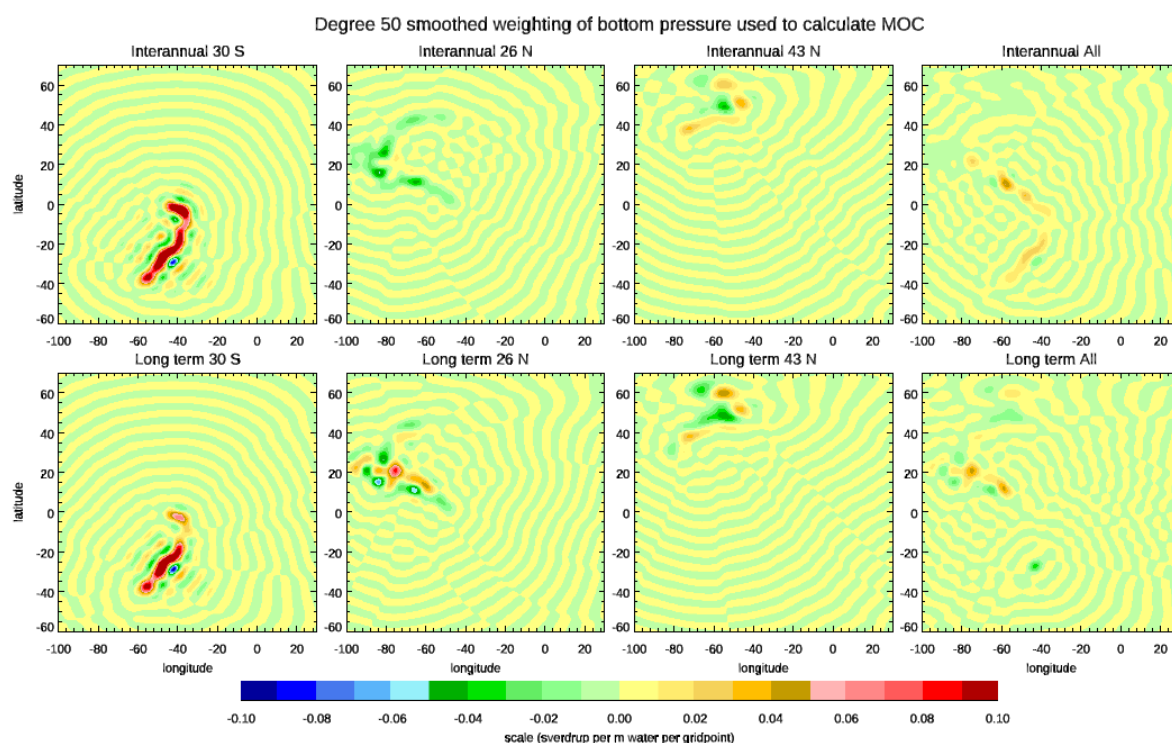
Figure 47-33: Averaging kernels for the 8 AMOC time series, truncated to spherical harmonic degree 50.
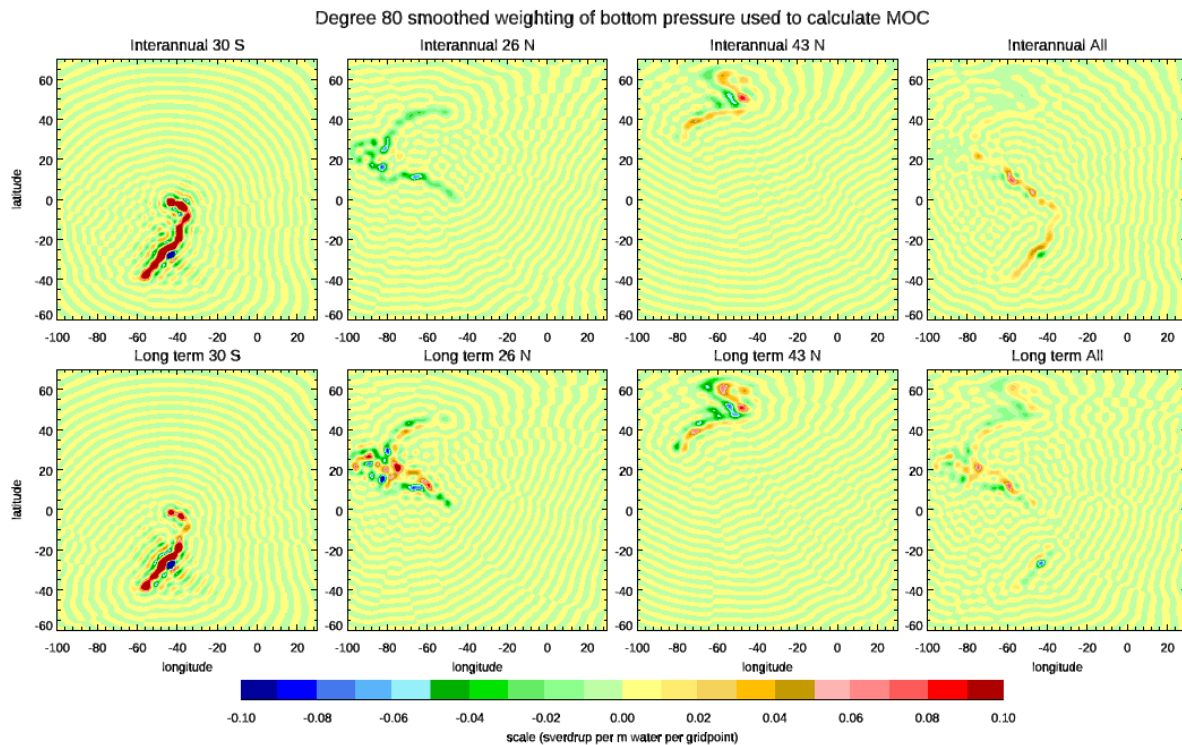
Figure 47-34: Averaging kernels for the 8 AMOC timeseries, truncated to spherical harmonic degree 80.

The results of using these averaging kernels are shown in Figure 47-35. Here we apply the noise, divided by $\sqrt{52}$ to make it more representative of annual means than weekly values, and, very speculatively, by $\sqrt{520}$ for decadal means, as an optimistic suggestion of what might be possible at the longest timescales. The results are very different for different regions and different timescales and require a degree of interpretation. For interannual variability, the no-noise case shows up to 50% variance explained by low degree variability, but a significant increase between approximately degrees 30 and 80. This fits with the greater localisation of the signal at higher degrees, and the relatively high number of degrees of freedom in the interannual case.

For 30°S, the "long term" case looks similar to the interannual case. As noted above, the full time series at 30°S is more dominated by interannual variability than the other cases, which may explain this pattern.

The other "long term" cases show significant skill even at degree 10-20. Given the low number of degrees of freedom, the lack of localisation at these degrees, and the basin-scale correlations seen in the model, it seems prudent to write this off as a reflection of large-scale dynamics which may be coincidentally correlated, or may be genuinely so but via dynamics that we do not yet understand. Either way, it is not the localised signal we are looking for.

Accordingly, our interpretation is that in order to detect the true, large-scale AMOC changes based on boundary pressures, we need the variance explained to remain high beyond degree 50, and ideally beyond degree 80. This is the case for the Bender scenario but not for GRACE, even with the most optimistic decadal scaling of noise.
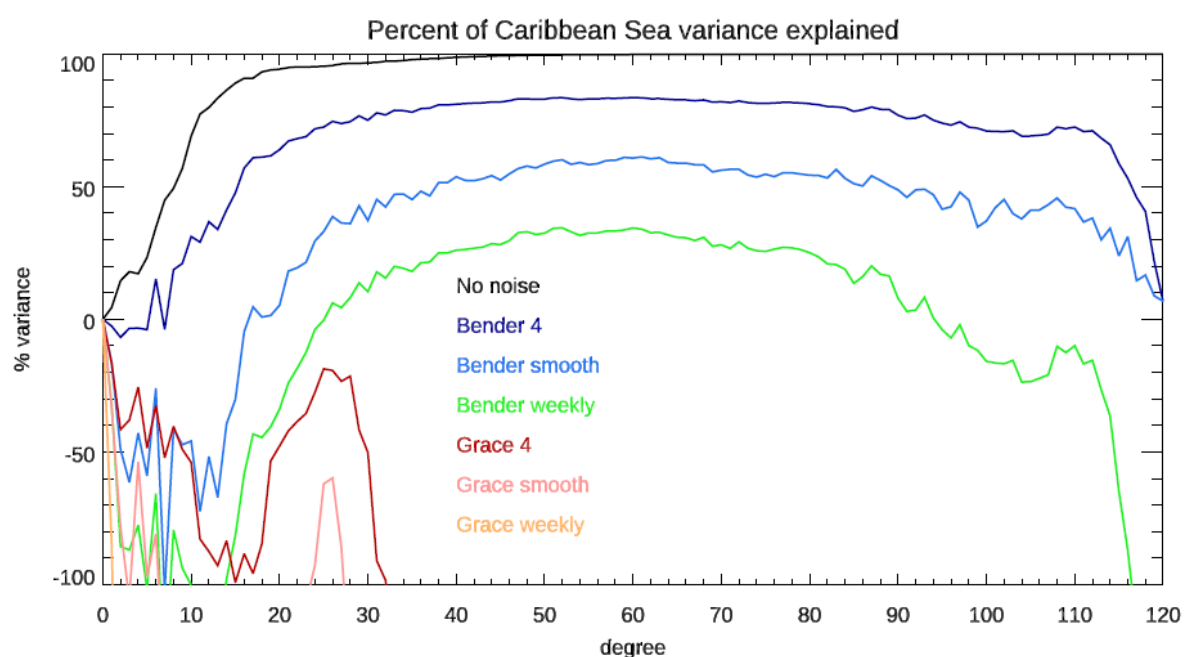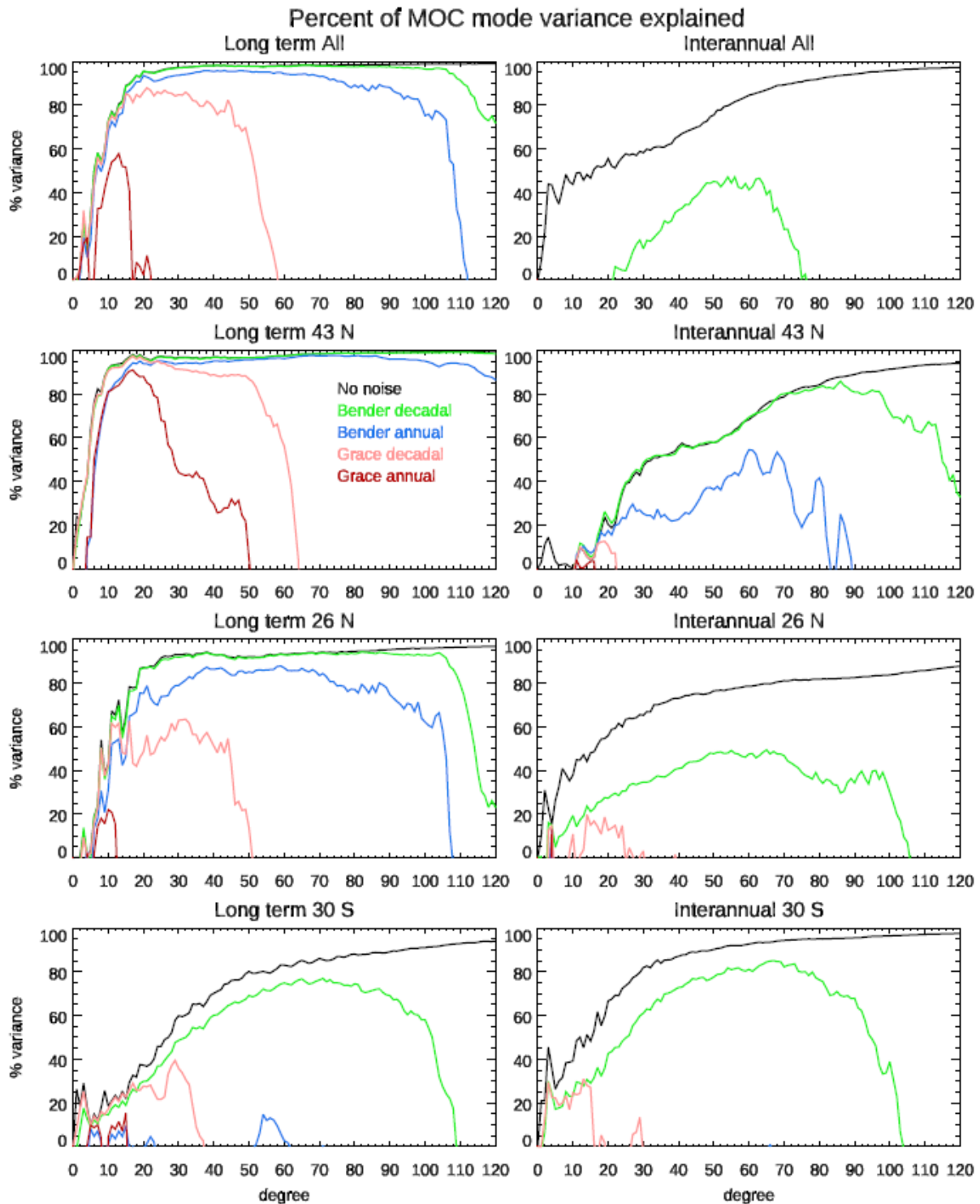
Figure 47-35: Percentage variance explained, of the 8 AMOC-related bottom pressure modes, by the pressures truncated at different spherical harmonic degrees and with noise of different amplitudes added. "annual" means noise has been reduced by a factor of square root of 52, "decadal" by square root of 520.

Translating the above into mission requirements and noise levels requires a combination of the interpretations and the noise values in Figure 47-29 and Figure 47-30. For the Caribbean Sea case we have seen that the Bender case with weekly noise divided by 4 is good (though this maybe pessimistic). Globally, since this basin is one with larger signals than most, we can

interpret this as marginal, and good would be 10 times smaller noise at low degrees in particular. Translating this into noise estimates, marginal becomes 0.4 cm at degree 20 (1000 km), 0.8 cm at degree 50 (400 km), and 3 cm at degree 80 (250 km), although signals beyond about degree 60 (333 km, 1.5 cm accuracy) may not be needed.

For the AMOC, the Bender annual noise simulation is marginal to good, depending on which scenario is assessed, and the higher degrees are particularly important. Using this to read off long-term noise values we obtain 0.1 cm/yr to degree 25 (800 km), 0.25 cm/yr to degree 50 (400 km), and 5 cm/yr to degree 111 (180 km). In this case, the extension to higher degrees is what gives the most trust in the signal, the variance explained starts tailing off at about degree 60 but remains useful, then drops sharply after about degree 105, so the degree 100 (200 km) value may be more relevant: 2.5 cm. Targets of 10 times better would produce some excellent results, pushing the resolution up significantly. The range that needs most attention is the low degrees, and the highest degrees beyond degree 100, for the most powerful results.

Conclusions

Whilst interpretation of the ocean results is complex, it is clear that the Next Generation Gravity Mission proposals for double-pair configurations produce a dramatic improvement in ocean bottom pressure determination over the single pair GRACE-style configuration. Detailed results for different configurations are not shown here, as all produce similar results for the cases studied, suggesting that ocean applications are not the best discriminator between scenarios, although this could be different if Arctic and Antarctic signals are considered.

As a rule of thumb, we find that GRACE-type configurations provide useful ocean dynamic information over the range of degrees ~5 to ~15-30, depending on the signal being investigated. This is insufficient to geographically localize boundary pressure signals, and any skill in measuring such signals is reliant on uncertain inferences of larger scale correlations from ocean model simulations. In contrast, the new configurations extend the valuable information out to degrees up to between degree ~50 and ~80, depending on the signal. This is a game-changing extension, permitting clear physical interpretation and showing the potential to monitor meridional overturning circulation changes on time scales of years and decades.

For other aspects of the ocean circulation, analysis is likely to be highly dependent on basin size. However, the Caribbean Sea study also illustrates the dramatic improvement to be expected over the GRACE configuration. There are subtleties which still need to be disentangled concerning how best to use (or not) very low degree signals, but the Caribbean Sea example shows a change from barely detectable signals (at about 1 cm RMS) to clearly detectable. In reality, we know that a better optimization of methods is currently capable of resolving useful signal in this region, and would expect the new configuration to improve this significantly from order 50% of variance explained to closer to 80%-90%. Similar conclusions can be expected for other basins which are significantly smaller than planetary scale.

Overall, the new mission configuration offers the possibility of a step change in ocean dynamic capability, from the present state in which GRACE measurements clearly measure only the large scale, rapid fluctuations which are of little climatic interest, to a future of unambiguous measurement of aspects of the ocean circulation which are of most relevance to the Earth System.

47.4 SOLID EARTH – EARTHQUAKE SIGNALS

We have analysed the problem to define a strategy that allows us to formulate the criterion whether the gravity field generated by the coseismic and postseismic movement of an earthquake is detectable by MAGIC. We conclude that we must distinguish the instrumental sensitivity of the mission and payload to gravity from the disturbing climatic effects of hydrology, glaciers oceanic tidal and non-tidal variations recorded by the payload. The reason is tied to the inhomogeneity of the glacier and hydrologic signals, which make these disturbing signals hardly relevant in some areas affected by high seismic risk. The glacier signal is relevant only where glaciers exist, which is confined to the polar regions, high latitudes, and to limited areas of high topography at mid-latitudes. The hydrologic basins cover the globe more homogeneously, but there are widespread arid areas where the hydrologic signal is negligible. We suspect that the inhomogeneous distribution of the disturbing signals contributes to the average MAGIC noise curve, such that the noise is overestimated respect to what can be expected for the regions where the disturbing effect is practically absent, allowing to lower the error curve, and reducing its gap to the instrumental error curve. The oceanic tidal signal is inhomogeneous both in space and in time, and is more relevant over oceanic and coastal regions. The tidal signal generates disturbance through aliasing, which creates the typical stripe-like pattern and again a periodic signal in time. Being a periodic apparent signal, it is reduced by time averaging of the single weekly MAGIC solutions. This has the consequence that increasing the time interval at which the MAGIC signal is determined, reduces the noise level of the recovered field. The coseismic earthquake waves down to magnitude M 5 or even M 4.5 are globally detected by existing international seismic networks, that provide the hypocentre and fault plane solution, and solution of the seismic moment. The slow postseismic deformation as well as the intermediate phases in the earthquake cycle generate the signal for which the gravity acquisitions compete most with the seismic networks. These movements are though slow, extending over decades or centuries, depending on the relative velocity of the moving plates across the fault discontinuity. Therefore, a reduced time interval of a month or year can be acceptable, if a lower magnitude can be detected by MAGIC. For this reason, we think it is useful to consider not only the weekly error curve of MAGIC in recovering the HIS signal, but also the time-averaged error curves, which are not much higher than the instrumental spectral noise curve.

For illustration, Figure 47-36 illustrates the noise curves expressed as degree variances of the 1 week MAGIC coefficients minus the 1 week HIS coefficients. The noise curves are shown for the GRACE like and Bender mission scenarios, using the average of all noise spectra, or the average of the coefficients, or the estimated 1-year average noise spectra using a scaling law. The averages are made on the available 52 weekly MAGIC error curves, covering one year. The scaling law is the following:

$$\sigma^2(l)_{\Delta t_1} = \sigma^2(l)_{\Delta t_0} \cdot (\Delta t_0 / \Delta t_1)$$

Where $\sigma^2(l)$ is the error degree variance at spherical harmonic (SH) degree l formulated for the solution timespan Δt_0 (original time interval) and Δt_1 (time interval we are scaling to). The MAGIC solutions are weekly, so Δt_0=1 week, and Δt_1=52 weeks for 1 year and 4 for 1 month [RD 5].

It is seen how the error curves are reduced by over one degree in variance by extending the sampling from one week to one year, and how the simple scaling law is a correct way to estimate

the noise curves for an extended time interval, starting from the weekly error curves. As will be shown later, the lowering of the noise curves, brings to lower the minimum magnitude of sensitivity of MAGIC.
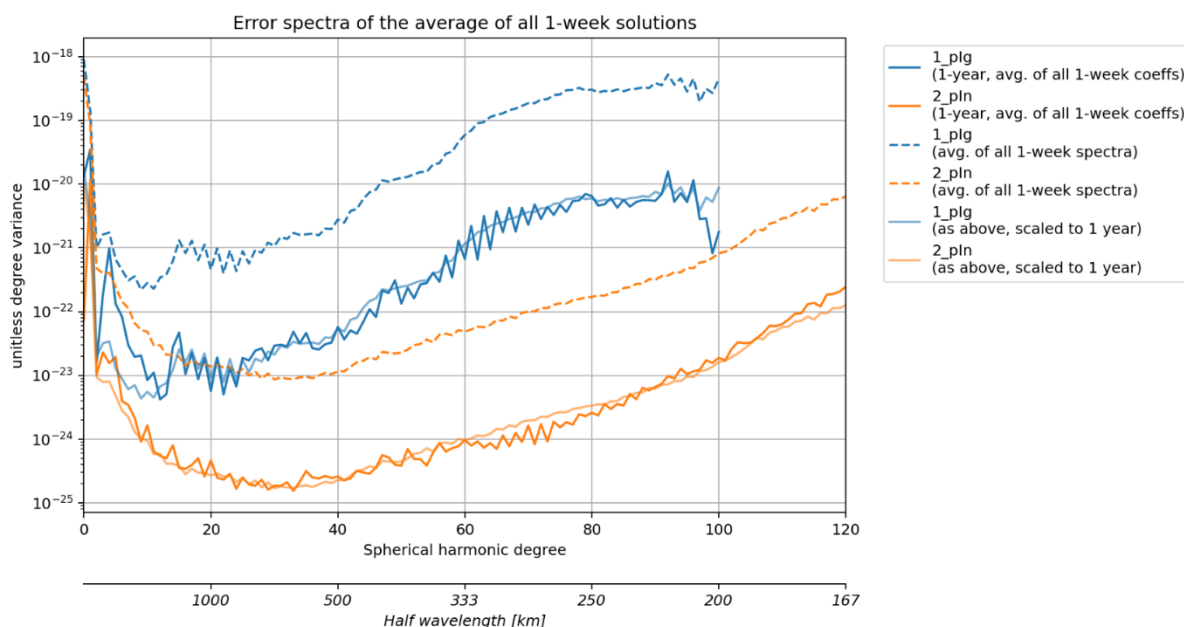
Figure 47-36: The MAGIC error weekly error curves defined as the MAGIC coefficients minus the HIS coefficients at weekly resolution. 1_plg: 1 couple, 2_pln: 2 couples. The graph shows: the average of the weekly coefficients over one year, the average of the degree variances over one year, and the estimated degree variances over one year calculated through a scaling law applied to the 1-week degree variances.

The earthquake is detectable if the signal spectrum in a given SH degree range is larger than the power of the degree error variance of MAGIC. Since the signal is local and not global, a spatial localization of the spectrum is required. We apply the spatio-spectral localization method in the spherical harmonic domain proposed by [RD-4], in its implementation in the SHTOOLS software [RD-6]. We adopt the spherical cap as localization domain, defined by its center coordinates and angular radius, and use the solutions to its concentration problem, defined as localization windows. The localization function parameters depend on the extent of the chosen phenomenon, on the calculation area used for its forward modelling, and on the degree range of interest. A pitfall of localization is loss of information on the synthesized signal spectrum of the earthquake in the lowest and highest SH degree range, due to the convolution-like operators employed. The smaller the cap radius, the more SH degrees at the spectrum ends of the earthquake spectrum cannot be used. This imposes an additional constrain on the cap radius to be employed. The noise curves of the satellite mission are not involved in the localization procedure, as noise at every SH degree is dominated by a stationary component, which if localized results in the same power spectrum as the non-localized signal. If the localization operation is not applied, an observable earthquake spectrum results to be much lower and seemingly undetectable by the mission, which is not realistic when comparing the earthquake signal amplitude with the noise amplitude calculated on the earth surface.

We compute the gravity field of an earthquake through the deformation in a radially layered spherical earth model. The method and software QSSPSTATIC [RD-7] allows modelling

coseismic and visco-elastic post-seismic deformation, and uses a hybrid approach. A separate solution of long-wavelength spheroidal modes, where the gravity effect is significant, using numerical integration. An analytical integration method using the Haskell propagator [RD-7] is used for solving the small-wavelength spheroidal modes and the complete toroidal modes. The underlying theory stems from the analytical solutions by [RD-8]. The layered earth model consists of a purely elastic lithosphere in the first 40 km, overlying a Burgers model up to 120 km, then by two Maxwell bodies separated by an interface at 660 km. Properties from 1400 km to the sphere center, are assumed constant. In Table 47-8, the model is shown in detail. Earthquake sources can be placed in any layer of the elastic or viscoelastic layers of the solid mantle.

Table 47-8: Crust and lithospheric mantle portion of the rheological and density model used for the gravity field calculation of earthquakes

	Depth [km] from	to	Density [kg/m^3]	Elastic and viscosity parameters
Upper crust	surface	20 km	2720 kg/m^3	Purely elastic (Hooke's Law)
Lower crust	20 km	35 km	2920 kg/m^3	
Lithosphere mantle	35 km	40 km	3320 kg/m^3	
Lower Lithosphere mantle	40 km	210 km	3320 kg/m^3 to 3426 kg/m^3	Burgers Model Viscoelastic
Sublithospheric mantle	210 km	1400 km	3426 kg/m^3 to 4795 kg/m^3	Maxwell body

The relevant parameters defining the earthquake source are the dip of the fault, the rake of slip and depth of fault. We have tested a multitude of combinations of the fault parameters, finding that the thrust fault maximizes the gravity signal. In the point-source approximation, for a given unit source-mechanism tensor, which characterizes the earthquake mechanism, the seismic moment tensor is linearly scaled with the seismic moment. The body forces which constitute the source term of the earthquake fault movement scale linearly with the seismic moment. In terms of degree variances, a consequence is that they scale with the square of the seismic moment. Due to the harmonicity of the gravity field, this holds true for any derived functional and/or upward continuation. Therefore, the seismic moment is the controlling parameter of the amplitude of the gravity field. This allows to calculate the gravity field for one reference seismic moment, scaling the degree variances then for other seismic moments, without the need to recalculate the gravity field for the different fault plane solutions again.
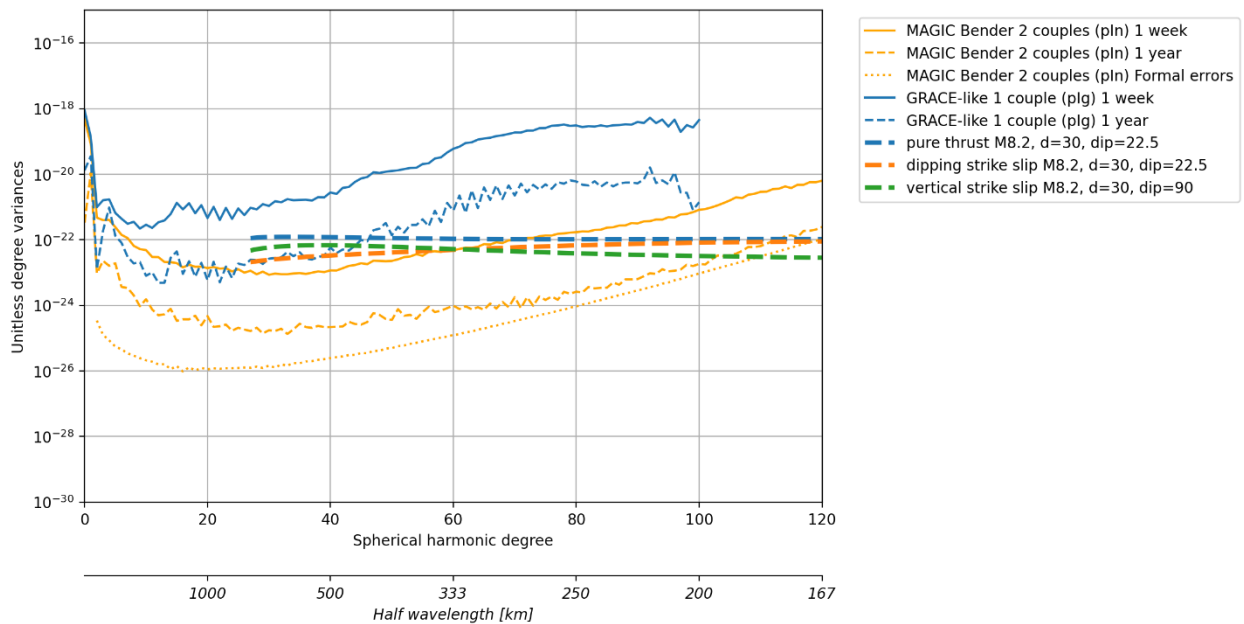
Figure 47-37: The localized spectrum of a M 8.2 magnitude earthquake. The MAGIC error curves are shown for 1 week and 1 year time resolution. The earthquake spectra are shown for a pure thrust, and a dipping and vertical strike-slip fault. Earthquake depth is 30 km.

We find that a magnitude M 8.2 earthquake is at the limit of observation of the single pair, the thrust event being seen up to degree N=45, and is well above the detection limit for the Bender pair, with maximum degree N=65 for the thrust event, with resolution of 1 week. An exploration of the limiting magnitude is done by calculating the signal to noise ratio for earthquakes of increasing magnitude, calculating the ratio of the degree variances of the localized spectral earthquake signal, and the degree variances of the noise curves. In the simulations we use the moment magnitude, which is related to the seismic moment by the formula found by Kanamori [RD 9], with M_w moment magnitude, and M_0 the seismic moment in dyne cm.

$$M_0 = 10^{(M_w+10.7)*\frac{3}{2}-1}$$

For an increase of moment magnitude of delta_M_w = [0.1, 0.5, 1], the seismic moment is increased by a factor [1.4, 5.6, 32]. The fault area scales by a factor [1.2, 2.9, 8.1), the displacement by a factor [1.2, 2.2, 4.9], and subsurface rupture length by a factor [1.14, 2.0, 3.9]. These numbers were calculated according to the regression relations of [RD 10], and have been calculated averaging over different fault plane mechanisms, and are based on estimates of moderate (M_w = 4.8) to big (M_w = 8.1) earthquake magnitudes. We refer to the publication of details and uncertainties.

The noise curves of the MAGIC single pair GRACE like and the Bender double pair are compared in Figure 47-38. The colour scale gives the SNR in function of degree and earthquake magnitude. The improvement of the Bender configuration is both in lowering the magnitude of detectable earthquakes, as well as increasing the highest degree, and therefore improving the spatial resolution of the gravity field generated by the earthquake. The limit for a crustal depth earthquake in the Bender configuration is close to magnitude M_w 8.2; for the single pair configuration it is about magnitude M_w 8.8. The Bender mission can detect a lower magnitude

earthquake, and the degradation of the detectable magnitude degrades less fast towards higher degrees, compared to the single pair mission.
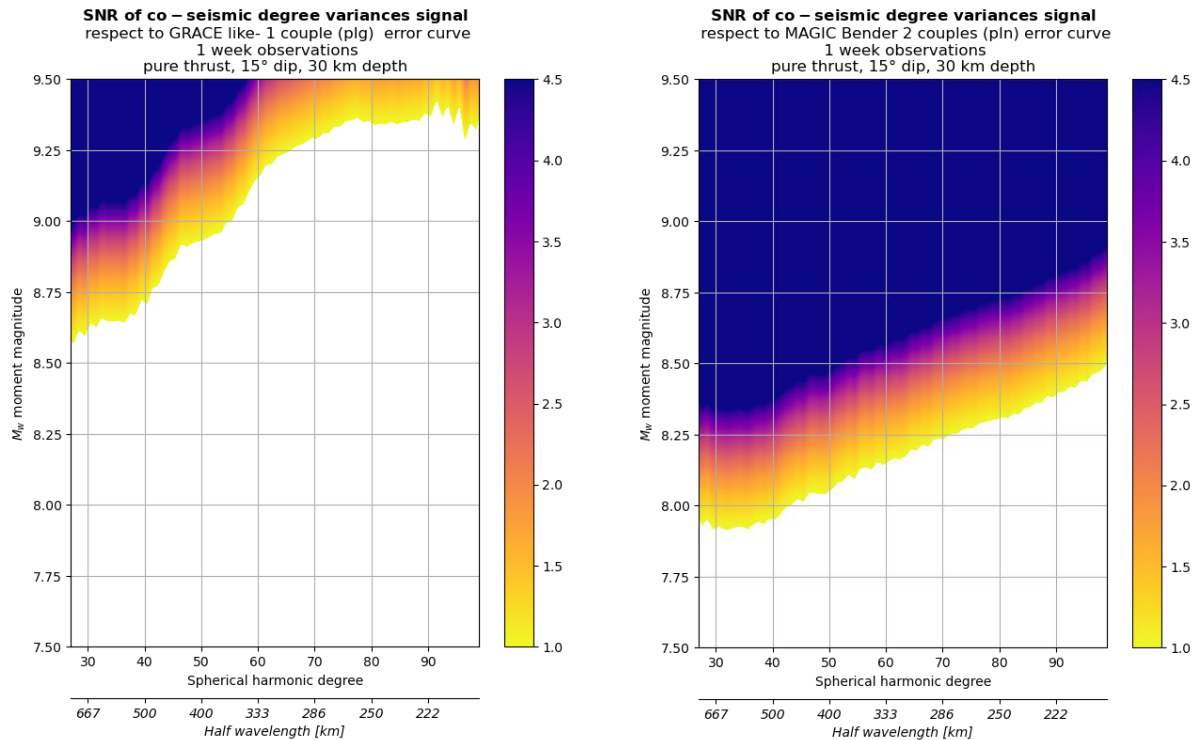
Figure 47-38. Signal to noise ratio of the earthquake signal localized spectral variances and the MAGIC noise degree variances. On the left for the single pair, on the right for the double pair constellation.

Finally, the dip and depth of the earthquake are explored, again using the SNR as a detectability criterion, and this time choosing the constant value of SNR=1 in the magnitude-SH degree space as a limiting value. Again, we give the results for the single pair and the double pair mission in Figure 47-39 and Figure 47-40, respectively. The depth dependence does not follow a simple rule of a decaying signal with increasing depth, because the density and rheology layering of the lithosphere model influence the result. For the chosen model it can be seen that the EQ depth of 30 km, that is a crustal earthquake above the Moho, gives a greater signal compared to a shallower or deeper source. The variation in terms of detectability is close to 0.2 M_w magnitude. For the pure thrust, a smaller magnitude EQ is detected for a 30° dipping event, compared to a flatter (15°) fault dip. The fault dip is characteristic of the geologic context, so the detectability will change geographically. The variation is on the 0.1 magnitude level, and is reduced at increasing SH degrees. The fault plane mechanism has a greater effect on detectability, with a pure thrust EQ requiring a smaller magnitude to be detected compared to a vertical or inclined strike slip fault. The magnitude difference for detectability is at the 0.25 M_w magnitude level, and affects low and high SH degrees. The fault plane mechanism is again a characteristic feature of the geologic context, with thrust events occurring at subducting plate margins, and continental convergent plate margins.
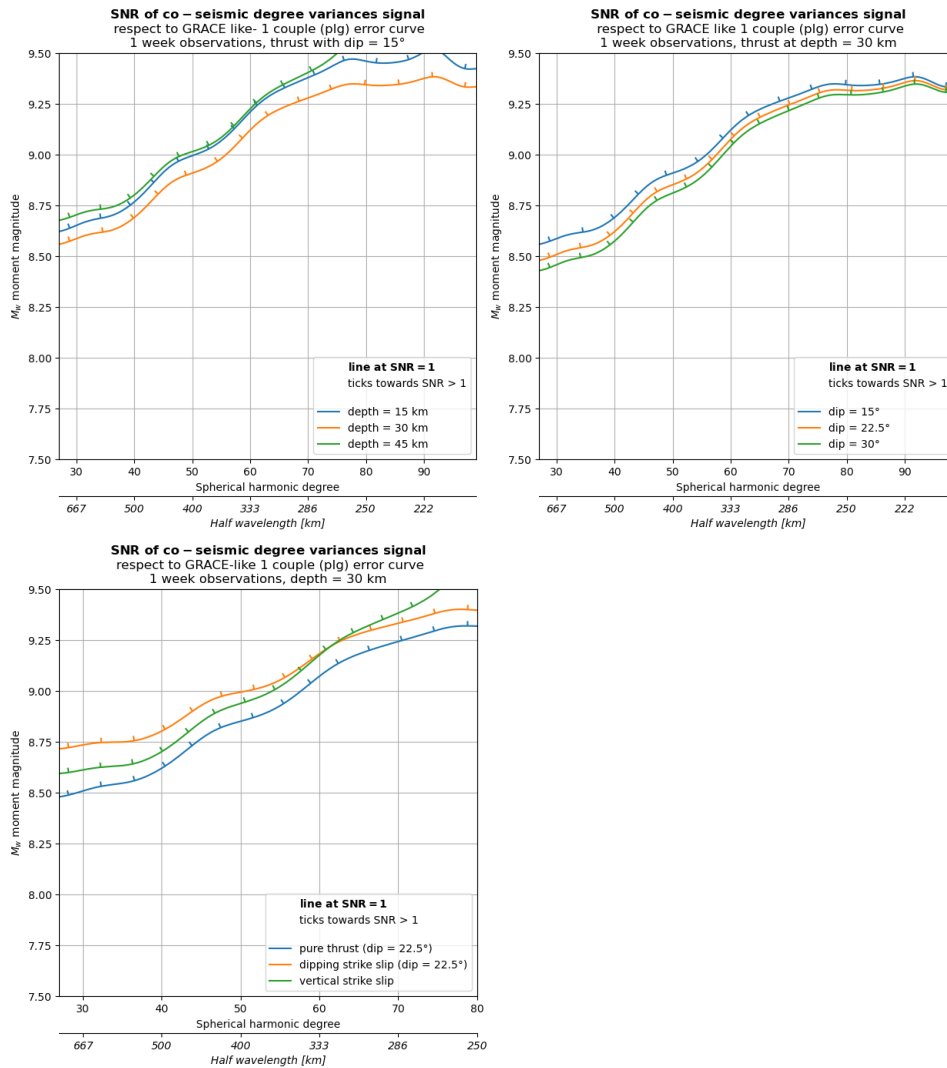
Figure 47-39. Earthquake degree variances and GRACE-like noise variances SNR isolines, for SNR = 1. The lines on the curve point towards detectable values in the magnitude-SH degree space. Single pair GRACE-like mission. The curves depend on earthquake mechanism, depth and fault plane dips.
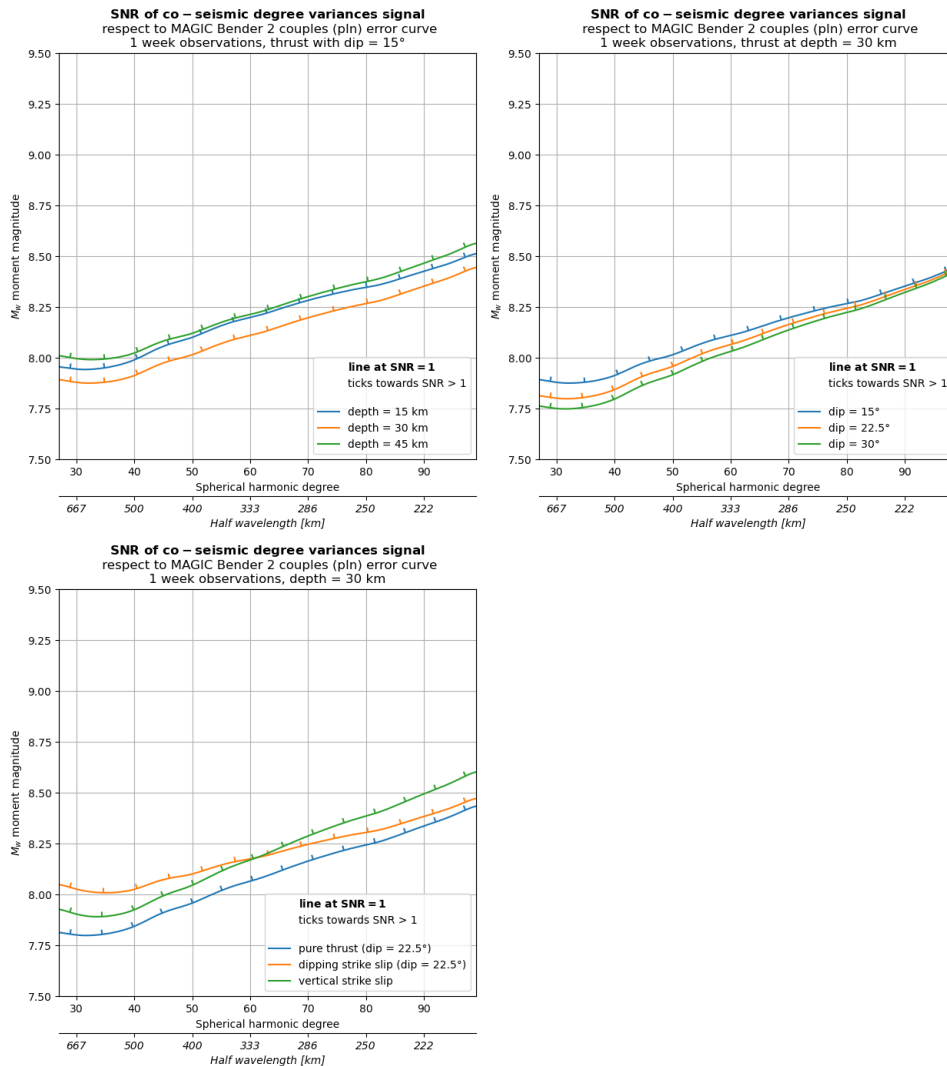
Figure 47-40. Earthquake degree variances and MAGIC noise variances SNR isolines, for SNR = 1. The lines on the curve point towards detectable values in the magnitude-SH degree space. Bender double pair MAGIC mission. The curves depend on earthquake mechanism, depth and fault plane dips.

We consider then the observation of the postseismic relaxation, which has the effect of reducing the coseismic gravity field generated by the coseismic movement, as shown in Figure 47-41. We consider the accumulation of the postseismic gravity change of an interval of 1 month, 2 and six months. The coseismic gravity field is compared to the weekly error curve of MAGIC in the GRACE-like and Bender configuration, whereas the error curves for the month and longer time accumulation correspond to the same time interval of the accumulated postseismic signal. Due to the lower noise curve with longer time interval, and the increased gravity change with time, the detectable magnitude is reduced with respect to the magnitude observable with the weekly noise in reference to the coseismic signal. An aspect which could be investigated further, is whether the decaying gravity field due to the postseismic relaxation could be used to give information on the state of the fault, and give information on the fact if a secondary main shock can be expected, or whether the first main shock completed the stress reduction on the fault. This information could be an added value of the gravity field monitoring on the fault movement, which would compete with the seismologic observations, which hardly could detect this relaxation process which besides from the aftershock sequence on the fault does not

generated seismic waves. Another aspect is to distinguish the afterslip from the post-seismic relaxation, by comparing the observation with the model. The gravity signature of afterslip and relaxation are different, so the difference of the observed gravity change, with the expected postseismic relaxation gravity change, can be used to define the amount of afterslip on the fault. This exercise has been made on the Sumatra Andaman earthquake of 2004 in [RD-11].
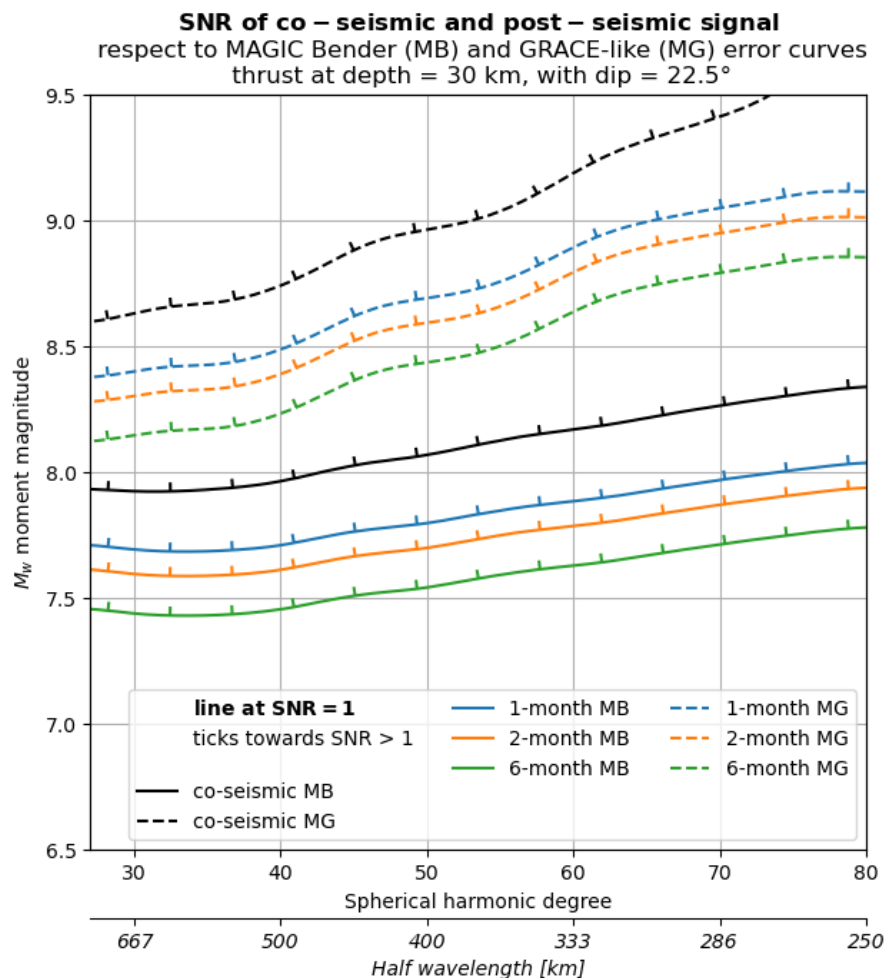
Figure 47-41. The figure shows the limiting moment magnitude versus spherical harmonic degree of the postseismic signal. Starting from the coseismic situation the postseismic relaxation reduces the gravity field generated by the coseismic fault movement gradually. The GRACE-like and Bender configurations of MAGIC are used starting from the weekly noise curves, which are scaled downwards the more the time period of observation is extended.

The next step is to calculate the cumulative spectral noise and signal curves, because at a certain SH degree these curves approximate the signal values we may expect to have at a given degree. To be consistent, we cumulate the curves starting from the lowest spectral degree resulting from the localized spectral analysis. The cumulative error is defined as follows, where 120 is the maximum degree of the retrieved model, and the coefficient errors are computed as

$$\Delta c_{nm} = c_{nm}(model) - c_{nm}(HIS)$$

$$cum.\,error(N) = \frac{a\,\rho_e}{3\,\rho_w} \sqrt{\sum_{n=27}^{N} \left(\frac{2n+1}{1+k_n}\right)^2 \sum_{m=0}^{n} [\Delta c_{nm}]^2 + [\Delta s_{nm}]^2}\,,$$

The average earth density ρ_e=5500 kg/m^3, water density ρ_w=1000 kg/m^3, a= 6378137 m. The starting degree is consequence of the localized spectra using a localization window of 8°. Given that the MRD documents use EWH as unit, we convert the SH coefficients into EWH using the conversion formulas summarized by [RD-12]. The cumulative curves for EWH spectral amplitude and amplitude for the gravity field at ground level are shown in Figure 47-42. The detection limits are the same if we consider gravity or EWH, which we use as control of the consistent conversion from SH coefficients to cumulated spectral curves. The coseismic signal for a magnitude M8.0 is about the limit for a weekly time resolution of MAGIC. Extending the resolution to 1 year, the lower magnitude of M 7.4 could be seen. The worldwide detection of a M7.4 and lower earthquake is done by seismological networks as well, but the information retrieved from gravity is the combined effect of aseismic afterslip and postseismic relaxation, the modelling of which allows to further define the fault properties. In particular, the postseismic relaxation can be predicted starting from the coseismic fault dislocation and depending in the crust and mantle rheology, and therefore subtracted from the observed gravity signal to determine the fault afterslip. With weekly sampling the limit of detection is about a M8.0 magnitude earthquake of thrust mechanism, with strike slip mechanism requiring a slightly increased magnitude. We have added the presently valid threshold values we find in the MRD document in the Solid Earth section, which request 1.0 cm EWH@350 km and 18 cm EWH@180 km (month), and 0.5 cm/yr EWH@250 km and 5 cm/yr EWH@150 km (long period). The long period request would correspond to the observation of the M7.4 earthquake signal change with a yearly sampling, and is slightly more stringent than the error curves of the MAGIC Bender noise curve. The requirement for the monthly acquisition corresponds to the signal of magnitude M7.7 earthquake, and is close to what can be expected for a MAGIC Bender type mission.
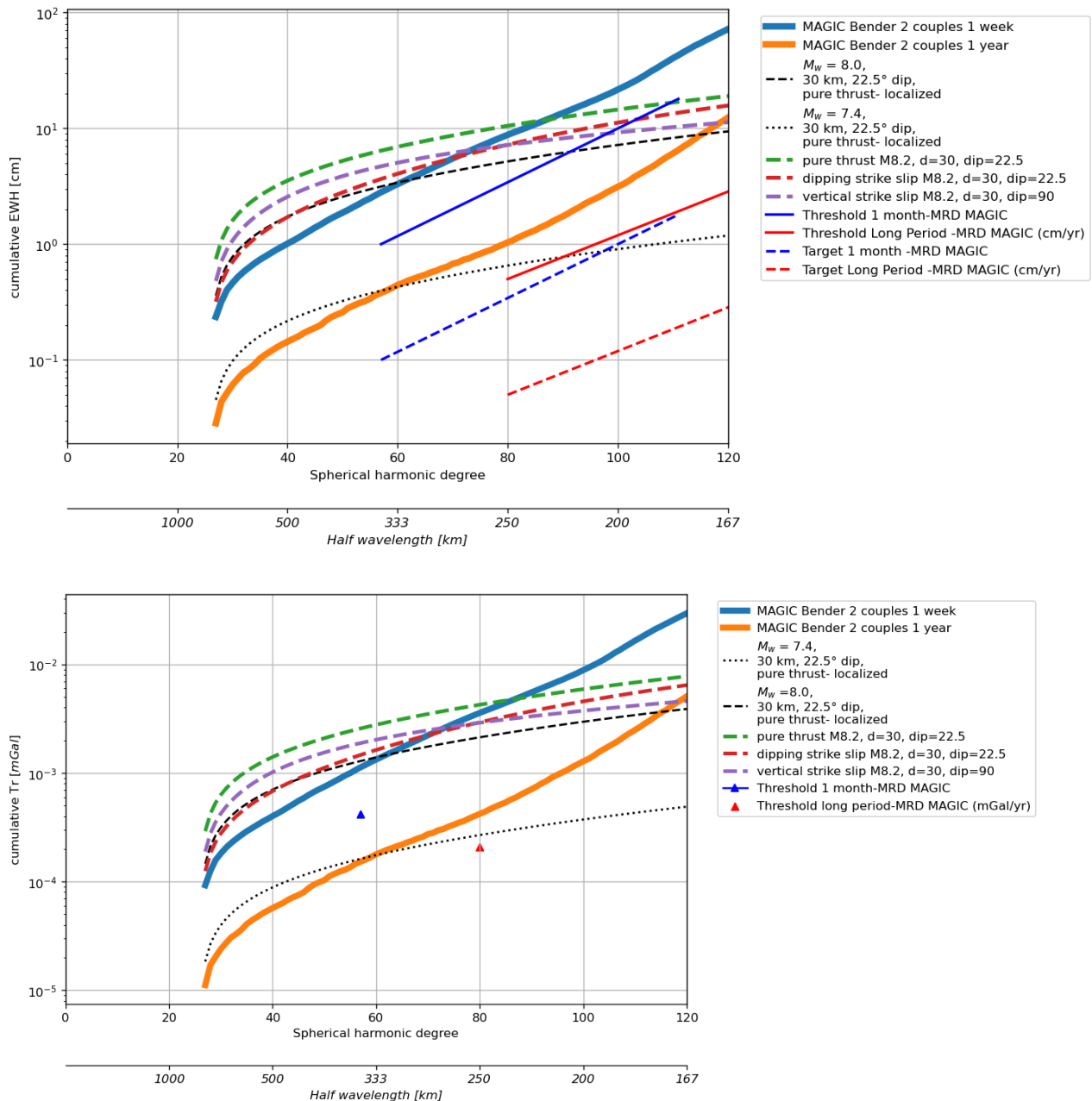
Figure 47-42. Cumulative noise curves and cumulative spectral signal curves for some selected earthquake mechanisms. EWH amplitude and gravity amplitude spectra at ground. In the gravity spectrum, the blue and red triangle correspond to the MRD threshold requirement for the solid earth section of 1.0 cm EWH@350 km and 18 cm EWH@180 km (month), and 0.5 cm/yr EWH@250 km and 5 cm/yr EWH@150 km (long period). Only the longer wavelength point is shown.

Conclusions

To analyse the performance of the MAGIC mission in detecting a gravity signal generated by an earthquake of a limiting magnitude M, we simulate the gravity signal that is generated by slip on a fault, given a seismic moment, to which a seismic magnitude is calculated. We define an earthquake to be observable if at least part of its spectral curve is above the spectral noise curve of the satellite mission. The seismic moment could be interpreted as due to a coseismic

signal, or due to a slow fault slip, and the gravity signal generated either in short time, or developing a trend distributed over time. The noise curve for a yearly time resolution has a degree variance that is smaller by a factor of 2/100 compared to a weekly time resolution, lowering the smallest observable seismic moment by the factor 0.14, which translates into a moment magnitude reduction of 0.57. This is because the degree variance of the gravity signal scales with the square of the seismic moment. Comparing single and double pair configurations with weekly solutions shows that the double pair significantly lowers the detectable moment magnitude from M=8.8 to M=8.2, and increases the highest observable degree up to about 60 (333 km resolution). Given a certain earthquake magnitude, the highest observable degree is defined by the SNR being equal to one or higher. Observing that the limiting SNR curve of value equal to 1 increases with increasing degree, the highest resolvable degree of the earthquake depends on its magnitude. Fixing the requested spatial resolution of an earthquake to 333 km at weekly sampling, which corresponds to degree 60, the Bender configuration requires the magnitude to be M=8.2, whereas the GRACE-like configuration requires the magnitude to be M=9.2. Lowering the time resolution to 1 year, the Bender configuration would detect earthquakes with magnitude M=7.4 upwards, at a spatial resolution of 333 km (degree 60). At higher degrees for this magnitude, the noise is expected to be larger than the EQ signal. The MAGIC configuration will bring a definitive improvement compared to the present observation technologies of a GRACE-like configuration.

47.5 CLIMATE CHANGE STUDIES

Following theories about climate change might leading to an "intensification" of the global water cycle resulting in, e.g. an increase in the annual amplitude of water storage change, and/or that climate-induced changes in atmospheric circulation patterns changing the phase of the annual peak, [RD-1] investigated the detectability of such changes in the annual water cycle using satellite gravimetry. A satellite mission that is able to observe and quantify these changes would be beneficial in two ways: (i) Satellite gravity could be used as tool to proof (or falsify) the postulate of an intensification of the water cycle in different regions of the world, and (2) the data could serve to validate whether climate models correctly simulate such changes. Figure 47-43 shows the projected changes in amplitude (left) and phase (right) derived from an ensemble of global climate models taking part in the CMIP6 model inter-comparison project. According to the models, in the majority of the land area (56%) the seasonal amplitude will increase in the future with a median of 0.12 mm/yr while in large parts (55% of the land area) the models project a positive phase shift, i.e., the maximum of the annual cycle will be reached later [RD-1]. As an example, the reason for the substantially later peak of the annual TWS maximum in large parts of Africa a later onset of the rainy season caused by a position shift in the tropical rain belt was identified.

Projected change of annual cycle from climate models
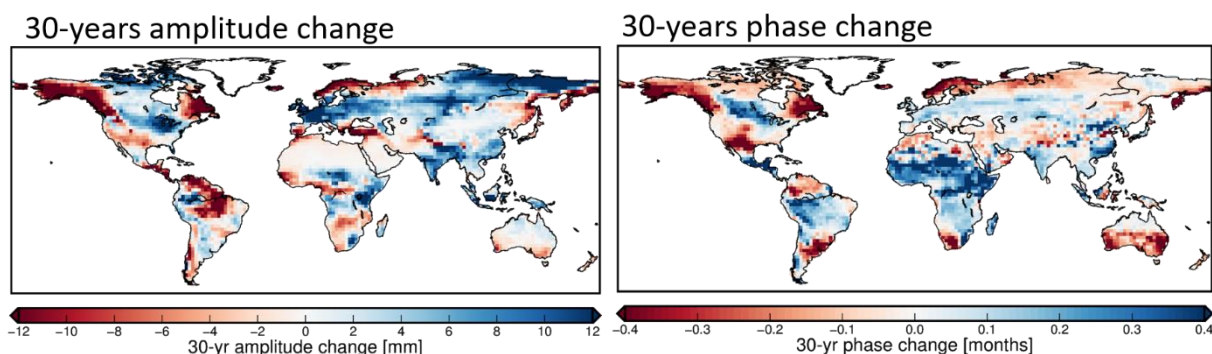
Figure 47-43: Projection of amplitude (left) and phase (right) change from 17 CMIP6 models, estimated over 2000-2100, scaled to 30 years from Jensen et al. (2020).

To analyze the detectability of these projected changes of the annual cycle by current or future satellite gravimetry missions, they were compared to the achievable accuracies of these quantities from the GRACE-like and the MAGIC simulation output. To this end the grid-wise RMSD values of the simulated 7-days temporal residuals were error propagated using the to derive standard deviations of amplitude/phase change after 30 years. For the amplitude change these standard deviations are shown in Figure 47-44 (top) for the GRACE-like mission (left) and for the MAGIC mission (right). Here we use VADER filtered solutions applying a comparably less strong filter (alpha=10) to come closer to the spatial resolution of the climate models. The projected amplitude changes (from Figure 47-43) are now challenged against these accuracies and colored pixels in Figure 47-44 (bottom) denote regions where the projected amplitude change exceeds the magnitude of the accuracy. While, according to the simulations at hand, a GRACE-like mission can only detect the anticipated amplitude changes in 36% of the land area after 30 years of observation, MAGIC-like missions would be able to identify such changes in 64% of the land area.

Propagated accuracy of a 30-years amplitude change

GRACE-like mission:

MAGIC:

Detectabililty of 30-years amplitude change

GRACE-like mission:

MAGIC:

36% of land area

64% of land area
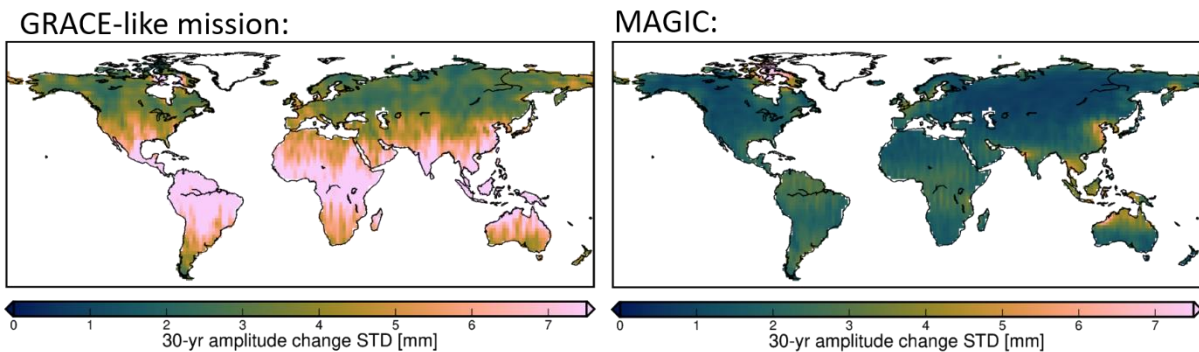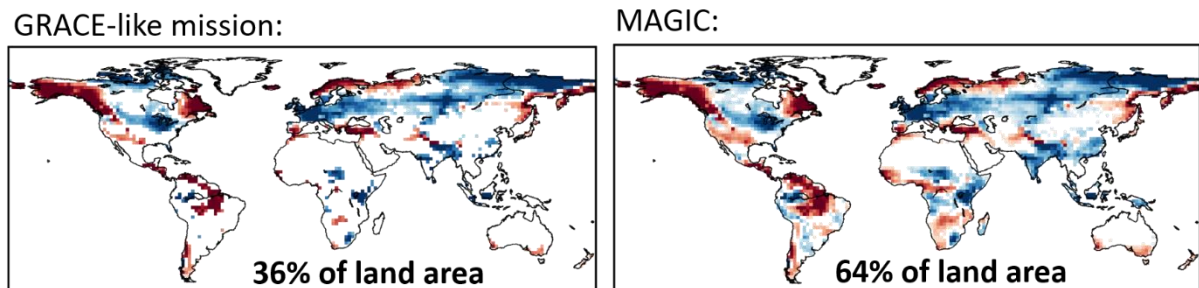
Figure 47-44: Top: Standard deviation of GRACE-like (left) and MAGIC (right) TWS amplitude change of annual cycle over 30 years. Bottom: Detectability of amplitude change: coloured pixels denote where projected amplitude change exceeds the magnitude of the accuracy.

The same analysis was repeated for the change in the phase of the annual cycle (Figure 47-45). Here again the top part shows the error-propagated accuracies of the phase change derived from the GRACE (left) and MAGIC (right) 7-day simulation output. The comparison with the projected changes (bottom) shows a detectability of a 30-years phase change from the single-pair scenario (left) in 30% of the land area and a significant increase of this portion (56% of land area) for the MAGIC scenario.

Propagated accuracy of a 30-years phase change
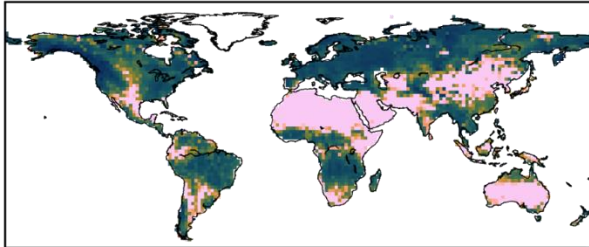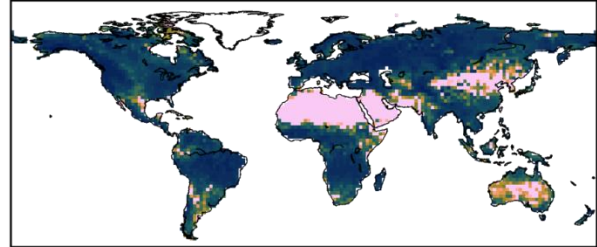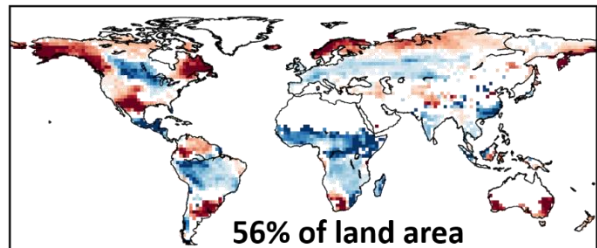
Detectabililty of 30-years phase change

Figure 47-45: Top: Standard deviation of GRACE-like (left) and MAGIC (right) TWS phase change of annual cycle over 30 years. Bottom: Detectability of phase change: coloured pixels denote where projected phase change exceeds the magnitude of the accuracy.

48 UPDATES AND REPHRASING OF SCIENCE QUESTIONS

48.1 UPDATES AND REPHRASING OF MRD REQUIREMENTS

The science panel revised the science questions and objectives of the MRD [AD-1]. The suggested modifications are given below, with the current text in the MRD given in black, and the suggested re-phrasing and additional comments are given in red.

3.2.1 Hydrology

- **H1**: Quantification of change. How is the water cycle changing? How are these changes expressed in frequency and magnitude of extremes events such as droughts and floods? Is it possible to close the water budget on various spatial and temporal scales?
  - ➢ **H1-a.** Develop and evaluate an integrated Earth system analysis with sufficient observational input to accurately quantify the components of the water and energy cycles and their interactions, and to close the water balance from headwater catchments to continental-scale river basins (confined to scales larger or equal than 250x250 km²). Provide constraints of the net fluxes.
  - ➢ **H1-b**. Quantify rates of snow accumulation, snowmelt and ice melt at regional scales.
  - ➢ **H1-c.** Estimate water storage change in small river basins and separate medium-scale drainage basins (confined to scales larger or equal than 250x250 km²).
- **H2**: Attribution of change. How do anthropogenic changes in climate, land use, water use, and water storage interact and modify the water and energy cycles locally, regionally, and globally, and what are the short- and long-term consequences? Is it possible to identify the climate change signature on the hydrological cycle?
  - ➢ **H2-a.** Quantify the magnitude of processes that cause changes in snowmelt, and ice melt, as they alter downstream water quantity (See CL2).
  - ➢ **H2-b**. Quantify how changes in land use, land cover, and water use related to agricultural activities, food production, and forest management, affect water storage and especially groundwater recharge, threatening sustainability of future water supplies.
  - ➢ **H2-c.** Drive and constrain predictive hydrological models with gravity data. Quantify individual natural and human-driven influences on the water cycle, as well as the separation of the different effects in a joint effort of combining modelling approaches and observations.
- **H3**: Impact on water availability. How do changes in the water cycle impact local and regional freshwater availability and related services ~~these provide~~?
  - ➢ **H3-a.** Monitor and understand the coupled natural and anthropogenic processes that change water quality, fluxes, and storages in and between all reservoirs (atmosphere, rivers, lakes, groundwater, and glaciers) and the response to extreme events as a basis for developing sustainable water resource management strategies
- **H4**: Prepardness for hazards. How does the water cycle interact with other Earth system processes to change the predictability and impacts of hazardous events and hazard chains (e.g. floods, wildfires, landslides, coastal loss, subsidence, droughts,

human health, and ecosystem health[Do all these issues need to be listed here? Can they all realistically be covered in the present context? Suggestions to remove at least coastal loss, subsidence, human health], and how do we improve preparedness and mitigation of water-related extreme events? How can we improve seasonal climate forecasts and the predictions of such extreme scenarios?

➢ **H4-a.** Improve drought and flood monitoring to forecast short-term impacts more accurately and to assess potential mitigations based on near real-time observations. Include gravity data into operational forecasting of drought and flood events (from long- to short-term).

Thematic field	Time scale **D**: Daily to weekly; **M**: Monthly; **L**: Long-term trend	Threshold: Resolution & Accuracy [EWH]	Target: Resolution & Accuracy [EWH]
Hydrology	**D**	Threshold-a: 600 km @ 3.2 cm; Threshold-b: 300 km @ 5.9 cm; Threshold-c: 280 km @ 6.0 cm	Target-a: 600 km @ 0.3 cm; Target-b: 300 km @ 0.6 cm; Target-c: 280 km @ 0.6 cm
	M	Threshold-a: 400 km @ 0.5 cm; Threshold-b: 260 km @ 4.8 cm	Target-a: 400 km @ 0.05 cm; Target-b: 260 km @ 0.48 cm
	L	Threshold-a: 350 km @ 0.1 cm/yr; Threshold-b: 150 km @ 5.0 cm/yr	Target-a: 350 km @ 0.01 cm/yr; Target-b: 150 km @ 0.5 cm/yr

Recommendation to relax threshold requirements at monthly time scale for the lower spatial resolution (i.e., Threshold-a: 400km@1.2 to 1.7 cm), and be more stringent with threshold requirements at monthly time scale for the higher spatial resolution.

3.2.2 Cryosphere

☐ **C1**: Reducing SLR projection uncertainty through improved process understanding: How much will ice sheets contribute to sea level change, globally and regionally, over the next decade and beyond? How can we determine the changes of ice sheets?

➢ **C1-a.** Current contribution: Determine the contribution of the ice sheets and mountain glaciers to global mean sea level change to within 0.1 mm/yr over the course of a decade (assuming 15 Gt/yr [See C2-b]).

➢ **C1-b.** Process understanding: Improve the knowledge on the dynamic response of ice flow to changing oceanic and atmospheric boundary conditions, including interactions with intra- and sub-glacial hydrology [See C2].

➢ **C1-c.** Regional impact: Determine the contribution of ice sheets and mountain glaciers to regional patterns of sea-level change to within 0.05 mm/yr over the course of a decade.

☐ **C2**: What will be the consequences of climate change on mass changes of ice sheets and glaciers?

➢ **C2-a.** Quantification: Reduce current uncertainties related to mountain glaciers and ice caps relative to the "eustatic" contribution to sea level rise.

➢ **C2-b.** Process attribution: Determine the changes in surface mass balance and glacier ice discharge and uncertainties within the 15 Gt~~on~~/yr accuracy over the entire ice sheets, continuously, for decades to come. Disentangle the superimposed processes from a combination of geodetic observations and modelling approaches (See Solid Earth).

➢ **C2-c.** Process understanding and modelling: Improve modelling capabilities to fully understand ice sheet and glacier changes and provide enhanced robust predictions. Enhance number and accuracy of observations. Validate model developments, provide boundary conditions and allow model initialization. Understand the processes revealed by observations for further developing models with the aim of reaching predicting capabilities for emergency applications like meltwater flooding.

➢ **C2-d.** Process separation: Separating ice sheet changes from coastal ocean changes. This task includes the account for the gravitationally consistent ocean changes induced by the ice mass changes themselves, as well as changes due to ocean dynamics.

➢ **C2-e.** Quantification: Cryosphere mass balance at monthly to decadal time scales to understand climate forcing on ice sheets and glaciers.

☐ **C3**: Interactions: How can we improve the description of geodynamic processes, induced by continental ice mass changes, which act globally? How can we better interpret Glacial Isostatic Adjustment (GIA) and distinct spatial "fingerprints" of global oceanic mass redistributions?

➢ **C3-a.** Improve the information on glacial history and solid Earth rheology, as well as consistency in the observing systems, and therefore embrace a large range of geoscience disciplines. Gravity has a key role due to its integrative nature and its direct relationship to conditions of mass conservation between changes in the cryosphere, the oceans and continental hydrology.

Thematic field	Time scale D: Daily to weekly; M: Monthly; L: Long-term trend	Threshold: Resolution & Accuracy [EWH]	Target: Resolution & Accuracy [EWH]
Cryosphere	D	Threshold-a: 400 km @ 5.0 cm; Threshold-b: 300 km @ 5.9 cm; Threshold-c: 250 km @ 6.3 cm	Target-a: 400 km @ 0.5 cm; Target-b: 300 km @ 0.6 cm; Target-c: 250 km @ 0.6 cm
	M	Threshold-a: 250 km @ 5.5 cm; Threshold-b: 150 km @ 50.0 cm	Target-a: 250 km @ 0.55 cm; Target-b: 150 km @ 5.0 cm
	L	Threshold-a: 170 km @ 2.6 cm/yr; Threshold-b: 130 km @ 15.0 cm/yr	Target-a: 170 km @ 0.26 cm/yr; Target-b: 130 km @ 1.5 cm/yr

3.2.3 Oceanography

- **O1**: How are decadal-scale global ocean circulation patterns changing, and what are the effects of these changes on seasonal climate processes, extreme events, and longer term environmental change?
  - ➢ ~~O1-a. Quantify the changes in the oceanic circulation patterns, reducing the uncertainty by a factor of 2.~~[As it stands, it is hard to see why MAGIC would quantify changes in ocean circulation, as its primary output relevant to this is the geoid, allowing mean dynamic topography to be calculated, and commonly considered to be static. Suggestion for new O1-a:]
  - ➢ **O1-a.:** Separate out changes in ocean dynamics, seen in sea level measurements, from changes in the geoid, removing an uncertainty in interpretation of satellite altimetry measurements which is steadily growing over time.
  - ➢ **O1-b.** Quantify the linkage between natural and anthropogenic forcing and oscillations in the climate system and the one between the dynamical and thermodynamic state of the ocean on decadal time scales. For both, reduce the uncertainty by a factor of 2.
  - ➢ **O1-c.** Quantify the linkage between global climate sensitivity and circulation change on regional scales, including the occurrence of extremes and abrupt changes. Quantify the changes in the strength of AMOC to within 5% per decade; ~~changes in ENSO spatial patterns, amplitude, and phase~~ [Any gravitational contribution to this is likely to be very small, related to quantifying the small changes in geoid over the tropical Pacific which interfere with interpretation of sea level changes (from altimetry) as dynamic topography changes. There are interesting questions about whether ENSO has a signal in ocean bottom pressure, beyond the continental shelf, but these are not addressed by this point.]
  - ➢ **O1-d.** Provide observational verification of models used for climate projections. Enhanced simulations on evolution of the large-scale patterns in the ocean circulation and tides are necessary. Improving descriptions nearby coasts and current de-aliasing is crucial. Improved tidal models by co-estimation of ocean tide parameters requires long time series as well as increased accuracy compared to the current state.
  - ➢ ~~O1-e. The ocean bottom pressure variations and the time mean dynamic topography can be provided by satellite gravity missions which are a powerful tool for investigating the ocean's internal dynamics. It mainly requires an improvement in spatial resolution. Combination with altimetry needs further improvement.~~ [This seems a rather vague bullet, and is formulated differently from other bullets in that it is a description of issues rather than an outcome. Suggestion for modified O1-e:]
  - ➢ **O1-e.** Quantify changing storage of dense waters in abyssal basins, and pressure differences across basins, which allow the diagnosis of mass transport. These processes play an important role in the global thermohaline circulation, in ocean heat storage, and in reconciling the global ocean volume budget for understanding of sea level change. They are currently poorly observed by other means, so observations have the potential to greatly improve process understanding.

Thematic field	Time scale D: Daily to weekly; M: Monthly; L: Long-term trend	Threshold: Resolution & Accuracy [EWH]	Target: Resolution & Accuracy [EWH]
Oceanography	D	N.A.	N.A.
	M	Threshold-a: 1000 km @ 0.2 cm; Threshold-b: 400 km @ 0.5 cm; Threshold-c: 250 km @ 5.5 cm.	Target-a: 1000 km @ 0.02 cm; Target-b: 400 km @ 0.05 cm; Target-c: 250 km @ 0.55 cm.
	L	Threshold-a: 800 km @ 0.015 cm/yr; Threshold-b: 400 km @ 0.05 cm/yr; Threshold-c: 180 km @ 1.8 cm/yr.	Target-a: 800 km @ 0.0015 cm/yr; Target-b: 400 km @ 0.005 cm/yr; Target-c: 180 km @ 0.18 cm/yr.

3.2.4 Solid Earth

☐ **S1**: How can large-scale geological hazards be accurately forecast in a socially relevant time frame? How do geological disasters directly impact the Earth system and society following an event? How can we monitor geohazards associated with earthquakes, tsunamis and volcanoes?

➢ **S1-a.** Measure and forecast inter-seismic, pre-seismic, co-seismic, and post-seismic activity over tectonically active areas on time scales ranging from hours to decades to distinguish the instant effects from long-term movements. Detect tectonic, aseismic creep events equivalent to magnitude >7. [In this study, we find a limit of 7.4 with a 1 year time resolution, but if we allow more years for observation, then M>7 is correct.] Rapid capture of the transient processes following disasters is needed for improved predictive modelling, as well as response and mitigation through optimal re-tasking and analysis of space data. A spatial resolution of 200 km with an accuracy of 0.5 µGal is needed. [200km@0.5 microGal corresponds to 1.3 cm EWH for monthly acquisition. This corresponds to the target performance, which is not fulfilled by MAGIC, as far as we see from the noise curves we have received in this study. A value of 5 microgal@200km monthly seems more feasible, corresponding to 10 cmEWH@200km cumulative signal.] Monthly resolution is required, acquisition of daily to weekly data with low latency is vital for specific short-term monitoring.

➢ **S1-b.** Forecast, model, and measure tsunami generation, propagation, and run-up for major tsunamigenic events.

☐ **S2**: How does energy flow from the core to Earth's surface? Can we better quantify the physical properties in the deep interior and their relationship to deep and shallow geodynamic processes?

➢ **S2-a.** Determine the effects of convection within Earth's interior, specifically the dynamics of Earth's core and its changing magnetic field and the

interaction between mantle convection and plate motions.

If high accuracy (signals amplitude: 0.5-1 mm EWH in 10 years) can be reached at long wavelengths (thousands km) and decadal timescales, on-going deep Earth dynamics may become observable: geostrophic flows near the top of the core that change pressures at the CMB [RD15], on-going large-scale convective mantle flow [RD13].

Time-integrated body tides perturbations from the heterogeneous mantle mass distribution are 10 times larger than the above deep Earth dynamics signals, reaching 0.5-1 mm EWH in one year [RD14]. Observe gravimetric perturbations caused by tidal forcing of convection-induced mantle heterogeneity.

☐ **S3**: How can we jointly quantify and improve separation of the ongoing solid Earth deformation in response to surface loads, as the last deglaciation (i.e., the post-glacial rebound (GIA) signal), or resulting from the internal dynamics, together with the present-day ice sheet loss and water mass variations [RD1][RD16]?

➤ **S3-a.** Separate signals: Identification of long-term effects and the separation from annual to inter-annual climatic factors which affect surface deformation of the crust: time series length in combination with past and existing missions of at least 30 years is required. A long time series characterized by a trend accuracy of 0.05 µGal/yr on scales of 200 km will be critical to provide regional-scale estimates of ongoing crustal deformation across the topographic land surface, ocean bottom and lower crustal boundary.

➤ **S3-b.** Surface processes: Quantify global, decadal landscape change produced by abrupt events and by continuous reshaping of Earth's surface due to surface processes, tectonics, and societal activity.

➤ **S3-c.** Internal creeping: Distinguish the creeping portions of subduction zones from the locked portion, which is crucial for hazard estimation of the inter-seismic interval of large earthquakes, or to observe regional tectonic processes as mountain building. By constraining Earth's low viscosity layers, it will enable characterization of the coupling between the plates and the mantle in active and oceanic areas.

➤ **S3-d.** Time series extension: As long-term processes are involved, the most important aspect is a continuous time series in combination with an increased spatial resolution. The minimum required time series for this mission is 6 years. Monthly resolution is adequate.

☐ **S4**: How much water is traveling deep underground and how does it affect geological processes over the long term and short term (earthquakes) and water supplies (e.g. water management)? How do we improve discovery and management of energy, mineral, and soil resources? How can we achieve sustainable exploitation of natural resources?

➤ **S4-a.** Crust and mantle structure: Improve spatial resolution for imaging of the 3D structure of the crust and mantle using the static gravity field. This is needed in order to locate and monitor changes in key resources.

- ➢ **S4-b.** Anthropogenic changes detection: Monitor underground anthropogenic driven mass variations. Monthly resolution is adequate, weekly resolution is desirable.
- ➢ **S4-c.** Hydrologic monitoring: Measure all significant fluxes in and out of the groundwater system across the recharge area. Determine the transport and storage properties in situ within a factor of 3 for shallow aquifers and an order of magnitude for deeper systems. Assess the impact of these water redistributions on earthquakes. [Should be consistent with hydrological requirements,]

Thematic field	Time scale D: Daily to weekly; M: Monthly; L: Long-term trend	Threshold: Resolution & Accuracy [EWH]	Target: Resolution & Accuracy [EWH]
Solid Earth	D	Threshold: 300 km @ 6.0 cm	Target: 300 km @ 0.6 cm
	M	Threshold-a: 350 km @ 1.0 cm; Threshold-b: 180 km @ 18 cm.	Target-a: 350 km @ 0.1 cm; Target-b: 180 km @ 1.8 cm.
	L	Threshold-a: 250 km @ 0.5 cm/yr; Threshold-b: 150 km @ 5.0 cm/yr	Target-a: 250 km @ 0.05 cm/yr; Target-b: 150 km @ 0.5 cm/yr

3.2.4 Climate Change

- ☐ **CL1**: How much will sea level change, globally and regionally, and along coastlines over the next decade and beyond, and what will be the role of ocean heat storage?
  - ➢ **CL1-a.** Observation and modelling: Quantify the rates of sea-level change and its driving processes at global and regional scales.
  - ➢ **CL1-b.** Procedures-interactions: Determining how and where heat is being taken up by the ocean, estimating how much is being stored in the deep ocean, and understanding the processes that control this are all important to understand sea level rise and improve the predictive skill of climate models.

- ☐ **CL2**: Is it possible to separate the effects of natural climate variability, long-term climate change and direct anthropogenic impacts on the water cycle?
  - ➢ **CL2-a.** Interaction with climate models: Evaluate seasonal to decadal climate predictions and assess long-term climate model projections [RD11] [RD10].
  - ➢ **CL2-b.** Continuity requirement: Ensure the continuation of current mass transport observations to provide multidecadal time series [RD21] [RD22].

48.2 NEW THEMATIC FIELD: GEODESY

As additional thematic field, "geodesy" was identified to be included in the MRD. The following text was prepared by Thomas Gruber, with inputs and feedback from Roland Pail, Reiner Rummel and Laura Sánchez. Feedback from further international experts is expected.

Within the "Geodesy" thematic field, the following societal and science questions and objectives need to be answered and achieved by MAGIC with complementary information:

G1: How to achieve a **global unification of height systems** with sufficient accuracy required by cross-border geodetic applications? How can regional and national height systems be unified independently of local datums realised by tide gauges measuring the local mean sea level? How can we complement local terrestrial and airborne gravimetry surveys by globally homogeneous and consistent satellite observations?

- **G1-a**. Develop a global reference geoid as an optimum combination of satellite and ground/airborne gravity data covering all relevant spatial wavelength, in order to minimize omission errors which currently can amount to high frequency geoid height errors of several decimetres in mountainous areas.
- **G1-b**. Develop a global satellite-only reference geoid with highest possible resolution, which serves as basis for computing the omission error at height reference stations from local gravity observations (in case station is not covered with ground data available for G1-a).
- **G1-c**. Generate a reference geoid which accounts for temporal changes of gravity field with improved spatial resolution and accuracy particularly needed in regions with strong gravity variations, like trends due to GIA, large scale surface and/or ground water variations or seismic events.

G2: How can we improve **GNSS levelling** to benefit national geodetic control networks and surveying applications, in particular in countries with a less developed geodetic infrastructure? Can GNSS levelling substitute costly and time-consuming traditional spirit levelling techniques? How do physical heights vary with redistribution of mass in the Earth system? How do changes in frequency and magnitude of the time variable gravity field affect the reference geoid used as zero-height level from which physical heights are measured?

- **G2-a**. Resolve temporal variations of physical heights induced by gravity variations originating from geophysical signals such as post-glacial rebound effects or other large scale mass redistributions, by including temporal gravity field variations of sufficient spatial resolution and accuracy.

G3: How are satellite-derived **geometric heights** affected by redistribution of mass in the Earth system? How can we improve the determination of geometric heights to derive enhanced products of Earth Observation missions such as SAR and altimetry missions?

- **G3-a**. Improve the accuracy of Earth Observation satellite orbits by including the time variable gravity field information in the precise orbit determination process.
- **G3-b**. Improve the accuracy of geometric heights by benefiting from improved orbits from G2-a and generate enhanced products from Earth Observation missions such as altimetry and SAR missions.

The previous science and societal questions and objectives are connected to the specific signals in the following Table 48-1. The user requirements are collected in Table 48-2.

Table 48-1: Societal and science questions and objectives link to specific geodetic quantities.

Thematic field	Quantity of interest	Scientific/societal **Q**uestions & **O**bjectives
Geodesy	Physical heights	Q: G1, G2; O: G1-a, G1-b, G1-c, G2-a;
	Geometric heights	Q: G3, C1, C2, C3, O1, S1, S3, CL1; O: G3-a, G3-b, C1-a, C1-b, C1-c, C2-a, C2-b, C2-c, C2-d, C2-e, C3-a, O1-a, O1-b, O1-c, O1-d, O1-e, S1-a, S1-b, S3-a, S3-b, S3-c, S3-d, CL1-a, CL-1b;

Table 48-2: MAGIC user requirements for Geodesy (Physical heights, Geometric heights). Values are obtained from IUGG user requirements [RD-21] and the e.motion2 proposal [RD-20].

Thematic field	**Time scale** **D**: Daily to weekly; **M**: Monthly; **L**: Long-term trend; **A**: Long-term average	**Threshold:** **Resolution & Accuracy [Geoid]** *Resolution & Accuracy [EWH]*	**Target:** **Resolution & Accuracy [Geoid]** *Resolution & Accuracy [EWH]*
Geodesy	**D**	N.A.	N.A.
	M	Threshold-a: 400 km @ 50 µm *Threshold-a: 400 km @ 0.7 cm;* Threshold-b: 200 km @ 500 µm *Threshold-b: 200 km @ 13 cm*	Target-a: 400 km @ 5 µm *Target-a: 400 km @ 0.07 cm;* Target-b: 200 km @ 50 µm *Target-b: 200 km @ 1.4 cm*
	L	Threshold-a: 400 km @ 5 µm/yr *Threshold-a: 400 km @ 0.07 cm/yr;* Threshold-b: 200 km @ 50 µm/yr *Threshold-b: 200 km @ 1.4 cm/yr*	Target-a: 400 km @ 0.5 µm/yr *Target-a: 400 km @ 0.01 cm/yr;* Target-b: 200 km @ 5 µm/yr *Target-b: 200 km @ 0.14 cm/yr*
	A	Threshold-a: 100 km @ 0.5 cm *Threshold-a: 100 km @ 264 cm;* Threshold-b: 30 km @ 1 cm *Threshold-b: 30 km @ 1740 cm*	Target-a: 100 km @ 0.1 cm *Target-a: 100 km @ 53 cm;* Target-b: 30 km @ 0.5 cm *Target-b: 30 km @ 870 cm*
Thematic sub-field			
Physical heights	**L, A**	See Geodesy	See Geodesy
Geometric heights	**L, A**	See Geodesy	See Geodesy

Remarks:

- For monthly (M) and long-Term (L) the numbers from the e.motion^2 proposal [RD-20] equivalent to the numbers in the IUGG report [RD-21] were taken, 400 km and 200 km resolution were used.
- Another line for the average field (A) was added. A resolution of 30 km (corresponding to degree 720) was selected, because it is unlikely that a 2160 model with 10 km resolution can reach that goal in average (may be in some areas with very good terrestrial data coverage).

49 APPLICABLE DOCUMENTS, REFERENCE DOCUMENTS, AND PUBLICATIONS TO PART 7

49.1 APPLICABLE DOCUMENTS

[AD-1] Mission Requirements Document, Next Generation Gravity Mission as a Mass-change And Geosciences International Constellation (MAGIC) - A joint ESA/NASA double-pair mission based on NASA's MCDO and ESA's NGGM studies (2020). ESA-EOPSM-FMCC-MRD-3785

[AD-2] Scientific Readiness Levels (SRL) Handbook, Issue 1, Revision 0, 05-08-2015

[AD-3] Statement of Work - ESA Express Procurement - EXPRO NGGM/MAGIC science support study during Phase A, Issue 1, Revision 0, 18/01/2021 Ref ESA-EOPSM-FUTM-SOW-3813

49.2 REFERENCE DOCUMENTS

[RD-1] Jensen, L., Eicker, A., Dobslaw, H., & Pail, R. (2020): Emerging Changes in Terrestrial Water Storage Variability as a Target for Future Satellite Gravity Missions. Remote Sensing, 12(23), 3898.

[RD-2] Wouters, B., Chambers, D., Schrama, E.J.O. (2008): GRACE observes small-scale mass loss in Greenland. Geophysical Research Letters 35(20), doi: 10.1029/2008gl034816.

[RD-3] Ran, J. J., et al. (2018): Seasonal mass variations show timing and magnitude of meltwater storage in the Greenland Ice Sheet, Cryosphere, 12(9), 2981-2999, doi: 10.5194/tc-12-2981-2018.

[RD-4] Wieczorek, M.A. (2007): Simons, F.J. Minimum-Variance Multitaper Spectral Estimation on the Sphere. J Fourier Anal Appl, 13, 665–692, doi:10.1007/s00041-006-6904-1.

[RD-5] Pivetta, T.; Braitenberg C.; Pastorutti, A. (2022) Sensitivity to lakes and glaciers mass changes of the quantum technology gravity gradients and time observations on satellite MOCAST+ Remote Sens., 14, x. https://doi.org/10.3390/xxxxx, under review.

[RD-6] Wieczorek, M.A.; Meschede, M. SHTools: Tools for Working with Spherical Harmonics. Geochem. Geophys. Geosyst. 2018, 19, 2574–2592, doi:10.1029/2018GC007529.

[RD-7] Wang, R., Heimann, S., Zhang, Y., Wang, H., Dahm, T., 2017. Complete synthetic seismograms based on a spherical self-gravitating Earth model with an atmosphere–ocean–mantle–core structure. Geophysical Journal International 210, 1739–1764. https://doi.org/10.1093/gji/ggx259

[RD-8] Takeuchi, H., Saito, M., 1972. Seismic Surface Waves, in: Methods in Computational Physics: Advances in Research and Applications. Elsevier, pp. 217–295. https://doi.org/10.1016/B978-0-12-460811-5.50010-6

[RD-9] Kanamori, H., Anderson, D.L., 1975. Theoretical basis of some empirical relations in seismology. Bulletin of the Seismological Society of America 65, 1073–1095. https://doi.org/10.1785/BSSA0650051073

[RD-10] Wells, D.L., Coppersmith, K.J., 1994. New empirical relationships among magnitude, rupture length, rupture width, rupture area, and surface displacement. Bull. Seismol. Soc. Am. 84, 974–1002.

[RD-11] Tanaka, Y., Hasegawa, T., Tsuruoka, H., Klemann, V., Martinec, Z., 2015. Spectral-finite element approach to post-seismic relaxation in a spherical compressible Earth: application to gravity changes due to the 2004 Sumatra–Andaman earthquake. Geophysical Journal International 200, 299–321. https://doi.org/10.1093/gji/ggu391

[RD-12] Murböck, M., 2015. Virtual Constellations of Next Generation Gravity Missions. Technical University Munich, http://mediatum.ub.tum.de/doc/1241150/268203.pdf.

[RD-13] Pail R., Bingham R., Braitenberg C., Dobslaw H., Eicker A., Güntner A., Horwath M., Ivins E., Longuevergne L., Panet I., Wouters B., IUGG Expert Panel (2015). Science and User Needs for Observing Global Mass Transport to Understand Global Change and to Benefit Society. Surveys in Geophysics, 36(6), 743-772, DOI:10.1007/s10712-015-9348-9.

[RD-14] Hughes, C. W., Joanne Williams, A. Hibbert, C. Boening and J. Oram, 2016: A Rossby whistle: A resonant basin mode observed in the Caribbean Sea. Geophys. Res. Lett. 43, 7036-7043, doi: 10.1002/2016GL069573.

[RD-15] Hughes, C. W., J. Williams, A. Blaker, A. Coward and V. Stepanov, 2018: A window on the deep ocean: The special value of ocean bottom pressure for monitoring the large-scale, deep-ocean circulation. Progress in Oceanography 161, 19-46. doi: 10.1016/j.pocean.2018.01.011.

[RD-16] Horvath, A., Murböck, M., Pail, R., Horwath, M. (2018): Decorrelation of GRACE Time Variable Gravity Field Solutions Using Full Covariance Information. - Geosciences, 8, 9., DOI:10.3390/geosciences8090323

[RD-17] Noël, B., van de Berg, W. J., Lhermitte, S., and van den Broeke, M. R.: Rapid ablation zone expansion amplifies north Greenland mass loss, Sci Adv, 5, eaaw0123, https://doi.org/10.1126/sciadv.aaw0123, 2019.

[RD-18] Sasgen, I., van den Broeke, M., Bamber, J. L., Rignot, E., Sørensen, L. S., Wouters, B., Martinec, Z., Velicogna, I., and Simonsen, S. B.: Timing and origin of recent regional ice-mass loss in Greenland, Earth and Planetary Science Letters, 333–334, 293–303, https://doi.org/10.1016/j.epsl.2012.03.033, 2012.

[RD-19] Zwally, H. Jay, Mario B. Giovinetto, Matthew A. Beckley, and Jack L. Saba, 2012, Antarctic and Greenland Drainage Systems, GSFC Cryospheric Sciences Laboratory, http://icesat4.gsfc.nasa.gov/cryo_data/ant_grn_drainage_systems.php.

[RD-20] Gruber, Th., Murböck, M., NGGM-D Team: e2.motion - Earth System Mass Transport Mission (Square) - Concept for a Next Generation Gravity Field Mission. C.H. Beck, 2014.

[RD-21] Pail, R.; Bingham, R.; Braitenberg, C.; Dobslaw, H.; Eicker, A.; Güntner, A.; Horwath, M.; Ivins, E.; Longuevergne, L.; Panet, I.; Wouters, B.: Science and User Needs for Observing Global Mass Transport to Understand Global Change and to Benefit Society. Surveys in Geophysics 36 (6), 2015, 743-772.

PART 8:

CALIBRATION OF ACCELEROMETERS

50 INTRODUCTION

This Part 8 refers to Task 7 of the SoW and covers the work performed under WP 700 of the WBS. It refers to the deliverable document TN D17 "Calibration of accelerometers".

The main purpose is to investigate if embarking a DORIS receiver has the potential to enhance the calibration of accelerometers..

51 EMBARKING DORIS RECEIVERS

In order to study the impact of embarking DORIS receivers on board of the gravity field satellites, accelerometer calibration simulations have been conducted for the scenario **3d_H** as outlined in [RD-1]. This scenario has a repeat cycle of 31 days with 3- and 7-day sub-cycles. The end-to-end simulator as used in precursor NGGM studies [RD-2][RD-3][RD-4] includes the DORIS observable type and is in fact also capable of processing real DORIS observations, as is done for, e.g., CryoSat-2 [RD-12]. DORIS has a proven capability of providing precise orbit solutions for Low Earth Orbiting satellites at the sub-decimeter level in terms of 3-dimensional position, and approaching the cm-level for the radial direction (see again, e.g., [RD-12]).

It will be assessed if DORIS, in addition to precise cm-level kinematic orbit solutions derived from GNSS observations, has the capability to enhance the calibration of accelerometers. The use of satellite tandems allows to form differential DORIS observations, which mitigates (largely) common errors such as tropospheric delay correction errors. Therefore, the accelerometer calibration simulations will include solutions based on both absolute and differential DORIS observations.

52 CALIBRATION OF ACCELEROMETERS

The accelerometer calibration scheme and setup are identical to the ones for the gravity field retrievals [RD-13], except for the parameters that are estimated. The accelerometer calibration is based on daily purely dynamic precise orbit determinations per satellite pair, where only the initial position and velocity for each parameter are estimated, thus 2x2x3 = 12 parameters. In addition, for each accelerometer 3 constant biases and 3 scale factors can be estimated in the X, Y and Z direction (predominantly along-track, cross-track and radial direction), again 2x2x3 = 12 parameters. Depending on the magnitude of the non-gravitational signal (see below), accelerometer scale factors can be more or heavily constrained.

For the accelerometer calibration, different combinations of observation types can be taken. The accuracy of estimated accelerometer biases and scale factors will be assessed for the following 10 combinations of observations:
- kinematic orbit coordinates (GNSS);
- absolute or differential DORIS observations (DORIS undif/dif);
- GNSS and DORIS observations (GNSS+DORIS dif/undif);
- kinematic orbits and ll-SST (GNSS+LRI);
- absolute or differential DORIS observations and ll-SST (DORIS undif/dif +LRI);

- all observations (DORIS undif/dif +GNSS+LRI).

When different observation types are combined, use will be made of the optimal weights (Table 3-1 in [RD-13]). By using a setup per satellite pair, the possible use of the ll-SST observations for accelerometer calibration can be assessed as well, in addition to the use of differential DORIS observations.

First, the proper estimation of accelerometer calibration parameters will be verified (Section 52.1). Second, the accelerometer calibration performance will be assessed for nominal drag-free flight (Section 52.2). Third, the use of maneuvers for improving the accelerometer calibration will be investigated (Section 52.3). Finally, the possibility to calibrate the accelerometer during the commissioning phase when the satellite fly non-drag-free will be explored (Section 52.4).

52.1 VERIFICATION OF ACCELEROMETER CALIBRATION PARAMETERS ESTIMATION

Before testing the estimation of accelerometer calibration parameters in the presence of the full error model, and before adopting possible maneuver schemes, consistency tests were conducted to validate the estimation of accelerometer biases. In a first test, constant biases were added to the accelerometer observations in the X, Y and Z direction equal to, respectively, 50, -50, and 50 nm/s^2 for all satellites. The estimated biases are displayed in Table 52-1 (left) for several combinations of observations. It can be observed that the biases are in general retrieved with high precision, especially when the kinematic position coordinates (GNSS) are included. For the ll-SST only solutions, the retrieved biases can have an error up to about 4 nm/s^2. The errors can be explained by near-singularity of the associated estimation process when using ll-SST observations only causing the need for applying slight constraints leading to a biased estimation process. Second, the consistency of scale factor estimation was tested by specifying the prior values for the scale factor equal to 0.8, 1.2 and 0.9 for, respectively, the X, Y and Z accelerometer axis. Please note that the correct value for the scale factors is 1.0. Table 52-1 shows that the retrieved scale factors are indeed close to 1.0 for all tested combinations of observations, except for the Y axis. The residual non-gravitational accelerations as used are according to the specifications in [RD-4] and display relatively large low-frequency signal for the Z axis as compared to the X axis, whereas the signal for the Y axis appears almost as Gaussian noise. The latter makes the estimation of the Y axis scale factors very unreliable and sensitive to the convergence settings of the iterative weighted least-squares precise obit determination process, where the iterations are required because of the linearized observation equations (for this test the maximum number of iterations was set at 6 or 2% convergence in terms of RMS of fit of the tracking observations, whichever comes first). The deviation of the Y axis scale factor can be as large as almost 0.04 for the ll-SST only solutions, but is below 0.0001 for the GNSS only solutions.

52.2 DRAG-FREE FLIGHT

The baseline for the satellites is to fly in drag-free mode, where the residual non-gravitational accelerations are of the order of 10 nm/s^2 (Table 3-1 in [RD-13]). Typically, accelerometers that fly on space-borne gravimetry missions require the estimation of biases, often with daily frequency, and scale factors for each accelerometer axis (X, Y and Z). However, the drag-free flight leaves a very small non-gravitational signal to be observed by the accelerometers, which makes the estimation of accelerometer scale factors less crucial and also very unstable. The latter is shown by a representative 1-day estimation of both accelerometer biases and scale factors.

The formal errors and retrieval errors are displayed in Table 52-2 and Table 52-3 for both the single and the combination of all observation types, when adopting the full error model (see Table 3-1 in [RD-13]). The formal errors (Table 52-2) are in general too optimistic, but give an indication of the achievable precision. As expected, the smallest formal errors are obtained when combining all available observations. The biggest contribution for precise accelerometer calibration comes from the kinematic orbit coordinates (GNSS). Accelerometer calibration is expected to be much less precise when using either absolute or differential DORIS observations. Adding DORIS to kinematic orbit coordinates leads to slightly smaller errors for the X (predominantly along-track) and Z (predominantly radial) axes. The ll-SST observations hardly contain information for (improving) the accelerometer calibration for the Y (predominantly cross-track) and Z axes, and only slightly for the X axis. In all cases, the retrieval of the Y axis accelerometer scale factor is very unreliable.

Table 52-1 Validation of accelerometer bias (left) and scale factor (right) estimation for different combinations of observations: error-free case (scenario 3d_H). Optimal weighting. The results hold for drag-free flight on 1 January 2002, which is representative for other days as well.

Satellite/obs	Bias retrieval (nm/s^2)			Scale factor retrieval		
	X	Y	Z	X	Y	Z
1/All	50,00000	-49,99993	50,00150	1,00000	0,99610	1,00000
1/G.+D undif	50,00000	-50,00292	49,99704	1,00000	0,99996	1,00000
1/G.+D. dif	50,00000	-50,00000	49,99999	1,00000	0,99973	1,00000
1/GNSS	49,99999	-50,01660	50,07645	1,00000	0,99999	1,00000
1/DORIS undif	49,99999	-50,01184	50,04298	1,00000	0,99820	1,00000
1/DORIS dif	49,99927	-50,26175	50,13205	1,00000	0,99816	1,00000
1/ll-SST	50,00000	-50,00103	49,99622	1,00000	0,96978	1,00000
2/All	50,00000	-49,99993	50,00152	1,00000	1,00276	1,00000
2/G.+D undif	50,00000	-49,99686	50,00378	0,99999	1,00006	1,00002
2/G.+D. dif	50,00000	-50,00000	50,00000	0,99999	1,00039	1,00002
2/GNSS	49,99999	-50,01634	50,07772	0,99999	1,00007	1,00002
2/DORIS undif	49,99999	-49,99142	50,01701	0,99999	0,99940	1,00002
2/DORIS dif	49,99935	-50,26030	49,63704	1,00000	1,00241	1,00000
2/ll-SST	50,00000	-49,99993	49,98112	1,00000	0,99926	1,00000
3/All	50,00000	-49,99987	49,97988	1,00000	1,00190	1,00000
3/G.+D undif	50,00000	-50,00120	49,97642	1,00000	0,99999	0,99999
3/G.+D. dif	50,00000	-50,00000	49,99997	1,00000	1,00036	0,99999

3/GNSS	50,00019	-50,04108	49,30366	1,00000	1,00000	0,99999
3/DORIS undif	50,00025	-50,04292	49,04758	1,00000	0,99985	0,99999
3/DORIS dif	49,99878	-49,82433	53,72764	1,00000	1,00204	0,99999
3/ll-SST	50,00000	-49,99722	49,97947	1,00000	0,96894	1,00000
4/All	50,00000	-49,99985	49,97991	1,00000	1,01322	1,00000
4/G.+D undif	50,00001	-49,99865	49,96240	1,00000	0,99994	1,00000
4/G.+D. dif	50,00000	-50,00000	50,00002	1,00000	0,99977	1,00000
4/GNSS	50,00020	-50,04033	49,30319	1,00000	0,99997	1,00000
4/DORIS undif	50,00020	-50,03283	49,24825	1,00000	0,99836	1,00000
4/DORIS dif	49,99878	-49,82028	53,74177	1,00000	1,00107	1,00000
4/ll-SST	50,00000	-49,99993	50,00150	1,00000	1,02153	1,00000

All = combination of GNSS, ll-SST and undifferenced DORIS observations

G.+D. = GNSS+DORIS

Satellite 1 = trailing polar satellite

Satellite 2 = leading polar satellite

Satellite 3 = trailing inclined satellite

Satellite 4 = leading inclined satellite

The actual retrieval errors (Table 52-3) indeed confirm that the most reliable accelerometer calibration parameters are obtained when using the kinematic orbit coordinates, and also that accurate retrieval of the Y axis accelerometer scale factor is very unreliable. By adding DORIS observations, accelerometer calibration parameters estimates do not significantly improve or deteriorate. Great care has to be taken when using the ll-SST observation for accelerometer calibration. In the presence of the full error model, the values for the accelerometer biases and scale factors become very unreliable for especially the Y axis, but also to a lesser extent for the Z axis. The ll-SST observations predominantly provide information for the differential motion in the flight direction (predominantly X axis) of the satellites in a certain tandem and hardly for the cross-track direction (Y axis). Because of the high precision of the ll-SST observation, a high weight is assigned in the estimation process (Table 3-1 in [RD-13]). The estimation process thus predominantly aims at minimizing the ll-SST observation residuals, which thus leads to unrealistic values for especially the bias and scale factors for the Y axis.

As mentioned above, the small residual non-gravitational accelerations because of drag-free flight, make the estimation of accelerometer scale factor parameters less useful. Therefore, also an estimation was done where the scale factors were fixed at their nominal value of 1.0 and only the daily accelerometer biases were estimated (Table 52-4). Also, when fixing the scale factors, the accelerometer bias estimates are predominantly determined by the kinematic orbit positions (GNSS). In addition, by adding DORIS observations, the bias estimates again do not significantly improve or deteriorate. Finally, accelerometer bias estimates for the Y axis become unreliable when adding ll-SST observations.

Table 52-2 Daily accelerometer calibration formal errors (scenario 3d_H) for different combinations of observations. Optimal weighting for the full error model. Estimation of both daily accelerometer biases and scale factors. The results hold for drag-free flight on 1 January 2002, which is representative for other days as well.

Satellite/obs	Bias (nm/s^2)			Scale factor		
	X	Y	Z	X	Y	Z
1/All	0,00040	0,32775	1,32529	0,00015	1,47143	0,00027
1/G.+D undif	0,00507	0,46209	1,37864	0,00517	1,53234	0,00855
1/G.+D. dif	0,00378	0,43463	1,27495	0,00380	1,42060	0,00639
1/GNSS	0,00552	0,46644	1,39684	0,00562	1,54819	0,00925
1/DORIS undif	0,01305	3,45245	8,72273	0,01319	10,89114	0,02316
1/DORIS dif	0,00678	2,78845	7,26123	0,00649	3,81236	0,01102
1/ll-SST	0,03585	14,65871	95,86904	0,00020	8,74426	0,00040
2/All	0,00037	0,35486	1,32383	0,00009	1,41534	0,00030
2/G.+D undif	0,00056	0,49881	1,38164	0,00579	2,02492	0,01895
2/G.+D. dif	0,00044	0,46922	1,27461	0,00369	1,88145	0,01215
2/GNSS	0,00061	0,50338	1,40078	0,00634	2,04490	0,02074
2/DORIS undif	0,00194	3,76765	8,72158	0,01427	14,67102	0,04702
2/DORIS dif	0,00171	2,82556	7,20965	0,00461	5,05134	0,01542
2/ll-SST	0,03500	14,78889	83,00046	0,00010	2,96026	0,00038
3/All	0,00048	0,33948	1,35074	0,00015	1,66474	0,00031
3/G.+D undif	0,00345	0,47771	1,39009	0,00422	1,82244	0,01609
3/G.+D. dif	0,00231	0,44548	1,27941	0,00310	1,65984	0,01041
3/GNSS	0,00385	0,48297	1,41015	0,00467	1,84594	0,01798
3/DORIS undif	0,00815	3,33094	8,36984	0,01005	11,52653	0,03643
3/DORIS dif	0,00402	2,50085	6,66460	0,00553	3,93513	0,01506
3/ll-SST	0,05004	13,07816	93,04685	0,00017	6,11400	0,00034
4/All	0,00048	0,33066	1,35134	0,00009	1,93601	0,00018
4/G.+D undif	0,00178	0,46749	1,39123	0,00250	2,25037	0,00387
4/G.+D. dif	0,00119	0,43593	1,27861	0,00159	2,06032	0,00284
4/GNSS	0,00197	0,47268	1,41155	0,00277	2,27723	0,00429
4/DORIS undif	0,00462	3,26487	8,37548	0,00584	14,85443	0,00903
4/DORIS dif	0,00259	2,49077	6,62061	0,00204	4,94794	0,00509
4/ll-SST	0,04938	13,12836	91,23193	0,00011	4,89990	0,00020

All = combination of GNSS, ll-SST and undifferenced DORIS observations

G.+D. = GNSS+DORIS

Satellite 1 = trailing polar satellite

Satellite 2 = leading polar satellite

Satellite 3 = trailing inclined satellite

Satellite 4 = leading inclined satellite

Table 52-3 Daily accelerometer calibration retrieval errors (scenario 3d_H) for different combinations of observations. Optimal weighting for the full error model. Estimation of both daily accelerometer biases and scale factors. The results hold for drag-free flight on 1 January 2002, which is representative for other days as well.

Satellite/obs	Bias (nm/s^2)			Scale factor		
	X	Y	Z	X	Y	Z
1/All	-0,04632	5,50508	-1,51325	-0,01478	-6,27065	-0,06826
1/G.+D undif	-0,06100	0,97915	3,29631	-0,01977	7,88388	0,04288
1/G.+D. dif	-0,08604	0,44998	2,74492	-0,05398	5,74837	-0,01103
1/GNSS	-0,05808	0,98910	2,41335	-0,01662	8,47424	0,03962
1/DORIS undif	-0,08347	0,22445	38,26178	-0,03779	-22,71732	0,06857
1/DORIS dif	-0,10699	-7,32049	24,91276	-0,07912	-11,98058	-0,03195
1/ll-SST	4,45181	2686,88415	-28915,59370	0,01572	54,41495	-0,14926
2/All	-0,00369	30,25259	-3,98538	0,01842	335,12331	0,01202
2/G.+D undif	-0,00934	0,95932	2,52145	0,04240	2,94293	-0,13267
2/G.+D. dif	-0,00911	0,96808	2,14091	0,04114	1,09738	-0,12597
2/GNSS	-0,00973	0,97117	1,72580	0,04654	3,15322	-0,14253
2/DORIS undif	-0,01240	0,85479	36,58174	0,02212	-6,22576	-0,08530
2/DORIS dif	-0,00943	-5,99447	24,18216	0,03479	-19,12969	-0,11319
2/ll-SST	4,65227	2733,75356	-29767,87386	0,00781	856,00502	-0,01820
3/All	0,02788	11,64669	-11,61860	0,00922	92,28509	-0,06101
3/G.+D undif	-0,01398	0,61804	-0,16673	0,10787	5,87130	0,07288
3/G.+D. dif	-0,01273	0,04739	-1,05274	0,10321	5,15162	0,07098
3/GNSS	-0,01439	0,52179	-1,49269	0,10880	5,20995	0,07742
3/DORIS undif	-0,02530	9,15145	43,99814	0,10748	25,47001	0,06273
3/DORIS dif	0,00965	-7,14039	-13,48666	0,05919	8,04861	-0,00052
3/ll-SST	-0,01550	1873,57597	842,25360	0,01462	446,92253	-0,04722
4/All	0,07042	5,60676	11,39019	-0,03106	12,59976	-0,17037

4/G.+D undif	0,03329	-0,40551	-0,11886	-0,05789	-2,66745	-0,06177
4/G.+D. dif	0,05317	-0,23570	-2,89493	-0,03859	-5,31339	-0,10025
4/GNSS	0,03509	-0,47771	-1,42981	-0,05581	-3,22082	-0,06287
4/DORIS undif	0,01490	7,65601	44,77296	-0,06605	26,02943	-0,05621
4/DORIS dif	0,07115	-6,06471	-16,93114	-0,03486	-18,47254	-0,15342
4/ll-SST	-1,71111	1827,97184	7108,02417	-0,02877	-554,29821	-0,17541

All = combination of GNSS, ll-SST and undifferenced DORIS observations
G.+D. = GNSS+DORIS
Satellite 1 = trailing polar satellite
Satellite 2 = leading polar satellite
Satellite 3 = trailing inclined satellite
Satellite 4 = leading inclined satellite

Table 52-4 Daily accelerometer calibration formal (left) and retrieval (right) errors (scenario 3d_H) for different combinations of observations. Optimal weighting for the full error model. Estimation of only daily accelerometer biases. The results hold for drag-free flight on 1 January 2002, which is representative for other days as well.

Satellite/obs	Bias formal error (nm/s^2)			Bias retrieval (nm/s^2)		
	X	Y	Z	X	Y	Z
1/All	0,00037	0,32512	1,32496	-0,04020	5,79266	-14,10456
1/G.+D undif	0,00047	0,45789	1,37311	-0,03960	0,65869	2,64974
1/G.+D. dif	0,00040	0,43044	1,27116	-0,03967	0,29227	3,14203
1/GNSS	0,00050	0,46227	1,39066	-0,03972	0,64680	1,81106
1/DORIS undif	0,00182	3,39694	8,70567	-0,04396	1,54365	36,36913
1/DORIS dif	0,00170	2,76735	7,21945	-0,04295	-5,34471	42,19101
1/ll-SST	0,03327	12,0291	47,05265	6,51213	909,01008	-16957,584
2/All	0,00037	0,32515	1,32362	-0,00323	-1,00490	4,17666
2/G.+D undif	0,00047	0,45789	1,37317	-0,00721	0,66995	1,52908
2/G.+D. dif	0,00040	0,43028	1,27065	-0,00728	0,85895	1,69269
2/GNSS	0,00051	0,46227	1,39071	-0,00741	0,66305	0,67275
2/DORIS undif	0,00183	3,39212	8,71058	-0,01128	1,60472	36,07148
2/DORIS dif	0,00170	2,75881	7,18207	-0,01053	-2,84918	40,42896
2/ll-SST	0,03332	12,04212	46,17123	6,52304	885,77894	-16627,508
3/All	0,00048	0,32918	1,35023	0,01056	5,02583	17,30439
3/G.+D undif	0,00056	0,46464	1,38924	0,01722	0,19835	-1,63306
3/G.+D. dif	0,00048	0,43383	1,27849	0,01714	-0,62724	-2,26453

3/GNSS	0,00060	0,46972	1,40914	0,01787	0,15765	-2,97512
3/DORIS undif	0,00254	3,26032	8,36882	0,00362	6,29870	41,97336
3/DORIS dif	0,00208	2,48756	6,65232	0,01752	-13,29511	-2,78907
3/ll-SST	0,04800	11,94962	77,01161	-12,49259	-1965,4388	40407,9013
4/All	0,00047	0,32923	1,35052	0,04879	0,81357	-3,28562
4/G.+D undif	0,00056	0,46465	1,38919	0,04635	-0,29831	1,10504
4/G.+D. dif	0,00049	0,43369	1,27778	0,04769	0,12440	-0,71633
4/GNSS	0,00060	0,46972	1,40914	0,04682	-0,37385	-0,20487
4/DORIS undif	0,00253	3,25995	8,35879	0,03390	8,60589	45,01206
4/DORIS dif	0,00206	2,48557	6,61195	0,04916	-9,18408	-4,33045
4/ll-SST	0,04773	11,97299	77,77135	-11,27387	-1936,742	36345,6528

All = combination of GNSS, ll-SST and undifferenced DORIS observations

G.+D. = GNSS+DORIS

Satellite 1 = trailing polar satellite

Satellite 2 = leading polar satellite

Satellite 3 = trailing inclined satellite

Satellite 4 = leading inclined satellite

52.3 MANEUVERS

As shown in Section 52.2, scale factors cannot be estimated accurately if the drag-free control of the satellites leaves small residual non-gravitational accelerations, especially for the Y axis. Therefore, dedicated maneuver schemes might be considered which aims at an accurate calibration of the accelerometers, including their scale factors.

Tests have been conducted with the maneuver schemes as specified in Table 52-5. The first two schemes introduce constant accelerations along the X, Y and Z accelerometer axes for a duration of 6 hours in the 2nd quarter of the day, with magnitudes of respectively 50 and 500 nm/s^2. By having different magnitudes, it can be verified if scale factors can be estimated better in case of larger maneuvers. A 3rd scheme introduces continuous accelerations which are piecewise constant with a magnitude of 50 nm/s^2, but with random sign for consecutive periods. The sign is obtained by using a uniform Gaussian distribution and by taking the sign of the random values.

Table 52-5 Maneuvers along the accelerometer axes (nm/s^2). The maneuvers consist of constant thrusts for specified periods. Use is made if daily arcs from midnight to midnight.

	Satellite	X	Y	Z	
Scheme 1	Trailing	-50	50	-50	06:00-12:00
	Leading	50	-50	50	
Scheme 2	Trailing	-500	500	-500	06:00-12:00
	Leading	500	-500	500	
Scheme 3	Leading	50	50	50	Entire arc: random ± 50
	Trailing	50	50	50	per 30 minutes

For each maneuver scheme, the formal and retrieval errors have been computed for 1 daily arc, namely 1 January 2002, in the presence of the full error model with optimal weighting (Table 3-1 in [RD-13]). As shown in Section 52.2, the accelerometer calibration largely depends on the kinematic position coordinated (GNSS). It is interesting to assess if, in the presence of maneuvers, the accelerometer calibration can be enhanced by adding DORIS observations, especially in the form of differential observations because of the mitigation of systematic errors. Therefore, for all the maneuver cases, accelerometer calibration parameter estimates are obtained for the kinematic position coordinates only and for their combination with differential DORIS observations. The results are included in **Table 52-6** and **Table 52-7**. For all schemes, it can be observed that the estimation of the Y axis accelerometer scale factors becomes much more accurate and reliable. It can also be observed that by increasing the magnitude of maneuvers, the formal and retrieval error of accelerometer scale factors improve proportionally. The use of maneuvers has a small impact on the quality of estimated accelerometer biases for all axes: X, Y and Z (*cf.* Table 52-2 and Table 52-3). The impact on the quality of estimated accelerometer scale factor is significant: very accurate values can be obtained for the X and Z axes (accuracy generally better than 0.001), and more reliable estimates for the Y axis scale factors are obtained (better than 0.05). In most cases, the addition of DORIS observations has a small impact.

Table 52-6 Daily accelerometer calibration formal errors (scenario 3d_H) for different combinations of observations, and for different maneuver schemes (Table 52-5). Optimal weighting for the full error model. Estimation of both daily accelerometer biases and scale factors. The results hold for calibration maneuvers according to Table 52-5 on 1 January 2002, which is representative for other days as well.

Satellite/obs	Scheme	Bias (nm/s^2)			Scale factor		
		X	Y	Z	X	Y	Z
1/GNSS	1	0,00404	0,55871	1,39295	0,00010	0,01331	0,00094
	2	0,00398	0,55977	1,39305	0,00001	0,00134	0,00010
	3	0,00070	0,46252	1,39080	0,00007	0,00285	0,00102
1/G.+D. dif	1	0,00306	0,51930	1,27348	0,00007	0,01229	0,00071
	2	0,00302	0,52029	1,27297	0,00001	0,00123	0,00008
	3	0,00051	0,43079	1,27147	0,00004	0,00265	0,00064
2/GNSS	1	0,00400	0,56099	1,39212	0,00010	0,01340	0,00083
	2	0,00400	0,56002	1,39042	0,00001	0,00134	0,0001
	3	0,00136	0,46255	1,39112	0,00014	0,00235	0,00104
2/G.+D. dif	1	0,00303	0,52112	1,27202	0,00008	0,01237	0,00063
	2	0,00303	0,52025	1,26953	0,00001	0,00123	0,00007
	3	0,00084	0,43048	1,27111	0,00009	0,00216	0,00069
3/GNSS	1	0,00393	0,57827	1,41118	0,00010	0,01383	0,00105
	2	0,00397	0,57870	1,41166	0,00001	0,00138	0,00010
	3	0,00073	0,46983	1,40971	0,00008	0,00293	0,00102
3/G.+D. dif	1	0,00285	0,52996	1,28006	0,00007	0,01261	0,00077
	2	0,00288	0,53032	1,27946	0,00001	0,00126	0,00008
	3	0,00054	0,43394	1,27873	0,00004	0,00263	0,00060
4/GNSS	1	0,00385	0,57859	1,41084	0,00010	0,01380	0,00127
	2	0,00400	0,57874	1,40924	0,00001	0,00138	0,00010

	3	0,00158	0,46983	1,40951	0,00014	0,00238	0,00106
4/G.+D. dif	1	0,00280	0,52992	1,27855	0,00007	0,01257	0,00094
	2	0,00293	0,53002	1,27577	0,00001	0,00126	0,00008
	3	0,00097	0,43386	1,27821	0,00008	0,00214	0,00063

G.+D. = GNSS+DORIS

Satellite 1 = trailing polar satellite

Satellite 2 = leading polar satellite

Satellite 3 = trailing inclined satellite

Satellite 4 = leading inclined satellite

Table 52-7 Daily accelerometer calibration retrieval errors (scenario 3d_H) for different combinations of observations, and for different maneuver schemes (Table 52-5). Optimal weighting for the full error model. Estimation of both daily accelerometer biases and scale factors. The results hold for calibration maneuvers according to Table 52-5 on 1 January 2002, which is representative for other days as well.

Satellite/obs	Scheme	Bias (nm/s^2)			Scale factor		
		X	Y	Z	X	Y	Z
1/GNSS	1	-0,02867	-0,25423	1,85613	0,00027	0,03827	0,00075
	2	-0,02826	-0,24502	1,46116	0,00003	0,00379	0,00008
	3	-0,03711	0,48952	1,89800	0,00119	0,00255	0,02267
1/G.+D. dif	1	-0,03605	-0,42323	2,07989	0,00009	0,03341	0,00065
	2	-0,03612	-0,46221	2,05907	0,00001	0,00339	0,00003
	3	-0,04015	0,15754	2,20799	0,00034	0,00221	0,01171
2/GNSS	1	0,06855	-0,32668	-0,01835	-0,00191	-0,04143	0,00990
	2	0,06612	-0,35683	0,18189	-0,00019	-0,00422	0,00119
	3	0,00367	0,54645	-0,49727	0,00060	-0,00223	0,02784
2/G.+D. dif	1	0,07252	-0,16814	1,32271	-0,00200	-0,04334	0,00797
	2	0,07058	-0,17572	1,67278	-0,00020	-0,00439	0,00093
	3	0,00619	0,80143	0,36801	0,00098	0,00135	0,02047
3/GNSS	1	0,05828	-1,29460	-0,34682	0,00119	0,03209	0,03519
	2	0,05668	-1,29043	-0,87965	0,00010	0,00325	0,00336
	3	0,02953	0,14447	-2,24559	0,00257	-0,02021	0,00683
3/G.+D. dif	1	0,05862	-1,89265	0,14355	0,00122	0,03605	0,03664
	2	0,05637	-1,91524	-0,94520	0,00010	0,00361	0,00348
	3	0,03466	-0,37147	-1,34699	0,00321	-0,01799	0,00018
4/GNSS	1	0,08937	-1,38367	-1,12742	-0,00127	-0,02755	0,03092
	2	0,09754	-1,41019	-0,96069	-0,00013	-0,00290	0,00239
	3	0,07442	-0,41422	-0,71770	0,00281	0,01372	0,00544
4/G.+D. dif	1	0,09201	-0,66879	-1,80969	-0,00133	-0,01783	0,03085
	2	0,10075	-0,70381	-2,33588	-0,00013	-0,00191	0,00249
	3	0,07918	0,03395	-1,74517	0,00327	0,01473	0,00734

G.+D. = GNSS+DORIS

Satellite 1 = trailing polar satellite

Satellite 2 = leading polar satellite

Satellite 3 = trailing inclined satellite

Satellite 4 = leading inclined satellite

52.4 COMMISSIONING PHASE

It is assumed that during at least part of the commissioning, the satellites will not fly drag-free ("non-DFC"). The satellite will then experience atmospheric drag and solar radiation pressure. It is assumed that the satellites have a shape and dimensions comparable to the CHAMP satellite without the boom (which resembles the GRACE satellites) with a mass of 522 kg and an average cross-sectional frontal area of 1.22 m^2. In fact, the satellites are modelled as boxes consisting of 6 panels (for a panel model for GRACE, see e.g. [RD-14]).

Density is computed with a DTM model included in the GOEDYN s/w suite [RD-15] which includes the use of F10.7 solar flux values. The drag is computed by assuming an earth-pointing satellite with a value of 2.2 for the drag coefficient C_D. In addition, solar radiation pressure is taken into account with a value of 1.0 for the C_R coefficient, where eclipses are modeled as well. Time series of the resulting non-gravitational accelerations are displayed in Figure 52-1 for a day during solar minimum (1 January 1996) and a day during solar maximum (1 January 2002). It can be observed that atmospheric density can change by an order of magnitude, which has a significant impact on the quality of estimated accelerometer calibration parameters.
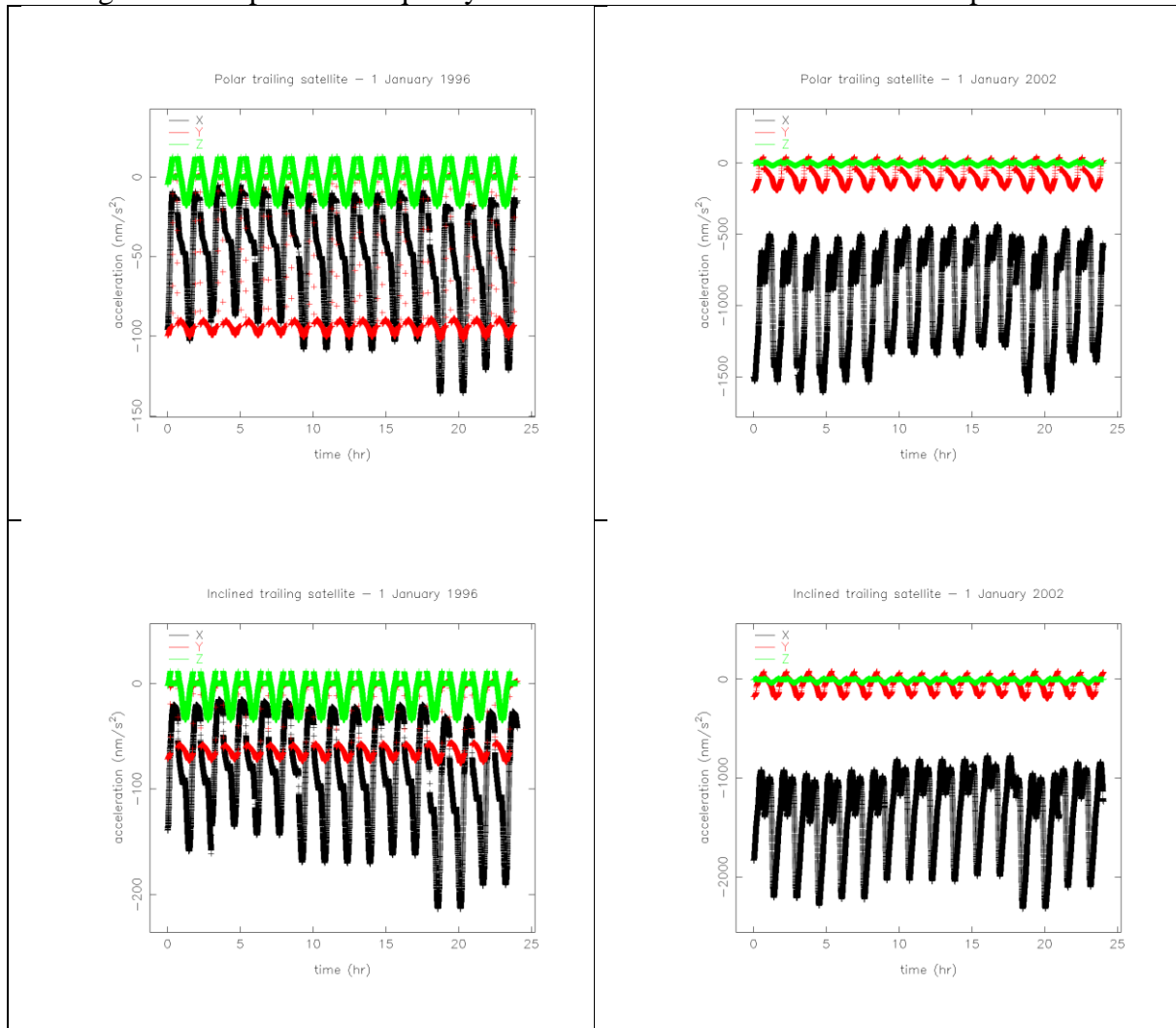

Figure 52-1 Non-gravitational accelerations in the accelerometer reference frame: X/Y/Z predominantly aligned with the along-track/cross-track/radial direction for the trailing satellites of the polar (top) and inclined (bottom) tandems. Similar time series are obtained for the leading satellites. The time series hold for periods of solar minimum (left) and maximum (right).

Accelerometer calibration results are displayed for the two selected days in Table 52-8 and Table 52-9 for the full error model (Table 3-1 in [RD-13]). The larger drag signal during the day at solar maximum causes a significantly lower formal error for the scale factors for the X (flight direction) and Y (cross-track direction) axes, whereas for the Z axis (radial direction) no improvement can be seen. The non-gravitational accelerations in the radial direction are predominantly caused by the solar radiation pressure, which is at the same level for days at solar minimum and maximum. The impact of solar activity on the formal errors for the accelerometer biases is insignificant for the Y and Z axes, and marginal for the Y axis (Table 52-8).

Table 52-8 Daily accelerometer calibration formal errors (scenario 3d_H) for different combinations of observations during commissioning phase (i.e. no drag-free control). Optimal weighting for the full error model. Estimation of both daily accelerometer biases and scale factors. The results hold for 1 January 1996 (solar minimum, top half) and 1 January 2002 (solar maximum, bottom half).

Satellite/obs	Bias error (nm/s^2)			Scale factor		
	X	Y	Z	X	Y	Z
1 January 1996 – Solar minimum						
1/GNSS	0,00895	0,47266	1,39092	0,00019	0,00123	0,00206
1/G.+D dif	0,00679	0,44027	1,27163	0,00015	0,00113	0,00157
2/GNSS	0,00897	0,47276	1,39092	0,00019	0,00123	0,00205
2/G.+D dif	0,00677	0,44017	1,27129	0,00015	0,00113	0,00157
3/GNSS	0,00921	0,47333	1,41122	0,00011	0,00129	0,00131
3/G.+D dif	0,00675	0,43754	1,27883	0,00008	0,00118	0,00097
4/GNSS	0,00925	0,47334	1,41122	0,00011	0,00129	0,00131
4/G.+D dif	0,00680	0,43734	1,27808	0,00008	0,00118	0,00096
1 January 2002 – Solar maximum						
1/GNSS	0,02276	0,46373	1,39132	0,00003	0,00053	0,00318
1/G.+D dif	0,01714	0,43189	1,27244	0,00002	0,00049	0,00237
2/GNSS	0,02280	0,46377	1,39131	0,00003	0,00053	0,00319
2/G.+D dif	0,01719	0,43176	1,27109	0,00002	0,00049	0,00238
3/GNSS	0,02373	0,47034	1,40968	0,00002	0,00045	0,00157
3/G.+D dif	0,01771	0,43443	1,27914	0,00001	0,00041	0,00117
4/GNSS	0,02372	0,47035	1,40969	0,00002	0,00045	0,00157
4/G.+D dif	0,01768	0,43425	1,27811	0,00001	0,00041	0,00118

G.+D. = GNSS+DORIS
Satellite 1 = trailing polar satellite
Satellite 2 = leading polar satellite
Satellite 3 = trailing inclined satellite
Satellite 4 = leading inclined satellite

Actual retrieval errors display the same pattern as the formal errors (Table 52-9): especially for the X axis, accelerometer scale factors can be determined with very high accuracy, better than 0.01 at solar minimum, and 0.001 at solar maximum. For the Y axis these values are 0.04 and 0.005, respectively. The Z axis accelerometer scale factor cannot be determined with high accuracy: errors range up to almost 0.1 (showing the formal errors in Table 52-8 are too optimistic). In general, accelerometer biases can be determined with an accuracy better than 3

nm/s2 for all axes, with again the best performance for the X axis: better than 1 nm/s2 for all cases listed. For all cases, adding differential DORUS observations to GNSS kinematic orbits leads to (slight) improvements.

Table 52-9 Daily accelerometer calibration retrieval errors (scenario 3d_H) for different combinations of observations during commissioning phase (i.e. no drag-free control). Optimal weighting for the full error model. Estimation of both daily accelerometer biases and scale factors. The results hold for 1 January 1996 (solar minimum, top half) and 1 January 2002 (solar maximum, bottom half).

Satellite/obs	Bias error (nm/s^2)			Scale factor		
	X	Y	Z	X	Y	Z
1 January 1996 – Solar minimum						
1/GNSS	0,12450	-0,50725	-0,11752	0,00345	-0,02382	-0,04006
1/G.+D dif	0,14992	-1,31244	2,25660	0,00399	-0,02494	-0,03666
2/GNSS	0,24629	-0,48281	-0,06767	0,00538	-0,02421	-0,03076
2/G.+D dif	0,22769	0,25062	-0,51362	0,00498	-0,02296	-0,03065
3/GNSS	-0,41038	-1,30154	-0,41598	-0,00499	-0,03289	0,06903
3/G.+D dif	-0,41358	-1,14039	0,82674	-0,00503	-0,03265	0,06957
4/GNSS	0,05513	-2,24236	1,07938	0,00034	-0,03388	0,08460
4/G.+D dif	0,04697	-2,52633	0,02666	0,00024	-0,03375	0,09547
1 January 2002 – Solar maximum						
1/GNSS	-0,06220	0,89211	0,99762	-0,00002	0,00129	0,07799
1/G.+D dif	-0,05144	0,64778	2,26215	-0,00001	0,00164	0,07927
2/GNSS	-0,45543	0,87720	-0,11628	-0,00050	0,00079	0,04004
2/G.+D dif	-0,46281	1,04855	-0,39200	-0,00051	0,00058	0,03799
3/GNSS	0,27978	0,00078	-2,75891	0,00020	-0,00225	0,02082
3/G.+D dif	0,25029	-0,40415	-2,34118	0,00018	-0,00203	0,01424
4/GNSS	-0,64259	-0,72480	-1,26061	-0,00053	-0,00179	-0,00742
4/G.+D dif	-0,61855	-0,43771	-1,73938	-0,00051	-0,00190	-0,00875

G.+D. = GNSS+DORIS

Satellite 1 = trailing polar satellite

Satellite 2 = leading polar satellite

Satellite 3 = trailing inclined satellite

Satellite 4 = leading inclined satellite

52.5 FINAL DRAG FREE FLIGHT SIMULATION WITH UPDATED NOISE TIME SERIES

The latest received noise characteristics received from TAS contain all noise contributions (accelerometers, LRI, attitude), only for the inclined pair (h=396 km, i=65°), were used in a final simulation. The noise time series were first analyzed spectrally, and examples for test Mass 2 (+Y axis) are displayed in Figure 52-2. The PSDs for test masses 5 (-Y), 3 (+Z) and 6 (-Z) all display essentially the same PSD, all with a noise level around 5E-11 m/s2 for the three axes.
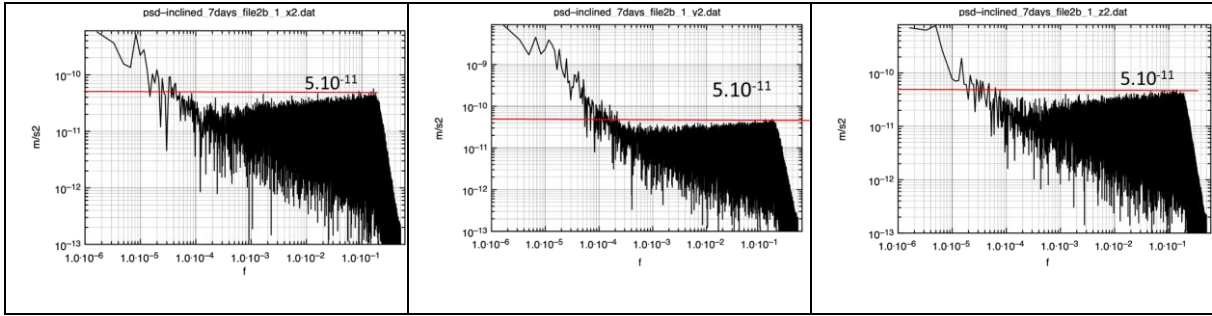
Figure 52-2 PSD of the noise time series for test mass 2 (+Y axis).

The active accelerometers are test mass 2 and 5 along the Y axis). We used in our simulation:
linear_acceleration = (TestMass2+TestMass5)/2

Noise =	$$\sqrt{\text{Noise\_TestMass2}^2 + \text{Noise\_TestMass5}^2}/2$$

A GRACE-like satellite geometry was used, and seven 1-day arcs were computed.

In order to get an idea of the differences the noise causes on orbit, Figure 52-3 shows this for the X, Y and Z directions, and it is up to 20 cm on X (i.e. well observable with GNSS).
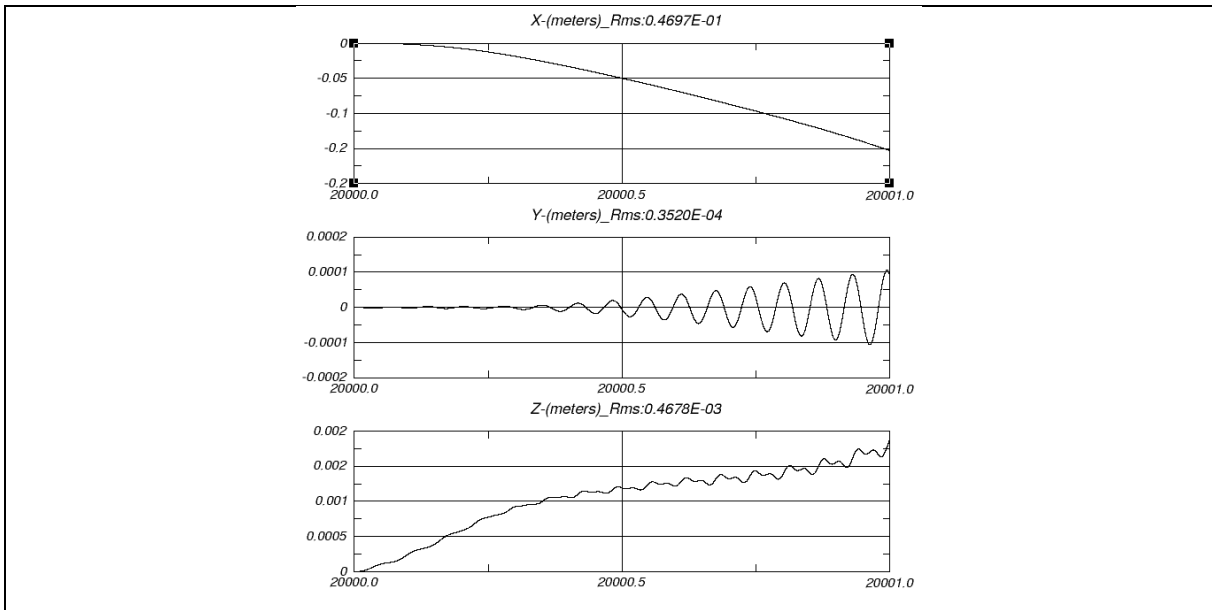
Figure 52-3 Example of orbit differences due to the noise after one day.

The following six scenarios were tested:
1. GNSS position of satellite perfectly known (reference test)
2. GNSS position + 1cm white noise
3. GNSS position + 2cm white noise
4. 5. and 6. same as 1. 2. 3 but accelerometer noise x2

For each case we add in X, Y, Z:

- Accelerometer biases of 150 nm/s²
- And accelerometer scale factor error 1.0002, 1.001, 1.001

And we evaluate the precision of their estimation. As for the noise, we calculated the differences the scale factors, the bias and a misalignment of the accelerometer with respect to the center of mass of 100 μm cause on orbit, and this is shown in Figure 3-4 for the X, Y and Z directions.
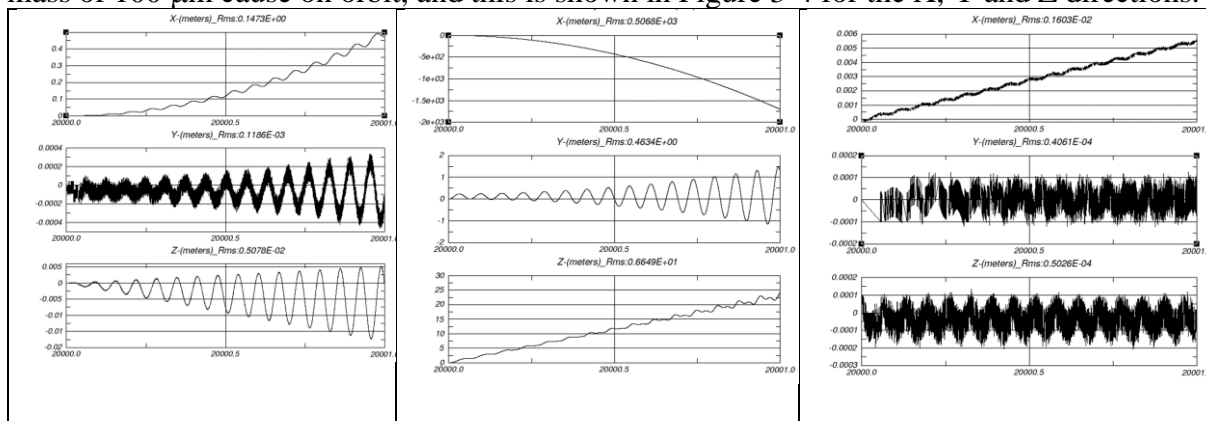
Figure 52-4 Example of orbit differences due to the scale factor error (left), bias (middle) and CoM misalignment of 100 ▯m after one day.

The maximum daily accelerometer calibration estimation errors found among the seven 1-day arcs are listed in Table 52-10.

Table 52-10 Maximum error in the daily accelerometer calibration retrieval errors.

Scenario	Bias (nm/s²)			Scale factor		
	X	Y	Z	X	Y	Z
1	0.567	0.0265	0.0047	-	0.000080	0.000075
2	0.641	0.0264	0.0189	-	0.000074	0.000303
3	0.715	0.0262	0.0340	-	0.000068	0.000563
4	1.134	0.0531	0.0092	-	0.000164	0.000150
5	1.208	0.0530	0.0227	-	0.000158	0.000343
6	1.281	0.0528	0.0379	-	0.000152	0.000604

All biases and scale factors retrieved precisely except the scale factor in X, which is too small to be adjusted. The effect of white noise on GNSS positions is very small. There is no detectable effect of the misalignment of 100 micro-meter from the SAT COM on the adjusted parameters (not shown in the table).

53 CONCLUSIONS

The biggest contribution for precise accelerometer calibration comes from the kinematic orbit coordinates (GNSS). The addition of DORIS or ll-SST observation hardly improves the accelerometer calibration by POD.

Drag-free flight leaves a very small non-gravitational signal to be observed by the accelerometers, which makes the estimation of accelerometer scale factors less crucial and also very unstable.

A proper maneuver scheme allows a very accurate kinematic orbit based calibration of the scale factor of the accelerometers: very accurate values can be obtained for the X and Z axes (accuracy generally better than 0.001), and more reliable estimates for the Y axis scale factors are obtained (better than 0.05). Periods of a few hours with thrust of the order of 50 nm/s^2 might be sufficient.

Accurate estimates of scale factors can be obtained as well when not flying drag-free (e.g. during the commissioning phase), especially for the X axis (much better than 0.001 during solar maximum, better than 0.01 during solar minimum). For the Y and Z axes, the performance is an order of magnitude worth, even more so for the Z axis during solar minimum.

The simulations with updated TAS noise for the inclined satellite pair are in agreement with all of the previous findings, i.e. previous simulations were equally realistic.

54   APPLICABLE DOCUMENTS, REFERENCE DOCUMENTS, AND PUBLICATIONS TO PART 8

54.1 APPLICABLE DOCUMENTS

[AD-1] Mission Requirements Document, Next Generation Gravity Mission as a Mass-change And Geosciences International Constellation (MAGIC) - A joint ESA/NASA double-pair mission based on NASA's MCDO and ESA's NGGM studies (2020). ESA-EOPSM-FMCC-MRD-3785

[AD-2] Scientific Readiness Levels (SRL) Handbook, Issue 1, Revision 0, 05-08-2015

[AD-3] Statement of Work - ESA Express Procurement - EXPRO NGGM/MAGIC science support study during Phase A, Issue 1, Revision 0, 18/01/2021 Ref ESA-EOPSM-FUTM-SOW-3813

54.2 REFERENCE DOCUMENTS AND BOOKS

[RD-1]   Statement of Work, ESA Express Procurement EXPRO+, Additional Constellation & Scientific Analysis Studies of the Next Generation Gravity Mission Concept, EOP-SM/2974, Issue 1, Revision 0, 19/04/2016

[RD-2]   Assessment of a Next Generation Mission for Monitoring the Variations of Earth's Gravity. Final Report, ESTEC Contract No. 22643/09/NL/AF, Issue 2, Date: 22.12.2010

[RD-3]   Assessment of a Next Generation Gravity Mission to Monitor the Variations of Earth's Gravity Field. Final Report, ESTEC Contract No. 22672/09/NL/AF, Issue 1, Date: 10.10.2011.

[RD-4]   Assessment of Satellite Constellations for Monitoring the Variations in Earth Gravity Field "SC4MGV", ESA Contract No 4000108663/13/NL/MV, Final Report, 04 November 2015

[RD-5]   R.D. Ray, Precise comparisons of bottom-pressure and altimetric ocean tides, J. Geophys. Res.: Oceans, Vol. 118, pp. 4870-4584, doi: 10.1002/jgrc.20336, 2013

[RD-6]   Savcenko, R. and Bosch, W. (2012): EOT11A - Empirical Ocean Tide Model from Multi-Mission Satellite Altimetry, München, Deutsches Geodätisches Forschungsinstitut (DGFI), hdl:10013/epic.43894

[RD-7]   GOCO, Gravity observation combination (GOCO), www.goco.eu, accessed 23 September 2021

[RD-8]   D.E . Pavlis, S. Poulouse, J.J. McCarthy, GEODYN operations manual, Contractor report, SGT Inc. Greenbelt, 2006

[RD-9]   ESA Earth System Model for Mass Distribution and Transport, https://isdc.gfz-potsdam.de/esmdata/esaesm/, last accessed 23 September 2021

[RD-10] D.N. Wiese, P. Visser, R.S. Nerem, Estimating Low Resolution/High Frequency Gravity Fields to Reduce Temporal Aliasing Errors, Adv. Space Res., 48(6), pp. 1094-1107, doi: 10.1016/j.asr.2011.05.027, 2011

[RD-11] TU Munich LRZ server (https://syncandshare.lrz.de/).

[RD-12] E Schrama, Precision orbit determination performance for CryoSat-2, Advances in Space Research 61 (1), pp. 235-247, doi: 10.1016/j.asr.2017.11.001, 2018

[RD-13] Pieter Visser, Next Generation Gravity Mission as a Mass-change And Geosciences International Constellation (MAGIC), Technical Note WP 320, DORIS aided orbit and gravity field determination, Issue 1.0, 15 November 2022

[RD-14] Srinivas Bettadpur, Gravity Recovery and Climate Experiment, Product Specification Document, GRACE 327-720 (CSR-GR-03-02), (Rev 4.5 – February 20, 2007), Center for Space Research The University of Texas at Austin

[RD-15] John JMcCarthy, Shelley Rowton, Denise Moore, Despina E. Pavlis, Scott B. Luthcke, Lucia S. Tsaoussie, GEODYN Systems Description Volume 1, Prepared For: Space Geodesy Branch, Code 926, NASA GSFC, Greenbelt, MD, February 23, 2015 from the original December 13, 1993 document

PART 9:

AD-HOC REQUEST:
SENSITIVITY ANALYSIS ON INTER-SATELLITE DISTANCE

55 INTRODUCTION

This document aims to assess and quantify the performance of GRACE-type (ll-SST-based) gravity field retrieval under assumption of various inter-satellite distances, orbit altitudes and sensor noise performances. The results presented in the following are based on numerical closed-loop simulations performed with IAPG's RSS (cf. Murböck, 2015 [RD-4], and Murböck et al., 2014 [RD-3]). For the sake of computational efficiency, the RSS uses Keplerian orbits, and the gravity retrieval is based on range acceleration differences (contrary to real GRACE/GRACE-FO data processing, where range resp. range-rate measurements are used). Any instrument noise contributor is projected onto the LOS and then accumulated into a single noise time series which is then added to the observations. The observation weighting is then carried out by means of digital ARMA filters (Siemes, 2008 [RD-6]). The filters are chosen in such a way that the cascade's frequency response poses an optimal approximation of the LOS-projected noise time series' inverse ASD.

56 SIMULATION PARAMETERS

The orbit parameters specified by ESA for this study are the orbital altitude ranging from 350 to 500 km as well as the ISD ranging from 100 to 250 km. Based on these prerequisites we generate Keplerian repeat orbits with the parameters specified in Table 56-1. Since it is not possible to generate repeat orbits which perfectly coincide with the altitude requirements of 350, 400, 450 and 500 km, we instead use the orbit which approximates these requirements in the best possible way (maximum deviation of 2.1 km). In order to realize these altitudes, however, different repeat parameters must be used for each scenario. Maximal consistency between scenarios is maintained by choosing orbits with smallest-possible variations between repeat cycles (26 to 29 days). The ISD is realized by optimally choosing the mean anomaly for Satellite B. The deviations between the actual ISD and the requirement of 100, 150, 200 and 250 km then constitute some decimetres at maximum and are therefore negligibly small.

Table 56-1: Orbit parameters

ISD [km]	Sat ID	Altitude [km]	Inclination [°]	Rev./nodal day	Ascending node [°]	Mean anomaly difference [°]
	SatA	351.503	89	407/26	0	-
100						0.851
150	SatB	351.503	89	407/26	0	1.277
200						1.703
250						2.129
	SatA	401.504	89	418/27	0	-
100						0.845
150	SatB	401.504	89	418/27	0	1.268
200						1.690
250						2.113
	SatA	452.074	89	444/29	0	-
100						0.839
150	SatB	452.074	89	444/29	0	1.258
200						1.678

						2.097
250						
	SatA	500.877	89	409/27	0	-
100						0.833
150						1.249
200	SatB	500.877	89	409/27	0	1.666
250						2.082

As specified in the SOW, only the two most dominant noise contributors are considered – the ACC and the LRI. For the accelerometer we differentiate between the NGGM performance according to

$$d_{acc(XZ)} = 2 \cdot 10^{-11} \sqrt{\left(\frac{10^{-3}Hz}{f}\right)^4 \bigg/ \left(\left(\frac{10^{-5}Hz}{f}\right)^4 + 1\right) + 1 + \left(\frac{f}{10^{-1}Hz}\right)^4} \frac{m}{s^2\sqrt{Hz}} \quad [1]$$

and the GRACE-I performance according to

$$d_{acc(XZ)} = 1 \cdot 10^{-10} \sqrt{1 + \frac{0.005\ Hz}{f}} \frac{m}{s^2\sqrt{Hz}} \quad [2]$$

For the simulations at hand only the accelerometer's performance in X-direction (along-track) is of relevance. Although the Y-axis (cross-track) features a worse performance by ca. one order of magnitude throughout all frequency bands (in both ACC noise scenarios), its contribution to the LOS projection is negligible as has been shown in other studies (e.g. Abrykosov et al., 2019 [RD-1]).

For the LRI noise we assume the performance empirically derived from GRACE-FO data according to

$$d_{lri} = (2\pi f)^2 \cdot 1.5 \cdot 10^{-9} \sqrt{\left(\left(\frac{0.028\ Hz}{f}\right)^3 + 1\right) \cdot \frac{\left(\frac{0.02\ Hz}{f}\right)}{\left(\left(\frac{0.00115\ Hz}{f}\right)^4 + 1\right)}} \frac{m}{s^2\sqrt{Hz}} \quad [3]$$

In addtion, we employ an additional LRI noise scenario which has been used in previous NGGM studies (e.g. Iran Pour et al., 2015 [RD-2], Pail et al., 2019 [RD-5]) according to

$$d_{lri} = (2\pi f)^2 \cdot 2 \cdot 10^{-8} \sqrt{\left(\frac{10^{-2}Hz}{f}\right)^2 + 1} \frac{m}{s^2\sqrt{Hz}} \quad [4]$$

The accelerometer and LRI noise ASDs are graphically summarized in Figure 56-1.
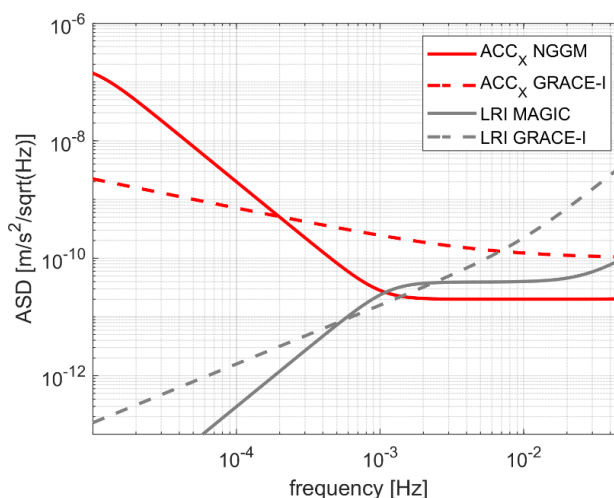
Figure 56-1: Instrument noise ASD

Since no temporal variations of the Earth's gravity field are taken into account (which corresponds to a perfect OT and AO de-aliasing in GRACE/GRACE-FO data processing), the simulation results are evaluated in terms of formal errors. The overall retrieval period is set to 30 days and the parameter estimation is carried out up to d/o 100.

57 RESULTS

The results are presented in Figure 57-1and Figure 57-2 in terms of degree RMS of formal errors.

It can be stated that the lowest orbit altitude obviously allows for the overall best retrieval performance. While the retrieval error rises with increasing SH degree in all cases, the increase is significantly more rapid the higher the chosen altitude. While the retrieval error is near-identical in the low-degree spectrum for all investigated orbital altitude scenarios (when comparing identical ISDs and instruments), the difference between h=350 km and h=500 km already constitutes a factor of 2 at n=30 and nearly one order of magnitude at n=100.

Further, it is evident that variations within the ISD result in a near-constant scaling of the retrieval error throughout the entire spectrum, which seems to be independent of the underlying orbital altitude. When all other parameters remain unchanged, the ISD of 250 km results in a retrieval performance improvement of 60% in the low degrees (which then decreases to around 50% at n=100) compared to an ISD of 100 km. In this way, the altitude-dependent increase of the retrieval error for h=500 km can be compensated up to n=38 (compared to h=350, ISD=100km, identical noise), resp. n=59 (compared to h=400, ISD=100 km, identical noise) when an ISD of 250 km is assumed.

The improved NGGM-type ACC noise performance also allows one to compensate for the increase of the altitude-related retrieval error. It can be established that a GRACE-type mission which employs an NGGM-type ACC (as well as any of the two studied LRIs) flying on 500 km altitude features a lower retrieval error up to n=57 (n=85) than a mission which uses a GRACE-type ACC flying on 350 km (400 km) altitude.

NGGM/MAGIC – Science Support Study During Phase A	*Final Report*	
	Doc. Nr:	MAGIC_FR
	Issue:	1.0
	Date:	15.11.2022
	Page:	457 of 466

It can further be asserted that the LRI's contribution to the overall retrieval error is fully superimposed by the GRACE-type ACC. The improved noise level of the NGGM ACC, on the other hand, allows one to clearly distinguish the LRI's contribution to the overall retrieval error (cf. Figure 57-2). Here, a retrieval error increase of up to 80% can be established in the low degree spectrum, which then decreases to 45% at n=100 in comparison to an NGGM-ACC-only scenario. The overall difference in performance when using the MAGIC and the ADDCON LRI is comparatively small, but it seems to correlate with the ISD – the variation between these two scenarios constitutes 9% at n=100 in case of ISD=100 km and 16% in case of ISD=250 km.

Figure 57-1: Formal error degree RMS for gravity solutions based on different combinations of ACC and LRI noise for varying orbit altitudes and ISD
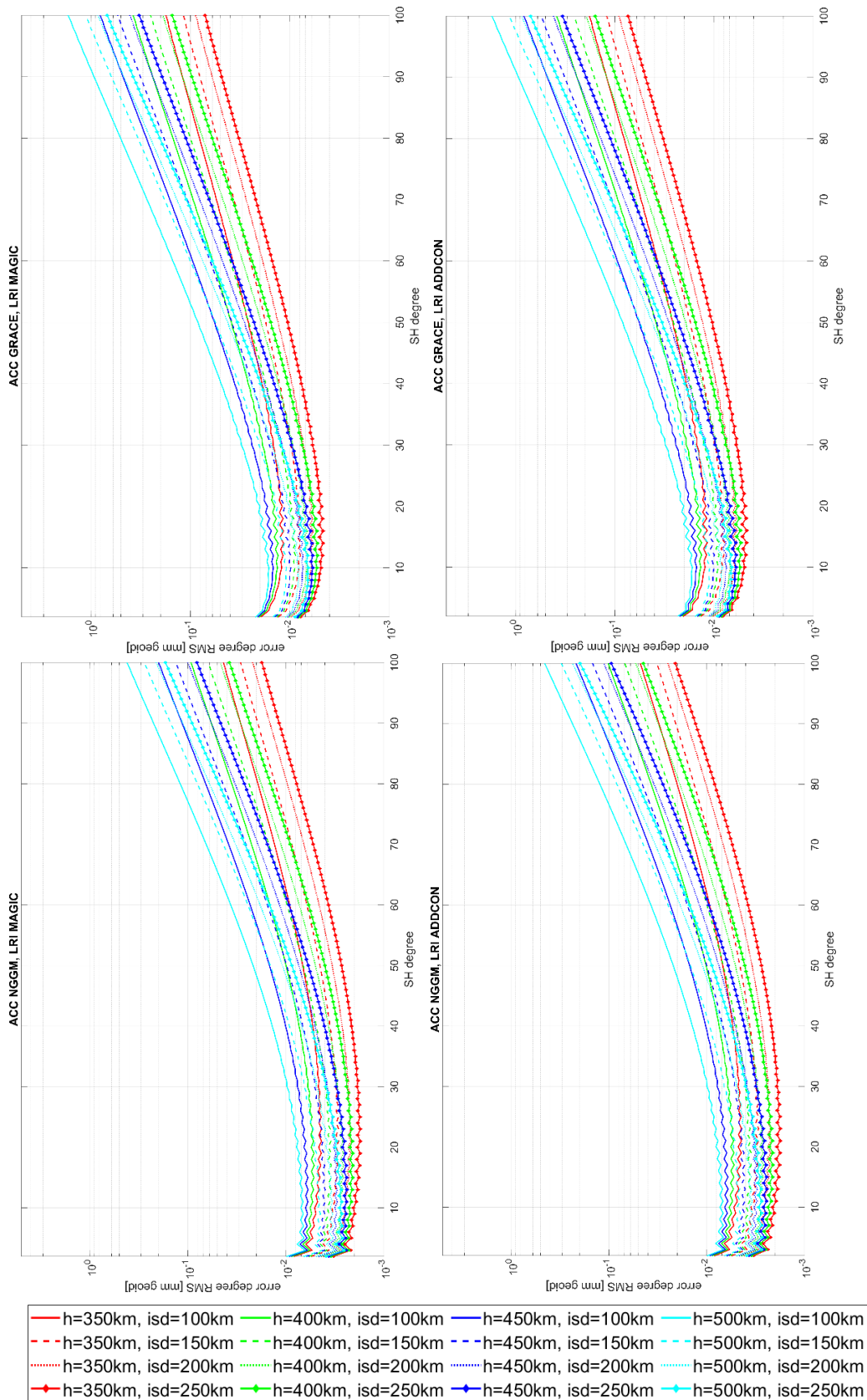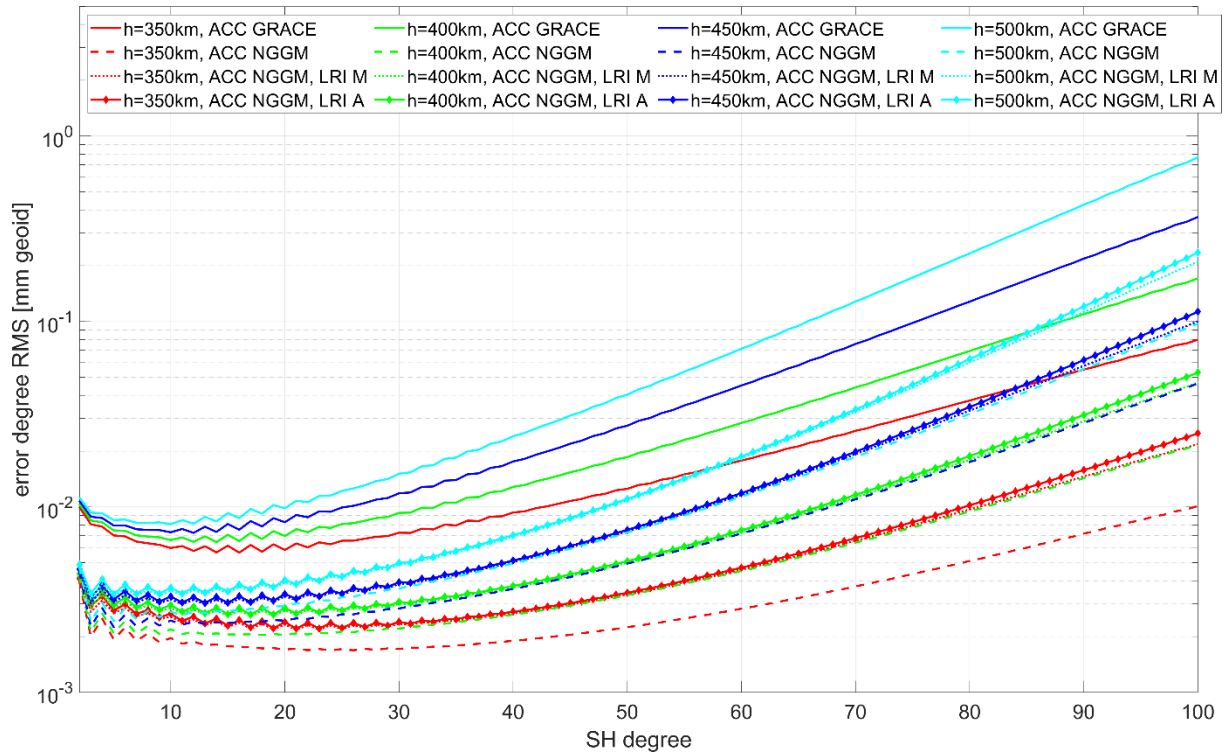
Figure 57-2: Formal error degree RMS for gravity solutions based on different combinations of ACC and LRI noise for varying orbit altitudes and an ISD of 200 km

58 APPLICABLE DOCUMENTS, REFERENCE DOCUMENTS, AND PUBLICATIONS TO PART 9

58.1 APPLICABLE DOCUMENTS

[AD-1] Mission Requirements Document, Next Generation Gravity Mission as a Mass-change And Geosciences International Constellation (MAGIC) - A joint ESA/NASA double-pair mission based on NASA's MCDO and ESA's NGGM studies (2020). ESA-EOPSM-FMCC-MRD-3785

[AD-2] Scientific Readiness Levels (SRL) Handbook, Issue 1, Revision 0, 05-08-2015

[AD-3] Statement of Work - ESA Express Procurement - EXPRO NGGM/MAGIC science support study during Phase A, Issue 1, Revision 0, 18/01/2021 Ref ESA-EOPSM-FUTM-SOW-3813

58.2 REFERENCE DOCUMENTS

[RD-1] Abrykosov P, Pail R, Gruber T, Zahzam N, Bresson A, Hardy E, Christophe B, Bidel Y, Carraz O, Siemes C (2019): Impact of a novel hybrid accelerometer on satellite gravimetry performance. Advances in Space Research 63 (2019), 325-3248. https://doi.org/10.1016/j.asr.2019.01.034.

[RD-2] Iran Pour S, Sneeuw N, Daras I, Pail R, Murböck M, Gruber T, Tonetti S, Cornara S, Weigelt M, Van Dam T, Visser P, Teixeira da Encarnação J (2015): Assessment of satellite constellations for monitoring the variations in earth gravity field. SC4MGV, ESA/ESTEC Constract No. AO/1-7317/12/NL/AF, Final Report.

[RD-3] Murböck M, Pail R, Daras I, Gruber T (2014): Optimal orbits for temporal gravity recovery regarding temporal aliasing. Journal of Geodesy 88 (2), 113-126. https://doi.org/10.1007/s00190-013-0671-y.

[RD-4] Murböck M (2015): Virtual Constellations of Next Generation Gravity Missions. Deutsche Geodästische Komission der Bayerischen Akademie der Wissenschaften, Reihe C, Dissertationen, Heft 750, Verlag der Bayerischen Akademie der Wissenschaften, ISBN(Print) 978-3-7696-5162-1, ISSN 0065-5325, 2016.

[RD-5] Pail et al. (2019): Additional Constellation & Scientific Analysis of the Next Generation Gravity Mission Concept (ADDCON), Final Report, ESA Contract No 4000118480/16/NL/FF/gp.

[RD-6] Siemes C (2008): Digital Filtering Algorithms for Decorrelation within Large Least Square Problems. Bonn: Rheinische Friedrich-Wilhelms-Universität, Hohe Landwirtschaftliche Fakultät, Dissertation.

PART 10:

AD-HOC REQUEST:
EMBARKING 3 ACCELEROMETERS ON EACH SATELLITE

59 EMBARKING 3 ACCELEROMETERS ON EACH SATELLITE

A proposed concept for NGGM satellites is to embark 3 accelerometers aligned with the Y-axis (predominantly cross-track), with one accelerometer in the centre-or-mass and the other two off-centred by 25 cm (Figure 59-1). For gravity field retrieval, such a configuration might lead to noise reduction: √3 in case of uncorrelated noise. Moreover, it might be interesting to investigate the benefit of one gradiometer arm for gravity field retrieval and possible enhance attitude reconstruction, made possible by differential accelerometery.
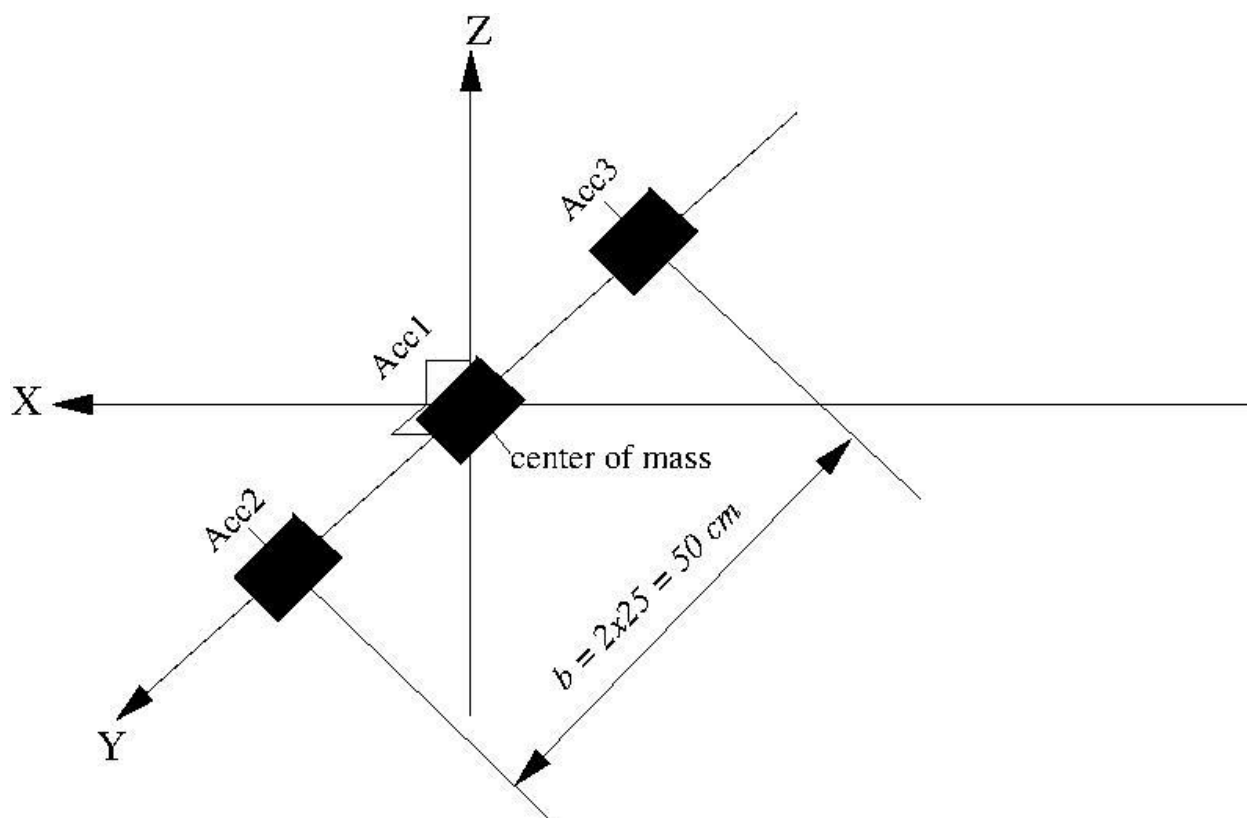
Figure 59-1 Accelerometer configuration

Regarding the calibration of accelerometers, this configuration of 3 accelerometers allows for additional possibilities for calibration: (1) comparison with star tracker derived angular accelerations [RD-16], (2) cross-verification by Precise Orbit Determination [RD-15], and (3) direct comparison between the accelerometer observations.

A possible point of attention concerns the sensitivity of the 3 axes of each accelerometer: will all axes have the same sensitivity, or will the accelerometers have two sensitive and one less sensitive axis, such as with GRACE and GOCE [RD-15][RD-16]?

Based on GOCE heritage, an assessment of the proposed 3-accelerometer configuration can be made. The baseline for the GOCE accelerometers aligned with the Y axis is 50 cm, equal to the proposed 2x25 cm for the off-centred NGGM accelerometers. The accelerometer in the centre-of-mass has high equivalence with common-mode accelerometery (at least in terms of signals, apart from of course rotational and gravity gradient terms).

Concerning calculations, an assessment can thus be based on e.g. the GOCE results/heritage. For the method based on star trackers [RD-16], it has to be known what is the setup of star trackers on the NGGM satellites (how many, bore sights) and what is their quality (observation noise/errors). For the calibration by Precise Orbit Determination [RD-15], it can be argued that similar results will be obtained for all three accelerometers, thus the calibration performance for the off-centred accelerometers is anticipated to be comparable to the one in the centre-of-mass if making use of POD (and thus results in the framework of WP710 [RD-18] are applicable, see also Table 59-1 for selected results). The latter is however based on the assumption that a sufficiently accurate attitude reconstruction can be done using the NGGM star tracker complement. This is because the individual, off-centred accelerometers have to be reduced by rotational, and also gravity gradient, terms. For GOCE, the rotational terms were derived from an optimal fusion product of star trackers and differential accelerometery. For NGGM, it has to be assessed how well this can be done with one instead of three gradiometer arms. It can be argued that the gravity gradient correction can be considered almost as "error-free" considering the small dimension of the off-centring (i.e. 25 cm).

Concerning the use of star tracker observations, an end-to-end simulation capability can be derived from the GOCE processing capability, but is not feasible in the framework of this study. For GOCE, rotation terms were derived from a fusion of two star trackers with different bore sights [RD-16]. The associated calibration method allows for the estimation of scale factors. Concerning accelerometer biases, a singularity arises for each axis (i.e. only differential accelerometer biases can be estimated).

Table 59-1 Daily accelerometer calibration retrieval errors (scenario 3d_H) when using GNSS observations. The results hold for 1 January 2002 for different scenarios: Drag-Free Flight (DFC), Manoeuvre Scheme 3 (MS3) and commissioning phase during solar minimum (CPMIN). Results are taken from [RD-18].

Satellite Scenario	Bias (nm/s^2)			Scale factor		
	X	Y	Z	X	Y	Z
1/DFC	-0,05808	0,98910	2,41335	-0,01662	8,47424	0,03962
3/DFC	-0,01439	0,52179	-1,49269	0,10880	5,20995	0,07742
1/MS3	-0,04015	0,15754	2,20799	0,00034	0,00221	0,01171
3/MS3	0,05862	-1,89265	0,14355	0,00122	0,03605	0,03664
1/CPMIN	0,12450	-0,50725	-0,11752	0,00345	-0,02382	-0,04006
3/CPMIN	-0,41038	-1,30154	-0,41598	-0,00499	-0,03289	0,06903

For GOCE, it was especially important to have a very accurate calibration of the scale factor of the accelerometers [RD-19]. Selected GOCE results for both common-mode accelerometery and individual accelerometers are displayed for the POD method in Figure 59-2 and for the star tracker method in Figure 59-3.

It can be observed that the scale factor for the X axis (predominantly along-track) can be retrieved with a consistency with the official GOCE calibrated accelerometer product much better than 0.001 for both common-mode accelerometery and the individual accelerometers when using the POD method. For the Z axis, the consistency is typically better than 0.01. For the Y axis, a worse consistency of around 0.03-0.04 is obtained, probably caused by uncertainties in the force modelling.

Table 5 Scale factors estimated by dynamically fitting the PSO kinematic co-ordinates for the selected 1213 daily arcs

	CM	1	2	3	4	5	6
2009, 62 daily arcs							
X axis	1.00009	1.00011	1.00015	1.00007	1.00009	1.00013	0.99998
Y axis	1.02669	1.02586	1.02724	1.02893	1.03036	1.02789	1.02904
Z axis	0.97686	0.97842	0.98030	0.97435	0.97276	0.97199	0.97778
2010, 243 daily arcs							
X axis	1.00012	1.00017	1.00019	0.99999	1.00009	1.00015	1.00000
Y axis	1.02653	1.02700	1.02596	1.02679	1.02765	1.02711	1.02718
Z axis	0.99365	0.99163	0.98475	0.97882	0.97868	0.99375	0.98197
2011, 323 daily arcs							
X axis	0.99997	1.00003	1.00006	0.99980	0.99992	1.00001	0.99985
Y axis	1.03619	1.03781	1.03595	1.03704	1.03495	1.03688	1.03743
Z axis	0.97388	0.97606	0.97616	0.97751	0.96843	0.96982	0.97547
2012, 328 daily arcs							
X axis	0.99987	0.99979	0.99994	1.00005	0.99996	0.99999	0.99988
Y axis	1.03567	1.03842	1.03501	1.03713	1.03476	1.03725	1.03617
Z axis	0.98430	0.98497	0.98602	0.98878	0.98125	0.98131	0.98799
2013, 257 daily arcs							
X axis	0.99994	0.99997	1.00003	0.99986	0.99993	1.00000	0.99986
Y axis	1.02796	1.02942	1.02751	1.02873	1.02743	1.02845	1.02759
Z axis	1.00110	1.00137	1.00154	1.00159	1.00010	1.00053	1.00081
Full mission period: 1 November 2009–20 October 2013, 1213 daily arcs							
X axis	0.99994	0.99992	1.00001	0.99997	0.99997	1.00002	0.99989
Y axis	1.03087	1.03225	1.03048	1.03186	1.03078	1.03171	1.03141
Z axis	0.99557	0.99590	0.99603	0.99612	0.99323	0.99438	0.99557

Figure 59-2 GOCE heritage: calibration of individual accelerometers and common mode by POD [RD-15]

The method based on attitude quaternions observations typically results in a consistency better than 0.01 for all axes for GOCE (Figure 59-3). As mentioned above, an open issue concerns the quality with which the attitude reconstruction for NGGM can be done based on a complement of star trackers and differential accelerations from the 3-accelerometer configuration.

Table 1 Estimated mean and RMS-about-mean values for the accelerometer bias and drift values, relative to accelerometer 1, and the scale factors obtained from the star tracker observations

	nr	X-axis	nr	Y-axis	nr	Z-axis
Bias (nm/s^2)						
Acc. 2	248	-328.94 ± 3.04	254	12939.45 ± 226.07	254	-21267.65 ± 746.46
Acc. 3	246	-301.41 ± 2.49	254	-9526.68 ± 364.70	251	-89.47 ± 5.16
Acc. 4	254	-279.24 ± 3.24	254	3312.12 ± 1303.77	254	15.34 ± 1.76
Acc. 5	248	-321.47 ± 1.80	254	13479.95 ± 294.43	254	-10121.48 ± 635.26
Acc. 6	246	-285.79 ± 2.57	254	9438.67 ± 180.87	245	24.46 ± 3.82
Drift (nm/s^2/day)						
Acc. 2	253	-0.038 ± 0.324	247	-0.224 ± 0.389	252	-2.139 ± 0.522
Acc. 3	254	0.007 ± 0.273	248	0.780 ± 0.551	253	0.000 ± 0.267
Acc. 4	245	0.017 ± 0.020	253	3.442 ± 1.003	253	-0.036 ± 0.534
Acc. 5	253	0.059 ± 0.321	249	-0.573 ± 0.469	254	3.114 ± 2.726
Acc. 6	253	0.024 ± 0.270	249	-0.195 ± 0.492	252	-0.018 ± 0.263
Scale factor						
Acc. 1	230	1.000 ± 0.001	254	0.996 ± 0.016	246	1.000 ± 0.004
Acc. 2	241	0.993 ± 0.003	254	0.996 ± 0.017	251	1.003 ± 0.004
Acc. 3	252	0.996 ± 0.015	254	0.995 ± 0.016	251	0.998 ± 0.005
Acc. 4	227	0.999 ± 0.001	254	0.996 ± 0.017	248	0.997 ± 0.007
Acc. 5	254	0.991 ± 0.003	254	0.996 ± 0.017	246	0.999 ± 0.003
Acc. 6	253	0.994 ± 0.015	254	0.997 ± 0.017	244	0.999 ± 0.004

Use was made of 254 daily arcs, where a 3σ editing was applied (number of used arcs indicated by nr)

Figure 59-3 GOCE heritage: calibration of accelerometers by attitude quaternions [RD-16]

60 APPLICABLE DOCUMENTS, REFERENCE DOCUMENTS, AND PUBLICATIONS TO PART 10

60.1 APPLICABLE DOCUMENTS

[AD-2]   NGGM/MAGIC – SCIENCE SUPPORT STUDY DURING PHASE A – EXPRO, RFP Proposal No. TUM/2021-MAGIC-Science, ESA RFP/3-17035/20/NL/FF/tfd, 16-03-2021

60.2 REFERENCE DOCUMENTS

[RD-14]   Statement of Work, ESA Express Procurement EXPRO, NGGM/MAGIC science support study during Phase A, Ref ESA-EOPSM-FUTM-SOW-3813, Date 18/01/2021

[RD-15]   Visser, P.N.A.M., and J.A.A. van den IJssel (2016b), Calibration and validation of individual GOCE accelerometers by precise orbit determination, J. Geod., 90(1), 1–13, doi: 10.1007/s00190–015–0850–0

[RD-16]   Visser, P.N.A.M. (2018), Using the GOCE star trackers for validating the calibration of its accelerometers, J. Geod., 92 (8), 833–846, DOI 10.1007/s00190–017–1097–8

[RD-17]   Pieter Visser, Next Generation Gravity Mission as a Mass-change And Geosciences International Constellation (MAGIC), Technical Note WPs 120 & 410, Generation of orbit parameters and analysis of ground tracks for baseline and alternative constellations, Issue 2.0, 20 November 2021

[RD-18]   Pieter Visser, Next Generation Gravity Mission as a Mass-change And Geosciences International Constellation (MAGIC), Technical Note WP 710, Calibration of accelerometers, Issue 2.0, 22 June 2022

[RD-19]   Johannes Bouman, Sophie Fiorot, Martin Fuchs, Thomas Gruber, Ernst Schrama, Christian Tscherning, Martin Veicherts, and Pieter Visser (2011), GOCE gravitational gradients along the orbit, J. Geod., 85, 791—805, doi: 10.1007/s00190-011-0464-0